

China's party line on the pandemic:
It didn't start here p. 805

Stabilizing high-pressure
nanoparticles pp. 814 & 870

Vaccine-induced T cells
offer protection p. 821

Science

\$15
19 AUGUST 2022
science.org

 AAAS

CATCHING THE LIGHT

Faster adaptation to
changing brightness raises
soy yield p. 851



PRIZE FOR IMMUNOLOGY

REWARDING HIGH-RISK RESEARCH.
SUPPORTING EARLY-CAREER SCIENTISTS.
HELPING TO FIND CURES FASTER.
APPLY TODAY

**Now accepting applications for the Michelson
Philanthropies & Science Prize for Immunology.**

The Michelson Philanthropies and Science Prize for Immunology focuses on transformative research in human immunology, with trans-disease applications to accelerate vaccine and immunotherapeutic discovery. This international prize supports investigators 35 and younger, who apply their expertise to research that has a lasting impact on vaccine development and immunotherapy. It is open to researchers from a wide range of disciplines including computer science, artificial intelligence/machine learning, protein engineering, nanotechnology, genomics, parasitology and tropical medicine, neurodegenerative diseases, and gene editing.

Application deadline: Oct. 1, 2022.

For more information visit:
www.michelsonmedicalresearch.org

#MichelsonPrizes



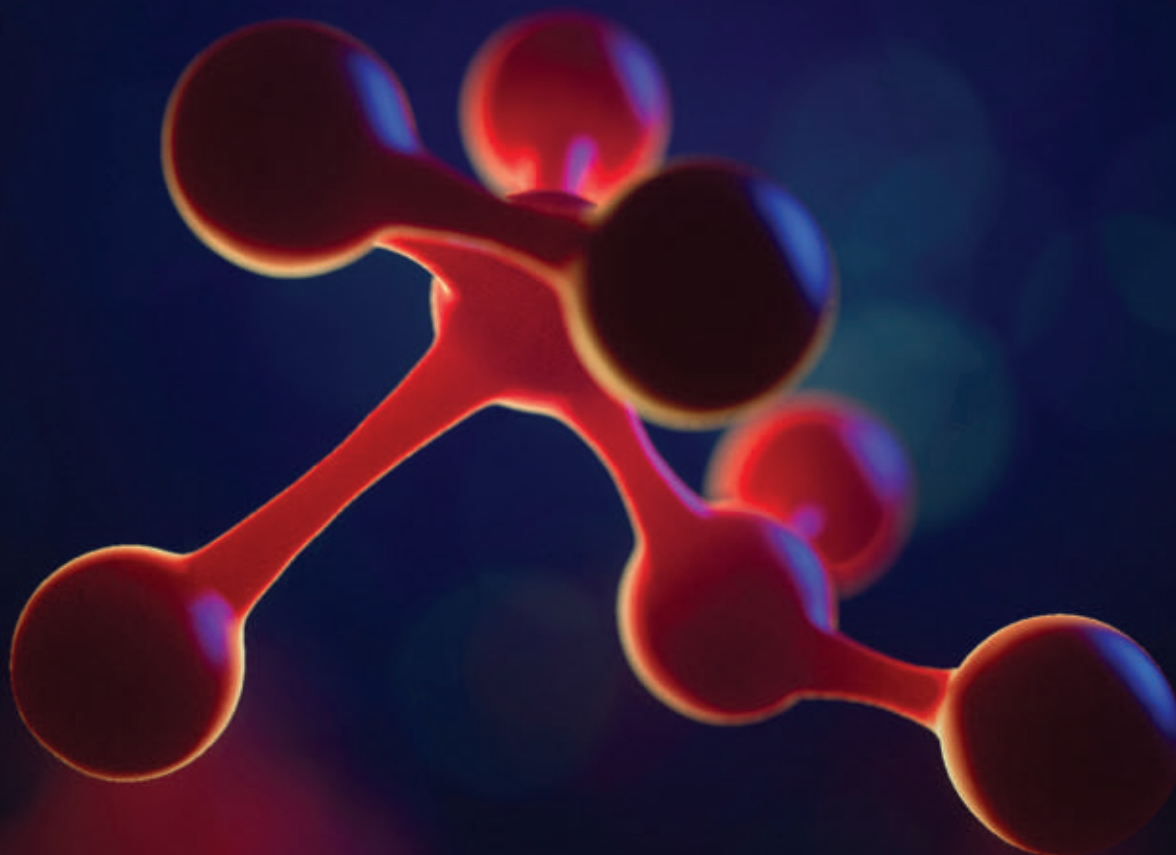
"The Michelson Philanthropies & Science Prize for Immunology will greatly impact my future work. As I am just starting my scientific career, it will illuminate my work, spark interest and support me to continue my research in this field."

Paul Bastard, MD, PhD,
Laboratory of Human Genetics
of Infectious Diseases, Imagine
Institute (INSERM, University of
Paris), Paris, France; and The
Rockefeller University, New York.

Dr. Bastard received the inaugural
Grand Prize for his essay: "Why
do people die from COVID-19:
Autoantibodies neutralizing type
I interferons increase with age."

GRAND PRIZE:
\$30,000

FINALIST PRIZE:
\$10,000



Publish your research in the *Science* family of journals

The *Science* family of journals (*Science*, *Science Advances*, *Science Immunology*, *Science Robotics*, *Science Signaling*, and *Science Translational Medicine*) are among the most highly-regarded journals in the world for quality and selectivity. Our peer-reviewed journals are committed to publishing cutting-edge research, incisive scientific commentary, and insights on what's important to the scientific world at the highest standards.

Submit your research today!

Learn more at **[Science.org/journals](https://www.science.org/journals)**



Dr. Moon Jeong Park (second from right) discusses her research with students in her lab.

The need for basic scientific research in an applied age

Since opening its doors in 1986, the Pohang University of Science and Technology in South Korea, commonly called POSTECH, has become a hub for groundbreaking research. In 2019, POSTECH ranked highest in Asia on Reuters' list of the World's Most Innovative Universities,¹ outflanking historic institutions such as the United Kingdom's Cambridge University, Caltech in the United States, and Tsinghua University in China.

The university's commitment to the growth of high-quality research is demonstrated by its investment in basic science research, which necessarily underpins and advances the organization's well-established applied science work.

For example, Moon Jeong Park leads a team within the Department of Chemistry that focuses on elucidating the interplay of transport and morphology in nanostructured charged polymer materials; the team's work is based on a fundamental understanding of molecular interactions.

Her team is currently working on developing new ion-containing polymeric materials with tailored molecular interactions that are more predictable, efficient, and sustainable for energy storage and transport. Advances in this area could include the development of artificial muscles, electric cars, and wearable devices.

Passion drives basic research at POSTECH

Thirteen years ago, Park moved from the University of California, Berkeley, back to South Korea. She recalls some challenges convincing colleagues in the United States who thought her work on such materials would not be practical

because of their low ionic conductivity and limited performance at high current densities. However, POSTECH supported her research, and over the past decade, her work has proved to be highly relevant to the field of battery technology. Scientific research into batteries has seen a surge in activity and investment due in large part to the growing demand for electric vehicles.

One major drawback of the most commonly used vehicle batteries is that they contain ions that are moved by a potentially flammable liquid electrolyte. In order to create the next generation of energy storage devices, Park's team has worked on developing highly efficient solid-state polymer electrolytes to replace the more unstable compounds.

"Now, it is becoming a common goal to try to obtain high conductivity and high transference numbers from solid-state polymer electrolytes. It is my belief that eventually this kind of fundamental research will drive and direct research in this field," says Park.

Her team recently developed a polymer electrolyte with a novel nanostructure that demonstrated a significant enhancement in ionic conductivity compared to previous versions. "This provides a potential route to accelerate the commercialization of safer, all-solid-state batteries," she says.

Tools that enable basic scientific research to flourish

Park appreciates the challenges posed to early-career researchers who conduct fundamental research. As opposed to applied research, basic research can appear frustratingly time-consuming. The key to motivating her team is to

¹<https://www.reuters.com/innovative-universities-2019>.

ensure that “fundamentals learned in school, and the ability to synthesize and analyze your own materials, will form a solid foundation for growing as a leader as you transition to becoming an independent researcher,” she says.

She speaks from personal experience. The reason Park was able to gain international recognition for her work at a such a young age was due to the level of support offered by the university, she says. “POSTECH encourages participation in international conferences and journal activities. Also, there are no major difficulties in purchasing equipment and setting up a lab.”

This supportive research environment leads to a highly cooperative and collaborative working style. “Even if I call for advice or support on a Saturday evening, there are staff members who are always there to help,” she says.

Small, research-focused community

For scientists whose research focus is long-term and necessarily involves steady and incremental steps, POSTECH is an ideal environment, says Young-Tae Chang.

In Chang’s lab, which is based in the Department of Chemistry, his team develops bioimaging probes for live cells. To understand complex biosystems, it is imperative to be able to discriminate between live and dead cells. Chang and his colleagues employ a diversity-oriented fluorescence library approach (DOFLA) to screen novel fluorescent molecules and have so far developed 30 cell-selective probes.

Chang started his research career at POSTECH, as one of the university’s first batch of students. After finishing his Ph.D., he moved to the United States and then to Singapore, where he spent 20 years exploring the different scientific environments in those two countries before deciding to come back to his alma mater. “I missed the small and research-focused environment of POSTECH,” he says.

His passion for his work comes from the promise of scientific discovery and its limitless possibilities for improving human health. “We have genes that generate millions of antibodies to fight any antigen. If we can correctly identify these antigens, it seems like a magic solution for any problem,” he says.

After two decades working in this field, Chang hopes to use his research to tackle issues around the aging of the human body. He hopes that his probes, which can correctly discriminate between old and young cells, will help identify novel biomarkers for the aging process.

“While the study of how our bodies age is attracting a lot of attention these days, the systematic discovery of biomarkers is far behind other fields, such as cancer research,” he says. Chang hopes that once scientists identify the molecules involved in aging, it will open the way to discovering a possible

molecular solution to slow or even reverse the process.

As a chemical biologist, Chang believes that adopting a molecular approach to human health interventions is safer than taking a gene-editing approach. “The sensor and molecular-imaging probes will provide unprecedented new tools for clinical checkups,” he says.

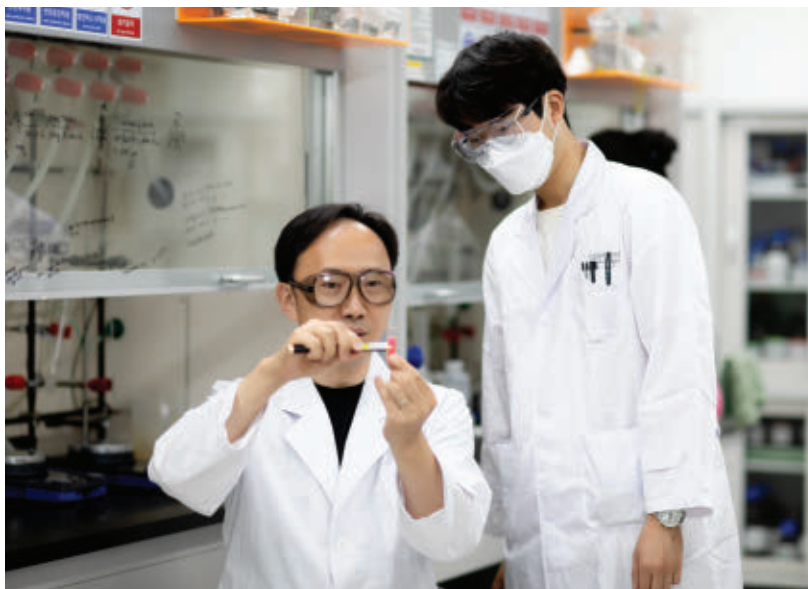
Aging-specific probes could make it possible to monitor specific molecules in our bodies and offer a guide to the early detection of problems, he adds. “The aging rate is not the same for

different organs. And the failure of a single organ will determine our lifespan, not the collapse of our entire body at once. Therefore, probes that detect age-related biomarkers may be able to guide preventative interventions as well as act as agents to reverse aging,” says Chang.

The future for basic science at POSTECH

Scientists at POSTECH are extremely optimistic about the future of fundamental research at their institution. The campus has a high concentration of top-level, motivated students and offers the right conditions to produce outstanding research, says Chang. Park adds that the superior research environment, which includes a synchrotron facility, attracts scientists from all over the country. This enables plentiful opportunities for collaboration and builds the university’s reputation as a hub for carrying out cutting-edge science.

“POSTECH was founded in the pursuit of being a world-class, research-oriented university, and I think all faculty members work hard to exemplify our founding spirit,” says Park. But it is important for people who do basic science not to get too caught up in their own research worlds, she adds. Park believes that having an open culture of collaboration creates positive feedback loops that benefit everyone’s work.



Dr. Young-Tae Chang’s (left) research team develops bioimaging probes for use in live cells.

Sponsored by

POSTECH
POHANG UNIVERSITY OF SCIENCE AND TECHNOLOGY

CONTENTS

19 AUGUST 2022
VOLUME 377 • ISSUE 6608

805

805

IN BRIEF

IN DEPTH

Batteries allowing, CubeSats will target lunar ice and more *By E. Hand*

Other methods still put the United States somewhat ahead *By J. Brainard and D. Normile*

Measures to capture carbon in soil may be less effective than hoped, scientists say
By E. Stokstad

Major physics projects and national lab infrastructure will get \$1.5 billion over 5 years *By J. Mervis and A. Cho*

Embryonic tissue samples reveal how pelvis shape—primed for bipedalism—comes to life *By M. Price*

Study implicates lack of key hormone, battle-weary immune cells, and awakened viruses

China now insists the pandemic didn't start within its borders. Its scientists are publishing a flurry of papers pointing the finger elsewhere
By J. Cohen

POLICY FORUM

Implications for nutrition, environment,
and work may be considerable
By E.-M. Meemken et al.

materials that are formed at high pressure
By W. L. Mao and Y. Lin
REPORT p. 870

Ductile inorganic semiconductors can help enable self-powered wearable electronics *By C. Hou and M. Zhu*
REPORT p. 854

The right solvent mix breaks down perfluorinated organic acids
By S. Joudan and R. J. Lundgren
RESEARCH ARTICLE p. 839

A glycoprotein is a possible biomarker of pathogenic progression for Parkinson's disease
By B. Mollenhauer and C. A. F. von Arnim
RESEARCH ARTICLE p. 833

Molecular structures provide a road map for understanding and controlling B cell receptor activation
By P. Tolar and S. K. Pierce
REPORTS pp. 875 & 880

T cell immunity may be critical for long-term protection by COVID-19 vaccines
By E. J. Wherry and D. H. Barouch

BOOKS ET AL.

823 Transforming urban environments

Resilient cities of the past hold lessons for creating adaptable communities of the future
By M. A. Palmer

824 The myth of meritocracy in scientific institutions

Inaccurate ideas about objectivity and merit perpetuate biases and inequality in academia
By L. Son Hing

LETTERS

826 Editorial Retraction

By H. H. Thorp

826 The Amur tiger needs transborder protection

By L. Zheng et al.

826 Genomic research data and the justice system

By D. Greenbaum and M. Gerstein

827 Response

By D. J. H. Mathews and N. Ram

827 Technical Comment abstracts

RESEARCH

IN BRIEF

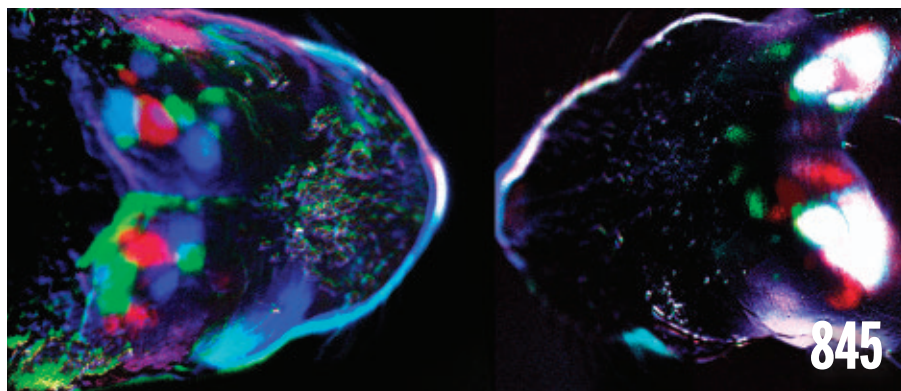
829 From *Science* and other journals

RESEARCH ARTICLES

832 Neurogenetics

Functional regulatory variants implicate distinct transcriptional networks in dementia
Y. A. Cooper et al.

RESEARCH ARTICLE SUMMARY; FOR FULL TEXT:
DX.DOI.ORG/10.1126/SCIENCE.ABI8654



Spontaneous brain activity in perinatal mouse refines the brain's visual and somatosensory circuits.

833 Parkinson's disease

GNPMB confers risk for Parkinson's disease through interaction with α -synuclein
M. E. Diaz-Ortiz et al.

RESEARCH ARTICLE SUMMARY; FOR FULL TEXT:
DX.DOI.ORG/10.1126/SCIENCE.ABK0637

PERSPECTIVE p. 818

834 Evolutionary ecology

Metabolic scaling is the product of life-history optimization
C. R. White et al.

839 Defluorination

Low-temperature mineralization of perfluorocarboxylic acids
B. Trang et al.

PERSPECTIVE p. 816

845 Neurodevelopment

Input-dependent segregation of visual and somatosensory circuits in the mouse superior colliculus
T. Guzmán-Vivancos et al.

851 Plant science

Soybean photosynthesis and crop yield are improved by accelerating recovery from photoprotection
A. P. De Souza et al.

REPORTS

854 Thermoelectrics

Flexible thermoelectrics based on ductile semiconductors
Q. Yang et al.

PERSPECTIVE p. 815

859 Flexible electronics

Chip-less wireless electronic skins by remote epitaxial freestanding compound semiconductors
Y. Kim et al.

865 Metalloenzymes

Structures of the nitrogenase complex prepared under catalytic turnover conditions
H. L. Rutledge et al.

870 Nanomaterials

Nanocrystals with metastable high-pressure phases under ambient conditions
T. Xiao et al.

PERSPECTIVE p. 814

Immunology

875 Cryo-EM structure of the human IgM B cell receptor
Q. Su et al.

880 Cryo-EM structures of two human B cell receptor isotypes
X. Ma et al.

PERSPECTIVE p. 819

885 Quantum physics

Tweezer-programmable 2D quantum walks in a Hubbard-regime lattice
A. W. Young et al.

890 Coronavirus

Omicron spike function and neutralizing activity elicited by a comprehensive panel of vaccines
J. E. Bowen et al.



DEPARTMENTS

793 Editorial

Rethinking the retraction process
By H. H. Thorp

898 Working Life

My life as a photon
By K. Rasmussen

ON THE COVER

Photograph of developing soybean pods. Leaves protect themselves in full sunlight by dissipating excess energy as heat. On shading, this dissipative process continues for many minutes, lowering photosynthesis. For the first time in a food crop,



multigenic manipulation has sped relaxation of this dissipative process on shading, raising photosynthesis and increasing field soybean yield by up to 30%. See page 851.
Photo: Igor Stevanovic/
Alamy Stock Photo

Science Staff 792
Science Careers 895

SCIENCE (ISSN 0036-8075) is published weekly on Friday, except last week in December, by the American Association for the Advancement of Science, 1200 New York Avenue, NW, Washington, DC 20005. Periodicals mail postage (publication No. 484460) paid at Washington, DC, and additional mailing offices. Copyright © 2022 by the American Association for the Advancement of Science. The title SCIENCE is a registered trademark of the AAAS. Domestic individual membership, including subscription (12 months): \$165 (\$74 allocated to subscription). Domestic institutional subscription (51 issues): \$2212; Foreign postage extra: Air assist delivery: \$98. First class, airmail, student, and emeritus rates on request. Canadian rates with GST available upon request. GST #125488122. Publications Mail Agreement Number 1069624. Printed in the U.S.A.

Change of address: Allow 4 weeks, giving old and new addresses and 8-digit account number. Postmaster: Send change of address to AAAS, P.O. Box 96178, Washington, DC 20090-6178. Single-copy sales: \$15 each plus shipping and handling available from backissues.science.org; bulk rate on request. Authorization to reproduce material for internal or personal use under circumstances not falling within the fair use provisions of the Copyright Act can be obtained through the Copyright Clearance Center (CCC), www.copyright.com. The identification code for Science is 0036-8075. Science is indexed in the Reader's Guide to Periodical Literature and in several specialized indexes.

Editor-in-Chief Holden Thorp, hthorp@aaas.org

Executive Editor Valda Vinson

Editor, Research Jake S. Yeston Editor, Insights Lisa D. Chong Managing Editor Lauren Kmec

DEPUTY EDITORS Stella M. Hurlty (UK), Phillip D. Szurmi, Sacha Vignieri SR. EDITORS Gemma Alderton (UK), Caroline Ash (UK), Brent Grocholski, Pamela J. Hines, Di Jiang, Priscilla N. Kelly, Marc S. Lavine (Canada), Mattia Maroso, Yevgeniya Nusinovich, Ian S. Osborne (UK), L. Bryan Ray, Seth Thomas Scanlon (UK), H. Jesse Smith, Keith T. Smith (UK), Jelena Stajic, Peter Stern (UK), Valerie B. Thompson, Brad Wible, Yuen Yiu ASSOCIATE EDITORS Michael A. Funk, Bianca Lopez, Corinne Simonti, Yury V. Suleymanov, Ekeoma Uzogara LETTERS EDITOR Jennifer Sills LEAD CONTENT PRODUCTION EDITORS Chris Filiatreau, Harry Jach SR. CONTENT PRODUCTION EDITOR Amelia Beyna CONTENT PRODUCTION EDITORS Jeffrey E. Cook, Julia Haber-Katris, Nida Masulis, Abigail Shashikanth, Suzanne M. White SR. EDITORIAL MANAGERS Carolyn Kyle, Beverly Shields SR. PROGRAM ASSOCIATE Maryrose Madrid EDITORIAL ASSOCIATE Joi S. Granger SR. EDITORIAL COORDINATORS Aneera Dobbins, Jeffrey Hearn, Lisa Johnson, Shannon McMahon, Jerry Richardson, Hilary Stewart (UK), Alice Whaley (UK), Anita Wynn EDITORIAL COORDINATORS Maura Byrne, Alexander Kief, Ronnel Navas, Isabel Schnaidt, Qiyam Stewart, Brian White RESEARCH & DATA ANALYST Jessica L. Slater ASI DIRECTOR, OPERATIONS Janet Clements (UK) ASI SR. OFFICE ADMINISTRATOR Jessica Waldo (UK)

News Editor Tim Appenzeller

NEWS MANAGING EDITOR John Travis INTERNATIONAL EDITOR Martin Enserink DEPUTY NEWS EDITORS Shradha Chakradhar, Elizabeth Culotta, Lila Guterman, David Grimm, Eric Hand (Europe), David Malakoff SR. CORRESPONDENTS Daniel Clery (UK), Jon Cohen, Jeffrey Mervis, Elizabeth Pennisi ASSOCIATE EDITORS Jeffrey Brainard, Kelly Servick NEWS REPORTERS Adrian Cho, Jennifer Couzin-Frankel, Jocelyn Kaiser, Rodrigo Pérez Ortega (Mexico City), Robert F. Service, Erik Stokstad, Paul Voosen, Meredith Wadman INTERNS Zack Savitsky, Viviana Flores, Katherine Irving CONTRIBUTING CORRESPONDENTS Warren Cornwall, Andrew Curry (Berlin), Ann Gibbons, Sam Kean, Eli Kintisch, Kai Kupferschmidt (Berlin), Andrew Lawler, Mitch Leslie, Eliot Marshall, Virginia Morell, Dennis Normile (Tokyo), Elisabeth Pain (Careers), Chris Pillar, Gabriel Popkin, Michael Price, Joshua Sokol, Richard Stone, Emily Underwood, Gretchen Vogel (Berlin), Lizzie Wade (Mexico City) CAREERS Rachel Bernstein (Editor), Katie Langin (Associate Editor) COPY EDITORS Julia Cole (Senior Copy Editor), Morgan Everett, Cyra Master (Copy Chief) ADMINISTRATIVE SUPPORT Meagan Weiland

Creative Director Beth Rakouskas

DESIGN MANAGING EDITOR Marcy Atarod GRAPHICS MANAGING EDITOR Chris Bickel MULTIMEDIA MANAGING PRODUCER Kevin McLean WEB STRATEGY MANAGER Kara Estelle-Powers DESIGN EDITOR Chrystal Smith DESIGNER Christina Aycock INTERACTIVE GRAPHICS EDITOR Kelly Franklin SENIOR GRAPHICS SPECIALISTS Holly Bishop, Nathalie Cary SENIOR SCIENTIFIC ILLUSTRATOR Valerie Altounian SCIENTIFIC ILLUSTRATORS Kellie Holoski, Ashley Mastin SENIOR PODCAST PRODUCER Sarah Crespi VIDEO PRODUCER Meagan Cantwell SENIOR PHOTO EDITOR Emily Petersen PHOTO EDITORS Charles Borst, Kaitlyn Dolan SOCIAL MEDIA STRATEGIST Jessica Hubbard SOCIAL MEDIA PRODUCER Sabrina Jenkins WEB DESIGNER Jennie Pajeroski INTERN Khafia Choudhary

Chief Executive Officer and Executive Publisher Sudip Parikh

Publisher, Science Family of Journals Bill Moran

DIRECTOR, BUSINESS SYSTEMS AND FINANCIAL ANALYSIS Randy Yi DIRECTOR, BUSINESS OPERATIONS & ANALYSIS Eric Knott DIRECTOR OF ANALYTICS Enrique Gonzales MANAGER, BUSINESS OPERATIONS Jessica Tierney MANAGER, BUSINESS ANALYSIS Cory Lipman BUSINESS ANALYSTS Kurt Ennis, Maggie Clark FINANCIAL ANALYST Isacco Fusi BUSINESS OPERATIONS ADMINISTRATOR Taylor Fisher SENIOR PRODUCTION MANAGER Jason Hillman SENIOR MANAGER, PUBLISHING AND CONTENT SYSTEMS Marcus Spiegler CONTENT OPERATIONS MANAGER Rebecca Doshi SENIOR CONTENT & PUBLISHING SYSTEMS SPECIALIST Jacob Hedrick SENIOR PRODUCTION SPECIALIST Kristin Wovk PRODUCTION SPECIALISTS Kelsey Cartelli, Audrey Diggs DIGITAL PRODUCTION MANAGER Lisa Stanford CONTENT SPECIALIST Kimberley Oster ADVERTISING PRODUCTION OPERATIONS MANAGER Deborah Tompkins DESIGNER, CUSTOM PUBLISHING Jeremy Huntsinger SR. TRAFFIC ASSOCIATE Christine Hall SPECIAL PROJECTS ASSOCIATE Sarah Dhery

ASSOCIATE DIRECTOR, BUSINESS DEVELOPMENT Justin Sawyers GLOBAL MARKETING MANAGER Allison Pritchard DIGITAL MARKETING MANAGER Aimee Aponte JOURNALS MARKETING MANAGER Shawana Arnold MARKETING ASSOCIATES Aaron Helmbrecht, Ashley Hylton, Mike Romano, Tori Velasquez, Jenna Voris SENIOR DESIGNER Kim Huynh

DIRECTOR AND SENIOR EDITOR, CUSTOM PUBLISHING Sean Sanders ASSISTANT EDITOR, CUSTOM PUBLISHING Jackie Oberst PROJECT MANAGER Melissa Collins

DIRECTOR, PRODUCT & PUBLISHING DEVELOPMENT Chris Reid DIRECTOR, BUSINESS STRATEGY AND PORTFOLIO MANAGEMENT Sarah Whalen ASSOCIATE DIRECTOR, PRODUCT MANAGEMENT Kris Bishop PRODUCT DEVELOPMENT MANAGER Scott Chernoff PUBLISHING TECHNOLOGY MANAGER Michael Di Natale SR. PRODUCT ASSOCIATE Robert Koepke PRODUCT ASSOCIATE Caroline Breul, Anne Mason SPJ ASSOCIATE MANAGER Samantha Bruno Fuller SPJ ASSOCIATE Casey Buchta

MARKETING MANAGER Kess Knight BUSINESS DEVELOPMENT MANAGER Rasmus Andersen SENIOR INSTITUTIONAL LICENSING MANAGER Ryan Rexroth INSTITUTIONAL LICENSING MANAGER Marco Castellani, Claudia Paulsen-Young SENIOR MANAGER, INSTITUTIONAL LICENSING OPERATIONS Judy Lillibridge SENIOR OPERATIONS ANALYST Lana Guz SYSTEMS & OPERATIONS ANALYST Ben Teincuff FULFILLMENT ANALYST Aminta Reyes

DIRECTOR, GLOBAL SALES Tracy Holmes US EAST COAST AND MID WEST SALES Stephanie O'Connor US MID WEST, MID ATLANTIC AND SOUTH EAST SALES Chris Hoag US WEST COAST SALES Lynne Stickrod ASSOCIATE DIRECTOR, ROW Roger Goncalves SALES REP, ROW Sarah Lelarge SALES ADMIN ASSISTANT, ROW Victoria Glasbey DIRECTOR OF GLOBAL COLLABORATION AND ACADEMIC PUBLISHING RELATIONS, ASIA Xiaoying Chu ASSOCIATE DIRECTOR, INTERNATIONAL COLLABORATION Grace Yao SALES MANAGER Danny Zhao MARKETING MANAGER Kilo Lan ASCA CORPORATION, JAPAN Rie Rambelli (Tokyo), Miyuki Tani (Osaka)

DIRECTOR, COPYRIGHT, LICENSING AND SPECIAL PROJECTS Emilie David RIGHTS AND PERMISSIONS ASSOCIATE Elizabeth Sandler LICENSING ASSOCIATE Virginia Warren CONTRACT SUPPORT SPECIALIST Michael Wheeler

MAIN HEADQUARTERS

Science/AAAS
1200 New York Ave. NW
Washington, DC 20005

SCIENCE INTERNATIONAL

Clarendon House
Clarendon Road
Cambridge, CB2 8FH, UK

SCIENCE CHINA

Room 1004, Culture Square
No. 59 Zhongguancun St.
Haidian District, Beijing, 100872

SCIENCE JAPAN

ASCA Corporation
Sibaura TY Bldg. 4F, 1-14-5
Shibaura Minato-ku
Tokyo, 108-0073 Japan

EDITORIAL

science_editors@aaas.org

NEWS

science_news@aaas.org

INFORMATION FOR AUTHORS

science.org/authors/
science-information-authors

REPRINTS AND PERMISSIONS

science.org/help/
reprints-and-permissions

MEDIA CONTACTS

scipak@aaas.org

MULTIMEDIA CONTACTS

SciencePodcast@aaas.org

ScienceVideo@aaas.org

INSTITUTIONAL SALES

AND SITE LICENSES

science.org/librarian

PRODUCT ADVERTISING

AND CUSTOM PUBLISHING

advertising.science.org/
products-services

science_advertising@aaas.org

CLASSIFIED ADVERTISING

advertising.science.org/
science-careers

advertise@sciencecareers.org

JOB POSTING CUSTOMER SERVICE

employers.sciencecareers.org

support@sciencecareers.org

MEMBERSHIP AND INDIVIDUAL

SUBSCRIPTIONS

science.org/subscriptions

MEMBER BENEFITS

aaas.org/membership/benefits

AAAS BOARD OF DIRECTORS

CHAIR Susan G. Amara

PRESIDENT Gilda A. Barabino

PRESIDENT-ELECT Keith Yamamoto

TREASURER Carolyn N. Ainslie

CHIEF EXECUTIVE OFFICER

Sudip Parikh

BOARD Cynthia M. Beall

Ann Bostrom

Janine Austin Clayton

Kaye Husbands Fealing

Maria M. Klawe

Jane Maienschein

Robert B. Millard

Babak Parviz

William D. Provine

Juan S. Ramírez Lugo

Susan M. Rosenberg

BOARD OF REVIEWING EDITORS

(Statistics board members indicated with \$)

Erin Adams, U. of Chicago

Takuzo Aida, U. of Tokyo

Leslie Aiello, Wenner-Gren Fdn.

Deji Akinwande, UT Austin

Judith Allen, U. of Manchester

Marcella Alsan, Harvard U.

James Analytis, UC Berkeley

Trevor Archer, NIEHS, NIH

Paola Arlotta, Harvard U.

Delia Baldassarri, NYU

Nenad Ban, ETH Zürich

Nandita Basu, U. of Waterloo

Franz Bauer, Pontificia U. Católica de Chile

Ray H. Baughman, UT Dallas

Carlo Beenakker, Leiden U.

Yasmine Belkaid, NIAID, NIH

Philip Benfey, Duke U.

Kiros T. Berhane, Columbia U.

Joseph J. Berry, NREL

Alessandra Biffi, Harvard Med.

Chris Bowler, École Normale Supérieure

Ian Boyd, U. of St. Andrews

Malcolm Brenner, Baylor Coll. of Med.

Emily Brodsky, UC Santa Cruz

Ron Brookmeyer, UCLA (\$)

Sabine Büchel, UKE Hamburg

Dennis Burton, Scripps Res.

Carter Tribble Butts, UC Irvine

György Buzsáki, NYU School of Med.

Mariana Byndloss, Vanderbilt U. Med. Ctr.

Annmarié Carlton, UC Irvine

Simon Cauchemez, Inst. Pasteur

Ling-Ling Chen, SIBCB, CAS

Ib Chorkendorff, Denmark TU

Karlene Cimprich, Stanford U.

James J. Collins, MIT

Robert Cook-Deegan, Arizona State U.

Virginia Cornish, Columbia U.

Carolyn Coyne, Duke U.

Roberta Croce, VU Amsterdam

Christina Curtis, Stanford U.

Ismaila Dabo, Penn State U.

Jeff L. Dangl, UNC

Chiara Daraio, Caltech

Nicolas Dauphas, U. of Chicago

Frans de Waal, Emory U.

Claude Desplan, NYU

Sandra Diaz, U. Nacional de Córdoba

Samuel Diaz-Muñoz, UC Davis

Ulrike Diebold, TU Wien

Stefanie Dimmeler, Goethe-U. Frankfurt

Hong Ding, Inst. of Physics, CAS

Dennis Discher, UPenn

Jennifer A. Doudna, UC Berkeley

Ruth Drdla-Schutting, Med. U. Vienna

Raissa M. D'Souza, UC Davis

Bruce Dunn, UCLA

William Dunphy, Caltech

Scott Edwards, Harvard U.

Todd Ehlers, U. of Tübingen

Nader Engheta, UPenn

Karen Ersche, U. of Cambridge

Beate Escher, UFZ & U. of Tübingen

Barry Everitt, U. of Cambridge

Vanessa Ezenwa, U. of Georgia

Toren Finkel, U. of Pitt. Med. Ctr.

Gwenn Flowers, Simon Fraser U.

Peter Fratzi, Max Planck Inst. Potsdam

Elaine Fuchs, Rockefeller U.

Jay Gallagher, U. of Wisconsin

Daniel Geschwind, UCLA

Ramon Gonzalez, U. of South Florida

Sandra González-Bailón, UPenn

Nicolas Gruber, ETH Zürich

Hua Guo, U. of New Mexico

Taejiip Ha, Johns Hopkins U.

Daniel Haber, Mass. General Hos.

Sharon Hammes-Schiffer, Yale U.

Wolf-Dietrich Hardt, ETH Zürich

Louise Harra, U. Coll. London

Carl-Philipp Heisenberg, IST Austria

Janet G. Hering, Eawag

Christoph Hess, U. of Basel & U. of Cambridge

Heather Hickman, NIAID, NIH

Hans Hilgenkamp, U. of Twente

Janneke Hille Ris Lambers, ETH Zürich

Kai-Uwe Hinrichs, U. of Bremen

Nandita Basu, U. of Waterloo

Franz Bauer, Pontificia U. Católica de Chile

Ray H. Baughman, UT Dallas

Carlo Beenakker, Leiden U.

Yasmine Belkaid, NIAID, NIH

Philip Benfey, Duke U.

Kiros T. Berhane, Columbia U.

Joseph J. Berry, NREL

Alessandra Biffi, Harvard Med.

Chris Bowler, École Normale Supérieure

Ian Boyd, U. of St. Andrews

Malcolm Brenner, Baylor Coll. of Med.

Emily Brodsky, UC Santa Cruz

Ron Brookmeyer, UCLA (\$)

Sabine Büchel, UKE Hamburg

Dennis Burton, Scripps Res.

Carter Tribble Butts, UC Irvine

György Buzsáki, NYU School of Med.

Mariana Byndloss, Vanderbilt U. Med. Ctr.

Annmarié Carlton, UC Irvine

Simon Cauchemez, Inst. Pasteur

Ling-Ling Chen, SIBCB, CAS

Ib Chorkendorff, Denmark TU

Karlene Cimprich, Stanford U.

James J. Collins, MIT

Robert Cook-Deegan, Arizona State U.

Virginia Cornish, Columbia U.

Carolyn Coyne, Duke U.

Roberta Croce, VU Amsterdam

Christina Curtis, Stanford U.

Ismaila Dabo, Penn State U.

Jeff L. Dangl, UNC

Chiara Daraio, Caltech

Nicolas Dauphas, U. of Chicago

Frans de Waal, Emory U.

Claude Desplan, NYU

Sandra Diaz, U. Nacional de Córdoba

Samuel Diaz-Muñoz, UC Davis

Ulrike Diebold, TU Wien

Stefanie Dimmeler, Goethe-U. Frankfurt

Hong Ding, Inst. of Physics, CAS

Dennis Discher, UPenn

Jennifer A. Doudna, UC Berkeley

Ruth Drdla-Schutting, Med. U. Vienna

Raissa M. D'Souza, UC Davis

Bruce Dunn, UCLA

William Dunphy, Caltech

Scott Edwards, Harvard U.

Todd Ehlers, U. of Tübingen

Nader Engheta, UPenn

Karen Ersche, U. of Cambridge

Beate Escher, UFZ & U. of Tübingen

Barry Everitt, U. of Cambridge

Vanessa Ezenwa, U. of Georgia

Toren Finkel, U. of Pitt. Med. Ctr.

Gwenn Flowers, Simon Fraser U.

Peter Fratzi, Max Planck Inst. Potsdam

Elaine Fuchs, Rockefeller U.

Jay Gallagher, U. of Wisconsin

Daniel Geschwind, UCLA

Ramon Gonzalez, U. of South Florida

Sandra González-Bailón, UPenn

Nicolas Gruber, ETH Zürich

Hua Guo, U. of New Mexico

Taejiip Ha, Johns Hopkins U.

Daniel Haber, Mass. General Hos.

Sharon Hammes-Schiffer, Yale U.

Wolf-Dietrich Hardt, ETH Zürich

Louise Harra, U. Coll. London

Carl-Philipp Heisenberg, IST Austria

Janet G. Hering, Eawag

Christoph Hess, U. of Basel & U. of Cambridge

Heather Hickman, NIAID, NIH

Hans Hilgenkamp, U. of Twente

Rethinking the retraction process

High-profile examples of scientific fraud continue to plague research. Recently, *Science* published two news stories on alleged image manipulation in Alzheimer's research and unreliable data in an ecology study, sadly showing that the problem persists. Each case involved back and forth among the journal, authors, and institutions to correct the scientific record. Journalists and advocates for research integrity (including courageous whistleblowers) are understandably frustrated about how long it takes to retract papers or at least to post editorial expressions of concern. It's time to devise a more efficient solution.

Most journals follow guidelines for research misconduct promoted by the Committee on Publication Ethics (COPE). Accordingly, should *Science* receive a report of alleged image manipulation or other problems, our first step is to contact the authors. Most of the time, authors will deny the problem or insist it can be solved with a minor correction. Much of the time, we know that neither answer is satisfactory but before moving to retract, our next step is to contact the authors' institutions. This is because we're not an investigatory body. Again, the most likely answer we will get is inconclusive, if there is an answer at all. According to COPE, we're then supposed to contact the institution every 3 to 6 months for a response. And this exasperating wait can last for a year or more.

So, what's the alternative? We could be more aggressive in retracting things without consulting as widely, but that could have a very big impact on scientists' careers, and a mistake would be costly. We could try to get the universities to respond more quickly and more transparently. As a former provost myself, I received many such inquiries over the years. Now that I've experienced both sides of this interaction, I've been thinking about how the process could be improved.

In 2000, the US Department of Health and Human Services issued a lengthy and legalistic set of regulations for what universities are supposed to do about research misconduct. A quick read of this labyrinth makes it easy to see how university administrators become paralyzed by the fear of running afoul of the

agency's regulations. Add to this the possibility that an unhappy author could threaten litigation against the institution, drawing legal counsel and public relations into the equation, and the only possible outcome is gridlock. With a university's reputation at risk and legal action looming, the last thing on their mind is the paper that is under dispute.

The journals have a different goal. *Science* just wants to know if the paper should be retracted or not. Although we're curious about the details—and sometimes our news division, which is editorially independent of the research department, might decide to look deeper—the matter of whether the problem was a rogue postdoc or graduate student, sloppy science, or outright fraud by the principal investigator is not for us to adjudicate. At the same time, the university is

focused on the personnel questions, making them prone to err on the side of revealing less than the full story.

The solution would be for the universities, federal government, funding agencies, and journals to come together and agree that these investigations should be a two-stage process. The first stage should evaluate the validity of the paper without attributing blame. The university would then feel free to determine the validity of the

paper before it plunges into a lengthy and more complicated investigation of the underlying wrongdoing. If the paper is not valid, it can then be retracted much more quickly. The second stage, with journals out of the picture, would be for the university to determine whether there was fraud that rises to the level of research misconduct. This plan would accelerate correction of the scientific record.

I asked prominent research integrity advocate Elisabeth Bik what she thought of this. "It would be beneficial for misconduct cases to split the investigations into two," she said. "On one hand, there is the question whether the data in a paper is reliable or not, while on the other hand, one can question who has been responsible for generating that data. These are two separate questions."

Indeed, they are separate, and the process to address retractions needs to change.

—H. Holden Thorp



H. Holden Thorp
Editor-in-Chief,
Science journals.
hthorp@aaas.org;
@hholdenthorp

**"...advocates for
research integrity...
are...frustrated about
how long it takes
to retract papers..."**

BUILDING ON A MILLENNIUM OF ARAB INNOVATION

The Middle East was once at the forefront of invention. Algebra, universities, inoculation against disease, coffee, windmills, the arch and even the three-course meal: all had their genesis in the region. Yet over the past 150 years, the focus on innovation on a global scale has not been as sharp as it once was.

That's why, as we enter the second quarter of the Digital Century, the Kingdom of Saudi Arabia will reinvigorate that inventive tradition with a range of new research, development and innovation priorities aimed at addressing the most pressing issues affecting mankind today.

Through a focus on Health and Wellness, Sustainable Environment and Supply of Essential Needs, Energy and Industrial Leadership, and Economies of the Future, the newly established Research, Development and Innovation Authority (RDIA) will be a steward for the Kingdom's work with global partners, deploying a multi-billion-dollar budget over the coming years.

We are determined to help make world-class healthcare accessible and equitable across society. As an existing leader in digital health, the Kingdom will continue investing to advance the technology even further. As we demonstrated during the Covid-19 pandemic, this is an area in which we lead the world.

Saudi Arabia is intent on addressing not only domestic but also global health challenges through focusing on ultra-early disease detection and biotechnology to prevent the blight of illnesses such as cancer and chronic heart disease from ending lives prematurely.

A good life isn't limited to good health. Security of food, water and energy are vital for happiness and wellbeing.

The world's largest solar-powered desalination plant is located in Al Khafji in Saudi Arabia and we continue to invest in innovation to make desalination environmentally friendly, more accessible to many more households and businesses, cheaper to achieve and, crucially for food security, able to be used easily in farming.

Saudi Arabia has prospered over the past century thanks, in large part, to our oil revenue. We're now investing that revenue in finding cleaner, greener sources of energy to power our way into a brighter future. The Kingdom is building what will be the world's largest green hydrogen facility, with a production target of 50 tonnes a day, aiming to produce 5 million tonnes of clean hydrogen by 2030.

Though the innovation and invention timescale can be frustratingly long, the Kingdom is committed to becoming an innovation superpower in the next two decades. We expect that by 2040, our total expenditure on innovation will reach 2.5% of GDP, more than the G20 average.

We can't do this alone.

At the heart of our commitment to innovation is the desire to build globally collaborative schemes and institutions which, together, will help mankind harness technology to improve lives. Saudi Arabia will invest in bringing scientific talent from other nations to work with our own brightest minds.

KACST (the King Abdulaziz City for Science and Technology) – the Kingdom's leading research and innovation centre – is already working with Cambridge University, Harvard, Berkley and MIT to pool knowledge, resources, information, and ability. As our programme expands in capability, so will our world advance in possibility.

Innovation, investment and people: the Research, Development and Innovation Authority brings all these together. Building on 1,500 years of our region's exceptionally inventive history, the Kingdom of Saudi Arabia will use the fruits of our prosperity to build a better future for everyone, everywhere.

His Excellency Munir Eldesouki – President of King Abdul Aziz City for Science and Technology (KACST)



“Wellcome remains an institutionally racist organisation.”

Jeremy Farrar, director of the Wellcome Trust, in *Times Higher Education*, announcing a new push to support applicants from diverse backgrounds in its grantmaking, but with no details on funding. A report found the large biomedical research charity's antiracism program, launched 2 years ago, has made limited progress.

IN BRIEF

Edited by Jeffrey Brainard and Greg Miller

COVID-19

U.K. OKs anti-Omicron vaccine

The United Kingdom this week became the first country to approve an updated COVID-19 booster directed at two different strains of the coronavirus. The “bivalent” booster, made by Moderna, will have the same dose of messenger RNA as the company's prior boosters but will target both the original version of the coronavirus and the first Omicron variant, BA.1, which emerged in late 2021. Clinical trials and other research by Moderna suggest its retooled booster generates a stronger immune response against BA.1 and other versions of Omicron now in circulation than its existing vaccine, introduced in December 2020. The new shot will be available in the fall. A similar booster is expected in the United States, although in June the Food and Drug Administration asked Moderna and a second manufacturer, Pfizer, to include the spike protein component for more recent versions of Omicron, BA.4 and BA.5, rather than BA.1.

A health school's colonial past

HISTORY OF SCIENCE | A report on the history of the London School of Hygiene & Tropical Medicine (LSHTM) has found the prestigious institution “embraced British colonialism and the notions of racism and white supremacy.” The review, commissioned by LSHTM and released last week, describes the institute's history from its founding in 1899 to 1960, when it was funded by the government ministry that administered colonies and overseas territories and by companies with commercial interests there. The school's research sought to protect the health of Europeans in the colonies and the companies' profits rather than the health of the other people who lived there, the report concludes. It details an experiment by physician Patrick Manson, before he founded the school, in which he exposed his servant to nematode-carrying mosquitoes to study the parasite's life cycle. The investigation was recommended by a 2020 report on racism and equality commissioned by LSHTM, which has prompted the school to adopt new measures to improve its diversity,

equity, and inclusion. LSHTM will offer a new funding scheme for Ph.D. scholars at partner institutions in five African countries.

Polio boosters for London kids

INFECTIOUS DISEASES | Citing new data indicating poliovirus continues to circulate in at least eight of London's 32 boroughs, U.K. authorities recommended last week that all the city's children between the ages of 1 and 9 receive an additional booster dose of polio vaccine. The virus, detected by routine wastewater samples starting in February, is a type derived from the oral polio vaccine, which contains live, weakened virus. Virus in the live vaccine, which is no longer used in richer countries, can spread and mutate into a version that can cause paralysis in unvaccinated people. Travelers probably introduced the virus into the United Kingdom; the country has had no cases of polio so far, but genetic analysis of the samples suggests the virus is spreading beyond a small group of people, according to a 10 August report by the UK Health Security Agency. Authorities are adding at

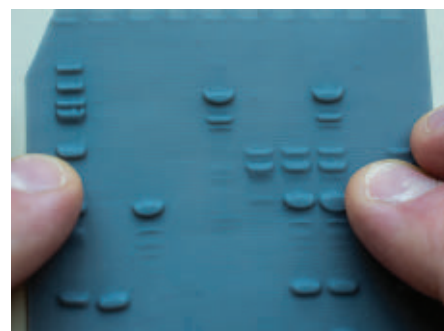
least two dozen sewage sampling sites in London and across the country to check the full extent of the spread.

CDC puts health equity on the map

PUBLIC HEALTH | The U.S. Centers for Disease Control and Prevention (CDC) and other health agencies have launched the first national index of how pollution, illness, and poverty affect health equity. The Environmental Justice Index, which debuted last week, combines several existing indices of environmental justice—based on data from CDC, the Environmental Protection Agency, and other sources—into an overall measure of environmental harm to health and well-being. The maps display data down to the scale of neighborhoods. That's a useful innovation, says Philip Alberti, senior director of health equity research and policy at the Association of American Medical Colleges. “The impacts of environmental injustice tend to be hyperlocal.” Another novelty is a focus on the combined effects of multiple health inequities. CDC hopes the website will help public health officials respond to areas with the highest risk of illness, set goals, and track progress.

3D data may aid blind scientists

DIVERSITY | Visually impaired scientists often rely on text readers to read journal articles, but until now there has been no easy way to render graphics and data in a way they could perceive. A group of researchers has developed a solution: 3D print a lithophane, a thin plastic sheet that



3D-printed lithophanes can help optically impaired scientists “see” data, such as from protein separation gels, with their fingertips.

PHOTO: ELIZABETH SHAW



IN FOCUS Scientists rallied outside Canada's Parliament on 11 August, carrying a 70-meter-long letter with more than 7000 signatures. The letter to lawmakers calls for increases in the stipends paid by graduate student scholarships and postdoctoral fellowships awarded by the Natural Sciences and Engineering Research Council of Canada. "We can't do science if we can't pay rent," one rallygoer's sign read.

displays visual data in the form of bumps and other surface features. Users can run their finger across the surface and perceive features of graphs such as data points, axes, and curves. For a stained protein or nucleic acid gel, a lithophane can represent the intensities of the stain as variations in relief. 3D printers have become widely available, and the printing only takes minutes. Bryan Shaw, a chemist at Baylor University, and his team collaborated with four optically impaired scientists to develop and describe the method on 17 August in *Science Advances*. (See a *Science* interview with them at <https://scim.ag/LithophaneQA>.)

NAS can suspend, not just expel

MISCONDUCT | The U.S. National Academy of Sciences (NAS) has changed its bylaws to permit members to be temporarily suspended, rather than permanently ejected, from the prestigious body if they breach its code of conduct, *Science* has learned. Separately, the academy made public that last week it has for 5 years barred a member, Jane Lubchenco, a White House official and former head of the National Oceanic and Atmospheric Administration, from receiving NAS honors and working on publications or programs for the academy or the National Research Council. The bylaw change was approved on 24 June in an online vote open to all 2500 NAS members, with more than 75% of participating members voting in favor. Requested by the standing

committee that reviews alleged violations of the academy's code of conduct, the change "will allow the NAS to take meaningful actions on conduct issues with less severe consequences," its president, Marcia McNutt, said in a statement to *Science*. A two-thirds vote of NAS's 17-member governing council will be required to restore a suspended membership. The new policy modifies one approved in 2019 that allows the body to expel members who breach its code, which prohibits scientific and financial misconduct, discrimination, harassment, and bullying. NAS has since permanently ejected at least three members: evolutionary biologist Francisco Ayala, astronomer Geoffrey Marcy, and Peruvian archaeologist Luis Jaime Castillo Butters. The sanctions on Lubchenco, who is now deputy director for climate and environment in the Office of Science and Technology Policy, stem from her role in editing a paper in the *Proceedings of the National Academy of Sciences* on which her brother-in-law was an author. She has previously apologized for the conflict of interest and now accepts the sanctions.

Museum to bury disputed skulls

ANTHROPOLOGY | The University of Pennsylvania's archaeology museum is planning a proper burial for 13 skulls of Black residents of Philadelphia it has held since 1966. The skulls are part of a controversial collection of more than 1300 skulls at the museum. They were gathered in the

mid-19th century by anthropologist Samuel Morton and others, and used by Morton to justify racist ideas about human intelligence. The skulls to be reburied were dug up from the Blockley Almshouse, a charity hospital at the site where the museum now stands, and probably came from enslaved people, a 2021 report said. The museum and some observers see the planned reburial, in the historically Black Eden Cemetery, as a step toward reconciliation. But some members of the city's Black community say the museum's decision was rushed and descendants should have the final say in where the remains are laid to rest. The disposition of the remaining skulls in the collection has yet to be resolved.

Accident kills 21,000 research fish

LAB SAFETY | Chlorine poisoning likely caused the deaths last week of more than 21,000 fish at a research center on aquatic biology and aquaculture at the University of California, Davis. About three-quarters of the fish lost were part of ecological physiologist Nann Fangué's research into the conservation and physiology of native California species. The animals lost included green and white sturgeon, one at least 20 years old, and endangered Chinook salmon. Chlorine, which is used for disinfection, is toxic to fish even in small amounts. The university apologized for the unprecedented "catastrophic failure" and is investigating the incident and reviewing plumbing and procedures at the center and elsewhere on campus.



NASA's Space Launch System, seen here in a June dress rehearsal, will be its most powerful rocket ever.

SPACE SCIENCE

Small stowaways on new NASA rocket promise big science

Batteries allowing, CubeSats will target lunar ice and more

By **Eric Hand**

When NASA's most powerful rocket ever attempts its first flight this month, its highest profile payload will be three instrumented mannequins, setting off on a 42-day journey beyond the Moon and back. They are stand-ins for the astronauts that the 98-meter-tall rocket, known as the Space Launch System (SLS), is supposed to carry to the Moon as soon as 2025, as part of NASA's Artemis program. But when the SLS lifts off on 29 August, other voyagers will be along for the ride: 10 CubeSats, satellites no bigger than a small briefcase, to probe the Moon, asteroids, and effects of deep-space radiation.

The teams that built those satellites have more than the usual launch jitters: Half of the devices may not have enough power to begin their missions. Stuck within the rocket for more than a year because of launch delays,

their batteries have drained and some may be unable to boot up and unfurl solar panels. "The longer we wait, the higher the risk," says Ben Malphrus of Morehead State University, principal investigator for Lunar IceCube, one of the probes with power concerns.

At stake is not just data, but a test of CubeSats as deep-space probes. "We're in the transition phase from being a curiosity and a training tool to being a platform for real science," Malphrus says. CubeSats are easy to assemble out of standardized parts, from thrifty ion propulsion systems to pint-size radio transmitters. That lets researchers focus on developing instruments capable of gathering novel data—if they can be shrunk into a CubeSat package.

At millions of dollars a pop compared with hundreds of millions for a bigger, stand-alone satellite on its own rocket, the spacecraft can take on riskier missions, including hitchhiking on the unproven SLS. "When it comes to

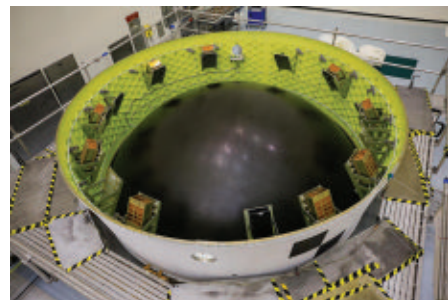
CubeSats, failure is an option," Bhavya Lal, NASA's associate administrator for technology, policy, and strategy, said at a briefing earlier this month.

Several SLS CubeSats will focus on lunar ice, which has intrigued researchers ever since NASA's Lunar Prospector discovered a signal suggestive of water in the late 1990s. Using a neutron detector, it peered into frigid, permanently shadowed regions in polar craters. In many, the probe detected a curious suppression of neutrons—best explained by extra hydrogen in the topmost meter of soil.

Researchers assume much of the hydrogen represents water ice trapped in the craters' coldest, darkest recesses. Ancient impacts of comets or asteroids could have delivered the ice, but the hydrogen could also be implanted by the solar wind. When hydrogen ions in the wind strike oxygen-bearing minerals in lunar soil, the barrage creates hydroxyl, which can be transformed into water through subsequent reactions. If the Moon holds enough water, it could be used for agriculture and life support, and split into hydrogen and oxygen for rocket propellant. "That will be more economical than bringing it from Earth," says Hannah Sargeant, a planetary scientist at the University of Central Florida.

The Lunar Polar Hydrogen Mapper (LunaH Map), led by Craig Hardgrove of Arizona State University, Tempe, will attempt to improve on Lunar Prospector's maps with a daring orbit that swoops just 12 to 15 kilometers above the Moon's south pole. Over the course of 280 passes, the team hopes the probe's neutron detector will map excess hydrogen with a resolution of 20 to 30 kilometers, about twice as good as Lunar Prospector. "We can distinguish one [deep crater] from another," Hardgrove says. Craters lacking hydrogen, or enrichments outside the frigid hideouts, might indicate a relatively recent impact that blasted out ice and redistributed it, he says.

Another CubeSat, Lunar IceCube, will carry a spectrometer that can detect the infrared fingerprints of either water or hy-



Ten CubeSats will be ejected from a ring that sits below the crew capsule on NASA's new rocket.

PHOTOS: (TOP TO BOTTOM) EVA MARIE UZCATEGUI/AFP/GETTY IMAGES; NASA

droxyl. Because the device depends on reflected light, it will be most sensitive to signs of hydroxyl and water in sunlit regions at lower latitudes. “They’re really looking at the [effect of] the solar wind, day by day,” says Benjamin Greenhagen, a planetary scientist at the Johns Hopkins University Applied Physics Laboratory.

Some of the CubeSats are headed beyond the Moon. After the SLS leaves Earth’s orbit and releases the probes, Near-Earth Asteroid Scout (NEA Scout) will unspool a thin solar sail the size of a racquetball court. Propelled by photons, it will navigate to 2020GE, a miniature asteroid between 5 and 15 meters across. About 2 years from now, it should sail as close as 800 meters to the asteroid in a 3-hour flyby. Many larger asteroids are loosely bound rubble piles, but NEA Scout will test the expectation that the faint pressure of sunlight has spun up 2020GE too fast for it to hold any rubble, says Julie Castillo-Rogez, NEA Scout’s science principal investigator at NASA’s Jet Propulsion Laboratory.

BioSentinel, led by Sergio Santa Maria, a biologist at NASA’s Ames Research Center, will carry out NASA’s first test of the biological effects of radiation beyond low-Earth orbit since the last Apollo mission in 1972. Unprotected by Earth’s magnetic field, organisms are more vulnerable to DNA damage caused by solar outbursts and galactic cosmic rays. BioSentinel will carry strains of yeast in hundreds of microscopic wells to a Sun-orbiting perch beyond the Moon. There, its optical sensors will gauge the health of the yeast strains as they accumulate radiation damage by measuring cell growth and metabolism.

BioSentinel, NEA Scout, and three other CubeSats were allowed to recharge their batteries during their long wait aboard the SLS. But five others were out of luck, including both LunaH Map and Lunar IceCube. Some could not be recharged without removing them from the rocket; in other cases NASA engineers feared the process might spark discharges that could harm the rest of the rocket. “We have to be very cognizant of the risk to the primary mission when we interface with these CubeSats,” says Jacob Bleacher, NASA’s chief exploration scientist.

Hardgrove says LunaH Map’s battery reserve is probably at 50%; at 40% it will not be able to run through initial operations and maneuvers before the solar panels can unfurl and begin to recharge the batteries. He pushed hard for the opportunity to recharge but says he was rebuffed by NASA. “You can’t agree to take stowaways and then kill them,” he says. Still, Hardgrove is resigned to rolling the dice. “It wouldn’t be a CubeSat mission if you weren’t anxious.” ■

SCIENCE METRICS

China rises to first place in one key metric of research impact

Other methods still put the United States somewhat ahead

By Jeffrey Brainard and Dennis Normile

For the first time, China has slightly edged out the United States in the number of most cited papers, a key measure of research impact, according to a Japanese science policy institute. The milestone provides fresh evidence that China’s scholarship, known for its burgeoning quantity, is catching up in quality as well. “People are writing off China, [saying] they’re putting out a lot of stuff but it’s not good quality,” says Caroline Wagner, who studies science policy and innovation at Ohio State University, Columbus. “That’s just short-sighted.”

Scholars disagree about the best methodology for measuring publications’ impact, however, and other metrics suggest the United States is still ahead—but barely.

For the new report, Japan’s National Institute of Science and Technology Policy (NISTEP) tallied the top 1% papers in terms of citations, a rarified stratum inhabited by many Nobel laureates. Many such elite articles have authors from multiple countries, however, which complicates the analysis. In one study, NISTEP used a method called “fractional counting” to divide the credit. If, for example, one French and three Swedish institutions contributed to a paper, France received 25% of the credit and Sweden 75%.

Using that measure, China accounted for 27.2% of the most cited papers published in 2018, 2019, and 2020, and the United States for 24.9%. Next was the United Kingdom, with 5.5%; Japan was in 10th place. (U.S. researchers were still slightly ahead when NISTEP used a less fine-grained method that credits every country that contributed to a highly cited paper equally, regardless of how many of its institutions were involved.)

Cao Cong, a science policy scholar at the University of Nottingham’s campus in Ningbo, China, says the methodology may overstate China’s contributions to internationally co-authored papers. “The question is who—the Chinese or their international

collaborators—led the studies,” he says.

Still, China’s rising production of top-cited papers is “remarkable,” NISTEP says; 2 decades ago it only ranked 13th in the fractional counting metric. In recent years, critics faulted the quality of Chinese research, pointing to policies—now being phased out—that provided professional rewards for authors based on the sheer number of papers published. They also noted that China-based paper mills, which provide researchers with authorship slots in exchange for money, appear to be growing in number.

Other measures still put the United States ahead. *The State of U.S. Science and Engineering 2022*, a report published by the U.S. National Science Foundation (NSF) in January, addressed one problem with reports such as NISTEP’s: By counting numbers of highly cited papers, they favor big

“The question is who—the Chinese or their international collaborators—led the [high-impact] studies.”

Cao Cong,

University of Nottingham, Ningbo

countries and those that spend more on research, just as big countries tend to do better in Olympic medal rankings. NSF instead measured the share of each country’s papers that are highly cited, which allows for comparisons across countries regardless of how much they publish. Its analysis showed U.S. papers were highly influential: Of those published

in 2018, more than twice as many ended up among the 1% most cited papers as expected based on the country’s total output. China published 20% more top-cited papers than would be expected.

Another paper, published by Wagner and others in 2020, concluded China’s research is slightly more innovative than the world average. That study tracked how often papers’ reference lists included atypical combinations of journals in disparate fields as a proxy for innovative new ideas.

The impact of publications is just one measure of a country’s scientific prowess, however. The United States still leads in other indicators, such as the number of doctorates awarded—but there’s little doubt China’s scientific enterprise is catching up with the rest of the world at an unprecedented speed. ■



After harvest, a Maryland cornfield is planted with a cover crop—a practice that boosts soil carbon.

AGRICULTURE

New law's big payout for farming has uncertain climate payoff

Measures to capture carbon in soil may be less effective than hoped, scientists say

By Erik Stokstad

When settlers plowed the North American prairie, they uncovered some of the most fertile soil in the world. But tilling those deep-rooted grasslands released massive amounts of underground carbon into the atmosphere. More greenhouse gases wafted into the skies when wetlands were drained and forests cleared for fields. Land conversion continues today, and synthetic fertilizer, diesel-hungry farm machinery, and methane-belching livestock add to the climate effects; all told, farming generates 10% of climate-affecting emissions from the United States each year. Now, Congress would like to turn back the clock and return some of that carbon to the soil.

The Inflation Reduction Act, a broad bill signed into law this week, has historic climate provisions, including massive subsidies for clean power and electric vehicles (*Science*, 5 August, p. 564). But lawmakers also included more than \$25 billion to expand and safeguard forests and promote farming practices thought to be climate friendly. Those include no-till agriculture and “cover crops,” plants cultivated simply

to protect the soil. Researchers, environmental groups, and the farm industry agree that paying and training farmers to adopt those measures will improve soil health and water and air quality. “I think pretty much everyone across the board is pretty happy,” says Haley Leslie-Bole, a climate policy analyst with the World Resources Institute. But how much these practices will slow global warming is unclear.

“It’s probably going to be positive, but how positive we don’t really know yet,” says Jonathan Sanderman, a soil scientist at the Woodwell Climate Research Center. A major factor is whether the U.S. Department of Agriculture (USDA) spends the money on the practices most likely to have climate benefits. Another challenge is measuring and quantifying the reductions, a task complicated by the great diversity of U.S. land and farming practices and the complex biogeochemistry of the carbon cycle.

Sanderman and others think bigger climate gains could come from other changes in farming, such as lessening emissions from fertilizer and livestock. And climate and agriculture expert Tim Searchinger of Princeton University sees a need for more research on climate-beneficial farming

practices. USDA “needs to come up with an ambitious, creative plan and include a really good system for tracking progress.”

U.S. farmers have long received payments for conserving soil and reducing the pollution that can run off their fields. The new bill expands funding for those programs, allowing more farmers to get a per-acre payment for a wide range of activities expected to reduce or sequester carbon emissions, including no-till and cover crops.

Yet how those practices will affect the soil’s ability to accumulate and hold carbon depends on a complex interplay between plants, which add organic material to the soil, and microbes and other tiny organisms that break down everything they can, sometimes releasing greenhouse gases. Those interactions vary enormously with soil type and environmental conditions, and it can take years for the impact of changes in crop types or farming techniques to emerge.

Planting cover crops such as cowpeas and vetch, for example, boosts soil carbon on average each year by one-third of a ton per hectare, according to a 2015 meta-analysis in *Agriculture, Ecosystems & Environment*. The cover crops help control weeds and make the soil more porous, says Cristine Morgan, scientific director of the Soil Health Institute. “Grab a shovel and jump on it,” she says. “And the shovel goes deeper.” Yet the net climate benefits remain uncertain. On the one hand, leguminous cover crops such as cowpeas and vetch add nitrogen to the soil, which microbes can transform into nitrous oxide, a potent greenhouse gas. But farmers might then add less fertilizer, which would reduce emissions.

Another reputedly climate-friendly practice is no-till farming, which is growing in popularity. By not plowing fields, farmers protect the topsoil from erosion. They also save on diesel, which benefits their bottom line and reduces carbon dioxide emissions. Crop yields can increase as carbon accumulates in the upper root zone, enriching the soil and helping it retain moisture.

At the same time, studies have shown that carbon decreases in deeper layers of certain soils, making the net change small or zero. And during the first decade, no-till fields release higher levels of nitrous oxide as microbes break down crop residues, although the levels eventually decline. A further complication is permanence: Few U.S. farmers continue the practice uninterrupted. Factors such as the growth of herbicide-resistant weeds and the need to rotate crops eventually convince them to plow

again, which can allow nearly one-third of the accumulated carbon to escape into the atmosphere.

Still, Keith Paustian, a soil scientist at Colorado State University, and others argue that together, these regenerative soil practices are powerful climate tools. “We can regain potentially quite a fair amount of that lost carbon,” he says, by combining no-till and cover crops with other steps, such as planting trees on farms and improving grazing management to revitalize pastures. “We need to get agriculture to a new paradigm where these kinds of practices are the norm and not the exception,” he says.

In addition to fields and forests, the bill’s climate-related provisions target livestock, which emit methane that accounts for 27% of all greenhouse emissions from U.S. agriculture. As part of one USDA program awarded \$8.5 billion, the bill instructs the agency to prioritize projects that will reduce these emissions from cows and other ruminants by modifying their feed. An additive called 3-NOP can cut methane burped by dairy cattle by about 30% and is used in the United Kingdom and Europe. But it hasn’t been greenlighted yet by the U.S. Food and Drug Administration, which considers it a drug, slowing the approval process.

Searchinger and others hope USDA will also emphasize the incentives the bill provides to cut fertilizer use. Nitrification inhibitors, compounds that slow microbial conversion of fertilizer into nitrous oxide, can help farmers apply less and also cut emissions, he and others say. Farmers may be receptive because of fertilizer shortages and high prices. USDA this week said it will streamline applications for fertilizer management.

Many climate advocates say the most cost-effective way to help the climate through agriculture is simply to farm less land and raise less livestock. That means persuading farmers not to convert grasslands or other carbon-rich lands to row crops such as corn and soybeans. But the bill includes no additional funding for USDA’s main program for protecting sensitive private land, the Conservation Reserve Program.

What might it all add up to? Paustian admits it’s hard to pin down the total climate benefit of the \$25 billion. But the bill also includes a special pot of \$300 million for USDA and partners to collect field data on carbon sequestered and emissions reduced—data could help target future climate efforts more effectively, he and others say. “That’s really significant,” says Alison Eagle, an agricultural economist with the Environmental Defense Fund. “This investment can help direct the next set of funding to the right place.” ■

FUNDING

Massive climate and health bill also benefits U.S. energy labs

Major physics projects and national lab infrastructure will get \$1.5 billion over 5 years

By Jeffrey Mervis and Adrian Cho

An ambitious climate, health care, and tax reform bill passed last week by the U.S. Congress also contains a 5-year, \$2 billion windfall for the national laboratories run by the U.S. Department of Energy (DOE). Most of the money—\$1.5 billion—will go to DOE’s science office for new facilities and upgrades at the 10 national labs it oversees, which carry out basic research in an array of fields.

“This is a nice little bump for the science budget,” says Bill Madia, former director of two DOE national laboratories. “I’m surprised science got anything in this bill.” Leland Cogliani of Lewis-Burke Associates, a science lobbying firm, cautions that the extra money is only a down payment for many projects in the pipeline. “It may sound like a lot of money, but \$1.5 billion doesn’t really go very far,” he says.

The new spending, part of the Inflation Reduction Act (IRA) of 2022, is much less than President Joe Biden had envisioned last year in proposing a \$3.2 trillion blueprint for sweeping social, environmental, and economic reforms. That ambitious agenda, called the Build Back Better Act, included nearly \$13 billion for DOE’s Office of Science and tens of billions of dollars for other federal research agencies.

Those numbers shrank as the legislation went through many iterations and names. But the IRA still delivers a sizable investment in DOE lab infrastructure despite the removal of funding for the other research agencies.

The IRA, which offsets some \$370 billion in additional spending with revenue from an array of taxes, was the result of protracted negotiations between Senate Majority Leader Chuck Schumer (D-NY) and Senator Joe Manchin (D-WV). Manchin’s opposition to climate and spending provisions in Biden’s original plan and a subsequent \$2 trillion version was sufficient to kill both bills. But Manchin had a change

of heart that allowed the Democrats to prevail in the Senate on 7 August, with Vice President Kamala Harris breaking a 50-50 tie. On 12 August, the House of Representatives approved the measure on a party-line vote of 220 to 207, and Biden signed it into law on 16 August.

Despite his concerns about additional federal spending, Manchin has repeatedly sought to boost support for DOE’s network of 17 national labs, including the National Energy Technology Laboratory in his home state. That lab is funded through DOE’s Office of Fossil Energy and Carbon Management, which in the IRA would receive \$150 million over 5 years.

The House’s original version of Build Back Better spelled out how much DOE should spend on each of dozens of specific projects. In contrast, the IRA simply divides the \$1.5 billion among the office’s seven research programs and leaves other decisions to DOE officials, an approach Madia applauds because it enables DOE to be selective.

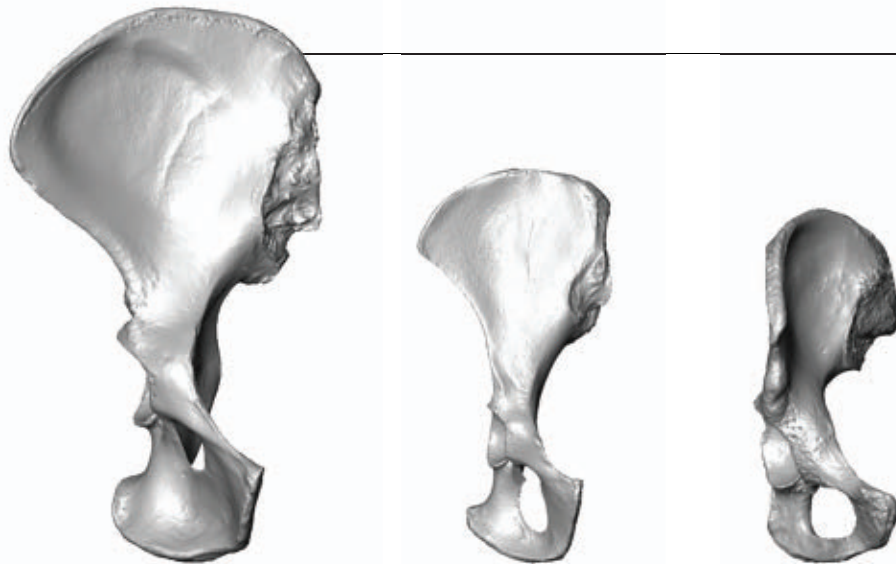
“The specific spend plan is being finalized internally in the Office of Science,” says Harriet Kung, the agency’s deputy director for science programs. But it’s not hard to guess where much of the money is likely headed.

High energy physicists at Fermi National Accelerator Laboratory in Batavia, Illinois—DOE’s only high energy physics lab—are gearing up to build a massive neutrino experiment. Its price tag has doubled to \$3 billion, so it could certainly use the help. Similarly, the extra money could kick-start a proposed Electron-Ion Collider to be built at Brookhaven National Laboratory in Upton, New York, at a cost of between \$1.7 billion and \$2.8 billion.

DOE will prioritize “signature facility projects” to advance schedules and reduce risks, Kung says, and will favor projects nearing completion. It will also consult with the White House and Congress, Kung says. “All of these approvals are necessary before any funding will be allocated.” ■

“I’m surprised science got anything in this bill.”

Bill Madia,
former Department of Energy
lab director



Compared with gorilla and chimp pelvises (left and middle), the human pelvis is curved and rotates out to the side to support upright walking.

EVOLUTIONARY BIOLOGY

Scientists isolate the genes that shape the human pelvis

Embryonic tissue samples reveal how pelvis shape—primed for bipedalism—comes to life

By Michael Price

The wide, basin-shaped human pelvis is a defining physical feature of our species. Without it, we couldn't walk upright or give birth to big-brained babies. Now, a new study of human embryos has pinpointed the window in embryonic development during which the pelvis begins to look humanlike and identified hundreds of genes and regulatory RNA regions that drive this transformation. Many bear the hallmarks of strong natural selection for bipedalism, the authors conclude.

"It is a really impressive study, especially the genomic part, which uses all the bells and whistles of state-of-the-art-analysis," says Marcia Ponce de León, an anthropologist at the University of Zürich (UZH) who was not involved with the work, which was reported this week in *Science Advances*. The results, she adds, support the idea that evolution often produces new physical features by acting on genetic switches that affect early embryonic development. Such predictions are "easy to state but very difficult to actually demonstrate, and this is what the authors did," she says.

The pelvic girdle in primates consists of three major parts: blade-shaped bones, called ilia, that fan out to form the hips and, below those, two tube-shaped fused bones known as the pubis and ischium, which give

shape to the birth canal. Great apes have relatively elongated ilia that lie flat against the back of the animals, as well as relatively narrow birth canals. Humans have shorter, rounded ilia that flare out and curve around. The reshaped ilia provide attachment points for the muscles that make upright walking more stable, and a wider birth canal accommodates our big-brained babies. Terence Capellini, an evolutionary biologist at Harvard University, says those pelvic patterns were already emerging in early human ancestors such as the 4.4-million-year-old hominin *Ardipithecus ramidus*, which had slightly turned-out ilia and is thought to have at least occasionally walked on two feet.

When and how those features take shape in human gestation had been mysterious, however. Many of the key human pelvic features, such as its curved, basinlike shape, are already developed by week 29. But Capellini wondered whether they might emerge earlier, when the pelvis has not yet turned to bone, but instead has scaffolding made from cartilage.

With the consent of women who had legally terminated their pregnancies, the researchers examined 4- to 12-week-old embryos under a microscope. They found that roughly around the 6- to 8-week mark, the ilium begins to form and then rotates into its telltale basinlike shape. Even as other cartilage within the embryo starts to ossify into bone, Capellini's team found this cartilage stage in the pelvis

seems to persist for several more weeks, giving the developing structure more time to curve and rotate. "These aren't bones, this is cartilage that is growing and expanding and taking that shape," Capellini says.

Next, the researchers extracted RNA from different regions of the embryos' pelvises to see which genes were active at different developmental stages. Then, they identified hundreds of human genes within specific pelvic sections whose activity seemed turned up or down during the first trimester. Of these, 261 genes were in the ilium. Many of the downregulated genes are involved in turning cartilage to bone, whereas many of the upregulated genes maintain cartilage, Capellini says, and possibly act to keep the ilium in a cartilaginous stage for longer.

By comparing the developing pelvis' genetic activity with a mouse model's, the researchers also identified thousands of genetic on/off switches seemingly involved in shaping the human pelvis. Stretches of DNA within those switches appear to have evolved rapidly since our species' split from our common ancestor with chimpanzees. But among modern humans, those regulatory bits in the ilium show strikingly little variation. That uniformity, the researchers say, is a sign that natural selection put—and continues to put—intense pressure on the ilium to develop in a highly specific way.

"We think this is really pointing to the origins of bipedalism in our genome," Capellini says of his team's work.

Martin Häusler, an anthropologist at UZH, says he's not surprised at the evidence for intense selective pressure on the pelvis, but adds that the findings offer an impressive look into some of the pelvic changes "at the very origin of what makes us human." Future work comparing human embryos with other primate embryos—rather than mouse models—would allow for an even better look at how natural selection reshaped the human pelvis, he adds.

The emerging understanding could also help scientists devise treatments for hip joint disorders or predict complications in childbirth, says Nicole Webb, a paleoanthropologist who studies pelvic anatomy at the University of Tübingen. Deviations from the genetic program that Capellini's team identified can result in disorders such as hip dysplasia and hip osteoarthritis, she notes. "I hope that it has major implications for making people's lives better. That would be huge, to connect paleoanthropology with real life," Webb says. ■

IMAGE: TERENCE CAPELLINI

COVID-19

Long Covid clues emerge from patients' blood

Study implicates lack of key hormone, battle-weary immune cells, and awakened viruses

By Jennifer Couzin-Frankel

An ambitious study of people with Long Covid, the mysterious, disabling symptoms that can trail a SARS-CoV-2 infection, has turned up a host of abnormalities in their blood. The clues add to a body of evidence hinting at drivers of the condition and potential treatments worth testing. They also suggest that, as many scientists and patients have suspected, Long Covid shares certain features with myalgic encephalomyelitis/chronic fatigue syndrome (ME/CFS), another condition thought to follow an infection.

The new study, posted as a preprint last week, was modest in size, examining just 99 people with Long Covid. “But it went very deep, it went into granular aspects of the T cells, the antibody response,” says Eric Topol, director of the Scripps Research Translational Institute, who was not involved in the work. “This is exploratory, but it’s the foundation for much bigger studies.”

The Long Covid patients, most of them struggling with intense fatigue, brain fog, and other symptoms, had low levels of cortisol, a stress hormone that helps the body control inflammation, glucose, sleep cycles, and more. Features of their T cells indicated their immune system was battling unidentified invaders, perhaps a reservoir of SARS-CoV-2 or a reactivated pathogen such as Epstein-Barr virus.

Other groups studying Long Covid patients have reported similar results this year, including in a January *Cell* paper that documented low cortisol in those with long-lived respiratory symptoms, and reactivation of viruses in patients with neurological issues. Collectively, these data “make me think about what other drugs we can test,” such as virus-directed antibodies or targeted anti-inflammatories to tame the immune system, says Emma Wall at University College London and the Francis Crick Institute, who co-leads a large trial of potential Long Covid therapies.

The new Long Covid project began in late 2020, when Yale University immunologist Akiko Iwasaki teamed up with David Putrino, a

neurophysiologist at the Icahn School of Medicine at Mount Sinai who was caring for affected patients. The pair wanted to compare those patients with people who had never been infected—and those who had recovered. To Putrino’s surprise, “It was quite challenging to find people who were fully recovered from COVID.” Many post-COVID-19 volunteers described themselves as healthy but then admitted, for example, that their once-normal gym workouts were too exhausting to resume. In the end, the team signed on 39 COVID-19-recovered volunteers among a total of 116 controls.

The low cortisol levels in the Long Covid patients, about half of normal levels, aren’t a total surprise: Symptoms such as fatigue and muscle weakness are associated with less of the hormone. The cause remains a mystery. ACTH, a hormone made by the pituitary gland that controls cortisol production, was at normal levels in the Long Covid group. Furthermore, note Putrino and others, some Long Covid patients outside the study have tried short courses of steroids, which can treat low cortisol, but say they haven’t helped. Next, the researchers plan to track cortisol levels throughout the day in

Long Covid; the steroid rises and falls on a daily cycle, and the

initial research only tested it in the morning.

The Long Covid blood samples were also awash with a category of “exhausted” T cells that can be recognized by certain markers they express. Such cells surge in the ongoing presence of pathogens—suggesting “the bodies of people with Long Covid are actively fighting something,” Putrino says.

This battle would produce chronic inflammation, which matches many Long Covid symptoms. By measuring levels of antibodies against viral proteins released in the blood, the study also noted reactivation of Epstein-Barr virus and other herpesviruses whose genes can sit dormant inside infected cells for extended periods. Iwasaki was intrigued to learn that the degree of T cell exhaustion appeared to track with Epstein-Barr virus reactivation, though she doesn’t consider that virus the only potential culprit. SARS-CoV-2 may linger in Long Covid patients, too, she and others say. Epstein-Barr reactivation, low cortisol, and T cell exhaustion have all turned up in some ME/CFS patients.

Long Covid is far from uniform, the new study makes clear—for example, only about 20% to 30% of the study’s patients had very high levels of exhausted T cells. But, “The level of consistency is great” among recent studies probing Long Covid biology, says James Heath, president of the Institute for Systems Biology, an author of the *Cell* paper that found low cortisol and virus reactivation. He notes that his group’s study examined patients about 3 months after SARS-CoV-2 infection, whereas Iwasaki and Putrino’s cohort was on average more than a year out from their COVID-19.

Putrino and Iwasaki say it’s time to forge ahead with new trials of potential therapies, which could also elucidate Long Covid’s causes and whether subsets of patients are more likely to respond to certain interventions. Iwasaki’s experimental therapy wish list is long and includes cortisol supplementation; Epstein-Barr virus-targeting therapy; the antiviral drug Paxlovid, now used for acute COVID-19; and even therapies that deplete B cells, which are used to treat autoimmune disease and calm the immune system.

“We should be trying these right now,” Iwasaki says. “As a basic scientist, of course I’d like to have all the pieces of the puzzle” before launching trials. “But the patients, they can’t wait.” ■



Subscribe to **News from Science** for unlimited access to authoritative, up-to-the-minute news on research and science policy.



bit.ly/NewsFromScience



ANYWHERE BUT HERE

China now insists the pandemic didn't start within its borders. Its scientists are publishing a flurry of papers pointing the finger elsewhere

When Alice Hughes downloaded a preprint from the server Research Square in September 2021, she could hardly believe her eyes. The study described a massive effort to survey bat viruses in China, in search of clues to the origins of the COVID-19 pandemic. A team of 21 researchers from the country's leading academic institutions had trapped more than 17,000 bats, from the subtropical south to the frigid

By **Jon Cohen**

northeast, and tested them for relatives of SARS-CoV-2.

The number they found: zero.

The authors acknowledged this was a surprising result. But they concluded relatives of SARS-CoV-2 are "extremely rare" in China and suggested that to pinpoint the pandemic's roots, "extensive" bat surveys should take place abroad, in the Indochina Peninsula.

"I don't believe it for a second," says Hughes, a conservation biologist who's now

at Hong Kong University. Between May 2019 and November 2020, she had done her own survey of 342 bats in the Xishuangbanna Tropical Botanical Garden, a branch of the Chinese Academy of Sciences (CAS) in Yunnan province where she worked at the time. As her team reported in *Cell* in June 2021, it found four viruses related to SARS-CoV-2 in the garden, which is about three times the size of New York City's Central Park.

The new study had sampled bats near that same location, at an abandoned mine that had yielded another close SARS-CoV-2

CREDITS: (ILLUSTRATION) KLAWE RZECZY; (PHOTOS) (FLAG) NATIONAL PEOPLE'S CONGRESS OF PRC; (VIRUSES) V. ALTOUNIAN/SCIENCE; (RACCOON DOG) ALVIN HUANG/GETTY IMAGES; (BATS) FLETCHER & BAYLIS/SCIENCE SOURCE; (GUARD HAND) NG HAN GUAN/AP PHOTO; (HUANAN MARKET) HECTOR RETAMAL/AFP/GETTY IMAGES; (GURNEY AND BARRICADE) HECTOR RETAMAL/AFP/GETTY IMAGES; (SPRAYER) ZHANG GUANJUN/NANFANG DAILY/VCG/GETTY IMAGES; (POLICE TAPE) GWENGOAT/ISTOCK.COM; (WUHAN, YELLOW CRANE TOWER) SLEEPINGPANDA/SHUTTERSTOCK



◀ Police closed the Huanan Seafood Market in Wuhan in January 2020, shortly after the first cluster of COVID-19 cases surfaced.

China has rejected calls for independent probes of the Wuhan Institute of Virology and dismissed the theory that SARS-CoV-2 leaked from its labs. ▶



relative in 2013, and at other sites in nearly half of China's 31 provinces. And yet the only thing researchers found were viruses close to SARS-CoV-1, which caused the outbreak of severe acute respiratory syndrome 2 decades ago.

Edward Holmes, an evolutionary biologist at the University of Sydney who co-authored the *Cell* paper with Hughes, dismisses the preprint with a single word: "Bullshit." Although Holmes has no evidence the team behind the study did anything underhanded, "There is a big contradiction between this study and others that needs to be explained," he says.

But the paper meshed with a growing political reality in China. From the start of the pandemic, the Chinese government—like many foreign researchers—has vigorously rejected the idea that SARS-CoV-2 somehow originated in the Wuhan Institute of Virology (WIV) and escaped. But over the

past 2 years, it has also started to push back against what many regard as the only plausible alternative scenario: The pandemic started in China with a virus that naturally jumped from bats to an "intermediate" species and then to humans—most likely at the Huanan Seafood Market in Wuhan.

Beijing was open to the idea at first. But today it points to myriad ways SARS-CoV-2 could have arrived in Wuhan from abroad, borne by contaminated frozen food or infected foreigners—perhaps at the Military World Games in Wuhan, in October 2019—or released accidentally by a U.S. military lab located more than 12,000 kilometers from Wuhan. Its goal is to avoid being blamed for the pandemic in any way, says Filippa Lentzos, a sociologist at King's College London who studies biological threats and health security. "China just doesn't want to look bad," she says. "They need to maintain an image of control and compe-

tence. And that is what goes through everything they do."

The idea of a pandemic origin outside China is preposterous to many scientists, regardless of their position on whether the virus started with a lab leak or a natural jump from animals. There's simply no way SARS-CoV-2 could have come from some foreign place to Wuhan and triggered an explosive outbreak there without first racing through humans at the site of its origin. "The idea that the pandemic didn't originate in China is inconsistent with so many other things," says Jesse Bloom, a virologist at the Fred Hutchinson Cancer Research Center who has argued for more intensive studies of the WIV lab-accident scenario. "When you eliminate the absurd, it's Wuhan," says virologist Gregory Towers of University College London, who leans toward a natural origin.

Yet Chinese researchers have published a flurry of papers supporting their government's

“anywhere-but-here” position. Multiple studies report finding no signs of SARS-CoV-2-related viruses or antibodies in bats and other wild and captive animals in China. Others offer clues that the virus hitched a ride to China on imported food or its packaging. On the flip side, Chinese researchers are not pursuing—or at least not publishing—obvious efforts to trace the sources of the mammals sold at the Huanan market, which could yield clues to the virus’ origins.

Wu Zhiqiang, a virologist at Peking Union Medical College who is the lead author of the Research Square preprint, wouldn’t say whether the government vetted his study, which is still under review at a journal. But he denies that his results were influenced by Beijing, let alone cooked up to please it. “We do not represent the government or anyone else,” writes Wu, who says his team is not arguing that the pandemic originated outside China. “We just stand by our data, and all our data are open access.”

Yet Holmes, who has close and long-standing ties with Chinese scientists, worries they have become entangled in the government’s political messaging. “There’s clearly an official narrative that’s come down from on high that appears to be: ‘The investigations have been completed now, and they couldn’t find where it came from,’” Holmes says. “It’s no longer China’s problem—this is about a problem from elsewhere.” He says his collaborators in China have become increasingly guarded, wary of contradicting that narrative with their own findings and opinions.

Hughes left Xishuangbanna in December 2021 after 9 years in China because it had become too difficult to continue her bat research there. Most origin-related research required government review, she says, and she also needed a green light from CAS. “The dialogue is just: ‘We don’t want it to have come from here in any form,’” she says. “And that’s not a sensible way of doing science.”

Science attempted to discuss these issues with George Gao, who until last month headed the Chinese Center for Disease Control and Prevention (CCDC) and is a lead author on several key papers about the pandemic’s origins. “What can I say?” Gao texted back. “Best wishes.”

THE NOTION THAT it all began at the sprawling Huanan market in downtown Wuhan was not controversial at first. A 31 December 2019 report from the Wuhan Municipal Health Commission announced a cluster of 27 unexplained pneumonia cases linked to the market, which was immediately closed. Three weeks later, after a novel coronavirus had been identified as the cause,

government researchers concluded in the *China CDC Weekly* that “all current evidence points to wild animals sold illegally in the Huanan Seafood Wholesale Market.” On 27 January, the official Chinese news agency Xinhua reported that 33 “environmental samples” from the market had tested positive for the virus and all but two came from areas selling wildlife. Again, the results suggested “the virus stems from wild animals on sale at the market,” the article stated.

That spring and summer, origin research continued apace in China, Hughes says. Her group dug into bat samples it had collected in 2019 at the Xishuangbanna gardens and discovered one of the closest relatives of SARS-CoV-2 yet found, which shared 93.3% of its genetic sequence, a finding it published in June 2020 in *Current Biology*.

 **The dialogue is just: ‘We don’t want it to have come from here in any form.’**
Alice Hughes, Hong Kong University

“Throughout 2020, we were encouraged to do more work,” Hughes says.

But the Chinese government’s counter-narrative had started to take shape. By the end of January, published reports about the earliest cases suggested almost half had no connection to Huanan, raising doubts about its role as the outbreak’s origin. The lab-leak theory had also started to circulate internationally, and before long, then-U.S. President Donald Trump began blaming WIV, which had studied bat coronaviruses for 15 years, for sparking the “kung flu” pandemic with the “China virus.” In March 2020, Zhao Lijian, a spokesperson for China’s foreign ministry, flipped the tables, asking whether the virus came from a U.S. Army lab at Fort Detrick in Maryland.

The Chinese government also began to clamp down on interactions between origin researchers and the media. Suddenly, giving an interview required permission from the Ministry of Science and Technology. “Part of that was for a good reason,” Hughes says. “There was some very bad science going on, and they didn’t want that to come out.”

The country’s new mindset colored a March 2021 report from an international team sent to China earlier in the year to study the origin of the pandemic under the auspices of the World Health Organization (WHO). The report deemed a laboratory accident “extremely unlikely” but ranked the frozen food

scenario as “possible.” A direct zoonotic spillover ranked higher, as “possible-to-likely,” yet the report questioned whether the jump could have happened at the Huanan market, claiming animals that might have carried the virus weren’t there. “No verified reports of live mammals being sold around 2019 were found,” the report flatly stated.

Dutch virologist Marion Koopmans, a prominent member of the WHO team, acknowledges politics played a role in both statements. Koopmans says she never put much stock in the frozen food route. As to the notion that mammals weren’t sold at the Huanan market, she says the international scientists on the mission were “highly skeptical” of the claim. They even showed their Chinese counterparts a photo Holmes had taken a few years earlier at that very market that showed a caged raccoon dog—a species known to be highly susceptible to SARS-CoV-2 and able to transmit it.

But in the end, hard evidence that the market sold mammals in 2019 was lacking, and the international scientists went along with the “no verified reports” phrasing, Koopmans says, to avoid “the political situation.”

To Chris Newman, an ecologist at the University of Oxford who has long studied the illegal sale of wildlife at Chinese markets, the report marked a significant shift in the Chinese government’s strategy. “They tried to start to change the narrative, and they’ve been sort of trapped in that ever since,” Newman says. “They’re trying to look for any alternative explanation, however implausible that might be. It’s almost like being caught in a childish lie.”

As it happened, Newman knew the statement about the Huanan market was dead wrong. “Somebody was misleading the World Health Organization here,” he says. Newman had helped conceptualize and write a study led by Zhou Zhao-Min of China West Normal University that surveyed mammals sold in Wuhan markets for 2 years prior to the pandemic, looking for the source of a tick-borne infection. It documented nearly 50,000 mammals for sale at Wuhan’s animal markets, including Huanan. Among the species were raccoon dogs and civets, also highly vulnerable to SARS-CoV-2.

The team could have published the study as a preprint, but it wanted the “credibility” of a peer-reviewed paper, Newman says. That took a long time. The paper finally appeared in *Scientific Reports* in June 2021—revealing the glaring misdirection in the WHO report published 3 months earlier. Zhou and Newman had sent a draft of their paper to WHO in October 2020, realizing its potential significance for the origins debate,

but the agency had not done anything with it. “That was a big glitch,” Koopmans says. “I find that annoying—I’m putting it mildly.”

Zhou and the other Chinese co-author, Xiao Xiao, did not respond to repeated requests from *Science* for interviews about the study. “When the paper did finally come out, they were both taken aside by their institutions and told off,” Newman says. “They were told to cease all work on wildlife trade. And they were quite worried.”

The paper left out a key detail that might help clarify the pandemic’s origin: It did not say whether the researchers collected ticks—which suck mammalian blood—or took biological samples directly from the animals. Either could be tested for antibodies to SARS-CoV-2 or genetic remnants of the virus itself to find out which animal species harbored it. Newman wasn’t involved with the sample collection, so he asked Zhou, but to no avail. “Zhou is not at liberty to say, and he doesn’t reply,” Newman says. “It’s so self-evident that surely somebody in the Chinese CDC has done exactly that. Surely somebody knows the answer.”

EVERYONE FROM LAB-LEAK proponents to WHO Director-General Tedros Adhanom Ghebreyesus and U.S. President Joe Biden criticized the WHO report, and in its wake, China’s willingness to probe the origins of the pandemic took another nosedive. The government scuttled ambitious follow-up plans proposed by the group: studies of viral genomes of the earliest cases, to trace the initial spread; retrospective analyses of Chinese hospital records prior to the outbreak and of illnesses in high-risk groups such as farmers and veterinarians; and mapping supply chains of farms that sold to the Huanan market. “The derailment of this whole process is horrible,” Koopmans says.

The finger-pointing at other countries also ramped up. On 17 September 2021, *The Lancet* published a four-page correspondence by Wu and authors at CCDC and several of the country’s top academic institutions claiming the WHO committee had carried out “an extensive investigation in Wuhan in the past year.” The letter argued it was now “reasonable” to start a “worldwide” hunt for the origin and laid out a plan for doing so. Invoking the lofty rhetoric common in global health circles—“humankind must work together”—the article stressed that the massive global investigation it proposed “should be carried out by scientists on the basis of science alone, without interference or coercion from political forces.”

By now more than two dozen reports from Chinese scientists have suggested the virus

came from elsewhere. Many, including Wu’s *Lancet* letter, explored the imported frozen food hypothesis. After China had all but stopped COVID-19 transmission by March 2020, researchers linked small outbreaks to imported salmon at a Beijing market, frozen cod offloaded at shipping docks in Qingdao, and imported pollock packaged by a company in Dalian. Other scientists tested more than 50 million swabs of frozen food packages from across China and found that nearly 1500 had genetic remnants of the virus. In the *China CDC Weekly* they asserted it “cannot be ruled out” that just such contamination triggered the initial Huanan market outbreak.

Yet researchers rarely detected infectious virus on the food—only viral RNA—and food regulators in the United States, Europe, Australia, and New Zealand have dismissed this route of transmission. There’s also nothing

tified people as having the disease who did not, the authors contended. They combined spatial analyses of where infected people lived and worked, genetic sequencing of early viral samples, and the location of positive environmental samples and the stalls that sold mammals highly susceptible to SARS-CoV-2 to conclude the market was the “epicenter” of the pandemic.

But a preprint from China published a day earlier by Gao and many co-authors from CCDC reached a starkly different conclusion. The study analyzed more than 1000 environmental samples from the Huanan market and found SARS-CoV-2 in 73 of them, indicating the virus was in the sewer, on the ground, and in “containers,” some of which Worobey suspects may have been cages that held mammals, based on their location.

In a so-called metagenomic analysis, the researchers also found several samples had a blend of viral and human RNA, “which highly suggests the SARS-CoV-2 might have derived from *Homo sapiens*” in the market, the authors wrote. In other words, humans didn’t catch SARS-CoV-2 from animals at the market. Instead, people might have brought it to the market from elsewhere.

Again, the researchers mentioned viral traces on imported frozen food and the retrospective studies from other countries as clues to a foreign origin. “Definitely, more work involving international coordination is needed to investigate the real origins of SARS-CoV-2,” they concluded.

Worobey and Holmes were gobsmacked by what the study didn’t say. In a graphic that illustrates the metagenomic analysis, dots show the virus mixed with RNA from several species other than humans, but the preprint does not specify which species. “They ignore all the other animals in there,” Holmes says.

A researcher who claims to have reviewed the manuscript for *Nature* says it’s not clear whether the omission was intentional or due to sloppy science, but either way, “I said you cannot publish this unless they release the raw data.” The reviewer, who asked not to be named, noted that the paper also includes an analysis of a sample from a defeathering machine at the market that found only human DNA. “Either only humans were defeathered or the analysis was wrong—pick your favorite,” the reviewer says. Gao did not reply to *Science*’s specific request to discuss the metagenomic data.

IN AN ATTEMPT to reboot the origin probe, WHO last year created the Scientific Advisory Group for the Origins of Novel Pathogens (SAGO), a new international team of 26 people. SAGO’s preliminary report,

“China just doesn’t want to look bad. They need to maintain an image of control and competence.”
Filippa Lentzos, King’s College London

that connects imported frozen food at the Huanan market to the outbreak there.

Besides, if the virus arrived in Wuhan on frozen food, “it means the virus had to be already circulating somewhere else, and there’s no evidence of that,” Koopmans says. Studies from Spain, Italy, France, Brazil, and the United States have reported finding genetic pieces of the virus—or antibodies to it—in stored tissue from patients or wastewater samples that predate the Wuhan outbreak. Chinese scientific papers and media have made much of such findings, but skeptics say the viral traces may be contaminants and the antibodies could be responses to other pathogens that “cross-react” with SARS-CoV-2.

As for the frozen food route, Holmes says it’s not even worth discussing. “You might as well just say it came from cosmic dust.”

CHINA HAS NOT allowed foreign researchers into the country to conduct independent origin studies, but that hasn’t stymied all investigations. On 26 February, a large international team that included Holmes and Michael Worobey, an evolutionary biologist at the University of Arizona, published two preprints that offered a new analysis of the outbreak’s early days—and pointed directly at the Huanan market. (*Science* published peer-reviewed versions online on 26 July.)

Early reports suggesting some cases were not connected to the market mistakenly iden-

Health officials
in Taiyuan
swab fish at a
market in January
2021. Chinese
researchers
say imported frozen
food has caused
COVID-19 outbreaks
in the country.



“
More and
more clues ...
are pointing the
origins of
SARS-CoV-2 to
sources around
the world.

Zhao Lijian,
Chinese foreign ministry

A bat is sampled for
viruses in Thailand.
China insists
SARS-CoV-2 likely
originated outside
its borders and
has advocated for
more global
efforts to find the
virus' origin.



issued on 15 May, offers recommendations echoing those of the earlier team, with two major differences: It calls for more studies of a potential “laboratory incident”—although members from China, Russia, and Brazil dissented—and it recognizes that the Huanan market did sell mammals susceptible to the virus.

But by then, “anywhere but here” had become the Chinese government’s party line. “More and more clues from the international science community are pointing the origins of SARS-CoV-2 to sources around the world,” Zhao, the foreign press ministry spokesperson, asserted at a 10 June press conference in response to the SAGO report. He again brought up the controversial reports of very early cases outside China and called for investigations at the “highly suspicious” Fort Detrick laboratory.

Wu says many Chinese researchers remain open to the idea that the virus origi-

nated in China. “We have never ruled out Wuhan or China in the next phase of the investigation, and Chinese researchers are still working on it and continuously getting data,” he says. He stresses that, in response to peer reviewers, his team has “toned down” some of its bold assertions in the Research Square preprint about the bat survey in China. For example, instead of calling viruses related to SARS-CoV-2 in Chinese bats “extremely rare,” the manuscript now says they “might be rare.”

But the clampdown on bat research that Hughes experienced has continued, especially at the local level, says Aaron Irving, a bat researcher at Zhejiang University. “People are now often scared to help out bat researchers in case they also get in trouble,” he says. Irving stresses that his institution still supports his work, but what he calls “non-scientific interference” has taken a toll. “Everyone in the bat field got a little secretive

and protective too because they don’t want to be targeted.”

Some researchers think too much time has passed to solve the origin mystery. But others who favor a natural origin say they only need a few more jigsaw pieces to complete the puzzle. Newman suspects Chinese officials and researchers may already hold some of those pieces. “They should be in a position to know an awful lot more than we are currently told,” he says.

There is no shame in admitting that the virus came from wild animals illegally sold at a market, Newman adds. “To leave it as an open question, it’s just going to breed intrigue about why the Chinese have not given us a clear explanation,” Newman says. “Why the smoke and mirrors? Whereas if they come up with something that we could all just accept, well, then it will be case closed. Can’t we persuade them that this is the right thing for everybody to do?” ■

INSIGHTS



POLICY FORUM

FOOD

Research and policy for the food-delivery revolution

Implications for nutrition, environment, and work may be considerable

By Eva-Marie Meemken¹, Marc F. Bellemare², Thomas Reardon^{3,4}, Carolina M. Vargas³

Globally, consumers have increasingly been getting the meals they consume delivered by third parties such as Doordash, Grubhub, Wolt, or Uber Eats. This trend is attributable to broader changes in food systems and technological and institutional innovation (such as apps and digital platforms and the increased reliance on third parties for food delivery) and has sharply accelerated as a consequence of the lockdowns resulting from the COVID-19 pandemic (1, 2). Global

PHOTO: CARSTEN KOALL/PICTURE ALLIANCE/GETTY IMAGES



A driver for food delivery service Uber Eats arrives to pick up food in Berlin's Friedrichshain district, September 2021.

DRIVING THE REVOLUTION

There has been a steady rise in all regions of the globe in the share of sales of food-service revenue from home delivery, from 2 to 7% in 2009 to 6 to 16% in 2019, and then a steep spike in 2021 to 13 to 27% (see the figure). All regions showed a similar growth pattern, and all remained within a tight band, except Latin American countries (LACs), which stayed well above the others. This delivery revolution is part of and driven by broader transformations of the entire food system (1, 4). We highlight three global trends in particular that are important: (i) the nutrition transition, (ii) growth and transformation in the food-service sector, and (iii) the spread of technological and institutional innovations.

Global diets have been changing as a result of economic growth, urbanization, increasing female labor market participation, and growing international trade of food and other commodities, among other factors (1, 4, 5). The nutrition transition refers to these changing dietary patterns, including rising demand for (i) higher-value products (such as fruits; vegetables; animal products; and products that meet high food safety, sustainability, or nutritional standards); (ii) processed foods that often contain high levels of sugar, salt, and fat and are often convenient and time-saving; and relevant to our context, (iii) food consumed away from home (such as in restaurants) and food prepared away from home (such as take-away food or food delivery) (1, 4, 5). The pandemic has—through lockdowns and quarantine orders—shifted much of the demand for food consumed away from home to food prepared away from home. With lockdowns and other COVID-19 measures being lifted in many countries, this trend is reversing somewhat, but we have good reason to believe that newly acquired food habits are here to stay (6).

Growth of the restaurant and broader food-service sector is a second trend that paved the way for the food delivery revolution. Restaurants and other food-service establishments have been spreading, first in high-income countries (HICs) from the 1960s on (6) and then in low- to middle-income countries (LMICs) over the past several decades, given increasing demand and reduced transaction costs by way of the agglomeration economies associated with greater urbanization. The restaurant sector emerged, first as informal-sector small and medium enterprises that eventually joined the formal sector, and then into large enter-

prises such as fast-food chains. In LMICs, this has been driven by domestic investment and by the liberalization of foreign direct investment inducing an influx of foreign chains (5). Historically, restaurants have often offered takeout or delivery services (6), but only with increasing competition has food delivery evolved as a profitable—and thus common—service offered by various types of restaurants.

Third, the spread of institutional and technological innovations has facilitated the delivery revolution. Delivery and takeout are as old as the restaurant as an economic institution. Delivery services were initially mainly offered by specialized lunch providers for lower-income workers (such as tiffin lunch boxes in India) and by restaurants serving easy-to-transport foods (such as pizza). Although food delivery was already widespread before the turn of the century as offered by restaurants themselves, the spread of information and communication technologies (ICT) was a key driver of the delivery revolution. The proliferation of landlines made remote ordering an accessible option for the masses. Remote ordering alters who travels (consumers versus producers) to bring food to homes, offices, or other locations and thus serves consumers eager to save time. The spread of ICT then made it more convenient to order remotely as well as to compare and discover different options (2).

The proliferation of ICT had another important implication: It led to restaurants outsourcing their delivery activities to new, third-party specialized actors. Providers such as Doordash and Grubhub act as middlemen, linking large numbers of consumers and large numbers of food providers. The outsourcing of delivery and the rise of these third-party intermediates is an institutional innovation that allows smaller establishments, which might hitherto not have had the capacity to offer delivery themselves, to reach a broader consumer base.

The “app-based” food-delivery sector has taken off over the past two decades. The COVID-19 pandemic accelerated the rise of delivery firms and the number of restaurants that pivoted toward delivery in order to remain profitable (1). Such unanticipated shocks often act as catalysts, spurring innovation and the adoption of new technologies.

revenues for the online food delivery sector were about \$90 billion in 2018, rose to \$294 billion in 2021, and are expected to exceed \$466 billion by 2026 (3). The consequences and policy implications of this “delivery revolution” remain poorly understood but deserve greater attention. We offer an overview of the drivers of the revolution and discuss implications for the environment, nutrition, and decent work, as well as recently implemented and potential policy options to address those consequences.

¹Food Systems Economics and Policy Group, ETH-Zurich, Zurich, Switzerland. ²Department of Applied Economics, University of Minnesota, St. Paul, MN, USA. ³Department of Agricultural, Food, and Resource Economics, Michigan State University, East Lansing, MI, USA. ⁴International Food Policy Research Institute, Washington, DC, USA. Email: emeemken@ethz.ch

IMPLICATIONS FOR POLICY AND RESEARCH

The food-delivery revolution has important implications for environmental protection, healthy diets, and poverty reduction through employment generation and decent work. In what follows, we discuss the small but growing body of scientific evidence in this area (2, 7) and highlight research gaps that are relevant for policy. Because of the limited nature of the empirical evidence on this topic, our discussion also draws on theoretical considerations and public discussions.

JOB CREATION AND DECENT WORK

The food-delivery revolution has created new jobs, with understudied implications for migrant workers and their households and communities, especially in LMICs. Most new jobs in this growing sector involve unskilled labor (more jobs created for delivery workers than for managers and tech personnel). In HICs, these jobs are often done by immigrants, including many undocumented migrants from LMICs (8), who send remittances home. During the COVID-19 pandemic, food-delivery jobs were also filled with local food-service employees who shifted from in-restaurant to delivery or warehouse work. In LMICs, those same urban jobs are often done by young rural migrants seeking opportunities outside of agriculture (9). Because fertility rates are high in many LMICs, the food delivery and broader food-services sector help absorb the “youth bulge.” The economic effects of the food-delivery revolution on workers’ households and communities remain poorly understood and are one direction for future research. Similarly, a better understanding of who selects into delivery jobs in different regions and countries can also help better design and target policies aimed at improving working conditions.

Delivery jobs are often precarious even in HICs, with poor safety standards and frequent traffic accidents, unpredictable schedules, long working hours, informal work arrangements, and low wages (8, 9). This is not only because delivery jobs are low skilled: Food delivery workers are also often freelance workers, like other gig-economy workers not directly hired but contracted with by the provider (8). The key concern is that the actual job meets many criteria of jobs that typically fall into the category of employment, and thus outsourcing shifts responsibilities and risks to workers. At the same time, those workers are often not supported by labor unions because they are self employed. Thus, even in regions with stringent labor regulations and high levels of unionization (such as Scandinavia), delivery workers often face precarious working conditions. In the case

of LMICs, many if not most delivery providers remain in the informal sector, where working conditions tend to be precarious. More research documenting working conditions among delivery workers in different regions and countries, and for different delivery firms would be useful and could focus on aspects such as payment and transportation modes, consumers’ tipping habits, recruitment strategies, and workers’ preferences and levels of satisfaction.

There are several policy options to improve working conditions among delivery workers, and key challenges differ across regions. In HICs, any real improvement would require addressing regulatory gray areas, especially those related to the mode of employment (for example, self employment and outsourcing of risks and costs by quasi-employers). In LMICs, monitoring

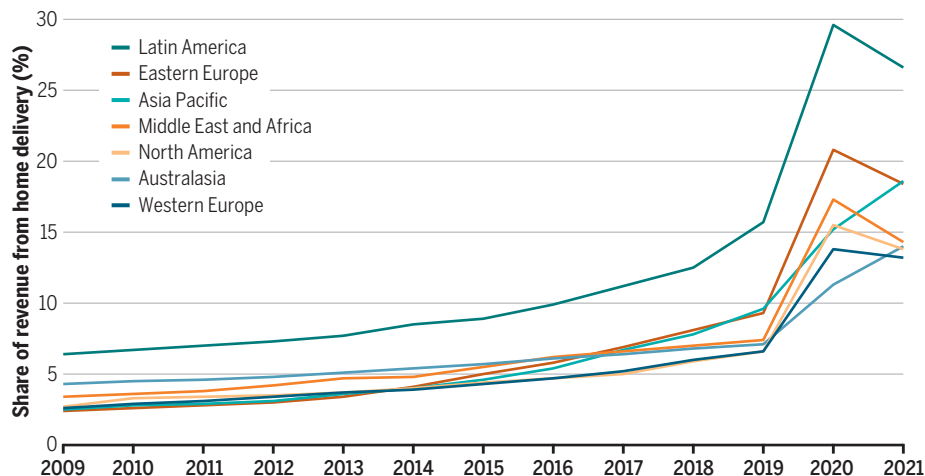
companies to pay for the maintenance of their worker’s bicycles. Some private sector-driven approaches have also emerged. In Switzerland, for example, some food-delivery providers have embraced public concerns around poor working conditions and recognized their consumers’ willingness to pay for better working conditions and have thus promised better employment conditions as part of their business and marketing model. Because all of these policies are new, their impact remains unclear and should be evaluated.

NUTRITION

The food-delivery revolution is both a cause and a consequence of the nutrition transition, exacerbating challenges to promoting healthy diets and food environments to reduce overweight [body-mass index

A global delivery revolution

Revenue from home delivery is growing, shown here as a share of the total revenue of food service (full and limited service restaurants, bars and cafes, and street stalls and kiosks). See the supplementary materials for details on the data.



is a key challenge. Because many delivery providers are small enterprises and operate in the informal sector, they are outside the reach of regulation and taxation. Even if new regulations are adopted, many LMIC governments are already strapped for resources to monitor and enforce regulations in fragmented industries in which there are many hundreds of thousands of small and informal providers. It would thus be a challenge to enforce worker payment and work-condition regulations in these contexts.

There are, however, several examples—mostly from HICs—of recent policies aimed at improving working conditions. For example, Australia is introducing regulations that require delivery companies to provide safety equipment and training to their workers. Germany is now requiring delivery

(BMI > 25], obesity (BMI > 30), and related noncommunicable diseases in HICs and increasingly in LMICs (4, 5).

Most of the research so far focuses on away-from-home food consumption in HICs without necessarily differentiating between delivery and restaurants, although the digitalization of food environments is an emerging research topic (7). Restaurant meals—especially fast food—often contain higher levels of salt, sugar, and fat than those of home-cooked meals. The evidence also suggests that eating restaurant food instead of eating home-cooked meals can incentivize overeating and a higher calorie intake (6)—for example, from high alcohol consumption (10) and selecting unhealthy meals (11). Yet in this comparison (restaurant versus home-cooked meals), the in-

come level of consumers matters because home-cooked meals of wealthy consumers tend to be healthier than those of less wealthy consumers (11).

An important question in this context is whether people eat more—or differently—when they get food delivered instead of eating in restaurants. Here, more research will be needed (7). Generally, the proliferation of delivery has increased the availability of both healthy and unhealthy options. The evidence so far suggests that many foods available by means of online platforms are of poor nutritional quality (12). Thus, an important empirical question is whether improved and more convenient access to especially unhealthy meals through delivery increases consumption rates of unhealthy meals. Beyond accessibility, social context might also matter (for example, ordering decisions can be influenced by peers). Whether delivery promotes overeating relative to dining in is also an open question. Delivery might promote overeating relative to restaurants given minimum ordering thresholds on many delivery apps and the absence of social control, which may limit the unhealthfulness of what one orders when eating in a restaurant. However, delivery could reduce overeating because leftover food from delivery might be saved for later or shared because getting food delivered reduces the near obligation, when dining in a restaurant, of ordering as many meal portions as there are diners.

Thus, more research is needed to inform policy, especially in LMICs, where our understanding of the food landscape is less complete than in HICs. Because unhealthy foods and ingredients are a key problem in the context of both restaurants and delivery, taxes on certain products (such as sugar-sweetened beverages) could be imposed, as has already been done in many countries (5). However, broader policies that address the underlying causes of poor food choices (for example, through health education, school feeding programs, social protection, safety nets, and pro-poor growth) are also likely needed.

ENVIRONMENT AND CLIMATE CHANGE

Some of the environmental challenges facing the food delivery sector include single-use packaging, food waste, and transportation and energy consumption (such as for cooking), which cause air and water pollution as well as CO₂ emissions (13).

It is likely that delivery causes more packaging waste than does home preparation, and also somewhat more than restaurants, because more packaging is used for food delivery, takeout, and fast food (such as trays, cups, utensils, and napkins). The use

of single-use packaging has soared recently with the rise of food delivery. This causes solid waste pollution, especially in LMICs, where solid waste and recycling systems are often of poor quality (14).

Several policy options are available to address these problems, but more research is needed to understand which approaches are most effective. In LMICs, investments in recycling systems and environmental education are required. In both LMICs and HICs, reducing the use of plastic items should be a policy goal, and several countries have already banned certain single-use items (such as plastic straws). Alternatively, firms using these items could be taxed. Policy-makers could also subsidize the development and use of reusable or compostable packaging, promoting a growing trend. An increasing share of consumers wants environmentally friendly restaurant and delivery practices. Over time, this trend will lead to more firms—especially those targeting higher-income, environmentally conscious consumers—to use compostable or reusable packaging (14, 15).

Whether food prepared away from home causes more food waste is an empirical question. It is also an open question whether where an individual eats affects how much food waste is generated; consumers might order more food when that food is delivered given that delivery fees are higher per unit when small quantities are ordered. When there is poor coordination between restaurants and food delivery, meals might not get picked up in time and thus go to waste. Policies to encourage food waste reduction include education and regulation. Some European countries, for example, require supermarkets and bakeries to donate food that is not sold in time. During the pandemic, some food-delivery firms partnered with community organizations to donate leftover meals to the poor. Some restaurants also offer leftover meals late at night at very reduced prices through online platforms. Policy-makers could support such initiatives.

Transportation-related carbon dioxide (CO₂) emissions occur irrespective of where meals are consumed. Ingredients need to be transported to the place where the food is prepared. Then, meals and consumers need to be in the same place, whether that place is a restaurant or consumers' homes. When consumers do not drive themselves (when they order food delivered), average distances that meals travel might increase. Large-scale food delivery and preparation, however, likely exploit economies of scale in various areas relevant to resource use and environmental protection. For example, delivery workers, unlike consumers,

plan routes to deliver more than one order. Similarly, buying larger quantities of ingredients at once also reduces transport emissions per unit of food, and cooking larger quantities might also reduce resource use (such as water and energy) per unit of food.

We are unaware of research on this topic, but given the many different scenarios and means of transportation (such as bicycle, motorcycle, or car), cooking, and other forms of energy use (such as refrigeration), it seems that making generalizable statements about the relationship between CO₂ emissions and delivery is going to be difficult. For transportation, one's best hope to do so might be to look at the progressive spread of adoption over time and compare it with air quality over the same time period for several metropolitan areas. That said, in many European cities, delivery workers use bicycles because they are faster and cheaper. The most effective way to reduce transport-related emissions might be to make cities more bicycle-friendly.

As of writing this paper, several countries have implemented new policies related to the food delivery sector. Such efforts may help advance progress toward the United Nations' Sustainable Development Goals (SDGs), especially those focusing on reducing all forms of malnutrition (SDG 2) and poverty, ensuring decent work, and spurring economic growth (SDGs 1 and 8), and sustainable farming and consumption (SDG 12). More research will nonetheless be needed to evaluate various policies related to the delivery sector, both *ex ante* and *ex post*. ■

REFERENCES AND NOTES

1. T. Reardon *et al.*, *Agric. Econ.* **52**, 459 (2021).
2. A. Shroff, B. J. Shah, H. Gajjar, *Int. J. Contemp. Hosp. Manag.* **34**, 2852 (2022).
3. Statista, "eServices Report 2021 - Online Food Delivery" (statista, 2021); <https://www.statista.com/study/40457/food-delivery>.
4. W. A. Masters, A. B. Finaret, S. A. Block, in *Handbook of Agricultural Economics* (Elsevier, 2022), vol. 6, pp. 4997–5083.
5. B. M. Popkin, T. Reardon, *Obes. Rev.* **19**, 1028 (2018).
6. C. Roberts, L. Young, M. Johanson, *J. Hosp. Tour. Res.* **10**, 1177/1096348020988338 (2021).
7. S. I. Granheim, A. L. Løvhaug, L. Terragni, L. E. Torheim, M. Thurston, *Obes. Rev.* **23**, e13356 (2022).
8. C. Popan, *J. Urb. Technol.* **10**, 1080/10630732.2021.2001714 (2021).
9. P. Sun, Y. Zhao, *Environ. Plann. A* **0308518X2210902** (2022).
10. P. Orfanos *et al.*, *Eur. J. Clin. Nutr.* **71**, 407 (2017).
11. J. A. Wolfson, C. W. Leung, C. R. Richardson, *Public Health Nutr.* **23**, 2384 (2020).
12. S. R. Partridge *et al.*, *Nutrients* **12**, 3107 (2020).
13. J. Chu, H. Liu, A. Salvo, *Nat. Hum. Behav.* **5**, 212 (2021).
14. G. Song, H. Zhang, H. Duan, M. Xu, *Resour. Conserv. Recycling* **130**, 226 (2018).
15. L. Camps-Posino *et al.*, *Sci. Total Environ.* **794**, 148570 (2021).

SUPPLEMENTAL MATERIALS

science.org/doi/10.1126/science.abo2182

10.1126/science.abo2182

PERSPECTIVES

METASTABLE MATERIALS

Making the most of metastability

Researchers seek to preserve materials that are formed at high pressure

By Wendy L. Mao^{1,2} and Yu Lin²

Extreme environments are useful for studying previously uncharacterized phases and properties of materials (1). Researchers may discover materials with desirable features, which would be especially attractive if they can be retained under ambient conditions. Although the thermodynamically stable state of a material is generally determined by its lowest energy configuration, there is also the possibility of a metastable state at local energy minima—a “valley” on a curve that is not the overall lowest point. A local energy minimum allows phases to exist outside their stability field for an extended period of time, making metastability a rich subject for exploring material properties. On page 870 of this issue, Xiao *et al.* (2) report using nanocrystals to explore the processes that influence the height of the kinetic energy barrier between different structures to preserve, at ambient conditions, phases that occur at high pressure.

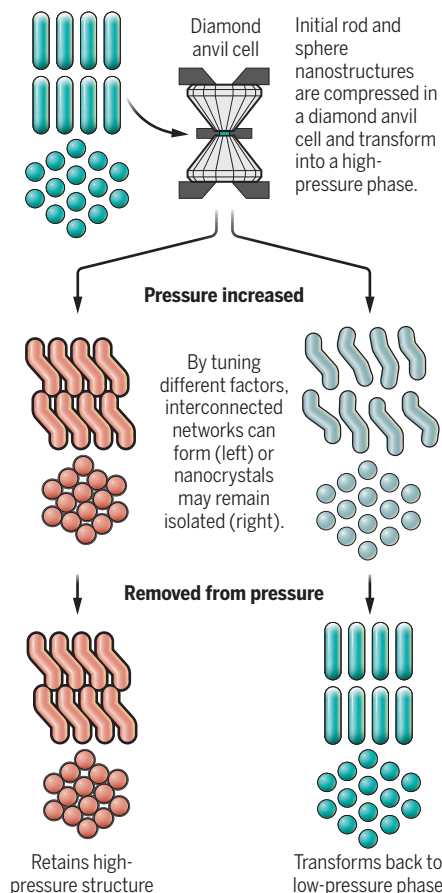
Materials with the same composition can have substantially different properties based on their structure, making them desirable for different applications. A well-known example of a metastable material is diamond, which is stable at high pressure and temperature but whose metastability field extends far beyond equilibrium and back to ambient conditions. Knowledge about this high-pressure phase of carbon has guided the development of techniques to mimic the high-pressure and temperature conditions for creating synthetic diamonds. An understanding of diamond's carbon bonding has inspired an alternative synthesis pathway for creating diamonds, by using the chemical vapor deposition of carbon in a methane plasma under near-vacuum conditions. This process allows the generation of the metastable diamond phase without requiring high pressure.

Although metastability can sometimes offer alternative ways to access the compet-

ing structural phases, much of the research remains limited to certain materials and is not generally applicable for materials design. A key consideration shared by all metastable phases is the kinetic energy barrier, which can prevent the material from transforming back to the thermodynamically stable phase. Xiao *et al.* studied the rock-salt structure phase—the same structure found in sodium chloride (NaCl)—in cadmium sulfide (CdS) and cadmium selenide (CdSe) semiconducting nanocrystals.

Preserving high-pressure phases in nanocrystals

Model nanocrystal systems help determine how ambient conditions can support phases observed at high pressure.



Previous theoretical predictions and experimental observations indicated that defects and strain can reduce the intrinsic energy barrier and the metastability of this phase under ambient conditions.

Xiao *et al.* explored numerous factors that can be tuned in their model nanocrystal systems. The factors include different compositions, starting atomic arrangements, nanoparticle shapes, and the addition of ligands bound at the nanocrystal surface. The authors observed the degree of long-range ordering in the nanocrystal assemblies to see how these factors influence defects and strain in the crystals (see the figure). They also investigated the effects of pressure, such as the highest pressure applied to the system and the rate of the pressure release, in preserving the high-pressure metastable phase under ambient conditions. Xiao *et al.* found that there is a noticeable interplay between these parameters and identified the formation of interconnected nanocrystal networks with reduced strain and defects as a key mechanism for maximizing barrier height and metastability. The interconnected nanocrystals help preserve the metastable rock-salt phase at ambient conditions. This revelation provides insight into developing generalized strategies for engineering transformation barriers that retain metastable phases in these and similar semiconductors and transition metal chalcogenides.

Another recent effort to control metastability involves designing pressure-temperature synthetic pathways and directing subtle structural differences in a halide perovskite system (3). Halide perovskites are a class of versatile, crystalline semiconductors that have shown great promise in a range of optoelectronic applications, such as photovoltaics (4) and solid-state lighting (5). By understanding the structural properties that determine the energy requirements between competing metastable structures, a narrow set of conditions were identified for accessing a useful, metastable halide perovskite phase. The application of pressure drives delicate atomic rearrangements and minimizes the energy difference between the metastable phase and the thermodynamically stable one. Subsequent rapid quenching from high temperature preserves the desired metastable structure at ambient conditions. This presents a promising strategy to control the structure of a material by tuning the thermodynamic and kinetic conditions, preserving certain desirable metastable phases.

A challenge when considering the potential for metastable materials is that many high-pressure transitions have small kinetic energy barriers, which results in the high-pressure phase transforming back to the

¹Department of Geological Sciences, Stanford University, Stanford, CA 94305, USA. ²Stanford Institute for Materials and Energy Sciences, SLAC National Accelerator Laboratory, Menlo Park, CA 94025, USA. Email: wmao@stanford.edu

low-pressure forms. In addition, metastable phases may also lose their outstanding high-pressure properties when the conditions are removed. For example, elemental hydrogen and some hydrogen-rich compounds are high-temperature superconductors at extremely high pressure, but they do not retain their superconductivity after the pressure is released (6). To preserve desirable phases and properties under ambient conditions, one may learn from the geological diamond-inclusion process, where a piece of something else is trapped, that is, included, inside a diamond as both form deep underground. As a result, the diamond can maintain the high-pressure conditions for the embedded compound when exposed to ambient atmospheric pressure (7). This process enables the preservation of high-pressure phases that are not metastable at ambient conditions and the potential for retaining favorable high-pressure properties. It may be mimicked by using carbon precursors to form capsules around a sample of interest and then converting the carbon precursor into diamond at high pressure and temperature. Once formed, the nanocrystalline diamond capsule can maintain high-pressure conditions in the sample even after the external pressure is released (8).

There is a need to investigate general approaches for leveraging metastability for accessing a broader range of material systems under practical conditions using both experiments and computational tools (9, 10). Extreme environments are a playground for discovering phases with enhanced materials functionality and their transition mechanisms and for exploring pathways to recover these phases under ambient conditions. The goal is to learn enough about these systems to rationally design materials with exceptional properties that can be preserved and ultimately synthesized under practical conditions. ■

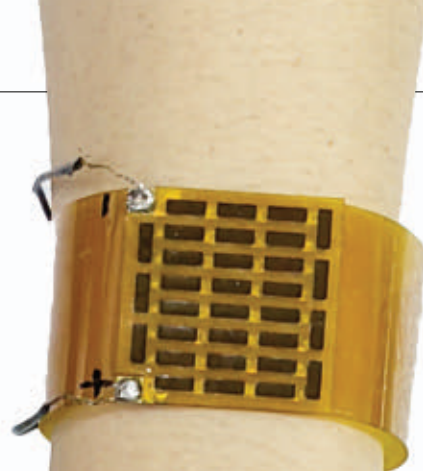
REFERENCES AND NOTES

1. P. F. McMillan, *Nat. Mater.* **1**, 19 (2002).
2. T. Xiao *et al.*, *Science* **377**, 870 (2022).
3. F. Ke *et al.*, *Nat. Commun.* **12**, 461 (2021).
4. M. A. Green, A. Ho-Baillie, H. J. Snaith, *Nat. Photonics* **8**, 506 (2014).
5. M. D. Smith, H. I. Karunadasa, *Acc. Chem. Res.* **51**, 619 (2018).
6. J. A. Flores-Livas *et al.*, *Phys. Rep.* **856**, 1 (2020).
7. O. Tschauer *et al.*, *Science* **374**, 891 (2021).
8. Z. Zeng *et al.*, *Nature* **10.1038/s41586-022-04955-z** (2022).
9. M. Amsler, V. I. Hegde, S. D. Jacobsen, C. Wolverton, *Phys. Rev. X* **8**, 041021 (2018).
10. W. Sun *et al.*, *Sci. Adv.* **2**, e1600225 (2016).

ACKNOWLEDGMENTS

We are supported by the US Department of Energy, Office of Science, Basic Energy Sciences, Materials Sciences and Engineering Division, under contract no. DE-AC02-76SF00515.

10.1126/science.add5433



THERMOELECTRICS

Semiconductors flex thermoelectric power

Ductile inorganic semiconductors can help enable self-powered wearable electronics

By **Chengyi Hou**^{1,2} and **Meifang Zhu**¹

Thermoelectric materials can convert a temperature gradient into electricity or convert electricity into a temperature gradient. They can be used to harvest waste heat and help to reduce the carbon footprint of many applications, ranging from computers to industrial equipment. Because the heat sources usually have a large area, planar thermoelectric generators with series-connected thermoelectric materials can satisfy the requirements. However, these materials—mostly inorganic thermoelectric semiconductors—are normally rigid and brittle, which restricts their application. On page 854 of this issue, Yang *et al.* (1) report a room-temperature ductile inorganic thermoelectric semiconductor that is flexible. This material opens the door to new applications such as wearable devices that can be powered by converting body heat to electricity.

Heat is continuously generated by the human body, of which about 40 mW/cm² is dissipated through the skin (2). Thermoelectric generators can convert this heat into electricity by using the temperature difference between the human body and the ambient environment. To realize the application for powering wearable devices, researchers

Yang *et al.* created a ductile inorganic thermoelectric semiconductor that can be used to generate power for wearable devices by using body heat. Shown here is a wristband-like thermoelectric generator that integrates series-connected superthin ductile thermoelectric semiconductors on flexible polymer substrates.

have sought flexibility by using conductive polymers and organic-inorganic hybrids. However, the poor electrical transport of known organic-based thermoelectric materials leads to low thermoelectric efficiency, as measured by a “figure of merit” denoted as “*zT*” and calculated by using the electrical conductivity, the thermal conductivity, and Seebeck coefficient (3).

To meet the demand for high-performance flexible thermoelectrics, Yang *et al.* developed a series of room-temperature ductile inorganic semiconductors with a high *zT*. In contrast to other inorganic semiconductors and ceramics that are usually brittle, these semiconductors can change shape instead of breaking—tolerating up to 18% strain—and can be machined to produce thin films with a thickness in the 10⁻⁵ m range. Being ductile and made thin enough, these inorganic thermoelectric materials can be easily bent (4), thus facilitating the fabrication of high-performance flexible thermoelectric generators.

The first room-temperature ductile inorganic semiconductor was discovered in 2018 (5). Since then, researchers have worked on many ductile thermoelectric materials, such as indium selenide (InSe) and silver sulfide (Ag₂S) (5–9). Most of these materials and their derivatives are n-type, where the main carriers are electrons (5–8), with a

¹State Key Laboratory for Modification of Chemical Fibers and Polymer Materials, College of Materials Science and Engineering, Donghua University, Shanghai 201620, P. R. China. ²Key Laboratory of Smart Fiber Technologies and Products, China National Textile and Apparel Council, Shanghai 201620, P. R. China. Email: hcy@dhu.edu.cn; zmfm@dhu.edu.cn

maximum zT value of around 0.44 at room temperature. The only known p-type ductile inorganic semiconductor, where the main carriers are electron holes instead of electrons, is a mixture of Ag, copper (Cu), Se, and S known as AgCu(Se,S) solid solution. However, the material has a poor zT value (0.01) at room temperature (9). Generally, an optimal thermoelectric generator would contain alternating grains of p- and n-type thermoelectric materials known as p-n couples; thus, being the weaker link in p-n couples, good p-type ductile thermoelectric materials are urgently pursued.

Yang *et al.* added tellurium (Te) to AgCuSe to convert its electrical conduction from n-type to p-type. This helped to increase the concentration of cation vacancy, but the resulting AgCu(Se,Te) solid solution is just as brittle as AgCuSe. The authors found that by mixing in a tiny amount of S in AgCu(Se,Te), a brittle-to-ductile transition occurs in the resulting AgCu(Se,S,Te). The increased amount of strongly polar Ag-S bonds increases the energy required for crystal plane cleaving, so these planes can hold the material together under an outer force instead of forming cracks during slipping. However, the Ag-S bonds also suppress the cation deficiency in the solid solution. Therefore, the amount of new Ag-S bonds also need to be balanced so as not to decrease the zT value too much.

After optimization, Yang *et al.* observed a p-type ductile thermoelectric semiconductor with a zT of 0.45 at room temperature. This leads to a promising possibility for realizing practical p-n thermoelectric couples, of which the thickness also determines the material's electrical resistance in addition to the bendability. The intrinsic brittleness of classic inorganic thermoelectric semiconductors, such as Bi₂Te₃ (10), prevents the fabrication of a thin and flexible thermoelectric generator. By contrast, the flexible device fabricated by Yang *et al.*, which contains six superthin p-n thermoelectric couples connecting in series, has an internal resistance of only 18 milliohm, which is more than 100 times less than that of bulk Bi₂Te₃-based thermoelectric generators. This eventually resulted in a record-breaking maximum normalized power density of 30 $\mu\text{W cm}^{-2} \text{K}^{-2}$, which is four times greater than that of the Bi₂Te₃-based thermoelectric generators and 10,000 times greater than that of the organic-based flexible thermoelectric generators. The improved output performance can help enable self-powered wearable electronics such as a smart wristwatch with an LED display, a heart rate monitor, and other functional units that are all powered by a flexible thermoelectric wristband.

From an application viewpoint, additional

attention should be paid to the flexible thermoelectric generator's performance stability. Yang *et al.* demonstrated a 5% internal resistance increment in the thermoelectric generator after bending and unbending it 500 times around a radius of 15 mm. Whether the ductile feature or other unexplored mechanisms will support good elastic stability under cyclic strain remains an open question. Because the thermoelectric output power increases with increasing temperature difference, it is also pertinent to maximize the temperature difference across the superthin thermoelectric generator from the skin-facing side to the other side. Although experimental results suggest that thermal convection and diffusion on the exposed thin film surface may enhance temperature difference to 1 to 2 K, it is still not competitive to the value measured in many millimeter-thick rigid thermoelectric generators, which ranges up to 20 K. Hopefully, passive radiative cooling and/or the combined thermoregulation approaches (11) will be useful for this purpose. Continuous efforts from interdisciplinary collaborations are thus required.

It is also important to consider the wearing comfortability of the material. Wearable electronics need to have a certain level of air and moisture permeability, softness, and lightness (12). Although thermoelectric fibers have been developed and integrated into textiles for comfortable wearable body heat harvesting (13), most of them are made of polymers and have relatively poor thermoelectric properties. The good machinability of ductile inorganic semiconductors may enable the fabrication of high- zT thermoelectric fibers, which potentially are set to hold advantages over existing thermoelectric fibers. This research will help to guide future studies on flexible heat harvesting and sensing applications and is beneficial to the growth of portable, flexible, and wearable electronics. ■

REFERENCES AND NOTES

1. Q. Yang *et al.*, *Science* **377**, 854 (2022).
2. P. J. Rodríguez de Rivera *et al.*, *J. Therm. Anal. Cal.* **81**, 178 (2019).
3. X.-L. Shi, J. Zou, Z.-G. Chen, *Chem. Rev.* **120**, 7399 (2020).
4. J. Peng, M. Grayson, G. J. Snyder, *Matter* **4**, 2694 (2021).
5. X. Shi *et al.*, *Nat. Mater.* **17**, 421 (2018).
6. T.-R. Wei *et al.*, *Science* **369**, 542 (2020).
7. J. Liang *et al.*, *Energy Environ. Sci.* **12**, 2983 (2019).
8. S. Yang *et al.*, *Adv. Mater.* **33**, 2007681 (2021).
9. Z. Gao *et al.*, *Adv. Energy Mater.* **11**, 2100883 (2021).
10. Q. Jin *et al.*, *Nat. Mater.* **18**, 62 (2019).
11. Y. Fang, G. Chen, M. Bick, J. Chen, *Chem. Soc. Rev.* **50**, 9357 (2021).
12. Q. Shi *et al.*, *Adv. Fiber Mater.* **1**, 3 (2019).
13. H. Xu *et al.*, *ACS Appl. Mater. Interfaces* **12**, 33297 (2020).

ACKNOWLEDGMENTS

C.H. thanks the Donghua University Distinguished Young Professor Program (LZB2019002) and Shanghai Rising-Star Program (20QA1400300) for support. M.Z. thanks the National Key Research and Development Program of China (2021YFA1201301/2021YFA1201300).

ENVIRONMENTAL CHEMISTRY

Taking the “F” out of forever chemicals

The right solvent mix breaks down perfluorinated organic acids

By Shira Joudan¹ and Rylan J. Lundgren²

Per- and polyfluoroalkyl substances (PFAS)—sometimes called “forever chemicals” because of their chemical stability—are synthetic molecules widely used in consumer products (1). Ironically, the characteristics that make these compounds useful, such as lipophilicity and hydrophobicity, high thermal stability, and resistance to chemical degradation, also lead to pervasive contamination in the environment (2). Moreover, chronic exposure to these chemicals has been associated with a host of negative human health effects (3). Unfortunately, the carbon-fluorine bonds in PFAS are among the most inert in organic compounds, which means that their destruction requires brutal treatment, such as incineration at high temperatures. On page 839 of this issue, Trang *et al.* (4) show that under specific mild conditions, perfluoroalkyl carboxylic acids (PFCAs), which are a type of PFAS, undergo spontaneous decomposition into benign inorganic fluoride ions and simple oxygenated organic molecules.

Ideally, all anthropogenic chemicals would easily break down to innocuous components once released into the environment. However, many of the approximately 5000 different PFAS are persistent. Several PFAS do go through transformations in the environment and become PFCAs (5), although once they have reached this stage, they remain a persistent contaminant.

PFAS can be destroyed by incineration (6), electro- or photochemical oxidation, or reductive defluorination. However, these methods require substantial energy input and are usually expensive to operate. Trang *et al.* discovered a low-energy pathway for decomposing PFCAs in which decarboxylation of the compound's acid group turns it into carbon dioxide (CO₂) and a perfluorinated

¹Department of Chemistry, York University, Toronto, Ontario, Canada. ²Department of Chemistry, University of Alberta, Edmonton, Alberta, Canada. Email: rylundgren@gmail.com

ated carbanion (a trivalent carbon anion). The carbanion can then undergo a series of chemical reactions to eventually break all the carbon-fluorine (C-F) bonds in the parent compound, producing inorganic fluoride and a combination of CO_2 , formate (CHO_2^-), and other oxygenated small molecules that no longer contain C-F units. The reaction occurs under mild temperatures (80° to 120°C). Outside of the reaction media, only the addition of sodium hydroxide (NaOH) is needed for the reaction to occur, making it potentially much cheaper than the processes currently used.

In addition to providing a simple approach to PFAS destruction, Trang *et al.* explored mechanisms of the transformation by looking at reaction mixtures, kinetic studies, and computational analysis. The key elementary chemical step that leads to a cascade of C-F bond breaking is decarboxylation of the acid group in the molecule. Decarboxylation of a related class of chemicals, perfluoroalkyl ether carboxylic acids, was previously observed as an inconvenient stability issue (7, 8). The key to the observed decarboxylation by Trang *et al.* is the addition of the polar aprotic solvent dimethyl sulfoxide (DMSO) (see the figure). In solvents such as water, PFCA is extremely stable against degradation, but in DMSO, the reaction proceeds. This simple difference explains how a molecule so persistent in the environment can degrade so readily in the lab.

Past studies have shown the importance of selecting the right solvent to enable low-temperature uncatalyzed decarboxylation reactions (9, 10). It is necessary to have reaction media that stabilize charge build-up through dipole-dipole interactions without overly stabilizing the carboxylic acid itself through hydrogen bonding (11). With a large dipole moment, the DMSO identified by Trang *et al.* is well-suited to stabilize charged reactive intermediates without forming strong hydrogen bonds with the carboxylate substrate. In quantified terms, the decarboxylation step was estimated by computational analysis to be the rate-determining step, with an activation barrier of 28 kcal/mol. This was in close agreement with the experimental value of 30 kcal/mol.

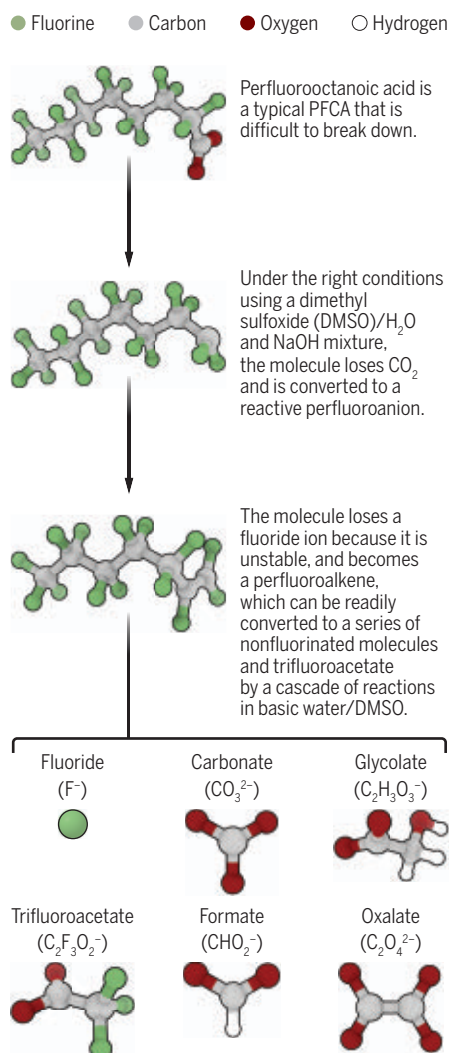
In Trang *et al.*'s experiment, after the perfluoroalkyl anion is generated, the breakdown of the fluorocarbon is energetically favorable and fast because the subsequent reaction steps have relatively low kinetic barriers. The perfluoroalkyl anion eliminates a fluoride ion to give a fluorinated alkene. The strongly electron-withdrawing C-F bonds make the fluorinated alkene unit electron-poor and thus highly reactive toward the addition of hydroxide. This process proceeds rapidly and leads to the expulsion of

another fluoride ion. This step produces an unstable acyl fluoride intermediate, which then undergoes several reactions to shed every fluorine atom from the organic framework, resulting in a mixture of innocuous oxygenated organic molecules.

The proposed mechanisms for PFCA degradation help to explain the optimized reaction conditions. DMSO is the solvent needed for decarboxylation, but aqueous sodium NaOH is also needed to promote defluorination of the perfluoroanion to complete the reaction. In the end, the solution used by Trang *et al.* was 1 part water to 8 parts DMSO—and 30 equivalents of NaOH per

Breaking down forever chemicals

Per- and polyfluoroalkyl substances are contaminants typically resistant to degradation, leading to their accumulation in the environment. Trang *et al.* designed a chain of reactions that can decompose perfluoroalkyl carboxylic acids (PFCAs)—a kind of such chemicals—into relatively harmless fluoride ions and oxygenated organic molecules.



molecule of perfluorooctanoic acid (PFOA), which comes out to roughly the same amount of NaOH as the water by weight.

In addition to the perfluorooctanoic acid used in their initial experiment, Trang *et al.* examined other PFCAs with varying carbon chain lengths, which also undergo similar degradation under the described experimental condition. In general, >80% fluoride recovery is observed for acids with a carbon chain between four and nine carbons long. In cases of one- or two-carbon perfluorocarboxylic acids, decarboxylation is slower because less-stable perfluoroalkyl anion intermediates are produced. The mechanism of degradation for these PFAS contrasts with those described in previous studies, which postulate sequential one-carbon removals along the chain to generate increasingly shorter molecules (12). Trang *et al.* demonstrate an approach to PFAS degradation that also works for branched perfluoroalkyl ether carboxylic acids, such as the hexafluoropropylene oxide dimer acid. Often known by its trade name “GenX,” the chemical has emerged as a replacement for certain PFAS and is now a ubiquitous environmental contaminant itself (13). Computational analysis by Trang *et al.* suggests a similar pathway for decomposition for GenX compared to PFOA, with initial substrate decarboxylation occurring at 40°C .

Given that nearly 5000 different PFAS are in use, it is imperative to understand the fundamental reactivity of these molecules. Especially important is the fact that most PFAS eventually form PFCAs, which remain in the environment practically forever (14). Trang *et al.* provide insight into how these seemingly robust compounds can undergo nearly complete decomposition under unexpectedly mild conditions. Hopefully, the fundamental findings of Trang *et al.* can be coupled with efficient capture of PFAS from contaminated environmental sites to provide a possible solution to the forever chemical problem. ■

REFERENCES AND NOTES

1. J. Glüge *et al.*, *Environ. Sci. Process. Impacts* **22**, 2345 (2020).
2. M. G. Evich *et al.*, *Science* **375**, eabg9065 (2022).
3. S. E. Fenton *et al.*, *Environ. Toxicol. Chem.* **40**, 606 (2021).
4. B. Trang *et al.*, *Science* **377**, 839 (2022).
5. S. Joudan, R. Liu, J. C. D'Eon, S. A. Mabury, *Trends Analyt. Chem.* **124**, 115431 (2020).
6. K. Jansen, *Chem. Eng. News* **97**, <https://cen.acs.org/environment/persistent-pollutants/Forever-chemicals-technologies-aim-destroy/97/i12> (2019).
7. H. K. Liberatore, S. R. Jackson, M. J. Strynar, J. P. McCord, *Environ. Sci. Technol. Lett.* **7**, 477 (2020).
8. C. Zhang *et al.*, *Environ. Sci. Technol.* **56**, 6103 (2022).
9. D. Kong *et al.*, *Science* **369**, 557 (2020).
10. G. Destro *et al.*, *Angew. Chem. Int. Ed.* **59**, 13490 (2020).
11. S. Zhou *et al.*, *J. Am. Chem. Soc.* **143**, 137 (2021).
12. J. Wang *et al.*, *Environ. Sci. Technol.* **56**, 5355 (2022).
13. Y. Pan *et al.*, *Environ. Sci. Technol.* **52**, 7621 (2018).
14. E. F. Houtz, D. L. Sedlak, *Environ. Sci. Technol.* **46**, 9342 (2012).

10.1126/science.add1813

NEURODEGENERATION

Toward preventing Parkinson's disease

A glycoprotein is a possible biomarker of pathogenic progression for Parkinson's disease

By **Brit Mollenhauer**¹ and
Christine A. F. von Arnim²

The diagnosis of Parkinson's disease (PD) relies on the presence of motor symptoms that occur when 50 to 70% of dopaminergic neurons in the substantia nigra degenerate. However, this happens after at least 20 years of the prodromal (premotor) phase. The spreading of α -synuclein (α Syn) aggregates, called fibrils, is pathologically associated with PD (1). However, the mechanisms leading to neurodegeneration continue to be debated. Alterations in the gene encoding α Syn are associated with increased risk of PD. Similarly, single-nucleotide polymorphisms (SNPs) that drive expression of glycoprotein nonmetastatic melanoma protein B (GPNMB) are associated with increased risk of PD (2, 3). On page 833 of this issue, Diaz-Ortiz *et al.* (4) report confirmation that SNPs increase GPNMB expression and confer PD risk. GPNMB was increased in the blood of PD patients and associated with disease severity, suggesting that GPNMB could be a biomarker of PD progression.

GPNMB is a transmembrane glycoprotein, which was first described in 1995 as more highly expressed in low-metastatic melanoma cell lines. The extracellular domain can be cleaved, and the soluble fragment binds many receptors, triggering an intracellular response. GPNMB has different functions in different cell types, and its roles in metastasis and inflammation are still a matter of debate (5). In 2016, GPNMB was found to be highly expressed in the brains of patients with Gaucher disease. This lysosomal storage disorder is caused by mutations in the glucocerebrosidase (*GBA*) gene, which is also an important risk factor for PD. Mutations in *GBA* may lead to loss of glucocerebrosidase activ-

ity and lysosomal dysfunction, which may lead to α Syn accumulation through the autophagic-lysosomal pathway (6).

Increased concentrations of GPNMB have been described in postmortem brain samples from patients with PD as well as samples from patients with Alzheimer's disease. Increased amounts of GPNMB in cerebrospinal fluid (CSF) have also been suggested as a promising biomarker in other neurological disorders, such as amyotrophic lateral sclerosis (ALS) (7). However, measurements of GPNMB concentrations in CSF could not distinguish between Alzheimer's disease and other neurological diseases, but they correlated with parameters such as aging and phosphorylated Tau in CSF (a marker of Alzheimer's disease), which indicates that increased GPNMB in CSF is not specific (8).

Neuroinflammation and activation of glia have been proposed to be possible mechanisms of neurodegeneration, suggesting a link between α Syn aggregation, neurodegeneration, and neuroinflammation in PD. GPNMB appears to be associated with the suppression of inflammatory processes and has been demonstrated to reduce proinflam-

matory cytokine secretion in macrophages outside of the brain (9). Conversely, GPNMB has been proposed to play a role in neuroinflammation and was found in microglia in the substantia nigra of PD patients by single-cell sequencing (10).

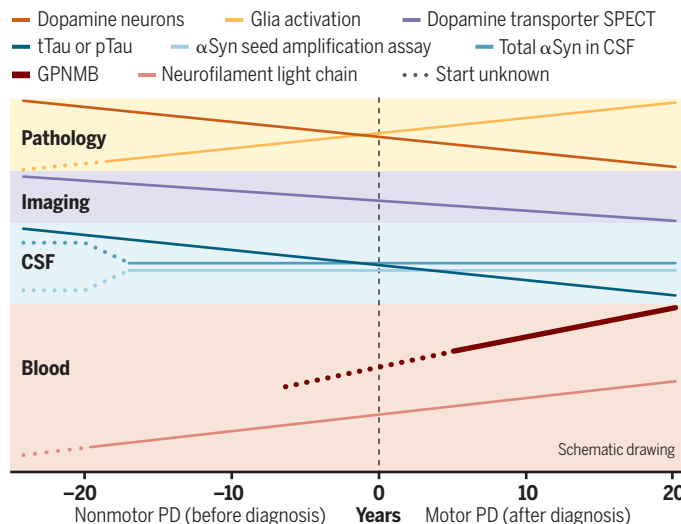
To analyze GPNMB function in neurons, Diaz-Ortiz *et al.* depleted its expression in human induced pluripotent stem cell (iPSC)-derived neurons and observed a decrease in synaptosomal α Syn. Further analyses revealed that α Syn and GPNMB interact. α Syn was found to be a hub for protein-protein interactions of synapse-related proteins, which were affected by the loss of GPNMB. Moreover, loss of GPNMB in iPSC-derived neurons specifically prevented internalization of α Syn fibrils. This study shows that GPNMB promotes synaptic uptake and cellular pathology of α Syn. To date, GPNMB has been associated with neuroinflammation and microglia but has not been directly linked to neurons. It will be important to assess whether GPNMB is also directly involved in α Syn uptake by microglia. This could enable understanding of the overall and GPNMB-specific roles of inflammatory reactions in PD

and whether they are a cause or consequence of neurodegeneration. Promoting loss of GPNMB could also be a therapeutic strategy for early PD.

Neuroprotective strategies have largely failed to prevent neurodegeneration in PD for various reasons, including because targeting the complex molecular mechanisms involved is challenging. There are diverse contributing genetic and environmental factors, and identifying patients undergoing the prodromal phase of the disease is difficult. Imaging dopamine transporter activity with single-photon emission computed tomography (SPECT) is currently used in the differential diagnosis of PD and to confirm early PD. Therefore, there is an urgent need to not only better understand the pathophysiology of PD but also establish a panel of biomarkers that identifies individuals at risk of developing PD, similar to emerging blood-based

Changes in Parkinson's disease

Increases of pathology and possibly neuroinflammation can occur up to 30 years before diagnosis of Parkinson's disease (PD) (year 0). People at risk of PD or disease progression could be identified with panels of biomarkers, including imaging with dopamine transporter single-photon emission computed tomography (SPECT); total Tau (tTau) or phosphorylated Tau (pTau), seeding of α -synuclein (α Syn) fibrils, or total α Syn from cerebrospinal fluid (CSF); and blood plasma biomarkers, such as glycoprotein nonmetastatic melanoma protein B (GPNMB).



¹Department of Neurology, University Medical Center Göttingen and Paracelsus-Elena-Klinik, Kassel, Germany. ²Department of Geriatrics, University Medical Center, Göttingen, Germany. Email: christine.arnim@med.uni-goettingen.de

biomarker panels for Alzheimer's disease (17).

Diaz-Ortiz *et al.* found that there were increased concentrations of GPNMB in the plasma of 781 early symptomatic and advanced PD patients compared with 59 healthy controls and that the concentrations increase with disease stage, indicating that GPNMB could be a biomarker of disease progression. Despite previous findings, the authors found no changes in GPNMB in CSF. Because GPNMB concentrations are increased in the CSF of ALS patients, further studies should assess GPNMB in CSF and blood from patients with other neurodegenerative diseases, including dementia with Lewy bodies, multiple system atrophy, and progressive supranuclear palsy. The changes in plasma GPNMB with PD stage also need to be validated in longitudinal samples from PD patients, and prodromal participants should be optimally included to assess the suitability of plasma GPNMB as a biomarker.

GPNMB seems not to work as a single predictive marker, so panels of biomarkers will be needed. The recently developed seeding aggregation assays for α Syn in CSF (12) come close to an ideal marker for indicating PD, with sensitivity and specificity both above 90% (13). Tau, phosphorylated Tau, and neurofilament light chain (14, 15), as well as microRNAs, may also be added to the biomarker panel, perhaps along with GPNMB (see the figure). This could allow people with early disease, or perhaps even prodromal disease, to be identified, and it would be a useful addition to allow monitoring in clinical trials. ■

REFERENCES AND NOTES

1. H. Braak *et al.*, *Neurobiol. Aging* **24**, 197 (2003).
2. M. N. Murthy *et al.*, *Neurogenetics* **18**, 121 (2017).
3. D. A. Kia *et al.*, *JAMA Neurol.* **78**, 464 (2021).
4. M. E. Diaz-Ortiz *et al.*, *Science* **377**, 833 (2022).
5. M. Saade *et al.*, *Front. Immunol.* **12**, 674739 (2021).
6. L. Smith, A. H. V. Schapira, *Cells* **11**, 1261 (2022).
7. P. Oeckl *et al.*, *Acta Neuropathol.* **139**, 119 (2020).
8. F. Aichholzer *et al.*, *Alzheimers Res. Ther.* **13**, 94 (2021).
9. V. M. Ripoll *et al.*, *J. Immunol.* **178**, 6557 (2007).
10. S. Smajic *et al.*, *Brain* **145**, 964 (2022).
11. C. E. Teunissen *et al.*, *Lancet Neurol.* **21**, 66 (2022).
12. M. Shahnewaz *et al.*, *JAMA Neurol.* **74**, 163 (2017).
13. U. J. Kang *et al.*, *Mov. Disord.* **34**, 536 (2019).
14. S. Hallaway *et al.*, *Neurology* **98**, e2185 (2022).
15. B. Mollenhauer *et al.*, *Mov. Disord.* **35**, 1999 (2020).

ACKNOWLEDGMENTS

B.M. has received honoraria for consultancy from Roche, Biogen, AbbVie, Servier, 4D Pharma PLC, and Amprion; is a member of the executive steering committee of the Parkinson Progression Marker Initiative, a co-principal investigator of the Systemic Synuclein Sampling Study, and a member of the Therapeutic Evaluation Committee of the P2P initiative of the Michael J. Fox Foundation for Parkinson's Research (MJFF); and has received research funding from the Deutsche Forschungsgemeinschaft (DFG), the European Union (Horizon2020), Parkinson Fonds Deutschland, Deutsche Parkinson Vereinigung, the Parkinson's Foundation, Hilde-Ulrichs-Stiftung für Parkinsonforschung, Aligning Science Across Parkinson's (ASAP), and MJFF. C.A.F.v.A. received honoraria from serving on the scientific advisory board of Biogen, Roche, Novo Nordisk, and Dr. Willmar Schwabe GmbH & Co. KG; has received funding for travel and speaker honoraria from Biogen, Roche diagnostics AG, and Dr. Willmar Schwabe GmbH & Co. KG; and has received research support from Roche diagnostics AG.

IMMUNOLOGY

Unveiling the B cell receptor structure

Molecular structures provide a road map for understanding and controlling B cell receptor activation

By Pavel Tolar¹ and Susan K. Pierce²

B cells took center stage in the COVID-19 pandemic as the world waited anxiously for a vaccine. Nearly all vaccines in use today depend on activating B cells by binding to the surface-expressed B cell receptors (BCRs) that recognize antigens and stimulate antibody production. However, even recent vaccines were developed without a detailed understanding of how BCRs function, and many fail to provide optimal long-lived immunity. On pages 875 and 880 of this issue, Su *et al.* (1) and Ma *et al.* (2), respectively, reveal the structures of the BCR complex, which is composed of membrane forms of antibodies [immunoglobulin M (IgM), IgG, etc.] bound to two transmembrane proteins, Ig α (CD79A) and Ig β (CD79B). These structures are likely to inform the development of highly effective vaccines, therapies that eliminate cancers, and treatments that control and prevent autoimmune diseases.

Earlier studies showed that the membrane antibody of the BCR has the familiar Y shape, with two fragment antigen-binding (Fab) arms connected through hinges to one fragment crystallizable (Fc) leg, which in this case is linked to a transmembrane domain. Ig α and Ig β chaperone the membrane antibody to the B cell surface and, crucially, initiate biochemical signaling inside the B cell when the membrane antibody binds antigen (3, 4). The critical interactions that hold the membrane antibody to Ig α and Ig β are buried within the cell membrane (5), making the BCR resistant to structural studies by crystallography.

The BCR is a multifunctional machine that is responsible for regulating most functions of a B cell. Under the appropriate conditions, antigen binding triggers B cell proliferation and differentiation into antibody-secreting cells. However, this activation requires second signals, without which

BCR signaling leads to cell death. Many second signals are provided by CD4⁺ helper T cells. To solicit T cell help, the BCR functions as an endocytic receptor that captures the antigen and delivers it to intracellular vesicles for proteolytic processing and loading onto major histocompatibility complex class II (MHC II) molecules, which are recognized by antigen-specific helper T cells. T cells also stimulate class-switching from the default IgM and IgD antibodies to IgG, IgA, or IgE. All of these antibody classes form distinct BCRs on B cell surfaces and fine-tune the responses to antigens (6). For example, IgG BCRs stimulate antibody secretion better than IgM BCRs.

Another important feature of the BCR is sensing the affinity of the antigen binding. Rather than being an on-off switch, the BCR grades the responses to advantage B cells that are better at recognizing the antigen at the expense of B cells that bind it poorly. This is the basis for antibody affinity maturation, which is mediated by the selection of B cells that have acquired somatic mutations in the antigen-binding site of their antibodies (7). The BCR is not idle in the absence of antigen but provides survival signals to resting B cells (8). Clearly, understanding all the nuances of B cell activation is not possible without a detailed structure of the BCR.

The physical signal through which antigen binding is transmitted through the BCR to the interior of the cell has itself been an enigma. Originally, antigens were thought to simply aggregate BCRs on the B cell surface because antigens are overwhelmingly multivalent (e.g., virus particles). BCR aggregation was an attractive mechanism because it obviated the need for conformational changes induced by antigen binding to be propagated to the cytoplasm through the highly flexible hinge region of the BCR antibody. Instead, the model proposed that aggregation of the Ig α -Ig β intracellular domains leads to cross-phosphorylation of their immunoreceptor tyrosine-based activation motifs (ITAMs) by associated tyrosine kinases (9). However, phosphorylation was observed to spread to BCRs that were not engaged by antigen, suggesting that the process can also work the opposite way:

¹Institute of Immunology and Transplantation, University College London, London, UK. ²Laboratory of Immunogenetics, National Institute of Allergy and Infectious Diseases, National Institutes of Health, Rockville, MD, USA. Email: spierce@niaid.nih.gov

Resting BCR oligomers can be separated by antigen binding, exposing their ITAM phosphorylation sites (10). Furthermore, given that the BCR often needs to wrestle antigens from other cell surfaces, a mechanical tug on the BCR could induce distant conformational changes or clustering (11), likely in conjunction with regulation from the submembrane cytoskeleton, which helps to keep the BCR in the resting state (12). The new structures presented by Ma *et al.* and Su *et al.* are the first steps toward testing these models in B cell activation or pathology.

To provide a high-resolution view of the BCR, both groups purified the BCR from cells and imaged them using cryo-electron microscopy (cryo-EM). It took more than 6 million single BCR particles to refine each of the final structures up to atomistic detail. Both papers present structures of the IgM BCR, and Ma *et al.* also report that of the IgG1 BCR (see the figure). The structures agree with each other and confirm in vivid detail what was previously only depicted in schematic cartoons. The membrane antibody retains its Y shape in which the Fab arms remain free, whereas the Fc portion binds the Ig α -Ig β heterodimer with

1:1 stoichiometry (10). Linker peptides introduce the extracellular portions into the cell membrane, where the transmembrane helices form a tight bundle, glued together by numerous polar residues interacting inside the hydrophobic environment. These intramembrane interactions are highly conserved across species and across different antibody classes and explain why this region is so critical for BCR assembly (5). By contrast, the cytoplasmic tails of the BCR are invisible in the reconstruction, indicating that they are flexible.

The structures also reveal unexpected features. They demonstrate the central importance of the linker peptides. The tightly knitted linkers are stabilized in specific positions by a network of interactions, suggesting that they are essential in keeping the BCR together and in the correct orientation. For example, one of the antibody linkers threads in between Ig α and Ig β . Therefore, the BCR complex must assemble from the individual chains while they are still folding and will be difficult to dismantle once fully formed.

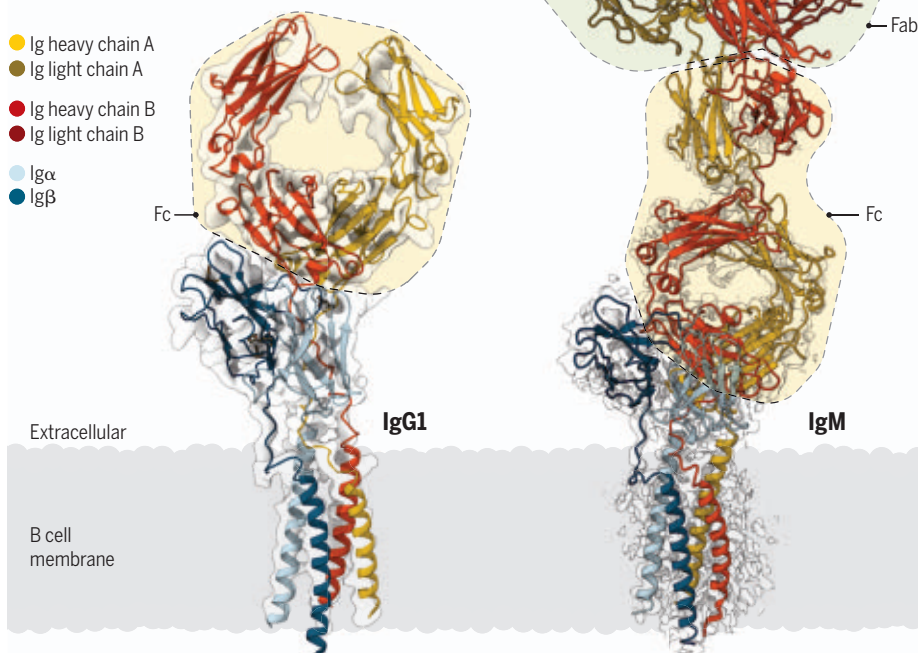
Although the interactions within the membrane are conserved between the IgM and the IgG BCRs, the two BCRs differ in

their extracellular domains. The IgM membrane antibody sits closer to the membrane and interacts with Ig α -Ig β on its side. By contrast, the IgG is spaced further out and sits on top of Ig α -Ig β . This structural disparity may underlie some of the signaling differences between IgM and IgG BCRs. It also predicts that BCRs of other classes adopt distinct structures, which may be important for class-specific functions and therapeutic targeting. Additionally, the Fab arms of the IgM BCR show only limited flexibility compared with soluble IgM (13). Apparently, association with Ig α alters the position of one of the C μ 3 domains in the IgM Fc, which in turn stabilizes the hinge movement of the C μ 2 domains. This suggests that in the IgM BCR, there is a communication between the Fab movement and the Ig α -Ig β heterodimer. It will be interesting to see whether such communication is involved in signal transmission after antigen binding and how this may contrast with the IgG BCR, in which the Fab arms move freely.

Where might these pioneering BCR structures lead us? One hope is that cryo-EM can be used to solve the structures of the antigen-engaged BCR complexes. Activated BCR structures could address the mechanisms by which antigens stimulate B cells and guide the engineering of vaccines for optimal B cell activation (14). Another area of interest is to prevent unwanted activation of B cells. Rational approaches to inhibit the BCR may help to quell the recognition of self-antigens by B cells in autoimmunity. Similarly, targeting the BCR can be beneficial in chronic lymphocytic leukemia and some types of B cell lymphomas in which BCR signaling drives malignant proliferation (15). Inhibiting intracellular signaling or marking the diseased cells for elimination will extend the range of therapeutic options in these diseases. ■

The structure of the BCR

Ma *et al.* and Su *et al.* present cryo-electron microscopy structures of the immunoglobulin M (IgM) B cell receptor (BCR), and Ma *et al.* also report that of the IgG1 BCR. The membrane antibody, with two fragment antigen-binding (Fab) arms connected through hinges to one fragment crystallizable (Fc) leg, is linked to a transmembrane domain that threads between Ig α and Ig β . The cytoplasmic tails of the BCR are not seen in the structures, and the Fab is not seen in IgG1.



REFERENCES AND NOTES

1. Q. Su *et al.*, *Science* **377**, 875 (2022).
2. X. Ma *et al.*, *Science* **377**, 880 (2022).
3. J. Hombach, T. Tsubata, L. Leclercq, H. Stappert, M. Reth, *Nature* **343**, 760 (1990).
4. K. S. Campbell, J. C. Cambier, *EMBO J.* **9**, 441 (1990).
5. A. C. Shaw *et al.*, *Cell* **63**, 381 (1990).
6. A. R. Venkitaraman, G. T. Williams, P. Dariavach, M. S. Neuberger, *Nature* **352**, 777 (1991).
7. G. D. Victora, M. C. Nussenzweig, *Annu. Rev. Immunol.* **40**, 413 (2022).
8. K.-P. Lam, R. Kühn, K. Rajewsky, *Cell* **90**, 1073 (1997).
9. M. Reth, J. Wienands, *Annu. Rev. Immunol.* **15**, 453 (1997).
10. W. W. A. Schamel, M. Reth, *Immunity* **13**, 5 (2000).
11. P. Tolar, J. Hanna, P. D. Krueger, S. K. Pierce, *Immunity* **30**, 44 (2009).
12. B. Treanor *et al.*, *Immunity* **32**, 187 (2010).
13. Y. Li *et al.*, *Science* **367**, 1014 (2020).
14. A. P. West Jr. *et al.*, *Cell* **156**, 633 (2014).
15. R. M. Young, A. L. Shaffer III, J. D. Phelan, L. M. Staudt, *Semin. Hematol.* **52**, 77 (2015).

10.1126/science.add8065

T cell immunity to COVID-19 vaccines

T cell immunity may be critical for long-term protection by COVID-19 vaccines

By **E. John Wherry**¹ and **Dan H. Barouch**²

The development of multiple COVID-19 vaccines in record time is a major biomedical achievement, but mechanistic immune correlates of vaccine protection remain to be determined. Most studies on COVID-19 vaccines have focused on neutralizing antibody (NAb) responses, with little emphasis on cellular immunity. However, accumulating data suggest that T cell responses play an important role in vaccine protection against severe COVID-19 disease, particularly against viral variants that partially escape from recognition by NABs. These insights have implications for using current COVID-19 vaccines and for developing next-generation vaccines against COVID-19 and other infectious diseases.

Protective immunity can be induced by vaccination or infection and is mediated by two arms of the adaptive immune system: humoral immunity mediated by antibodies and memory B cells, and cellular immunity that includes helper CD4⁺ T cells and cytotoxic CD8⁺ T cells. Antibodies block infection by binding virus and preventing viral entry into host cells and are correlates of protection for many vaccines. For severe acute respiratory syndrome coronavirus-2 (SARS-CoV-2), antibodies can prevent acquisition of infection if they are present at high enough concentrations, as demonstrated by immunoglobulin G (IgG) transfer studies in macaques (1).

Memory T cells can provide an important additional layer of protective immunity. Because T cells do not recognize infecting viruses until they have entered the host cell, the mechanisms of protection by T cells are different from those of antibodies. For example, T cells cannot prevent host cells from initially becoming infected, but they can respond rapidly once infection has occurred to limit virus replication and spread (see the figure). Thus, T cell immunity likely does not prevent acquisition of infection. However, emerging evidence supports a key role for SARS-CoV-2-specific T cell immunity in protection from severe disease.

Immunological memory to SARS-CoV-2 from vaccination or infection can protect the host through multiple mechanisms. If virus breaches NAB defenses in the upper respiratory tract, protection from severe disease could still be mediated if immune mechanisms prevent virus spread to the lower respiratory tract and control virus replication in the lungs. Such protection can involve antibodies, but T cells are ideally suited to limit virus replication by eliminating virus-infected cells. Thus, although an ideal vaccine would prevent acquisition of infection, immune responses that operate rapidly and efficiently after initial infection could prevent progression to severe disease. Indeed, even for vaccines with outstanding and durable efficacy, such as the measles vaccine, clinical protection may be mediated by rapid control of virus replication in infected cells and prevention of disease progression (2).

For SARS-CoV-2, there are four main goals of vaccination: protection from acquisition of infection; prevention of transmission; protection from severe disease; and prevention of Long Covid. When vaccines were initially rolled out, the early high NAB titers following immunization led to hopes that the vaccines would largely block infection and transmission. However, two issues have emerged that question whether these goals are still achievable with current vaccines. The high NAB titers observed at peak immunity several weeks after messenger RNA (mRNA) vaccination wane rapidly and substantially, often within 4 to 6 months (3, 4). NAB titers after adenovirus type 26 (Ad26) vector vaccination are more durable over time but peak at lower levels (4). The serum concentration of NABs needed to provide durable protection from infection and transmission remains unclear but is likely much higher for the current highly infectious SARS-CoV-2 variants.

Additionally, SARS-CoV-2 variants such as Omicron show increased transmissibility and substantial escape from NAB responses, both of which reduce the ability of vaccine-induced NABs to block infection (5, 6). The combination of waning antibody levels and the emergence of viral variants has now forced a recalibration of the expectations of current COVID-19 vaccines. Protective efficacy against acquisition of infection appears to be transient and limited against Omicron, even after third and fourth mRNA vaccine boosters (7, 8). By contrast, protection against

severe disease has largely been maintained in otherwise healthy individuals. For example, data from South Africa during the Omicron surge have shown that both BNT162b2 and Ad26.COV2.S vaccines still provided robust protection against hospitalization even in the absence of high-titer NABs (5, 6, 9). These data suggest that other mechanisms protect from severe disease.

Multiple layers of the immune system contribute to immunological memory and protective immunity to viruses. Antibody responses, produced by B cells, are generated in two waves. Short-lived plasma cells are usually generated without entering a germinal center (GC) and function to rapidly produce high titers of low-quality antibodies. A second set of B cells enters the GC, where they undergo somatic hypermutation and affinity maturation to generate higher-quality antibodies. Long-lived plasma cells emerge from the GC and migrate to the bone marrow, where they produce high-quality, affinity-matured antibodies. The other output of the GC is a pool of memory B cells, the cellular storage unit of high-quality antibody sequences. These cells persist, and upon reinfection (or booster vaccination), can rapidly convert into plasma cells to make new antibodies and seed new GCs to reinitiate antibody affinity maturation. For COVID-19 vaccines, although serum antibody titers wane rapidly, memory B cells are highly durable and may contribute to protection from disease along with memory T cells (10, 11).

T cells recognize short peptides presented on the cell surface in complex with human leukocyte antigen (HLA) class I or class II molecules. Upon recognition of their cognate peptide presented by HLA molecules, memory T cells can rapidly elaborate effector functions to suppress viral replication, limit infection, and prevent spread within the host. For example, CD8⁺ T cells directly kill infected cells and produce antiviral cytokines, as well as inflammatory molecules that recruit additional immune cells to sites of infection. CD4⁺ T cells contribute to various aspects of immunity, including supporting B cell responses in the GC; some CD4⁺ T cells can also have direct antiviral properties similar to those of CD8⁺ T cells. Once generated, memory T cells can be stably maintained for decades in humans, and SARS-CoV-2-specific memory T cells durably persist after vaccination or infection (11, 12).

¹Institute for Immunology and Department of Systems Pharmacology and Translational Therapeutics, University of Pennsylvania Perelman School of Medicine, Philadelphia, PA, USA. ²Center for Virology and Vaccine Research, Beth Israel Deaconess Medical Center, Harvard Medical School, Boston, MA, USA. Email: wherry@pennmedicine.upenn.edu; dbarouch@bidmc.harvard.edu

Because antibodies and T cells recognize virus and contribute to protection by different mechanisms, the impact of viral mutations on immune escape is distinct. NABs recognize conformational epitopes on viral proteins and typically mediate their effects by blocking engagement of a viral coat protein with the host cell entry receptor. In the case of SARS-CoV-2, NABs bind to the spike protein receptor binding domain (RBD) and N-terminal domain (NTD), blocking engagement with the host receptor, angiotensin-converting enzyme 2 (ACE-2). Mutations in the spike RBD and NTD can substantially influence antibody binding. Immune pressure from antibodies is likely driving evolution of the spike protein, resulting in incomplete neutralization of new viral variants by NABs induced by vaccination or infection (5, 6). Similarly, multiple therapeutic monoclonal antibodies have lost efficacy against current SARS-CoV-2 variants.

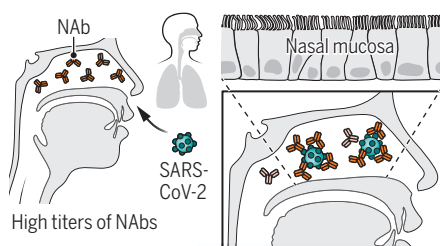
By contrast, T cells recognize short, 8- to 15-amino acid linear peptides, which are not limited to the spike RBD and NTD domains, where most mutations occur. As a result, T cell responses remain largely intact against variants such as Omicron, with >80% of T cell epitopes conserved across variants (12, 13). Moreover, if escape from a T cell epitope occurs, differences in HLA-peptide presentation suggest that a mutation that causes escape from T cell immunity in one person is unlikely to do so in another person. Overall, emerging viral variants substantially affect antibody neutralization but so far have had a minimal impact on T cell responses.

What is the evidence that memory T cells contribute to protective immunity to SARS-CoV-2? In cancer patients with B cell deficiencies that experience COVID-19, CD8⁺ T cell responses correlated with milder disease (14). CD8⁺ T cell depletion studies in macaques have demonstrated a contribution of CD8⁺ T cells to protection from SARS-CoV-2 challenge (1). In addition, vaccine failures against experimental Omicron challenge in macaques were associated with a lack of Omicron-specific CD8⁺ T cells, despite moderate Omicron NAB titers (15). Moreover, robust protection against severe disease in the absence of high NAB titers (5, 9) suggests a role for T cell responses. There have been surges in SARS-CoV-2 infections driven by Omicron subvariants that largely escape NAB responses, but hospitalization, intensive care unit admission, and death rates have not increased proportionally. The disconnect between infection and severe disease suggests a substantial level of population immunity, which likely includes both hu-

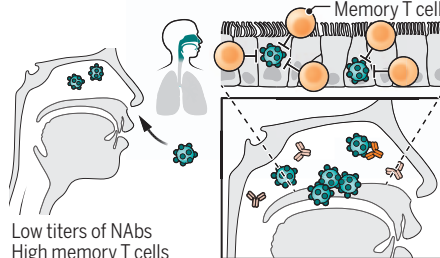
Neutralizing antibodies and T cells in COVID-19 vaccine efficacy

When vaccines induce high titers of neutralizing antibodies (NABs), severe acute respiratory syndrome coronavirus 2 (SARS-CoV-2) infection of the upper respiratory track is blocked. But, when NAB titers wane or the virus evades antibody recognition, robust T cell responses block progression of infection to the lower respiratory tract. Disease progression occurs with low titers of NABs and weak T cell responses.

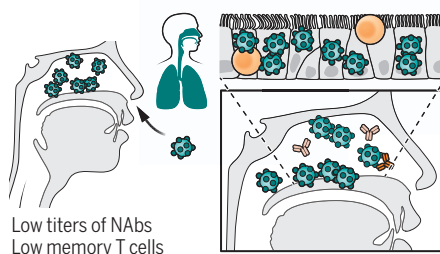
Protection from infection



Protection from severe disease



Viral dissemination and severe disease



moral and cellular immunity. Together, these observations support a role for cellular immunity, and particularly CD8⁺ T cell responses, in contributing to vaccine protection against severe COVID-19. Furthermore, the durability and reactivity of CD8⁺ T cells against variants (4, 11–13) suggest their relevance for preventing severe disease against viral variants that increasingly escape NABs.

A key question moving forward is how to optimize T cell immunity with COVID-19 vaccines. Boosting with current mRNA or vector-based vaccines should increase spike-specific cellular immunity, but better understanding of which T cell subpopulations protect against disease is needed. Adding into next-generation vaccines other

immunogens, such as SARS-CoV-2 nucleocapsid or membrane proteins, or conserved regions, represents another strategy to broaden cellular immunity. Such approaches may also contribute to the development of pan-betacoronavirus vaccines. Whether vaccine-induced memory T cells establish long-term residence at sites of mucosal entry for durable protection is also important to address.

Another knowledge gap is whether updated booster vaccines will improve clinical efficacy compared with current vaccine boosters. Recent clinical data suggest that boosting with bivalent mRNA vaccines expressing the ancestral and Omicron BA.1 spike resulted in less than twofold higher Omicron BA.1 NAB titers compared to boosting with vaccines based on the ancestral spike. T cell responses have not yet been reported with these updated vaccines. The clinical relevance of the modestly increased NAB titers for protection against infection with Omicron remains unclear.

Future research should define the precise mechanisms by which T cells contribute to vaccine efficacy, including the role of mucosal resident T cells, optimal memory T cell differentiation states, and the role, if any, of SARS-CoV-2 escape from T cell immunity. T cell responses should be included in studies of immune correlates of protection. Moreover, future studies should define optimal methods for monitoring T cell responses. A deeper understanding of the role of T cell immunity for protection against SARS-CoV-2 infection and disease should provide a foundation for improving the use of current vaccines and the development of next-generation vaccines. ■

REFERENCES AND NOTES

1. K. McMahan et al., *Nature* **590**, 630 (2021).
2. N. Sundell et al., *Euro Surveill.* **24**, 1900114 (2019).
3. A. Pegu et al., *Science* **373**, 1372 (2021).
4. A. Y. Collier et al., *N. Engl. J. Med.* **385**, 2010 (2021).
5. S. Cele et al., *Nature* **602**, 654 (2022).
6. L. Liu et al., *Nature* **602**, 676 (2022).
7. J. M. Ferdinands et al., *MMWR Morb. Mortal. Wkly. Rep.* **71**, 255 (2022).
8. Y. M. Bar-On et al., *N. Engl. J. Med.* **386**, 1712 (2022).
9. G. Gray et al., *N. Engl. J. Med.* **386**, 2243 (2022).
10. J. S. Turner et al., *Nature* **596**, 109 (2021).
11. R. R. Goel et al., *Science* **374**, abm0829 (2021).
12. J. Liu et al., *Nature* **603**, 493 (2022).
13. A. Tarke et al., *Cell* **185**, 847 (2022).
14. E. M. Bange et al., *Nat. Med.* **27**, 1280 (2021).
15. A. Chandrashekar et al., *Cell* **185**, 1549 (2022).

ACKNOWLEDGMENTS

E. J.W. is a member of the Parker Institute for Cancer Immunotherapy. He is also an adviser for Danger Bio, Merck, Marengo, Janssen, Related Sciences, Syntheke, and Surface Oncology and a founder of Surface Oncology, Danger Bio, and Arsenal Biosciences. D.H.B. is a coinventor on provisional vaccine patents that have been licensed to Janssen (63/121,482; 63/133,969; 63/135,182), serves as a consultant to Pfizer, and collaborates with Moderna as part of the Massachusetts Consortium for Pathogen Readiness.

10.1126/science.add2897

Iranian wind towers, an ancient and natural cooling system, could inform modern urban planning.

nature. Doing so avoids the overexploitation and waste of resources that can lead to fragility.

They encourage cities to maximize multifunctionality by capitalizing on fundamental ecological linkages that contribute to both social and environmental sustainability. For example, maintaining river-floodplain connectivity for access to drinking water, food, and socio-cultural practices not only ensures that communities have clean water, it also protects the rivers' self-renewing nutrient and sediment cycles, which support food webs and riparian plants that minimize harmful floods.

Cooperation and coordination among people and institutions (formal and informal) at multiple levels is another tenet of adaptable cities, argue the authors, helping communities avoid problems that can arise when sharing common-pool resources. This idea harkens back to one of the arguments made by Nobel Prize-winning economist Elinor Ostrom: that cities can successfully manage resources through collective ownership (2).

The book applies thinking that is most akin to the notion of adaptive cycle resilience advanced by Lance Gunderson and Buzz Holling, who also include the idea of major reorganization as a necessary component of socio-ecological resilience (3). (The authors of this book use the term "durability" rather than resilience, but the sentiment is seemingly the same.)

Ultimately, I found the book to be a clear, informative, and useful resource that I plan to use to teach about socio-environmental systems. It successfully makes the case that historical cities that exhibited durability can offer us valuable insights into how to build modern cities that can reinvent themselves in the face of change, providing a collection of interesting case studies and a look at how archaeologists think about human-nature interactions. An easy-to-read book, it is suitable as inspiration for urban design experts and for teachers and scholars of socio-ecological sustainability. ■

REFERENCES AND NOTES

1. IHOPE, <https://ihopenet.org>.
2. E. Ostrom, *Governing the Commons: The Evolution of Institutions for Collective Action* (Cambridge Univ. Press, 1990).
3. L. H. Gunderson, C. S. Holling, Eds., *Panarchy: Understanding Transformations in Human and Natural Systems* (Island Press, 2002).

ACKNOWLEDGMENTS

The reviewer is director of the National Socio-Environmental Synthesis Center, which provided support for the conference from which this book arose. She was not involved in any way with the book's production or promotion.

10.1126/science.ade1308

BOOKS *et al.*

SUSTAINABILITY

Transforming urban environments

Resilient cities of the past hold lessons for creating adaptable communities of the future

By Margaret A. Palmer

Cities are highly dynamic socio-environmental systems in which people, communities, and institutions interact with mosaics of green space, contaminated brown fields, and remnants of once thriving ecosystems. Over diverse time scales, these systems can thrive, decline, or reinvent themselves across multiple spatial scales. And while economic forces, environmental threats, urban unrest, and other challenges may result in the demise of some cities, others are able to persist—often by reinventing themselves.

A new book titled *If the Past Teaches, What Does the Future Learn?* argues that communities that were able to pivot in the face of change in the past provide key lessons in how to strengthen cities' adaptability moving forward. The book's authors suggest that these historical examples can "inspire new possibilities, provide useful guiding principles, and suggest solutions to new challenges" cities face today.

The book—resulting from activities conducted as part of the Integrated History and Future of People on Earth (IHOPE) project and edited by archaeologists Carol Crumley

and John Murphy—opens with an engaging chapter on what the authors call "durability," the capacity of a city to either adapt or succumb to change (1). To illustrate the concept, they carefully select case studies that capture the variability in cities around the world and through time. From highland Ethiopia to the Maya lowlands, Atlantic Europe, and southern Mesopotamia, the authors use these places, their landscapes, and their regional settings to "build a bridge from archaeology to mainstream architectural and design theory." Although there are examples of extant cities that have prehistoric antecedents (e.g., Phoenix, Arizona) and exhibit durability, archaeological examples are the primary focus.

"How can we transform urban environments to encourage durability and mediate the social price of myriad risks and vulnerability?" ask the book's authors. They argue that there are guiding management principles that have led to urban durability in the past that we should apply today. These include maximizing diversity in all its forms—natural resources, people, ideas, views, institutions—which allows for flexibility and, in turn, permits adaptation to changing forces and challenges.

The authors also advocate for the integration of the city in its natural setting—that is, ensuring that it optimizes inherent natural cycles and reuse principles, thereby tapping into the self-sustaining processes built into



If the Past Teaches, What Does the Future Learn?
John T. Murphy and
Carole L. Crumley, Eds.
TU Delft Publishing,
2022. 124 pp.

The reviewer is at the National Socio-Environmental Synthesis Center, University of Maryland, College Park, MD 20742, USA. Email: mpalmer@umd.edu

SOCIOLOGY

The myth of meritocracy in scientific institutions

Inaccurate ideas about objectivity and merit perpetuate biases and inequality in academia

By **Leanne Son Hing**

Written by sociologists Mary Blair-Loy and Erin Cech, *Misconceiving Merit* investigates how STEM (science, technology, engineering, and math) faculty in the United States understand scientific merit and how these understandings can lead to subtle biases and perpetuations of inequality. The authors propose that cultural processes and beliefs concerning devotion to work and the independence of the scientific enterprise shape how STEM faculty view, treat, evaluate, and reward their peers. Critically, although STEM professionals define excellence as groundbreaking research conducted by means of objective methods, the pair find that faculty often fail to consider how their professional culture can lead to bias against certain groups, which can ultimately undermine knowledge production and its application.

Written for nonexperts, the book reports on a comprehensive study of STEM faculty at an anonymized US university that is large, prestigious, and research intensive. Complex phenomena are explained in an easy-to-grasp fashion, and rigorous data are used to provide evidence for the authors' assertions.

Researchers will likely see their own experiences in the book's rich descriptions of the priorities and pressures of a competitive academic environment. These descriptions, paired with ample quotes from interviewees, make for compelling reading, painting a portrait of STEM faculty who work all the time, are highly engaged with their work, struggle to balance personal and professional obligations, and feel that they are always behind and never enough.

"Most want objective, neutral STEM work without reference to the identities of individual scientists. But there's a catch," argue Blair-Loy and Cech. "Historically—and today—that unmarked, unobtrusive

identity of scientist can be embodied only by white, heterosexual men." The authors weave together a compelling case for this argument by drawing on findings from multiple sources of data, including university data (e.g., rank, pay, group memberships, research funding) for all 502 STEM faculty in their case university and indicators of performance (e.g., number of publications, citation counts). They match these data to survey responses from an impressive 53% of potential respondents, allowing them to make strong claims about generalizability.

Drawing on these data, the authors found, for instance, that, although STEM faculty believed that researchers who are mothers are



Bias against underrepresented groups, including mothers, hinders innovation.

not as devoted to their work as researchers who are fathers, the mothers they surveyed reported working as many hours per week as their male counterparts and performed at equal or higher levels (e.g., yearly publication rates), despite spending many more hours a week performing childcare than male researchers who were also parents. Nonetheless, female researchers who were mothers earned less than their peers.

The veracity of such findings might be called into question given the study's small sample size, low reliability of measures, and lack of evidence of validation of measures. However, any potential weaknesses are more than made up for by additional data sources, including survey findings from more than 7000 STEM faculty from universities across

Misconceiving Merit

Mary Blair-Loy and
Erin A. Cech
University of Chicago Press,
2022. 232 pp.



the US and qualitative interviews with 85 STEM faculty from the authors' case university, which provide a rich sense of the meaning making in which STEM researchers engage in their efforts to understand merit.

One of the most compelling parts of the book details how the authors asked interviewees to reflect on a study published in *Science*, which found evidence of anti-Black bias in NIH funding rates, when controlling for key factors such as the applicants' previous funding and research productivity (1). The participants' responses revealed strong inclinations to reject this finding and to continue to justify the system as meritorious. Many called the study methodology into question and insisted that grant reviewers steadfastly ignore cues about applicants' identities. Such assertions stand in stark contrast with interviews conducted with researchers from marginalized groups that appear earlier in the book, in which they recount working to hide one's identity and feeling excluded at work, and with other interviews that appear throughout the book, in which straight white male researchers

expressed discomfort with interacting with colleagues from marginalized groups.

I wish the authors had spent more time laying out avenues for change, as this book will likely be of interest to university administrators, professional associations, and STEM thought leaders. However, they do provide some clear observations that STEM faculty and their institutions must recognize to move forward, including the fact that bias exists in this setting, that collaborative work and mentorship of students and junior colleagues is essential, and that a healthier work-family culture can benefit all. ■

REFERENCES AND NOTES

1. D. K. Ginther *et al.*, *Science* **333**, 1015 (2011).

10.1126/science.add5909

The reviewer is at the Department of Psychology, University of Guelph, Guelph, ON N1G 2W1, Canada. Email: sonhing@uoguelph.ca



Cyborg and Bionic Systems

Cyborg and Bionic Systems is an online-only, Open Access journal published in affiliation with the **Beijing Institute of Technology (BIT)** and distributed by the **American Association for the Advancement of Science (AAAS)**. The journal publishes original, peer-reviewed articles based on fundamental, applied science, or their interaction. *Cyborg and Bionic Systems* promotes the knowledge interchange and hybrid system codesign between living beings and robotic systems. The journal also covers a wide range of fields related to cybernetic organisms (cyborg) and bionic systems (CBS), mainly including robotics, biomedical engineering and neuro-engineering.

Submit your research to *Cyborg and Bionic System* today!

Learn more at spj.sciencemag.org/cbsystems

The Science Partner Journal (SPJ) program was established by the American Association for the Advancement of Science (AAAS), the nonprofit publisher of the *Science* family of journals. The SPJ program features high-quality, online-only, Open Access publications produced in collaboration with international research institutions, foundations, funders and societies. Through these collaborations, AAAS furthers its mission to communicate science broadly and for the benefit of all people by providing top-tier international research organizations with the technology, visibility, and publishing expertise that AAAS is uniquely positioned to offer as the world's largest general science membership society. Visit us at spj.sciencemag.org



LETTERS

Edited by Jennifer Sills

Editorial Retraction

On 22 August 2014, *Science* published the Research Article “Chemically mediated behavior of recruiting corals and fishes: A tipping point that may limit reef recovery” by D. L. Dixon *et al.* (1). On 17 February, we published an Editorial Expression of Concern (2) after being made aware of data manipulation accusations pertaining to this paper. In August, the University of Delaware informed us that the data in Figures 1A, 2, 3, and 4 were questioned and that they no longer have confidence in the validity of the data. In agreement with the recommendation of the University of Delaware, *Science* is retracting the paper.

H. Holden Thorp
Editor-in-Chief

REFERENCES AND NOTES

1. D. L. Dixon, D. Abrego, M. E. Hay, *Science* **345**, 892 (2014).
2. H. H. Thorp, *Science* **375**, 729 (2022).

Published online 9 August 2022
10.1126/science.ade2691

The Amur tiger needs transborder protection

Of the nine subspecies of tiger, three—the Bali, Javan, and Caspian tigers—became extinct in the 20th century. The South China tiger, unique to China, became extinct in the wild in the 1990s (1). Human activities, including migration, war, wildlife trade that includes illegal sales, and deforestation, caused their extinction (2–4). The remaining five tiger subspecies, which are all Endangered or Critically Endangered (5), continue to face these threats. Thanks to effective conservation policies, the population of one subspecies, China’s Amur tiger (*Panthera tigris altaica*), has grown substantially in the past few years. However, the Amur tigers often cross China’s border into Russia, complicating protection efforts. China and Russia can better protect the Amur tiger by working together.

The Amur tiger was listed in 2011 as Endangered by the International Union for Conservation of Nature (IUCN) (6). It is also a Class I key protected cat species in China due to its population decline (7). China has taken important steps to recover the population, such as bans on culling and deforestation, captive breeding,

and the establishment of tiger reserves in Heilongjiang and Jilin provinces (8, 9). As a result of these policies, the Amur tiger population in the wild, including in reserves, has increased from 27 in 2017 to more than 60 in 2022 (10). However, when the tigers cross from China into Russia, chances of human-wildlife conflicts increase.

To ensure consistent protection, Russia should implement the strategies that have worked in China. Both countries should also put in place penalties and strict enforcement to discourage the capture and hunting of tigers for commercial gain (11). In addition, China and Russia each need a well-publicized wildlife compensation policy to provide reimbursement for property losses caused by tigers, mitigating the risk of ranchers killing tigers who attack or threaten livestock. News media and other educational outlets in both China and Russia should emphasize the importance of protecting endangered species and preventing human-tiger conflicts.

Given the threats to the remaining tiger populations, it is crucial to build on examples of conservation success. The Amur tiger population has shown signs of recovery; transboundary cooperation could help save this vulnerable subspecies.

Li Zheng¹, Joe Mac Regenstein², Lianzhou Jiang¹, Zhongjiang Wang^{1*}

¹College of Food Science, Northeast Agricultural University, Harbin, Heilongjiang 150030, China.

²Department of Food Science, Cornell University, Ithaca, NY 14853, USA.

*Corresponding author.

Email: wzjname@neau.edu.cn

REFERENCES AND NOTES

1. S. J. Luo *et al.*, *PLOS Biol.* **2**, 12 (2004).
2. P. Villalva, E. Moracho, *Science* **364**, 743 (2019).
3. S. Cho *et al.*, *PLOS One* **7**, 17 (2022).

4. J. H. Liew *et al.*, *Sci. Adv.* **7**, eabf7679 (2021).
5. Tiger Species Information (2022); <https://endangeredtigers.org/tiger-species/>.
6. D. Miquelle *et al.*, *Panthera tigris ssp. altaica* (The IUCN Red List of Threatened Species, 2011); www.iucnredlist.org/species/15956/5333650#assessment-information.
7. National Forestry and Grassland Administration of China, “Official release of the updated list of wild animals under special state protection in China” (2021); www.forestry.gov.cn/main/586/20210208/095403793167571.html [in Chinese].
8. A. Rabinowitz *et al.*, *Science* **333**, 1824 (2011).
9. F. Perez, Z. J. Piao, X. H. Liu, *Environ. Sci. Pollut. Res.* **8**, 29 (2022).
10. National Forestry and Grassland Administration of China, CCTV13 EWS (2022); www.forestry.gov.cn/main/5980/20220801/084323515836212.html [in Chinese].
11. F. Courchamp *et al.*, *PLOS Biol.* **4**, 12 (2006).

10.1126/science.ade0807

Genomic research data and the justice system

In their Policy Forum “Get law enforcement out of biospecimen authentication” (17 June, p. 1274), D. J. H. Mathews and N. Ram propose an identification system for cells and tissues used in biomedical research that would be separate and distinct from the Combined DNA Index System (CODIS) used by the US criminal justice system. Their proposal could potentially create artificial silos between genomic data in the justice system and in biomedical research, making it inefficient and ultimately counterproductive.

CODIS was purposefully designed to guarantee that people could be identified while their personal data, such as health information, remained private (1). In this system, short tandem repeats (STRs) create a unique DNA fingerprint as an identifier for each person. These STRs were initially thought to



Efforts by China and Russia could save the Amur tiger from extinction.

PHOTO: XUEFENG ZHENG

be unrelated to any phenotypic information, although evidence may now suggest otherwise (2). However, preserving anonymity remains a fundamental intent of the system. The design of CODIS reflects the fact that suspected criminals (3) and even prison inmates (4) retain some privacy rights under the US Constitution.

Mathews and Ram acknowledge the economies of scale and the sound practical reasons for using the same genetic loci in research settings and in CODIS but argue that using alternative loci for tissue and cell-line authentication would be preferable. We disagree. The use of CODIS loci within a research-based authentication system—with the necessary safeguards in place, such as the penalties legislated under the Justice for All Act of 2004 (5)—would be unlikely to exacerbate problems of bias. This is especially true given that DNA fingerprints are otherwise easily attainable: Currently, a deluge of private genomic data has been made public through various direct-to-consumer platforms, and it is increasingly trivial to sequence and deanonymize DNA from tissues and cells.

Mathews and Ram note that the criminal justice system is unwilling to share any DNA fingerprints for research purposes, which makes sense given the strict criminal penalties for the misuse of CODIS data (6). Thus, under Mathews and Ram's proposed system, research into determining problematic correlations between phenotypes and CODIS STRs will ultimately be limited, as these data will be collected primarily by the justice system, not by bioscientists.

We believe that using an alternative STR system would be a lost opportunity. With research-based authentication using the same loci as CODIS, the amount of useful data that could be collected and correlated with the CODIS STRs will grow as we expand research into these STRs. Collecting such data could provide an invaluable service in either supporting or refuting concerns that CODIS may not be as privacy friendly as first thought. If the resulting research were to show strong phenotypic correlations with CODIS loci, we would then demand new loci not only for researchers, as Mathews and Ram suggest, but for the criminal justice system as well.

Dov Greenbaum^{1,2,3*} and Mark Gerstein^{3,4,5}

¹Harry Radzyner Law School, Reichman University, Herzliya, Israel. ²Zvi Meitar Institute for Legal Implications of Emerging Technologies, Reichman University, Herzliya, Israel. ³Department of Molecular Biophysics and Biochemistry, Yale University, New Haven, CT 06520, USA. ⁴Program in Computational Biology and Bioinformatics, Yale University, New Haven, CT 06520, USA.

⁵Department of Computer Science, Yale University, New Haven, CT 06520, USA.

*Corresponding author.

Email: dov.greenbaum@yale.edu

REFERENCES AND NOTES

1. Office of Technology Assessment, US Congress, "Genetic witness: Forensic uses of DNA tests" (Publication OTA-BA-438, 1990).
2. N. Wyner *et al.*, *Front. Genet.* **11**, 884 (2020).
3. *Carpenter v. US*, 585 U.S. 2018 (2018).
4. *Florence v. Board of Chosen Freeholders*, 566 U.S. 318 (2012).
5. "Justice for All Act 2004," Public Law No. 108–405 (2004).
6. 42 U.S. Code § 14133(c).

10.1126/science.add7974

Response

Greenbaum and Gerstein argue that we should embrace the dissolving of silos between contexts and data sources by using Combined DNA Index System (CODIS) markers for research authentication purposes. However, we believe the silos that isolate research data from law enforcement data and activities are both justified and critical. The research community must take steps to reduce the risk that these silos fall.

Greenbaum and Gerstein assert that we should instead maximize the amount of research data that can be collected and compared with the CODIS short tandem repeats (STRs). As they rightly note, the assumption that CODIS STRs and phenotypic information are not related is increasingly untenable (1). However, this observation does not necessitate that researchers use CODIS STRs specifically for authentication. We support Greenbaum and Gerstein's call for further research on CODIS STR data, and we trust that researchers interested in such work do not intend to "misuse" the data. But CODIS-focused research should be undertaken directly and described to research participants as such, rather than occurring as a by-product of authentication standards. Whereas the Justice for All Act might apply to certain researchers funded by the Department of Justice, its protections do not appear to cover any genetic data outside the criminal legal system. Furthermore, law enforcement's refusal to permit access to CODIS itself should not be used to argue for increasing risks to all research participants.

Greenbaum and Gerstein also argue that avoiding CODIS markers for authentication is unnecessary because, effectively, the cat is out of the bag. Given the preponderance of direct-to-consumer platforms and the ease with which data from tissues can be deanonymized, Greenbaum and Gerstein suggest that CODIS marker-based authentication standards do little harm.

We disagree. As we explain in our Policy Forum, the risk of attracting law enforcement interest to research data increases when the data are available in a recognizable way, which is precisely what CODIS

marker-based authentication standards do. Data produced pursuant to these standards may be, and indeed likely are, even easier for law enforcement to exploit than the sprawling family trees that investigative genetic genealogy with consumer genetic data requires.

Finally, Greenbaum and Gerstein do not respond to the other serious harms our Policy Forum identified. Using CODIS markers could undermine the trust and subsequently recruitment of research participants, including those from historically marginalized and excluded groups (whose trust may be particularly undermined when research uses the language and tools of law enforcement), and impose additional potential harms on already vulnerable populations, including children (whose inclusion in genetic research is predicated on a "minimal risk" analysis that may no longer be tenable). The risks are substantial, and the benefits of both biospecimen authentication and scientific research can be secured in ways that are less likely to erode trust in science.

Debra J. H. Mathews^{1,2*} and Natalie Ram³

¹Berman Institute of Bioethics, Johns Hopkins University, Baltimore, MD 21205, USA.

²Department of Genetic Medicine, Johns Hopkins University, Baltimore, MD 21205, USA. ³Carey School of Law, University of Maryland, Baltimore, MD 21201, USA.

*Corresponding author. Email: dmathews@jhu.edu

REFERENCES AND NOTES

1. N. Ram, *Va. L. Rev.* **105**, 1357 (2019).

10.1126/science.add8413

TECHNICAL COMMENT ABSTRACTS

Comment on "The missing ocean plastic sink: Gone with the rivers"

Lei Mai, Xiang-Fei Sun, Eddy Y. Zeng

Weiss *et al.* (Reports, 2 July 2021, p. 107)

incorrectly conclude that the residence time for floating microplastic stock at the ocean surface is ~2.4 years. We contend that this conclusion is fundamentally flawed, because the residence time is obtained through dividing a published oceanic stock of plastic debris by a doubtful river microplastic flux estimated by the authors.

Full text: dx.doi.org/10.1126/science.abl6433

Response to Comment on "The missing ocean plastic sink: Gone with the rivers"

Lisa Weiss and Wolfgang Ludwig


Mai *et al.* are mistaken in their assertions that we incorrectly calculated the residence time for floating microplastic stock at the ocean surface and that most of our results are not novel. Their claim that our field-measured data and methods were not rigorous is wrong, as shown by a more careful consideration of what was done.

Full text: dx.doi.org/10.1126/science.abm7305

PUT YOUR RESEARCH OUT IN FRONT

Submit your research:
[cts.ScienceMag.org](https://cts.science.org)

Science Signaling


 Twitter: @SciSignal

 Facebook: @ScienceSignaling

RESEARCH

IN SCIENCE JOURNALS

Edited by Michael Funk

EVOLUTIONARY ECOLOGY

Optimized strategies for life

Metabolic theory posits that physical constraints on energy uptake and allocation drive biological processes. This theory predicts broad ecological patterns such as the observed allometric scaling relationship between animals' metabolic rate and body size. White *et al.* developed a new theory showing that such patterns can also be explained by evolution acting concurrently on metabolism, growth, and reproduction. Using data from over 10,000 species from 12 animal phyla, the authors found support for the prediction that species' lifetime reproduction is optimized, with growth and reproduction both increasing with metabolic level. This work proposes a bridge between metabolic and life history theory, two basic ways of understanding ecological patterns. —BEL

Science, abm7649, this issue p. 834

Theory helps to explain observed ecological and metabolic patterns such as the many sizes and life histories of fish.



SYNTHETIC BIOLOGY

Decoding a multisite mechanism

A multisite phosphorylation mechanism defines a complex signaling system in which the countervailing influences of the phosphorylation of more than one site create a highly nuanced cellular response, in contrast to the simple on-off switch of single-site phosphorylation. Faustova *et al.* have unraveled the “code” for one such system, the signals from cyclin-dependent kinases controlling nuclear localization and nuclear export. Controlling the phosphorylation sites, cyclin-specific short linear motifs, phosphoprimering, and other manipulations enabled synthetic alteration of the observed signaling with control

of the delay in the responses, the magnitude of responses, and the localization dynamics. —PLY

Sci. Adv. 10.1126/sciadv.abp8992 (2022).

NEURODEVELOPMENT

Allocating sensory responsibilities

During late embryogenesis, the developing mouse brain has inputs from both visual and sensory systems that activate overlapping regions of the cortex. Guillamón-Vivancos *et al.* now show how spontaneous activity in the perinatal retina tunes the visual cortex to specialize in interpreting retinal activity as vision. Without such spontaneous retinal activity,

this part of the brain will take on somatosensory responsibilities instead. This handshake between the sensory system and the cortical recipient is established during a limited time in the perinatal phase of development. —PJH

Science, abq2960, this issue p. 845

QUANTUM PHYSICS

Combining lattices and tweezers

Optical lattices have been used as a platform for quantum simulation for the past two decades. More recently, arrays of optical tweezers, which have the advantage of rapid reconfigurability, have risen to prominence. Young *et al.* combined these tools to perform large-scale quantum

walks of strontium-88 atoms prepared in optical tweezers, and then implanted into the sites of an optical lattice. The combined platform holds promise for applications in quantum science. —JS

Science, abo0608, this issue, p. 885

METALLOENZYMES

Caught N the act

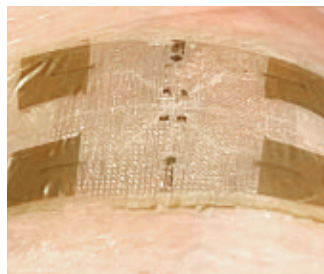
Although the nitrogen-fixing enzyme nitrogenase has been studied extensively by x-ray crystallography, enzymes in crystals cannot move or form transient complexes as they would in solution. This is a particular problem for nitrogenase because the protein that harbors the site of nitrogen reduction requires a dynamic interaction with

an ATP-hydrolyzing subunit. Rutledge *et al.* used cryo-electron microscopy to examine nitrogenase samples prepared under turnover conditions with abundant ATP and the chemical reductant dithionite. They observed an asymmetric complex of the two proteins and, correspondingly, differences between subunits at the interface and near the key nitrogenase cofactor, FeMoco. These structures generate many new questions about electron delivery and coupling between the proteins, which are key to understanding this essential reaction. —MAF

Science, abq7641, this issue p. 865

FLEXIBLE ELECTRONICS Chip-less electronic skin

Flexible electronic materials, or e-skins, can be limited by the need to include rigid components. A range of techniques have emerged to bypass this problem, including approaches for wireless communication and charging based on silicon, carbon nanotubes, or conducting polymers. Kim *et al.* show that epitaxially grown, single-crystalline gallium nitride films on flexible substrates can be used for chip-less, flexible e-skins. The main advantage is that the material is flexible and breathable, thus providing better comfort. The devices convert electrical energy into surface acoustic waves using a piezoelectric resonator. The resonator is sensitive to changes in strain, mass changes due to the absorption or loss of ions, and ultraviolet



A new flexible film may be of use in wearable electronics.

light, all of which can be used for different sensing measurements. —MSL

Science, abn7325, this issue p. 859

CANCER Contextually complicated CAFs

Cancer-associated fibroblasts (CAFs) are often implicated in drug resistance and tumor progression, but they can also be associated with tumor suppression. Remsing Rix *et al.* discovered another twist in the role of CAFs in drug efficacy: The same CAFs that induced drug resistance in some lung cancer cell lines promoted drug sensitivity in others. In certain tumors, drug-induced compensatory signaling was attenuated by certain proteins secreted by CAFs, thus enhancing or restoring drug efficacy in treatment-naïve and drug-resistant cells. —LKF

Sci. Signal. **15**, eabj5879 (2022).

CORONAVIRUS Boosting a weakened response

The Omicron strain of severe acute respiratory syndrome coronavirus 2 (SARS-CoV-2) was first detected in 2021 and is now dominant across the globe. Bowen *et al.* show that the Omicron sublineages BA.1, BA.2, BA.2.12, and BA.4/5 have increased affinity for the ACE2 receptor on human cells, but show decreased cell-cell fusion. The authors used pseudovirus to measure neutralizing activity against Omicron sublineages in plasma from individuals who were previously infected or vaccinated with one of seven vaccines, all based on the Wuhan-Hu-1 variant. For both vaccinees and convalescents, there was severe dampening of neutralizing activity. Boosting with either the same vaccine used initially or one of the other Wuhan-Hu-1-based vaccines increased neutralization across all vaccines evaluated. —VV

Science, abq0203, this issue p. 890

IN OTHER JOURNALS

Edited by **Caroline Ash**
and **Jesse Smith**



PUBLIC HEALTH How to nudge in the right direction

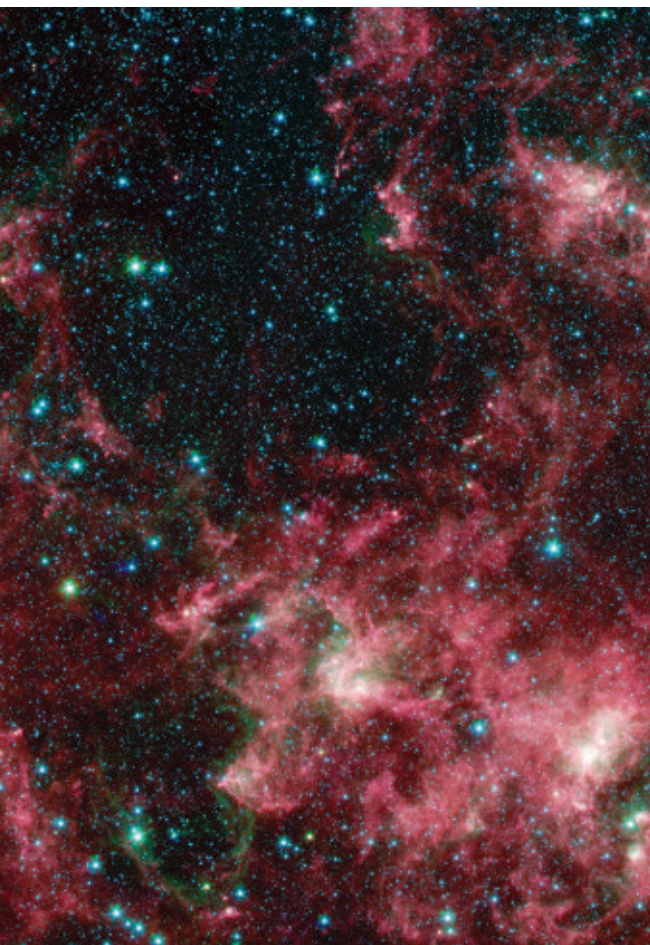
Public health communications during the COVID-19 pandemic emphasized guidance from medical authorities to practice social distancing, masking, and handwashing. However, these authoritative messages (i.e., “don’t break official COVID-19 guidelines”) may not be the most effective way to motivate compliance because of psychological reactance. In a field study during January 2021, Banker *et al.* analyzed data from over 57,000 travelers in a major US airport that presented color-coded visual indicators about crowdedness levels. The visual indicators were accompanied by short messages called nudges (e.g., “Protect yourself. Go toward green for less crowded areas”). Compared with authoritative

nudges from the Centers for Disease Control and Prevention (CDC), the visual indicators that accompanied informal nudges motivated more social distancing in the airport and may be more effective at preventing transmission of pathogens than more officious messages. —EEU

Proc. Natl. Acad. Sci. U.S.A. **119**, e2116156119 (2022).

NEUROSCIENCE Coronavirus in cortical astrocytes

Many patients suffering with or having recovered from COVID-19 present with neurological symptoms. Are these symptoms a result of direct infection of the nervous system or are they a secondary consequence of widespread inflammation in other tissues? Andrews *et al.* used primary cortical tissue from both the developing



STELLAR ASTROPHYSICS

Zooming into the most massive star

The most massive individual star known is R136a1 in the Tarantula Nebula, but its exact mass has been the subject of debate. R136a1 is located in a dense stellar cluster, so atmospheric distortion causes blending with other cluster members, contaminating measurements. Kalari *et al.* performed ground-based speckle imaging of R136a1, achieving spatial resolution of 30 to 40 milliarcseconds, which is better than previous observations, including those taken from space. This resolves R136a1 from two contaminating stars. Combining their photometric measurements with stellar models, the authors determined that R136a1 formed with 200 ± 30 solar masses, which is lower than previous estimates but still the most massive individual star known. —KTS *Astrophys. J.* [Preprint] arXiv:2207.13078 (2022).

The Tarantula Nebula, photographed here by NASA's Spitzer Space Telescope, hosts the most massive individual star known.

Way show that positioning of phosphotyrosine residues can have particular importance in signal output. Phosphotyrosine residues are modular, in that they recruit adaptor proteins that bind phosphotyrosine-containing motifs. The authors focused on two phosphotyrosine residues in the protein A36 from Vaccinia virus that allows the virus to interact with a host cell's cytoskeleton to enable its transport and release. Results indicate that the positioning of the two sites is optimized for efficient signaling output. Such findings may be valuable for synthetic biology applications, in which such modules could be used to design signaling outcomes. —LBR

eLife **11**, e74655 (2022).

MALARIA

Plastic parasites elude control

Malaria parasites, *Plasmodium* spp., are genetically plastic and resistant to control efforts despite—or possibly even because of—their complex life cycles. Public health interventions could therefore have effects beyond the induction of drug resistance. Early *et al.* applied a modeling approach, supported by genomics, to *Plasmodium falciparum* obtained in French Guiana to determine how control efforts might influence the parasite's life cycle. Only sexual forms of *P. falciparum* can infect mosquitoes and be transmitted to new hosts, but only asexual forms can replicate and amplify in humans. As the number of human cases declined, the authors found that the most strongly selected genes were enriched for the transcription factors required for sexual development. Higher rates of sexual conversion that lead to greater transmission potential from humans to mosquitoes, which could undermine the impact of control measures. —CA

Proc. Natl. Acad. Sci. U.S.A. **119**, e2122165119 (2022).

brain and the adult brain, paired with stem cell–derived cortical organoids, to evaluate which human neural cell types can be directly infected by SARS-CoV-2. In primary cortical tissue cultures and cortical organoids exposed to SARS-CoV-2, the authors observed significant infection and viral replication specifically in immature and mature astrocytes, which has downstream consequences for neurological function. —PRS

Proc. Natl. Acad. Sci. U.S.A. **119**, e2122236119 (2022).

CARBON CAPTURE

Protecting quinones with ethanol

Developing robust technology to capture carbon dioxide emissions from combustion streams is a key factor in mitigating climate change.

Most current approaches focus on amines that bind chemically to carbon dioxide and release it upon heating. An electrochemical approach to toggling the catch-and-release modes could be more efficient. However, in such cases, capture agents such as reduced quinones may react with oxygen instead of carbon dioxide. Barlow and Yang report that added ethanol can head off this undesired pathway through hydrogen bonding, raising prospects for further investigation of this method. —JSY

J. Am. Chem. Soc. 10.1021/jacs.2c04044 (2022).

PHOTOSYNTHESIS

Building chlorophyll b

Photosynthetic organisms use a wide range of pigments to absorb light energy and convert it into chemical energy. Chlorophyll is a familiar green pigment, but there are in fact

several kinds of chlorophyll with differences in peripheral functional groups that tune the absorption spectrum and redox potential. Liu *et al.* characterized an oxidase involved in the synthesis of chlorophyll *b*, an essential, blue-shifted pigment. In addition to uncovering the details of the mechanism and specificity that may be useful in engineering efforts, the authors show that this enzyme can accept a substrate analog, leading to a non-native chlorophyll derivative. —MAF

ACS Cent. Sci. 10.1021/acscentsci.2c00058 (2022).

SIGNAL TRANSDUCTION

Positioning signaling adaptors

Phosphorylation of tyrosine residues in proteins is a common mechanism for cellular signal transduction. Basant and

ALSO IN *SCIENCE* JOURNALS

Edited by Michael Funk

CORONAVIRUS

T cells in vaccine immunity

Whether a person has protective immunity derived from a vaccine is usually measured in terms of neutralizing antibody responses. Severe acute respiratory syndrome coronavirus 2 (SARS-CoV-2) variants have mutations that reduce neutralization by antibodies, which has increased breakthrough infections in vaccinated people. However, these infections have not proportionally increased hospitalization and deaths, indicating that antibodies are not the whole story. In a Perspective, Wherry and Barouch discuss the emerging role of T cell immunity in preventing severe COVID-19, even when it is caused by antibody-escape variants. Measuring T cell responses to vaccines will improve our understanding of their role in immune protection, especially in the long term after antibody waning. This work should also lead to optimized immune protection strategies, including the development of updated COVID-19 or pan-beta-coronavirus vaccines. —GKA

Science, add2897, this issue p. 821

NEUROGENETICS

Zooming in on dementia genes

Neurodegenerative disorders are a major problem worldwide, and their incidence is continuing to increase. These are usually complex polygenic traits, and although many gene loci have been identified in association with these disorders, the functional roles of these loci are unclear and most of them fall within noncoding regions of the genome. Cooper *et al.* used massively parallel reporter assays to screen noncoding variants reported in genome-wide association studies of two neurodegenerative disorders, followed by functional validation

in neurons and microglia. With this combination of methods, the authors identified regulatory variants in several different genes that play functional roles in disease pathogenesis, as well as interactions between these genes. —YN

Science, abi8654, this issue p. 832

PARKINSON'S DISEASE

Uncovering a contributor

Genome-wide association studies (GWAS) have uncovered nearly 100 loci that contribute to risk for Parkinson's disease (PD), which affects an estimated 6 million people worldwide. However, target genes and biological mechanisms associated with these loci remain largely unexplored. Diaz-Ortiz *et al.* examined a PD GWAS risk locus on chromosome 7, linking it to the transmembrane protein Glycoprotein Nonmetastatic Melanoma Protein B (GPNMB). GPNMB was found to interact with alpha-synuclein (aSyn), the key protein that forms the pathological inclusions that characterize PD (see the Perspective by Mollenhauer and von Arnim). In cells, GPNMB was both necessary and sufficient for the uptake of fibrillar forms of aSyn and the subsequent development of aSyn pathology. —SMH

Science, abk0637, this issue p. 833;

see also add7162, p. 818

DEFLUORINATION

Forever chemicals' Achilles' heel

Per- and polyfluoroalkyl substances (PFAS) have been referred to as "forever chemicals" because of their resistance to most biological and chemical degradation mechanisms. Most current methods use very harsh conditions to decompose these compounds. Trang *et al.* found that there is a potential weak spot in carboxylic acid-containing PFAS: Decarboxylation in

polar, non-protic solvents yields a carbanion that rapidly decomposes (see the Perspective by Joudan and Lundgren). The authors used computational work and experiments to show that this process involves fluoride elimination, hydroxide addition, and carbon-carbon bond scission. The initial decarboxylation step is rate limiting, and subsequent defluorination and chain-shortening steps occur through a series of low barrier steps. The procedure can accommodate perfluoro-ether carboxylic acids, although sulfonic acids are not currently compatible. —MAF

Science, abm8868, this issue p. 839;

see also add1813, p. 816

PLANT SCIENCE

More soybeans by light management

Plants protect themselves from too much sun by dissipating excess light energy. Unfortunately, the switch from dissipating light energy to using light energy for photosynthesis is not as nimble as the clouds moving across the sky. De Souza *et al.* applied a bioengineered solution that speeds up accommodation by nonphotochemical quenching in soybeans, a widely cultivated and essential crop. In field trials, seed yield increased in some cases up to 33%. —PJH

Science, adc9831, this issue p. 851

NANOMATERIALS

Ligand-driven metastability

A high-pressure phase of a solid can persist at ambient pressure if there are kinetic barriers to its relaxation. Xiao *et al.* performed detailed mechanistic studies on the reversibility of four- to six-coordinate pressure-driven solid-phase transitions in well-controlled model systems of nanospheres or nanorods of cadmium selenide, cadmium

sulfide, or both (see the Perspective by Mao and Lin). The choice of surface ligands could control the reversibility of the transformations. Interparticle sintering helped to eliminate crystal defects and relaxed lattice distortions from the high-pressure rock-salt structures to maintain their ambient-pressure metastability. —PDS

Science, abq7684, this issue p. 870;

see also add5433, p. 814

THERMOELECTRICS

A flexible power source

Thermoelectric materials can harvest heat and turn it into power. Heat sources potentially include the heat generated by humans through wearable devices and might enable self-powering systems, but the lack of ductility for most thermoelectrics poses a major problem. Yang *et al.* found a thermoelectric silver/copper-based semiconductor that also is ductile (see the Perspective by Hou and Zhu). This material allows for a thin, flexible device capable of producing power, even when adhered to a wrist. —BG

Science, abq0682, this issue p. 854;

see also add7029, p. 815

IMMUNOLOGY

The complete BCR comes into focus

B cell activation is initiated by antigen binding to the B cell receptor (BCR), resulting in proliferation and differentiation into either plasma cells or memory cells. A better understanding of B cell signaling depends on a more complete picture of the BCR's structure. Two groups resolved cryo-electron microscopy (cryo-EM) structures of the intact BCR complex, which comprises a membrane-bound immunoglobulin (Ig) linked to a transmembrane Ig- α /Ig- β (CD79) signaling complex (see the Perspective by Tolar and Pierce). Su *et al.* determined the

cryo-EM structure of the IgM BCR, and Ma *et al.* describe cryo-EM structures of both IgG and IgM BCRs. Both studies reveal important features of the BCR's structure in its native state before engagement by antigen, and this work opens up the field to future studies of B cell activation and function. —STS

Science, abo3923, abo3828, this issue p. 875, p. 880; see also add8065, p. 819

AUTOIMMUNITY

Turning down TRAF3 revs up B cells

TRAF3 is a cytoplasmic adaptor protein involved in multiple intracellular signal transduction pathways. Rae *et al.* identified nine individuals with a previously undescribed monogenic immune dysregulatory syndrome caused by a loss-of-function mutation in one of their two *TRAF3* alleles. Patients with this haploinsufficiency syndrome exhibited B cell hyperactivity leading to hypergammaglobulinemia and autoimmunity, but they also displayed increased susceptibility to recurrent bacterial infections. Common human genetic variants of *TRAF3* associated with lower gene expression were found to carry an increased risk of autoimmune disease and some B cell malignancies. These findings point to functional impairment of TRAF3 as a shared mechanism leading to B cell dysfunction, hyperactivity, and disease in the presence of either rare loss-of-function germline mutations or much more common genetic variants. —IRW

Sci. Immunol. **7**, eabn3800 (2022).

AUTISM SPECTRUM

Exploiting face processing

The heterogeneity observed in patients with autism spectrum disorder (ASD) highlights the need for better patient stratification methods. Mason *et al.* evaluated the use of the speed of early-stage face processing

(N170 latency) for patient stratification and prognosis in subjects with ASD and in age-matched healthy individuals. N170 latency was slower in individuals with ASD and was correlated with response to faces measured with functional magnetic resonance imaging and with polygenic risk score. Among subjects with ASD, the N170 values stratified patients according to socialization prognosis and improved power in a simulated clinical trial. The results suggest that including N170 evaluation in patient stratification might help in the design and development of patient-specific therapies for ASD. —MM

Sci. Transl. Med. **14**, eabf8987 (2022).

CELL BIOLOGY

Phosphorylated XPD regulates mitosis

Xeroderma pigmentosum group D protein (XPD) is a DNA helicase involved in DNA repair and transcription. *XPD* mutations cause a variety of human recessive disorders, including neurological and skin abnormalities, elevated cancer rates, and intellectual and growth deficits. Compe *et al.* show that XPD phosphorylated by the CDK1 mitotic kinase interacts with Eg5, a motor protein required to establish a mitotic spindle. Cells from XP-D patients with mutations that block the XPD-Eg5 interaction display defective mitosis and chromosome segregation. The authors conclude that, in addition to changes in DNA repair and transcription, mitotic defects contribute to XP-D patient phenotypes. —DLD

Sci. Adv. **10**, 1126/sciadv.abp9457 (2022).

RESEARCH ARTICLE SUMMARY

NEUROGENETICS

Functional regulatory variants implicate distinct transcriptional networks in dementia

Yonatan A. Cooper, Noam Teyssier, Nina M. Dräger, Qiuyu Guo, Jessica E. Davis, Sydney M. Sattler, Zhongan Yang, Abdulsamie Patel, Sarah Wu, Sriram Kosuri, Giovanni Coppola, Martin Kampmann, Daniel H. Geschwind*

INTRODUCTION: The widespread adoption of genome-wide association studies (GWASs) has revolutionized the detection of genetic loci associated with complex traits. However, identification of the causal variants and mechanisms underlying genotype–phenotype associations poses an enormous challenge because most common susceptibility loci reside in noncoding genomic regions and are composed of many correlated polymorphisms owing to linkage disequilibrium (LD). Massively parallel reporter assays (MPRAs) permit the high-throughput functional characterization of noncoding genetic variation, yet they have not been systematically applied to neurodegenerative disease. In this study, we used MPRA coupled with CRISPR-based vali-

dation to identify likely causal genetic variants underlying two neurodegenerative conditions that are neuropathologically linked by intracellular tau protein aggregation—Alzheimer's disease (AD) and progressive supranuclear palsy (PSP).

RATIONALE: Neurodegenerative dementias such as AD and PSP are a major cause of morbidity and mortality worldwide. There are no disease-modifying therapeutics for either disorder, motivating major efforts to characterize disease pathogenesis. Identifying causal genetic factors and downstream associated risk genes are fundamental initial steps in developing a mechanistic understanding that would enable therapeutic development.

RESULTS: We tested the transcriptional regulatory activity of 5706 noncoding single-nucleotide variants, representing 25 genome-wide significant loci associated with AD and nine loci associated with PSP, by MPRA, using the neuroepithelial-like human embryonic kidney 293T (HEK293T) cell line. We identified 320 different functional regulatory variants (frVars) that affect gene expression within 27 of these loci. AD frVars were enriched within microglial enhancers, whereas PSP frVars were enriched within neuronal enhancers and, to a lesser extent, oligodendrocytes, consistent with differential cellular impact in each disease.

The majority of frVars (94%) overlapped two or more known functional annotations in human brain tissue or blood, nearly two-thirds of which were predicted to disrupt transcription factor binding, indicating their potential relevance in human disease. Forty-two high-confidence regulatory variants distributed across 15 AD loci and three PSP loci were selected for validation, using either CRISPR droplet sequencing (CROP-seq) or direct CRISPR excision in induced pluripotent stem cell–derived neurons, microglia, and astrocytes, enabling validation of 19 functional variants, implicating 20 risk genes across 11 loci.

Our data provide evidence implicating *C4A*, *PVRL2*, and *APOC1* as risk genes in AD and *PLEKHM1* and *KANSL1* as risk genes in PSP, as well as additional validation for more than a dozen other genes. MPRA-defined functional variants preferentially disrupt predicted transcription factor binding sites (TFBSs) that converge on enhancers with differential cell type–specific activity in PSP and AD, implicating a neuronal *SP1*-driven regulatory network in PSP pathogenesis.

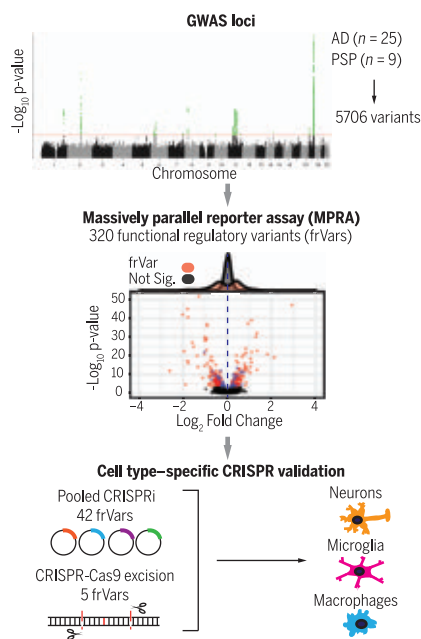
CONCLUSION: We provide systematic characterization of common variants underlying disease risk for two distinct neurodegenerative disorders, AD and PSP. Our work illustrates the utility of integrating multiplexed reporter and CRISPR assays to efficiently characterize noncoding disease-associated variation, thereby permitting the identification of risk genes, even in complex loci with high LD. These analyses support a mechanism underlying noncoding genetic risk, whereby common genetic variants drive disease risk in aggregate through polygenic cell type–specific regulatory effects on specific gene networks. ■

The list of author affiliations is available in the full article online.

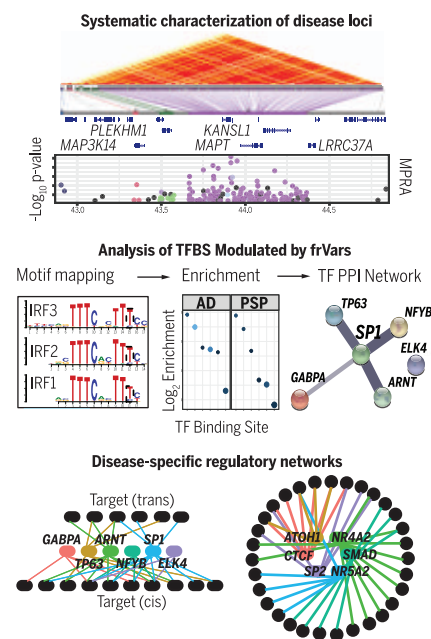
*Corresponding author. Email: dhg@mednet.ucla.edu
Cite this article as Y. A. Cooper et al., *Science* 377, eabi8654 (2022). DOI: 10.1126/science.abi8654

READ THE FULL ARTICLE AT
<https://doi.org/10.1126/science.abi8654>

Regulatory variant identification



Biological insight



Massively parallel functional genomics identifies genes and mechanisms in dementia. We used MPRA to screen thousands of common genetic variants associated with either AD or PSP to identify 300 likely functional regulatory variants. When coupled with CRISPR editing, this approach permitted the dissection of multiple risk loci and identification of several risk genes. The ability to view the aggregate activity of genetic risk shows convergence on disease- and cell type–specific transcriptional networks. TF, transcription factor; PPI, protein–protein interaction.

RESEARCH ARTICLE

NEUROGENETICS

Functional regulatory variants implicate distinct transcriptional networks in dementia

Yonatan A. Cooper^{1,2,3}, Noam Teyssier⁴, Nina M. Dräger⁴, Qiuyu Guo³, Jessica E. Davis⁵, Sydney M. Sattler⁴, Zhongang Yang³, Abdulsamie Patel³, Sarah Wu³, Sriram Kosuri⁵, Giovanni Coppola^{3,6}, Martin Kampmann^{4,7}, Daniel H. Geschwind^{1,8,9,10,*}

Predicting the function of noncoding variation is a major challenge in modern genetics. In this study, we used massively parallel reporter assays to screen 5706 variants identified from genome-wide association studies for both Alzheimer's disease (AD) and progressive supranuclear palsy (PSP), identifying 320 functional regulatory variants (frVars) across 27 loci, including the complex 17q21.31 region. We identified and validated multiple risk loci using CRISPR interference or excision, including complement 4 (*C4A*) and *APOC1* in AD and *PLEKHM1* and *KANSL1* in PSP. Functional variants disrupt transcription factor binding sites converging on enhancers with cell type-specific activity in PSP and AD, implicating a neuronal SP1-driven regulatory network in PSP pathogenesis. These analyses suggest that noncoding genetic risk is driven by common genetic variants through their aggregate activity on specific transcriptional programs.

Neurodegenerative disorders such as Alzheimer's disease (AD) and progressive supranuclear palsy (PSP) are a major cause of morbidity and mortality worldwide (1). Given the paucity of disease-modifying therapeutics, there is a considerable need for investigation of causal disease mechanisms. Sporadic AD and PSP, both known as tauopathies because of the pathological deposition of tau in the brains of affected individuals (2), are complex polygenic traits with heritability estimates of between 40 and 80% (3, 4) and numerous susceptibility loci identified by genome-wide association studies (GWASs) (5–8). Most of these loci overlap noncoding regions and encompass hundreds of variants that are difficult to study owing to linkage disequilibrium (LD), which hampers the identification of underlying regulatory variants and associated risk genes (9). Salient examples

include regions harboring multiple independent association signals, such as the H1 pan-neurodegenerative risk haplotype at 17q21.31 that includes the *MAPT* locus (10) and the AD risk locus at 19q13.32 that harbors *APOE* (11, 12).

Computational methods alone have limited predictive utility, especially in noncoding regions or regions of high LD (13–15). It is increasingly recognized that functional methods are necessary to identify true causal variants within most loci, but the sheer numbers of variants challenge most experimental approaches. Massively parallel reporter assays (MPRAs) provide a solution, enabling high-throughput experimental characterization of the transcriptional-regulatory potential of noncoding DNA elements. In an MPRA, various regulatory elements are cloned into an expression vector harboring a reporter gene and a unique DNA barcode to create an expression library that is assayed by means of high-throughput sequencing (16, 17). MPRAs have prioritized functional common variation for multiple traits and disorders (18, 19) but have yet to be systematically applied to neurodegenerative disease.

Results

MPRA to identify candidate regulatory GWAS variants

We conducted a staged analysis to identify regulatory variants underlying GWAS loci for two neurodegenerative tauopathies—Alzheimer's disease and progressive supranuclear palsy (Fig. 1A). First, we performed two MPRAs to screen both alleles of 5706 noncoding variants in linkage disequilibrium [squared correlation coefficient (R^2) > 0.8] with

all genome-wide significant polymorphisms from two recent AD GWASs (5, 6) and a PSP GWAS (8). In the first MPRA (MPRA 1), we tested 5223 variants encompassing 14 AD and five PSP GWAS loci. In the second MPRA (MPRA 2), we replicated 326 variants from MPRA 1 to determine assay reproducibility and screened another 483 variants encompassing 11 additional AD loci and four newly identified suggestive loci for PSP (Fig. 1, B and C; fig. S1; and Table 1) (20).

The performance of MPRAs to detect allelic skew depends on high library transfection efficiency, favoring the use of easy-to-transfect immortalized cell lines, such as human embryonic kidney 293T (HEK293T) cells (21). However, we recognized that gene regulatory elements may differ between primary and immortalized cell lines, as well as between different primary cell types. Indeed, AD-associated variants fall within open chromatin across several different neuronal and glial cell types, which are largely nonoverlapping (6). We explored this further using ENCODE deoxyribonuclease (DNase) hypersensitive site (DHS) data (22), confirming poor DNA accessibility overlap between different brain cell types, such as astrocytes and neural progenitors (mean Jaccard index = 0.14). Notably, when we compared this overlap to that of the neuroepithelial-derived HEK293T cell line, we found that HEK293T cells had the highest mean pairwise Jaccard index (0.22; Fig. 1D) compared with active regulatory regions identified across all brain tissues. Moreover, we found that AD and PSP GWAS variants that fell within open chromatin in any brain cell type were also likely to fall within open chromatin in HEK293T cells (mean = 60%; Fig. 1E). These data indicated that HEK293T cells would provide a technically tractable model for efficient screening within a single line.

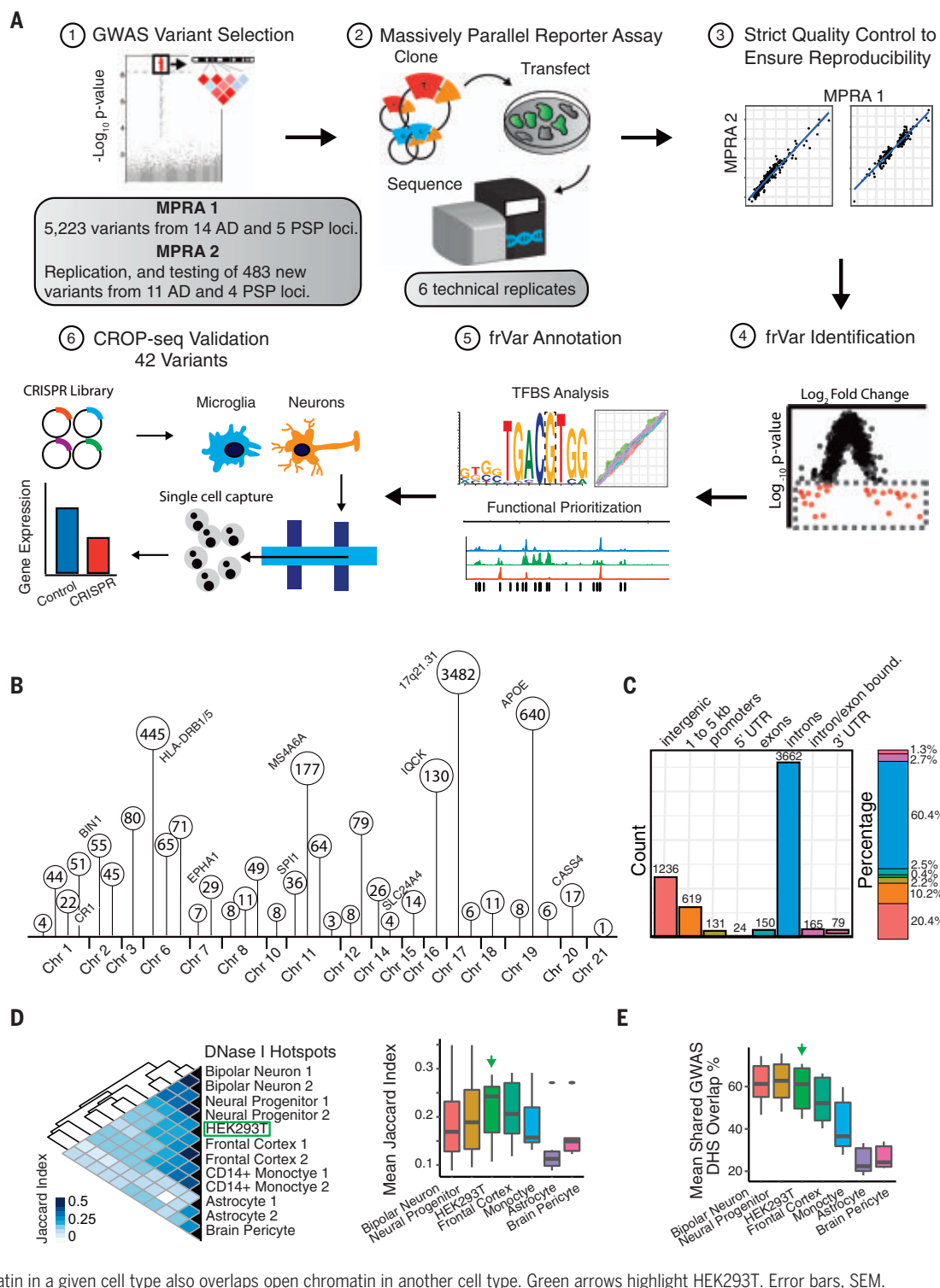
We performed both MPRAs in six independent technical replicates, obtaining activity measurements from at least five unique barcodes for both alleles of 5340 of 5706 different variants (93.6%; data S1) with median library complexities of 40 and 54 barcodes per allele, respectively (fig. S2). Consistency within (fig. S2) and between the separate MPRA experiments was high, highlighting the MPRA's reproducibility [activity scores, Pearson's correlation coefficient (r) = 0.98, $P < 2 \times 10^{-16}$; effect sizes, $r = 0.94$, $P < 2 \times 10^{-16}$; Fig. 2A]. Overall, we observed that ~19% of library elements were transcriptionally active (fig. S3A), in concordance with previous estimates (18, 19). Relative to nonactive elements, transcriptionally active elements were enriched within genomic annotations (HEK293T cells), including DHS (open and active chromatin), H3K27Ac (active enhancers and promoters), H3K4Me3 (active promoters), and chromatin immunoprecipitation sequencing (ChIP-seq) peaks

¹Department of Human Genetics, David Geffen School of Medicine, University of California, Los Angeles, CA 90095, USA. ²Medical Scientist Training Program, David Geffen School of Medicine, University of California, Los Angeles, CA 90095, USA. ³Center for Neurobehavioral Genetics, Jane and Terry Semel Institute for Neuroscience and Human Behavior, University of California, Los Angeles, CA 90095, USA. ⁴Institute for Neurodegenerative Diseases, University of California, San Francisco, CA 94158, USA. ⁵Department of Chemistry and Biochemistry, University of California, Los Angeles, CA 90095, USA. ⁶Department of Psychiatry and Biobehavioral Sciences, David Geffen School of Medicine, University of California, Los Angeles, CA 90095, USA. ⁷Department of Biochemistry and Biophysics, University of California, San Francisco, CA 94143, USA. ⁸Program in Neurogenetics, Department of Neurology, University of California, Los Angeles, CA 90095, USA. ⁹Center for Autism Research and Treatment, Jane and Terry Semel Institute for Neuroscience and Human Behavior, University of California, Los Angeles, CA 90095, USA. ¹⁰Institute of Precision Health, University of California, Los Angeles, CA 90095, USA.

*Corresponding author. Email: dhg@mednet.ucla.edu

Fig. 1. Project overview.

(A) Workflow: (1) 5223 genome-wide significant variants and LD partners encompassing 14 AD and five PSP GWAS loci were selected in MPRA 1. For MPRA 2, select variants identified in MPRA 1 were replicated. An additional 483 variants from 11 AD and four PSP loci were also tested. (2) Both alleles of each variant were barcoded and cloned into an expression library that was transfected into HEK293T cells. Allele expression was quantified by next-generation sequencing of associated barcodes. (3) Strict quality control was performed to confirm assay reproducibility. (4) Identification of variants with significant allele-specific transcriptional skew (frVars). (5) FrVars were further prioritized using brain-specific genomic annotations, and (6) 42 prioritized frVars were validated using a pooled CRISPRi screen (CROP-seq) in iPSC-derived neurons and microglia in addition to five loci validated by direct CRISPR excision. **(B)** The number of variants screened per GWAS locus and their chromosomal location. **(C)** The bar charts (counts and percentages) show genomic annotations for 5223 variants tested in MPRA 1. **(D)** (Left) Heatmap quantifying overlap (Jaccard index) of DNase hotspots between primary brain cell types and HEK293T cells. (Right) Boxplot displaying the mean pairwise Jaccard index for each cell type. **(E)** Tested GWAS variants were overlapped with DNase hotspots from each cell type. The boxplot displays the mean pairwise probability that a GWAS variant within open chromatin in a given cell type also overlaps open chromatin in another cell type. Green arrows highlight HEK293T. Error bars, SEM.



for specific transcription factors (fig. S3B), consistent with their likely functionality. We also identified significant enrichment of transcription factor binding sites (TFBSs) within active elements, including *SP/KLF*, *ETS*, and *AP-1* family members, and did not find major differences in TFBS enrichment when stratifying our results by disorder (fig. S3C).

We applied a stringent statistical threshold to define functional regulatory variants (frVars)—those with significantly different transcriptional efficacy between alleles [two-sided Mann-Whitney *U* test, false discovery rate (FDR) $q < 0.01$, Benjamini-Hochberg (BH)], identifying 320 different frVars distributed across 17 chromosomes (6.0%; Fig. 2B) within

27 of 34 tested GWAS loci, with a median of two frVars per locus (Fig. 2C and Table 1). As expected, effect sizes were generally modest (mean absolute log₂ fold change = 0.53; Fig. 2D). FrVars were highly enriched within library elements that were transcriptionally active [odds ratio (OR) = 6.2; $P < 2 \times 10^{-16}$] (20) and within open chromatin from major

Table 1. AD and PSP GWAS loci. Description of GWAS loci and variants tested in this study. Shown are the locus lead SNPs and annotated genes, as described in the listed GWASs. For each locus, the table shows: the MPRA stage in which it was tested, the number of variants tested per locus, and the number of functional regulatory variants with significant allelic skew (FDR $q < 0.01$; frVars) ultimately identified. Chr, chromosome; Pos, position.

Chr	Pos/cytoband	Lead SNP	Annotated gene	GWAS*	MPRA stage	No. of SNPs tested	frVars
1	85603051	rs114573015	WDR63	PSP	2	4	0
1	180993146	rs57113693	STX6	PSP	1	44	2
1	207692049	rs6656401	CR1	AD 1	1	22	2
1	221995092	rs12125383	DUSP10	PSP	2	51	3
2	127892810	rs6733839	BINI	AD 1	1	55	7
2	234068476	rs35349669	INPP5D	AD 1	2	45	2
3	39510287	rs10675541	MOBP	PSP	1	80	2
6	32578530	rs9271192	HLA-DRB5– HLA-DRB1	AD 1	1	445	13
6	45499614	rs35740963	RUNX2	PSP	1	65	1
6	47487762	rs10948363	CD2AP	AD 1	1	71	3
7	100004446; 100091795	rs1476679; rs12539172	ZCWPW1; NYAP1	AD 1 and 2	2	7	0
7	143110762	rs11771145	EPHA1	AD 1	1	29	3
8	27195121	rs28834970	PTK2B	AD 1	1	8	2
8	27467686	rs9331896	CLU	AD 1	1	11	1
8	131075859	rs2045091	ASAP1	PSP	2	49	2
10	11720308	rs7920721	ECHDC3	AD 2	2	8	1
11	47557871; 47380340	rs10838725; rs3740688†	CELF1/ SPII-PU.1	AD 1 and 2	2	36	5
11	59923508	rs983392	MS4A6A	AD 1	1	177	4
11	85867875	rs10792832	PICALM	AD 1	1	64	0
11	121435587	rs11218343	SORL1	AD 1	1	3	0
12	21314281	rs7966334	SLC01A2	PSP	1	8	0
12	53788003	rs147124286	SP1	PSP	2	79	5
14	53400629; 53391680	rs17125944; rs17125924	FERMT2	AD 1 and 2	2	26	2
14	92926952; 92932828	rs10498633; rs12881735	SLC24A4/RIN3	AD 1 and 2	1	4	1
15	59045774	rs593742	ADAM10	AD 2	2	14	3
16	19808163	rs7185636	IQCK	AD 2	2	130	17
17	17q21.31	NA	MAPT	PSP	1	3482	194
17	61538148	rs138190086	ACE	AD 2	2	6	1
18	29088958	rs8093731	DSG2	AD 1	1	11	2
19	1063443	rs4147929	ABCA7	AD 1	1	8	0
19	19q13.32	NA	APOE/TOMM40	AD 1	1	640	37
19	51727962	rs3865444	CD33	AD 1	2	6	0
20	55018260; 54997568	rs7274581; rs6024870	CASS4	AD 1 and 2	2	17	4
21	28156856	rs2830500	ADAMTS1	AD 2	2	1	1

*Source GWAS for tested loci and variants: PSP, (8); AD 1, (5); AD 2, (6). †Locus remapped in AD GWAS 2. Lead SNPs are not in LD. Both lead SNPs were tested here.

brain cell types, as well as monocytes, which derive from the same lineage as microglia (Fig. 2E). However, when we separated frVars derived from AD versus PSP GWAS loci and identified those that were found to overlap enhancer marks from recent work in purified nuclei from postmortem human brain (23), we observed that the cell types affected by each disorder were distinct. A plurality of PSP frVars fell within neuronal enhancers, which was significantly above chance ($P = 8.3 \times 10^{-5}$; χ^2 test of equal proportion) (20). In contrast, a plurality of AD frVars fell within microglial enhancers ($P = 0.08$), in concordance with recent estimates of cell type-specific enrichment in single-nucleotide polymorphism (SNP)-based heritability for these two disorders (24) (Fig. 2F). Across both disorders, 55/78 (71%) of these variants overlapped with cell type-

specific enhancer annotations identified in postmortem human brain (Fig. 2G), further supporting the correspondence of these findings with regulatory elements active in human brain tissue. Of note, we found functional predictions from four popular computational algorithms to have poor concordance with regulatory annotations identified in this study and another published MPRA dataset (fig. S4) (18, 20).

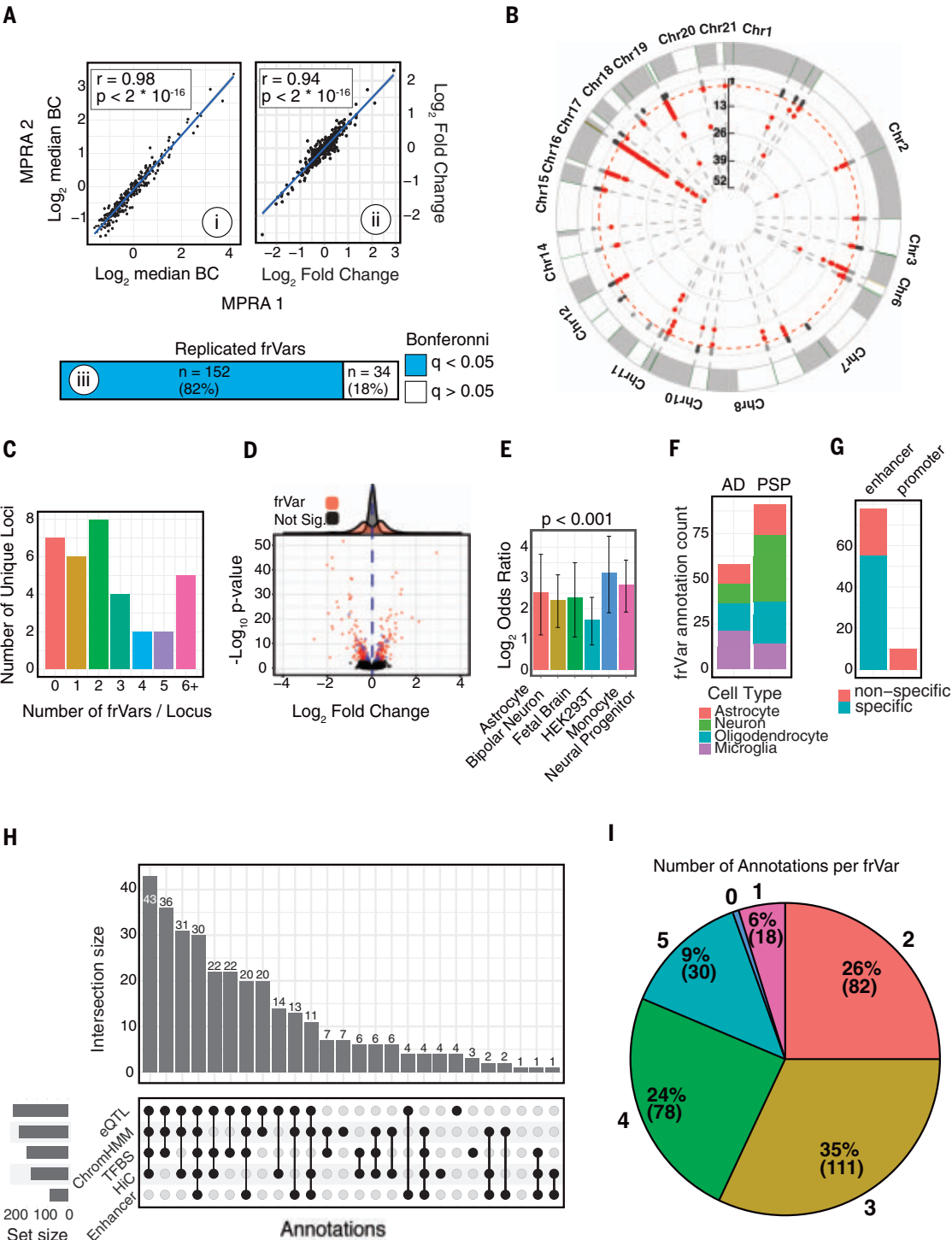
Refinement of frVar annotations for high-confidence prediction of regulatory variants

We next sought to determine the extent to which empirical predictions derived from HEK293T cells translate to the regulatory landscape of the human brain. We characterized frVars using functional annotations from postmortem human brain tissue (23, 25, 26), brain and microglial- or monocyte-specific expression

quantitative trait loci (eQTLs) (27–29), predicted disruption of TFBSs (30, 31), and brain-specific chromatin interaction data (28) (data S2). Blood eQTLs (27) were also assessed as a more powered approximation of microglia eQTLs, for which study sample sizes are relatively small. Of 320 frVars, all except one (319/320, 99.7%) had at least one functional regulatory annotation in brain, and the majority (301, 94%) overlapped two or more functional annotations (Fig. 2, H and I, and data S2): 270 (84%) were brain, microglial, or blood eQTLs; 238 (74%) overlapped transcriptionally active regions in human brain; 88 (28%) fell within a promoter or enhancer in at least one brain cell type; and 200 (63%) significantly (all $P < 0.05$) (20) altered transcription factor binding. This indicates that most of the regulatory variants identified by our assay likely have an

Fig. 2. Identification of MPRA functional regulatory variants.

(A) Reproducibility of MPRA across experimental stages. A total of 326 variants, including 186 frVars identified from the preliminary assay (MPRA 1), were retested in a follow-up assay (MPRA 2). (i) Reference allele transcriptional activity and (ii) log₂ effect sizes (alternative divided by reference allele) show strong correlation (Pearson's $r = 0.98, 0.94$; $P < 2 \times 10^{-16}$) between experiments. BC, barcode count. (iii) One hundred fifty-two of 186 assessed frVars from MPRA 1 were replicated in MPRA 2 (Bonferroni $P < 0.05$). **(B)** Manhattan plot of 5340 different variants assayed across both experiments. Red indicates frVars at FDR-adjusted $q < 0.01$ (BH method). **(C)** Histogram of the number of frVars identified per GWAS locus LD block (median = 2). **(D)** Volcano plot shows log₂ allelic skew effect sizes and -log₁₀ P values for 5340 different variants tested by MPRA. FrVars for MPRA stage 1 (red) and 2 (blue) highlighted. Blue dashed line indicates median effect size. **(E)** Enrichment log₂ odds ratios (Fisher's exact test) of frVars within DHSs of various brain cell types (ENCODE project). Error bars, 95% confidence interval (CI); all FDR-adjusted $q < 0.001$. **(F and G)** FrVars were separated into those derived from AD or PSP GWAS and annotated for overlap with enhancer marks from sorted brain tissue (23). **(F)** Bar plot shows cell type-specific enhancer annotation counts for overlapping frVars separated by disease. A plurality of AD frVars fell within microglial enhancers, whereas PSP frVars fell within neuronal enhancers. **(G)** Most frVars overlap enhancers present in only one cell type. **(H)** Upset plot shows the number of frVars (bars) overlapping combinations (dots and lines below bars) of different functional genomic annotations. Marginal probability of each specific annotation shown in the graphic (lower left). **(I)** Pie chart depicts frVars binned by total number of overlapping genomic annotations (percentages and counts).



active regulatory role in human brain tissue. We used these annotations to further prioritize the highest-likelihood regulatory variants and nominate downstream cognate target genes.

Experimental validation of frVars

On the basis of these functional annotations, we selected 42 high-likelihood regulatory variants for additional validation, choosing those that reside within regulatory regions active in

brain tissue [Table 2; selection rationale (20)]. These variants were distributed across 15 distinct AD loci (*APOE*, *BINI*, *CASS4*, *CELF1/SP1*, *CLU*, *CRI*, *ECHDC3*, *EPHA1*, *FERMT2*, *HLA-DRB1/5*, *INPP5D*, *IQCK*, *MS4A*, *PTK2B*, and

Table 2. CRISPR validation of 42 frVars. Summarized results for the 42 frVars validated using CRISPR-Cas9-mediated editing. MPRA frVars are listed with log ₂ fold changes. Predicted disruption of transcription factor binding sites (TFBSx) using the union of two algorithms (30, 31) is shown. The method used to validate each variant is shown: (i) pooled CRISPRi screen (CROP-seq), (ii) CRISPR enhancer excision assay (CRISPR-ex), or (iii) “None” if the variant failed validation. FDR-adjusted (Benjamini-Hochberg method) q-values for CRISPR experiments shown. All CRISPR q < 0.05.								
rsID	chr:pos_A0_A1	Locus	Disorder	MPRA log ₂ FC	TFBSx	Validation method	Gene_cell type	CRISPR q-value
rs6701713	chr1:207786289_A_G	CR1	AD	1.33	CTCF, ATOH1	CROP-seq	CR1_Microglia	0.02
rs7920721	chr10:11720308_A_G	ECHDC3	AD	0.65	–	None	–	–
rs10838726	chr11:47568344_C_G	CELF1/SPI1	AD	0.17	–	CROP-seq	CELF1_Microglia; SPI1_Microglia	1.5 × 10 ^{–4} ; 0.02
rs12223593	chr11:47789082_T_G	CELF1/SPI1	AD	–0.46	CEBP, NFY, YBX1	CROP-seq	FNBP4_Neuron	9.00 × 10 ^{–3}
rs667897	chr11:59936979_A_G	MS4A	AD	–1.01	NFE2, MAFK	CROP-seq	MS4A4E_Microglia	3.00 × 10 ^{–3}
rs636317	chr11:60019150_C_T	MS4A	AD	–1.95	CTCF, ATOH1	CROP-seq/CRISPR-ex	MS4A4E_Microglia, MS4A6A_THP1	0.02; 0.04
rs10876450	chr12:53811034_T_C	SP1	PSP	–0.40	ESR1, GATA5	None	–	–
rs7144029	chr14:53333616_C_A	FERMT2	AD	0.27	PRRX2, DLX3	None	–	–
rs17125924	chr14:53391680_A_G	FERMT2	AD	0.61	ELF3, ETV7	None	–	–
rs36026988	chr14:92938382_T_C	SLC24A4/RIN3	AD	0.40		CRISPR-ex	RIN3_Microglia	0.01
rs9935063	chr16:19710702_A_G	IQCK	AD	0.18	ARNT2	CROP-seq	KNOPI_Microglia	0.01
rs11646891	chr16:19711351_C_T	IQCK	AD	–0.24		CROP-seq	GPRC5B_Neuron; IQCK_Neuron; KNOPI_Neuron	1.6 × 10 ^{–89} ; 1.9 × 10 ^{–14} ; 9 × 10 ^{–3}
rs3829539	chr16:19722366_T_C	IQCK	AD	–0.29	–	None	–	–
rs4782272	chr16:19729016_G_C	IQCK	AD	–0.43	STAT3	None	–	–
rs13331873	chr16:19749709_A_G	IQCK	AD	0.24	GLIS3, PLAG1	None	–	–
rs4792846	chr17:43367152_G_A	17q21.31	PSP	0.45	–	None	–	–
rs112275793	chr17:43563304_A_C	17q21.31	PSP	0.60	–	None	–	–
rs111392251	chr17:43568928_T_A	17q21.31	PSP	–0.39	IRF1-3	CROP-seq	PLEKHM1_Neuron	0.01
rs76594404	chr17:43971457_G_C	17q21.31	PSP	0.16	EGR1, USF	CROP-seq	MAPT_Neuron; MAPT_Microglia	9.7 × 10 ^{–18} ; 6.8 × 10 ^{–4}
rs76324150	chr17:43973233_C_T	17q21.31	PSP	0.55	ZFX	CROP-seq	MAPT_Neuron	1.50 × 10 ^{–3}
rs80346216	chr17:43974476_G_T	17q21.31	PSP	0.79	–	CROP-seq	MAPT_Neuron	0.04
rs7212857	chr17:44132301_C_A	17q21.31	PSP	–1.79	SP1	None	–	–
rs2532404	chr17:44302881_C_T	17q21.31	PSP	0.49	IRF4	CROP-seq	KANSL1_Neuron	1.30 × 10 ^{–3}
rs2732652	chr17:44345114_C_T	17q21.31	PSP	–0.46	PAX5	None	–	–
rs9912530	chr17:44836302_T_C	17q21.31	PSP	–1.76	–	None	–	–
rs2927437	chr19:45241638_A_G	APOE	AD	0.47	MAZ, TP73	None	–	–
rs11666329	chr19:45354296_A_G	APOE	AD	–0.33	SP2	None	–	–
rs412776	chr19:45379516_G_A	APOE	AD	1.05	GLI3	None	–	–
rs12972156	chr19:45387459_C_G	APOE	AD	–0.42	TFAP	None	–	–
rs10423208	chr19:45453656_G_A	APOE	AD	–0.24	HNF4	CROP-seq	APOC1_Neuron	0.04
rs117316645	chr19:45458212_G_A	APOE	AD	–0.93	–	CROP-seq	APOC1_Neuron	1.50 × 10 ^{–6}
rs13025717	chr2:127886158_C_T	BIN1	AD	–1.77	KLF1, KLF4, SP1	CRISPR-ex	BIN1_Microglia	<0.0001
rs36181881	chr2:234055276_A_G	INPP5D	AD	0.27		None	–	–
rs6064392	chr20:54984768_G_T	CASS4	AD	–1.03	ATF6	None	–	–
rs9271171	chr6:32577907_C_T	HLA-DRB1/5	AD	–0.35	–	CRISPR-ex	C4A_Astrocyte; C4A_THP1	0.04; 0.003
rs2790095	chr6:45439307_C_G	RUNX2	PSP	0.22	TCF3	None	–	–
rs75045569	chr7:143109208_T_G	EPHA1	AD	–0.76	RUNX	None	–	–
rs10224310	chr7:143126994_A_C	EPHA1	AD	–0.35	SPI1	CRISPR-ex	EPHA1_Microglia; TAS2R60_Microglia	<0.0001; 0.02
rs755951	chr8:27226790_A_C	PTK2B	AD	0.76	CTCF	None	–	–
rs17057051	chr8:27227554_A_G	PTK2B	AD	0.48	HBP1	None	–	–
rs1532277	chr8:27466181_T_C	CLU	AD	0.26	ARNT	CROP-seq	CLU_Neuron	2.30 × 10 ^{–3}
rs2045091	chr8:131075859_C_T	ASAP1	PSP	–0.25	NFE2, MAFG	None	–	–

SLC24A4/RIN3) and three distinct PSP loci (17q21.31, ASAP1, and RUNX2). We used two CRISPR-Cas9-mediated strategies to assay regulatory regions in their native genomic context within neurons, microglia, and astro-

cytes derived from human induced pluripotent stem cells (iPSCs). The first leveraged a pooled CRISPR interference (CRISPRi) platform in neurons (32) and microglia (33) using CRISPR droplet sequencing (CROP-seq) (34) to target

all 42 variants. Recognizing that the pooled screening method using previously untested guides would not effectively edit all of the targeted regions, we additionally performed direct enhancer excision on a subset (five) of

these 42 variants that were highly significant MPRA hits and whose potential regulatory role was supported by functional genomic data, such as eQTL and high-throughput chromosome conformation capture (Hi-C)—rs13025717, rs636317, rs9271171, rs36026988, and rs10224310—assaying downstream effects on gene expression using quantitative polymerase chain reaction. We identified the candidate target genes for a given variant using eQTL or chromatin interaction data based on Hi-C from the relevant neural tissue (Table 2).

For CROP-seq, each variant was targeted using two different guide RNAs, which were introduced into iPSCs that were subsequently differentiated into neurons or microglia. We captured and sequenced 174,983 single neurons and 130,137 microglia corresponding to a median of 1030 distinct neurons and 739 microglia per guide (fig. S5, A and B). Single-cell clustering and expression of marker genes confirmed effective differentiation of both cell types (fig. S5C). CROP-seq results for all surveyed variant-gene pairs for both cell types are summarized in fig. S6. In total, we were able to validate 19 variants that regulated at least one predicted gene in at least one target cell type (Table 2 and data S3), representing a validation efficiency of 45%. This validation rate was higher than the 11% enhancer validation probability defined in a previous CROP-seq study (35). We verified the activity of frVars at 11 separate GWAS loci, identifying regulatory relationships with multiple previously unidentified risk genes outside of the *MAPT* and *APOE* loci, including *MS4A4E*, *C4A*, *APOC1*, and *GPRC5B* for AD and *PLEKHM1* for PSP (Fig. 3, fig. S6, and Table 2).

Several canonical risk genes, including *CRI*, *CLU*, and *BIN1*, have been consistently associated with AD risk across multiple GWASs (36), but the causal variants and relevant cell types underlying these associations remain to be fully clarified. We were able to identify and validate functional variants regulating each of these three established risk genes. At the Clusterin (*CLU*) locus, we validated intronic variant rs1532277 as regulating *CLU* expression within neurons (Fig. 3, A and B). Although previous studies proposed additional risk genes at this locus based solely on chromatin interaction assays (23), we did not detect any effects of rs1532277 on the expression of distal genes *CCDC25* or *CHRNA2* (Fig. 3B).

At the complement receptor 1 locus (*CRI*), we validated the distal intronic variant rs6701713 as regulating *CRI* expression specifically within microglia, with the disease-associated allele (A) predicted to disrupt binding of *CTCF* and increase expression of *CRI* [Genotype-Tissue Expression (GTEx)] (Fig. 3, C and D; Table 2; and data S2). Within the *BIN1* locus, previous work had rigorously established rs6733839

as a causal variant acting specifically in microglia (23). However, two other studies proposed rs13025717 as an additional independent risk variant at the locus on the basis of allele-specific differential chromatin accessibility and chromatin interaction data (37, 38). MPRA identified rs13025717 as a highly significant frVar ($P = 2.6 \times 10^{-38}$; Fig. 3E), and we experimentally confirmed that this variant regulates *BIN1* expression in microglia using CRISPR-mediated enhancer excision (Fig. 3F). We also experimentally validated regulatory variants at other canonical loci including rs10224310 and rs36026988, which we show regulate *EPHA1* and *RIN3* expression, respectively, in microglia (Fig. 3, G to J; fig. S6; and Table 2).

We also identified variants with pleiotropic regulatory activity, allowing us to identify candidate risk genes underlying AD risk. The membrane-spanning 4-domains (*MS4A*) cluster on chromosome 11 contains more than 16 genes and harbors numerous variants conferring risk for AD (37, 38). Previous work at this locus implicated rs636317 as a likely causal variant and nominated *MS4A6A* as the cognate risk gene (37, 38). In this study, we confirmed the regulatory function of rs636317, as well as another variant, rs667897, within the *MS4A* locus (Fig. 3K). Notably, we found that both variants regulate expression of *MS4A4E*, but not *MS4A4A*, specifically within microglia, with rs667897 also suggestive for regulation of *MS4A6A* (Fig. 3, L to O). Additionally, using enhancer excision in THP-1-derived macrophages, we found that rs636317 also regulates *MS4A6A* expression (fig. S7A), although this was not significant in the CRISPRi screen (Fig. 3M). The disease-associated (T) allele of rs636317 disrupts binding of transcriptional repressor *CTCF*, thereby increasing gene expression (38). Conversely, the disease-associated (A) allele of rs667897 creates an *NFE2-MAFG* TFBS, increasing *MS4A6A* and *MS4A4E* expression in microglia to confer AD risk (Table 2).

We next explored the *HLA-DRB1/5* AD GWAS locus, which is a highly polymorphic region of extended LD with numerous AD-associated variants and potential risk genes. MPRA identified 13 significant variants in the locus falling within the intergenic region between *HLA-DRB1* and *HLA-DQAI*. We further validated rs9271171 using enhancer excision in iPSC-derived astrocytes, because brain chromatin conformation data from PsychENCODE predicted that rs9271171 regulates the distal gene complement 4 (*C4A*), which is most highly expressed in astrocytes (39). Indeed, we observed that excision of this variant significantly reduced *C4A* expression in both astrocytes ($P = 0.04$; Fig. 3, P and Q) and THP-1 macrophages ($P = 0.003$; fig. S7B), highlighting *C4A* as a risk gene for AD. Other examples of loci wherein we

identified variants regulating multiple downstream target genes include *IQCK* (rs9935063, rs11646891; *GPRC5B*, *IQCK*, *KNOP1*) and *SPI1* (rs10876450, rs12223593; *SPI1*, *CELF1*, *FBNP4*) (fig. S6 and Table 2). Whether all, or a subset, of the genes regulated at these loci contribute to disease risk will require individual functional validation in model systems.

Characterization of 17q21.31 and 19q13.32

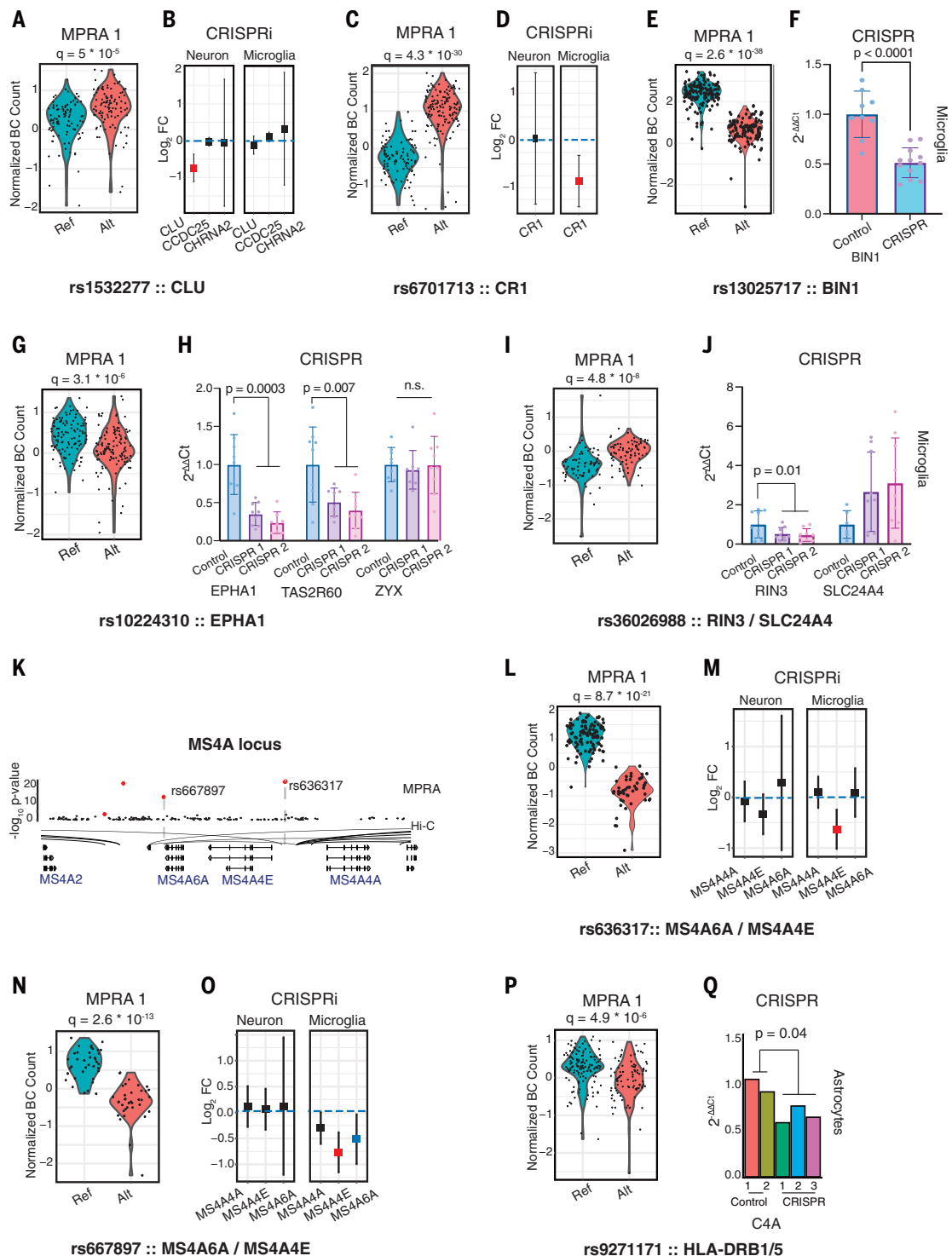
The chromosome 17q21.31 locus is noteworthy for harboring the tau-encoding *MAPT* gene within a common 900-kb inversion polymorphism and is a major risk locus for PSP (H1 haplotype OR = 4 to 5) as well as AD, Parkinson's disease, and corticobasal degeneration (10). 17q21.31 contains complex haplotypic substructural variation and extensive LD, hampering interrogation with traditional statistical genetics approaches (13). We leveraged the ability to functionally dissect this region with MPRA, testing 3482 variants within 17q21.31 in strong LD with lead SNPs from a PSP GWAS (8), which comprise ~24% of the more than 14,000 common variants in the region, identifying a total of 194 frVars, or 5.6% of those within this region.

We next clustered these frVars according to LD (minimum $R^2 = 0.5$), identifying seven distinct LD clusters (Fig. 4A), which suggests multiple distinct loci within this region. The largest LD cluster includes 42 frVars within the core *MAPT* gene itself [–5 kb upstream of the transcriptional start site (TSS) to the 3' untranslated region (3'UTR)], of which 13 are variants within annotated enhancers predicted to disrupt TFBSs (Fig. 4B) and are in strong LD ($R^2 > 0.9$) with the H1 marker rs8070723 (data S4). We also highlight a cluster of eight contiguous frVars overlapping a large oligodendrocyte enhancer within a distal regulatory element of the *MAPT* first intron (Fig. 4B). These variants were of interest because tau pathology within oligodendrocytes is a defining pathological feature of PSP (40). All eight of these regulatory variants are in low LD ($D' = 1$, $R^2 = 0.18$) with rs242557, a marker SNP for the H1C subhaplotype known to confer risk for PSP (10) (data S4 shows pairwise LD for rs242557).

A core promoter beginning ~300 bp from the TSS (41) has been previously characterized in a variety of cell types (41, 42). As basal *MAPT* expression (in addition to splicing) is thought to be a key molecular driver of tauopathy pathogenesis (8), we used the functional data from MPRA to further clarify the cis-regulatory landscape of the *MAPT* gene. The MPRA element corresponding to positions –226 to –63 of the *MAPT* gene was highly transcriptionally active, whereas elements within the region –349 to –186 drove only modest expression (data S1), suggesting a core promoter starting –226 bp upstream of the *MAPT* TSS (Fig. 4C).

Fig. 3. CRISPR validation of eight MPRA frVars across seven AD loci.

(A and B) rs1532277 in the *CLU* locus. (A) Violin plot shows MPRA normalized barcode (BC) distributions for each allele. FDR-adjusted q -values displayed. (B) CRISPRi targeting suppresses *CLU* (z-score = -3.8, $q = 2.3 \times 10^{-3}$) but not *CCDC25* or *CHRNA2* expression specifically in iPSC-derived neurons. Error bars, 95% CI. FC, fold change. (C and D) rs6701713 in the *CR1* locus. (C) MPRA data as in (A). (D) CRISPRi targeting suppresses *CR1* expression (z-score = -2.8, $q = 0.04$) specifically in microglia. Error bars, 95% CI. (E and F) rs13025717 in the *BIN1* locus. (E) MPRA data. (F) CRISPR-mediated excision of genomic region containing rs13025717 in microglia reduces *BIN1* expression compared with gRNA-scramble controls [control $n = 9$, CRISPR $n = 12$, $t_{19} = 5.8$; $P < 0.0001$]. Error bars, SEM. (G and H) rs10224310 in the *EPHA1* locus. (G) MPRA data. (H) CRISPR deletion of genomic region containing rs10224310 in microglia reduces *EPHA1* [control $n = 9$, CRISPR $n = 17$, $t_{24} = 6.6$; $P < 0.0001$] and intronic gene *TAS2R60* but not *ZYX* expression. Error bars, SEM. (I and J) rs36026988 in the *SLC24A4/RIN3* locus. (I) MPRA data. (J) CRISPR deletion of genomic region containing rs36026988 in microglia reduces *RIN3* [control $n = 9$, CRISPR $n = 19$, $t_{35} = 1.7$; $P = 0.05$] but not *SLC24A4* expression. (K) *MS4A* locus variants, highlighting rs667897 and rs636317. (L) rs636317 MPRA data. (M) CRISPRi targeting of rs636317 reduces *MS4A4E* (z-score = -3.0, $q = 0.02$) expression. (N) rs667897 MPRA data. (O) CRISPRi targeting of rs667897 significantly reduces *MS4A4E* (z-score = -3.7, $q = 0.003$) and shows a trend toward reducing *MS4A6A* expression (z-score = -2.2, uncorrected $P = 0.01$) in microglia. Error bars, 95% CI. (P and Q) rs9271171 in the *HLA-DRB1/5* locus. (P) MPRA data. (Q) CRISPR deletion of rs9271171 significantly reduces *C4A* expression in iPSC-derived astrocytes [CRISPR $n = 3$, control $n = 2$; $t_3 = 3.5$; $P = 0.04$]. All CRISPR excision assessed using two-tailed Student's t test comparing the averages of the control and the CRISPR conditions.



(K) *MS4A* locus variants, highlighting rs667897 and rs636317. (L) rs636317 MPRA data. (M) CRISPRi targeting of rs636317 reduces *MS4A4E* (z-score = -3.0, $q = 0.02$) expression. (N) rs667897 MPRA data. (O) CRISPRi targeting of rs667897 significantly reduces *MS4A4E* (z-score = -3.7, $q = 0.003$) and shows a trend toward reducing *MS4A6A* expression (z-score = -2.2, uncorrected $P = 0.01$) in microglia. Error bars, 95% CI. (P and Q) rs9271171 in the *HLA-DRB1/5* locus. (P) MPRA data. (Q) CRISPR deletion of rs9271171 significantly reduces *C4A* expression in iPSC-derived astrocytes [CRISPR $n = 3$, control $n = 2$; $t_3 = 3.5$; $P = 0.04$]. All CRISPR excision assessed using two-tailed Student's t test comparing the averages of the control and the CRISPR conditions.

We next sought to identify functional variants likely to control *MAPT* gene expression. We chose three frVars for further experimental validation prioritized by regulatory annotations in brain and chromatin looping to the

MAPT TSS (data S2): rs76594404, within the proximal promoter (predicted to disrupt *EGR1/USF* binding); rs76324150, which falls within the proximal first *MAPT* intron (disrupts *ZFX*); and rs80346216, within the distal

first intron (Fig. 4C). These loci were confirmed using CRISPRi to regulate *MAPT* expression within iPSC-derived neurons (Fig. 4, D and E; fig. S6; and Table 2). Additionally, we identified a frVar just distal to the *MAPT* gene

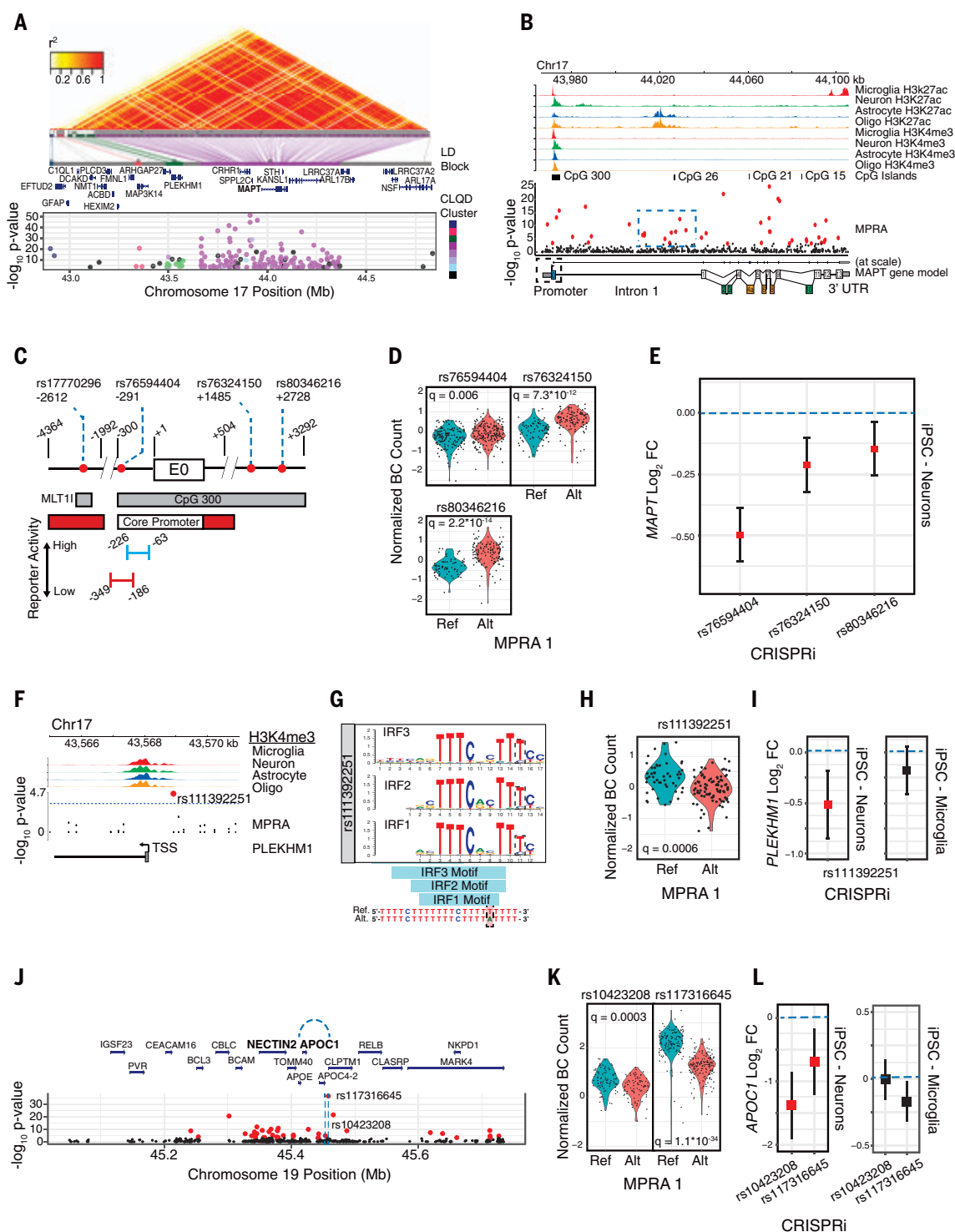


Fig. 4. Systematic characterization of 17q21.31. (A) (Top) 17q21.31 LD plot (1000 Genomes, CEU) above MPRA frVars clustered by LD. (Bottom) frVars plotted by position and MPRA significance ($-\log_{10} P$ values; colors indicate clusters, black indicates unclustered). Most variants fall within LD cluster 4 (purple) centering on *MAPT*. (B) Chromatin annotations and frVars across *MAPT*. Tracks (1 through 8) show H3K27ac (active) and H3K4me3 (promoter) ChIP-seq peaks for microglia (red), neurons (green), astrocytes (blue), and oligodendrocytes (orange) from (23); CpG islands (track 9); and tested variants plotted by $-\log_{10} P$ value (track 10). FrVars in red. *MAPT* gene model (track 11). Exons: blue, untranslated; white, constitutive; green,

alternative neuronal; and yellow, rarely expressed in brain. Blue square shows frVars within an oligodendrocyte enhancer. (C) Annotation of the *MAPT* promoter [−4364 to +3292 from TSS, features from (42)] with frVars (red dots). Red, repressor regions. (Bottom) MPRA relative reporter activity for two elements. (D and E) Three frVars regulating *MAPT* expression. (D) MPRA violin plots show normalized allelic barcode distributions. (E) CRISPRi targeting suppresses *MAPT* expression for rs76594404 (z -score = −9.1, $q = 9.7 \times 10^{-18}$), rs76324150 (z -score = −4.0, $q = 1.5 \times 10^{-3}$), and rs80346216 (z -score = −2.8, $q = 0.04$) in iPSC-neurons. (F to I) rs111392251: frVar in *PLEKHM1* promoter (±3 kb). (F) Tracks (1 through 4) show H3K4me3 peaks

[as in (B)]. (G) The alternate allele of rs111392251 disrupts *IRF1-3* TFBSs. (H) MPRA data as in (D). (I) CRISPRi targeting of rs111392251 suppresses *PLEKHM1* expression (z -score = -3.1 , $q = 0.01$) in neurons but not microglia. Error bars, 95% CI. (J) Variants within the *APOE* locus plotted by coordinate

and MPRA $-\log_{10} P$ value. FrVars in red, blue dashes loop to *APOC1* promoter. (K) MPRA data and (L) CRISPRi targeting of rs10423208 (z -score = -5.5 , $q = 1.5 \times 10^{-6}$) and rs117316645 (z -score = -2.8 , $q = 0.04$) suppresses *APOC1* expression in neurons but not microglia. Error bars, 95% CI.

body, rs2532404, that we confirmed strongly regulates *KANS1* expression in neurons, but not microglia (fig. S6).

We also identified three separate LD clusters at 17q21.31 harboring variants predicted to regulate genes besides *MAPT*. Putative risk genes overlapping regulatory variants in independent LD blocks implicated here include *MAP3K14*, *PLEKHM1*, and *LRRC37A4P* (table S1). One such cluster harbors rs111392251, a high-confidence regulatory variant located in the promoter of *PLEKHM1* that is predicted to disrupt binding of *IRF*-family TFs (Fig. 4, F to H). We used CRISPRi to validate that this locus regulates *PLEKHM1* expression within neurons but not microglia (Fig. 4I). *PLEKHM1* regulates autophagosome-lysosome formation (43) and has been previously suggested as a PSP risk gene on the basis of proximity (7), but has yet to be functionally characterized in a disease context. These results indicate that *PLEKHM1* dysregulation within human neurons contributes to PSP risk, independent of *MAPT* expression.

The *APOE* locus on 19q13.32 harbors the strongest common genetic association with late-onset AD, tagging the well-characterized *APOE4* risk haplotype (5, 6). However, the extensive LD in the region has resulted in identification of hundreds of additional disease-associated variants (11, 12). Recent work has uncovered evidence for *APOE*-independent risk for AD in the locus, implicating *PVRL2/NECTIN2* and *APOC1* (11), although some have argued that *APOE* coding variants mediate the entire association signal (12). We reasoned that identification of functional variants at 19q13.32 would inform our understanding of this complex regulatory architecture. We tested 640 variants in LD with the 538 genome-wide significant SNPs (5) at this locus and identified 37 frVars (5.8%; Fig. 4J). Through integration with whole brain and blood eQTLs, we show that 10 of these were predicted to regulate *PVRL2* expression, identifying *PVRL2* as a strong candidate risk gene at this locus (table S2). With respect to *APOC1*, we examined a distal segment of open chromatin within an intergenic region downstream from the *APOC2-APOC4* gene carrying two frVars, rs10423208 and rs117316645 (Fig. 4J), neither of which are in LD with the *APOE* haplotype tag SNPs rs7412 and rs429358 (all $R^2 < 0.01$, EUR ancestry). CRISPRi targeting of both loci robustly down-regulated *APOC1* expression specifically within neurons (Fig. 4, K and L, and Table 2). Our results provide support for

APOC1 as an AD risk gene, warranting its further study.

MPRA frVars enrich for TFBS disruption

We next hypothesized that functional variants defined by our frVars distributed across the genome would be enriched for variants that disrupt TF binding as a class, which was what we observed [enrichment OR = 1.4, $P = 0.003$; SNP2TFBS (30)]. We observed a similar magnitude of enrichment of TFBS-disrupting variants among frVars in another published dataset (18) (OR = 1.9, $P = 8.7 \times 10^{-8}$). Both enrichments were replicated using an alternative TFBS scoring method [motifbreakR (31)]. Furthermore, the magnitude and directionality of predicted TFBS disruption correlated with MPRA effect sizes for frVars in both our dataset (Spearman's $\rho = 0.44$, $P = 2.3 \times 10^{-4}$) and the other dataset (18) ($\rho = 0.52$, $P < 8.7 \times 10^{-9}$; Fig. 5, A and B). In general, we did not find that TFBS disruption alone predicts MPRA allelic skew (positive predictive value = 0.14) (20), although disruption of a subset of specific TFs such as *ELK4*, *ETS1*, *GABPA*, and *SP*-family members did modestly predict allelic skew captured by MPRA in these data (fig. S8).

Enrichment of functional risk variants within disease-specific transcriptional networks

We next assessed whether frVars were enriched within binding sites for specific transcription factors, and we found that TFBSs disrupted by risk variants differed by disease. In AD, CTCF (\log_2 OR = 4.5, $P = 3 \times 10^{-5}$), NR4A2 (\log_2 OR = 4.9, $P = 0.002$), NR5A2 (\log_2 OR = 3.6, $P = 0.01$), ATOH1 (\log_2 OR = 3.8, $P = 0.009$), SP2 (\log_2 OR = 2.3, $P = 0.008$), and SMAD-family (SMAD2,3,4 heterotrimer, \log_2 OR = 3.7, $P = 0.0002$) binding sites were enriched for disrupting risk variants, which is consistent with previous work identifying enrichment of AD risk variation in microglial enhancers containing CTCF, SMAD, and SP binding motifs (38). In contrast, PSP showed a different pattern of TFBS enrichment, in which five of the six TFs predicted to be enriched for binding site disruption physically interact with the transcription factor SP1 (including SP1 itself; OR = 1.8, $P = 0.007$; Fig. 5C). Of note, the set of PSP-enriched TFs forms a significant protein-protein interaction (PPI) network with SP1 (STRING $P = 1.7 \times 10^{-5}$; permutation $P = 0.05$; Fig. 5C) (20). This finding is consistent with SP1's multimerization capabilities and its activity as a core component of a broad array of gene regulatory complexes that regulate

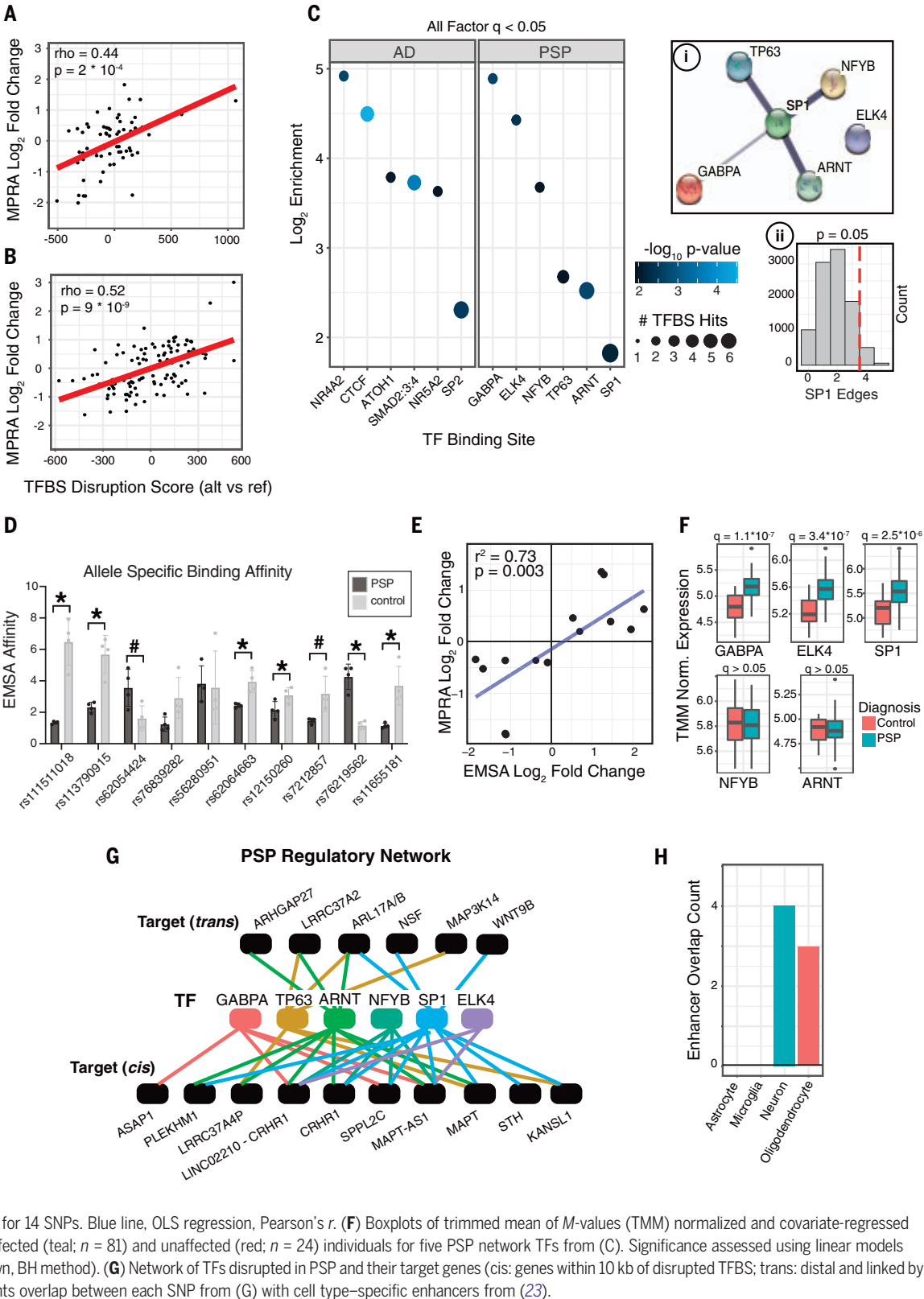
tissue-specific gene expression (44). Notably, 11.1% of annotated PSP frVars are predicted to participate specifically within this network. We also assessed enrichments at a lower statistical threshold (TFBS enrichment $q < 0.1$), finding additional *ETS*-family TFs and SP1 interactors to be enriched within functional PSP risk variants (fig. S9). Although these TFs are highly expressed in HEK293T cells, we did not find a general relationship between relative TF abundance and MPRA allelic skew ($P > 0.05$; Spearman's correlation) (20), indicating that expression levels do not explain our results. Additionally, we did not identify a significant enrichment for disrupted TFBS motifs among equivalently sized random collections of GWAS variants (20), demonstrating that our results are not explained by the initial SNP selection.

Given these findings, we sought to verify whether our computational predictions of TFBS disruption were robust by performing electrophoretic mobility shift assays (EMSAs). We focused on SP1 because it was the core hub gene in the PPI network, testing the relative SP1 binding affinity for each of the 14 frVars predicted to disrupt SP1 binding. We identified significant differential allele-specific binding affinities in 10 of 14 variants ($q < 0.1$; Fig. 5D and fig. S10) and found a strong correlation between EMSA results and MPRA effect sizes (Fig. 5E), confirming the bioinformatic regulatory predictions of SP1 activity.

We next reasoned that we could leverage expression data from postmortem human brain tissue to garner additional evidence for dysregulation of SP1 network TFs in disease. Indeed, gene expression analysis confirmed that a majority of these network TFs, including SP1, were differentially expressed within the temporal cortex of individuals with PSP and matched controls (Fig. 5F and fig. S11A). Of note, the coding region for *SP1* itself falls within a suggestive PSP risk locus that did not reach genome-wide significance (locus combined $P = 4.1 \times 10^{-7}$) (8). Taken together, these data provide converging evidence for broad dysregulation of an SP1-centered transcriptional network in PSP pathophysiology.

To explore this further, we generated a two-layer directed network composed of these six PSP TFs and their likely targets, defined as genes within the cis-regulatory window of TFBS-disrupting frVars, as well as genes linked by brain Hi-C (Fig. 5G; fig. S11B for AD network) (20). These TFBS-disrupting variants were then annotated using cell type-specific

Fig. 5. FrVars disrupt disease-specific TF networks. (A and B) MPRA variant effect sizes correlate with predicted TFBS disruption scores for our dataset (A) and a published dataset (18) (B). Red line, OLS regression, Spearman's rho. (C) Shows the log₂ enrichments for significantly disrupted TFBSs (FDR $q < 0.05$, BH method), with frVars from AD and PSP analyzed separately (color indicates $-\log_{10}$ enrichment P values, dot size indicates the number of disrupted TFBSs). (Inset) (i) PPI network from the STRING (55) database for significantly disrupted PSP TFs. Network hub is the transcription factor SP1. Line thickness indicates the strength of evidence. (ii) Empirical distribution for expected PPI network SP1 connectivity generated by resampling. Red dashed line indicates the observed number of PSP TF network edges. (D) Normalized binding affinities to SP1 for both alleles of 10 PSP-associated SNPs predicted to alter SP1 TFBSs tested by EMSA ($n = 4$ replicates). Dark gray bars, PSP risk allele; light gray bars, protective allele. Two-tailed Student's t test with FDR correction (BH method). $*q < 0.05$, # $q < 0.1$. Error bars, SEM. (E) Correlation between EMSA and MPRA effect sizes for 14 SNPs. Blue line, OLS regression, Pearson's r . (F) Boxplots of trimmed mean of M -values (TMM) normalized and covariate-regressed gene expression from PSP affected (teal; $n = 81$) and unaffected (red; $n = 24$) individuals for five PSP network TFs from (C). Significance assessed using linear models (FDR-corrected q -values shown, BH method). (G) Network of TFs disrupted in PSP and their target genes (cis: genes within 10 kb of disrupted TFBS; trans: distal and linked by brain Hi-C). (H) Bar plot counts overlap between each SNP from (G) with cell type-specific enhancers from (23).



enhancers derived from human brain (23) to identify the cell types in which target gene expression is most likely dysregulated. Variants mostly overlapped enhancers in neurons (Fig. 5H) and a few in oligodendrocytes, suggesting

that this SP1 regulatory network primarily operates in neurons and, to a lesser extent, oligodendrocytes, consistent with the observation of overall neuronal enrichment of PSP risk variants identified in GWAS (45).

Discussion

Predicting functionality of noncoding variation is one of the major challenges in modern genetics. Here, we provide a systematic characterization of common variants underlying

disease risk for two neurodegenerative disorders, AD and PSP, identifying regulatory variants at 27 of 34 tested genomic loci. We use functional genomic annotations from human brain tissue to prioritize these variants, experimentally validating the activity of 19 variants and their cognate target genes using direct genome manipulation. Our work illustrates the utility of integrating multiplexed reporter and CRISPR assays to efficiently characterize noncoding disease-associated variation, suggesting a framework for future work in other complex traits. In agreement with previous studies (14), we found that four existing computational prediction algorithms for a priori variant prioritization were not highly concordant among themselves, nor were they predictive of functional variants identified by our MPRA or in a previously published dataset (18) [fig. S4; see (20)]. This emphasizes the necessity for further development and utilization of high-throughput experimental methods to prioritize noncoding regulatory variants from GWAS, especially in regions with extensive LD. In this study, we used MPRA and CRISPR to identify regulatory variants within two such regions, 17q21.31 and 19q13.32, risk factors for PSP and AD, respectively, enabling identification of risk genes within these complex loci, including *PLEKHM1* and *APOC1*.

A potential limitation of this study was the technical challenge of performing MPRA within human brain cell types, with the specific trans-regulatory environment of HEK293T cells likely influencing the generalizability of our screen (19). Recognizing that HEK293T cells are not primary neural cells, we directly addressed the question of cell type specificity through integration with orthogonal genomics annotations from the human brain (which reassuringly showed high overlap), followed by CRISPR validation of 42 variants within their native genomic context in neurons and microglia. In doing so, we provide strong evidence for multiple risk genes, implicating *PLEKHM1* and *KANSL1* in PSP and *MS4A4E*, *APOC1*, and *C4A* in AD. Of note, our analysis did not address regulatory function within neurovasculature and epithelial cells, which may also contribute to AD pathogenesis (46). Additionally, some associated loci likely operate by means of mechanisms independent of direct transcriptional regulation (i.e., splicing, posttranslational modification), requiring other approaches to delineate causal variants and their mechanisms. However, this work takes an important step forward by providing large-scale functional annotation of these dementia risk loci.

SNP-based heritability is known to enrich in regulatory regions within disease-relevant tissues (47). For AD, this enrichment affects networks of genes downstream of several TFs, including *CTCF* and *SMAD*, which have been

described as acting in multiple brain and peripheral cell types to affect risk for AD (38, 48). For PSP, our analysis identified an enrichment of TFBS-disrupting frVars in a PPI network with the transcription factor SPI1, which regulates a broad array of cellular processes, including chromatin remodeling, apoptosis, immune regulation, and response to oxidative stress in neurons (49). Although SPI1 network dysregulation has been identified in the AD brain (50), it does not appear to harbor AD genetic risk and therefore is likely to play a reactive or secondary role in AD. Overall, our data are consistent with PSP risk primarily affecting neurons and, to a lesser extent, oligodendrocytes (24, 45). This includes an oligodendrocyte enhancer within the tau locus, which we speculate may be related to the distinctive glial pathology in PSP.

These observations suggest a refined model for understanding the combinatorial effects of common genetic risk. Signals from intergenic GWAS loci are typically interpreted as deriving from causal regulatory variants that influence downstream expression of specific cognate risk genes. Our results, implicating a TF network converging on SPI1 in PSP, are consistent with a model whereby common genetic variants function in aggregate across multiple TFBSs to disrupt key cell type-specific transcriptional programs. We speculate that this genetic mechanism may manifest itself only upon induction of the relevant transcriptional network, which may occur specifically within a disease context. Our data show that disease-relevant transcriptional networks regulate a large number of cell type-enriched genes, providing a mechanism whereby genetic risk is expressed not by affecting a few core genes (51) but by means of polygenic cell type-specific regulatory effects on networks of genes (52).

Materials and methods summary

A full description of the materials and methods is provided in the supplementary materials (20). An abbreviated version is provided below.

Massively parallel reporter assay

Variant selection and MPRA were performed as described (20). To identify functional regulatory variants with significant allelic skew (frVars), normalized barcode counts were combined across replicates and significance determined using a two-way Mann-Whitney *U* test comparing barcode counts between each allele. FrVars were defined at an FDR threshold $q < 0.01$ (Benjamini-Hochberg method). MPRA \log_2 effect sizes were defined as the median summed normalized barcode count for the alternate allele minus the reference allele.

Genome engineering

For CRISPR excision experiments, a single line from a healthy male donor (#1205-4) was

derived and cultured as previously documented at the University of California, Los Angeles (53). iPSC differentiation into mature astrocytes or microglia, as well as further description of the CRISPR excision experiments, is described here (20).

For the CROP-seq (pooled CRISPRi) screen, two iPSC lines were maintained at the University of California, San Francisco. For microglial differentiation, a transcription factor-based protocol (iTF-microglia) was used as described by Dräger *et al.* (33). Similarly, neurons for the CROP-seq screen were generated using the transcription factor-based i³N approach as described by Tian *et al.* (32). For CROP-seq validation, we picked 42 frVars that were also annotated as lying within transcriptionally active regulatory regions defined as overlapping either brain enhancer and promoter marks from (23) or overlapping “active” brain ChromHMM marks from the NIH Roadmap Epigenomics Mapping Consortium (25), and analysis performed as described (20).

Bioinformatic analysis

Variant annotation

FrVars were annotated for TFBS disruption and overlapped with functional brain annotations to create a high-confidence list of likely regulatory variants (data S2). We calculated TFBS disruption using both the motifbreakR package (37) and the SNP2TFBS webtool (30). We then identified frVar overlap with enhancer and promoter annotations from sorted microglia, neurons, astrocytes, and oligodendrocytes (23) as described (20).

TFBS analysis

Predicted TFBS enrichment within “active” MPRA elements was calculated using the HOMER (4.11) software suite (54) against a background set of all other oligos (20). Predicted TFBS disruption was also scored for all variants using the SNP2TFBS webtool (30), and an enrichment OR for frVars was calculated using Fisher’s exact test. We also partitioned frVars into those derived from AD or PSP GWAS (20) and ran these sets through the SNP2TFBS algorithm, filtering for TFBSs with at least two predicted disruptions. Only TFBSs significantly ($q < 0.05$ or $q < 0.1$) enriched for disruption by frVars were plotted and considered further. For these significantly disrupted TFs, we created PPI networks using the STRING (v11) webtool and standard parameters (55), identifying target genes and cell type enrichment as described using functional genomic data (20).

Additional analyses

Pairwise Jaccard index calculations, open chromatin enrichment analysis, bulk RNA-seq analysis, LD analysis within the 17q21.31 locus,

and other analyses are further described in the supplemental methods (20).

Statistical reporting

Statistical analysis was performed using the stats package in R. All hypothesis testing was two-sided, and all enrichment was determined using a Fisher's exact test, except when explicitly stated. For MPRA allelic skew multiple testing correction, unique variants from MPRA 1 and 2 were combined (5340 total) and Mann-Whitney *U* *P* values were FDR-adjusted (Benjamini-Hochberg method). FrVars were called at a threshold of $q < 0.01$. For CRISPR excision experiments, a two-tailed Student's *t* test was performed by comparing the average value of controls against the average value of enhancer-targeting conditions. For CRISPRi experiments, SNP:gene *P* values were computed and FDR-adjusted as described (20).

REFERENCES AND NOTES

1. M. G. Erkkonen, M. O. Kim, M. D. Geschwind, Clinical neurology and epidemiology of the major neurodegenerative diseases. *Cold Spring Harb. Perspect. Biol.* **10**, a033118 (2018). doi: [10.1101/cshperspect.a033118](https://doi.org/10.1101/cshperspect.a033118); pmid: 28716886
2. M. G. Spillantini, M. Goedert, Tau pathology and neurodegeneration. *Lancet Neurol.* **12**, 609–622 (2013). doi: [10.1016/S1474-4422\(13\)70090-5](https://doi.org/10.1016/S1474-4422(13)70090-5); pmid: 23684085
3. R. Sims, M. Hill, J. Williams, The multiplex model of the genetics of Alzheimer's disease. *Nat. Neurosci.* **23**, 311–322 (2020). doi: [10.1038/s41593-020-0599-5](https://doi.org/10.1038/s41593-020-0599-5); pmid: 32112059
4. S. L. Forrest *et al.*, Heritability in frontotemporal tauopathies. *Alzheimers Dement. (Amst.)* **11**, 115–124 (2019). doi: [10.1016/j.dadm.2018.12.001](https://doi.org/10.1016/j.dadm.2018.12.001); pmid: 30723775
5. J. C. Lambert *et al.*, Meta-analysis of 74,046 individuals identifies 11 new susceptibility loci for Alzheimer's disease. *Nat. Genet.* **45**, 1452–1458 (2013). doi: [10.1038/ng.2802](https://doi.org/10.1038/ng.2802); pmid: 24162737
6. B. W. Kunkle *et al.*, Genetic meta-analysis of diagnosed Alzheimer's disease identifies new risk loci and implicates Aβ, tau, immunity and lipid processing. *Nat. Genet.* **51**, 414–430 (2019). doi: [10.1038/s41588-019-0358-2](https://doi.org/10.1038/s41588-019-0358-2); pmid: 30820047
7. G. U. Hoglinger *et al.*, Identification of common variants influencing risk of the tauopathy progressive supranuclear palsy. *Nat. Genet.* **43**, 699–705 (2011). doi: [10.1038/ng.859](https://doi.org/10.1038/ng.859); pmid: 21685912
8. J. A. Chen *et al.*, Joint genome-wide association study of progressive supranuclear palsy identifies novel susceptibility loci and genetic correlation to neurodegenerative diseases. *Mol. Neurodegener.* **13**, 41 (2018). doi: [10.1186/s13024-018-0270-8](https://doi.org/10.1186/s13024-018-0270-8); pmid: 30089514
9. L. D. Ward, M. Kellis, Interpreting noncoding genetic variation in complex traits and human disease. *Nat. Biotechnol.* **30**, 1095–1106 (2012). doi: [10.1038/nbt.2422](https://doi.org/10.1038/nbt.2422); pmid: 23138309
10. K. R. Bowles *et al.*, 17q21.31 sub-haplotypes underlying H1-associated risk for Parkinson's disease are associated with LRR37A/2 expression in astrocytes. *Mol. Neurodegener.* **17**, 48 (2022). doi: [10.1186/s13024-022-00551-x](https://doi.org/10.1186/s13024-022-00551-x); pmid: 35841044
11. X. Zhou *et al.*, Non-coding variability at the APOE locus contributes to the Alzheimer's risk. *Nat. Commun.* **10**, 3310 (2019). doi: [10.1038/s41467-019-10945-z](https://doi.org/10.1038/s41467-019-10945-z); pmid: 31346172
12. G. Jun *et al.*, Comprehensive search for Alzheimer disease susceptibility loci in the APOE region. *Arch. Neurol.* **69**, 1270–1279 (2012). doi: [10.1001/archneurol.2012.2052](https://doi.org/10.1001/archneurol.2012.2052); pmid: 22869155
13. D. J. Schaid, W. Chen, N. B. Larson, From genome-wide associations to candidate causal variants by statistical fine-mapping. *Nat. Rev. Genet.* **19**, 491–504 (2018). doi: [10.1038/s41576-018-0016-z](https://doi.org/10.1038/s41576-018-0016-z); pmid: 29844615
14. L. Liu *et al.*, Biological relevance of computationally predicted pathogenicity of noncoding variants. *Nat. Commun.* **10**, 330 (2019). doi: [10.1038/s41467-018-08270-y](https://doi.org/10.1038/s41467-018-08270-y); pmid: 30659175
15. K. Eilbeck, A. Quinlan, M. Yandell, Settling the score: Variant prioritization and Mendelian disease. *Nat. Rev. Genet.* **18**, 599–612 (2017). doi: [10.1038/nrg.2017.52](https://doi.org/10.1038/nrg.2017.52); pmid: 28804138
16. A. Melnikov *et al.*, Systematic dissection and optimization of inducible enhancers in human cells using a massively parallel reporter assay. *Nat. Biotechnol.* **30**, 271–277 (2012). doi: [10.1038/nbt.2137](https://doi.org/10.1038/nbt.2137); pmid: 22371084
17. R. P. Patwardhan *et al.*, Massively parallel functional dissection of mammalian enhancers in vivo. *Nat. Biotechnol.* **30**, 265–270 (2012). doi: [10.1038/nbt.2136](https://doi.org/10.1038/nbt.2136); pmid: 22371081
18. R. Tewhey *et al.*, Direct identification of hundreds of expression-modulating variants using a multiplexed reporter assay. *Cell* **165**, 1519–1529 (2016). doi: [10.1016/j.cell.2016.04.027](https://doi.org/10.1016/j.cell.2016.04.027); pmid: 27259153
19. J. C. Ulirsch *et al.*, Systematic functional dissection of common genetic variation affecting red blood cell traits. *Cell* **165**, 1530–1545 (2016). doi: [10.1016/j.cell.2016.04.048](https://doi.org/10.1016/j.cell.2016.04.048); pmid: 27259154
20. See supplementary materials.
21. A. Melnikov, X. Zhang, P. Rogov, L. Wang, T. S. Mikkelsen, Massively parallel reporter assays in cultured mammalian cells. *J. Vis. Exp.* **2014**, 51719 (2014). doi: [10.3791/51719](https://doi.org/10.3791/51719); pmid: 25177895
22. ENCODE Project Consortium, An integrated encyclopedia of DNA elements in the human genome. *Nature* **489**, 57–74 (2012). doi: [10.1038/nature11247](https://doi.org/10.1038/nature11247); pmid: 22955616
23. A. Nott *et al.*, Brain cell type-specific enhancer-promoter interactome maps and disease-risk association. *Science* **366**, 1134–1139 (2019). doi: [10.1126/science.aay0793](https://doi.org/10.1126/science.aay0793); pmid: 31727856
24. V. Swarup *et al.*, Identification of conserved proteomic networks in neurodegenerative dementia. *Cell Rep.* **31**, 107807 (2020). doi: [10.1016/j.celrep.2020.107807](https://doi.org/10.1016/j.celrep.2020.107807); pmid: 32579933
25. B. E. Bernstein *et al.*, The NIH Roadmap Epigenomics Mapping Consortium. *Nat. Biotechnol.* **28**, 1045–1048 (2010). doi: [10.1038/nbt1010-1045](https://doi.org/10.1038/nbt1010-1045); pmid: 20944595
26. J. Ernst, M. Kellis, ChromHMM: Automating chromatin-state discovery and characterization. *Nat. Methods* **9**, 215–216 (2012). doi: [10.1038/nmeth.1906](https://doi.org/10.1038/nmeth.1906); pmid: 22373907
27. GTEx Consortium, The GTEx Consortium atlas of genetic regulatory effects across human tissues. *Science* **369**, 1318–1330 (2020). doi: [10.1126/science.aaz1776](https://doi.org/10.1126/science.aaz1776); pmid: 32913098
28. D. Wang *et al.*, Comprehensive functional genomic resource and integrative model for the human brain. *Science* **362**, eaat8464 (2018). doi: [10.1126/science.aat8464](https://doi.org/10.1126/science.aat8464); pmid: 30545857
29. K. P. Lopes *et al.*, Genetic analysis of the human microglial transcriptome across brain regions, aging and disease pathologies. *Nat. Genet.* **54**, 4–17 (2022). doi: [10.1038/s41588-021-00976-y](https://doi.org/10.1038/s41588-021-00976-y); pmid: 34992268
30. S. Kumar, G. Ambrosini, P. Bucher, SNP2TFBS – a database of regulatory SNPs affecting predicted transcription factor binding site affinity. *Nucleic Acids Res.* **45**, D139–D144 (2017). doi: [10.1093/nar/gkw1064](https://doi.org/10.1093/nar/gkw1064); pmid: 27899579
31. S. G. Coetzee, G. A. Coetzee, D. J. Hazelett, motifbreakR: An R/Bioconductor package for predicting variant effects at transcription factor binding sites. *Bioinformatics* **31**, 3847–3849 (2015). doi: [10.1093/bioinformatics/btv470](https://doi.org/10.1093/bioinformatics/btv470); pmid: 26272984
32. R. Tian *et al.*, CRISPR interference-based platform for multimodal genetic screens in human iPSC-derived neurons. *Neuron* **104**, 239–255.e12 (2019). doi: [10.1016/j.neuron.2019.07.014](https://doi.org/10.1016/j.neuron.2019.07.014); pmid: 31422865
33. N. M. Dräger *et al.*, A CRISPRi/a platform in iPSC-derived microglia uncovers regulators of disease states. *Nat. Neurosci.* **10**, 1038/s41593-022-01131-4 (2022).
34. P. Datlinger *et al.*, Pooled CRISPR screening with single-cell transcriptome readout. *Nat. Methods* **14**, 297–301 (2017). doi: [10.1038/nmeth.4177](https://doi.org/10.1038/nmeth.4177); pmid: 28099430
35. M. Gasperini *et al.*, A genome-wide framework for mapping gene regulation via cellular genetic screens. *Cell* **176**, 1516 (2019). doi: [10.1016/j.cell.2019.02.027](https://doi.org/10.1016/j.cell.2019.02.027); pmid: 30849375
36. S. M. Neuner, J. Tcw, A. M. Goate, Genetic architecture of Alzheimer's disease. *Neurobiol. Dis.* **143**, 104976 (2020). doi: [10.1016/j.nbd.2020.104976](https://doi.org/10.1016/j.nbd.2020.104976); pmid: 32565066
37. M. R. Corces *et al.*, Single-cell epigenomic analyses implicate candidate causal variants at inherited risk loci for Alzheimer's and Parkinson's diseases. *Nat. Genet.* **52**, 1158–1168 (2020). doi: [10.1038/s41588-020-00721-x](https://doi.org/10.1038/s41588-020-00721-x); pmid: 33106633
38. G. Novikova *et al.*, Integration of Alzheimer's disease genetics and myeloid genomics identifies disease risk regulatory elements and genes. *Nat. Commun.* **12**, 1610 (2021). doi: [10.1038/s41467-021-21823-y](https://doi.org/10.1038/s41467-021-21823-y); pmid: 33712570
39. M. Druart, C. Le Magueresse, Emerging roles of complement in psychiatric disorders. *Front. Psychiatry* **10**, 573 (2019). doi: [10.3389/fpsyt.2019.00573](https://doi.org/10.3389/fpsyt.2019.00573); pmid: 31496960
40. I. Ferrer *et al.*, Glial and neuronal tau pathology in tauopathies: Characterization of disease-specific phenotypes and tau pathology progression. *J. Neuropathol. Exp. Neurol.* **73**, 81–97 (2014). doi: [10.1097/NEN.000000000000030](https://doi.org/10.1097/NEN.000000000000030); pmid: 24335532
41. M. L. Caillaud-Boudin, L. Buée, N. Sergeant, B. Lefebvre, Regulation of human MAPT gene expression. *Mol. Neurodegener.* **10**, 28 (2015). doi: [10.1186/s13024-015-0025-8](https://doi.org/10.1186/s13024-015-0025-8); pmid: 26170022
42. B. Maloney, D. K. Lahiri, Structural and functional characterization of H2 haplotype MAPT promoter: Unique neurospecific domains and a hypoxia-inducible element would enhance rationally targeted tauopathy research for Alzheimer's disease. *Gene* **501**, 63–78 (2012). doi: [10.1016/j.jgene.2012.01.049](https://doi.org/10.1016/j.jgene.2012.01.049); pmid: 22310385
43. D. G. McEwan *et al.*, PLEKHM1 regulates autophagosome-lysosome fusion through HOPS complex and LC3/GABARAP proteins. *Mol. Cell* **57**, 39–54 (2015). doi: [10.1016/j.molcel.2014.11.006](https://doi.org/10.1016/j.molcel.2014.11.006); pmid: 25498145
44. P. Bouwman, S. Philipsen, Regulation of the activity of Sp1-related transcription factors. *Mol. Cell. Endocrinol.* **195**, 27–38 (2002). doi: [10.1016/S0303-7207\(02\)00221-6](https://doi.org/10.1016/S0303-7207(02)00221-6); pmid: 12354670
45. V. Swarup *et al.*, Identification of evolutionarily conserved gene networks mediating neurodegenerative dementia. *Nat. Med.* **25**, 152–164 (2019). doi: [10.1038/s41591-018-0223-3](https://doi.org/10.1038/s41591-018-0223-3); pmid: 30510257
46. A. C. Yang *et al.*, A human brain vascular atlas reveals diverse mediators of Alzheimer's risk. *Nature* **603**, 885–892 (2022). doi: [10.1038/s41586-021-04369-3](https://doi.org/10.1038/s41586-021-04369-3); pmid: 35165441
47. H. K. Finucane *et al.*, Partitioning heritability by functional annotation using genome-wide association summary statistics. *Nat. Genet.* **47**, 1228–1235 (2015). doi: [10.1038/ng.3404](https://doi.org/10.1038/ng.3404); pmid: 26414678
48. T. Town *et al.*, Blocking TGF-β-Smad2/3 innate immune signaling mitigates Alzheimer-like pathology. *Nat. Med.* **14**, 681–687 (2008). doi: [10.1038/nm1781](https://doi.org/10.1038/nm1781); pmid: 18516051
49. N. Y. Tan, L. M. Khachigian, Sp1 phosphorylation and its regulation of gene transcription. *Mol. Cell. Biol.* **29**, 2483–2488 (2009). doi: [10.1128/MCB.01828-08](https://doi.org/10.1128/MCB.01828-08); pmid: 19273606
50. B. A. Citron, J. S. Dennis, R. S. Zeitlin, V. Echeverria, Transcription factor Sp1 dysregulation in Alzheimer's disease. *J. Neurosci. Res.* **86**, 2499–2504 (2008). doi: [10.1002/jnr.21695](https://doi.org/10.1002/jnr.21695); pmid: 18449948
51. E. A. Boyle, Y. I. Li, J. K. Pritchard, An expanded view of complex traits: from polygenic to omnigenic. *Cell* **169**, 1177–1186 (2017). doi: [10.1016/j.cell.2017.05.038](https://doi.org/10.1016/j.cell.2017.05.038); pmid: 28622505
52. N. R. Wray, C. Wijmenga, P. F. Sullivan, J. Yang, P. M. Visscher, Common disease is more complex than implied by the core gene omnigenic model. *Cell* **173**, 1573–1580 (2018). doi: [10.1016/j.cell.2018.05.051](https://doi.org/10.1016/j.cell.2018.05.051); pmid: 29906445
53. A. Gordon *et al.*, Long-term maturation of human cortical organoids matches key early postnatal transitions. *Nat. Neurosci.* **24**, 331–342 (2021). doi: [10.1038/s41593-021-00802-y](https://doi.org/10.1038/s41593-021-00802-y); pmid: 33619405
54. S. Heinz *et al.*, Simple combinations of lineage-determining transcription factors prime cis-regulatory elements required for macrophage and B cell identities. *Mol. Cell* **38**, 576–589 (2010). doi: [10.1016/j.molcel.2010.05.004](https://doi.org/10.1016/j.molcel.2010.05.004); pmid: 20513432
55. D. Szklarczyk *et al.*, STRING v11: Protein-protein association networks with increased coverage, supporting functional discovery in genome-wide experimental datasets. *Nucleic Acids Res.* **47**, D607–D613 (2019). doi: [10.1093/nar/gky1131](https://doi.org/10.1093/nar/gky1131); pmid: 30476243
56. Y. Cooper, Tauopathy-MPRA/Tauopathy-MPRA: Tauopathy-MPRA, version 1, Zenodo (2022); <https://doi.org/10.5281/zenodo.6549628>.

ACKNOWLEDGMENTS

We thank Geschwind lab member J. Grundman for assistance with bulk RNA-seq data analysis, as well as the UCLA TCGB and Flow Cytometry cores for their assistance and technical expertise. We also thank H. Goodarzi for valuable discussions. **Funding:** Y.A.C. was supported by National Institute of Aging fellowship 1F30AG064832 and UCLA-Caltech MSTP training grant T32-GM008042. D.H.G. and G.C. were funded by National Institute of Neurological Disorders and Stroke grant 5UG3NS104095-04. D.H.G. and G.C. were additionally funded by award 20180629 from the Rainwater Charitable Foundation. M.K. and D.H.G. were funded by National Institute of Neurological Disorders and Stroke grant U54 NS123746. M.K. was additionally supported by award A130323 from the Rainwater Charitable Foundation. **Author contributions:** Conceptualization: Y.A.C., G.C., and D.H.G. Data curation: Y.A.C. and N.T. Formal analysis: Y.A.C. and N.T. Funding acquisition: Y.A.C., G.C., M.K., and D.H.G. Investigation: Y.A.C.,

N.T., N.M.D., Q.G., S.M.S., Z.Y., A.P., and S.W. Methodology: Y.A.C., J.E.D., S.K., and D.H.G. Project administration: Y.A.C., G.C., and D.H.G. Resources: S.K., G.C., M.K., and D.H.G. Software: Y.A.C. Supervision: S.K., G.C., M.K., and D.H.G. Validation: Y.A.C. Visualization: Y.A.C. and N.T. Writing – original draft: Y.A.C. and D.H.G. Writing – review & editing: Y.A.C., J.E.D., S.K., G.C., M.K., and D.H.G. **Competing interests:** S.K. is an employee of and holds equity in Octant, Inc. M.K. holds equity in and serves on the scientific advisory boards of Engine Biosciences, Casma Therapeutics, Cajal Neuroscience, and Alektor and advises Modulo Bio and Recursion Therapeutics. M.K. is an inventor on US patent 11,354,933 related to CRISPRi and CRISPRa screening. G.C. is now a full-time employee of Regeneron Pharmaceuticals and has received stock and stock options from Regeneron Pharmaceuticals. The authors have no additional competing interests to declare. **Data and materials availability:** Raw and processed sequencing data for both MPRA experiments are

available from the Gene Expression Omnibus (GEO) under accession number GSE163855. Raw CROP-seq data are available from GEO under accession number GSE207099. To facilitate downstream analyses, preprocessed MPRA count data have also been uploaded to Zenodo (56). Processed and normalized MPRA data for both experimental stages are provided in data S1. All MPRA frVars with functional annotations as in Fig. 2, H and I, are available for download in data S2. Processed CROP-seq results for all SNP gene comparisons are provided in data S3. Data underlying Figs. 3, F, H, J, and Q, 4A, and 5, C to E, and figs. S3A, S4, S7, S8, and S13A are provided in data S5. As part of a complete description of the methods, additional accession numbers and materials are provided in data S6. Custom Python scripts used for preprocessing MPRA data have been uploaded to Zenodo (56). **License information:** Copyright © 2022 the authors, some rights reserved; exclusive licensee American Association for the Advancement of Science. No claim to original

US government works. <https://www.science.org/about/science-licenses-journal-article-reuse>

SUPPLEMENTARY MATERIALS

science.org/doi/10.1126/science.abi8654

Materials and Methods

Supplementary Text

Figs. S1 to S13

Tables S1 and S2

References (57–74)

MDAR Reproducibility Checklist

Data S1 to S6

Submitted 5 April 2021; accepted 19 July 2022
10.1126/science.abi8654



AAAS.ORG/COMMUNITY



AAAS' Member Community is a one-stop destination for scientists and STEM enthusiasts alike. It's "Where Science Gets Social":
a community where facts matter, ideas are big and there's always a reason to come hang out, share, discuss and explore.

**Member
COMMUNITY**
AAAS

AMERICAN ASSOCIATION FOR THE ADVANCEMENT OF SCIENCE

RESEARCH ARTICLE SUMMARY

PARKINSON'S DISEASE

GPNMB confers risk for Parkinson's disease through interaction with α -synuclein

Maria E. Diaz-Ortiz[†], Yunji Seo[†], Marijan Posavi, Marc Carceles Cordon, Elisia Clark, Nimansha Jain, Rakshita Charan, Michael D. Gallagher, Travis L. Unger, Noor Amari, R. Tyler Skrinak, Roseanne Davila-Rivera, Eliza M. Brody, Noah Han, Rebecca Zack, Viviana M. Van Deerlin, Thomas F. Tropea, Kelvin C. Luk, Edward B. Lee, Daniel Weintraub, Alice S. Chen-Plotkin*

INTRODUCTION: An estimated 6 million people worldwide are affected by Parkinson's disease (PD), for which there are no disease-modifying therapies. Since 2005, genome-wide association studies (GWASs) have aimed to find common variant risk loci for PD. These PD GWASs have now uncovered 90 genome-wide significant risk signals. However, target genes and mechanisms remain largely unknown, hampering the field's ability to develop downstream therapeutic approaches from these genomic studies.

RATIONALE: We dissected a chromosome 7 locus linked to risk for PD by GWASs to find the target gene and understand its role in PD pathophysiology. We first performed colocalization analyses of expression quantitative trait locus (eQTL) and PD risk signals, confirming eQTL effects with allele-specific expression (ASE) studies of candidate target genes in the human brain. We then characterized the consequences of manipulating target gene expression in human induced pluripotent stem cell-derived neurons (iPSC-Ns) and other cell models. Finally,

we determined whether levels of the target gene or protein were associated with disease state and severity in humans.

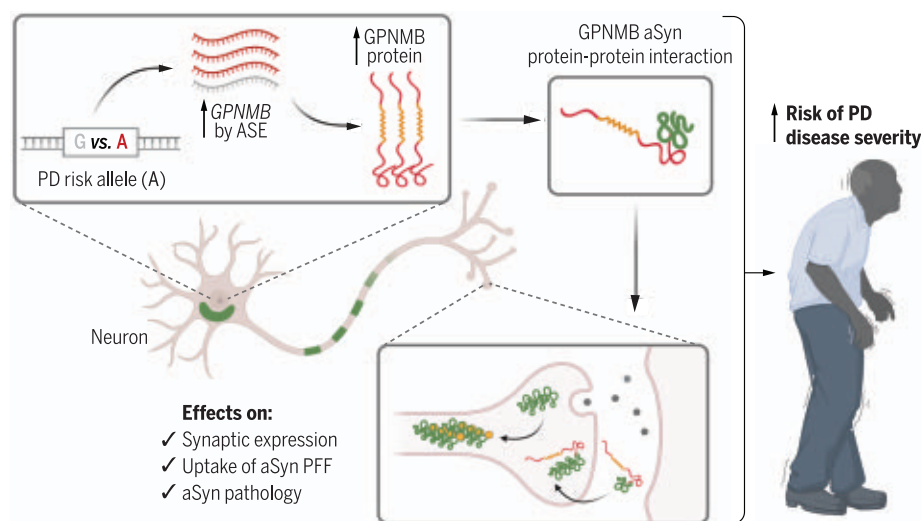
RESULTS: We linked the GWAS-derived chromosome 7 PD risk locus [sentinel single-nucleotide polymorphism (SNP) rs199347] to *GPNMB*—which encodes the transmembrane protein glycoprotein nonmetastatic melanoma protein B (GPNMB)—with a 94% posterior probability of the PD risk and caudate *GPNMB* eQTL signals sharing a causal variant. In human brain samples across multiple brain regions (the caudate, cerebellum, and cingulate cortex) from both PD cases ($n = 4$) and neurologically normal controls ($n = 2$), ASE studies confirmed that the PD risk-associated haplotype was associated with threefold higher *GPNMB* expression.

Having linked *GPNMB* expression levels to PD risk, we generated iPSC-N lines with normal levels of *GPNMB* [wild-type (WT)], heterozygous loss of *GPNMB* (Het), or homozygous loss of *GPNMB* [knockout (KO); two different lines generated] by CRISPR-Cas9 genome

editing. Analyzing these iPSC-Ns using confocal microscopy, we found that loss of *GPNMB* was accompanied by a marked reduction in α -synuclein (aSyn) at the synapse—a result confirmed by immunoblotting of synaptosomal preparations for aSyn. Culturing the iPSC-Ns for an additional week, to a state of greater maturity, only exaggerated the differences in synaptic aSyn when comparing WT versus all other lines. Moreover, transcriptomic profiling of these genome-edited iPSC-N lines revealed that aSyn served as a key protein-protein interaction hub for genes with dysregulated expression in *GPNMB* Het and KO states.

Because aSyn is the protein that accumulates in the hallmark pathological inclusions of PD, and because progression of PD may result from the uptake and cell-to-cell spread of pathological forms of aSyn, we further explored the relationship between GPNMB and aSyn. In HEK293 and HeLa cells, we found that GPNMB and aSyn colocalized and coimmunoprecipitated. In iPSC-Ns, we observed minimal uptake of fibrillar forms of aSyn in *GPNMB* Het and KO iPSC-Ns, in contrast to rapid and obvious uptake of fibrillar aSyn by WT iPSC-Ns. Additionally, when iPSC-Ns were cultured for 14 days after a one-time addition of fibrillar aSyn to the culture medium, WT iPSC-Ns developed hyperphosphorylated, insoluble inclusions of aSyn, but these forms of aSyn pathology were minimal in *GPNMB* Het and KO iPSC-Ns. These experiments, together, demonstrated that GPNMB was necessary for internalization of fibrillar aSyn and subsequent development of aSyn pathology. Meanwhile, in cell lines with low *GPNMB* expression that do not normally internalize fibrillar aSyn, exogenous expression of *GPNMB* was sufficient to confer ability to take up aSyn. Finally, using samples from 731 PD and 59 neurologically normal control individuals, we found that plasma GPNMB is elevated in PD and that PD individuals with higher plasma GPNMB levels have more severe disease.

CONCLUSION: Computational, cell biological, and human tissue-based studies establish *GPNMB* as a GWAS-derived risk gene for PD, with higher expression levels mediating pathogenicity through interactions with aSyn. As a transmembrane protein that is expressed at the cell surface, with an extracellular, soluble form generated by cleavage, GPNMB is a candidate for biomarker development and therapeutic targeting in PD. ■



GPNMB and aSyn in PD. Haplotypes associated with PD result in increased expression of *GPNMB*, encoding GPNMB. GPNMB interacts with aSyn, with effects on aSyn expression at the synapse, cellular uptake of fibrillar aSyn, and development of aSyn pathology in neurons. Together, these cellular processes mediate risk for development and progression of PD. Created with BioRender.com. PFF, preformed fibril.

The list of author affiliations is available in the full article online.

*Corresponding author. Email: chenplot@penmedicine.upenn.edu

[†]These authors contributed equally to this work.

Cite this article as M. E. Diaz-Ortiz et al., *Science* 377, eabk0637 (2022). DOI: 10.1126/science.abk0637

READ THE FULL ARTICLE AT
<https://doi.org/10.1126/science.abk0637>

RESEARCH ARTICLE

PARKINSON'S DISEASE

GNMB confers risk for Parkinson's disease through interaction with α -synuclein

Maria E. Diaz-Ortiz^{1,2†}, Yunji Seo^{1†}, Marijan Posavi¹, Marc Carceles Cordon¹, Elisia Clark¹, Nimansha Jain^{1,3}, Rakshita Charan^{1,4}, Michael D. Gallagher^{1,5}, Travis L. Unger¹, Noor Amari¹, R. Tyler Skrinak¹, Roseanne Davila-Rivera¹, Eliza M. Brody¹, Noah Han¹, Rebecca Zack¹, Vivianna M. Van Deerlin⁶, Thomas F. Tropea¹, Kelvin C. Luk⁶, Edward B. Lee⁶, Daniel Weintraub^{7,8}, Alice S. Chen-Plotkin^{1*}

Many risk loci for Parkinson's disease (PD) have been identified by genome-wide association studies (GWASs), but target genes and mechanisms remain largely unknown. We linked the GWAS-derived chromosome 7 locus (sentinel single-nucleotide polymorphism rs199347) to *GNMB* through colocalization analyses of expression quantitative trait locus and PD risk signals, confirmed by allele-specific expression studies in the human brain. In cells, glycoprotein nonmetastatic melanoma protein B (GNMB) coimmunoprecipitated and colocalized with α -synuclein (aSyn). In induced pluripotent stem cell-derived neurons, loss of *GNMB* resulted in loss of ability to internalize aSyn fibrils and develop aSyn pathology. In 731 PD and 59 control biosamples, *GNMB* was elevated in PD plasma, associating with disease severity. Thus, *GNMB* represents a PD risk gene with potential for biomarker development and therapeutic targeting.

Parkinson's disease (PD) is a progressive neurodegenerative disease affecting an estimated 5 million people worldwide (1). Although genome-wide association studies (GWASs) have nominated >80 genetic loci as PD risk factors (2), target genes and mechanisms for these loci remain largely unknown. To date, drug development in PD has focused on pathways related to α -synuclein (aSyn)—the main component of disease-defining neuropathological lesions—or a handful of other genes causal for PD in a small minority of patients (3, 4). However, these efforts have not yet yielded successful disease-modifying therapies.

In this work, we sought to widen the net for PD therapeutic targets by dissecting a common variant GWAS-derived PD risk locus. We used computational, cell biological, and human tissue-based approaches to ascertain that *GNMB* is a bona fide PD risk gene. Moreover, we implicated glycoprotein nonmetastatic

melanoma protein B (GNMB)-aSyn interactions and GNMB expression levels in the development of PD.

GNMB is the target gene at the rs199347 PD risk locus

Multiple GWASs have linked a chromosome 7 locus [sentinel single-nucleotide polymorphism (SNP) rs199347] with PD (2, 5). Because rs199347 and linked variants are noncoding, we hypothesized that this locus confers PD risk through the modulation of expression levels of one or more target genes, as has been shown for a number of common variant GWAS-derived risk factors in other diseases (6–9). To nominate candidate target genes, we used the Genotype Tissue Expression (GTEx) database (10), finding genes for which a shared causal variant could be linked to both PD risk and expression levels in normal human tissue. Target genes within a 1-Mb window of the sentinel SNP were evaluated in colocalization analyses (11, 12): *GNMB*, *KLHL7*, and *NUPL2* (fig. S1). Among these, *GNMB* demonstrated the greatest overlap between PD risk and expression quantitative trait locus (eQTL) effects, with the most significant colocalization effects seen in the PD-affected caudate brain region (fig. S1B). Moreover, when we examined eQTL effects more broadly, we found that rs199347 genotypes associated significantly with *GNMB* expression levels in all GTEx-characterized brain regions as well as in whole blood (fig. 1A). Thus, computational analyses of existing databases strongly implicated *GNMB* as the target gene at this locus, with higher levels of brain and blood expression linked to PD risk.

The mechanistic basis for eQTL effects lies in allele-specific expression (ASE), whereby different alleles at a given locus show different levels of expression (13). Thus, to validate the database-predicted eQTL relationship between rs199347 and *GNMB* expression, we developed a capture RNA sequencing (RNA-seq)-based (14) ASE assay for human brain tissue (Fig. 1B) and used it to investigate whether individuals carrying two different alleles for the rs199347 haplotype demonstrated ASE for *GNMB*. Moreover, to understand whether rs199347 haplotype effects on brain tissue expression extended to PD brains, we characterized multiple brain regions with varying degrees of pathological involvement in PD (in order of greatest to least aSyn pathological involvement: the caudate, cingulate, and cerebellum) from both PD cases ($n = 4$) and neurologically normal controls (NCs) ($n = 2$); extended demographic information is available in table S1).

We found a high degree of ASE for *GNMB* regardless of PD status or brain region, with 15 of 15 brain samples showing significant ASE (Fig. 1C). Moreover, all samples displayed the same direction of effect, with the PD risk haplotype associating with higher expression levels, averaging approximately threefold higher than the PD protective haplotype. By contrast, ASE analyses for another gene at this locus, *KLHL7*, did not show preferential expression of either haplotype (Fig. 1C). Finally, we confirmed that *GNMB* is expressed at the protein level in the human brain, examining multiple postmortem cases (table S1) by immunoblotting (Fig. 1D), which demonstrated a main band at the predicted molecular weight of 72 kD across all cases, as well as a variably expressed higher-molecular weight band that collapses to 72 kD with deglycosylation (fig. S2), consistent with prior accounts of GNMB's variably glycosylated forms (15). To better understand what cell types might be expressing GNMB, we also performed immunohistochemical staining of human brain tissue (Fig. 1E and table S1) and found GNMB expression in multiple cell types, consistent with studies of spinal cord tissue (16). Thus, both database-predicted and empirically validated eQTL studies in human PD samples support *GNMB* as the target gene at the rs199347 locus, with protein expression in the brain.

Loss of GNMB in iPSC-Ns decreases synaptic aSyn

Having nominated *GNMB* as the mechanistic link between a GWAS locus and PD risk, we sought to define its function in a disease-relevant context. *GNMB* encodes the GNMB protein, a transmembrane glycoprotein first identified in a screen of human melanoma cells with varying potential for metastasis (17). Although GNMB has subsequently been

¹Department of Neurology, Perelman School of Medicine, University of Pennsylvania, Philadelphia, PA, USA.

²Department of Bioengineering, School of Engineering and Applied Sciences, University of Pennsylvania, Philadelphia, PA, USA. ³Department of Neurology, Hope Center for Neurological Disorders, Knight Alzheimer Disease Research Center, Washington University, St. Louis, MO, USA. ⁴Flagship Pioneering, Cambridge, MA, USA. ⁵Whitehead Institute for Biomedical Research, Cambridge, MA, USA. ⁶Center for Neurodegenerative Disease Research, Department of Pathology and Laboratory Medicine, Perelman School of Medicine, University of Pennsylvania, Philadelphia, PA, USA. ⁷Department of Psychiatry, Perelman School of Medicine, University of Pennsylvania, Philadelphia, PA, USA.

⁸Parkinson's Disease Research, Education and Clinical Center (PADRECC), Corporal Michael J. Crescenz VA Medical Center, Philadelphia, PA, USA.

*Corresponding author. Email: chenplot@pennmedicine.upenn.edu

†These authors contributed equally to this work.

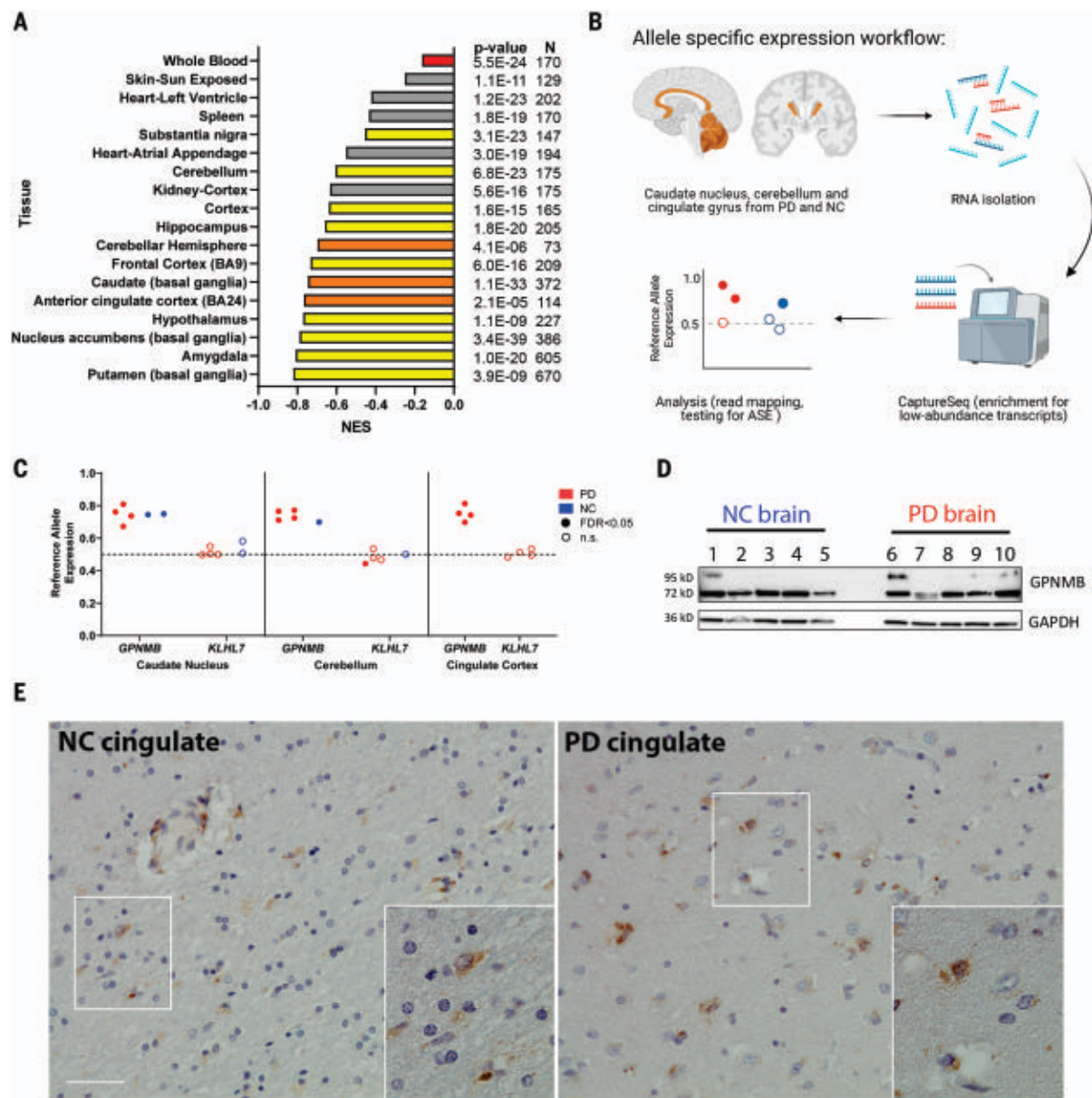


Fig. 1. Chromosome 7 PD risk locus is a multitissue *GPNMB* eQTL and shows ASE. (A) GTEx normalized expression size (NES) coefficients for rs199347's effect on *GPNMB* expression in various tissues (10). Red indicates whole blood, and yellow and orange indicate brain regions. Orange bars correspond to brain regions analyzed for ASE. The PD risk allele at rs199347 (allele = A) is uniformly associated with higher *GPNMB* mRNA expression. (B) Workflow for ASE experiment in brain samples from PD patients ($n = 4$) and NCs ($n = 2$). (C) ASE analysis for rs199347 target gene candidates *GPNMB* and *KLHL7* in caudate, cerebellum, and cingulate cortex brain samples of PD (red) and NC (blue) individuals heterozygous at this locus. Shaded dots indicate

significant (Benjamini-Hochberg-adjusted $P < 0.05$) ASE, whereas empty dots do not show significant ASE. In the absence of ASE, the allelic ratio would be 0.5. For *GPNMB*, the allelic ratio approached 0.8, with higher expression for the *GPNMB* allele carrying the PD risk haplotype. n.s., not significant. (D) Immunoblots showing *GPNMB* expression in caudate brain lysates from NC ($n = 5$) and PD ($n = 5$) individuals. A 72-kD band was detected by the E1Y7J antibody in all cases, with variable expression of a higher-molecular weight glycosylated form. A glyceraldehyde-3-phosphate dehydrogenase (GAPDH) loading control is also shown. (E) Representative immunohistochemical staining of *GPNMB* in NC and PD brains demonstrates expression in multiple cell types. Scale bar, 50 μ m.

found to enhance malignant phenotypes in a number of cancers (18), characterization of its function in the brain or in neurons is scant (15, 16, 19–21). We thus turned to a rapidly inducible human induced pluripotent stem cell-derived cortical neuron (iPSC-N) model (22) in which we could directly manipulate *GPNMB* levels to investigate its neuronal function.

Using CRISPR-Cas9 genome editing, we generated iPSC-N lines with normal levels of *GPNMB* [wild-type (WT)], heterozygous loss of *GPNMB* (Het), or homozygous loss of *GPNMB* [two lines: knockout 1 (KO1) and KO2; figs. S3 and S4] and assessed them by confocal microscopy. At a time point when morphology, expression of neuronal markers, and ability

to fire trains of action potentials reportedly indicate maturity [14 days after neuronal induction (22)], loss of *GPNMB* was accompanied by a marked reduction in aSyn at the synapse (Fig. 2, A and B). Moreover, similar levels of decrease were observed in the Het, KO1, and KO2 lines when we quantified microscopy results (Fig. 2C). By contrast, staining

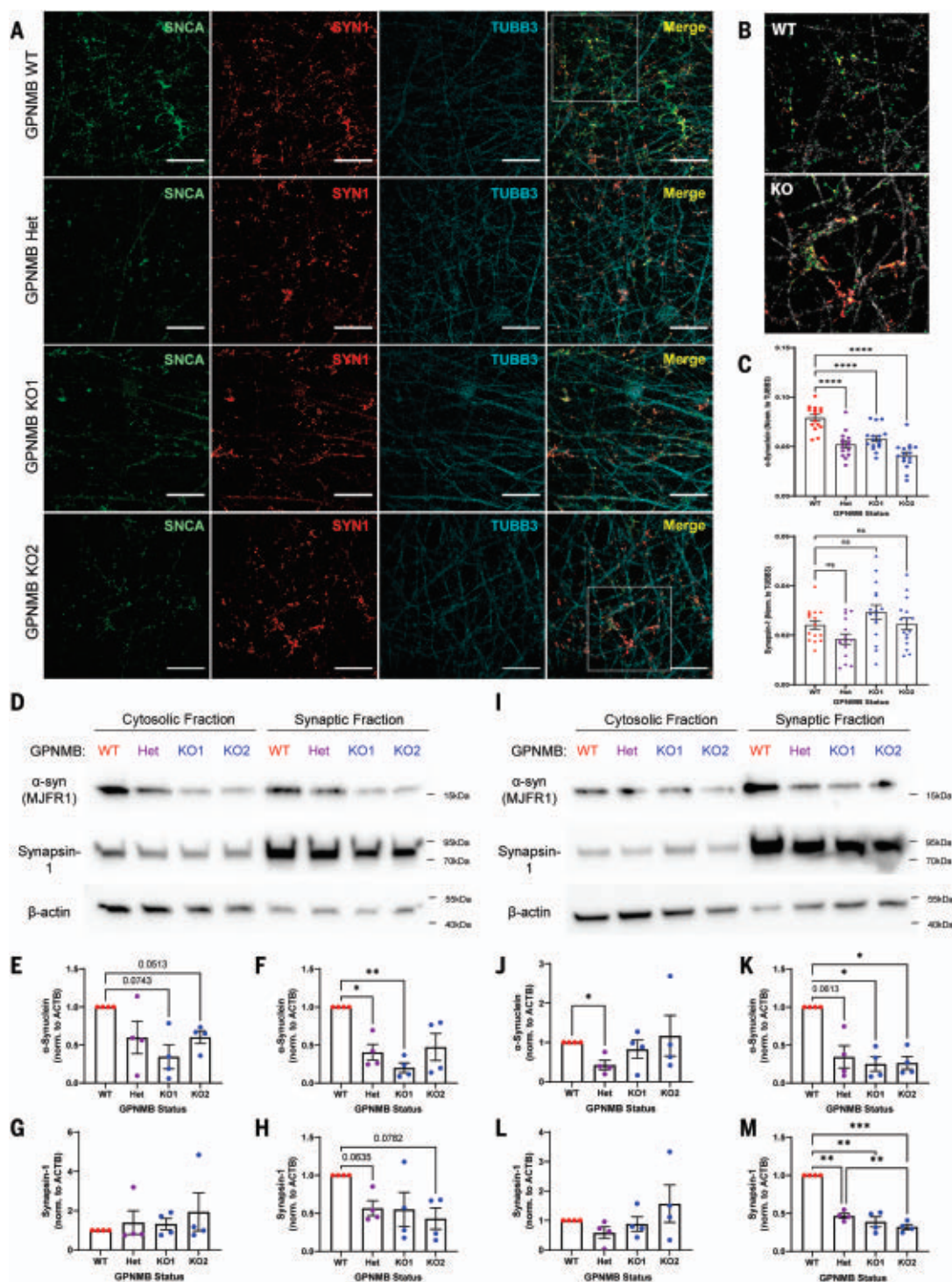


Fig. 2. Heterozygous and homozygous loss of GPNMB results in altered aSyn expression and localization. (A) Immunofluorescence imaging of aSyn (SNCA, green, stained with MJFR1 antibody), synapsin-1 (SYN1, red), and β-tubulin (TUBB3, cyan) in GPNMB WT, Het, KO1, and KO2 iPSC-Ns acquired 14 days after induction of neuronal differentiation. Scale bars, 20 μm. (B) 2x magnified images of merged insets from (A) demonstrate greatly reduced localization of aSyn (SNCA, green) to synapses (labeled with SYN1, red) in GPNMB KO iPSC-Ns compared with WT. TUBB3 is converted to gray. (C) Quantification of aSyn (top) and synapsin-1 (bottom). $N = 15$ images (five images from each of three wells) per condition. Means \pm SEMs, as well as individual data points, are shown. Statistics are by one-way ANOVA followed by post hoc Dunnett's test comparing all other groups

to WT. ns = $P > 0.05$; **** $P < 0.0001$. (D and I) Western blots showing cytosolic and synaptosomal expression of aSyn, synapsin-1, and β-actin in iPSC-N lysates isolated at day 14 (D) and day 21 (I) after neuronal induction. (E to H) Quantification of day 14 immunoblots for either aSyn [(E) and (F)] or synapsin-1 [(G) and (H)] expression in the cytosolic [(E) and (G)] or synaptosomal [(F) and (H)] fractions. (J to M) Quantification of day 21 immunoblots for aSyn [(J) and (K)] or synapsin-1 [(L) and (M)] expression in the cytosolic [(J) and (L)] or synaptosomal [(K) and (M)] fractions. $N = 4$ blots per time point from four independent differentiations. Means \pm SEMs, as well as individual data points, are shown. Statistics are by one-way ANOVA with repeated measures followed by post hoc Tukey test. * $P < 0.05$; ** $P < 0.01$; *** $P < 0.001$.

of synapsin-1, another presynaptic terminal protein, did not differ significantly among the iPSC-N lines (Fig. 2C).

To corroborate our immunofluorescence findings, we isolated synaptosomes from the WT, Het, KO1, and KO2 iPSC-N lines and quantified aSyn by immunoblot in both the synaptosomal and cytosolic fractions (Fig. 2, D to M). At the same time point as our microscopy experiments, synaptosomal aSyn was decreased in the Het and KO1 lines (Fig. 2, D and F). By contrast, neither synaptosomal nor cytosolic synapsin-1 levels differed significantly among the WT, Het, KO1, and KO2 lines (Fig. 2, G and H).

Because aSyn expression at the synapse increases as neurons mature (23, 24), we investigated whether the observed loss of aSyn could be the result of a delay in neuronal maturation that would improve over time. However, after an additional week of neuronal differentiation, differences in aSyn only increased, with the *GPNMB* Het, KO1, and KO2 lines showing ~75% reduction in the synaptosomal aSyn fraction compared with the WT line (Fig. 2, I and K). In addition, by 21 days after induction, both aSyn and synapsin-1 were found primarily in the synaptosomal fraction, and synapsin-1 levels were also significantly decreased in the *GPNMB* Het, KO1, and KO2 lines compared with the WT line (Fig. 2M).

Thus, decreased expression of *GPNMB* in neurons leads to loss of aSyn at the synapse, which suggests direct links between the rs199347 risk haplotype, *GPNMB* expression, and aSyn. Moreover, loss of *GPNMB* may result in a broader synaptic defect.

Transcriptomic profiling of iPSC-Ns reveals *GPNMB* effects on synaptic biology and aSyn

To obtain an unbiased view of biological changes induced by loss of *GPNMB* in neurons, we transcriptionally profiled five independent replicates each of the *GPNMB* WT, Het, and KO2 (hereafter referred to as just KO) iPSC-N lines. Although all three lines showed similar gene expression at baseline, upon neuronal differentiation, distinct profiles emerged for the WT versus the Het and KO cells (fig. S5). Specifically, regardless of whether we performed hierarchical clustering using the top 35 differentially expressed genes (Fig. 3A and fig. S5) or principal components analysis (PCA) using all expressed genes (Fig. 3B and fig. S5), *GPNMB* WT lines separated from the Het and KO lines, whereas within-line replicates clustered together. As expected, across all cell lines, as neuronal differentiation occurred, neuronal genes (e.g., *MAP2*, *TUBB3*, and *SYN1*) were up-regulated, whereas pluripotency genes (e.g., *SOX2*) were down-regulated (fig. S6).

In the neuronally differentiated lines, overlap among genes dysregulated in the *GPNMB* Het and *GPNMB* KO lines compared with the

WT line was considerable, with 142 and 449 overlapping up-regulated and down-regulated genes, respectively (out of 177 and 610 up- and down-regulated genes, respectively, in the Het condition, and 176 and 525 up- and down-regulated genes, respectively, in the KO condition). By contrast, relatively few genes showed differential expression comparing the *GPNMB* Het versus KO lines (Fig. 3, C to E).

Globally, two modules of coexpressed genes distinguished WT from *GPNMB* Het and KO iPSC-Ns, with one module (M1) increased in expression in WT compared with *GPNMB* Het and KO iPSC-Ns and one module (M2) decreased in expression in WT iPSC-Ns (fig. S5). Biological pathway analysis of M1 genes revealed a highly significant overrepresentation of synapse-related categories (Fig. 3F and table S2), corroborating our cell biological findings. The top three categories overrepresented in M2 genes related to receptor tyrosine kinases (Fig. 3G and table S3).

Using module coexpression network analysis with the GeneMANIA (25) database of protein-protein interactions (Fig. 3, H and I), we found that aSyn (encoded by *SNC4*) served as a key protein-protein interaction hub for M1 genes with dysregulated expression in *GPNMB* Het and KO states. These data—from unbiased bottom-up analyses of global gene expression—highlight the strong functional effects of *GPNMB* loss on aSyn.

GPNMB is necessary and sufficient for cellular internalization of aSyn

Because data from the edited iPSC-N lines supported a functional interaction between *GPNMB* and aSyn from both targeted and unbiased lines of investigation, we investigated whether these two proteins might directly interact. In iPSC-Ns, *GPNMB* expression is not high, which makes visualization and co-immunoprecipitation (co-IP) experiments challenging, so we began with immortalized cell lines. Confocal microscopy of *GPNMB* and aSyn revealed colocalization between *GPNMB* and aSyn in LAMP1+ cytoplasmic punctae when transfected in both HeLa (Fig. 4A) and HEK293 (fig. S2) cells. Moreover, when expressed in both cell types, *GPNMB* and aSyn coimmunoprecipitated, regardless of whether the immunoprecipitated protein was *GPNMB* or aSyn (Fig. 4, B and C, and fig. S2).

Encouraged by these data that suggest that a *GPNMB*-aSyn protein-protein interaction might form the basis for the profound effects on aSyn caused by loss of *GPNMB*, we next investigated the functional interaction of these two proteins in a cellular model of PD. Specifically, when aSyn is fibrillized and introduced in the culture medium to neurons, including iPSC-Ns, these fibrillar forms of aSyn are known to be internalized by the cells, which will subsequently develop aSyn inclusions with patho-

logical hallmarks, including phosphorylation at serine 129 (S129) and decreased solubility (26). We thus used this PD model to probe the effects of neuronal loss of *GPNMB* by introducing fibrillar aSyn to cultures of our *GPNMB* WT, Het, and KO iPSC-Ns.

Although WT iPSC-Ns at a mature stage of differentiation readily internalized labeled pre-formed fibrils (PFFs) of aSyn (Fig. 4D, second row), we observed a significant reduction in aSyn internalization in the Het and KO iPSC-N lines, to levels barely above background (Fig. 4, D and F). Thus, *GPNMB* is necessary for the robust internalization of aSyn into iPSC-Ns.

To test whether *GPNMB* is also sufficient for aSyn internalization, we turned to a cell line that does not internalize aSyn at baseline. In HEK293 cells, *GPNMB* is expressed at very low levels endogenously and, in the absence of exogenous *GPNMB* expression, aSyn was not taken up by cells (Fig. 4E, top row). However, expression of *GPNMB*, but not of a control transmembrane protein (TMEM106B), conferred the ability to internalize aSyn (Fig. 4, E and G). Thus, *GPNMB* is sufficient for the internalization of aSyn.

GPNMB expression is permissive for the development of aSyn pathology in neurons

Having demonstrated that *GPNMB* is needed for robust internalization of fibrillar aSyn in iPSC-Ns, we next investigated whether loss of *GPNMB* would rescue the development of aSyn pathology in these cells. To test this, we introduced aSyn PFFs into the culture medium of *GPNMB* WT, Het, and KO iPSC-N lines at the same time point as the internalization experiments (day 14 after neuronal induction) and then continued to culture the neurons for 14 more days after the one-time addition of fibrillar aSyn. At the end of this period, in WT neurons, as expected, we observed abundant examples of S129-phosphorylated aSyn (Fig. 5A, second row), often along neuronal processes (Fig. 5C). In *GPNMB* Het or KO neurons, however, minimal phospho-aSyn staining was found (Fig. 5A). By extracting soluble proteins from our neuronal cultures, we found that WT *GPNMB* iPSC-Ns developed insoluble aSyn aggregates to a much greater degree than *GPNMB* Het or KO neurons (Fig. 5B, second row). These insoluble aggregates had a dense appearance and were often found in a perinuclear location (Fig. 5E). Moreover, quantifications of S129-phosphorylated aSyn, with (Fig. 5F) or without (Fig. 5D) first extracting soluble proteins, revealed a >70% reduction in hyperphosphorylated aSyn species in the *GPNMB* Het and KO neurons. Thus, *GPNMB* functions in the development of PD pathology through mechanisms related to the cellular internalization of fibrillar aSyn.

GPNMB measures reflect clinical status in PD

Findings from our human eQTL and ASE analyses and iPSC-N experiments support a model

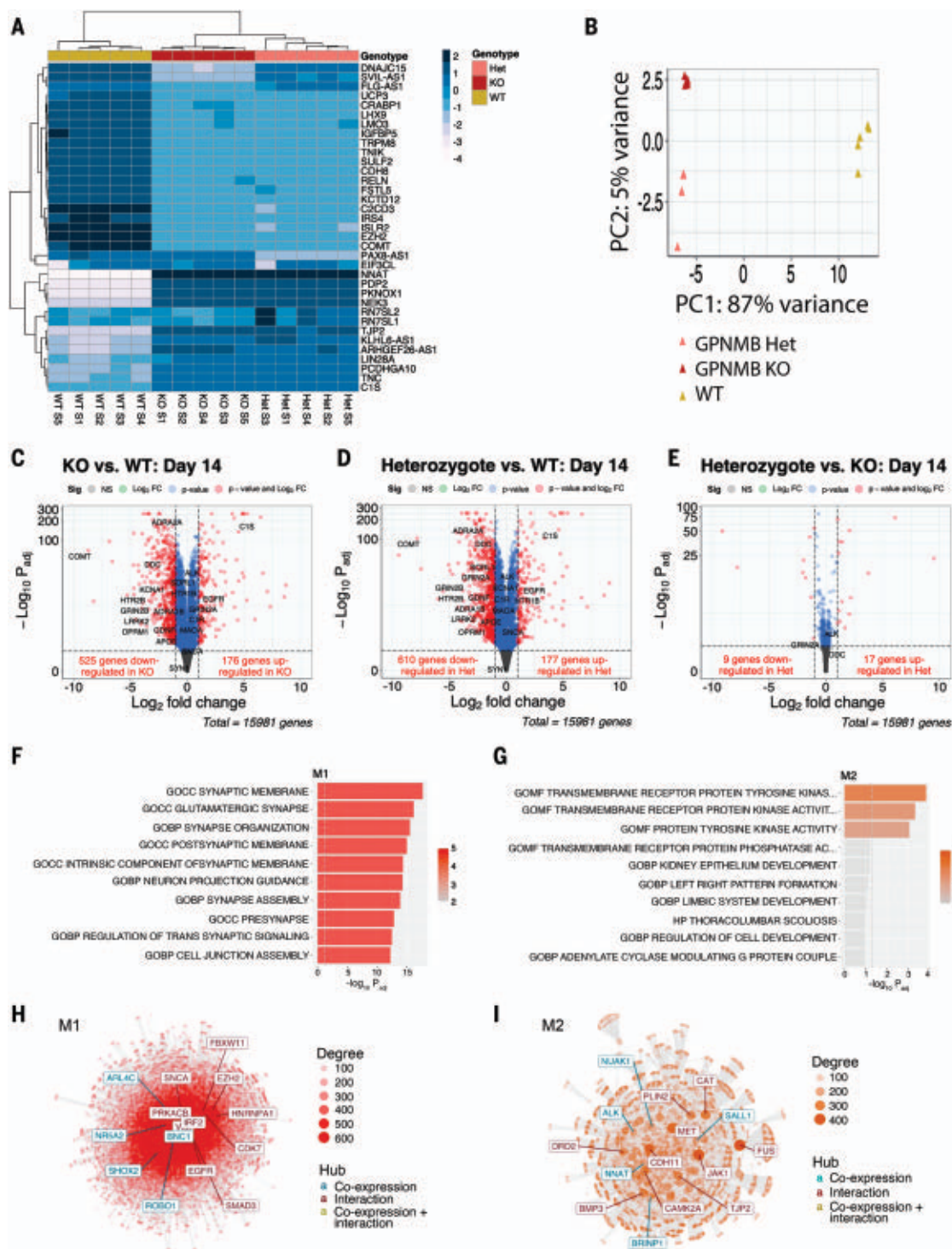


Fig. 3. Transcriptomic profiling of iPSC-Neurons with heterozygous or homozygous loss of GPNMB reveals altered synaptic biology. (A) Heatmap showing clustering of iPSC-Neurons (day 14 after neuronal induction) based on the top 35 genes. $N = 5$ replicate samples from three independent neuronal differentiations per GPNMB genotype. (B) PCA using all expressed genes. (C to E) Volcano plots for pairwise comparison of GPNMB KO cells compared with WT (C), GPNMB Het cells compared with WT (D), and GPNMB KO cells compared with Het (E). The horizontal axes indicate the log₂ fold-change (log₂FC) in gene expression. The vertical axes indicate the -log₁₀ of Benjamini-Hochberg-adjusted P value (P_{adj}), with dotted lines

indicating a $P_{adj} = 0.01$ significance threshold. (F and G) Two coexpression modules (M1 and M2) differentiated WT iPSC-Neurons from GPNMB Het and KO iPSC-Neurons. The top 10 enriched pathways for M1 (F)—decreased in GPNMB Het and KO iPSC-Neurons—and M2 (G)—increased in GPNMB Het and KO iPSC-Neurons—are listed. (H and I) Network analysis of genes in modules M1 (H) and M2 (I) constructed using the GeneMANIA (25) protein-protein interaction dataset. Each point represents a gene, with edges showing protein-protein interactions or coexpression. The most connected genes, or hubs, are labeled, with teal representing coexpression hubs and maroon representing protein-protein interaction hubs.

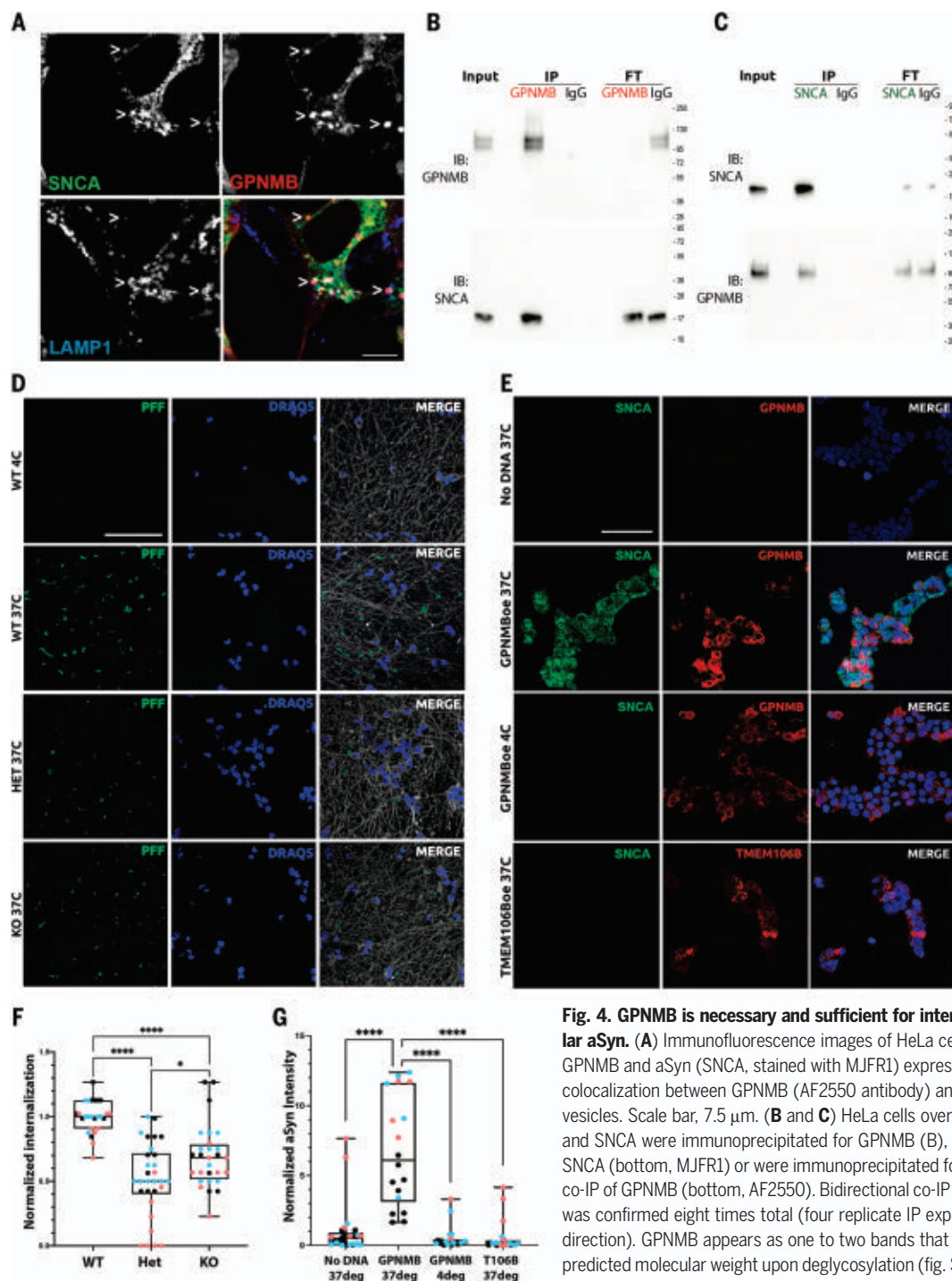


Fig. 4. GPNMB is necessary and sufficient for internalization of fibrillar aSyn. **(A)** Immunofluorescence images of HeLa cells transfected with GPNMB and aSyn (SNCA, stained with MJFR1) expression constructs show colocalization between GPNMB (AF2550 antibody) and SNCA in LAMP1+ vesicles. Scale bar, 7.5 μ m. **(B and C)** HeLa cells overexpressing GPNMB and SNCA were immunoprecipitated for GPNMB (B), showing co-IP of SNCA (bottom, MJFR1) or were immunoprecipitated for SNCA (C), showing co-IP of GPNMB (bottom, AF2550). Bidirectional co-IP of GPNMB and SNCA was confirmed eight times total (four replicate IP experiments from each direction). GPNMB appears as one to two bands that collapse to the predicted molecular weight upon deglycosylation (fig. S2). 1:10:1 Input:IP:FT (flow-through) for protein loading on immunoblots. **(D)** Representative images of Alexa Fluor 594 (AF594)-labeled human aSyn PFFs internalized

in iPSC-Ns (DIV14). All experiments were started at 4°C to allow for addition of PFF in the absence of active uptake. Cells were then maintained at 4°C (top row: negative control) or warmed to 37°C for 90 min to permit uptake (WT, GPNMB Het, and GPNMB KO are shown in rows 2, 3, and 4, respectively). Monochrome images were captured by confocal microscopy, then converted to color for visualization using Fiji software. In each case, PFFs are shown in green, nuclei are shown in blue, and β -tubulin (neuronal structural marker) is shown in gray. Scale bar, 50 μ m. Only WT iPSC-Ns demonstrate definite uptake of aSyn PFF. **(E)** Representative images of HEK293 cells, a human cell line that does not internalize aSyn PFF at baseline (top row: negative control). Overexpression of GPNMB (red, stained with D9 antibody) enables internalization of human WT PFFs (SNCA, green, stained with MJFR1 antibody) at 37°C (row 2). However, no internalization is observed when GPNMB-overexpressing cells are maintained at 4°C (row 3) or at 37°C when another protein (TMEM106B) is overexpressed in HEK293 cells (row 4, TMEM106B is shown in red for this row only, FLAG tag stained). Monochrome images were captured by confocal microscopy, then processed using Fiji imaging software. Nuclei are shown in blue. Scale bar, 50 μ m. **(F)** Quantification of aSyn PFF uptake in iPSC-N lines. $N = 30$ images from three independent differentiations (blue, pink, and black dots) per iPSC-N line. Groups were compared by Mann-Whitney test. $*P < 0.05$; $****P < 0.0001$. **(G)** Quantification of aSyn PFF uptake in HEK293 cells. $N = 30$ images from three independent transfections (blue, pink, and black dots) per condition. Groups were compared by Mann-Whitney test. $****P < 0.0001$. Boxplots [(F) and (G)] depict median, 25th, and 75th quartiles, and whiskers depict full ranges.

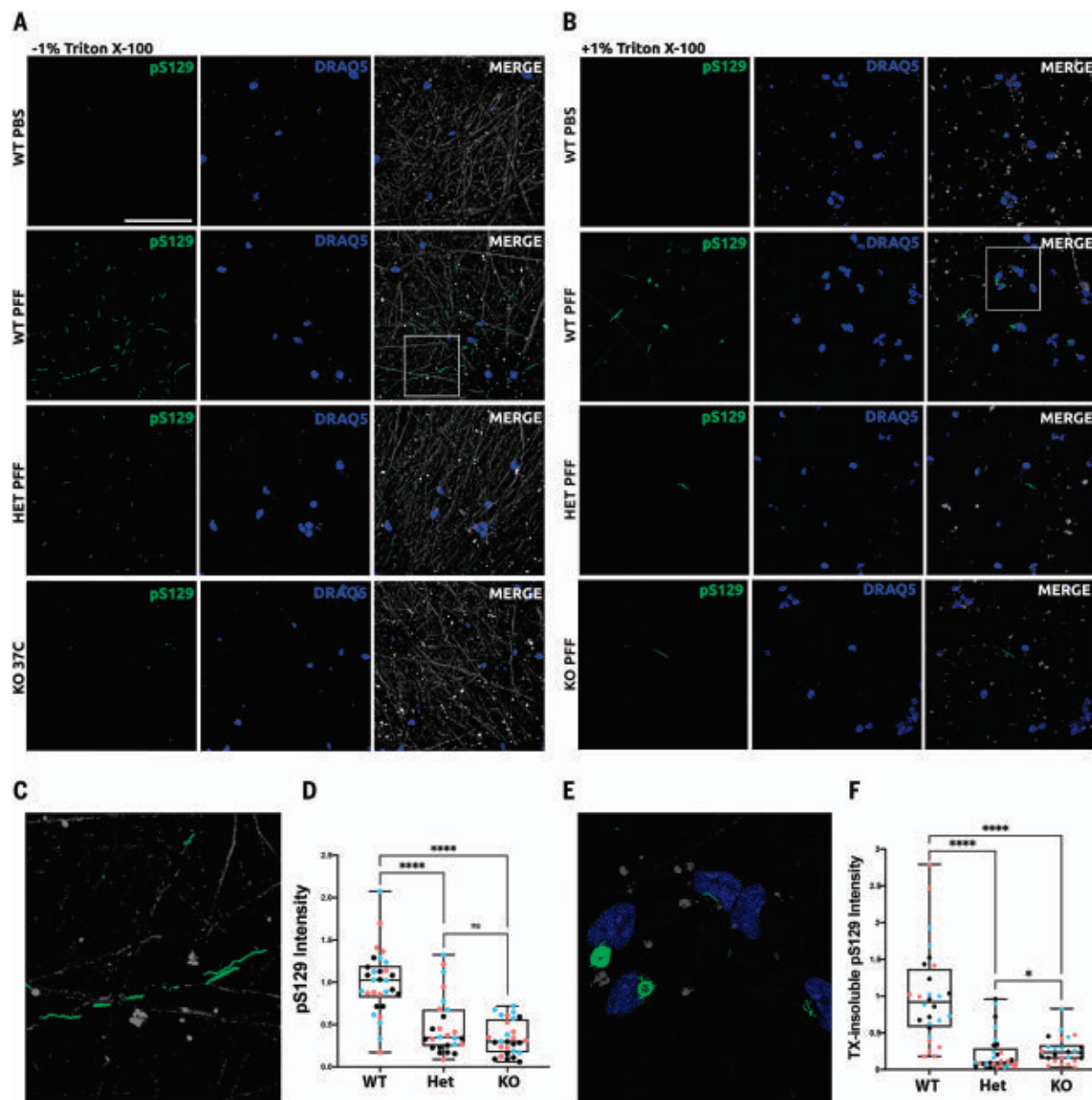


Fig. 5. GPNMB is necessary for development of aSyn pathology in iPSC-Ns.

(**A** and **B**) Untagged human aSyn PFFs were added to iPSC-Ns at DIV14. Neuronal cultures were maintained for 14 additional days to allow for development of aSyn pathology before cells were washed, fixed, and stained under conditions without 1% Triton X-100 (TX) extraction (**A**) or after extraction of soluble proteins with 1% TX (**B**). 81a antibody against aSyn phospho-S129 (pS129) was used to stain pathology (green). Neurons were also stained for nuclear DNA (blue) and tubulin (gray), although this structural protein was largely removed under 1% TX extraction conditions. Scale bar, 50 μ m. For each set, a negative control condition without addition of aSyn PFFs is shown in the top row, followed by addition

of aSyn PFFs in WT (row 2), GPNMB Het (row 3), and GPNMB KO (row 4) iPSC-Ns. Only the WT iPSC-Ns demonstrate abundant pS129 staining. (**C** and **E**) The pS129 staining shows a neuritic pattern [(**C**), inset from (**A**)] in the absence of 1% TX extraction and a dense perinuclear aggregate pattern [(**E**), inset from (**B**)] after extraction of soluble proteins, only in the WT iPSC-Ns. (**D** and **F**) Quantification of pS129 pathology scores is shown under conditions without 1% TX (**D**) and after extraction of soluble proteins with 1% TX (**F**). $N = 30$ images from three independent differentiations (shown as blue, pink, and black dots) per line. Boxplots depict median, 25th, and 75th quartiles, and whiskers depict full ranges. Groups were compared by Mann-Whitney test. **** $P < 0.0001$; * $P > 0.05$.

in which higher *GPNMB* expression levels confer risk for PD through interactions with aSyn that are permissive for neuronal internalization of fibrillar aSyn. Because the extracellular domain of GPNMB is known in cancer contexts to be shed and to circulate in bodily fluids, we explored whether GPNMB might be detected in plasma and cerebrospinal fluid (CSF)

samples from 731 PD and 59 NC individuals (Fig. 6; also see demographic data in tables S4 to S7). Furthermore, we sought to understand whether GPNMB measures in biofluids from living subjects might reflect either rs199347 genotype or disease.

Echoing our results from eQTL and ASE analyses in human brain samples (Fig. 1), we

found that rs199347 genotypes associated with GPNMB levels in CSF in the direction predicted by GTEx (10), whereas no protein quantitative trait locus (pQTL) effect was observed in the plasma (Fig. 6, A and B). Notably, however, plasma GPNMB levels were elevated in PD individuals compared with NCs (Fig. 6C), and this elevation persisted after adjustment

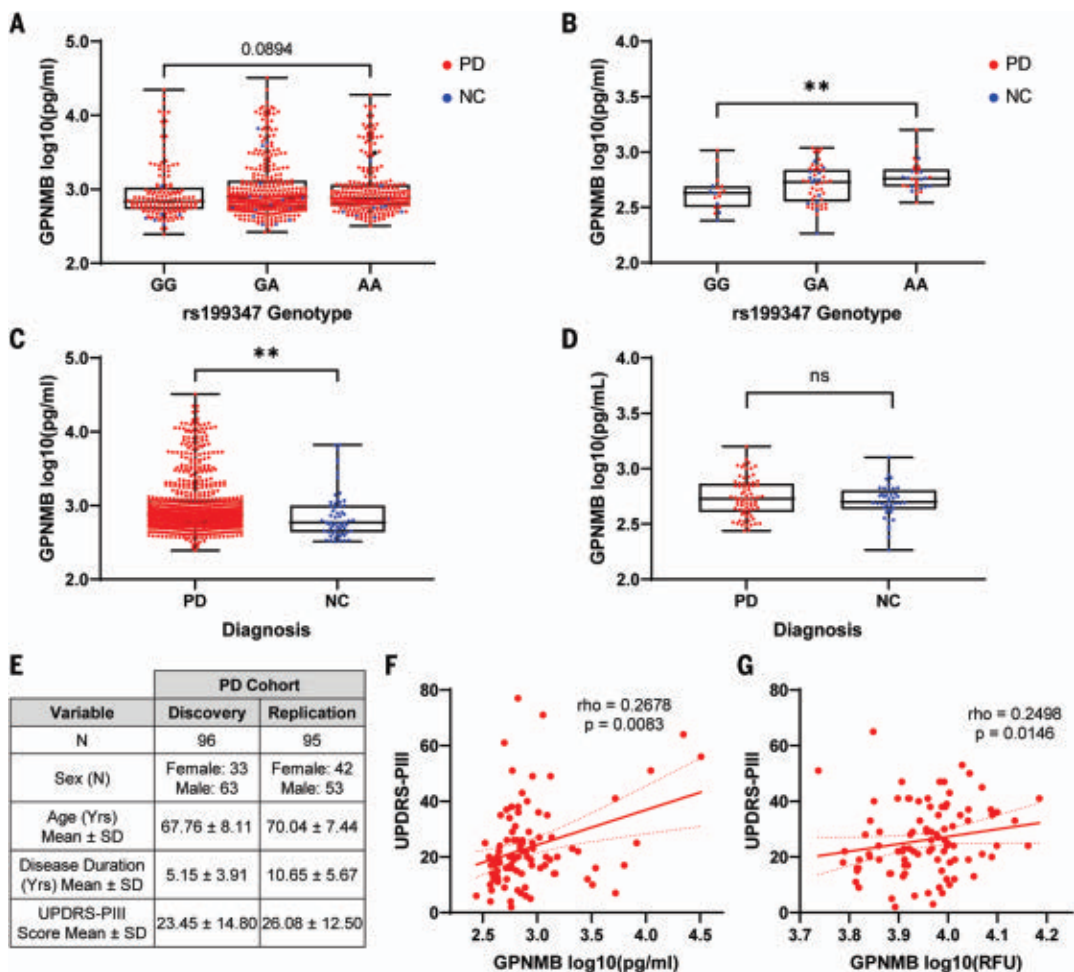


Fig. 6. Biofluid GPNMB protein levels associate with rs199347 genotype, PD diagnosis, and disease severity. (A and B) Plasma (A) and CSF (B) GPNMB levels grouped by rs199347 genotype. Genotypes were compared with Kruskal-Wallis test, followed by post hoc Dunn's test. ***P* < 0.01. (C and D) Plasma (C) and CSF (D) GPNMB levels grouped by diagnosis. PD (red) versus NCs (blue) were compared by Mann-Whitney test. Boxplots depict

median, 25th, and 75th quartiles, and whiskers depict full ranges. ***P* < 0.01. (E) Demographics for discovery and replication cohorts used for UPDRS-III analysis. (F and G) Scatterplots showing positive correlation between UPDRS-III scores and plasma GPNMB values in discovery (F) and replication (G) cohorts. Spearman's rho and *P* value are displayed. RFU, relative fluorescence unit.

for age, sex, and rs199347 genotype ($\beta_{PDvsNC} = 0.141$, *P* = 0.0397; tables S8 and S9). Moreover, in a subset of 96 PD individuals with clinical severity measures (Fig. 6E), plasma GPNMB levels were associated with disease severity as measured by the Unified Parkinson's Disease Rating Scale Part III (UPDRS-III) score (27), with higher plasma GPNMB levels found in more severely affected PD patients (Fig. 6F and table S10).

We confirmed these results in a second cohort of PD individuals from whom we had previously obtained GPNMB plasma measures using an aptamer-based method (28). Despite differences in measurement platform, disease duration, and severity between the original cohort of 96 individuals and this cohort of 95 additional, nonoverlapping PD individuals, GPNMB levels replicated their association with disease severity (Fig. 6G and table S11).

Discussion

Using statistical genetic methods, direct measures of ASE in human brain samples, CRISPR-based manipulation of gene levels in iPSC-Ns, and human biomarker studies, we establish *GPNMB* as a PD risk gene. Moreover, using a PD cellular model, we nominate GPNMB as a potential therapeutic target for interrupting the transmission of pathological aSyn. Finally, we demonstrate the importance of GPNMB expression levels, with even partial loss of expression exerting profound effects on aSyn and the synapse and increased expression associating with clinical severity in PD. Our results support a model in which PD risk-associated haplotypes at the rs199347 locus result in increased expression of *GPNMB* at the RNA and protein levels. Increase in *GPNMB* expression, in turn, may confer risk for development of PD through effects on the synapse and specifically on the cellular uptake of pathological forms of aSyn.

In this work, we integrated computational analyses of large databases with direct experimental verification of key predictions from these analyses. For example, statistical colocalization techniques and eQTL analyses suggested that the rs199347 haplotype affects *GPNMB* expression levels, and direct measures of *GPNMB* ASE in human brain samples confirmed these effects. Similarly, transcriptomic profiling of GPNMB-edited iPSC-Ns revealed broad effects on the synapse, with aSyn emerging as a hub protein from network analyses of genes affected by loss of GPNMB, and our cell biological studies confirmed a functional GPNMB-aSyn interaction with repercussions for the cellular transmission of pathological aSyn.

Additionally, we integrated the use of patient-derived samples with bench-based manipulation in a model system. The failure, to date, of many cell- and mouse model-based findings to translate to clinical utility in PD underlines the

importance of verifying that biological pathways implicated in model systems show corresponding signals in human disease. We used ~800 human samples to ground our study in clinical relevance. Direct manipulation of GPNMB in iPSC-Ns then allowed us to establish a causal effect for GPNMB in cellular processes that may mediate PD pathology.

What remains to be seen is whether GPNMB interacts with both normal and pathological conformations of aSyn to a similar extent and whether our neuronal findings will translate in vivo. A detailed analysis of the interaction between these two proteins, including whether the interaction with aSyn occurs with the soluble form of GPNMB versus the transmembrane protein before cleavage, would be key to downstream attempts at targeting. However, the discovery of a protein, expressed at the cell surface, which is both necessary and sufficient for internalization of fibrillar aSyn in neurons, opens up therapeutic avenues in PD.

Materials and methods

A more detailed version of the materials and methods is provided in the supplementary materials.

RNA isolation and library preparation from human brain samples

Human postmortem brain samples from NCs ($n = 2$) and PD ($n = 4$) individuals were obtained from the University of Pennsylvania Center for Neurodegenerative Disease Research (CNDP) Brain Bank and dissected as previously described (29). Demographics are summarized in table S1. The regions analyzed included the caudate nucleus, cingulate gyrus, and cerebellum. Samples were made up of predominantly gray matter. Genotypes for the brain samples were obtained as previously described (29, 30).

Library preparation was performed with the KAPA RNA HyperPrep Kit (KR1350, Illumina Platforms, Roche, WI). Briefly, RNA was fragmented using heat and magnesium for 8 min at 94°C to obtain 100– to 200–base pair (bp) fragments. The first cDNA strand was then synthesized using a thermocycler, followed by the second strand synthesis combined with A-tailing. Unique adapters were then ligated onto the library insert fragments and amplified using high-fidelity, low-bias polymerase chain reaction (PCR). The products then underwent a bead-based cleanup for purification of the cDNA libraries.

SeqCap RNA ChoiceTM probe pool design

The SeqCap RNA probe design pool was designed by Roche Sequencing Solutions Custom Design (Roche, WI). The pool was designed to contain probes ~60 bp in length with no more than 20 close matches in the genome, as determined by the Sequence Search and Align-

ment by Hashing Algorithm (SSAHA), for the purposes of providing sufficient coverage of transcripts of interest while minimizing potential off-target effects. A close match was defined as any genomic sequence that differed from one of the probe sequences by five or fewer single-base insertions, deletions, or substitutions. The majority of included probes had no off-target matches, with an exceedingly small percentage of probes displaying very few off-target matches. Only exonic probes covering the transcripts of interest were included and, to minimize SNP-mediated capture bias, probes that overlapped any SNPs in linkage disequilibrium ($r^2 > 0.2$, where r^2 is the coefficient of determination) with the sentinel PD GWAS SNPs were excluded.

Target cDNA enrichment and sequencing

Target cDNA enrichment and sequencing was performed as previously described (14) using the SeqCap EZ Accessory kit v2 (07145594001, Roche, WI). Briefly, equimolar amounts of cDNA libraries were combined for a total mass of 1 µg. Each of these libraries underwent multiplexed PCR with unique index oligonucleotides. The libraries were then hybridized with capture probes using the SeqCap EZ Hybridization and Wash Kit (05634261001, Roche, WI). Libraries were dried with heat in a vacuum and resuspended with hybridization reagents. Pooled capture probes for each region were added to the resuspended libraries and incubated for 20 hours in a thermocycler at 47°C, with the lid temperature at 57°C. The captured multiplex cDNA samples then underwent stringent washing steps and were amplified using ligation-mediated PCR (LM-PCR). These post-capture PCR-amplified libraries were pooled and sequenced on two lanes of an Illumina HiSeq 2500 with 150-bp paired-end reads, yielding ~150 million read pairs per lane.

Read mapping and ASE analyses

To assess RNA-seq reads quality, we used FastQC (31), and for reads quality filtering and trimming we used Trimmomatic (version 032) (32). We ran Trimmomatic to remove low-quality fragments in a 4-base-wide sliding window (average window quality below PHRED 20), and low-quality leading and trailing bases (below PHRED 10). We also dropped all the reads with average PHRED quality below 25, as well as reads shorter than 75 bases. Depending on the sample, 65 to 80% of reads passed this trimming and filtering step, resulting in 6.5 to 24 million read pairs per sample for mapping.

To perform unbiased allele-specific read mapping to the reference human genome (hg19) we applied WASP-STAR pipeline (fig. S7). First, we mapped reads with STAR (33), applying 2-step alignment and filtering them for mapping bias using WASP (34). Before proceeding with variant calling, we removed duplicate

reads using rmdup_pe.py script incorporated into WASP pipeline. To call and filter single-nucleotide variants (SNVs), we used GATK tools: HaplotypeCaller, SelectVariants, and VariantFiltration. We obtained allele-specific read counts by GATK – ASEReadCounter. To filter out intergenic variants, we functionally annotated SNVs using VariantAnnotation (35) and TxDb.Hsapiens.UCSC.hg19.knownGene (36) R packages. To test for ASE at the gene level, we first selected proxy SNPs that were highly linked ($r^2 > 0.6$) with rs199347 and located within a coding region for the gene of interest to assign allele of origin. For *GPNMB*, we assigned the allele of origin for each transcript read based on genotype at rs199355, and for *KLHL7*, we assigned the allele of origin based on genotype at rs2072368. We then tested for allelic imbalance with a beta-binomial model with overdispersion using the MBASED R package (13). *P* values were adjusted for false discovery rate using the Benjamini-Hochberg method (37).

Colocalization analysis

Colocalization analysis was performed as previously described (11) using the coloc package in R (version 4.0-2). The prior probabilities of p1, p2, and p12 were set to 1×10^{-4} , 1×10^{-4} , and 1×10^{-5} respectively. Significant colocalization was determined as having a PPH4 > 75%. Sensitivity analysis was performed to determine whether PPH4 is robust over plausible values of p12 (1×10^{-5} to 1×10^{-6}) (38). Association plots were generated using Locus-Compasser package (version 1.0.0) (39) in R.

Immortalized cell line transfection and collection

For co-IP experiments, HEK293 or HeLa cells were plated at 700,000 or 1 million cells per well, respectively, and 18 hours after plating, transfection was performed with 4 µg of each DNA construct and Lipofectamine 2000 (Thermo Scientific) in serum-free Dulbecco's minimum essential medium (DMEM). Cells were transfected with either GPNMB-myc-DDK pCMV6-Entry (Origene) and 5' untranslated region (5' UTR)-Syn pcDNA3.1+ (obtained from K. Luk) for the GPNMB-flag IP or GPNMB untagged clone pCMV6-XL4 (Origene) and Syn-Myc pcDNA3.1+ (obtained from K. Luk) for the Syn-Myc IP. Four hours after transfection, media was changed to DMEM with 10% fetal bovine serum (FBS), 1% L-Glut, and 1% Pen-Strep. At 20 hours posttransfection, cells were washed in Dulbecco's phosphate-buffered saline (dPBS) and lysed in CHAPS buffer (25 mM Tris, 150 mM NaCl, 1 mM EDTA, 1% CHAPS, 5% glycerol, pH to 7.4). Lysates were collected and spun down at 4°C for 30 min at 21380 xg. Bicinchoninic acid (BCA) assays (Thermo Scientific) were used to determine protein concentrations.

For immunofluorescence experiments, HEK293 or HeLa cells were plated at either 100,000 or

200,000 cells per well on either PDL-coated or untreated 12-mm glass coverslips in a 12-well format. 18 hours after plating, the cells were transfected with 1.6 µg of each DNA construct (GPNMB untagged clone pCMV6-XL4 and 5' UTR-Syn pcDNA3.1+) and Lipofectamine 2000 (Thermo Scientific) in serum-free DMEM.

Co-IP

To immunoprecipitate GPNMB, 300 µL of anti-Flag-conjugated beads (Sigma A2220) or mouse immunoglobulin G (IgG)-conjugated beads (Sigma A0919, used as a negative control) were used to immunoprecipitate from 1000 µg of lysate from GPNMB-myc-DKK and 5'UTR-syn double-transfected cells in CHAPS buffer overnight at 4°C. To immunoprecipitate aSyn, 300 µL of anti-c-Myc-conjugated beads (Sigma A7470) or rabbit IgG-conjugated beads (Sigma A2909, used as a negative control) were used to immunoprecipitate from 1000 µg of lysate from GPNMB untagged clone and Syn-Myc double-transfected cells in CHAPS buffer overnight at 4°C. After 24 hours, the protein-conjugated beads were washed three times with CHAPS buffer and the bound protein was competitively eluted from the beads using either 250 µM 3x flag peptide (Sigma) or 250 mM myc peptide (Sigma) for 1 hour at 4°C.

CRISPR-Cas9 KO of human iPSCs

Human iPSCs with *Neurog1* and *Neurog2* in a bicistronic doxycycline-inducible expression cassette (22) were used for generation of GPNMB KO iPSCs and rapid induction of iPSC-Ns. The protocol for generating CRISPR-edited iPSCs is summarized in fig. S3 and detailed in the supplementary materials and methods.

Culture and differentiation of iPSC-Ns

Before differentiation, iPSC cultures were maintained on Matrigel-coated 6-cm tissue culture plates with mTeSR1 media and mechanically passaged every 4 days with StemMACS passaging solution XF. The neural induction protocol is summarized in fig. S4, based on prior studies (40), and detailed in the supplementary materials and methods.

Immunofluorescence

The media was aspirated from coverslip-containing wells, and the cells were fixed in 2% paraformaldehyde in dPBS for 15 min at room temperature. After fixing, the coverslips were rinsed five times with dPBS and blocked/permeabilized with blocking buffer (3% bovine serum albumin + 0.05% saponin in dPBS) for 1 hour before incubating in primary antibody overnight. Image stacks of 1-µm thickness were acquired by confocal microscopy (Leica SP5) using a 40x oil immersion objective with 2x zoom. Antibody concentrations are summarized in the key resources tables in the supplementary materials.

Image processing and quantification

Image processing to quantify synaptic proteins was performed using a Cell Profiler pipeline based on Danielson *et al.*'s previously published work (41). A single slice was chosen from each stack to focus our analysis on the plane with the most abundant synapsin-1 staining. TUBB3 images underwent image enhancement for neurite-like features and were used to calculate TUBB3+ area for normalization and expanded to generate a mask. Synapsin-1 and aSyn images underwent enhancement for speckle-like features, followed by object identification and characterization of object size/intensity. The total integrated intensity (i.e., sum for all particles) was used for analysis. The pipeline used has been made publicly available in the supplementary materials.

aSyn pathology in iPSC-Ns was also quantified using CellProfiler. Maximum intensity projections of z-stack images were created using FIJI. Desired 81a+ objects were identified with intensity thresholding and the total area of 81a+ objects were normalized with total area of DRAQ5+ objects. To quantify MJFR1+ staining in HEK293 overexpressing GPNMB, nuclei artifact staining was removed by generating DRAQ5+ nuclei mask and excluding MJFR1+ speckles within the mask. Total area of MJFR1+ objects was normalized by total area of DRAQ5+ objects.

A researcher blinded to sample identity was provided with randomly ordered maximum intensity projection of z-stack images of iPSC-Ns treated with AF594-PFF. Scores ranging from 0 to 3 were given for each criterion: intensity, length, and frequency of internalized PFFs. The three scores were added and were normalized to the average score of WT iPSC-Ns.

Synaptosome extraction

Synaptosomes were extracted using Syn-PER Synaptic Protein Extraction Reagent (Thermo-Fisher) per the user instructions.

Immunoblotting

Samples were diluted in 5X concentrated sample buffer [10 g Sucrose, 1.85 mL 0.5 M Tris, pH 6.8, 1.0 mL 0.1 M EDTA, 1.0 mL of 0.1% Bromophenol Blue, 1.0 mL of 0.05% Pyronine Yellow, 0.615 g of dithiothreitol (DTT), 10 mL of 10% sodium dodecyl sulfate (SDS), and adjusted to a final volume of 20 mL with Milli-Q Water] and boiled at either 100°C for 10 min or 70°C for 15 min for heat-sensitive proteins (GPNMB). Samples were run on 4 to 20% polyacrylamide TGX gels (Bio-Rad Laboratories) and transferred onto 0.2 nitrocellulose membrane (Bio-Rad Laboratories). When blotting for aSyn, membranes were fixed in 0.4% PFA for 30 min (42). Membranes were blocked in 5% milk in tris-buffered saline (TBS) for 1 hour and blotted overnight at 4°C with specific antibodies. The membranes were incubated for 2 hours in

horseradish peroxidase (HRP)-conjugated secondary antibodies and developed using Western Bright ECL and Sirius HRP substrates (Advansta). Antibody concentrations are summarized in the key resources tables. Densitometry was performed using the Bio-Rad Image Lab Software.

RNA-seq of iPSC-Ns

RNA was extracted from iPSC-Ns on days 0 and 14 after doxycycline induction using QIAGEN RNeasy mini kit. RNA integrity was measured using RNA nano chips (Agilent) on an Agilent 2100 Bioanalyzer. All samples had RIN > 9.4. Library preparation was performed with the TruSeq Stranded mRNA Library Prep kit (Illumina cat no. 20020595) using 225 ng of total RNA and following manufacturer instructions. High-sensitivity DNA chips (Agilent) were used to balance libraries before sequencing. In total, 30 RNA samples [three genotypes (WT, Het, and KO) × two differentiation times (days 0 and 14) × five biological replicates] were sequenced. All 30 samples were sequenced together on a single S2 flow-cell generating $>1.1 \times 10^9$ of 100-bp single-end reads in total (on average 3.69×10^7 reads per sample, ranging from 2.9×10^7 to 5.3×10^7). A summary of the Illumina NovaSeq run is provided in table S12.

Read quality control and filtering

A quality check of the raw reads was assessed using FastQC (31) and summarized with MultiQC (43). Next, the adapters were removed and filtering of the low-quality reads was conducted using Trimmomatic, version 0.39 (32), with the following parameters: *ILLUMINACLIP:TruSeq3-SE,fa:2:30:10 LEADING:5 TRAILING:5 SLIDINGWINDOW:5:20 MINLEN:50 AVGQUAL:30 HEADCROP:10*. The adapters that matched the sequences provided by TruSeq3-SE.fa were removed. The low-quality bases were cut off the start and off the end of reads if their PHRED score was below 5. The sliding window of 5 bp was applied to trim the bases if the window PHRED score dropped below 20. The 10 bases from the start of the reads were also cropped. Finally, the reads were discarded if the average PHRED score of the read was below 30.

Read alignment and quantification

The sequence alignment BAM files generated by Bowtie 2 were used as the input to RSEM software tool, to quantify gene expression levels (44). On average, 3.61×10^7 (97.8%) of reads per sample passed the filtering steps and were mapped versus reference genome GRCh38 using Bowtie 2 with the following parameters: *bowtie2 -q-phred33-sensitive-dpad 0-gbar 999999999-mp 1,1-np 1-score-min L,0,-0.1-nofw -p 32 -k 200 -x*, as suggested by RSEM manual. The read alignment rate was on average >89% (table S12). To obtain the raw read counts at the gene level, an expectation

maximization algorithm (RNA-seq by Expectation Maximization) was run by the following RSEM command: *rsem-calculate-expression-bowtie2-forwardprob 0*.

Differential gene expression (DGE) analysis

To detect significant differences in iPSC-N gene expression data between day 0 and day 14 and between the genotypes (WT, Het, and KO), DESeq function from DESeq2 Bioconductor's R package (45) was used. RNA-seq data were modeled using the negative binomial distribution that accounts for overdispersion. To conduct the pairwise comparisons (day 14 versus day 0 in WT, KO versus WT, Het versus WT, and KO versus Het at day 14) for each gene, the *nbinomWaldTest* statistic was used. The Wald test *P* values were calculated by scaling the coefficients by their standard errors and then compared with a standard Normal distribution. After DGE analysis, the *lfcShrink* function from R package *apeglm* (46) was applied to shrink the log2FC. We corrected for false discovery rate (FDR) using the Benjamini-Hochberg method (37). Genes with a Benjamini-Hochberg-corrected *P* < 0.01 and a |log2 fold-change| > 1 were considered to be significantly differentially expressed. To visualize the results of DGE analyses we used EnhancedVolcano R package version 1.10.0 (47).

Modular coexpression network analysis

Modular coexpression network analysis of iPSC-Ns was performed using R package *CEMiTool* (CoExpression Molecules identification Tool), version 1.14.1 (48). The log normalized expression data (15981 genes in 15 samples) were used as an input to *cemitool* function. As a first step, *cemitool* conducted an unsupervised filtering of expression data using the inverse gamma distribution to model the variance of genes. Out of 15981 genes, 1100 genes with *P* < 0.1 survived this filtering and were used for downstream analyses. The genes were then separated into modules using the dissimilarities measures and the *Dynamic Tree Cut* package (49). The minimum number of genes per module was set to 20, and similar modules were merged together based on correlation.

To determine biological functions associated with the coexpression modules, the gene ontology (GO) gene sets *c5.all.v7.4*, which contain GO resources (BP, biological process; CC, cellular component; MF, molecular function) and human phenotype ontology (HPO) from MSigDB database (50), were used in overrepresentation analysis (ORA). The module gene set enrichment analysis (GSEA) was performed using the *fgsea* R package (51) within the CEMiTool pipeline. First, a *z*-score gene normalization on all input genes was performed, followed by calculation of the mean for each sample class (GPNMB WT, Het, and KO). Next, a preranked GSEA was performed

independently for each *GPNMB* genotype. The module activity was visualized by normalized enrichment score.

To construct the gene interactions network in the coexpression modules, the combined human protein-protein interaction data, downloaded from GeneMANIA, were added to the CEMiTool object using the function *interactions_data*. The interactions between the genes were visualized using the *plot_interactions* function.

aSyn PFF internalization and immunofluorescence experiments

Human WT PFFs and fluorescent fibrils including Alexa Fluor594 (AF594)-conjugated aSyn were provided by K. Luk at the Penn CNDR. All fibrils were kept at -80°C until use. After the stock of 5 mg/mL was diluted to a working concentration of 0.1 mg/mL in dPBS, fibrils were sonicated (Diagenode Biorupter Plus) on high, sonicating for 30 s followed by 30 s of rest for a total of 10 min. Sonicated PFFs were then added to classic neuronal media according to appropriate concentrations.

For AF594-PFF internalization experiments using iPSC-Ns, 10 µg of PFFs were added per well of a 12-well plate. iPSC-Ns were incubated in 4°C for 30 min, followed by an additional 30-min incubation at 4°C for the negative control or 1 hour and 30 min in 37°C for experimental wells. All cells were immediately fixed and stained afterward.

To demonstrate aSyn pathology after PFF transduction, we replaced regular media of iPSC-Ns at day 14 with classical neuronal media containing total of 1 µg of human WT PFFs per well. iPSC-Ns were fixed and stained after 14 days (at day 28 of neuronal induction). To extract soluble proteins, coverslips were fixed with 2% paraformaldehyde and 1% Triton X-100 in dPBS. 3% bovine serum albumin without saponin in dPBS was used as blocking buffer.

For WT PFF internalization experiments using HEK293, cells were plated at 200,000 cells per well in PDL-coated 12-mm glass coverslips in a 12-well format. 18 hours after plating, the cells were transfected with 1 µg of DNA (GPNMB untagged clone pCMV6-XL4 or TMEM106B-Flag) and Lipofectamine 2000 (Thermo Scientific) in serum-free DMEM. At 20 hours posttransfection, media was replaced with DMEM containing 1 µg of PFFs per well. The plates were incubated for 30 min at 4°C followed by an additional 30-min incubation at 4°C for negative control (to inhibit endocytosis) or 1 hour and 30 min in 37°C for experimental wells. All cells were immediately fixed and stained for immunofluorescence afterward.

Patient samples and genotypes

Plasma and CSF samples of PD patients and NCs were obtained as part of the Penn CNDR Neuropathology, Biomarker, and Genetics Bio-

Integration in Neurological Diagnosis Initiative (MIND) studies. PD patients had a clinical diagnosis of PD made by a movement disorders specialist at the Parkinson's Disease and Movement Disorder Clinic (PDMDC) at the University of Pennsylvania, whereas controls had no known neurological disorder. Data were stored in the Penn Integrated Neurodegenerative Disease Database (INDD) (30). These studies were approved by the UPenn Institutional Review Board (IORG0000029). Informed consent was obtained at study enrollment. Participant demographics are reported in tables S4 to S7. Individuals with known *GBA1* mutations (N370S, E365K, and L444P) were excluded from the analysis because GPNMB elevation has been reported in patients with Gaucher disease, a lysosomal storage disorder caused by homozygous mutations in *GBA1* (52, 53). Genotyping of SNP rs199347 was performed by Infinium Global Screening Assay (Illumina), NeuroX genotyping platform, PANDORA (Sequenom) panel (30), or MIND panel based on allele-specific PCR performed using FlexSIX Dynamic Array integrated fluidic circuits (Fluidigm) and genotyping using BioMark HD system (Fluidigm) (54).

A subset of PD individuals from the previously described University of Pennsylvania U19 Cohort (55) had UPDRS-PIII scores for disease severity.

Enzyme-linked immunosorbent assay (ELISA)

GPNMB protein levels within human plasma and CSF samples were measured with ELISA kits (R&D systems) according to manufacturer's instructions. CSF and plasma samples were diluted by factors of 1 in 2 and 1 in 30 respectively to obtain optical density measurements within the standard range. All samples were run in duplicates and absorbance at 450 nm was determined by a microplate reader (Berthold Technologies, Tristar LB 941). Only duplicate samples with a coefficient of variation (CV) of <25% were retained for analysis, and the average CV across all samples used was 3.3%. Moreover, replicate samples assayed by ELISA on different days, by different operators, across multiple freeze-thaw cycles, demonstrated excellent reproducibility (Pearson's correlation coefficient *r* = 0.97).

Multiple linear regression analyses

Multiple linear regression was used to determine factors that are significant predictors of GPNMB concentration in plasma and CSF. Age, sex, PD status, and rs199347 genotype were included as independent variables. A codominant genetic model, which considers each allele combination (GG, AG, and AA) as a separate factor (56), was used to model the effect of rs199347. Regression coefficients were calculated with GG as the reference.

The relationship between GPNMB levels and disease severity was established in two

different PD cohorts. GPNMB values for the discovery cohort were generated by ELISA (R&D systems), whereas GPNMB values for the replication cohort were generated using an aptamer-based platform (26). UPDRS-PIII values were downloaded from the Penn INDD.

Statistical analyses

Statistical analyses were performed with either PRISM or R. Data were tested for normality with a Shapiro-Walk test. Data with more than two categorical groups were analyzed by either one-way analysis of variance (ANOVA) (followed by post hoc Tukey or Dunnett tests) or Kruskal-Wallis test (followed by post hoc Dunn's test) depending on the data's distribution. Data with only two groups were analyzed by either a Welch's two-sample *t* test or Mann-Whitney *U* test depending on the data distribution. Correlations were determined using Spearman's rank correlation. Multiple linear regression (glm) was used to determine associations between two variables adjusting for potentially confounding covariates. Outlier determination was performed using ROUT method, *Q* (FDR) = 1%.

Immunohistochemistry

Formalin-fixed, paraffin-embedded cingulate and temporal cortex samples were obtained from the Penn CNDR. Patient demographics are reported in table S1. 6- μ m sections were cleared in xylene and a descending EtOH series. Endogenous peroxidases were quenched in 30% H₂O₂ and 70% MeOH solution for 30 min. Slides were microwaved in citric acid Antigen Unmasking Solution (Vector Laboratories). After cooling, slides were rinsed in TBS-T (0.1 M Tris Buffer/0.05% TWEEN) and blocked (TBS-T/2%FBS/3%BSA). Sections were incubated overnight at 4°C in the primary antibody (see the key resources tables for antibody conditions). Once washed with TBS-T, sections were incubated for 1 hour at room temperature in the secondary antibody (see the key resources tables for antibody conditions). VECTASTAIN ABC Standard (Vector Laboratories) was applied for 1 hour at room temperature followed by ImmPACT DAB (Vector Laboratories). Sections were counterstained with Harris Hematoxylin (Thermo Scientific) for 40 s. Slides were dehydrated in an ascending EtOH series and xylenes then coverslipped with Cytoseal (Thermo Scientific).

Dephosphorylation and deglycosylation

For deglycosylation of cell and brain lysates, 5.0 μ L of PNGase F was added to 125 μ g of brain lysates or 60 μ g of cell lysates and incubated at 37°C for 30 min. For dephosphorylation experiments, 1 μ L of Lambda protein phosphatase was added to 125 μ g of brain lysates or 50 μ g of cell lysates and incubated at 30°C for 30 min.

REFERENCES AND NOTES

- E. R. Dorsey et al., Projected number of people with Parkinson disease in the most populous nations, 2005 through 2030. *Neurology* **68**, 384–386 (2007). doi: [10.1212/01.wnl.0000247740.47667.03](https://doi.org/10.1212/01.wnl.0000247740.47667.03); pmid: 17082464
- M. A. Nalls et al., Identification of novel risk loci, causal insights, and heritable risk for Parkinson's disease: A meta-analysis of genome-wide association studies. *Lancet Neurol.* **18**, 1091–1102 (2019). doi: [10.1016/S1474-4422\(19\)30320-5](https://doi.org/10.1016/S1474-4422(19)30320-5); pmid: 31701892
- K. McFarthing, T. Simuni, Clinical Trial Highlights: Targeting Alpha-Synuclein. *J. Parkinsons Dis.* **9**, 5–16 (2019). doi: [10.3233/JPD-189004](https://doi.org/10.3233/JPD-189004); pmid: 30741694
- S. A. Schneider, R. N. Alcalay, Precision medicine in Parkinson's disease: Emerging treatments for genetic Parkinson's disease. *J. Neurol.* **267**, 860–869 (2020). doi: [10.1007/s00415-020-09705-7](https://doi.org/10.1007/s00415-020-09705-7); pmid: 31974807
- D. Chang et al., A meta-analysis of genome-wide association studies identifies 17 new Parkinson's disease risk loci. *Nat. Genet.* **49**, 1511–1516 (2017). doi: [10.1038/ng.3955](https://doi.org/10.1038/ng.3955); pmid: 28892059
- M. D. Gallagher et al., A Dementia-Associated Risk Variant near *TMEM106B* Alters Chromatin Architecture and Gene Expression. *Am. J. Hum. Genet.* **101**, 643–663 (2017). doi: [10.1016/j.ajhg.2017.09.004](https://doi.org/10.1016/j.ajhg.2017.09.004); pmid: 29056226
- K. Musunuru et al., From noncoding variant to phenotype via *SORT1* at the 1p13 cholesterol locus. *Nature* **466**, 714–719 (2010). doi: [10.1038/nature09266](https://doi.org/10.1038/nature09266); pmid: 20686566
- M. Claussnitzer et al., FTO Obesity Variant Circuitry and Adipocyte Browning in Humans. *N. Engl. J. Med.* **373**, 895–907 (2015). doi: [10.1056/NEJMoa1502214](https://doi.org/10.1056/NEJMoa1502214); pmid: 26287746
- F. Soldner et al., Parkinson-associated risk variant in distal enhancer of α -synuclein modulates target gene expression. *Nature* **533**, 95–99 (2016). doi: [10.1038/nature17939](https://doi.org/10.1038/nature17939); pmid: 27096366
- GTEX Consortium, Genetic effects on gene expression across human tissues. *Nature* **550**, 204–213 (2017). doi: [10.1038/nature24277](https://doi.org/10.1038/nature24277); pmid: 29022597
- C. Giambartolomei et al., Bayesian Test for Colocalisation between Pairs of Genetic Association Studies Using Summary Statistics. *PLOS Genet.* **10**, e1004383 (2014). doi: [10.1371/journal.pgen.1004383](https://doi.org/10.1371/journal.pgen.1004383); pmid: 24830394
- M. N. Murthy et al., Increased brain expression of GPNMB is associated with genome wide significant risk for Parkinson's disease on chromosome 7p15.3. *Neurogenetics* **18**, 121–133 (2017). doi: [10.1007/s10048-017-0514-8](https://doi.org/10.1007/s10048-017-0514-8); pmid: 28391543
- O. Mayba et al., MBASED: Allele-specific expression detection in cancer tissues and cell lines. *Genome Biol.* **15**, 405 (2014). doi: [10.1186/s13059-014-0405-3](https://doi.org/10.1186/s13059-014-0405-3); pmid: 25315065
- T. R. Mercer et al., Targeted sequencing for gene discovery and quantification using RNA CaptureSeq. *Nat. Protoc.* **9**, 989–1009 (2014). doi: [10.1038/nprot.2014.058](https://doi.org/10.1038/nprot.2014.058); pmid: 24705597
- H. Tanaka et al., The potential of GPNMB as novel neuroprotective factor in amyotrophic lateral sclerosis. *Sci. Rep.* **2**, 573 (2012). doi: [10.1038/srep00573](https://doi.org/10.1038/srep00573); pmid: 22891158
- Y. Nagahara et al., GPNMB ameliorates mutant TDP-43-induced motor neuron cell death. *J. Neurosci. Res.* **95**, 1647–1665 (2017). doi: [10.1002/jnr.23999](https://doi.org/10.1002/jnr.23999); pmid: 27935101
- M. A. J. Weterman et al., *nmb*, a novel gene, is expressed in low-metastatic human melanoma cell lines and xenografts. *Int. J. Cancer* **60**, 73–81 (1995). doi: [10.1002/ijc.2910600111](https://doi.org/10.1002/ijc.2910600111); pmid: 7814155
- A. A. N. Rose, M. Biondini, R. Curiel, M. Siegel, Targeting GPNMB with glenatamumab vedotin: Current developments and future opportunities for the treatment of cancer. *Pharmacol. Ther.* **179**, 127–141 (2017). doi: [10.1016/j.pharmthera.2017.05.010](https://doi.org/10.1016/j.pharmthera.2017.05.010); pmid: 28546082
- M. Hüttenrauch et al., Glycoprotein NMB: A novel Alzheimer's disease associated marker expressed in a subset of activated microglia. *Acta Neuropathol. Commun.* **6**, 108 (2018). doi: [10.1186/s40478-018-0612-3](https://doi.org/10.1186/s40478-018-0612-3); pmid: 30340518
- E. B. Moloney, A. Moskites, E. J. Ferrari, O. Isacson, P. J. Hallett, The glycoprotein GPNMB is selectively elevated in the substantia nigra of Parkinson's disease patients and increases after lysosomal stress. *Neurobiol. Dis.* **120**, 1–11 (2018). doi: [10.1016/j.nbd.2018.08.013](https://doi.org/10.1016/j.nbd.2018.08.013); pmid: 30149180
- M. L. Neal, A. M. Boyle, K. M. Budge, F. F. Safadi, J. R. Richardson, The glycoprotein GPNMB attenuates astrocyte inflammatory responses through the CD44 receptor. *J. Neuroinflammation* **15**, 73 (2018). doi: [10.1186/s12974-018-1100-1](https://doi.org/10.1186/s12974-018-1100-1); pmid: 29519253
- V. Busskamp et al., Rapid neurogenesis through transcriptional activation in human stem cells. *Mol. Syst. Biol.* **10**, 760 (2014). doi: [10.15252/msb.20145508](https://doi.org/10.15252/msb.20145508); pmid: 25403753
- J. E. Galvin, T. M. Schuck, V. M. Y. Lee, J. Q. Trojanowski, Differential expression and distribution of α -, β -, and γ -synuclein in the developing human substantia nigra. *Exp. Neurol.* **168**, 347–355 (2001). doi: [10.1006/exnr.2000.7615](https://doi.org/10.1006/exnr.2000.7615); pmid: 11259122
- D. D. Murphy, S. M. Ruetter, J. Q. Trojanowski, V. M.-Y. Lee, Synucleins are developmentally expressed, and α -synuclein regulates the size of the presynaptic vesicular pool in primary hippocampal neurons. *J. Neurosci.* **20**, 3214–3220 (2000). doi: [10.1523/JNEUROSCI.20-09-03214.2000](https://doi.org/10.1523/JNEUROSCI.20-09-03214.2000); pmid: 10777786
- D. Warde-Farley et al., The GeneMANIA prediction server: Biological network integration for gene prioritization and predicting gene function. *Nucleic Acids Res.* **38**, W214–W220 (2010). doi: [10.1093/nar/gkq537](https://doi.org/10.1093/nar/gkq537); pmid: 20576703
- L. A. Volpicelli-Daley, K. C. Luk, V. M.-Y. Lee, Addition of exogenous α -synuclein preformed fibrils to primary neuronal cultures to seed recruitment of endogenous α -synuclein to Lewy body and Lewy neurite-like aggregates. *Nat. Protoc.* **9**, 2135–2146 (2014). doi: [10.1038/nprot.2014.143](https://doi.org/10.1038/nprot.2014.143); pmid: 25122523
- S. Fahn, R. Elton, Members of the UPDRS Development Committee, in *Recent Developments in Parkinson's Disease*, S. Fahn, C. D. Marsden, M. Goldstein, D. B. Calne, Eds. (Macmillan Healthcare Information, 1987), pp. 153–163.
- M. Posavi et al., Characterization of Parkinson's disease using blood-based biomarkers: A multicohort proteomic analysis. *PLOS Med.* **16**, e1002931 (2019). doi: [10.1371/journal.pmed.1002931](https://doi.org/10.1371/journal.pmed.1002931); pmid: 31603904
- A. S. Chen-Plotkin et al., Variations in the progranulin gene affect global gene expression in frontotemporal lobar degeneration. *Hum. Mol. Genet.* **17**, 1349–1362 (2008). doi: [10.1093/hmg/ddn023](https://doi.org/10.1093/hmg/ddn023); pmid: 18223198
- J. B. Toledo et al., A platform for discovery: The University of Pennsylvania Integrated Neurodegenerative Disease Biobank. *Alzheimers Dement.* **10**, 477–484.e1 (2014). doi: [10.1016/j.jalz.2013.06.003](https://doi.org/10.1016/j.jalz.2013.06.003); pmid: 23978324
- S. Andrews, FastQC: A Quality Control Tool for High Throughput Sequence Data (Java, 2010); <https://www.bioinformatics.babraham.ac.uk/projects/fastqc/>.
- A. M. Bolger, M. Lohse, B. Usadel, Trimmomatic: A flexible trimmer for Illumina sequence data. *Bioinformatics* **30**, 2114–2120 (2014). doi: [10.1093/bioinformatics/btu170](https://doi.org/10.1093/bioinformatics/btu170); pmid: 24695404
- A. Dobin, T. R. Gingeras, in *Data Mining Techniques for the Life Sciences*, O. Carugo, F. Eisenhaber, Eds. (Springer, 2016), pp. 245–262.
- B. van de Geijn, G. McVicker, Y. Gilad, J. K. Pritchard, WASP: Allele-specific software for robust molecular quantitative trait locus discovery. *Nat. Methods* **12**, 1061–1063 (2015). doi: [10.1038/nmeth.3582](https://doi.org/10.1038/nmeth.3582); pmid: 26366987
- V. Obenchain et al., VariantAnnotation: A Bioconductor package for exploration and annotation of genetic variants. *Bioinformatics* **30**, 2076–2078 (2014). doi: [10.1093/bioinformatics/btu168](https://doi.org/10.1093/bioinformatics/btu168); pmid: 24681907
- M. Carlson, TxDb.Hsapiens.UCSC.hg19.knownGene: Annotation package for TxDb object(s), R package version 3.2.2 (2015).
- Y. Benjamini, Y. Hochberg, Controlling the False Discovery Rate: A Practical and Powerful Approach to Multiple Testing. *J. R. Stat. Soc. B* **57**, 289–300 (1995). doi: [10.1111/j.2517-6161.1995.tb02031.x](https://doi.org/10.1111/j.2517-6161.1995.tb02031.x)
- C. Wallace, Eliciting priors and relaxing the single causal variant assumption in colocalisation analyses. *PLOS Genet.* **16**, e1008720 (2020). doi: [10.1371/journal.pgen.1008720](https://doi.org/10.1371/journal.pgen.1008720); pmid: 32310995
- B. Liu, M. J. Gloudemans, A. S. Rao, E. Ingelsson, S. B. Montgomery, Abundant associations with gene expression complicate GWAS follow-up. *Nat. Genet.* **51**, 768–769 (2019). doi: [10.1038/s41588-019-0404-0](https://doi.org/10.1038/s41588-019-0404-0); pmid: 31043754
- R. Tian et al., CRISPR Interference-Based Platform for Multimodal Genetic Screens in Human iPSC-Derived Neurons. *Neuron* **104**, 239–255.e12 (2019). doi: [10.1016/j.neuron.2019.07.014](https://doi.org/10.1016/j.neuron.2019.07.014); pmid: 31422865
- E. Danielson et al., Molecular Diversity of Glutamatergic and GABAergic Synapses from Multiplexed Fluorescence Imaging. *eNeuro* **8**, ENEURO.0286-20.2020 (2020). doi: [10.1523/JNEURO.0286-20.2020](https://doi.org/10.1523/JNEURO.0286-20.2020); pmid: 33355295
- B. R. Lee, T. Kamitani, Improved Immunodetection of Endogenous α -Synuclein. *PLoS One* **6**, e23939 (2011). doi: [10.1371/journal.pone.0023939](https://doi.org/10.1371/journal.pone.0023939); pmid: 21886844
- P. Ewels, M. Magnusson, S. Lundin, M. Källér, MultiQC: Summarize analysis results for multiple tools and samples in a single report. *Bioinformatics* **32**, 3047–3048 (2016). doi: [10.1093/bioinformatics/btw354](https://doi.org/10.1093/bioinformatics/btw354); pmid: 27312411

44. B. Li, C. N. Dewey, RSEM: Accurate transcript quantification from RNA-Seq data with or without a reference genome. *BMC Bioinformatics* **12**, 323 (2011). doi: [10.1186/1471-2105-12-323](https://doi.org/10.1186/1471-2105-12-323); pmid: [21816040](https://pubmed.ncbi.nlm.nih.gov/21816040/)
45. M. I. Love, W. Huber, S. Anders, Moderated estimation of fold change and dispersion for RNA-seq data with DESeq2. *Genome Biol.* **15**, 550 (2014). doi: [10.1186/s13059-014-0550-8](https://doi.org/10.1186/s13059-014-0550-8); pmid: [25516281](https://pubmed.ncbi.nlm.nih.gov/25516281/)
46. A. Zhu, J. G. Ibrahim, M. I. Love, Heavy-tailed prior distributions for sequence count data: Removing the noise and preserving large differences. *Bioinformatics* **35**, 2084–2092 (2019). doi: [10.1093/bioinformatics/bty895](https://doi.org/10.1093/bioinformatics/bty895); pmid: [30395178](https://pubmed.ncbi.nlm.nih.gov/30395178/)
47. K. Blighe, S. Rana, M. Lewis, EnhancedVolcano: Publication-ready volcano plots with enhanced colouring and labeling. Github (2021); <https://github.com/kevinblighe/EnhancedVolcano>.
48. P. S. T. Russo *et al.*, CEMiTool: A Bioconductor package for performing comprehensive modular co-expression analyses. *BMC Bioinformatics* **19**, 56 (2018). doi: [10.1186/s12859-018-2053-1](https://doi.org/10.1186/s12859-018-2053-1); pmid: [29458351](https://pubmed.ncbi.nlm.nih.gov/29458351/)
49. P. Langfelder, B. Zhang, S. Horvath, Defining clusters from a hierarchical cluster tree: The Dynamic Tree Cut package for R. *Bioinformatics* **24**, 719–720 (2008). doi: [10.1093/bioinformatics/btm260](https://doi.org/10.1093/bioinformatics/btm260); pmid: [18024473](https://pubmed.ncbi.nlm.nih.gov/18024473/)
50. A. Liberzon *et al.*, Molecular signatures database (MSigDB) 3.0. *Bioinformatics* **27**, 1739–1740 (2011). doi: [10.1093/bioinformatics/btr260](https://doi.org/10.1093/bioinformatics/btr260); pmid: [21546393](https://pubmed.ncbi.nlm.nih.gov/21546393/)
51. G. Korotkevich *et al.*, Fast gene set enrichment analysis. *bioRxiv* 060012 (2021). <https://doi.org/10.1101/060012>.
52. H. Zigdon *et al.*, Identification of a Biomarker in Cerebrospinal Fluid for Neuronopathic Forms of Gaucher Disease. *PLOS One* **10**, e0120194 (2015). doi: [10.1371/journal.pone.0120194](https://doi.org/10.1371/journal.pone.0120194); pmid: [25775479](https://pubmed.ncbi.nlm.nih.gov/25775479/)
53. G. Kramer *et al.*, Elevation of glycoprotein nonmetastatic melanoma protein B in type 1 Gaucher disease patients and mouse models. *FEBS Open Bio* **6**, 902–913 (2016). doi: [10.1002/2211-5463.12078](https://doi.org/10.1002/2211-5463.12078); pmid: [27642553](https://pubmed.ncbi.nlm.nih.gov/27642553/)
54. T. F. Tropea *et al.*, Whole Clinic Research Enrollment in Parkinson's Disease: The Molecular Integration in Neurological Diagnosis (MIND) Study. *J. Parkinsons Dis.* **11**, 757–765 (2021). doi: [10.3233/JPD-202406](https://doi.org/10.3233/JPD-202406); pmid: [33492247](https://pubmed.ncbi.nlm.nih.gov/33492247/)
55. K. Pigott *et al.*, Longitudinal study of normal cognition in Parkinson disease. *Neurology* **85**, 1276–1282 (2015). doi: [10.1212/WNL.0000000000002001](https://doi.org/10.1212/WNL.0000000000002001); pmid: [26362285](https://pubmed.ncbi.nlm.nih.gov/26362285/)
56. C. M. Lewis, Genetic association studies: Design, analysis and interpretation. *Brief. Bioinform.* **3**, 146–153 (2002). doi: [10.1093/bib/3.2.146](https://doi.org/10.1093/bib/3.2.146); pmid: [12139434](https://pubmed.ncbi.nlm.nih.gov/12139434/)

ACKNOWLEDGMENTS

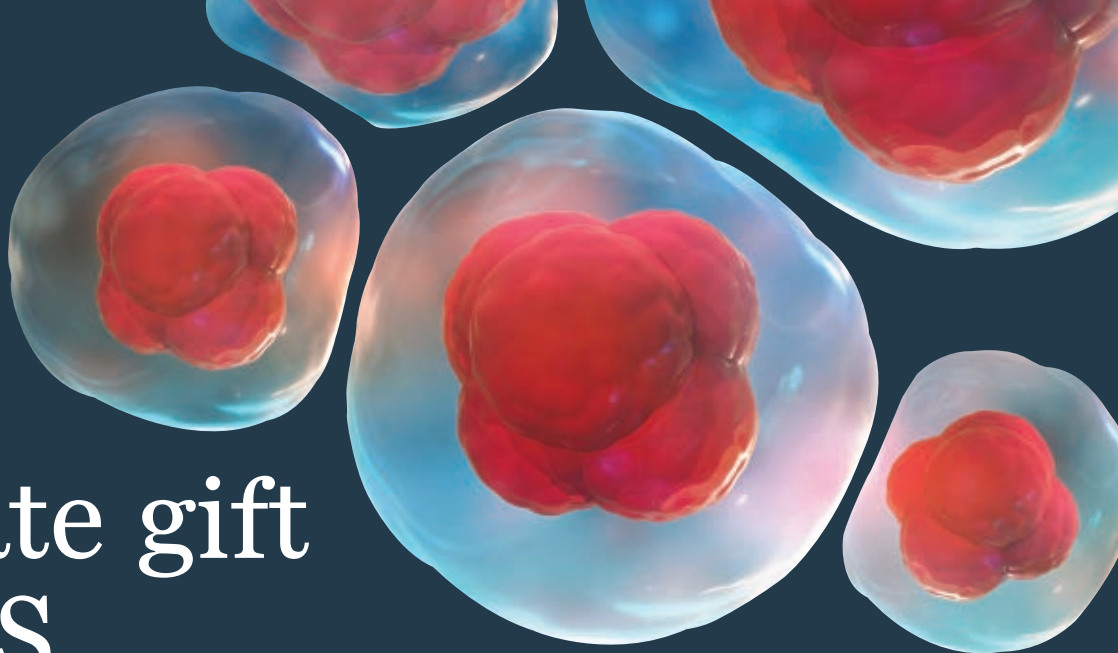
The authors thank G. Church for providing the iPSC-N cell line. We also thank the Penn Institute for Regenerative Medicine (IRM) iPSC core members (directors: W. Yang, R. Truitt, and J. McCormick) for guidance on iPSC culture and experimental design as well as the Penn Next Generation Sequencing (NGS) core members (directors: J. Schug, K. Rutherford, and O. Smirnova) for assistance in library preparation and RNA-seq services. Lastly, we thank the patients who donated their brain, blood, and CSF samples for research and J. Trojanowski for his vision in creating a neurodegenerative disease biobank that has served so many. **Funding:** This study was supported by National Institutes of Health (NIH) grant K23NS114167 (T.F.T.), NIH grant F31NS113481 (M.E.D.-O.), NIH grant R01NS115139 (A.S.C.-P.), NIH grant P30AG072979 (A.S.C.-P., E.B.L., and V.M.V.D.), NIH grants U19 AG062418 and P50 NS053488 (A.S.C.-P., D.W., and V.M.V.D.), and a Biomarkers Across Neurodegenerative Diseases (BAND) grant from the Michael J. Fox Foundation/Alzheimer's Association/Weston Institute (A.S.C.-P. and T.F.T.). A.S.C.-P. is additionally supported by the Parker Family Chair, the Chan Zuckerberg Initiative Neurodegeneration Challenge Network, and the AHA/Allen Brain Health Initiative. T.F.T. is additionally supported by the Parkinson Foundation. **Author contributions:** Conceptualization: M.E.D.-O., Y.S., and A.S.C.-P. Data curation: M.E.D.-O., Y.S., M.P., N.A., T.F.T., and D.W. Formal analysis: M.E.D.-O., Y.S., M.P., and A.S.C.-P. Methodology: M.E.D.-O., Y.S., M.C.C., M.P., N.J., M.D.G., V.M.V.D.,

K.C.L., and A.S.C.-P. Investigation: M.E.D.-O., Y.S., M.C.C., M.P., E.C., N.J., R.C., M.D.G., T.L.U., R.T.S., R.Z., R.D.-R., and E.M.B. Visualization: M.E.D.-O., Y.S., M.P., and A.S.C.-P. Resources: E.B.L., D.W., V.M.V.D., K.C.L., and A.S.C.-P. Validation: A.S.C.-P. Funding acquisition: M.E.D.-O. and A.S.C.-P. Project administration: M.E.D.-O., Y.S., and A.S.C.-P. Supervision: A.S.C.-P. Writing – original draft: M.E.D.-O., Y.S., and A.S.C.-P. Writing – review & editing: all authors. **Competing interests:** M.E.D.-O., Y.S., and A.S.C.-P. are the inventors of a provisional patent submitted by the University of Pennsylvania that relates to targeting GPNMB as a potential therapeutic in PD. T.F.T. has received consulting fees and honoraria from Sanofi Genzyme. The authors declare no other competing interests. **Data and materials availability:** All transcriptome data have been deposited in the National Center for Biotechnology Information (NCBI)'s Gene Expression Omnibus (GEO dataset GSE206327). Human data are available upon request subject to a data use agreement to ensure the maintenance of personal privacy. Requests for data or materials should be addressed to the corresponding author. **License information:** Copyright © 2022 the authors, some rights reserved; exclusive licensee American Association for the Advancement of Science. No claim to original US government works. <https://www.science.org/about/science-licenses-journal-article-reuse>

SUPPLEMENTARY MATERIALS

science.org/doi/10.1126/science.abk0637
Materials and Methods
Figs. S1 to S7
Tables S1 to S12
MDAR Reproducibility Checklist
Data S1

Submitted 4 August 2021; resubmitted 13 April 2022
Accepted 1 July 2022
[10.1126/science.abk0637](https://doi.org/10.1126/science.abk0637)



An estate gift to AAAS

Going all the way back to 1848, our founding year, the American Association for the Advancement of Science (AAAS) has been deeply committed to advancing science, engineering and innovation around the world for the benefit of all people.

Today, we are dedicated to advocating for science and scientific evidence to be fully and positively integrated into public policy and for the community to speak with one voice to advance science and engineering in the United States and around the world.

By making AAAS a beneficiary of your will, trust, retirement plan or life insurance policy, you will become a member of our 1848 Society and will help fuel our work on behalf of science and society – including publishing the world's most promising, innovative research in the *Science* family of journals and engaging in the issues that matter locally, nationally and around the world.

"As a teacher and instructor, I bear responsibility for the younger generations. If you have extra resources, concentrate them on organizations, like AAAS, that are doing work for all."

—Prof. Elisabeth Ervin-Blankenheim, 1848 Society member

If you intend to include AAAS in your estate plans, provide this information to your lawyer or financial adviser:

Legal Name: American Association for the Advancement of Science

Federal Tax ID Number: 53-0196568

Address: 1200 New York Avenue, NW, Washington, DC 20005

If you would like more information on making an estate gift to AAAS, cut out and return the form below or send an email to philanthropy@aaas.org. Additional details are also available online at www.aaas.org/1848Society.

AMERICAN ASSOCIATION FOR THE ADVANCEMENT OF SCIENCE

cut here

Yes, I would like more information about joining the AAAS 1848 Society.

PLEASE CONTACT ME AT:

Name: _____

Address: _____

City: _____ State: _____ Zip code: _____ Country: _____

Email: _____ Phone: _____

RETURN THIS FORM TO:

AAAS Office of Philanthropy and Strategic Partnerships • 1200 New York Avenue, NW • Washington, DC 20005 USA



RESEARCH ARTICLES

EVOLUTIONARY ECOLOGY

Metabolic scaling is the product of life-history optimization

Craig R. White*, Lesley A. Alton, Candice L. Bywater†, Emily J. Lombardi, Dustin J. Marshall

Organisms use energy to grow and reproduce, so the processes of energy metabolism and biological production should be tightly bound. On the basis of this tenet, we developed and tested a new theory that predicts the relationships among three fundamental aspects of life: metabolic rate, growth, and reproduction. We show that the optimization of these processes yields the observed allometries of metazoan life, particularly metabolic scaling. We conclude that metabolism, growth, and reproduction are inextricably linked; that together they determine fitness; and, in contrast to longstanding dogma, that no single component drives another. Our model predicts that anthropogenic change will cause animals to evolve decreased scaling exponents of metabolism, increased growth rates, and reduced lifetime reproductive outputs, with worrying consequences for the replenishment of future populations.

Metabolism and production (growth and reproduction) affect every aspect of biology, but attempts to understand the relationships between these processes often take very different approaches. Broadly speaking, two schools of thought are applied to understand the interplay between metabolism and biological production (usually growth): metabolic theory and life-history theory. Metabolic theories assume that the exchange or transport of wastes or nutrients across surfaces and through distribution networks constrains patterns of energy allocation to tissue synthesis (1–4). Metabolism and body size trajectories therefore emerge from these theories as a consequence of assumed physical and chemical constraints on resource acquisition or usage. Life-history theory seeks to understand ontogenetic trajectories through the lens of evolution. It assumes that total resource allocation to survival, growth, and reproduction is limited, and thus allocation to each life-history trait is constrained by trade-offs among traits that have emerged as an outcome of evolutionary selection (5, 6).

Metabolic and life-history theories each have their own strengths and weaknesses. A strength of metabolic theories is that they seek to explore the relationship between metabolism and growth from first principles and are explicit in terms of mass and energy. However, these strengths can also be a weakness if they are applied with a rigid emphasis on the role of intrinsic, absolute constraints without incorporating the capacity of these constraints

to evolve in response to selection. A strength of the life-history approach is that it focuses on the ultimate driver of biological production, evolution. An important weakness of this approach is that, for simplicity, overall rates of energy expenditure and net allocation to production are themselves assumed to be evolutionarily inert. It is increasingly clear, however, that metabolism itself is evolutionarily labile and subject to selection (7). Here, in contrast to metabolic and life-history theories, we propose that the invocation of constraints is unnecessary to explain the ontogenetic trajectories of metabolism and growth. We explore this idea by modeling how the relationships among metabolism, growth, and reproduction emerge from selection to maximize lifetime reproduction.

Our approach builds on decades of work investigating how metabolism (and its relationship to body mass), growth, and reproduction have coevolved (8–18). Our approach does not assume that life is unconstrained by physics and chemistry, but instead assumes that there is substantial (and underappreciated) opportunity for evolutionary optimization within these constraints. For example, the evolution of vascular distribution networks has allowed organisms to increase in size beyond the physical and chemical constraints imposed by the slow diffusion of respiratory gases through tissue. Similarly, the large and complex surfaces of lungs, gills, and guts demonstrate how evolution has increased the capacity for exchange of resources beyond the Euclidian geometric constraints imposed by simple surface area-to-volume relationships. Here, we apply that same logic but expand it to consider how whole-organism metabolism might coevolve with the other fundamental components of life: growth and reproduction.

A model for metabolism, growth, and reproduction

Our model is built upon an energy-expenditure budget for an animal in which the total rate of energy expenditure (E_T) is equal to the sum of the rates of energy allocation to self-maintenance (E_M), production (E_P), digestion (E_D), and activity (E_A). E_P is equal to the sum of the rates of energy allocation to growth (E_G) and reproduction (E_R). All energy expenditure values are expressed as joules per hour. The overhead costs of production continue when an animal is postprandial (i.e., no longer spending energy on digestion) (19); therefore, for an inactive postprandial animal when both E_A and E_D are zero,

$$E_T = E_M + E_P = E_M + E_G + E_R \quad (1)$$

The scaling of rates of energy expenditure (metabolic rates) with body mass (m , in grams) is usually well described by a power function $E = a_E m^{b_E}$, where a_E is the scaling coefficient and b_E is the scaling exponent, which is typically <1 for E_T and E_M (7, 13, 20, 21) and ≥ 1 for E_R (22, 23). Following Day and Taylor (24), we partitioned total production among growth and reproduction, with allocation to growth occurring early in life and growth ceasing when all of production is allocated to reproduction (e.g., Fig. 1A). Assuming that total production scales allometrically (24) with an exponent equal to $b_{E_T} = b_{E_M}$, it follows that animals allocate a fraction (f) of E_T to production [$f = (E_T - E_M)/E_T$]. Growth rate (in grams per hour) is the change in m over time (t) (dm/dt) and is dictated by E_G and a term that represents the overhead cost of tissue biosynthesis and serves to convert from units of energy to units of mass (C_m , in joules per gram). Before reproductive maturation at size M_{mat} , $E_R = 0$ and all of production is allocated to growth. Growth rate is then calculated by rearranging Eq. 1 to calculate E_G , converting E_G to the mass of tissue synthesized by dividing by C_m , and substituting scaling relationships for E_T as follows:

$$dm/dt = fE_T/C_m = fa_{E_T}m^{b_{E_T}}/C_m \quad (2)$$

After maturation, production is divided among growth and reproduction, and growth rate can be calculated by rearranging Eq. 1 to calculate E_G (i.e., subtracting E_R from f of E_T allocated to E_P) and substituting scaling relationships for both E_T and E_R

$$\begin{aligned} dm/dt &= [fE_T - E_R]/C_m \\ &= [fa_{E_T}m^{b_{E_T}} - a_{E_R}m^{b_{E_R}}]/C_m \quad (3) \end{aligned}$$

Growth ceases at maximum mass (M , in grams), when all of production is allocated to reproduction (i.e., $fa_{E_T}M^{b_{E_T}} = a_{E_R}M^{b_{E_R}}$), so a_{E_R} can be estimated from f , a_{E_T} , b_{E_T} , b_{E_R} ,

School of Biological Sciences and Centre for Geometric Biology, Monash University, Clayton 3800, Victoria, Australia.

*Corresponding author. Email: craig.white@monash.edu

†Present address: School of Biological Sciences, The University of Queensland, Brisbane 4072, Queensland, Australia.

ONTOGENETIC TRAJECTORIES OF SIZE (GROWTH), REPRODUCTION, AND METABOLISM:

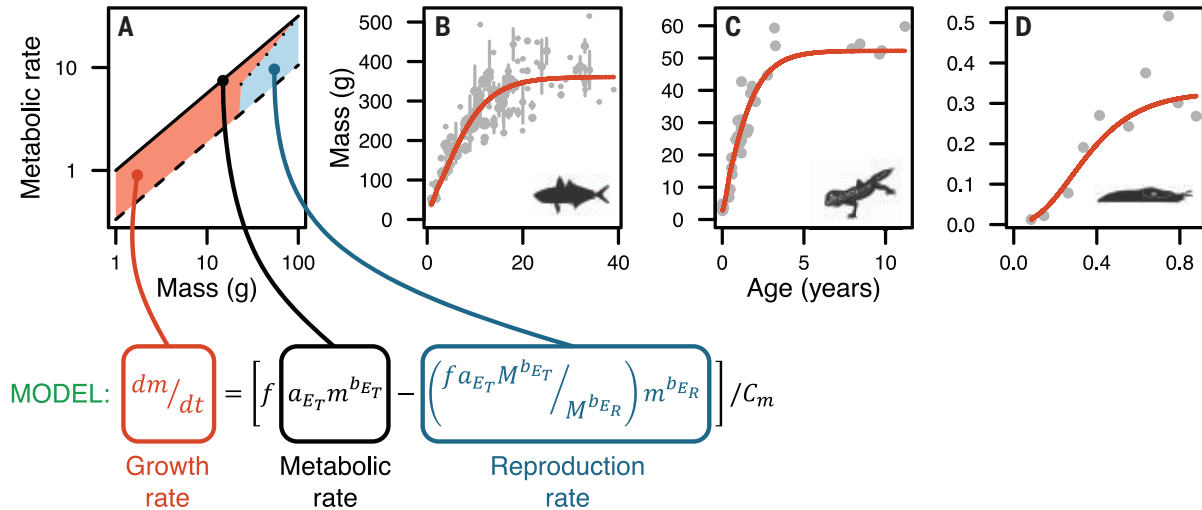


Fig. 1. Division of energy between growth and reproduction yields ontogenetic growth trajectories. (A) Size-dependent allocation of energy to production (E_P), which is partitioned among growth (E_G) and reproduction (E_R) and is equal to the difference between total metabolic rate (E_T , solid line) and maintenance metabolic rate (E_M , dashed line). E_R is represented by the

blue shaded area bounded by the dotted and dashed lines, and E_G is represented by the red shaded area. (B to D) Example fits of the growth model to mass-for-age data for Atlantic horse mackerel (B), leopard geckos (C), and gray field slugs (D) (25). Error bars in (B) are standard errors for the mean mass of animals of identical age.

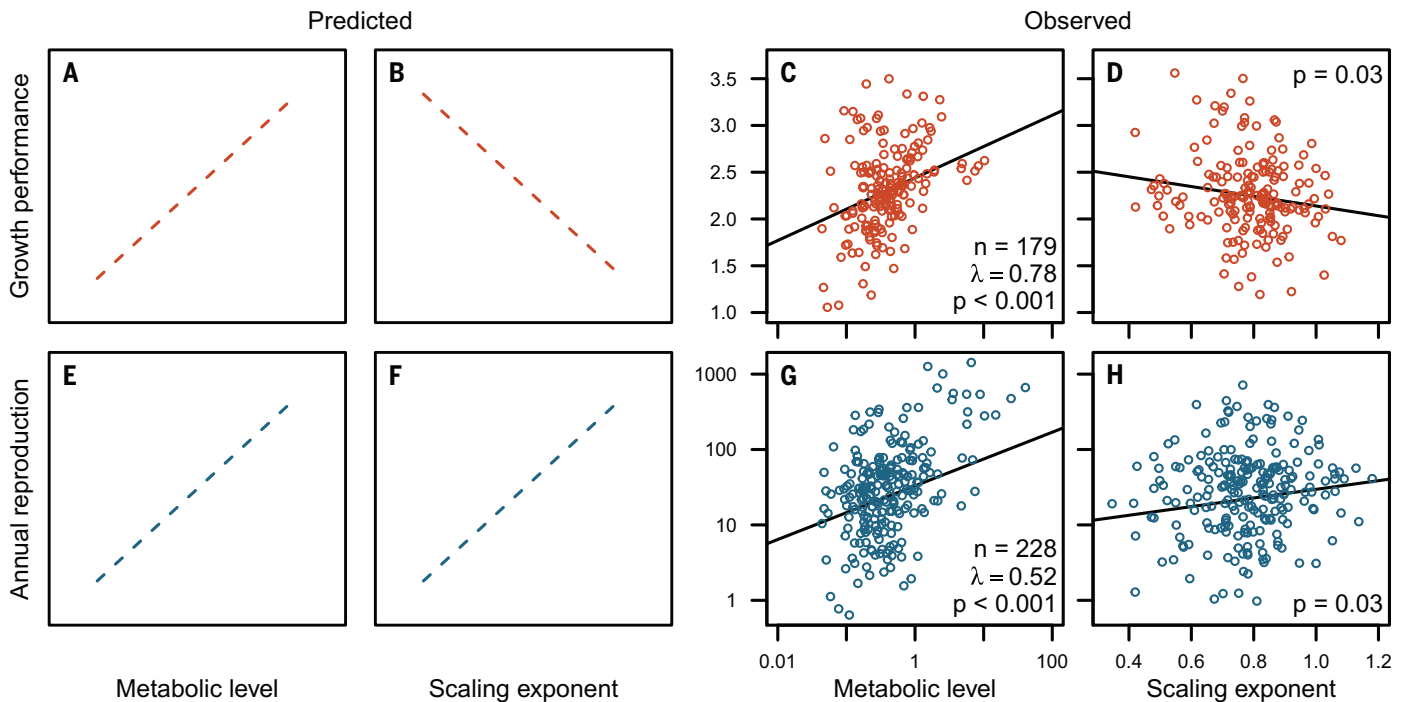


Fig. 2. Life history covaries with metabolic scaling. Predicted and observed effects of metabolic level and the metabolic scaling exponent on growth performance (A to D) and annual reproduction (E to H). Metabolic level (a , in milliliters of oxygen per hour) and the metabolic scaling exponent (b) are estimated from the scaling of metabolic rate (E) with mass (m) where $E = am^b$. Dashed lines in (A), (B), (E), and (F) depict the directionality of predictions derived from the model described in the text (see fig. S1 for further details).

Solid lines in (C), (D), (G), and (H) are empirical relationships estimated from phylogenetic generalized least-squares models including mass and temperature as covariates (tables S1 and S2). Points are shown adjusted for the effects of all other predictors in the model. Phylogenetic heritability (λ) was significantly greater than zero, and the effect of metabolic level and the metabolic scaling exponent was significant for all models (P values are shown in the relevant panel, along with sample size, n).

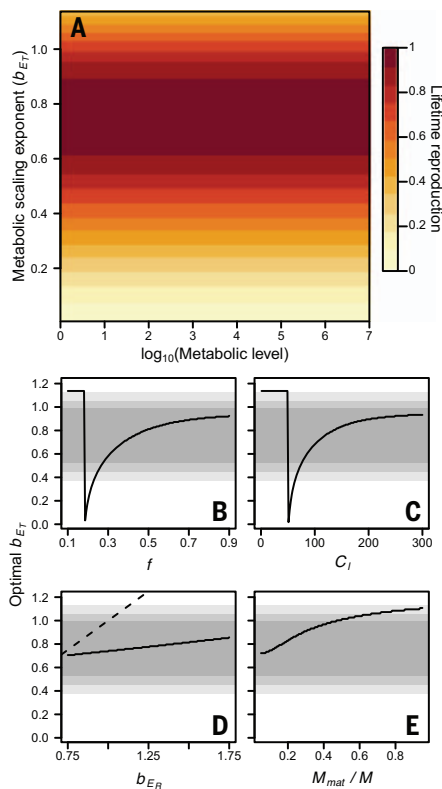


Fig. 3. Allometric scaling of metabolic rate maximizes lifetime reproduction. (A) Predicted effects of metabolic level (a_{E_T} , in arbitrary units) and the metabolic scaling exponent (b_{E_T}) on lifetime reproduction (scaled from 0 to 1), where metabolic rate scales with mass (m) as $a_{E_T} m^{b_{E_T}}$. (B) to (E) Sensitivity of the optimal value of b_{E_T} (the value that maximizes lifetime reproduction) to variation in key parameters describing growth and reproduction over the life of a hypothetical organism, including: f , the fraction of total metabolism that is allocated to production (growth and reproduction) (B); C_l , a constant linking a_{E_T} with life span (C); b_{E_R} , the scaling exponent of reproductive output (D); and M_{mat}/M , the ratio of mass at maturity to maximum mass (E). Shaded areas in (B) to (E) represent percentile ranges of the empirical distribution of b_{E_T} (Fig. 4), with the darkest shade bounding the 10th and 90th percentiles, the intermediate shade bounding the 5th and 95th percentiles, and the lightest shade bounding the 2.5th and 97.5th percentiles. The dashed line in (D) is the line of unity where $b_{E_T} = b_{E_R}$.

and M by rearrangement. By substituting $a_{E_R} = f a_{E_T} M^{b_{E_T}} / M^{b_{E_R}}$ into Eq. 3 and rearranging, growth rate can be estimated as follows:

$$\frac{dm}{dt} = \frac{f}{C_m} a_{E_T} \left[m^{b_{E_T}} - M^{b_{E_T}} \left(\frac{m}{M} \right)^{b_{E_R}} \right] \quad (4)$$

The integral of Eq. 4 yields a growth trajectory but has no closed-form solution and so must

be solved by numerical approximation (e.g., Fig. 1, B to D). Our approach is philosophically similar to that of Day and Taylor (24) (e.g., their equation 10) but differs in that we do not fix the scaling exponent of production. Instead, we assume that production is proportional to metabolic rate and set the scaling exponent of production equal to the scaling exponent of metabolic rate. We formulated Eq. 4 using a scaling relationship for reproduction so that it can be easily parameterized using empirical data (e.g., 22). We note that although the model is formulated for animals that exhibit indeterminate growth, it can also accommodate determinate growth. Determinate growth occurs if animals allocate all of production to reproduction immediately upon reaching maturity (in model terms, determinate growth can arise if the scaling exponents of metabolism and reproduction are equal, or if size at maturity is equal to M).

Conditions that optimize life history

To explore the relationships among metabolic scaling parameters (a_{E_T} and b_{E_T}), growth, and reproduction statistically, it is necessary to derive an estimate of a_{E_T} that is not correlated with b_{E_T} . To do so, we define metabolic level (L) as the metabolic rate estimated at a common mass (m') that results in a correlation of 0 between $\log_{10} L$ and b ($L = a_{E_T} m'^{b_{E_T}}$) (25). Defined in this way, L represents a mass-independent estimate of the elevation of the metabolic scaling relationship (i.e., animals with a high L have a high E_T at m'), and b_{E_T} represents the slope of the relationship between $\log_{10} E_T$ and $\log_{10} m$. If the assumptions stated above hold, then Eq. 4 makes four testable predictions, which are illustrated in Fig. 2 and further elaborated in fig. S1: (i) For a given metabolic scaling exponent b_{E_T} , growth will be positively correlated with metabolic level L (Fig. 2A); i.e., animals with a higher metabolic level grow faster [e.g., (17, 26, 27, 28)]. (ii) For a given L , growth will be negatively correlated with b_{E_T} (Fig. 2B); i.e., animals with shallower metabolic scaling relationships allocate more energy to production early in life and therefore grow faster. (iii) For a given b_{E_T} , maximum energy allocation to reproduction, $E_{R_{max}}$ ($=E_R$ when $m = M$), will be positively correlated with L (Fig. 2E); i.e., animals with a higher metabolic level allocate more energy to reproduction [e.g., (29, 30)]. (iv) For a given L , $E_{R_{max}}$ will be positively correlated with b_{E_T} (Fig. 2F); i.e., animals that have steeper metabolic scaling relationships allocate more energy to production later in life and therefore have higher maximum reproduction.

To test these four predictions, we compiled intraspecific metabolic scaling and life-history data from the literature and analyzed them in a phylogenetic generalized least-squares framework (25). The dataset includes new compila-

tions of ontogenetic scaling relationships expressed as a function of live mass or wet mass, growth trajectories, annual reproduction, and longevity (31). We restricted our compilation of growth data to animals that grow after maturation and show growth patterns that are reasonably well approximated by the von Bertalanffy growth equation. We calculated growth performance, a size-independent estimate of growth rate, as Pauly's (2) growth performance index (ϕ) from estimates of maximum length (L_∞) and the growth constant (k) derived from fits of von Bertalanffy growth curves to length-at-age data using the equation $\phi = \log_{10} k + 2 \log_{10} L_\infty$. Life histories for each species were characterized by mean growth performance, mean annual reproduction, and maximum longevity.

The patterns in the data match all four predictions from Eq. 4: Life histories have been optimized such that growth performance and reproduction both increase with metabolic level (predictions 1 and 3, Fig. 2, C and G), growth performance decreases with the metabolic scaling exponent (prediction 2, Fig. 2D), and reproduction increases with the metabolic scaling exponent (prediction 4, Fig. 2H). The data also show that longevity decreases with metabolic level (fig. S2A), in keeping with the predictions of both metabolic theory (1, 10) and life-history theory (11, 32). Longevity is not related to the metabolic scaling exponent (fig. S2B).

Life-history optimization yields allometric scaling of metabolism

After validating the predictions of our growth model, we next explored the effects of metabolic level and the metabolic scaling exponent to determine whether any combination of these parameters maximizes lifetime reproduction. To do this, we used Eqs. 3 and 4 to generate growth trajectories and estimated lifetime reproduction from the time dependence of m and the scaling of E_R with m for values of m greater than M_{mat}

$$E_R = [f a_{E_T} M^{b_{E_T}} / M^{b_{E_R}}] m^{b_{E_R}} \quad (5)$$

We used a numerical model to estimate growth and reproduction through 1 million time steps from birth to maximum longevity (25). As a first approximation, we modeled animals growing from a starting mass of $m = 1$ to $M = 100$ and assumed that $b_{E_R} = 1.137$ (22, 23) and $f = 0.43$ (33). This estimate of f derived from growth data is broadly consistent with estimates of the energetic cost of egg biomass production in female animals [$\sim 50\%$ of basal metabolic rate (34)]. The cost of gamete production is lower for males than females (34), but costs associated with mating effort can be higher [e.g., (35)], and the overall costs associated with reproduction can be similar for males

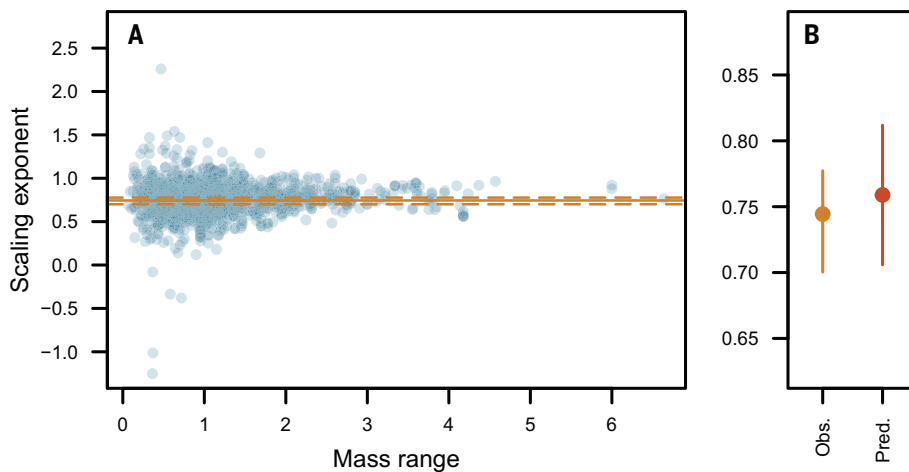


Fig. 4. Metabolic rate scales allometrically with body mass. (A) Funnel plot showing the relationship between the intraspecific scaling exponent of metabolic rate and mass range (orders of magnitude) over which the scaling exponent was estimated for scaling exponents estimated from the relationship between metabolic rate and live or wet body mass. The horizontal solid line is the mean of all values (0.743 ± 0.017) estimated in an intercept-only linear mixed model with random intercept terms for species identity and taxonomic group. Dashed lines are the 95% profile likelihood confidence interval (95% CI) for the mean (0.699, 0.777). (B) Mean observed scaling exponent (shown \pm 95% CI) from the empirical distribution in (A) compared with a scaling exponent predicted to maximize reproduction (Fig. 3A) based on a set of assumptions regarding energy allocation to production, the size dependence of reproduction, size at maturity, and longevity, as described in the text. Plastic or evolutionary changes in energy allocation to production, the size dependence of reproduction, size at maturity, or longevity will yield changes in the scaling exponent predicted to maximize lifetime reproduction (Fig. 3, B to E). The error bars associated with the predicted scaling exponent show the range of values over which lifetime reproduction is >99% of maximum.

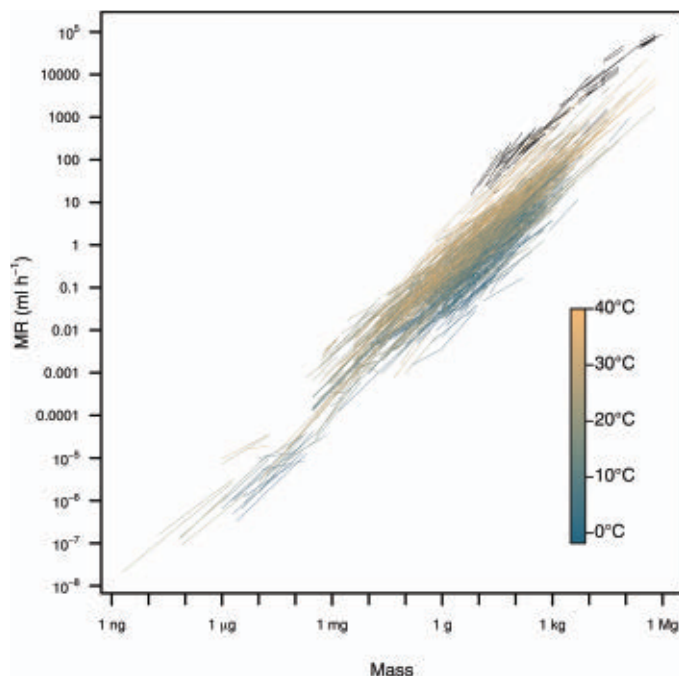


Fig. 5. Scaling of metabolic rate (MR) with body mass. Black lines depict intraspecific scaling relationships for endotherms (birds and mammals). Colored lines depict intraspecific scaling relationships for ectotherms (fishes, amphibians, reptiles, and invertebrates), which are colored by measurement temperature from 1.8° to 40°C.

and females [e.g., (36)]. We assumed that $M_{\text{mat}} = 0.223 M$ on the basis of data for fish showing that the mean length at maturity is equal to 0.61 of maximum length (37) and assuming that, on average, mass is proportional to length cubed. Finally, we assumed that life span is proportional to a constant (C_l) divided by a_{E_T} and first report the results of these analyses with C_l set to an arbitrary value of 120. The value of $C_l = 120$ was selected because, in combination with the other parameters drawn from data ($b_{E_R} = 1.137$, $f = 0.43$, $M_{\text{mat}} = 0.223 M$), this value yields an optimal value of the metabolic scaling exponent (b_{E_T}) that is broadly consistent with the mean value observed in the data (Figs. 3 and 4). We then used sensitivity analyses to explore how variations in the values of b_{E_R} , f , M_{mat} , and C_l alter the optimal value of b_{E_T} .

The model predicts that lifetime reproduction varies with the metabolic scaling exponent b_{E_T} but not with the metabolic level L . Lifetime reproduction is independent of metabolic level over a wide range (Fig. 3A) that far exceeds the approximately three orders of magnitude range of metabolic level observed at any given body mass in the dataset (Fig. 5). Other factors that are not included in our model probably set the upper and lower limits of metabolism at any given size. Such limits may be imposed by resource availability in the environment mediated by minimum viable population sizes (38) or by constraints on the capacity of organisms to ingest and process resources or expend energy (39).

A key outcome of our study is that the predicted metabolic scaling exponent that maximizes lifetime reproduction is almost always allometric and falls within the range of observed data (Fig. 3; 90% of the observed scaling exponents are <1 ; Fig. 4A). Our initial parameter estimates for b_{E_R} , f , and M_{mat} were drawn from published data, but the value of C_l was selected to yield an estimate of the optimal scaling exponent of metabolic rate b_{E_T} that closely matches the mean scaling exponent of metabolic rate from the literature compilation, which is $\sim 3/4$ (Fig. 4). However, the model does not predict a universally optimal b_{E_T} , but instead predicts that the value of b_{E_T} that maximizes lifetime reproduction depends on the values of f (Fig. 3B), C_l (Fig. 3C), b_{E_R} (Fig. 3D), and M_{mat} (Fig. 3E). The model therefore predicts that evolutionary or plastic changes in energy allocation to production, the size dependence of reproduction, the size at maturity, or the relationship between longevity and metabolism (and thereby production) will yield changes in the scaling of metabolic rate. This is consistent with empirical studies showing that the scaling exponent of metabolic rate varies in response to a wide range of biotic and abiotic variables [e.g., (12, 13, 20, 21)].

Our finding that allometric metabolic scaling emerges from the optimization of growth and reproduction within a finite life span to maximize lifetime reproduction offers a potential solution to one of the most enduring controversies in biology (20, 27). Metabolic theories have usually proposed explanations for the allometric scaling of metabolic rate on the basis of the assumption that allometry arises as a consequence of physical geometric constraints, such as those that are imposed by the geometry of resource distribution networks (3), the need to dissipate heat produced as a by-product of metabolism (18, 39, 40), and surface area-to-volume constraints on the fluxes of nutrients or wastes (1, 18). Others have countered that variation in metabolic allometry arises as a consequence of selection rather than constraint [e.g., (7, 9, 12, 15, 18, 21, 41–43)]. Our model and data support the latter view, that allometric scaling of metabolic rate is predicted to arise if selection optimizes growth and reproduction to maximize lifetime reproduction (Fig. 4). Metabolic allometry can therefore be explained without the need to invoke any of the assumed constraints traditionally imposed by metabolic theories [e.g., (1, 4, 18, 39, 40)].

Allometries are characteristic of life and are observed at the level of enzymes, mitochondria, cells, whole organisms, populations, and ecosystems (44–48). Kozłowski and colleagues have shown how intraspecific allometries, such as those predicted by our model, yield among-species metabolic scaling patterns that are also allometric (9, 41, 42). Thus, taken together, the work of Kozłowski and colleagues and our study offer a mathematically explicit explanation for biological allometries at multiple scales of organization. Intraspecific metabolic allometries arise as a consequence of evolutionary optimization of growth and reproduction (Fig. 3), and interspecific metabolic allometries arise as a consequence of evolutionary optimization of body size and metabolic rate [e.g., (9, 41, 42)]. We therefore suggest that the allometric scaling of metabolic rate arises not because it is inevitable but rather because it is advantageous.

Implications for life histories in the Anthropocene

Elevated extrinsic mortality is a signature of the Anthropocene (49). The framework that we provide here not only offers new insight into the origin of biological allometries but also gives us the opportunity to explore and predict how metabolism, growth, and reproduction will respond to future changes in the environment (25). Our model predicts that organisms living in a future environment with a 10% increase in mortality (an arbitrary but realistic figure) are predicted to have substantially re-

duced lifetime reproductive output (~36%) and to evolve lower metabolic scaling exponents (decreased from 0.76 to 0.73) that are associated with more rapid growth and earlier maturation (~1.5%). The substantial decrease in reproduction predicted by the model, and the consequences of this for population replenishment, is particularly concerning.

Conclusion

Our findings suggest that metabolism, growth, and reproduction have coevolved to maximize fitness (i.e., lifetime reproduction) and that the observed patterns in these fundamental characteristics of life can be explained by optimization rather than constraint. We offer this as an alternative way of viewing the origin of biological allometries at all scales, recognizing that it represents a profound departure from classic thinking. Our viewpoint is analogous to the concept of the Hutchinsonian niche (50): Constraints define the range within which life is possible (analogous to the fundamental niche), whereas optimization yields the (smaller) range of possibilities exploited by life (analogous to the realized niche). We reiterate that this viewpoint does not deny the existence of biophysical constraints and does not call forth Darwinian demons (hypothetical organisms that maximize all aspects of fitness simultaneously and would exist if there were no constraints on evolution). Rather, our approach expands the phenotypic space in which evolutionary optimization operates and avoids giving primacy of causation to any single pillar of multicellular life. It also emphasizes that the pillars of metabolism, growth, and reproduction have coevolved to shape each other, and, consequently, observed life-history strategies emerge from the optimization of these to maximize lifetime reproduction within a finite life span (8, 9, 15, 41, 42). Within this multivariate optimization dwells the great diversity of life histories in nature.

REFERENCES AND NOTES

1. S. A. L. M. Kooijman, *Dynamic Energy Budget Theory for Metabolic Organisation* (Cambridge Univ. Press, ed. 3, 2010).
2. D. Pauly, "Gill size and temperature as governing factors in fish growth: A generalization of von Bertalanffy's growth formula" (Institut für Meereskunde, 1979); <https://agris.fao.org/agris-search/search.do?recordID=AV2012092482>.
3. G. B. West, J. H. Brown, B. J. Enquist, *Nature* **413**, 628–631 (2001).
4. M. R. Kearney, *Biol. Rev. Camb. Philos. Soc.* **96**, 557–575 (2021).
5. A. J. Zera, L. G. Harshman, *Annu. Rev. Ecol. Syst.* **32**, 95–126 (2001).
6. S. C. Stearns, *Funct. Ecol.* **3**, 259 (1989).
7. C. R. White *et al.*, *Nat. Ecol. Evol.* **3**, 598–603 (2019).
8. R. H. Peters, *Cambridge Studies in Ecology: The Ecological Implications of Body Size* (Cambridge Univ. Press, 1986).
9. J. Kozłowski, J. Weiner, *Am. Nat.* **149**, 352–380 (1997).
10. J. H. Brown, J. F. Gillooly, A. P. Allen, V. M. Savage, G. B. West, *Ecology* **85**, 1771–1789 (2004).
11. J. R. Speakman, *J. Exp. Biol.* **208**, 1717–1730 (2005).
12. D. S. Glazier *et al.*, *Ecol. Monogr.* **81**, 599–618 (2011).

13. S. S. Killen, D. Atkinson, D. S. Glazier, *Ecol. Lett.* **13**, 184–193 (2010).
14. I. A. Hattton, A. P. Dobson, D. Storch, E. D. Galbraith, M. Loreau, *Proc. Natl. Acad. Sci. U.S.A.* **116**, 21616–21622 (2019).
15. D. S. Glazier, *Biol. Rev. Camb. Philos. Soc.* **90**, 377–407 (2015).
16. D. S. Glazier, *Systems* **2**, 451 (2014).
17. S. Wong, J. S. Bigman, N. K. Dulvy, *Proc. Biol. Sci.* **288**, 20210910 (2021).
18. D. S. Glazier, *Biol. Rev. Camb. Philos. Soc.* **85**, 111–138 (2010).
19. J. Rosenfeld, T. Van Leeuwen, J. Richards, D. Allen, *J. Anim. Ecol.* **84**, 4–20 (2015).
20. C. R. White, M. R. Kearney, *Compr. Physiol.* **4**, 231–256 (2014).
21. D. S. Glazier, *Biol. Rev. Camb. Philos. Soc.* **80**, 611–662 (2005).
22. D. R. Barneche, D. R. Robertson, C. R. White, D. J. Marshall, *Science* **360**, 642–645 (2018).
23. D. J. Marshall, C. R. White, *Trends Ecol. Evol.* **34**, 102–111 (2019).
24. T. Day, P. D. Taylor, *Am. Nat.* **149**, 381–393 (1997).
25. Materials and methods are available online in the supplementary materials.
26. T. J. Case, *Q. Rev. Biol.* **53**, 243–282 (1978).
27. R. Ton, T. E. Martin, *Funct. Ecol.* **30**, 743–748 (2016).
28. J. M. Grady, B. J. Enquist, E. Dettweiler-Robinson, N. A. Wright, F. A. Smith, *Science* **344**, 1268–1272 (2014).
29. B. K. McNab, *Physiological Ecology of Vertebrates* (Comstock Cornell, 2002).
30. D. S. Glazier, *Comp. Biochem. Physiol. A Comp. Physiol.* **80**, 587–590 (1985).
31. C. R. White, L. A. Alton, C. L. Bywater, E. J. Lombardi, D. J. Marshall, Metabolic scaling, growth, and reproduction data for animals for: Metabolic scaling is the product of life-history optimization, *Zenodo* (2022); <https://doi.org/10.5281/zenodo.6782436>.
32. R. E. Ricklefs, M. Wikelski, *Trends Ecol. Evol.* **17**, 462–468 (2002).
33. P. Rombough, in *Comparative Developmental Physiology: Contributions, Tools, and Trends*, S. J. Warburton, W. W. Burggren, B. Pelster, C. L. Reiber, J. Spicer, Eds. (Oxford Univ. Press, 2006), pp. 99–123.
34. A. Hayward, J. F. Gillooly, *PLOS ONE* **6**, e16557 (2011).
35. M. J. Chung, M. D. Jennions, R. J. Fox, *Evol. Lett.* **5**, 315–327 (2021).
36. J. E. Lane, S. Boutin, J. R. Speakman, M. M. Humphries, *J. Anim. Ecol.* **79**, 27–34 (2010).
37. A. C. Tsklikiras, K. I. Stergiou, *Rev. Fish Biol. Fish.* **24**, 219–268 (2014).
38. R. Lande, *Am. Nat.* **142**, 911–927 (1993).
39. J. R. Speakman, E. Król, *J. Anim. Ecol.* **79**, 726–746 (2010).
40. R. Sarrus, N. Rameaux, *Méd.* **3**, 1094 (1839).
41. J. Kozłowski, M. Konarzewski, A. T. Gawelczyk, in *Macroecology: Concepts and Consequences*, T. M. Blackburn, K. J. Gaston, Eds. (Blackwell Science, 2003), pp. 299–320.
42. J. Kozłowski, M. Konarzewski, M. Czarnoleski, *Biol. Rev. Camb. Philos. Soc.* **95**, 1393–1417 (2020).
43. P. A. C. L. Pequeno, F. B. Baccaro, J. L. P. Souza, E. Franklin, *Ecol. Entomol.* **42**, 115–124 (2017).
44. G. N. Somero, J. J. Childress, *J. Exp. Biol.* **149**, 319–333 (1990).
45. J. Damuth, *Biol. J. Linn. Soc. Lond.* **31**, 193–246 (1987).
46. V. M. Savage, J. F. Gillooly, J. H. Brown, E. L. Charnov, *Am. Nat.* **163**, 429–441 (2004).
47. A. P. Allen, J. F. Gillooly, J. H. Brown, *Funct. Ecol.* **19**, 202–213 (2005).
48. G. B. West, W. H. Woodruff, J. H. Brown, *Proc. Natl. Acad. Sci. U.S.A.* **99** (suppl. 1), 2473–2478 (2002).
49. S. P. Otto, *Proc. Biol. Sci.* **285**, 20182047 (2018).
50. G. E. Hutchinson, *Cold Spring Harb. Symp. Quant. Biol.* **22**, 415–427 (1957).

ACKNOWLEDGMENTS

C.R.W. is grateful for more than 20 years of discussions on the topic of biological allometry with R. Seymour, who provided comments on an earlier version of this manuscript. We also acknowledge J. Kozłowski's essential role in shaping our thinking on this topic. **Funding:** This work was supported by the Australian Research Council (grants DP180103925 and DP220103553).

Author contributions: Conceptualization: C.R.W., D.J.M.; Formal analysis: C.R.W.; Funding acquisition: C.R.W., L.A.A.; Investigation: C.R.W., L.A.A., C.L.B., E.J.L.; Methodology: C.R.W., D.J.M.;

Writing – original draft: C.R.W., L.A.A., D.J.M.; Writing – review & editing: C.R.W., L.A.A., C.L.B., E.J.L., D.J.M. **Competing interests:** The authors declare no competing interests. **Data and materials availability:** The data needed to reproduce the results described in this study are hosted at Zenodo (31). **License information:** Copyright © 2022 the authors, some rights reserved; exclusive licensee American Association for the Advancement of

Science. No claim to original US government works. <https://www.science.org/about/science-licenses-journal-article-reuse>

SUPPLEMENTARY MATERIALS

science.org/doi/10.1126/science.abm7649
Materials and Methods
Figs. S1 and S2

Tables S1 to S3
References (51–73)
MDAR Reproducibility Checklist

Submitted 10 October 2021; resubmitted 16 March 2022
Accepted 8 July 2022
[10.1126/science.abm7649](https://doi.org/10.1126/science.abm7649)

DEFLUORINATION

Low-temperature mineralization of perfluorocarboxylic acids

Brittany Trang^{1†}, Yuli Li^{2,3†}, Xiao-Song Xue⁴, Mohamed Ateia^{1†}, K. N. Houk^{3*}, William R. Dichtel^{1*}

Per- and polyfluoroalkyl substances (PFAS) are persistent, bioaccumulative pollutants found in water resources at concentrations harmful to human health. Whereas current PFAS destruction strategies use nonselective destruction mechanisms, we found that perfluoroalkyl carboxylic acids (PFCAs) could be mineralized through a sodium hydroxide-mediated defluorination pathway. PFCA decarboxylation in polar aprotic solvents produced reactive perfluoroalkyl ion intermediates that degraded to fluoride ions (78 to ~100%) within 24 hours. The carbon-containing intermediates and products were inconsistent with off-proposed one-carbon-chain shortening mechanisms, and we instead computationally identified pathways consistent with many experiments. Degradation was also observed for branched perfluoroalkyl ether carboxylic acids and might be extended to degrade other PFAS classes as methods to activate their polar headgroups are identified.

Per- and polyfluoroalkyl substances (PFAS) are anthropogenic substances containing multiple C–F bonds. PFAS are used as omniphobic surfactants in many industrial processes and products, including in poly(tetrafluoroethylene) production; as water-, oil-, and stain-resistant barriers for fabrics and food service containers; and as components of aqueous film-forming foams for fire suppression (1). As a result of their widespread global use, environmental persistence, and bioaccumulation, PFAS contamination is pervasive (2) and affects drinking water, surface waters, livestock, and agricultural products around the world (3). This persistent environmental contamination is alarming because chronic exposure to even low levels of these compounds is associated with negative health effects such as thyroid disease, liver damage, high cholesterol, reduced immune responses, low birth weights, and several cancers (4). Many of these effects have been ob-

scured by PFAS manufacturers for decades (5). The growing focus on removing parts-per-billion to parts-per-trillion levels of PFAS contamination from drinking water supplies has produced several PFAS-removal approaches, including established adsorbents such as activated carbon and ion-exchange resins, as well as emerging materials such as cross-linked polymers (6, 7). Adsorbents or membrane-based separation processes create PFAS-contaminated solid or liquid waste streams but do not address how to degrade these persistent pollutants. PFAS destruction is a daunting task because the strong C–F bonds that give PFAS their desirable properties also make these compounds resistant to end-of-life degradation. Harsh PFAS degradation methods include incineration (8), ultrasonication (9, 10), plasma-based oxidation (11), electrochemical degradation (12, 13), supercritical water oxidation (14), ultraviolet-initiated degradation using additives such as sulfite or iron (15–19), and other combinations of chemical and energy inputs (20) (table S1). Leveraging the reactivity of perfluoroalkyl species might, however, offer milder alternatives to address the PFAS contamination problem.

The opportunity to degrade PFAS at high concentrations in nonaqueous solvents has recently been developed using PFAS adsorbents that can be regenerated using a simple solvent wash. This development enables the destruction of these compounds after they have been removed from water resources, which broadens suitable degradation conditions beyond dilute

aqueous environments. Here, we accessed reactive perfluoroalkyl anions that are mineralized under mild conditions by decarboxylating perfluorocarboxylic acids (PFCAs), one of the largest classes of PFAS compounds, at low temperatures in dipolar aprotic solvents (Fig. 1). PFCAs of various chain lengths undergo efficient mineralization in the presence of NaOH in mixtures of water and dimethyl sulfoxide (DMSO) at mild temperatures (80 to 120°C) and ambient pressure. Under these conditions, perfluorooctanoic acid (PFOA, 1) is completely degraded with >90% defluorination and minimal formation of fluorocarbon by-products. Experimental observations and density functional theory (DFT) calculations offer strong evidence for degradation pathways distinct from the single-carbon-chain shortening processes proposed in prior PFAS degradation studies (11, 16, 18, 21–23). This reactivity mode is immediately promising for PFCA destruction and may prove generalizable to other PFAS classes as methods to activate their polar groups are identified.

Decarboxylation and defluorination of PFCAs in polar aprotic solvent

Perfluoroalkylcarbanions are easily accessed by decarboxylating PFCAs in dipolar aprotic solvents. In a solution of DMSO and H₂O (8:1 v/v) at 120°C, PFOA decarboxylates to form perfluoro-1H-heptane 2, which phase separates from solution as an oil. ¹H, ¹³C, and ¹⁹F nuclear magnetic resonance (NMR) spectroscopy of the isolated oil confirmed the formation of the decarboxylated product in high purity (figs. S1 to S4). This decarboxylation reaction is consistent with those reported by Kong *et al.*, who found that most carboxylic acids decarboxylate reversibly in dimethylformamide (24). Zhou *et al.* (25) studied the origins of this reversible carboxylation computationally and determined that the lower barrier to decarboxylation was fully induced by solvent effects from the polar aprotic solvent (figs. S45 and S58). Such reactivity has also been observed as a complication for analytical standards (26, 27). We found that when the same PFOA solution in DMSO/H₂O was subjected to the decarboxylation conditions but in the presence of NaOH (30 equiv), PFOA instead degraded to a mixture of fluoride, trifluoroacetate ions, and carbon-containing by-products (Fig. 2A). Degradation also occurred in other polar aprotic solvents such as dimethylacetamide and sulfolane but

¹Department of Chemistry, Northwestern University, Evanston, IL 60208, USA. ²Department of Chemistry, School of Science, Tianjin University, Tianjin 300354, China.

³Department of Chemistry and Biochemistry, University of California, Los Angeles, Los Angeles, CA 90095, USA. ⁴Key Laboratory of Organofluorine Chemistry, Shanghai Institute of Organic Chemistry, University of Chinese Academy of Sciences, Chinese Academy of Sciences, Shanghai 200032, P.R. China.

*Corresponding author. Email: houk@chem.ucla.edu (K.N.H.); wdichtel@northwestern.edu (W.R.D.)

†These authors contributed equally to this work.

‡Present address: Center for Environmental Solutions & Emergency Response, US Environmental Protection Agency, Cincinnati, OH, USA.

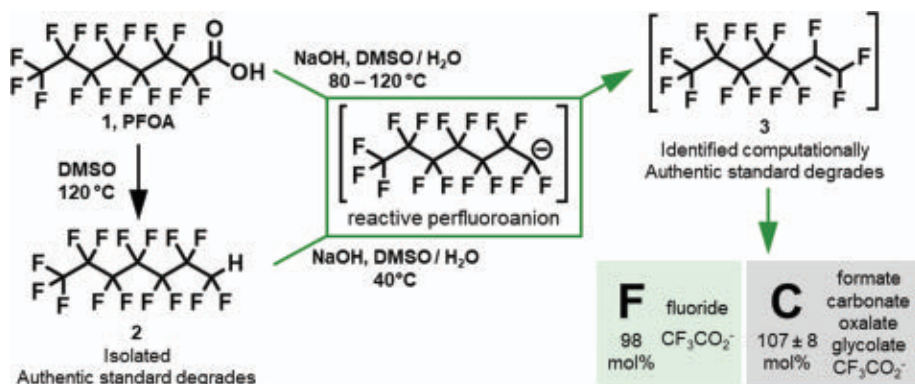


Fig. 1. Overview of degradation pathways identified in this study. Heating PFCAs in polar aprotic solvents such as DMSO decarboxylates them to 1H-perfluoroalkanes. When this reaction was performed in the presence of NaOH, the PFCa mineralized to fluoride, sodium trifluoroacetate, and nonfluorinated carbon-containing products. The 1H-perfluoroalkane underwent the same degradation process at even lower temperatures. Computational studies identified the corresponding perfluoroalkenes as likely intermediates, and an authentic standard of the seven-carbon perfluoroalkene was competent for the degradation.

did not proceed in pure water (fig. S20 and table S3). ¹⁹F NMR spectroscopy of reaction aliquots collected over 24 hours indicated that resonances corresponding to PFOA were no longer detectable within 14 hours. Unexpectedly, no resonances corresponding to perfluoroalkyl groups containing between four and seven carbons were observed. Resonances corresponding to sodium perfluoropropionate (CF₃CF₂CO₂Na) at -81.5 and -118.2 ppm were observed just above the baseline within spectra of aliquots collected at reaction times shorter than 24 hours but were absent in spectra of later aliquots (fig. S10). The only prominent fluorine resonance in the aliquot sampled at 24 hours corresponds to sodium trifluoroacetate (CF₃CO₂Na, -73.6 ppm; Fig. 2B). Integration of this resonance indicated that its intensity plateaued at ~4 to 24 hours, corresponding to only 7% of the F content and 9% of the C content relative to the initial PFOA concentration (Fig. 2, A and C). The resonance from CF₃CO₂Na ions eventually decreased in intensity and presumably degraded into fluoride, albeit much more slowly than the rate of PFOA disappearance (Fig. 2C, inset). This resonance disappeared over 300 hours, which we confirmed by subjecting an authentic sample of sodium trifluoroacetate to the same reaction conditions (fig. S24). PFOA degradation is thus rapid and forms CF₃CO₂Na and trace CF₃CF₂CO₂Na as the only identifiable perfluoroalkyl-containing liquid-phase by-products, each of which continues to degrade over extended reaction times. Subjecting perfluorooctane sulfonate ions to the basic decarboxylation conditions did not result in decreasing perfluoroalkyl ¹⁹F NMR integrations or fluoride formation (fig. S19 and table S3), indicating that decarboxylation to the reactive anion intermediate is the key first step of the defluorination process for PFCAs.

Ion chromatography (IC) indicated that 90 ± 6% of the fluorine atoms originating from the PFOA were recovered as fluoride ions after 24 hours of reaction at 120°C (fig. S29). Control experiments showed that the fluorinated polytetrafluoroethylene reaction vessels did not contribute an appreciable amount of fluoride to fluoride recovery (table S3). Fluoride analyses performed by IC at shorter reaction times indicated that fluoride increased proportionally to the decrease in [PFOA] observed by ¹⁹F NMR spectroscopy. This high fluoride recovery indicates that most of the perfluoroalkyl fluorines were defluorinated and mineralized rather than being transformed to smaller-chain PFAS or being lost as volatile fluorocarbons.

Degradation of varied PFAS and by-product analysis suggest a complex mechanism

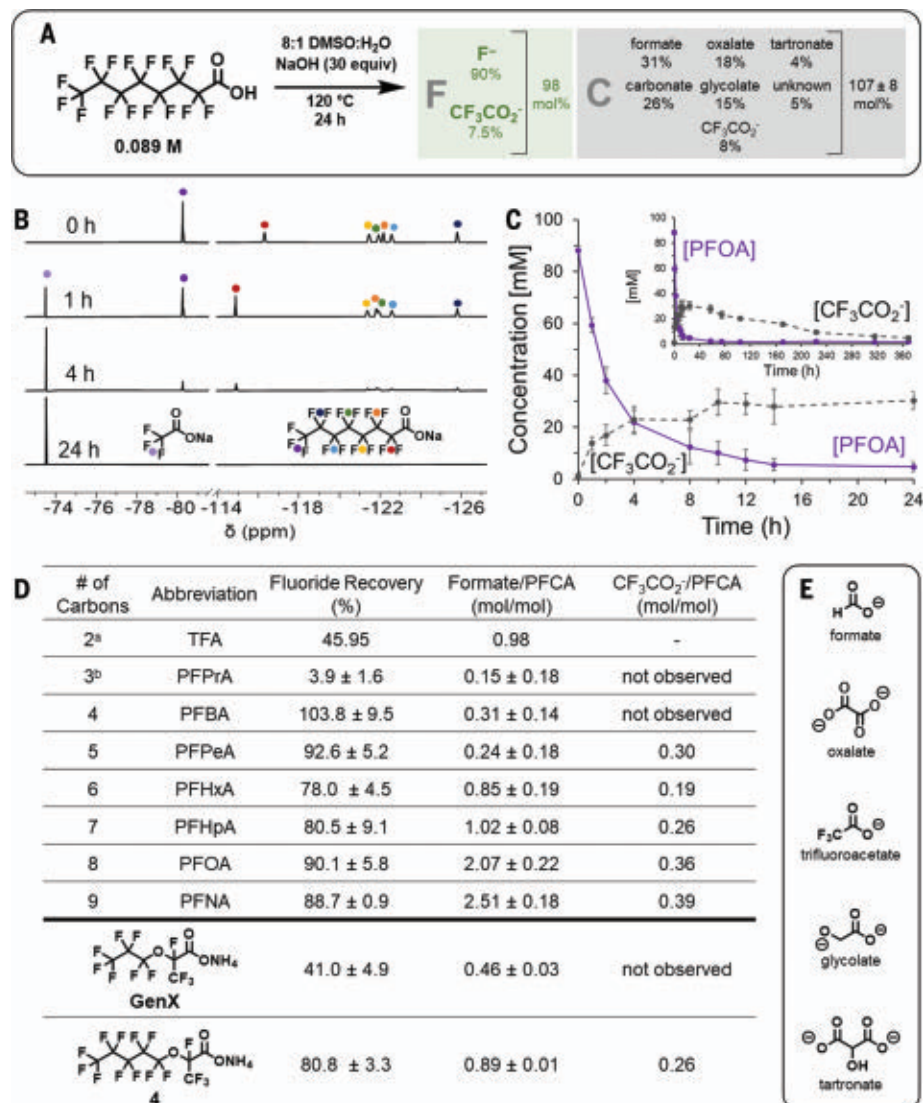
PFCAs with different chain lengths (two to nine carbons) were degraded, providing fluoride recoveries between 78% and quantitative at 24 hours for all PFCAs with four or more carbons (Fig. 2D). Although the longer-chain (C ≥ 4) PFCAs had a degradation profile similar to that of PFOA in that their perfluoroalkyl peaks disappeared from the ¹⁹F NMR spectra (fig. S22) and CF₃CO₂⁻ was formed (Fig. 2D and fig. S23), the destruction of shorter-chain PFCAs (C = 2, 3) was slower and appeared to occur by different mechanisms. For trifluoroacetate (C = 2), degradation is slow (>6 days; fig. S24), likely because the instability of the CF₃⁻ anion (28) hinders decarboxylation, such that destruction occurs either more slowly or by a different mechanism. The carbanion corresponding to perfluoropropionic acid (PFPrA) (C = 3) decarboxylation is similarly unstable (28), resulting in degradation faster than trifluoroacetate but slower than the longer PFCAs (fig. S22). Although the PFPrA ¹⁹F NMR peaks

disappeared completely over 3 days, fluoride recovery was lower than in other PFCAs (3.9 ± 1.6%; Fig. 2D). PFPrA, unlike others in the series, decarboxylates to form a volatile product; in the ¹⁹F NMR for PFPrA degradation, peaks corresponding to CF₃CF₂H can be identified (figs. S11 and S12). Headspace gas chromatography-electron-impact mass spectrometry (MS) also detected the CF₃CF₂⁺ fragment in the gas phase of the reaction (fig. S40). This finding was corroborated by atmospheric pressure chemical ionization-MS of a liquid aliquot of the reaction that had a prominent peak corresponding to CF₃CF₂⁻ (compare fig. S39 with figs. S38 and S40). It appears to be more favorable to produce volatile CF₃CF₂H than for the C = 3 PFCa to proceed down the destruction pathway; as discussed below, this supports our proposal that a γ-carbon is necessary for the major defluorination pathway to occur. Previous PFAS degradation studies have suggested that PFCAs (or other PFAS that are PFCa precursors) degrade through a decarboxylation-hydroxylation-elimination-hydrolysis (DHEH) pathway in which each PFCa is shortened by one carbon each cycle, producing successively shorter PFCAs (11, 16, 18, 21–23). However, the nonconformal degradation of the three-carbon acid and the products observed in the ¹⁹F NMR spectra of degradation reactions of PFCAs containing four or more carbons in the present study indicated that degradation instead occurs through distinct, non-single-carbon shortening mechanisms under these conditions.

The hypothesis that degradation does not occur by iterative one-carbon shortening was further supported by quantifying the carbon-containing by-products formed when PFOA was degraded for 24 hours. We examined a combination of solution ¹H and ¹⁹F NMR spectroscopy and quantitative ¹³C NMR spectroscopy of the precipitate isolated from the reaction and dissolved in D₂O. We also performed ion chromatography on the combined solution and precipitate by adding water to the reaction mixture until the precipitate redissolved. These measurements accounted for the complete carbon balance of the PFOA degradation (107 ± 8 mol% C relative to the [PFOA]₀; table S4 and fig. S30). Other than the residual CF₃CO₂⁻ ions described above, which continued to degrade at longer reaction times, no other organofluorine compounds were detected. Instead, one-, two-, and three-carbon products lacking C–F bonds were identified and quantified. Formate ions were found in solution (fig. S9) and in the precipitate, corresponding to 2.5 ± 0.3 mols formate ions/mol PFOA, as determined by combining the formate concentrations measured in the solution and precipitate by NMR spectroscopy. This amount is consistent with ion chromatography of the reaction mixture and redissolved precipitate,

Fig. 2. Overall reaction scheme, experiments monitoring PFOA and CF_3CO_2^- concentrations over the course of the reaction, and summary of degradation products from a series of PFCAs of different lengths. (A) Heating 0.089 M PFOA in 8:1 DMSO:H₂O with 30 equiv NaOH allowed 90% of the initial fluorine to be recovered as inorganic fluoride and residual trifluoroacetate with few other organofluorine by-products. Formate ions (26 mol %) and several other nonfluorinated by-products were identified (107 ± 8 mol %).

(B) ^{19}F NMR spectra from 0 to 24 hours. Peaks corresponding to PFOA perfluoroalkyl fluorines between -115 and -126 ppm, as well as at -80 ppm, disappeared in less than 24 hours. Trifluoroacetate (-73.6 ppm) appeared and disappeared (disappearance shown in inset of panel C) more slowly over the course of the reaction. (C) Amount of PFOA (purple, solid line) and sodium trifluoroacetate (gray, dashed line) in the reaction over time. Error bars correspond to the standard deviation of three experiments. (D) Fluoride recovery was calculated as mols fluoride after reaction as detected by ion chromatography per mol fluorine in PFOA reactant. Formate/PFOA was calculated as mols formate as detected by IC after reaction per mol PFOA reactant. $\text{CF}_3\text{CO}_2^-/\text{PFOA}$ was determined as mols CF_3CO_2^- as calculated from ^{19}F NMR spectroscopy after 24 hours of reaction per mol PFOA reactant. All measurements are expressed as the average of three trials unless specified otherwise, and error is expressed as a standard deviation. All reaction times are 24 hours unless specified otherwise. "a," 286 hours, single measurement; "b," 63% ± 12% of PFPrA starting material degraded after 24 hours. (E) Structures of the identified carbon-containing by-products.



which provided 2.1 ± 0.2 mols formate/mol PFOA. Formate formation and the varying amounts of formate produced by PFCAs of other chain lengths inspired a deeper mechanistic study (see below). Carbonate ions were detected exclusively in the precipitate, corresponding to 2.1 ± 0.3 mols/mol PFOA. The most likely source of carbonate ions was from the initial decarboxylation step, along with other downstream processes that generate carbon dioxide or single-carbon products at the same oxidation state. Two-carbon products, glycolate ions (0.6 ± 0.1 mol/mol PFOA) and oxalate ions (0.7 ± 0.1 mol/mol PFOA), were found in the precipitate, along with three-carbon-containing tartronate ions (0.2 ± 0.1 mol/mol PFOA). The glycolate and oxalate ions were identified by ^{13}C NMR spectroscopy and comparison with authentic standards. Tartronate ions were identified by a combination of ^{13}C and ^1H NMR spectroscopy, which were consistent with literature reports (29) and showed

the expected correlations in two-dimensional NMR experiments (figs. S31 and S32). Finally, a small amount of the PFOA carbon balance was found in an unknown product, which we designated as a secondary degradation product derived from the reaction of glycolate ions with other intermediates because it was formed in greater amounts when glycolic acid was included at the beginning of the PFOA degradation reaction. Identifying and quantifying these carbon products has important implications for PFOA degradation. First, the high recovery of products with no C-F bonds, along with the high fluoride ion recovery, confirms that these conditions efficiently mineralize PFCAs. Furthermore, identifying multiple two- and three-carbon by-products further implicates mechanisms more complicated than iterative one-carbon shortening processes.

PFCAs of different lengths degraded by different pathways, as indicated by the distinct

patterns in their formate and CF_3CO_2^- formation. If the chain-shortening DHEH mechanism were operative, then we would expect that resonances belonging to chain-shortened species would appear transiently in the ^{19}F NMR spectra as longer-chain PFCAs speciated into a distribution of shorter-chain PFCAs. Instead, only ^{19}F NMR peaks corresponding to CF_3CO_2^- and trace amounts of $\text{CF}_3\text{CF}_2\text{CO}_2^-$ were detected, and the following by-product patterns emerged. PFCAs containing four or fewer carbons did not produce any CF_3CO_2^- , but all PFCAs containing more than four carbons produced roughly the same substoichiometric amount of CF_3CO_2^- : ~0.3 equivalents of $\text{CF}_3\text{CO}_2^-/\text{mol}$ PFOA. PFCAs containing fewer than six carbons did not produce substantial amounts of formate (Fig. 2D), but PFCAs containing six or more carbons produced increasing amounts of formate, with C = 6 and 7 producing ~1 equivalent of formate per PFOA, C = 8 ~2 equivalents, and C = 9 ~2.5 equivalents. These observations indicate that

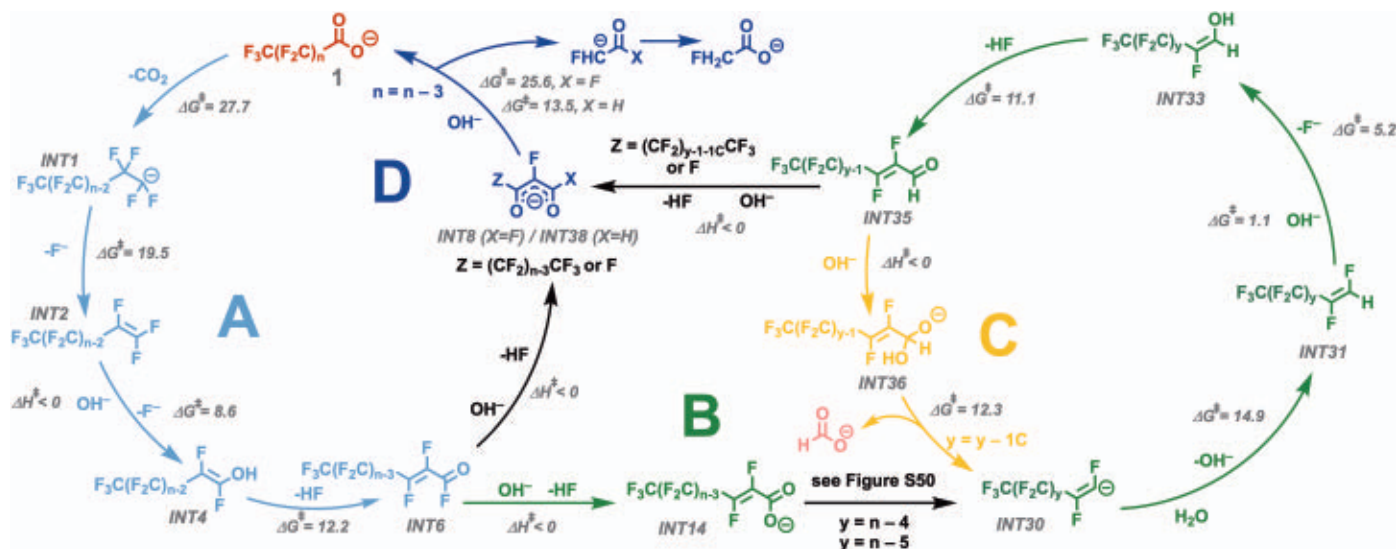


Fig. 3. Proposed PFCA degradation mechanism with activation energies (ΔG^\ddagger , kcal/mol) for each step as calculated at the M06-2X/6-311+G(2d,p)-SMD(DMSO) level. Cycle AD shows a three-carbon shortening of the original PFCA of n carbons ("1," red, top) with one carbon lost as CO_2 (converted to CO_3^{2-} under basic conditions) and two carbons lost to fluoroacetic acid, which readily degrades under these reaction conditions. Pathway B shows the reaction that results from the 1,2 addition of hydroxide to the carboxyl carbon of INT6.

Proposed pathways for the conversion of INT14 to INT30, along with pathways for nonfluorinated, carbon-containing by-products, are described in fig. S50. The alkene INT30 becomes protonated and proceeds through a similar pathway as pathway A. At INT35, the aldehyde analog of acid fluoride INT6, 1,2 addition to the carboxyl carbon leads to the formation of formate by elimination in pathway C, whereas 1,4 addition to the β carbon leads back to pathway D. All energies are expressed in units of kilocalories per mole.

CF_3CO_2^- and formate production occur by distinct pathways.

Experiments conducted at near-ambient temperatures showed that decarboxylation is the rate-limiting step and subsequent defluorination and chain-shortening steps can occur at near-ambient temperature, giving experimental insight into the possible mechanism. Substantial defluorination still occurred when the isolated PFOA degradation product (perfluoro-1H-heptane **2**) was subjected to degradation conditions but heated to only 40°C (table S3). PFCAs have historically been decarboxylated by heating PFCA salts in ethylene glycol at 190 to 230°C to yield perfluoro-1H-alkanes (30) or by pyrolyzing PFCA salts at 210 to 300°C to yield perfluoro-1-alkenes (31), but dipolar aprotic solvent-assisted degradation enabled decarboxylation at only 80 to 120°C, which can be followed by an even lower-temperature defluorination. When **2** was subjected to the basic degradation conditions, both fluoride and chain-shortened PFCAs were observed by IC and ^{19}F NMR at short reaction times (5 min at 120°C) and low temperatures (25 min at 40°C), in contrast to reactions starting from the carboxylated PFOA at the same conditions, in which no fluoride or short-chain PFCAs were formed at short reaction times or at low temperatures (table S3). Degradation of **2** at 40°C for 48 hours showed 57% defluorination (table S3). Although the insolubility of the polyfluoroalkane standard in the DMSO and water solvent precluded accurate measurements of its concentration

by NMR spectroscopy, the presence of the CF_3CO_2^- ^{19}F NMR peak (fig. S13) indicated that the decarboxylated material likely followed a similar degradation pathway. In this low-temperature experiment, intermediates that were not observed in the higher-temperature experiments became evident; at around -210 ppm, a triplet with $J = 48$ Hz appeared, which corresponds to the fluoroacetate ion (CH_2FCOO^- ; fig. S13). The fluoroacetate peak did not appear in the higher-temperature degradations because it degrades rapidly at those temperatures, as confirmed by the degradation of a pure standard. Temperature-dependent studies of the original PFOA degradation reaction showed that the reaction slowed slightly when the reaction was conducted at 100°C (time to $[\text{PFOA}] = 0$ is ~100 hours compared with 16 hours for 120°C; figs. S21 and S25 to S27) and slowed substantially when lowered to 80°C (>290 hours; figs. S21 and S28). Therefore, significant defluorination of **2** was unexpected at 40°C, suggesting that the steps after the decarboxylation were low-barrier or barrierless. These observations further indicate that degradation does not proceed by successive chain shortening through iterative decarboxylation steps.

Computational studies reveal steps in defluorination mechanism with negligible barriers

DFT was used to determine the mechanism of this degradation reaction. These studies predicted that decarboxylation is the rate-limiting step of the degradation and that a series of

low-barrier or enthalpically barrierless reactions can lead to levels of defluorination consistent with experimental observations. DFT calculations were performed at the M06-2X/6-311+G(2d,p)-SMD(DMSO) level (see the supplementary materials for details) and used PFOA as the starting point for the calculations. This mechanism should also be valid for the degradation of straight-chain PFCAs of other lengths. After the initial decarboxylation of PFOA (compound **1**; Fig. 3) at an activation energy of about 28 kcal/mol, calculations indicated that the resulting anion INT1 would eliminate a fluoride to become perfluoroalkene INT2 (Fig. 3 and fig. S44). Unlike previous PFCA degradation mechanisms in the literature predicting that the perfluoroalkyl fragment will hydroxylate after decarboxylation (11, 16, 18, 21–23), these computational results point to the formation of an alkene followed by an enthalpically barrierless hydroxylation of the activated electrophilic alkene. Hydroxylation of the alkyl fragment INT1, as postulated in previous studies, was calculated to have an activation energy of 29.7 kcal/mol under our study's conditions after protonation of the fragment (fig. S46), whereas formation of the alkene INT2 had a barrier of 19.5 kcal/mol, followed by a hydroxylation with no enthalpic barrier ($\Delta G = -44.3$ kcal/mol). The highly exothermic nature of this alkene hydroxylation step played a leading role in driving the degradation, consistent with observations that the defluorination and chain-shortening steps of the reaction neither have high energy barriers

nor lead to the formation of successively shorter PFCAs. Accordingly, when perfluoro-1-heptene **3** (INT2) was subjected to degradation conditions (table S3), it also degraded to similar products even at 40°C, corroborating the computational prediction and indicating that the alkene is likely on the degradation pathway. Further, calculations also suggested that the hydroxylation is specifically favored at the terminal position, because addition on the internal side of the alkene had a barrier of 8.9 kcal/mol (fig. S47). After this alkene hydroxylation (INT4), calculations suggested that a series of low- or no-barrier reactions occurred, as shown in Fig. 3 and fig. S44. The enol can then eliminate another fluoride, forming α,β -unsaturated acyl fluoride INT6 through retro 1,4-conjugate addition.

This resulting α,β -unsaturated acid fluoride INT6 has two plausible reaction pathways that are consistent with the experimental findings: a 1,4-conjugate addition that leads to CF_3CO_2^- formation (pathway D) or a 1,2 addition (pathway B) that can lead to formate formation (pathway C), which together explain the experimentally observed by-product distribution. Calculations indicated that neither option had enthalpic barriers and thus very low free energies of activation, indicating that both reactions occurred to some extent (fig. S48). In the enthalpically barrierless 1,4-conjugate addition (Fig. 3, pathway D, $X = \text{F}$) that leads to the formation of shorter PFCAs such as CF_3CO_2^- , the hydroxide adds to the β carbon of α,β -unsaturated acyl fluoride INT6, followed by an enthalpically barrierless fluoride elimination to form 1,3-diketone compound INT8. Hydroxide again adds to this intermediate on the ketone carbonyl side to generate INT9, which is more favorable than the addition on the acyl fluoride side (fig. S49). Finally, fragmentation occurs to generate an equivalent of PFCa three carbons shorter than the initial carboxylic acid and an equivalent of fluoroacetic acid, which was observed in the experiments conducted at 40°C (figs. S13 and S16). As an example, if five-carbon PFCa perfluoropentanoic acid (PFPeA) went through this cycle, it would produce an equivalent of carbon dioxide (1 carbon), an equivalent of trifluoroacetic acid (2 carbons), and an equivalent of fluoroacetic acid (2 carbons) by this pathway. However, from the experimental results, only about 0.3 equiv of CF_3CO_2^- were produced from PFPeA (Fig. 2D), indicating the PFCa degradation does not proceed quantitatively by this process. This pathway also does not account for the substantial amounts of formate produced in reactions from longer PFCAs.

Formate ion production is explained by a pathway stemming from the favorable 1,2-hydroxylation product, which provides an α,β -unsaturated PFCa (pathway B). As with

INT6, there are multiple possible sites for hydroxide addition to INT14, either to the α (13.6 kcal/mol) or β (12.0 kcal/mol) carbons. Possible pathways propagating from both of these processes, along with the formation of oxalate and other carbon by-products, are described in the supplementary materials (figs. S50 to S54). Although both of these pathways for the conversion of INT14 to INT30 are plausible and supported by computation, the possibility of other active mechanisms cannot be ruled out. However, both of these hydroxylations are more favorable than decarboxylating the α,β -unsaturated perfluoroacid (22.3 kcal/mol), and both lead to the formation of perfluoroalkene anion INT30. The chain length of the alkene depends on which hydroxylation pathway the substrate follows, either four carbons shorter than the original chain (1,3 addition) or five carbons shorter than the original chain (1,4 addition). Calculations showed that perfluoroalkene anion INT30 is protonated rather than eliminating a fluoride to generate the alkyne (figs. S55 and S56). After the protonation, hydroxide adds to the alkene, much like the first postdecarboxylation step in the first proposed pathway. Likewise, α,β -unsaturated aldehyde INT35, an analog to the α,β -unsaturated acid fluoride INT6, is generated through retro-1,4 addition. At this point, the intermediate again faces a bifurcation, with opportunities for both the 1,4-conjugate addition and the 1,2 addition of the hydroxide to the α,β -unsaturated aldehyde. Similar to the addition to the α,β -unsaturated acyl fluoride, both of these reactions were calculated to have no enthalpic barrier (fig. S57). Through the 1,4-conjugate addition (Fig. 3, pathway D, $X = \text{H}$; figs. S59 and S60), the 1,3-diketone compound generated will be attacked by hydroxide, followed by the same fragmentation as noted before. That is, a PFCa and a fluoroacetic aldehyde are formed, the latter of which can be transformed into fluoroacetic acid or be rapidly hydrolyzed. However, if INT35 undergoes 1,2 addition of hydroxide to the α,β -unsaturated aldehyde (Fig. 3, pathway C; figs. S55 and S60), the resulting aldehyde (INT36) cannot eliminate a hydride, whereas its acid fluoride counterpart INT13 can eliminate a fluoride. Instead, INT36 can eliminate the entire perfluoroalkyl chain, creating an equivalent of formate and a one-carbon-shorter alkene anion that can either exit the cycle through 1,4-conjugate addition or proceed through the cycle again to form more formate, thus giving rise to the trend of increased formate formation by PFCAs of longer chain length.

Experimental support for the computationally determined mechanism

Our calculations affirmed that decarboxylation is the rate-determining step of the degradation, and the calculated activation energy of

~28 kcal/mol is consistent with the experimentally determined value of 30.0 kcal/mol (see the supplementary materials, page 6 and table S2). The proposed mechanism is also supported by experimental observations of CF_3CO_2^- and the formate distribution shown in Fig. 2D. By this mechanism, CF_3CO_2^- was produced as a nonstoichiometric by-product, in accordance with the observation that only ~0.3 to 0.4 equivalents of CF_3CO_2^- were formed per mol PFCa for all PFCAs with $C \geq 5$. This proposed mechanism also explains why four-carbon perfluorobutanoic acid (PFBA) did not produce CF_3CO_2^- , whereas the five-carbon PFPeA did, because PFBA that has gone through cycle AD would create FCOO^- , which will decompose spontaneously to carbon dioxide and fluoride (32) or hydrolyze from INT8 to form tartronate. This two-cycle mechanism also explains why five-carbon PFPeA produced CF_3CO_2^- but no formate, because the carbon chain is not long enough to go through pathway C. The mechanism predicts that the amount of formate will increase as the length of the initial PFCa carbon chain increases; this was also affirmed by experimental results for PFCAs of six to nine carbons (Fig. 2D). The formation of carbonaceous by-products such as oxalate, glycolate, and tartronate is also consistent with this mechanism (figs. S50 to S54). Furthermore, when conducting reactions with protodecarboxylated perfluoro-1H-heptane **2** or perfluoro-1H-hexane **S1** (figs. S5 to S8) at 40°C, the formation of intermediate products containing five- or four-carbon fluorine chains was observed (figs. S14 and S17), respectively, which likely correspond to INT8/INT9 (figs. S15 and S18), the intermediate with the highest activation energy (25.6 kcal/mol) in this pathway. The peaks corresponding to this intermediate disappeared as peaks corresponding to the five- and four-carbon PFCAs appeared. These PFCAs that are shortened by three carbons are the logical products of a single-pathway AD cycle from their respective starting materials. The experimental observations confirm that the computed mechanism provides a complete model to describe the observations made experimentally about this complex degradation. We also performed calculations to test proposed difluorocarbene (fig. S62), perfluoroalkyl hydroxylation (fig. S46), and α -lactone (33, 34) (fig. S61) mechanisms that had been proposed for such degradations, but these were found to have barriers too high to be compatible with the experimental conditions.

Generalization of the PFCa destruction method to perfluoroalkyl ether carboxylates

Branched perfluoroalkyl ether carboxylic acids, another major class of PFAS contaminants, are also mineralized by perfluoroalkyl anion intermediates. The ammonium salt of hexafluoropropylene dimer acid (ammonium perfluoro

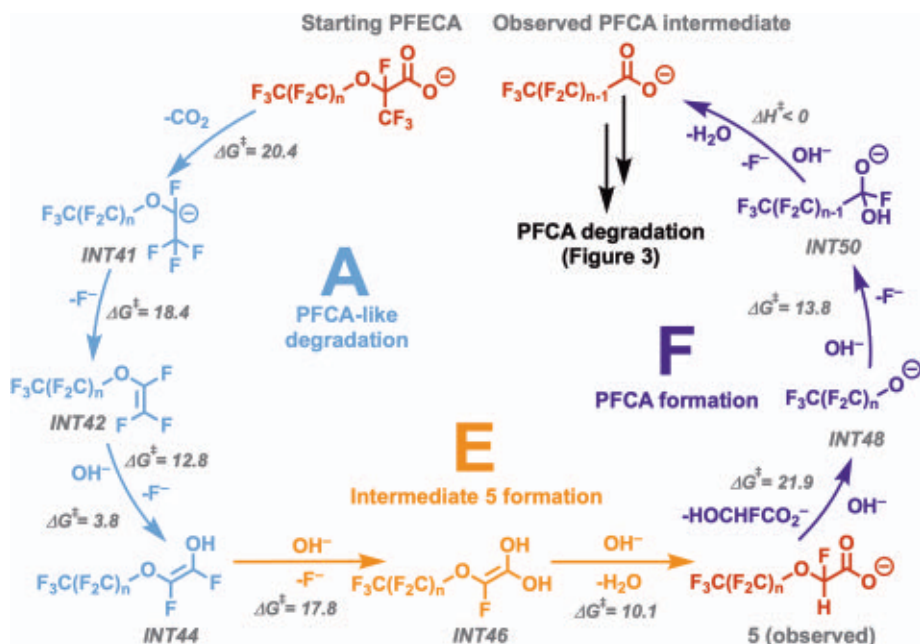


Fig. 4. Proposed mechanism for branched perfluoroalkyl ether carboxylic acid degradation. Pathway A (blue) shows the branched CF_3 defluorinating in the same manner as PFCAs in Fig. 3. The lack of γ -fluorines forces formation of **5** through pathway E (orange), as observed by NMR and MS. Calculations show the hydroxide-mediated $\text{S}_\text{N}2$ that eliminates the perfluoroalkoxide tail in pathway F (purple), leading to the formation of a PFECA that is degraded according to the mechanism described in Fig. 3. All energies are expressed in units of kilocalories per mole.

(2-methyl-3-oxahexanoate; also known as FRD-902, the trade name GenX, or HFPO-DA in its acid form) is a perfluoroalkyl ether carboxylic acid that was introduced as an industrial replacement for PFOA. This compound now contaminates water sources such as the Cape Fear River, which serves as the primary drinking water source for >350,000 residents of North Carolina (35). For this compound, the decarboxylation and branched CF_3 chain defluorination occurred at 40°C , an even lower temperature than for the PFCAs (fig. S35). This finding is consistent with computational results indicating that the barrier for GenX decarboxylation is only 20.4 kcal/mol (fig. S63). However, because of the presence of the ether oxygen in place of the γ -carbon, the structure was unable to eliminate a γ -fluorine and instead formed perfluoroalkyl ether carboxylic acid intermediate **5** through hydrolysis (Fig. 4), which built up in solution and was observed by both ^{19}F NMR and electrospray ionization MS (figs. S33, S35, and S42). Further degradation occurred at elevated temperatures (80°C ; fig. S35). Calculations showed that the decarboxylation of this intermediate was unfavorable (figs. S65); rather, a hydroxide-mediated $\text{S}_\text{N}2$ with a barrier of 21.9 kcal/mol occurred in which the perfluoroalkoxide tail was eliminated (fig. S66). This perfluoroalkoxide formed a carboxylic acid ($\Delta G^\ddagger = 21.9$ kcal/mol) with the same number of carbons as the original perfluoroether tail. Because GenX contains a

three-carbon tail, it produced the C3 PFECA (PFPrA), the degradation of which led to incomplete defluorination (41%; Fig. 2D) and the formation of $\text{CF}_3\text{CF}_2\text{H}$ (figs. S37, S40, and S41). These observations are consistent with those of the direct degradation of PFPrA (Fig. 2D and figs. S11, S12, S39, and S40). The experimental observations showed that temperatures of 40° , 80° , and 120°C are necessary to form intermediate **5**, to form the PFECA analog, and to initiate PFECA degradation, respectively. These temperature steps correspond to the calculated energy barriers of 20.4, 21.9, and 27.7 kcal/mol, respectively (figs. S35, S63, and S64). Degradation of a longer perfluoroalkyl ether carboxylic acid with a five-carbon perfluoroalkyl tail (compound **4**; figs. S34, S36, S40, and S43) proceeded by a similar mechanism as that of GenX and gave fluoride recoveries consistent with those obtained from the five-carbon PFECA PFPeA. These findings indicate that perfluoroalkyl ether carboxylates also degrade through perfluoroalkyl anion-based processes. Intermediates in the degradation of **4**, as observed by atmospheric pressure chemical ionization-MS (fig. S43), corroborated the proposed mechanism (Fig. 4).

Conclusions

The perfluorocarbon reactivity that we have described here leverages low-barrier defluorination mechanisms to mineralize PFAS at mild temperatures with high rates of defluorination

and low organofluorine side-product formation. In contrast to other proposed PFAS degradation strategies, the conditions described here are specific to fluorocarbons, destroy concentrated PFCAs, give high fluoride ion recovery and low fluorinated by-product formation, and operate under relatively mild conditions with inexpensive reagents. The proposed mechanism is consistent with both computational and experimental results, provides insight into the complexity of PFAS mineralization processes, and may be operative but unrecognized in other PFAS degradation approaches. This demonstration of the reactivity of perfluoroalkyl anions, and the ability to access such intermediates efficiently from PFCAs, may inform the development of engineered PFAS degradation processes and facilitate expanding this reactivity mode to PFAS with other polar head groups.

REFERENCES AND NOTES

1. A. Leeson et al., *Environ. Toxicol. Chem.* **40**, 24–36 (2021).
2. A. M. Calafat, L.-Y. Wong, Z. Kuklenyik, J. A. Reidy, L. L. Needham, *Environ. Health Perspect.* **115**, 1596–1602 (2007).
3. United Nations Stockholm Convention, “Perfluorooctanoic acid (PFOA), its salts and PFOA-related compounds” (UN, 2017); <http://chm.pops.int/Implementation/Alternatives/AlternativestoPOPs/ChemicalslistedinAnnexA/PFOA/tabid/8292/Default.aspx>.
4. “C-8 Medical Monitoring Program” (GCG, 2022); <http://www.c-8medicalmonitoringprogram.com/>.
5. N. Rich, “Rob Bilott v. DuPont,” *New York Times Magazine*, 17 January 2016; <https://hnbjps.blogspot.com/2016/01/rob-bilott-v-dupont.html>.
6. A. Maimaiti et al., *Chem. Eng. J.* **348**, 494–502 (2018).
7. M. Ateia, A. Alsbaiee, T. Karanfil, W. Dichtel, *Environ. Sci. Technol. Lett.* **6**, 688–695 (2019).
8. D. Bond, J. Enck, “First in the nation testing reveals toxic contamination in soil and water near Norlite incinerator” (Bennington University, 2020); <https://www.bennington.edu/sites/default/files/sources/docs/Norlite%20News%20Release%20%5Bdb%20final%20updated%5D.pdf>.
9. C. D. Vecitis, H. Park, J. Cheng, B. T. Mader, M. R. Hoffmann, *J. Phys. Chem. A* **112**, 4261–4270 (2008).
10. J. Cheng, C. D. Vecitis, H. Park, B. T. Mader, M. R. Hoffmann, *Environ. Sci. Technol.* **44**, 445–450 (2010).
11. R. K. Singh et al., *Environ. Sci. Technol.* **53**, 2731–2738 (2019).
12. C. E. Schaefer, C. Andaya, A. Urtiaga, E. R. McKenzie, C. P. Higgins, *J. Hazard. Mater.* **295**, 170–175 (2015).
13. A. M. Trautmann, H. Schell, K. R. Schmidt, K. M. Mangold, A. Tiehm, *Water Sci. Technol.* **71**, 1569–1575 (2015).
14. M. J. Krause et al., *J. Environ. Eng.* **148**, 05021006 (2022).
15. M. J. Bentel et al., *Environ. Sci. Technol. Lett.* **7**, 351–357 (2020).
16. M. J. Bentel et al., *Environ. Sci. Technol.* **53**, 3718–3728 (2019).
17. M. J. Bentel et al., *Environ. Sci. Technol.* **54**, 2489–2499 (2020).
18. H. Hori et al., *Environ. Sci. Technol.* **39**, 2383–2388 (2005).
19. X. Liang, J. Cheng, C. Yang, S. Yang, *Chem. Eng. J.* **298**, 291–299 (2016).
20. B. N. Nzeribe, M. Crimi, S. Mededovic Thagard, T. M. Holsen, *Crit. Rev. Environ. Sci. Technol.* **49**, 866–915 (2019).
21. Q. Zhuo, S. Deng, B. Yang, J. Huang, G. Yu, *Environ. Sci. Technol.* **45**, 2973–2979 (2011).
22. H. Hori et al., *Environ. Sci. Technol.* **38**, 6118–6124 (2004).
23. B. Wu et al., *Environ. Sci. Technol. Lett.* **6**, 630–636 (2019).
24. D. Kong, P. J. Moon, E. K. J. Lui, O. Bsharat, R. J. Lundgren, *Science* **369**, 557–561 (2020).
25. S. Zhou, B. T. Nguyen, J. P. Richard, R. Kluger, J. Gao, *J. Am. Chem. Soc.* **143**, 137–141 (2021).
26. H. K. Liberatore, S. R. Jackson, M. J. Strynar, J. P. McCord, *Environ. Sci. Technol. Lett.* **7**, 477–481 (2020).
27. C. Zhang, A. C. McElroy, H. K. Liberatore, N. L. M. Alexander, D. R. U. Knappe, *Environ. Sci. Technol.* **56**, 6103–6112 (2022).
28. D. A. Dixon, T. Fukunaga, B. E. Smart, *J. Am. Chem. Soc.* **108**, 4027–4031 (1986).
29. T. Chatterjee, E. Boutin, M. Robert, *Dalton Trans.* **49**, 4257–4265 (2020).

30. J. D. LaZerte, L. J. Hals, T. S. Reid, G. H. Smith, *J. Am. Chem. Soc.* **75**, 4525–4528 (1953).
31. R. N. Haszeldine, *J. Chem. Soc.* 4259 (1952).
32. X. Zhang, U. Gross, K. Seppelt, *Angew. Chem. Int. Ed.* **34**, 1858–1860 (1995).
33. M. J. Pellerite, *J. Fluor. Chem.* **49**, 43–66 (1990).
34. Y. Ge *et al.*, *Comput. Theor. Chem.* **1029**, 33–40 (2014).
35. G. McGrath, “Denied by Trump EPA, NC activists hope Biden EPA will force ‘forever chemical’ study,” *Fayetteville Observer*, 17 January 2021; <https://www.fayobserver.com/story/news/2021/01/27/denied-by-trump-epa-nc-activists-hope-biden-epa-force-forever-chemical-study/4265453001/>.

ACKNOWLEDGMENTS

We thank Y. Luo at Shanghai Institute of Organic Chemistry for helpful discussions about fluorine NMR; S. Shafaie at Northwestern University’s Integrated Molecular Structure Education and Research Center (IMSERC) facility for assistance with MS; and R. Sponenburg at Northwestern University’s Quantitative Bio-element Imaging Center (QBIC) for ion chromatography. **Funding:** B.B.T. is supported by the National Science Foundation Graduate Research Fellowship Program (NSF grant DGE-1842165). K.N.H. is supported by the National Science Foundation (grant CHE-1764328) and the Saul Winstein Chair in Organic Chemistry.

Ion chromatography was performed at the Northwestern University Quantitative Bio-element Imaging Center, which is generously supported by the NASA Ames Research Center (grant NNA04CC36G). This work made use of the IMSERC at Northwestern University, which has received support from the National Institutes of Health (NIH grants 1S100D012016-01 and 1S10RR019071-01A1), the Soft and Hybrid Nanotechnology Experimental (SHyNE) Resource (NSF grant ECCS-1542205), the State of Illinois, and the International Institute for Nanotechnology (IIN). Gas chromatography MS was performed at the REACT Core Facility at Northwestern University, which acknowledges funding from the U.S. Department of Energy, Office of Science, Office of Basic Energy Sciences, Catalysis Science program (DE-SC0001329) used for the purchase of the GC/MS analysis system. **Author contributions:** Conceptualization: B.B.T., K.N.H., W.R.D.; Data curation: L.Y.L.; Formal analysis: B.B.T., L.Y.L., M.A.; Funding acquisition: K.N.H., W.R.D.; Investigation: B.B.T., L.Y.L.; Methodology: B.B.T., L.Y.L., K.N.H., W.R.D.; Project administration: K.N.H., W.R.D.; Supervision: X.S.X., K.N.H., W.R.D.; Visualization: B.B.T., L.Y.L.; Writing – original draft: B.B.T., L.Y.L., K.N.H., W.R.D.; Writing – review & editing: B.B.T., L.Y.L., X.S.X., M.A., K.N.H., W.R.D. **Competing interests:** Northwestern University has filed a provisional patent (63/261,772) that describes methods to degrade PFCAs on behalf of inventors B.B.T. and W.R.D. W.R.D. is a founder and equity holder in Cyclopure, Inc., which is

commercializing technologies related to PFAS detection and remediation. Cyclopure is uninvolved in the research described in this manuscript. The remaining authors declare no competing interests. **Data and materials availability:** All data are available in the manuscript or the supplementary materials. **License information:** Copyright © 2022 the authors, some rights reserved; exclusive licensee American Association for the Advancement of Science. No claim to original US government works. <https://www.science.org/about/science-licenses-journal-article-reuse>

SUPPLEMENTARY MATERIALS

science.org/doi/10.1126/science.abm8868
Materials and Methods
Supplementary Text
Figs. S1 to S66
Tables S1 to S4
Data S1
References (36–57)

Submitted 19 October 2021; resubmitted 19 April 2022
Accepted 8 July 2022
10.1126/science.abm8868

NEURODEVELOPMENT

Input-dependent segregation of visual and somatosensory circuits in the mouse superior colliculus

Teresa Guillamón-Vivancos, Mar Aníbal-Martínez, Lorenzo Puche-Aroca, Juan Antonio Moreno-Bravo, Miguel Valdeolmillos, Francisco J. Martini, Guillermina López-Bendito*

Whereas sensory perception relies on specialized sensory pathways, it is unclear whether these pathways originate as modality-specific circuits. We demonstrated that somatosensory and visual circuits are not by default segregated but require the earliest retinal activity to do so. In the embryo, somatosensory and visual circuits are intermingled in the superior colliculus, leading to cortical multimodal responses to whisker pad stimulation. At birth, these circuits segregate, and responses switch to unimodal. Blocking stage I retinal waves prolongs the multimodal configuration into postnatal life, with the superior colliculus retaining a mixed somato-visual molecular identity and defects arising in the spatial organization of the visual system. Hence, the superior colliculus mediates the timely segregation of sensory modalities in an input-dependent manner, channeling specific sensory cues to their appropriate sensory pathway.

In the mature cerebral cortex, sensory modalities are segregated into specialized areas known as primary sensory cortices. So that cortical areas ultimately respond to a specific sensory stimulus, this segregation is thought to occur during development, and it is first instructed by intrinsic factors and later by sensory experience (1–5). However, this early inception of sensory identity has not been directly demonstrated because there is no functional evidence of the sensory specificity of emerging circuits. It remains to be determined whether sensory identities arise directly as unimodal entities or whether they are initially multimodal and become specified over time.

We found that the nascent somatosensory and visual pathways of mice are functionally interconnected, with both cortices responding to tactile stimulation at prenatal stages yet segregating into independent pathways at birth. This segregation happens in the superior colliculus (SC) and depends on retinal input. Blocking stage I retinal waves or removing retinal projections in embryos leads to a failure in the timely developmental segregation of visual circuits in the SC. Consequently, the activation of the visual cortex by somatosensory stimuli extends into postnatal life and is associated with long-term circuit abnormalities.

S1 and V1 emerge functionally intermingled

A functional map of the periphery is present in the mouse somatosensory cortex at perinatal stages, as shown through whisker pad stimu-

lation in a transgenic mouse line in which glutamatergic neurons in the neocortex express GCaMP6f (hereafter $Cx^{GCaMP6f}$) (6). Hence, there appears to be a high level of intramodal functional organization of sensory circuits at these early stages. We used the same approach to test whether developing sensory circuits also show early specificity to stimulus modalities. We found that at embryonic stages, a somatosensory stimulus not only triggered the expected contralateral response in the barrel field of the primary somatosensory cortex (S1) but also a bilateral response in the presumptive primary visual cortex (V1). This multimodal response was observed in 33% of the mice analyzed at embryonic day 18 (E18) but disappeared by postnatal day 0 (P0) (Fig. 1, A to C, and movies S1 and S2), suggesting that we were revealing the end of a developmental process. We next tested whether the disappearance of this cortical multimodal response might be related to the arrival of retinal inputs to central structures, which occurs close to birth (7–9). To test this possibility, we used $Cx^{GCaMP6f}$ mice in which their eyes were eliminated bilaterally at E14 (embBE mice) (10). Whereas whisker pad stimulation at P0 triggered only the cortical somatosensory response in control mice, in the embBE mice, this response was consistently multimodal, activating both S1 and V1 in 100% of the cases, even at E18 (Fig. 1, D to F, and movies S3 and S4). This multimodal response extended into the first postnatal days and lasted until P6 (Fig. 1G and fig. S1). Thus, it appears that somatosensory and visual circuits are not segregated by default but require the arrival of retinal input to do so.

We then designed experiments to identify the circuits responsible for this lack of segregation and the ensuing multimodal response in embBE mice. Electrical stimulation of either S1

Instituto de Neurociencias de Alicante, Universidad Miguel Hernández–Consejo Superior de Investigaciones Científicas (UMH-CSIC), San Juan de Alicante, Alicante, Spain.

*Corresponding author. Email: g.lbendito@umh.es

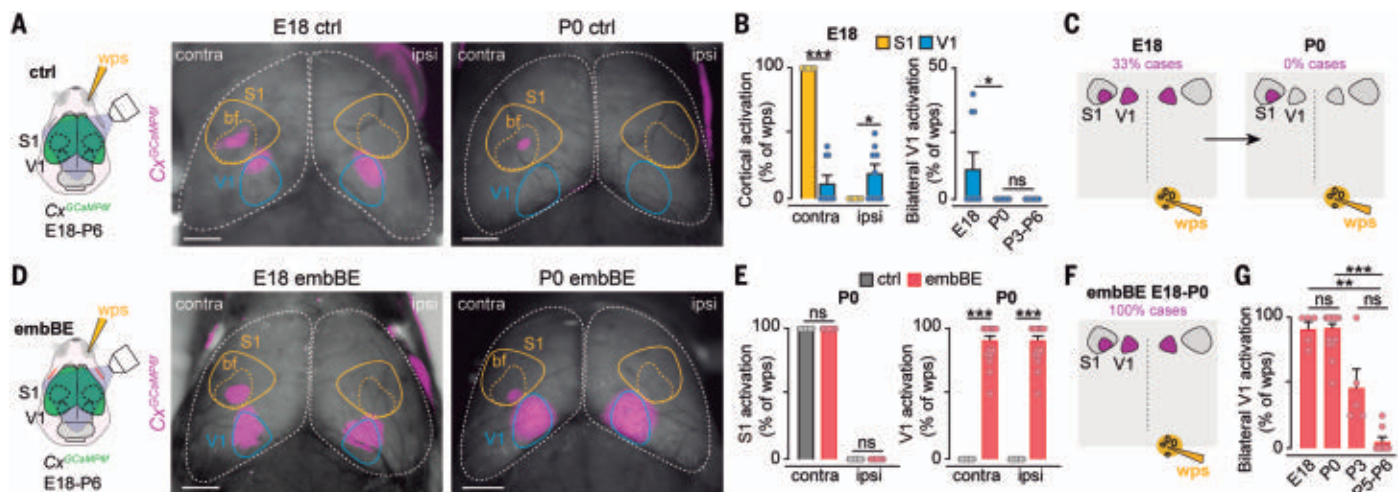


Fig. 1. Embryonic somatosensory and visual cortices originate as multimodal.

(A) (Left) Experimental design. (Right) Calcium responses in the cortex (pink) elicited by mechanical stimulation of the whisker pad in control mice at E18 and P0. (B) Proportion of the whisker pad stimulations that evoked a contralateral or ipsilateral response in S1 and V1 of control mice at E18, and in V1 from E18 to P6 (E18, $n = 9$ mice; P0, $n = 13$ mice; P3 to P6, $n = 8$ mice). (C) Scheme summarizing the results. (D) (Left) Experimental design. (Right) Calcium responses in the cortex (pink) elicited by

mechanical stimulation of the whisker pad in embBE mice at E18 and P0. (E) Proportion of the whisker pad stimulations that evoked a contralateral or ipsilateral response in S1 and V1 of control and embBE mice at P0 ($n = 19$ control mice, $n = 21$ embBE mice). (F) Scheme summarizing the results. (G) Proportion of the whisker pad stimulations that evoked a bilateral V1 response in embBE from E18 to P6 (E18, $n = 5$ mice; P0, $n = 21$ mice; P3, $n = 5$ mice; P5 to P6, $n = 8$ mice). Scale bars, 1000 μm . Bar graphs show the means \pm SEM. ns, not significant; * $P < 0.05$, ** $P < 0.01$, *** $P < 0.001$.

or V1 in the embBE mice failed to reproduce the bilateral V1 responses to whisker pad stimulation (fig. S2, A to D). Moreover, these responses were still triggered by whisker pad stimulation when the barrel field was inhibited by tetrodotoxin (TTX) (fig. S2, E and F). Hence, these experiments demonstrate that the sensory-modality interconnection in embBE mice is not driven by a cortico-cortical mechanism.

SC circuit reorganization provides sensory-modality specificity

Before reaching the cortex, sensory-modality pathways converge in nearby territories of the thalamus and also in the SC (11). Therefore, the multimodal responses observed might involve direct communication between modalities at either of these structures. The SC is a midbrain multisensory structure that receives visual input in its superficial layers (sSC) and somatosensory input in its deep layers (dSC) (11, 12). Using mice that express GCaMP6f in SC neurons (hereafter SC^{GCaMP6f}), we found that whisker pad stimulations at P0 evoked a bilateral response in the sSC of all embBE mice, whereas no responses were evoked in the sSC of control mice (Fig. 2, A to C, and movies S5 and S6). To confirm that the cortical multimodal response requires the SC, we inactivated the SC with TTX in embBE triple transgenic mice that expressed GCaMP6f in the cortex and SC (*Cx-SC^{GCaMP6f}*) and found that the cortical response became unimodal (Fig. 2, D to F). Similar results were found when the SC was acutely lesioned (fig. S3, A and B). Last, we looked for sensory modality changes in the circuits downstream of the SC

and, using dye tracing, demonstrated that the connectivity from the SC to the thalamus was normal in embBE mice (fig. S3, C and D). Similarly, we found no differences in the specificity of the sensory modality of thalamic afferents or efferents in these embBE mice (fig. S4). Therefore, these results demonstrate that the SC mediates the multimodal cortical responses in embBE mice and suggest that the SC is involved in the developmental segregation of sensory modalities observed in control mice.

We next assessed how the SC channels somatosensory information into the presumptive V1 by testing the connectivity between the dSC (somatosensory) and sSC (visual) layers in embBE mice. At P0, whereas unilateral electrical stimulation of the dSC layers in SC^{GCaMP6f} control slices only elicited responses in the contralateral dSC layer, the responses in the embBE mice also propagated to both the ipsilateral and contralateral sSC layers (Fig. 2, G and H, and movies S7 and S8), an effect that was not observed by stimulating the superficial layers (fig. S5). In addition, these functional results were supported by anatomical tracing. Unilateral injection of lentivirus-expressing enhanced green fluorescent protein (EGFP) into the SC produced widespread labeling of the contralateral dSC and sSC layers in embBE mice, whereas only the contralateral dSC layer was labeled in their control littermates (Fig. 2, I and J). Conversely, when the multimodal response finally switched to unimodal in the embBE mice at P6, we observed a significant reduction, as compared with P0, both in the number of axons in the

sSC and in the bilateral V1 or SC activation elicited by whisker pad stimulation (fig. S6).

The data from the embBE suggest that the multimodal embryonic response in control mice could also be mediated by the SC. Using the *Cx-SC^{GCaMP6f}*, we found that whisker pad stimulation at E18 in control mice elicited a bilateral V1 response in 37% of the cases, which was always accompanied by concomitant bilateral sSC activation. However, activation of the sSC was not detected when the cortical multimodal response switched to unimodal at P0 (Fig. 3, A to C). We then tested whether the switch from multimodal to unimodal cortical responses involved a developmental reconfiguration of the intracortical circuits. As such, we injected a lentivirus-expressing EGFP unilaterally into the SC at E14 and analyzed the disposition of the axons in the contralateral sSC at E18 and P0. We detected significantly more labeled axons in the sSC layer at E18 than at P0 (Fig. 3D). This unplugging of the sSC layer from the dSC layer, which was delayed in embBE mice, coincides with the peak innervation of retinocollicular axons (Fig. 3E) (7). These results suggest that the arrival of retinal axons to the SC prompts the segregation of somatosensory and visual circuits.

Perinatal retinal waves drive the SC circuit reorganization

Developing retinal axons convey a stereotyped pattern of spontaneous activity known as retinal waves. Stage I retinal waves, which are mediated by gap junctions, last approximately from E17 until P1 in mice (Fig. 3F) (13), and

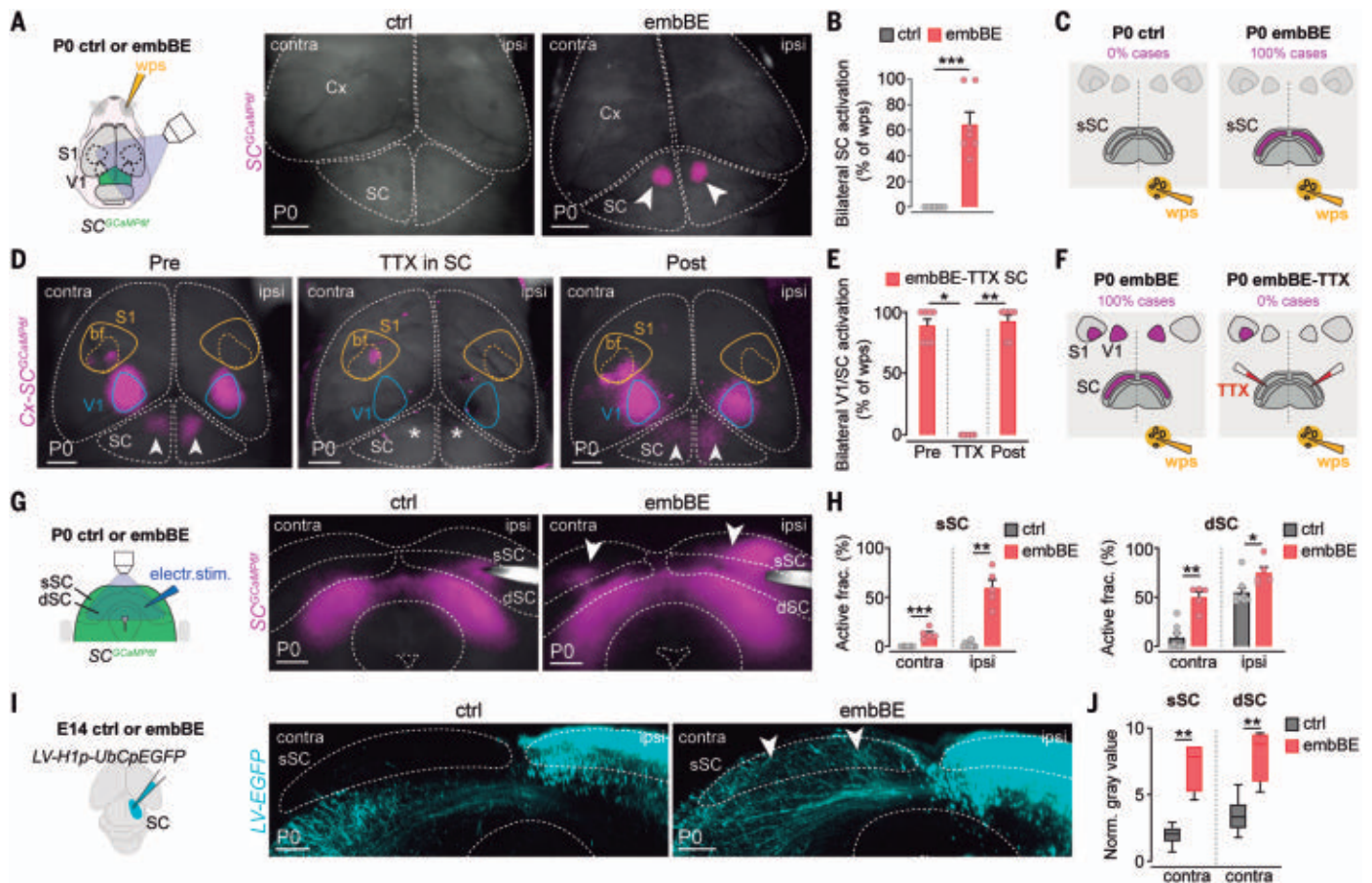


Fig. 2. Somatosensory and visual SC circuits remain intermingled in embBE mice. (A) (Left) Experimental design. (Right) Calcium responses (pink) in the SC elicited by mechanical stimulation of the whisker pad in control and embBE mice at P0. (B) (Left) Quantification of the data shown in (A) ($n = 7$ control mice, $n = 7$ embBE mice). (C) Scheme summarizing the data. (D) Cortical and SC calcium responses elicited by mechanical stimulation of the whisker pad in embBE mice at P0 before, during, and 1 hour after bilateral TTX injection in the SC (asterisks). (E) Quantification of the data shown in (D) ($n = 6$ mice). (F) Scheme summarizing the data. (G) (Left) Experimental design. (Right) Calcium responses elicited by electrical stimulation of the dSC in control and embBE slices at P0. There is spreading to the ipsilateral and contralateral

superficial layers of the SC in embBE mice (arrowheads). (H) Proportion of the total area (active fraction) of the sSC and dSC layers activated by a perithreshold stimulus in the dSC at P0 ($n = 8$ control mice, $n = 5$ embBE mice). (I) (Left) Experimental design. The lentivirus was injected into the SC at E14. (Right) Optical coronal sections from three-dimensional (3D) light-sheet images showing the EGFP lentiviral-labeled axons in the sSC of embBE mice at P0 (arrowhead). (J) Quantification of the normalized EGFP expression in contralateral sSC and dSC ($n = 8$ control mice, $n = 4$ embBE mice). Scale bars, (A) and (D) 1000 μ m; (G) and (I) 150 μ m. Boxplots show the medians with the interquartile range (box) and range (whiskers). The bar graphs show the means \pm SEM. ns, not significant; * $P < 0.05$, ** $P < 0.01$, *** $P < 0.001$.

therefore, we tested whether these waves might play a role in directing intracollicular sensory-modality segregation. We blocked stage I retinal waves by injecting the gap junction blocker carbenoxolone (cbx) (13, 14) into both eyes of *Cx^{GCaMP6f}* mice at P0. To confirm that cbx blocks gap junction-mediated retinal waves in vivo, we recorded spontaneous activity in V1, the frequency of which was reduced significantly 1 hour after the administration of cbx at P0 (fig. S7, A and B). This reduction was not due to the degeneration of retinofugal axons because these axons reached both the thalamus and the SC (fig. S7C), and visual spontaneous activity was recovered at P6 (fig. S7, A and B). Accordingly, acute administration of epibatidine, a high-affinity cholinergic agonist that inhibits postnatal stage II retinal

waves (15–17), significantly reduced the frequency of spontaneous activity in V1 at P6, whereas cbx had no such effect at this stage (fig. S7, D and E). Altogether, these experiments show that most of V1 activity at the perinatal stage in vivo is driven by gap junction-mediated retinal waves.

We next recorded the cortical activity after whisker pad stimulation in *Cx^{GCaMP6f}* mice treated with cbx at P0 (Fig. 3G). Seven to 8 hours after cbx administration, stimulation of the whisker pad triggered in all mice a multimodal response that was elicited in 44% of the trials and that rose to 64% after a second injection of cbx on the following day (Fig. 3, G to I, and movies S9 and S10). By contrast, this multimodal response was not triggered by the injection of saline or epibatidine (Fig. 3, G to

I). Cbx administration to *Cx-SC^{GCaMP6f}* mice at P0 showed concomitant bilateral responses in the V1 and SC at P1 (fig. S8, A to C, and movie S11), which were abolished by TTX acute injection into the SC (fig. S8, D and E). As in the embBE, lentiviral tracing in the SC of cbx-treated mice showed the abnormal invasion of axons from the dSC layer into the sSC layer at P1 (Fig. 3J). Last, we checked whether the responses to whisker pad stimulation eventually switch to unimodal in the cbx-treated mice. When we performed the whisker pad stimulation in the *Cx^{GCaMP6f}* and triple *Cx-SC^{GCaMP6f}* mice, we found that the multimodal responses both in the V1 and SC were almost absent by P6 (fig. S8, F to I). These data show that the timely segregation of somatosensory and visual pathways require a perinatal reorganization

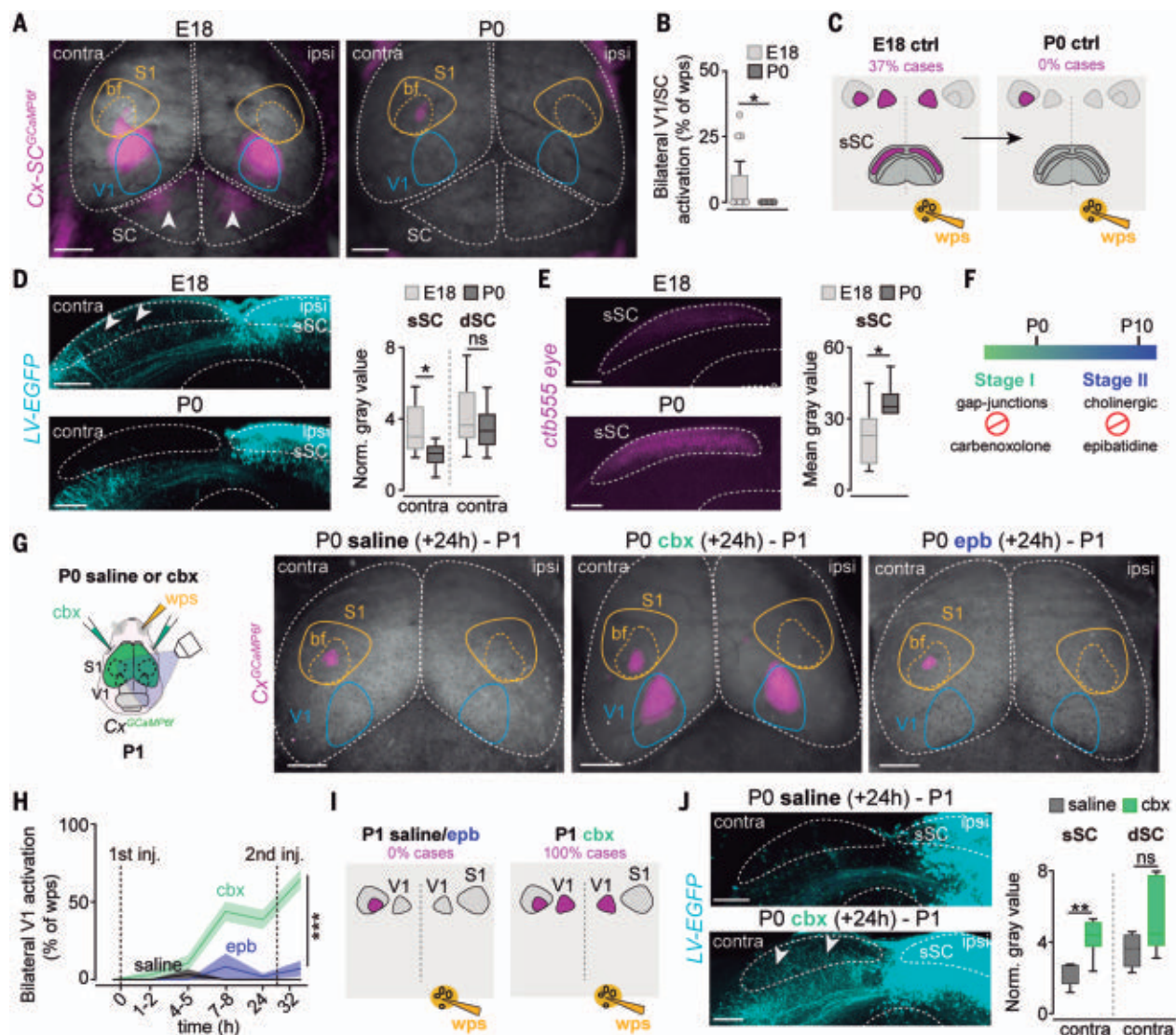


Fig. 3. Blocking stage I retinal waves prolongs the multimodal configuration.

(A) Whisker pad stimulation leads to the concomitant bilateral activation of both V1 and SC in control E18 mice, which switches to unimodal at P0. (B) Quantification of the data shown in (A) ($n = 8$ E18, $n = 13$ P0). (C) Scheme summarizing the data. (D) (Left) Optical coronal sections from 3D light-sheet images showing EGFP lentiviral-labeled axons in the sSC of control E18 (arrowheads) but not P0 mice. The lentivirus was injected into the SC at E14. (Right) Quantification of the normalized EGFP expression in contralateral sSC and dSC ($n = 9$ E18 mice, $n = 8$ P0 mice). (E) (Left) Coronal views of retinal axons labeled by CTB injection of the eye at E14 that reach the SC at E18 and P0. (Right) Quantification of the data shown at left ($n = 9$ E18 mice, $n = 6$ P0 mice). (F) Scheme showing early phases of retinal waves. (G) (Left) Experimental design. (Right) Cortical calcium responses at P1 elicited by mechanical stimulation of the whisker pad after bilateral injection of (left) saline, (middle) cbx, and (right) epibatidine (epb) into the eye at P0. (H) Proportion of the whisker pad

stimulations that evoked a bilateral V1 response before and after the injection of saline, cbx, or epb: time (t) = 0, $n = 20$ mice injected with saline, $n = 24$ cbx, $n = 17$ epb; $t = 1$ to 2 hours, $n = 4$ saline, $n = 8$ cbx, $n = 6$ epb; $t = 4$ to 5 hours, $n = 6$ saline, $n = 7$ cbx, $n = 9$ epb; $t = 7$ to 8 hours, $n = 7$ saline, $n = 4$ cbx, $n = 3$ epb; $t = 24$ hours, $n = 19$ saline, $n = 14$ cbx, $n = 13$ epb; and $t = 32$ hours, $n = 11$ saline, $n = 12$ cbx, $n = 7$ epb. (I) Scheme summarizing the data. (J) (Left) Optical coronal sections from 3D light-sheet images showing lentiviral EGFP-labeled axons in the sSC of P1 mice treated at P0 with cbx (arrowheads) but not with saline. The lentivirus was injected into the SC at E14. (Right) Quantification of the normalized EGFP expression in contralateral sSC and dSC ($n = 5$ saline, $n = 6$ cbx). Scale bars, (A) and (G) 1000 μ m; (D) 200 μ m; (E) 250 μ m; (J) 200 μ m. Boxplots show the medians with the interquartile range (box) and range (whiskers). The bold lines in (H) indicate the mean, and the shading indicates the SEM. The bar graphs in (B) show the mean \pm SEM. ns, not significant; * $P < 0.05$, ** $P < 0.01$, *** $P < 0.001$.

of intracollicular circuits that depends on gap junction-mediated retinal waves.

Failure to timely segregate drives long-lasting circuit alterations

Although reversed by the end of the first postnatal week, the transient expansion of the multimodal phase may have long-term effects

on the specification of sensory circuits. For example, perinatal blockage of retinal activity might cause enduring changes in the transcriptional program of SC layers. To assess this, we performed bulk RNA-sequencing (RNA-seq) of the sSC and dSC layers at P6 in mice treated with saline or cbx at P0 to P1 (Fig. 4A). A principal components analysis

(PCA) revealed that sSC and dSC cells clustered according to their anatomic origins (Fig. S9A). Moreover, a differential expression analysis (DEA) in saline conditions revealed 1544 differentially expressed genes (DEGs) enriched in the sSC as opposed to 1549 in the dSC layers (Fig. 4A and table S1). Among the DEGs enriched in each population, we found genes

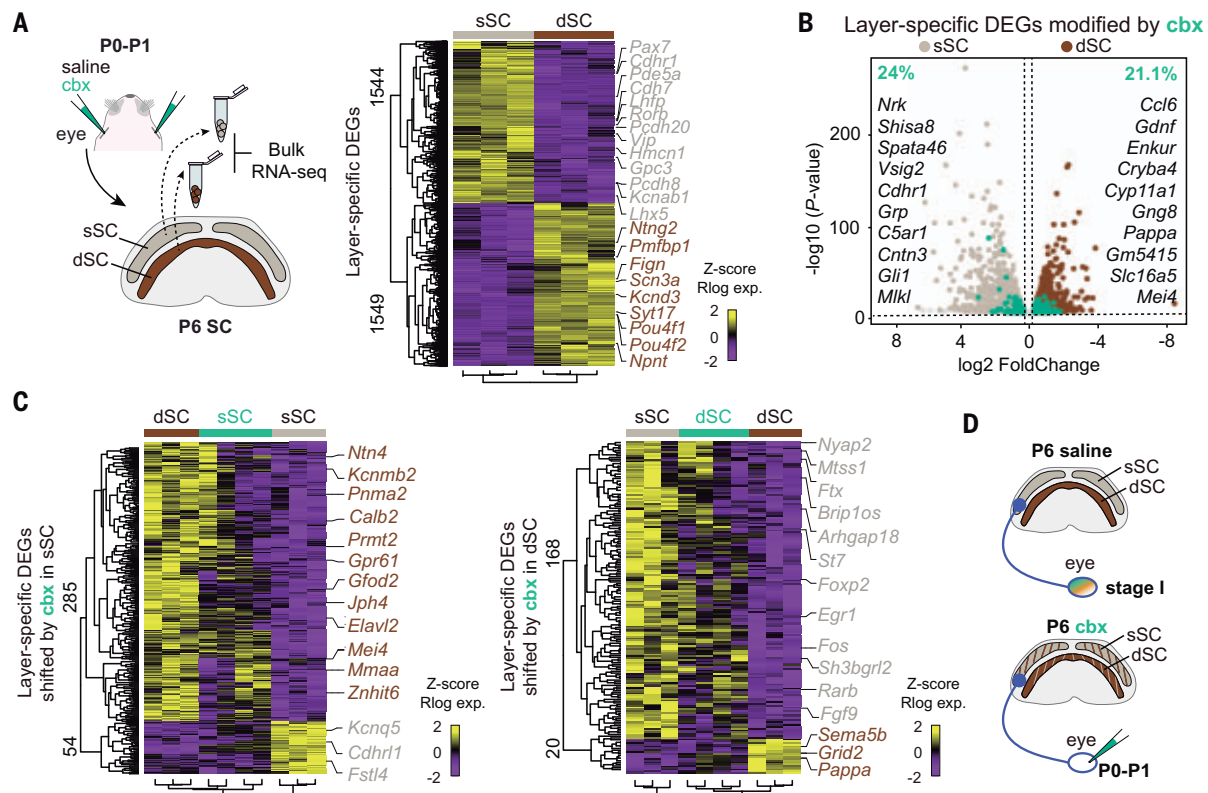


Fig. 4. Transcriptomic SC alterations following blockade of perinatal retinal waves. (A) (Left) Scheme of the RNA-seq experiments of sSC and dSC tissue from P6 mice treated with saline and *cbx* at P0-P1. (Right) Heatmap of normalized, regularized logarithm (Rlog) z-score of expression, and unbiased clustering of significant DEGs between the sSC and dSC in saline-treated mice. Each row represents a gene, and the columns are biological replicates. The color code indicates the normalized expression for up-regulated genes in yellow versus down-regulated genes in purple. Highlighted genes are those previously identified as

layer-specific markers. (B) Volcano plot showing the significance and *P* value distribution of DEGs. The light brown and dark brown dots indicate sSC and dSC DEGs, respectively, and the green dots and the percentages indicate layer-specific DEGs shifted by *cbx*, with the top 10 protein coding genes listed in every region. (C) Heatmaps of the normalized regularized logarithm (Rlog) z-score of expression and unbiased clustering of layer-specific DEGs whose expression was modified by *cbx* in the sSC and dSC regions. (D) Scheme summarizing the data.

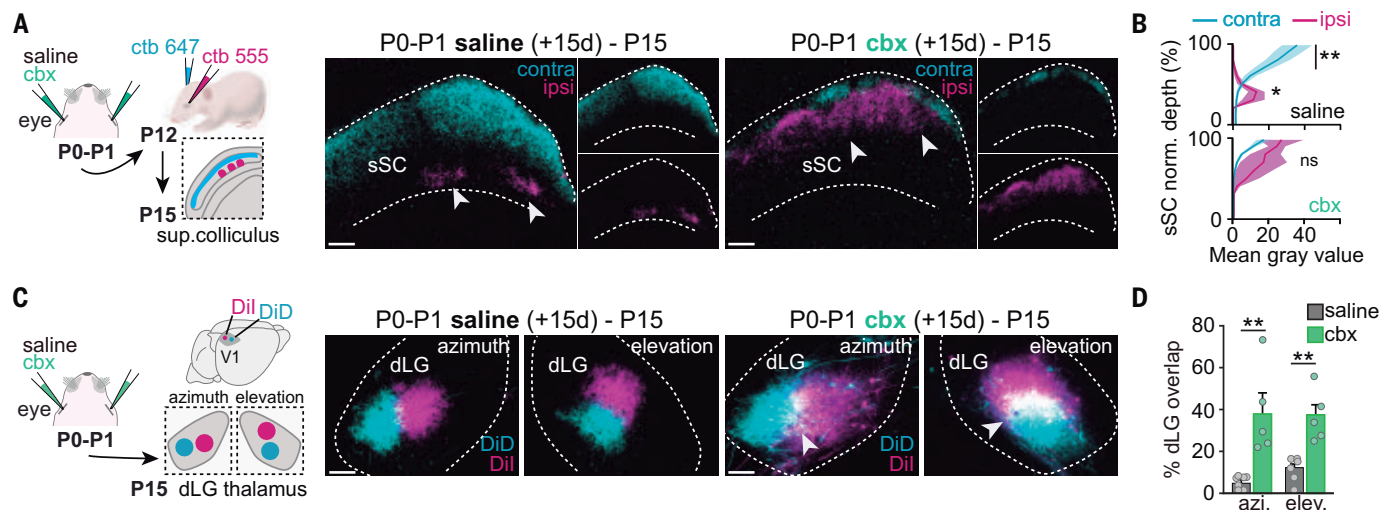


Fig. 5. Long-term alterations in eye-specific segregation and retinotopy after blockade of perinatal retinal waves. (A) (Left) Experimental design. (Right) Coronal view of the SC showing axons from the ipsilateral (CTB-555) and contralateral (CTB-647) eye at P15 in saline- and *cbx*-treated mice. (B) Quantification of the data in (A) (contralateral, *n* = 10 saline, *n* = 6 *cbx*; ipsilateral, *n* = 7 saline, *n* = 5 *cbx*). (C) (Left) Experimental design. (Right)

Coronal view of the dLG showing back label from DiI and DiD crystals in V1 at P15 in saline- and *cbx*-treated mice. (D) Quantification of the data shown in (C) (azimuth, *n* = 7 saline, *n* = 5 *cbx*; elevation, *n* = 6 saline, *n* = 5 *cbx*). Scale bars, 100 μ m. The bold lines in (B) indicate the mean, and the shading indicates the SEM. Bar graphs show the mean \pm SEM. ns, not significant; **P* < 0.05, ***P* < 0.01.

previously identified as layer-specific markers, including those encoding transcription factors such as *Rorb* and *Barhl1* in the sSC layer or *Pou4f1* and *Pou4f2* in the dSC layer (18, 19). To determine whether *cbx* may influence SC layer-specific genes, we compared the RNA-seq data between mice that received saline or *cbx* and found that *cbx* significantly modified 24% (370 genes) of the sSC-specific genes and 21.1% (326 genes) of the dSC-specific genes (Fig. 4B, fig. S9B, and table S2). Among these, *cbx* induced the expression of a large proportion of the dSC-specific genes (285 out of 326 genes) in the sSC layer, and that of sSC-specific genes (168 out of 370 genes) in the dSC layer. Likewise, it provoked the down-regulation of layer-specific gene expression to levels resembling those in the other layer (Fig. 4C and fig. S9, C and D). Together, these results demonstrate that the somatosensory and visual molecular identity of SC layers was altered by the blockade of stage I retinal waves (Fig. 4D).

The alterations to the modality-specific identity of sSC and dSC may somehow affect the stereotypic organization of incoming inputs to these layers. Within the visual system, retinocollicular axons are organized in eye-specific segregated clusters in the sSC (7, 20), and therefore, we tested whether eye-specific segregation is disrupted in *cbx*-treated mice. Cholera toxin subunit B (CTB) injection into the eyes of perinatally *cbx*-treated mice (fig. S10A) showed a compromised eye-specific segregation in the sSC at P15. Whereas in the saline condition, contralateral and ipsilateral axons segregated into dorsal and ventral sSC compartments, respectively, the ipsilateral axons in *cbx*-treated mice invaded the dorsal compartment and mingled with the contralateral axons (Fig. 5, A and B, and movies S12 and S13). In addition, small dye crystals placed in V1 at the azimuth and elevation axis at this stage also showed alterations in the fine-scale organization of the geniculo-cortical pathway (Fig. 5, C and D, and fig. S10, B to D). Together, these results demonstrate that early perturbations in retinal activity leads to long-lasting circuit reconfiguration at central stations within the visual pathway.

Discussion

Our findings demonstrate that visual and somatosensory pathways emerge as multimodal circuits, and that during perinatal life, they segregate in a manner that is orchestrated in the SC. The multimodal-to-unimodal transition requires a reconfiguration of intracollicular circuits at birth, in which dSC layers disconnect from the sSC layers. This reconfiguration drives the specificity of sensory circuits, so that whisker pad stimulation exclusively triggers S1 responses in the cortex after birth. The switch from multimodal to unimodal requires early retinal activity because perturbation of stage I

retinal waves prevents the reconfiguration of the circuits in the SC and leads to the extension of the multimodal phase into postnatal life. Therefore, these data broaden our understanding of retinal wave function by revealing their instructive role in the acquisition of sensory modality specificity, which is beyond their classic role in the postnatal refinement of visual circuits (21–25).

The segregation of visual from somatosensory systems must occur in a limited developmental window because any delay in this segregation will cause long-lasting changes in the intramodal organization of visual circuits. The mechanisms that mediate the final closing of the multimodal phase in embBE and *cbx*-treated mice remain unexplored, although they may include the influence of passive whisking during the first days of life (26) or the progressive assembly of inhibitory cells into the networks of the SC, as described for cortical networks (27). A longitudinal analysis of both the molecular identity of collicular neurons and the maturation of their connectivity in physiological and in manipulated scenarios will help identify the cell types and potential factors involved in this circuit segregation and plasticity.

Last, our findings reveal that the SC, a highly conserved structure in vertebrates (28, 29), participates in the construction of brain regions that appeared more recently in phylogenetic terms such as the neocortex, a role that goes far beyond the SC's well-established sensorimotor and multimodal integrative functions (30). From the phylogenetic perspective, it has been stated that the visual cortex has inherited an increasing number of functions from the SC related to the processing of visual features (31–33). Our results spotlight the ontogenetic perspective, in which the developing SC exerts a master control on cortical specification and configuration of visual circuits. Thus, we believe that a deeper understanding of the functional development of phylogenetically ancient structures is crucial to understand how the neocortex is formed and its functional areas are specified.

REFERENCES AND NOTES

1. B. Tasic et al., *Nature* **563**, 72–78 (2018).
2. C. R. Cadwell, A. Bhaduri, M. A. Mostajo-Radji, M. G. Keefe, T. J. Nowakowski, *Neuron* **103**, 980–1004 (2019).
3. A. Simi, M. Studer, *Curr. Opin. Neurobiol.* **53**, 96–102 (2018).
4. F. J. Martini, T. Guillamón-Vivancos, V. Moreno-Juan, M. Valdeolmillos, G. López-Bendito, *Neuron* **109**, 2519–2534 (2021).
5. Z. Molnár, H. J. Luhmann, P. O. Kanold, *Science* **370**, eabb2153 (2020).
6. N. Antón-Bolaños et al., *Science* **364**, 987–990 (2019).
7. P. Godement, J. Salaün, M. Imbert, *J. Comp. Neurol.* **230**, 552–575 (1984).
8. M. A. Edwards, V. S. Caviness Jr., G. E. Schneider, *J. Comp. Neurol.* **248**, 395–409 (1986).
9. M. A. Edwards, G. E. Schneider, V. S. Caviness Jr., *J. Comp. Neurol.* **248**, 410–421 (1986).
10. V. Moreno-Juan et al., *Nat. Commun.* **8**, 14172 (2017).

11. J. Cang, D. A. Feldheim, *Annu. Rev. Neurosci.* **36**, 51–77 (2013).
12. M. Ahmadiou, L. S. Zweifel, J. A. Heimel, *Nat. Commun.* **9**, 3895 (2018).
13. A. G. Blankenship, M. B. Feller, *Nat. Rev. Neurosci.* **11**, 18–29 (2010).
14. W. T. Wong, J. R. Sanes, R. O. Wong, *J. Neurosci.* **18**, 8839–8852 (1998).
15. J. B. Ackman, T. J. Burbridge, M. C. Crair, *Nature* **490**, 219–225 (2012).
16. A. A. Penn, P. A. Riquelme, M. B. Feller, C. J. Shatz, *Science* **279**, 2108–2112 (1998).
17. C. Sun, C. M. Speer, G. Y. Wang, B. Chapman, L. M. Chalupa, *J. Neurophysiol.* **100**, 3253–3263 (2008).
18. Z. Xie et al., *eLife* **10**, e69825 (2021).
19. A. Zeisel et al., *Cell* **174**, 999–1014.e22 (2018).
20. T. A. Seabrook, T. J. Burbridge, M. C. Crair, A. D. Huberman, *Annu. Rev. Neurosci.* **40**, 499–538 (2017).
21. T. J. Burbridge et al., *Neuron* **84**, 1049–1064 (2014).
22. J. B. Ackman, M. C. Crair, *Curr. Opin. Neurobiol.* **24**, 166–175 (2014).
23. C. L. Torborg, M. B. Feller, *Prog. Neurobiol.* **76**, 213–235 (2005).
24. J. Cang et al., *Neuron* **48**, 797–809 (2005).
25. H. P. Xu et al., *Neuron* **70**, 1115–1127 (2011).
26. A. Tiriak, B. D. Uitermarkt, A. S. Fanning, G. Sokoloff, M. S. Blumberg, *Curr. Biol.* **22**, 2075–2080 (2012).
27. L. Modol et al., *Neuron* **105**, 93–105.e4 (2020).
28. J. Cang, E. Savier, J. Barchini, X. Liu, *Annu. Rev. Vis. Sci.* **4**, 239–262 (2018).
29. M. A. Basso, P. J. May, *Annu. Rev. Vis. Sci.* **3**, 197–226 (2017).
30. T. Isa, E. Marquez-Legorreta, S. Grillner, E. K. Scott, *Curr. Biol.* **31**, R741–R762 (2021).
31. L. Zhaoping, *Curr. Opin. Neurobiol.* **40**, 94–102 (2016).
32. R. Beltramo, M. Scanziani, *Science* **363**, 64–69 (2019).
33. L. L. Glickfeld, M. H. Histed, J. H. Maunsell, *J. Neurosci.* **33**, 19416–19422 (2013).

ACKNOWLEDGMENTS

We thank L. M. Rodríguez, R. Susin, and B. Andrés for their technical support; S. Martínez for providing the *Engrailed 1-Cre* mouse; and S. Jurado for the plasmid used to generate the lentivirus-EGFP. We thank D. Jabaoud, J. López-Atalaya, and B. Berninger for critical reading of the manuscript and the members of López-Bendito's laboratory for stimulating discussions. **Funding:** This work was supported by the European Research Council (ERC-2014-CoG-647012), the Spanish Ministry of Science, Innovation and Universities (PGC2018-096631-B-I00), a Severo Ochoa Grant (SEV-2017-0723), and the European Research Council (ERC-2020-StG-950013). **Author contributions:** T.G.-V. and G.L.-B. designed the experiments. T.G.-V. and F.J.M. performed the analysis of the activity data. T.G.-V. conducted all the meso-scale calcium imaging in vivo. J.A.M.-B. and M.A.-M. performed the tracing experiments. M.A.-M. performed the bulk-sequence experiments, and L.P.-A. performed the bioinformatics analysis. F.J.M. adapted and developed the Matlab codes for the analysis. G.L.-B. acquired the funding, and T.G.-V., F.J.M., M.V., and G.L.-B. wrote the paper. **Competing interests:** The authors have no competing interests to declare. **Data and materials availability:** All the data are available in the main text or the supplementary materials. The RNA-seq data generated in this study has been deposited in the NCBI Gene Expression Omnibus repository under accession GSE198112 (<https://www.ncbi.nlm.nih.gov/geo/query/acc.cgi?acc=GSE198112>). **License information:** Copyright © 2022 the authors, some rights reserved; exclusive licensee American Association for the Advancement of Science. No claim to original US government works. <https://www.science.org/about/science-licenses-journal-article-reuse>

SUPPLEMENTARY MATERIALS

science.org/doi/10.1126/science.abq2960
Materials and Methods
Figs. S1 to S11
References (34–38)
MDAR Reproducibility Checklist
Movies S1 to S13
Tables S1 and S2

Submitted 10 April 2022; accepted 21 July 2022
10.1126/science.abq2960

PLANT SCIENCE

Soybean photosynthesis and crop yield are improved by accelerating recovery from photoprotection

Amanda P. De Souza¹, Steven J. Burgess^{1,2}, Lynn Doran¹, Jeffrey Hansen¹, Lusya Manukyan¹, Nina Maryn³, Dhananjay Gotarkar², Lauriebeth Leonelli^{1,4}, Krishna K. Niyogi^{3,5}, Stephen P. Long^{1,6*}

Crop leaves in full sunlight dissipate damaging excess absorbed light energy as heat. This protective dissipation continues after the leaf transitions to shade, reducing crop photosynthesis. A bioengineered acceleration of this adjustment increased photosynthetic efficiency and biomass in tobacco in the field. But could that also translate to increased yield in a food crop? Here we bioengineered the same change into soybean. In replicated field trials, photosynthetic efficiency in fluctuating light was higher and seed yield in five independent transformation events increased by up to 33%. Despite increased seed quantity, seed protein and oil content were unaltered. This validates increasing photosynthetic efficiency as a much needed strategy toward sustainably increasing crop yield in support of future global food security.

The number of people affected by food insufficiency continues to grow (1). Projections clearly show that food supply is not increasing fast enough to guarantee food security. As a result, it is expected that more than 840 million people worldwide will be undernourished by 2030. Providing seed that can achieve higher yield per unit land area is an effective way to reduce this food shortage, provide food security to the poorest, and avoid yet more land being brought into production. Improving photosynthesis has been suggested as a major opportunity to gain the needed jump in yield potential (2).

Plants dissipate potentially damaging excess absorbed light energy in full sunlight by inducing a mechanism termed nonphotochem-

ical quenching (NPQ) (3). This process is essential in avoiding the formation of reactive oxygen species that would damage the photosynthetic apparatus (4). However, NPQ mechanisms are slow to relax following the frequent sun-shade transitions that occur within crop canopies. This results in a substantial loss of photochemical energy (i.e., between 7.5 and 30%) that could otherwise be used for photosynthesis (5, 6). For soybean crop canopies, this slow NPQ relaxation upon sun-shade transitions was calculated to cost >11% of daily carbon assimilation (7).

NPQ combines several different mechanisms that vary in relaxation kinetics during sun-shade transitions (8, 9). Energy-dependent quenching (qE) is the major and most rapidly

induced component, initiated within seconds up to a few minutes upon transfer of leaves to high light (3, 10). The induction of qE during exposure to high light requires acidification of the thylakoid lumen to activate violaxanthin de-epoxidase (VDE), which converts violaxanthin to zeaxanthin via the intermediate antheraxanthin in the VAZ xanthophyll cycle (11). When the leaf transitions back to low light, the reverse reaction converts zeaxanthin back to violaxanthin on a much slower time scale via the activity of zeaxanthin epoxidase (ZEP) (12). Photosystem II (PSII) subunit S (PsbS) is also implicated in qE modulation of NPQ (13), causing PSII-associated antennae to undergo a conformational change. Zeaxanthin accumulation is also responsible for a more slowly induced and relaxing NPQ component that is independent from both PsbS and lumen acidification. This component, termed zeaxanthin-dependent quenching (qZ), is where zeaxanthin binds to light-harvesting complex proteins and is induced during the first ~8 to 10 min of high light (3).

¹Carl R Woese Institute for Genomic Biology, University of Illinois at Urbana-Champaign, Urbana, IL, USA. ²Department of Plant Biology, Morrill Hall, University of Illinois at Urbana-Champaign, Urbana, IL, USA. ³Howard Hughes Medical Institute, Department of Plant and Microbial Biology, University of California, Berkeley, CA, USA. ⁴Department of Agricultural and Biological Engineering, University of Illinois at Urbana-Champaign, Urbana, IL, USA. ⁵Molecular Biophysics and Integrated Bioimaging Division, Lawrence Berkeley National Laboratory, Berkeley, CA, USA. ⁶Lancaster Environment Centre, Lancaster University, Lancaster, UK. *Corresponding author. Email: slong@illinois.edu

Fig. 1. Protein expression, yield, and seed composition in engineered soybeans. (A) Representative immunoblots comparing the protein abundance of wild-type (WT) and eight independent transgenic soybean lines expressing *AtVDE*, *AtPsbS*, and *AtZEP* (VPZ) grown in the field at Urbana, IL, USA. Band corresponding to *AtPsbS* is the lower band; 30 μ g of total soluble protein was loaded per well; Coomassie Blue-stained gel (CB) is presented to show uniformity of loading. Immunoblots of all biological replicates are shown in figs. S1 and S2 for 2020, and in figs. S3 to S9 for 2021. (B) Seed yield in tonnes per hectare ($t \cdot ha^{-1}$) obtained at final harvest in 2020. (C) Protein, oil, fiber, and ash content in percentage of dry mass of seeds in 2020. Given the high similarity between biological replicates, statistical differences were obtained, even though most were <1% different from WT. These statistical differences are for protein between WT and ND-18-56, YZ-19-8A, and ND-18-44; for oil between WT and ND-18-56, YZ-26-1C, and ND-17-20; for fiber between WT and ND-18-56 and ND-17-20; and for ash, between WT and ND-18-56. Given the small magnitude of difference, these are very unlikely to have any physiological meaning. Bars and values are the mean (± 1 SE). Asterisks indicate significant differences between WT and VPZ transgenic line (** $P < 0.05$, * $P < 0.1$; $n = 15$ experimental blocks).

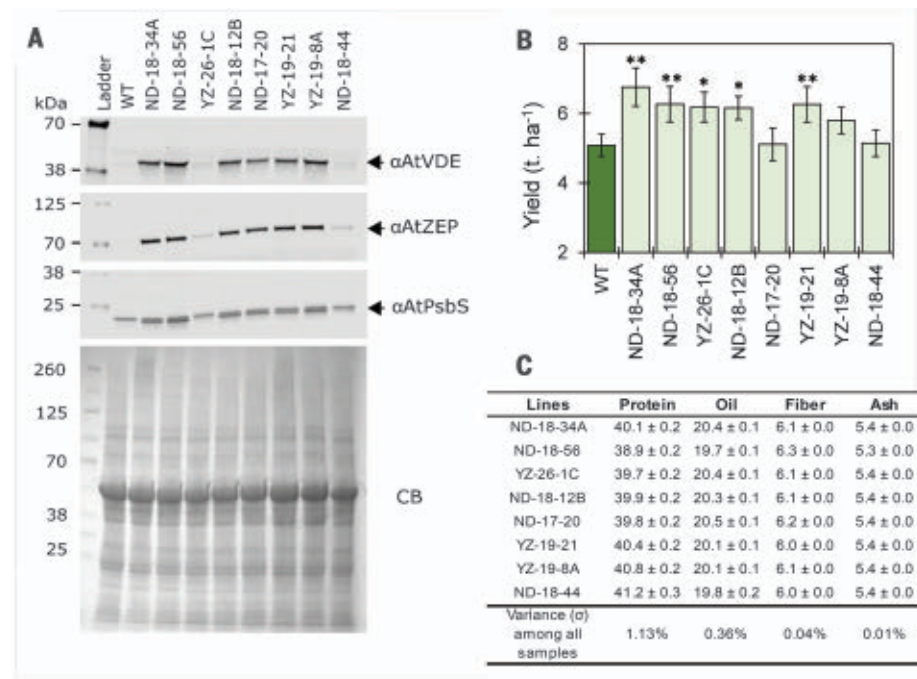
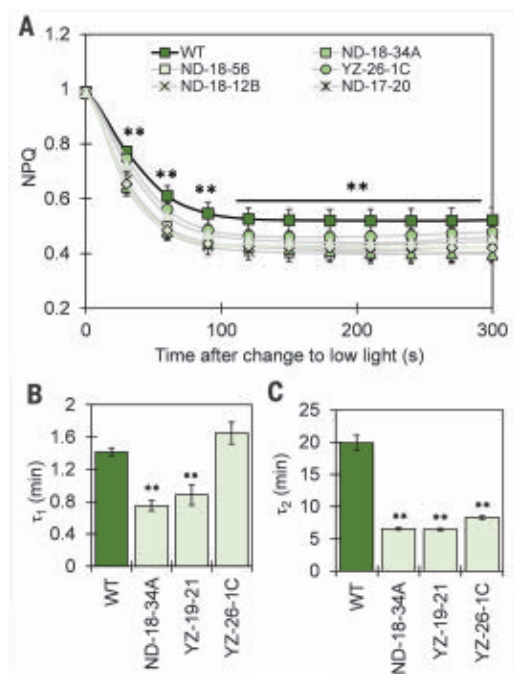


Fig. 2. Relaxation of NPQ on high- to low-light transitions.

(A) Relaxation of NPQ in the last of five cycles of 4 min under high light ($2000 \mu\text{mol m}^{-2} \text{s}^{-1}$ PFD) followed by 3 min under low light ($200 \mu\text{mol m}^{-2} \text{s}^{-1}$ PFD) in wild-type (WT) and independent transgenic soybean lines expressing *AtVDE*, *AtPsbS*, and *AtZEP* (*VPZ*) grown in the field at Urbana, IL, USA in 2020. NPQ throughout the five cycles is shown in fig. S12. Values were normalized to NPQ in high light to allow easier comparison among lines; points shown are means (± 1 SE) for each time point ($n = 8$ biological replicates). (B) Mean (± 1 SE) of the time constants (τ) of the fast (τ_1) and (C) medium (τ_2) relaxing components of NPQ in field-grown plants in 2021. Time constants were obtained by fitting a double exponential curve (8) to the time course of NPQ relaxation ($n = 16$ biological replicates). Semi-log plot of the NPQ values used for these calculations is shown in fig. S13. Asterisks indicate significant difference (** $P < 0.05$) between WT and transgenic lines.



Up-regulation of *VDE*, *PsbS*, and *ZEP* (*VPZ*) in tobacco significantly accelerated the violaxanthin xanthophyll cycle (VAZ), leading to faster induction and relaxation of NPQ. This increased the efficiency of CO_2 assimilation and electron transport through PSII in fluctuating light conditions, without altering photosynthetic efficiency at steady state. In replicated field trials, shoot biomass production was increased 14 to 21% across three independent transgenic events (14). However, a study in transgenic *Arabidopsis thaliana* (*At*) containing the *VPZ* expression cassette failed to show increased biomass accumulation. This observed discrepancy was suggested to be due to negative effects of faster relaxation on photoprotection, or the result of feedback controls related to lack of sink strength (15). Others have claimed that increases in biomass in *VPZ* tobacco can be due to reasons other than photosynthesis such as changes in hormone levels (16) or suggested that sink limitations will prevent any realization of increased seed yield in food crops (17–19). To test whether a yield increase could be achieved in a major agronomical crop, we introduced the *VPZ* construct into soybean [*Glycine max* (Gm)]. In terms of total global production, soybean is the fourth most important grain crop and the most important single source of vegetable protein.

Results

Engineered acceleration of NPQ relaxation increases soybean yield

During the summers of 2020 and 2021, field experiments were performed in Urbana, IL, USA to test the impact of the *VPZ* construct

on photosynthesis, growth, and seed yield in independent transgenic lines of T_4 and T_5 homozygote progeny of soybean (cv. Maverick). Maverick is an elite soybean genotype that is resistant to stress conditions and has been used as a proof of concept of different transgenes (20–22) because of its amenability to genetic transformation.

AtVDE, *AtPsbS*, and *AtZEP* protein and mRNA were detected in all transgenic lines in both years and at different stages of plant development (Fig. 1A, figs. S1 to S9, and table S1). The *PsbS* antibody detected both native *GmPsbS* and the transgenic *AtPsbS* proteins. The *AtPsbS* protein was observed as a lower band just below 23 kDa on a Western blot, which was absent in wild-type (WT) samples (Fig. 1A and figs. S1 to S9). Transgene expression was variable with the lowest abundance observed in YZ-26-1C and ND-18-44 lines in both protein and RNA levels (Fig. 1A and table S1). As might be expected, the ratio of increases in each of the three proteins appears more important than the total increase (fig. S10). For instance, YZ-26-1C had low overall increases and showed a 21.7% yield increase, whereas ND-17-20 had high amounts of protein without a significant increase in yield (Fig. 1, A and B). This is consistent with the mathematical simulations that show that the ratio of expression of *VDE*, *ZEP*, and *PsbS* is more important in achieving altered NPQ kinetics than is absolute abundance (fig. S10).

In 2020, the overexpression of *VPZ* transgenes led to a significantly higher seed yield (Fig. 1B). Of eight independent transgenic lines, five showed a significant increase in seed

yield, and none showed a lower yield. The yield increase averaged across these five transgenic lines was 24.5% compared to the WT with the largest difference being observed for the line ND-18-34A (+33%). Higher yields were due to a higher seed number per plant (fig. S11A). Except for the line YZ-19-21 that showed greater seed mass, seeds from transgenic lines were overall smaller than WT (fig. S11B). The same trend was observed during 2021 on number and size of seeds (fig. S12, A and B), although those differences did not translate into a significantly higher seed yield at the end of the 2021 season (fig. S12C). Increased seed production in 2020 was achieved with less than 1.3% change in protein and oil content, and most other components of seed quality (Fig. 1C and table S2). Similar results were obtained for seeds produced in 2021 (tables S2 and S3).

Did the overexpression of *AtVDE*, *AtPsbS*, and *AtZEP* (i.e., *VPZ* genes) lead to a faster NPQ relaxation and higher photosynthetic efficiency in soybean? As observed in tobacco (14), the overexpression of these three transgenes in soybean accelerated the relaxation of NPQ during sun-to-shade transitions (Fig. 2), resulting in increased photosynthetic efficiency under fluctuating light (Fig. 3). The difference in NPQ relaxation was assessed by comparing the normalized NPQ values at different time points or the time constant of NPQ components after the transition from high to low light. In both years, NPQ relaxation was faster in all transgenic lines (Fig. 2). Between 90 and 300 s after the sun-shade transition, reduction in NPQ across transgenic lines during 2020 was 11 to 23% greater than in WT (Fig. 2A). Similarly, in 2021, the fast (τ_1) and medium (τ_2) relaxing time constants for NPQ relaxation were 37 to 67% smaller in the transgenic lines than in WT; i.e., relaxed more rapidly (Fig. 2, B and C, and fig. S13).

Although all transgenic lines showed faster NPQ relaxation rates, the amplitude of NPQ varied between lines. For instance, ND-18-34A and YZ-19-21 had significantly higher NPQ under high light, whereas YZ-26-1C had NPQ values similar to those of the WT under the same conditions (fig. S14). The increased NPQ levels under high light did not confer any benefit to the plants, because the photoprotection index (23) did not differ throughout the day between any of the *VPZ* lines and WT (fig. S15).

Effects of the engineered change beyond yield

The overexpression of *VPZ* genes in soybean led to an overall reduction in levels of violaxanthin in ND-18-34A and YZ-19-21 with a concomitant increase in zeaxanthin in the periods of high light exposure (i.e., 2 p.m.) (figs. S16, A and C, and S17). Levels of antheraxanthin in all transgenic lines did not change relative to WT (fig. S16B). Differences

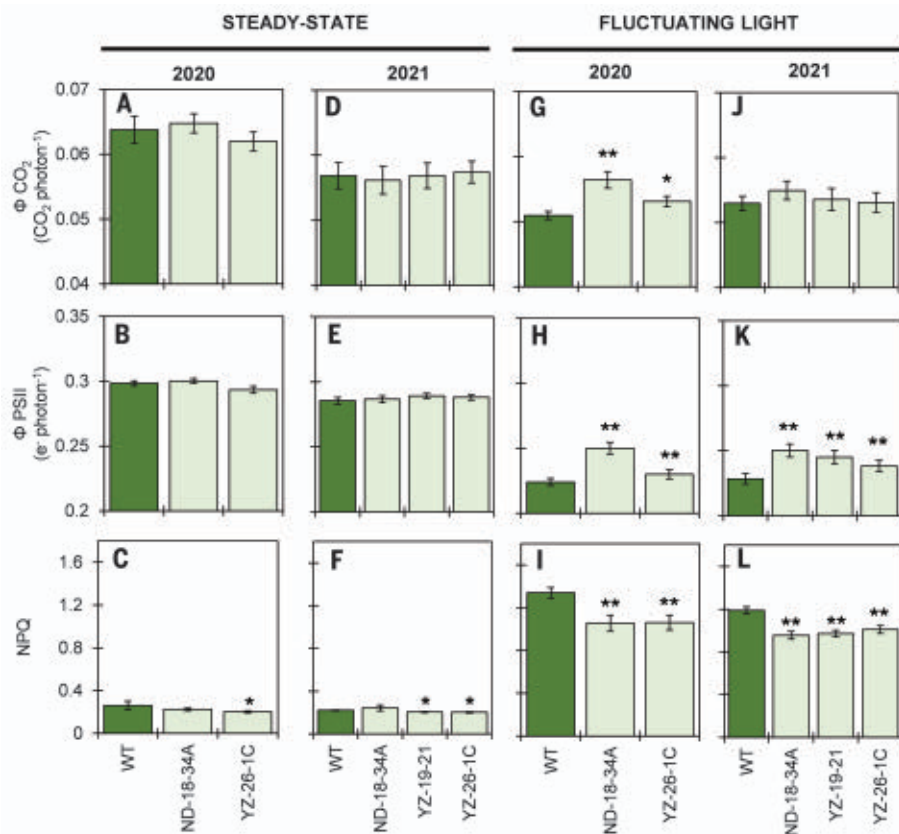


Fig. 3. Photosynthetic efficiency in steady-state and fluctuating light. (A and D) Quantum efficiency of CO_2 assimilation (ΦCO_2) under steady-state light. (B and E) Quantum efficiency of linear electron transport (ΦPSII) under steady-state light. (C and F) Average NPQ corresponding to A – B and D – E, respectively. Panels (G to L) are, respectively, the equivalent measures under fluctuating light. Data are for wild-type (WT) and soybean lines expressing AtVDE, AtPsbS, and AtZEP (VPZ) grown in the field at Urbana, IL, USA during 2020 and 2021. Bars are the mean (± 1 SE) for measurements made during vegetative and seed-filling stages ($n = 16$ biological replicates). Asterisks indicate significant differences between WT and VPZ transgenic lines (** $P < 0.05$; * $P < 0.1$). The separate values for each developmental stage are listed in table S4.

in zeaxanthin accumulation altered the de-epoxidation state (DES) in the VPZ lines. Whereas YZ-26-1C had a lower DES throughout the day, ND-18-34A and YZ-19-21 showed an increase in DES at mid-day in relation to the WT, but a faster decrease in DES in the late afternoon (fig. S16D). In both soybean and tobacco, VPZ expression was associated with faster epoxidation of zeaxanthin, faster τ_1 and τ_2 recovery, and less residual NPQ after transition from excess light to limiting light. Apparently, unlike tobacco, soybean has a second xanthophyll cycle, the lutein epoxide cycle (LxL cycle), which converts lutein epoxide into lutein during exposure to high light. The LxL cycle is catalyzed by the same enzymes as the VAZ cycle (24) and similarly contributes to the photoprotection mechanism, but is typically present only in trace amounts in those plant species examined (24–26). Here, overexpression of VPZ genes increased lutein epoxide levels relative to WT with a concomitant decrease of lutein and an average reduction of

5% in DES related to the lutein epoxide cycle (LxL DES; fig.S18). Introduction of the LxL cycle in *Arabidopsis* generated plants that had increased photosynthetic efficiency over the WT (27). Thus, activation of the LxL cycle in the VPZ soybean could potentially contribute to the phenotypes observed in the VPZ transgenic lines. However, epoxidation of lutein is significantly slower than that of zeaxanthin (28, 29) and would not explain the observed faster relaxation of NPQ.

Changes in photosynthetic efficiency were evaluated through the response of photosynthesis to different light levels under steady-state and fluctuating light conditions (Fig. 3). At steady state, there were no differences between transgenic lines and WT in quantum efficiencies of CO_2 assimilation (ΦCO_2) or of linear electron transport (ΦPSII) in 2020 (Fig. 3, A and B) and 2021 (Fig. 3, D and E). Under fluctuating light, ΦCO_2 was significantly increased by 1 to 10% relative to WT across the two years (Fig. 3, G and J). In parallel, ΦPSII

in fluctuating light was increased 2.5 to 11.5% (Fig. 3, H and K). These increases were consistent with those observed previously in tobacco (14). Consistent with the increase in ΦCO_2 and ΦPSII under fluctuating light, NPQ values in these fluctuating light conditions averaged 21% lower in 2020 (Fig. 3I) and 17% lower in 2021 (Fig. 3L) relative to WT. Increased photosynthetic efficiency did not alter plant growth, plant development, or stem biomass (figs. S19 to S21). Carbon and nitrogen ratio (C/N) and phosphorus levels in leaves during vegetative and reproductive stages or in seeds were not different between WT and transgenic lines (fig. S22), suggesting that the increase in photosynthetic efficiency did not alter nutrient contents per unit mass.

Weather may affect the yield response

So, how did the faster NPQ relaxation and increased photosynthetic efficiency promoted by the overexpression of VPZ genes lead to a higher seed production in 2020? Accelerating the rates of NPQ relaxation can only benefit productivity when there are fluctuations in light (Fig. 3) (14). Thus, it is expected that VPZ plants exposed to a larger number of sun-to-shade transitions during their growth will have an advantage over plants exposed to a lower number of those transitions. As evidenced by our 2020 field season findings, the VPZ plants significantly outperformed WT while yield gains were lacking in 2021. Strong interannual variation in seed production has been observed in other transgenic yield traits (30), so what may explain the difference between years in our study? First, in 2021, a severe storm just before the critical stage of seed filling lodged the crop, causing upper leaves to lie on lower leaves in the canopy, leading many to be permanently shaded and so, lacking the sunflecking that would have occurred in an upright canopy. Second, sun-shade transitions caused by intermittent cloud cover and of the duration in which photosynthesis would benefit from the bioengineered increase in NPQ relaxation were 20% fewer in 2021 compared to 2020 (fig. S23).

The number of pods produced by VPZ plants shows further evidence that the leaves of the middle canopy are important for the observed increase in yield in VPZ soybean. The number of pods in soybean is determined during the period from beginning of flowering to the beginning of seed filling (31) and shows a linear and positive correlation with canopy photosynthesis (32, 33). At harvest in 2021, transgenic plants had on average 13% more pods than WT (fig. S24F), indicating that prior to the lodging, VPZ soybeans were on track for a higher seed yield than WT plants in terms of pod numbers. However, at harvest, the number of pods with four seeds, typically the highest number, was lower in the transgenic lines

compared to WT, whereas the number of 0-seed and 2-seed pods was higher (fig. S24, A, C, and E). Although the number of seeds per pod in soybean has high heritability (34), reduced number of seeds per pod and increased abortion occur when photosynthate availability becomes limiting (35, 36).

In conclusion, the overexpression of *AtVDE*, *AtPsbS*, and *AtZEP* in soybean promoted acceleration of NPQ relaxation with a concomitant improvement in photosynthetic efficiency under fluctuating light over 2 years in field trials. By accelerating NPQ relaxation, an average seed yield increase of 24.5% across five independent events was observed in 2020. This is equivalent to the average biomass increase achieved previously for tobacco plants. This demonstrates that under field conditions, direct bioengineering of increased photosynthetic efficiency leads to increased yield in replicated plots in a major food and feed crop. Further, in line with agronomic practice, no nitrogen fertilizer was added to the soybean crop. Yet, more seed was produced without any reduction in protein, nitrogen, and oil content, showing this as a means to the sustainable increases in yield urgently needed to help ensure future food security.

REFERENCES AND NOTES

- FAO, IFAD, UNICEF, WFP, WHO, "The State of Food Security and Nutrition in the World 2020. Transforming food systems for affordable healthy diets." (FAO, Rome, 2020).
- S. P. Long, A. Marshall-Colon, X. G. Zhu, *Cell* **161**, 56–66 (2015).
- R. Bassi, L. Dall'Osto, *Annu. Rev. Plant Biol.* **72**, 47–76 (2021).
- S. P. Long, S. Humphries, P. G. Falkowski, *Annu. Rev. Plant Physiol. Plant Mol. Biol.* **45**, 633–662 (1994).
- C. Werner, R. Ryel, O. Correia, W. Beyschlag, *Plant Cell Environ.* **24**, 27–40 (2001).
- X. G. Zhu, D. R. Ort, J. Whitmarsh, S. P. Long, *J. Exp. Bot.* **55**, 1167–1175 (2004).
- Y. Wang, S. J. Burgess, E. M. de Becker, S. P. Long, *Plant J.* **101**, 874–884 (2020).
- S. P. Long et al., *Annu. Rev. Plant Biol.* **73**, 617–648 (2022).
- A. Malnoë, *Environ. Exp. Bot.* **154**, 123–133 (2018).
- A. V. Ruban, *Plant Physiol.* **170**, 1903–1916 (2016).
- B. Demmig, K. Winter, A. Krüger, F. C. Czygan, *Plant Physiol.* **84**, 218–224 (1987).
- B. Demmig-Adams, *Biochim. Biophys. Acta Bioenerg.* **1020**, 1–24 (1990).
- X.-P. Li et al., *Nature* **403**, 391–395 (2000).
- J. Kromdijk et al., *Science* **354**, 857–861 (2016).
- A. Garcia-Molina, D. Leister, *Nat. Plants* **6**, 9–12 (2020).
- E. Kaiser, V. Correa Galvis, U. Armbruster, *Biochem. J.* **476**, 2725–2741 (2019).
- M. R. Smith, I. M. Rao, A. Merchant, *Front. Plant Sci.* **9**, 1889 (2018).
- T. R. Sinclair, T. W. Rufty, R. S. Lewis, *Trends Plant Sci.* **24**, 1032–1039 (2019).
- J. L. Araus, R. Sanchez-Bragado, R. Vincente, *J. Exp. Bot.* **72**, 3936–3955 (2021).
- W.-S. Kim, J. Sun-Hyung, N. W. Oehle, J. M. Jez, H. B. Krishnan, *Sci. Rep.* **10**, 14989 (2020).
- P. T. Do et al., *BMC Plant Biol.* **19**, 311 (2019).
- S. K. Guttikonda et al., *Mol. Biol. Rep.* **41**, 7995–8008 (2014).
- A. V. Ruban, E. H. Murchie, *Biochim. Biophys. Acta* **1817**, 977–982 (2012).
- J. I. Garcia-Plazaola, S. Matsubara, C. B. Osmond, *Funct. Plant Biol.* **34**, 759–773 (2007).
- A. Young, in *Carotenoids in Photosynthesis*, A. Young, G. Britton, Eds. (Chapman & Hall, 1993), pp. 16–71.
- S. Matsubara et al., *Funct. Plant Biol.* **36**, 20–36 (2009).
- L. Leonelli, M. D. Brooks, K. K. Niyogi, *Proc. Natl. Acad. Sci. U.S.A.* **114**, E7002–E7008 (2017).
- S. Matsubara et al., *J. Exp. Bot.* **56**, 461–468 (2005).
- B. Förster, B. J. Pogson, C. B. Osmond, *Plant Physiol.* **156**, 393–403 (2011).
- J. Wu et al., *Proc. Natl. Acad. Sci. U.S.A.* **116**, 23850–23858 (2019).
- W. Fehr, C. Caviness, "Stages of soybean development," *Special Report* (Iowa State University, Ames, Iowa, USA, 1977).
- D. Egli, Z. Yu, *Crop Sci.* **31**, 439–442 (1991).
- R. van Roekel, L. Purcell, M. Salmerón, *Field Crops Res.* **182**, 86–97 (2015).
- R. Jain, A. Joshi, H. Chaudhary, A. Dashora, C. Khatik, *Legume Res.* **41**, 532–536 (2018).
- X. Liu et al., *Plant Soil Environ.* **52**, 150–158 (2006).
- T. J. Johnson, J. W. Pendleton, D. B. Peters, D. R. Hicks, *Crop Sci.* **9**, 577–581 (1969).

ACKNOWLEDGMENTS

We thank D. Drag, B. Harbaugh, B. Thompson, and R. Edquiang for help with the maintenance of the field experiment and its final harvest; D. Tarantino and A. Altschuler for help with biomass and growth data collection; and K. X. Chan, M. Burns, M. Blaszyński, and J. Milo for help with collection and processing of leaf tissue for molecular analysis. **Funding:** Supported by the Bill & Melinda Gates Foundation; Foundation for Food and Agriculture Research; and the UK Foreign, Commonwealth & Development Office grant OPPI1722157. S.J.B. was supported by a Carl R. Woese Institute for Genomic Biology Fellowship, and N.M. was supported by the National Science Foundation Graduate Research Fellowship Program grant DGE 1752814. Any opinions, findings, and conclusions or recommendations expressed in this material are those of the author(s) and do not necessarily reflect the views of the NSF. K.K.N. is an investigator of the Howard Hughes Medical Institute. **Author contributions:** A.D.S., S.J.B., and S.L. conceived the project. S.J.B., A.D.S., and L.M. performed initial molecular

and physiological screening of the transgenic plants. A.D.S., S.J.B., J.H., L.D., N.M., D.G., and L.L. performed experiments and collected data. A.D.S. and S.J.B. analyzed the data. K.K.N. and S.L. supervised research. A.D.S. wrote the manuscript with input from S.J.B., L.L., K.K.N., and S.L. **Competing interests:** L.L., K.N. and S.L. are inventors on a patent "Transgenic plants with increased photosynthesis efficiency and growth" WO2017205834A1. All authors declare no other competing interests. **Data and materials availability:** All data are presented in the paper or the supplementary materials. Seeds of the lines included in this article are available under a material transfer agreement with the Universities of Illinois at Urbana-Champaign and California at Berkeley and as long as supplies remain. **License information:** This article is subject to HHMI's Open Access to Publications policies. HHMI lab heads have previously granted a nonexclusive CC BY 4.0 license to the public and a sublicensable license to HHMI in their research articles. Pursuant to those licenses, the author-accepted manuscript of this article can be made freely available under a CC BY 4.0 license immediately upon publication.

SUPPLEMENTARY MATERIALS

science.org/doi/10.1126/science.adc9831
Material and Methods
Figs. S1 to S26
Tables S1 to S11
Datasets D1 to D27
References (37–48)
MDAR Reproducibility Checklist

Submitted 12 May 2022; accepted 12 July 2022
10.1126/science.adc9831

REPORTS

THERMOELECTRICS

Flexible thermoelectrics based on ductile semiconductors

Qingyu Yang^{1,2†}, Shiqi Yang^{1,2†}, Pengfei Qiu^{1,3*}, Liming Peng^{1,2}, Tian-Ran Wei⁴, Zhen Zhang⁵, Xun Shi^{1,2,4*}, Lidong Chen^{1,2*}

Flexible thermoelectrics provide a different solution for developing portable and sustainable flexible power supplies. The discovery of silver sulfide–based ductile semiconductors has driven a shift in the potential for flexible thermoelectrics, but the lack of good p-type ductile thermoelectric materials has restricted the reality of fabricating conventional cross-plane π -shaped flexible devices. We report a series of high-performance p-type ductile thermoelectric materials based on the composition-performance phase diagram in AgCu(S_xSe_{1-x}) pseudoternary solid solutions, with high figure-of-merit values (0.45 at 300 kelvin and 0.68 at 340 kelvin) compared with other flexible thermoelectric materials. We further demonstrate thin and flexible π -shaped devices with a maximum normalized power density that reaches 30 $\mu\text{W cm}^{-2} \text{K}^{-2}$. This output is promising for the use of flexible thermoelectrics in wearable electronics.

Wearable electronics are widely used in communication, medicine, health care, and other areas, but their usage is greatly limited by the low capacity and short lifetime of power supply from chemical batteries (1). Therefore, portable, reliable, super-thin, and sustainable flexible power supplies are in great demand (2–4). Flexible thermoelectric (TE) generators have the advantages of small volume, no moving parts, continuously working in all weather

conditions, and high reliability. They can directly convert the heat from the human body to electricity with a temperature gradient of several kelvins (or less) through the Seebeck effect, providing in principle a self-power supply solution for wearable electronics (5–7). The performance of flexible TE devices (Fig. 1A), which is usually characterized by the normalized power density ($P_{\text{max}}/A\Delta T^2$, where P_{max} is the maximum power output, A is the cross-sectional area, and ΔT is the temperature difference

across the device) (8), is strongly dependent on the TE figure of merit (zT) of n- and p-type TE materials, as well as device integration technology. Currently, three typical approaches are used to fabricate high-performance flexible thermoelectrics. The first approach is to deposit classic brittle, inorganic, thin-film TE materials such as Bi_2Te_3 -based alloys on flexible substrates or scaffolds (9–17). However, because of the difficulty in achieving dense films and/or in precisely controlling the chemical compositions, the material's zT obtained by this approach is usually low. This leads to a small normalized power density (Fig. 1B). The second approach is directly using organic TE materials to fabricate flexible devices (12). Unfortunately, because of their poor electrical transport, the zT s of organic TE materials (Fig. 1C), particularly for n-type materials (13, 14), are much lower than those for state-of-the-art inorganic TE materials. This also leads to very low normalized power density, on the order of 10^{-3} to $10^{-5} \mu\text{W cm}^{-2} \text{K}^{-2}$ (Fig. 1B) (15, 16).

Recently discovered ductile TE semiconductors provide a third avenue for high-performance flexible thermoelectrics because of their excellent metal-like machinability. Inorganic Ag_2S -based materials and InSe single crystals with good ductility and tunable electrical properties have been reported (17, 18). After this development, $\text{Ag}_2(\text{Se}, \text{Te}, \text{S})$ -based materials with both high zT and inherent ductility were developed, pushing the zT value of n-type ductile TE materials to 0.44 at room temperature, which is among the highest values in flexible TE materials (Fig. 1C). However, the current zT value of p-type ductile TE materials at room temperature is still very poor (0.01 at 300 K) (19). Thus, the fabrication of flexible TE devices based on ductile TE semiconductors with the conventional, and often most practical, cross-plane π -shaped structure (Fig. 1A) are quite challenging because of the lack of good p-type ductile TE materials. We report a series of high-performance p-type ductile TE materials, $\text{AgCu}(\text{Se}, \text{S}, \text{Te})$ pseudoternary solid solutions, with a zT of 0.45 at 300 K and 0.68 at 340 K, attractive values for flexible TE materials (Fig. 1C). We successfully developed the

flexible π -shaped TE devices (0.3 mm thick) based on inorganic materials, with a maximum normalized power density up to $30 \mu\text{W cm}^{-2} \text{K}^{-2}$. This value is about four times that of the Bi_2Te_3 -based TE devices (20–22), at least four orders of magnitude higher than that of organic-based flexible TE devices (Fig. 1B) (13–15), and one order of magnitude higher than that of other low-grade heat-to-electricity conversion technologies (8, 23, 24).

The phase diagram and chemical defects are quite complicated in the $(\text{Ag}, \text{Cu})\text{-X}$ ($\text{X} = \text{S}, \text{Se}, \text{Te}$) family, which includes Ag_2X , AgCuX , and their derivatives, and also provides an opportunity for tuning their transport and mechanical properties through composition and structure modulation. Generally, Ag-contained compounds are n-type, whereas Cu-contained ones are p-type; a high S content or a high Ag content tends to result in ductile materials, whereas high Se and Te contents or high Cu content are prone to be brittle materials (19). We focused on $\text{AgCu}(\text{Se}, \text{S}, \text{Te})$ pseudoternary solid solutions in an attempt to find high-performance p-type ductile TE materials. We use a composition-performance phase diagram to show the relationship that we obtained experimentally (Fig. 2). Additional details on the crystal structures and phase compositions of

$\text{AgCu}(\text{Se}, \text{S}, \text{Te})$ pseudoternary solid solutions can be found in the supplementary materials and in Figs. S1 to S3. AgCuSe is brittle and shows n-type conduction, with a maximum bending deformation of $\sim 3\%$ in the three-point bending test (fig. S4A). Alloying Te in AgCuSe does not change the brittle feature (fig. S4A) but does convert the electrical conduction to p-type. The boundary of p/n conduction in $\text{AgCu}(\text{Se}_{1-y}\text{Te}_y)$ is $\sim y = 0.5$ (fig. S5). Upon further alloying a tiny amount of S in $\text{AgCu}(\text{Se}_{1-y}\text{Te}_y)$ ($0.7 \geq y \geq 0.5$), a “brittle-ductile” transition occurred, and we obtained ductile p-type materials in $\text{AgCu}(\text{Se}_{1-y-x}\text{S}_x\text{Te}_y)$ with x between 0.05 and 0.08 and y between 0.5 and 0.7 (Fig. 2).

$\text{AgCuSe}_{0.3-x}\text{S}_x\text{Te}_{0.7}$ ($x = 0.06$ and 0.08) are ductile and plastic materials, as determined with mechanical tests (Fig. 3, A and B). Room temperature compression and three-point bending tests showed strain values of $>30\%$ and 10% , respectively, which are comparable to ductile Ag_2S and its derivatives (17, 25, 26). We also observed a similar metal-like ductility in other $\text{AgCu}(\text{Se}_{1-y-x}\text{S}_x\text{Te}_y)$ pseudoternary solid solutions over a broad composition range, such as $\text{AgCuSe}_{0.5-x}\text{S}_x\text{Te}_{0.5}$ ($x = 0.05$ and 0.07), $\text{AgCuSe}_{0.35}\text{S}_{0.05}\text{Te}_{0.6}$ (fig. S4B), and cation-deficient $(\text{AgCu})_{1-\delta}\text{Se}_{0.22}\text{S}_{0.08}\text{Te}_{0.7}$ ($\delta = 0.002$) (Fig. 3, A and B).

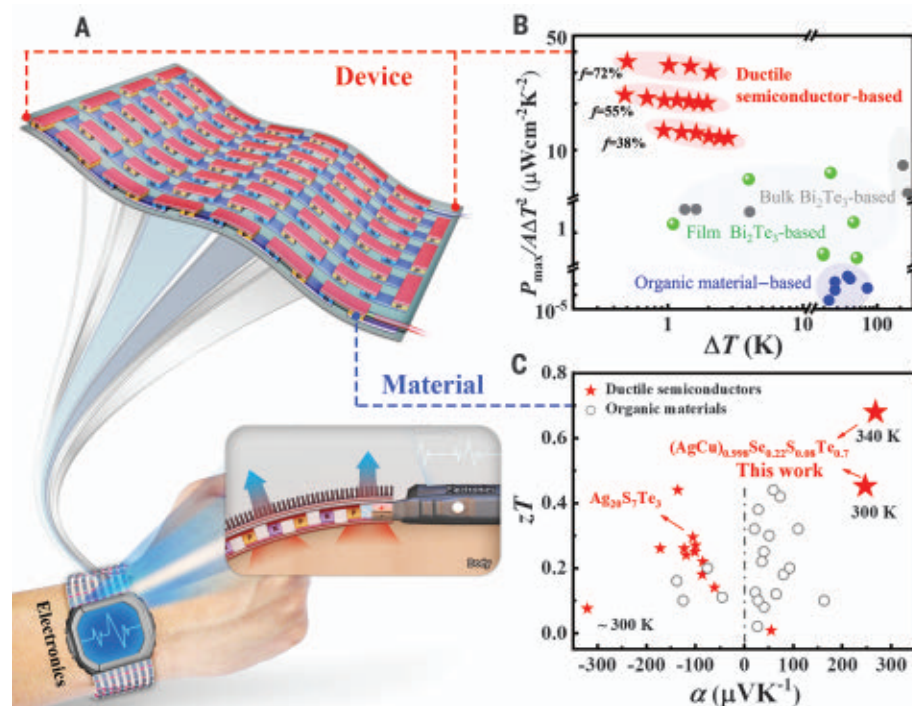


Fig. 1. Flexible TE materials and devices. (A) Schematics of flexible thermoelectrics that could be used in wearable electronics with a cross-plane π -shaped structure. (B) Normalized power density ($P_{\max}/A\Delta T^2$) of flexible TE devices achieved by using ductile materials with different filling factors (f). Data for Bi_2Te_3 film-based devices, organic material-based devices, and traditional Bi_2Te_3 -based bulk devices are included for comparison. (C) Room-temperature thermoelectric figure of merit (zT) and Seebeck coefficient (α) for ductile inorganic materials and organic-based materials. The detailed data in (B) and (C) and the related references are listed in tables S1 and S2.

¹State Key Laboratory of High Performance Ceramics and Superfine Microstructure, Shanghai Institute of Ceramics, Chinese Academy of Sciences, Shanghai 200050, China.

²Center of Materials Science and Optoelectronics Engineering, University of Chinese Academy of Sciences, Beijing 100049, China. ³School of Chemistry and Materials Science, Hangzhou Institute for Advanced Study, University of Chinese Academy of Sciences, Hangzhou 310024, China.

⁴State Key Laboratory of Metal Matrix Composites, School of Materials Science and Engineering, Shanghai Jiao Tong University, Shanghai 200240, China. ⁵Division of Solid-State Electronics, Department of Electrical Engineering, Uppsala University, 75103 Uppsala, Sweden.

*Corresponding author. Email: qiupf@mail.sic.ac.cn (P.Q.); xshi@mail.sic.ac.cn (X.S.); cld@mail.sic.ac.cn (L.C.)

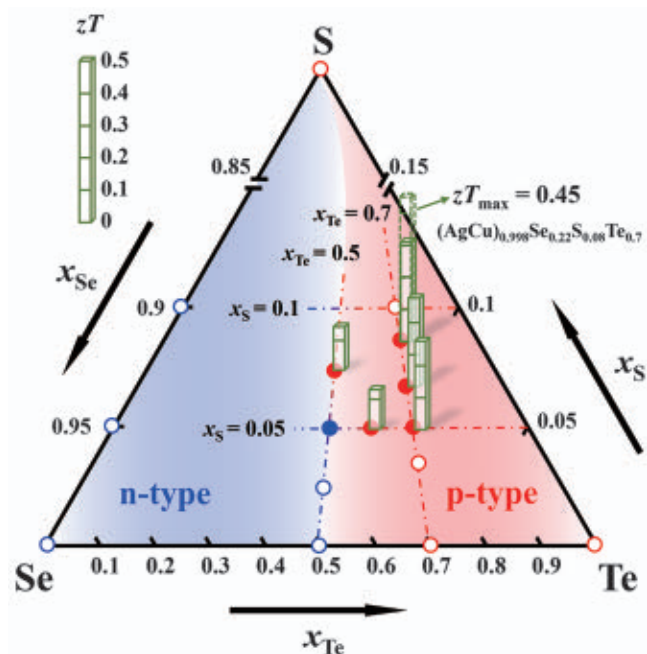
†These authors contributed equally to this work.

We used $\text{AgCuSe}_{0.22}\text{S}_{0.08}\text{Te}_{0.7}$, which has the highest zT among all of the fabricated p-type materials tested (Fig. 2), as the typical example to perform the detailed microstructure characterization. After compression tests, we observed obvious slip bands along different directions on the material's surface, indicating the existence of multiple slip bands (Fig. 3C). Inside each slip band, we observed numerous finer slip lines (fig. S6A). The space between the nearby parallel slip lines was dozens of nanometers. In addition, numerous dimples with sizes ranging from several hundred nanometers to several micrometers appeared on the fracture surface of $\text{AgCuSe}_{0.22}\text{S}_{0.08}\text{Te}_{0.7}$ (Fig. 3D), which was different from the river-like patterns on the fracture surface of brittle $\text{AgCuSe}_{0.3}\text{Te}_{0.7}$ (fig. S6B). Similar to many metals, these dimples are considered to be produced by the nucleation, growth, and aggregation of the microscopic cavity during plastic deformation (27, 28). Because of their good ductility, the $\text{AgCu}(\text{Se},\text{S},\text{Te})$ materials can be easily machined to flexible films with a thickness down to 100 μm (Fig. 3E).

The good ductility of $\text{AgCuSe}_{0.3-x}\text{S}_x\text{Te}_{0.7}$ ($x = 0.06$ and 0.08) comes from the alloyed S, even though the content is very low. The engineering strain was just 3% for S-free $\text{AgCuSe}_{0.3}\text{Te}_{0.7}$ in the three-point bending test, but was substantially enhanced to ~13 and 18% by alloying S contents of 0.06 and 0.08, respectively (Fig. 3F). We observed a similar phenomenon in S-alloyed $\text{AgCuSe}_{0.5}\text{Te}_{0.5}$ (fig. S4, A and B). To understand the underlying reason for this sort of brittle-ductile transition, we calculated the slipping energy barrier (E_b) and cleavage energy (E_c) of S/Te-alloyed AgCuSe . The E_b along the (010)[100] slip system was almost unchanged upon alloying either S or Te; however, the E_c was obviously increased upon alloying S but decreased upon alloying Te (fig. S7). The enhanced ratio of E_c/E_b caused by the increased amount of multicentered and diffused Ag-S bonds (17) is beneficial for the material's slip before fracture.

Beyond the attractive ductility, $\text{AgCuSe}_{0.3-x}\text{S}_x\text{Te}_{0.7}$ ($x = 0.06$ and 0.08) showed p-type conduction with relatively good TE properties. We measured a positive Seebeck coefficient α (fig. S8A) and Hall coefficients R_H (fig. S8B), indicating the p-type conduction behavior. Upon alloying S, the α was enhanced but the electrical conductivity σ was lowered (fig. S8, A and C) because of the lowered hole concentration p_H (fig. S8D). Because the Ag-S bond is more ionic than Ag-Se and Ag-Te bonds, the Cu-deficiency defects were greatly suppressed when alloying S, leading to the decreased reduced Fermi energy (fig. S8E) and hole concentrations. Likewise, both carrier thermal conductivity (κ_C) and lattice thermal conductivity (κ_L) were also reduced upon alloying S (fig. S8F), yielding the lowered thermal con-

Fig. 2. Composition-performance phase diagram of $\text{AgCuSe}-\text{AgCuS}-\text{AgCuTe}$ pseudoternary solid solutions. Columns represent zT at room temperature. Blue and red symbols represent n- and p-type conduction, respectively. Filled circles represent ductile compositions and hollow circles brittle compositions.



ductivity κ (fig. S8G). The power factors ($PF = \alpha^2 \sigma$) of $\text{AgCuSe}_{0.3-x}\text{S}_x\text{Te}_{0.7}$ ($x = 0.06$ and 0.08) were $\sim 3 \mu\text{W cm}^{-1} \text{K}^{-2}$ (fig. S8H), whereas the thermal conductivities κ (fig. S8G) were only ~ 0.3 to $0.4 \text{ W m}^{-1} \text{K}^{-1}$, leading to a zT of up to 0.31 at 300 K (Fig. 3G). Upon further introducing a tiny amount of cation deficiency, we were able to enhance the PF to $5.1 \mu\text{W cm}^{-1} \text{K}^{-2}$ at 300 K (fig. S8H). Although the κ of cation deficient material was slightly enhanced because of the increased κ_C (fig. S8, F and G), the zT was still improved to 0.45 at 300 K and 0.68 at 340 K (Fig. 3G) for $(\text{AgCu})_{0.998}\text{Se}_{0.22}\text{S}_{0.08}\text{Te}_{0.7}$, respectively. Likewise, good reproducibility of TE properties was observed in our ductile TE materials (fig. S9).

The zT values of our ductile semiconductors were much higher than those of organic materials (Fig. 1C), even close to the commercial zone-melted Bi_2Te_3 -based alloys. These high zT values can be mainly attributed to their ultralow κ_L originating from the severe atomic-lattice disorders caused by the complex chemical compositions (29). The κ of ductile $\text{AgCuSe}_{0.3-x}\text{S}_x\text{Te}_{0.7}$ ($x = 0.06$ and 0.08) was much lower than that of the classic Bi_2Te_3 -based materials (1.0 to $1.8 \text{ W m}^{-1} \text{K}^{-1}$ at 300 K) (21), and was even comparable to that of wood (0.1 to $0.3 \text{ W m}^{-1} \text{K}^{-1}$) (30). Such an ultralow κ is helpful for realizing a large temperature gradient across a TE device. In addition, ductile TE materials have larger α and PF than the organic TE materials (Fig. 3H), which is beneficial for achieving high onset voltage with fewer p/n couples in TE devices.

The discovery of high-performance n- and p-type ductile TE materials offers the opportunity to fabricate flexible cross-plane π -shaped TE

devices (Fig. 4A). We selected p-type $(\text{AgCu})_{0.998}\text{Se}_{0.22}\text{S}_{0.08}\text{Te}_{0.7}$ and n-type $\text{Ag}_{20}\text{S}_7\text{Te}_3$ (Fig. 1C) to connect electrically in series and thermally in parallel between two polyimide (PI)-based flexible circuit boards. Taking advantage of the materials' ductility, we cut n- and p-type ultra-thin plates with a thickness of 0.1 mm directly from bulk ingots. The intrinsic brittleness of traditional thermoelectric alloys such as the Bi_2Te_3 -based ones prevents fabricating a similar thickness in these materials. We metallized the thin plates by magnetron sputtering using tungsten (W) and tin (Sn) as contact layers with an electrical contact resistivity (ρ_c) of 19 and $2 \mu\Omega \text{ cm}^2$ for Sn/W/ $(\text{AgCu})_{0.998}\text{Se}_{0.22}\text{S}_{0.08}\text{Te}_{0.7}$ and Sn/W/ $\text{Ag}_{20}\text{S}_7\text{Te}_3$ interfaces (Fig. 4B), respectively. These small ρ_c values, as well as the large thermal conductivities of W and Sn, suggest that the additional thermal resistance introduced by the contact layer was very low. The metallized thin films were cut into the assigned shapes and then soldered onto the Cu/Au electrodes in PI-based flexible circuit boards using a low-temperature solder paste (fig. S10A).

We successfully fabricated a few flexible cross-plane π -shaped TE devices with six-couple $(\text{AgCu})_{0.998}\text{Se}_{0.22}\text{S}_{0.08}\text{Te}_{0.7}/\text{Ag}_{20}\text{S}_7\text{Te}_3$ legs (Fig. 4C). We designed the same dimensions of TE legs but different filling factors (f) with the values of 38, 55, and 72%. The total thickness of our flexible TE was only 0.3 mm with an upper limit of several millimeters, like a normal rigid device. Therefore, the thickness of our flexible device can be freely tuned from 0.3 mm to a few millimeters. We characterized the performance of these devices using a home-made test platform (fig. S10B). We show the

output voltage (V) and output power (P) as a function of current (I) under different ΔT for the device with $f = 72\%$ in Fig. 4D. The device internal resistance (R_{in}) was $\sim 18\text{ m}\Omega$, which is comparable to the theoretical value ($19\text{ m}\Omega$) calculated on the basis of the material's electrical resistance. This R_{in} was at least three orders of magnitude lower than that of flexible organic material-based TE devices (14, 15) and two orders of magnitude lower than that of classic bulk Bi_2Te_3 -based TE devices (fig. S11). Such low R_{in} , caused by the super-thin TE legs, is beneficial for achieving super-high output power P . The open circuit voltage (V_{OC}) and maximum output power ($P_{max} = V_{OC}^2/4R_{in}$) increased with increasing ΔT , reaching 3.7 mV and $203\text{ }\mu\text{W}$ at $\Delta T = 1.5\text{ K}$ (Fig. 4D), respectively. The maximum normalized power density $P_{max}/A\Delta T^2$ was $\sim 30\text{ }\mu\text{W cm}^{-2}\text{ K}^{-2}$, a high value compared with other reported flexible TE devices and even bulk TE devices (Fig. 1B) (14–16, 20–22).

We also tested the performance of the devices with $f = 38\%$ and $f = 55\%$ (fig. S12, A and B). Under similar ΔT , the device with higher f had higher V_{OC}/A and $P_{max}/A\Delta T^2$ (fig. S12, C and D). The $P_{max}/A\Delta T^2$ values were ~ 13 and $20\text{ }\mu\text{W cm}^{-2}\text{ K}^{-2}$ when $f = 38$ and 55% , respectively, still much higher than that of current TE devices (Fig. 1B) (14–16, 20–22). Such ultrahigh performances are mainly caused by the material's high TE figure of merit, short length of TE legs, and low energy loss at the material/electrode interfaces.

The super-thin and highly efficient flexible TE devices developed in this study can be implemented into the Internet of Things, quartz watches, or motion detectors, acting as a charge-free battery to monitor human health or the environment. Toward these potential applications, we fabricated a cross-plane π -shaped TE device including 31-couple ($\text{AgCu}_{0.998}\text{Se}_{0.22}\text{S}_{0.08}\text{Te}_{0.7}/\text{Ag}_{20}\text{S}_7\text{Te}_3$ with $f = 33\%$ (Fig. 4C, right). This device can easily and effectively adhere to the curved surface of human skin using adhesive tape (Fig. 4E). Under an ambient temperature of 298 K and humidity of 42% , directly adhering the device on a human's wrist gave a V_{OC} and P_{max} of 0.2 mV and 70 nW , respectively (fig. S13A). The $P_{max}/A\Delta T^2$ of this device was $\sim 11\text{ }\mu\text{W cm}^{-2}\text{ K}^{-2}$, the same as for the six-couple device with a similar filling factor. By shaking the arms to strengthen the convective heat transfer, the ΔT across the TE device could be enhanced to 0.1 K to yield a V_{OC} and P_{max} of 0.76 mV and $1\text{ }\mu\text{W}$, respectively (fig. S13B). Spraying alcohol on the device's upper surface could cause a large ΔT (0.35 K), yielding a high V_{OC} and P_{max} of 2.5 mV and $13\text{ }\mu\text{W}$, respectively (fig. S13C). In real applications, various heat-dissipation approaches (e.g., copper pipes and graphite sheets) will be applied to further enhance ΔT to 1 to 2 K to reach the threshold

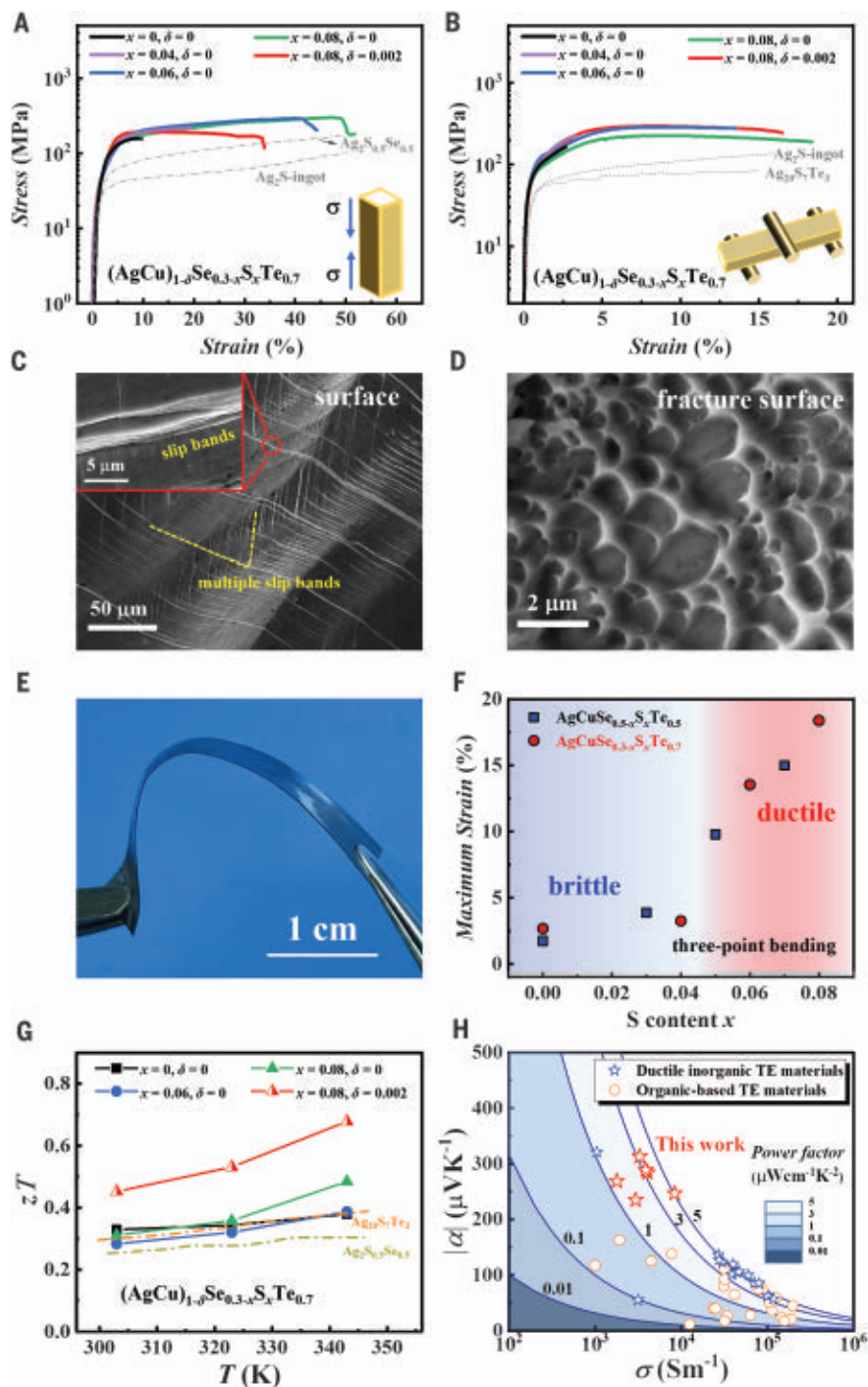


Fig. 3. Mechanical and thermoelectric properties of $(\text{AgCu})_{1-\delta}\text{Se}_{0.3-x}\text{S}_x\text{Te}_{0.7}$. (A and B) Engineering stress-strain curves for compression (A) and bending (B) tests for $(\text{AgCu})_{1-\delta}\text{Se}_{0.3-x}\text{S}_x\text{Te}_{0.7}$ ($x = 0, 0.04, 0.06$, and 0.08 ; $\delta = 0$ and 0.002) at room temperature. Data for Ag_2S and its n-type derivatives are included for comparison (17, 25, 26). (C and D) SEM images of the surface (C) and fracture surface (D) of $\text{AgCuSe}_{0.22}\text{S}_{0.08}\text{Te}_{0.7}$ after the compression test. (E) Optical image of the $\text{AgCuSe}_{0.22}\text{S}_{0.08}\text{Te}_{0.7}$ thin film showing good flexibility. (F) Maximum engineering strains of bending test as a function of S content for $\text{AgCuSe}_{0.5-x}\text{S}_x\text{Te}_{0.5}$ and $\text{AgCuSe}_{0.3-x}\text{S}_x\text{Te}_{0.7}$. (G) Temperature dependence of TE zT for $(\text{AgCu})_{1-\delta}\text{Se}_{0.3-x}\text{S}_x\text{Te}_{0.7}$ ($x = 0, 0.06$, and 0.08 ; $\delta = 0$ and 0.002). (H) Absolute value of Seebeck coefficient (α) as a function of electrical conductivity (σ) for p-type $\text{AgCu}(\text{Se},\text{S},\text{Te})$ ductile TE materials. Data for n-type Ag_2S -based ductile materials and typical organic-based TE materials are included for comparison. The detailed data in (H) and the related references are listed in table S1.

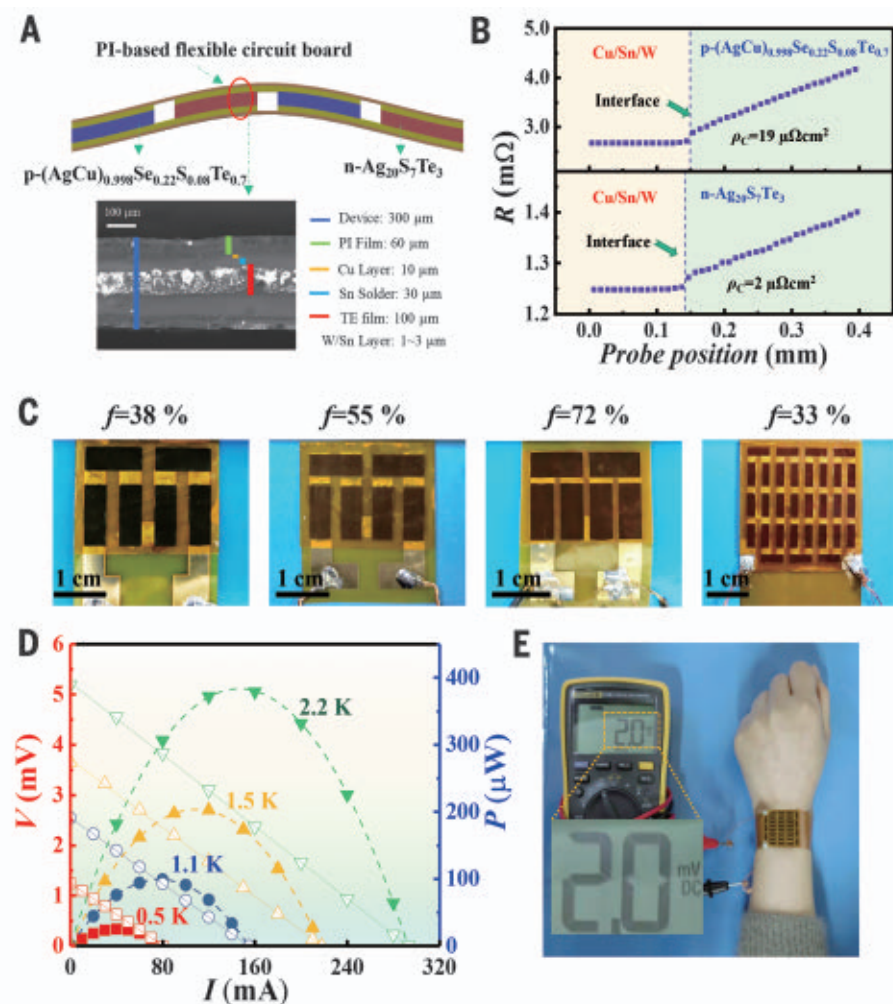


Fig. 4. Super-thin flexible TE devices based on ductile semiconductors. (A) Structure of the π -shaped flexible $(\text{AgCu})_{0.998}\text{Se}_{0.22}\text{S}_{0.08}\text{Te}_{0.7}/\text{Ag}_{20}\text{S}_7\text{Te}_3$ TE device. The bottom panel is the SEM image for the overall cross-section of the flexible device with the thicknesses of each layer labeled. (B) Resistance (R) line scanning across the interface for the p- and n-type TE elements. (C) Optical images of the as-prepared six-couple flexible TE devices with different filling factors ($f = 38, 55$, and 72%) and 31-couple flexible TE devices ($f = 33\%$). (D) Measured output voltage (V) and output power (P) as a function of current (I) under different temperature differences for the six-couple $(\text{AgCu})_{0.998}\text{Se}_{0.22}\text{S}_{0.08}\text{Te}_{0.7}/\text{Ag}_{20}\text{S}_7\text{Te}_3$ flexible TE device with $f = 72\%$. (E) Optical image of the 31-couple flexible TE device adhered on a human's wrist.

of 100 μW , which is strong enough to power many microelectronics such as quartz watches and wireless sensor nodes. Furthermore, the total thickness of our flexible device can be freely tuned for various working conditions with different temperature gradients and working spaces.

We also tested the service stability of our flexible TE device by cyclically bending the 31-couple device with a filling factor of 33% under a bending radius of 15 mm. After bending 500 times, the relative inner resistance ($R_{\text{in}}/R_{\text{in},0}$) was scarcely changed (fig. S13D). A service stability test was also performed in two long-strip-shaped devices with high filling factors of 55 and 71%. The maximum incre-

ment of $R_{\text{in}}/R_{\text{in},0}$ was $<5\%$ after bending 500 times (fig. S13, E to G). These tests indicate that the service stability of our device is acceptable. Furthermore, we found that humidity had little influence on the V_{OC} and P_{max} of the device (fig. S13H).

In summary, we have discovered p-type ductile TE materials with a relatively high TE figure of merit compared with other flexible materials. Coupled with high-performance n-type ductile materials, we successfully developed super-thin flexible TE devices with a conventional π -shape, ultra-high normalized power density, and reasonable service stability. Ductile semiconductors thus provide a different strategy for high-performance flex-

ible thermoelectrics, which can directly and efficiently convert low-grade heat energy such as the heat from human body into useful and sustainable electricity. Our study offers a promising example of applying a self-powered supply technology to wearable electronics.

REFERENCES AND NOTES

1. J. M. Tarascon, M. Armand, *Nature* **414**, 359–367 (2001).
2. S. Park et al., *Nature* **561**, 516–521 (2018).
3. D. P. Dubal, N. R. Chodankar, D. H. Kim, P. Gomez-Romero, *Chem. Soc. Rev.* **47**, 2065–2129 (2018).
4. W. Gao et al., *Nature* **529**, 509–514 (2016).
5. K. Nan et al., *Sci. Adv.* **4**, eaau5849 (2018).
6. C. Wan et al., *Nat. Mater.* **14**, 622–627 (2015).
7. Y. Wang et al., *Adv. Mater.* **31**, e1807916 (2019).
8. X. Shi, J. He, *Science* **371**, 343–344 (2021).
9. Q. Jin et al., *Nat. Mater.* **18**, 62–68 (2019).
10. S. J. Kim et al., *ACS Nano* **10**, 10851–10857 (2016).
11. S. J. Kim, J. H. We, B. J. Cho, *Energy Environ. Sci.* **7**, 1959–1965 (2014).
12. G. H. Kim, L. Shao, K. Zhang, K. P. Pipe, *Nat. Mater.* **12**, 719–723 (2013).
13. C. Y. Yang et al., *Nat. Commun.* **11**, 3292 (2020).
14. Y. Sun et al., *Adv. Mater.* **24**, 932–937 (2012).
15. T. Sun et al., *Nat. Commun.* **11**, 572 (2020).
16. O. Bubnova et al., *Nat. Mater.* **10**, 429–433 (2011).
17. X. Shi et al., *Nat. Mater.* **17**, 421–426 (2018).
18. T. R. Wei et al., *Science* **369**, 542–545 (2020).
19. Z. Gao et al., *Adv. Energy Mater.* **11**, 2100883 (2021).
20. C. S. Kim et al., *ACS Energy Lett.* **3**, 501–507 (2018).
21. R. Deng et al., *Energy Environ. Sci.* **11**, 1520–1535 (2018).
22. F. Suarez et al., *Appl. Energy* **202**, 736–745 (2017).
23. C. G. Han et al., *Science* **368**, 1091–1098 (2020).
24. B. Yu et al., *Science* **370**, 342–346 (2020).
25. J. Liang et al., *Energy Environ. Sci.* **12**, 2983–2990 (2019).
26. S. Yang et al., *Adv. Mater.* **33**, 2007681 (2021).
27. J. P. Bandstra, D. A. Koss, A. Geltmacher, P. Matic, R. K. Everett, *Mater. Sci. Eng. A* **366**, 269–281 (2004).
28. S. He et al., *Sci. Adv.* **6**, eaaz8423 (2020).
29. H. Liu et al., *Nat. Mater.* **11**, 422–425 (2012).
30. B. M. Suleiman, J. Larfeldt, B. Leckner, M. Gustavsson, *Wood Sci. Technol.* **33**, 465–473 (1999).

ACKNOWLEDGMENTS

We thank Z. Zhou for help with crystal structure analysis.

Funding: This work was supported by the National Natural Science Foundation of China (grants 91963208, 52122213, and 51625205), the Shanghai Government (grants 20JC1415100 and JCYJ-SHFY-2022-002), and the CAS-DOE Program of the Chinese Academy of Sciences (grant 121631KYSB20180060). Z.Z. is supported by the Swedish Research Council (grant VR 2018-06030). **Author contributions:** Q.Y. prepared the samples and measured the thermoelectric and mechanical properties. S.Y. and L.P. fabricated the devices and measured the output performance. Q.Y., S.Y., L.P., and T.W. collected the data and interpreted the results under the guidance of P.Q., X.S., and L.C.. Q.Y., S.Y., P.Q., Z.Z., X.S., and L.C. wrote the paper. All authors discussed the results and provided helpful suggestions. **Competing interests:** The authors declare no competing interests. **Data and materials availability:** All data are available in the manuscript or the supplementary materials. **License information:** Copyright © 2022 the authors, some rights reserved; exclusive licensee American Association for the Advancement of Science. No claim to original US government works. <https://www.science.org/about/science-licenses-journal-article-reuse>

SUPPLEMENTARY MATERIALS

science.org/doi/10.1126/science.abq0682
 Materials and Methods
 Supplementary Text
 Figs. S1 to S13
 Tables S1 to S4
 References (31–64)

Submitted 15 March 2022; accepted 28 June 2022
 10.1126/science.abq0682

FLEXIBLE ELECTRONICS

Chip-less wireless electronic skins by remote epitaxial freestanding compound semiconductors

Yeongin Kim^{1,2,3,†}, Jun Min Suh^{1,2,†}, Jiho Shin^{1,2,†}, Yunpeng Liu^{1,2,†}, Hanwool Yeon^{1,2,4}, Kuan Qiao^{1,2}, Hyun S. Kum^{1,2,5}, Chansoo Kim^{1,2}, Han Eol Lee^{1,2,6}, Chanyeol Choi⁷, Hyunseok Kim^{1,2}, Doyoon Lee^{1,2}, Jaeyong Lee¹, Ji-Hoon Kang², Bo-In Park², Sungsu Kang⁸, Jihoon Kim⁸, Sungkyu Kim⁹, Joshua A. Perozek⁷, Kejia Wang^{1,10}, Yongmo Park¹, Kumar Kishen¹, Lingping Kong¹, Tomás Palacios⁷, Jungwon Park^{8,11}, Min-Chul Park¹², Hyung-jun Kim^{12,13}, Yun Seog Lee¹⁴, Kyusang Lee¹⁵, Sang-Hoon Bae^{1,16}, Wei Kong^{1,17}, Jiyeon Han^{18*}, Jeehwan Kim^{1,2,19*}

Recent advances in flexible and stretchable electronics have led to a surge of electronic skin (e-skin)-based health monitoring platforms. Conventional wireless e-skins rely on rigid integrated circuit chips that compromise the overall flexibility and consume considerable power. Chip-less wireless e-skins based on inductor-capacitor resonators are limited to mechanical sensors with low sensitivities. We report a chip-less wireless e-skin based on surface acoustic wave sensors made of freestanding ultrathin single-crystalline piezoelectric gallium nitride membranes. Surface acoustic wave-based e-skin offers highly sensitive, low-power, and long-term sensing of strain, ultraviolet light, and ion concentrations in sweat. We demonstrate weeklong monitoring of pulse. These results present routes to inexpensive and versatile low-power, high-sensitivity platforms for wireless health monitoring devices.

Electronic skin (e-skin)-based health monitoring platforms have recently emerged, including flexible and stretchable sensors (1), electronic circuits (2), and skin-compatible adhesive patches (3, 4) that laminate conformally onto the skin. Their applications include biophysical tracking of fitness and wellness (5), as well as clinical management (4, 6). A key technical requirement for the broader use of e-skins in our daily lives is the capability to communicate data wirelessly. A major issue in conventional wireless e-skins is that they require rigid integrated circuit chips—near-field communication (NFC) or radio frequency identification (RFID) chips, microprocessors, or analog-to-digital converters (ADCs), for example—which can compromise overall flexibility. Moreover, given the power constraint in wireless e-skin systems, the high power consumption by these chips, which contain thousands of transistors (7), often leads to reduced sensitivity (due to the power-sensitivity trade-off in ADCs) (8), substantial heat generation (9), and reduced communication distance (10). To address these issues, inductor-capacitor (LC) resonator-based chip-less wireless e-skin sensors have been studied (11), but demonstrated applications are re-

stricted to strain and pressure sensing with relatively low sensitivity owing to the limitations of capacitive sensor designs.

We report a chip-less wireless e-skin technology based on surface acoustic wave (SAW) sensors that achieves marked improvement in strain sensitivity, power efficiency, versatility as a sensing platform for a broad range of external stimuli, and long-term wearability. This is achieved by integrating a freestanding ultrathin single-crystalline piezoelectric membrane of gallium nitride (GaN) on a flexible patch as the material for passive wireless sensing. The ultrathin GaN epitaxial layers are grown on graphene-coated GaN substrates by remote homoepitaxy and are easily released from the weak graphene-GaN interface by a two-dimensional (2D) material-based layer transfer (2DLT) process (12).

Figure 1A and fig. S1 show schematic illustrations comparing conventional chip-based wireless e-skins and our SAW-based chip-less wireless e-skin (see table S1 for additional details). Chip-based wireless e-skins integrate NFC or RFID chips, circuit elements (diodes, resistors, and capacitors), sensors, and radio frequency antenna on silicone patches (1). The large size and rigidity of these chips compro-

mise conformal lamination of e-skin on skin and necessitate thick silicone patches (300 to 500 μm), which disturb skin function over time owing to sweat impermeability and occlusion. Moreover, they consume substantial power.

In our SAW-based chip-less wireless e-skin, an ultrathin GaN SAW sensor replaces the chips, circuit components, and sensors. The changes in the resonant frequency of the GaN SAW sensor yield information about mechanical, optical, and biochemical stimuli (see supplementary text in the supplementary materials for the detailed mechanism). The ultrathin and light functional layers (GaN and metal electrodes) can be integrated on a thin patch of polydimethylsiloxane (PDMS; $\sim 20\ \mu\text{m}$) with perforations that allow removal of sweat and skin by-products (13), thereby improving the softness, skin-conformability, and long-term wearability compared with chip-based e-skins, while also consuming considerably less power.

Wireless SAW sensors have traditionally relied on thick, non-freestanding GaN films that are tethered to the wafer, which were difficult to integrate on flexible e-skins. We estimated that the GaN film thickness required for conformal skin adhesion is 300 nm (Fig. 1B; see supplementary materials for detailed calculation). Remote epitaxy can yield single-crystalline GaN membranes with a thickness of <300 nm and reduce material cost for GaN films (12).

We successfully performed the remote epitaxy of 200-nm-thick GaN membrane on graphene-coated GaN substrates, followed by exfoliation via 2DLT (fig. S2). High-resolution x-ray diffraction (HRXRD) phi scan data in Fig. 1C shows the perfect single-crystallinity of GaN on graphene. Figure 1D shows cross-sectional transmission electron microscopy (TEM) and associated selective-area diffraction images of the exfoliated GaN membrane on metal support layers indicating solely oriented atomic planes of GaN nanomembrane. Atomic force microscopy analysis (fig. S3) also confirms the atomically flat surface of GaN. These properties are important for high-performance electromechanical and optoelectronic devices. We further verified the capability of our GaN membranes to laminate conformally on skin by attaching them on a skin replica made of Eco-flex silicone [see methods for preparation steps and Fig. 1E for scanning electron microscopy

¹Department of Mechanical Engineering, Massachusetts Institute of Technology, Cambridge, MA 02139, USA. ²Research Laboratory of Electronics, Massachusetts Institute of Technology, Cambridge, MA 02139, USA. ³Department of Electrical Engineering and Computer Science, University of Cincinnati, Cincinnati, OH 45219, USA. ⁴School of Materials Science and Engineering, Gwangju Institute of Science and Technology, Gwangju 61005, South Korea. ⁵Department of Electrical and Electronic Engineering, Yonsei University, Seoul 03722, South Korea. ⁶Division of Advanced Materials Engineering, Jeonbuk National University, Jeonju 54896, South Korea. ⁷Department of Electrical Engineering and Computer Science, Massachusetts Institute of Technology, Cambridge, MA 02139, USA. ⁸School of Chemical and Biological Engineering, Institute of Chemical Process, Seoul National University, Seoul 08826, South Korea. ⁹Department of Nanotechnology and Advanced Materials Engineering, Sejong University, Seoul 05006, South Korea. ¹⁰School of Micro-Nano Electronics, Zhejiang University, Hangzhou 311200 Zhejiang, People's Republic of China. ¹¹Center for Nanoparticle Research, Institute for Basic Science (IBS), Seoul 08826, South Korea. ¹²Post-Silicon Semiconductor Institute, Korea Institute of Science and Technology (KIST), Seoul 02792, South Korea. ¹³Division of Nano and Information Technology, KIST School, Korea University of Science and Technology, Seoul 02792, South Korea. ¹⁴Department of Mechanical Engineering, Seoul National University, Seoul 08826, South Korea. ¹⁵Department of Electrical and Computer Engineering, University of Virginia, Charlottesville, VA 22904, USA. ¹⁶Department of Mechanical Engineering and Materials Science, Institute of Materials Science and Engineering, Washington University in St. Louis, MO 63139, USA. ¹⁷Department of Materials Science and Engineering, Westlake University, Hangzhou 310024 Zhejiang, People's Republic of China. ¹⁸SkinCare Division, Amorepacific R&D Center, Yongin 17074, South Korea. ¹⁹Department of Materials Science and Engineering, Massachusetts Institute of Technology, Cambridge, MA 02139, USA.

*Corresponding author. Email: jeehwan@mit.edu (J.K.); sviviria@amorepacific.com (J.H.) †These authors contributed equally to this work.

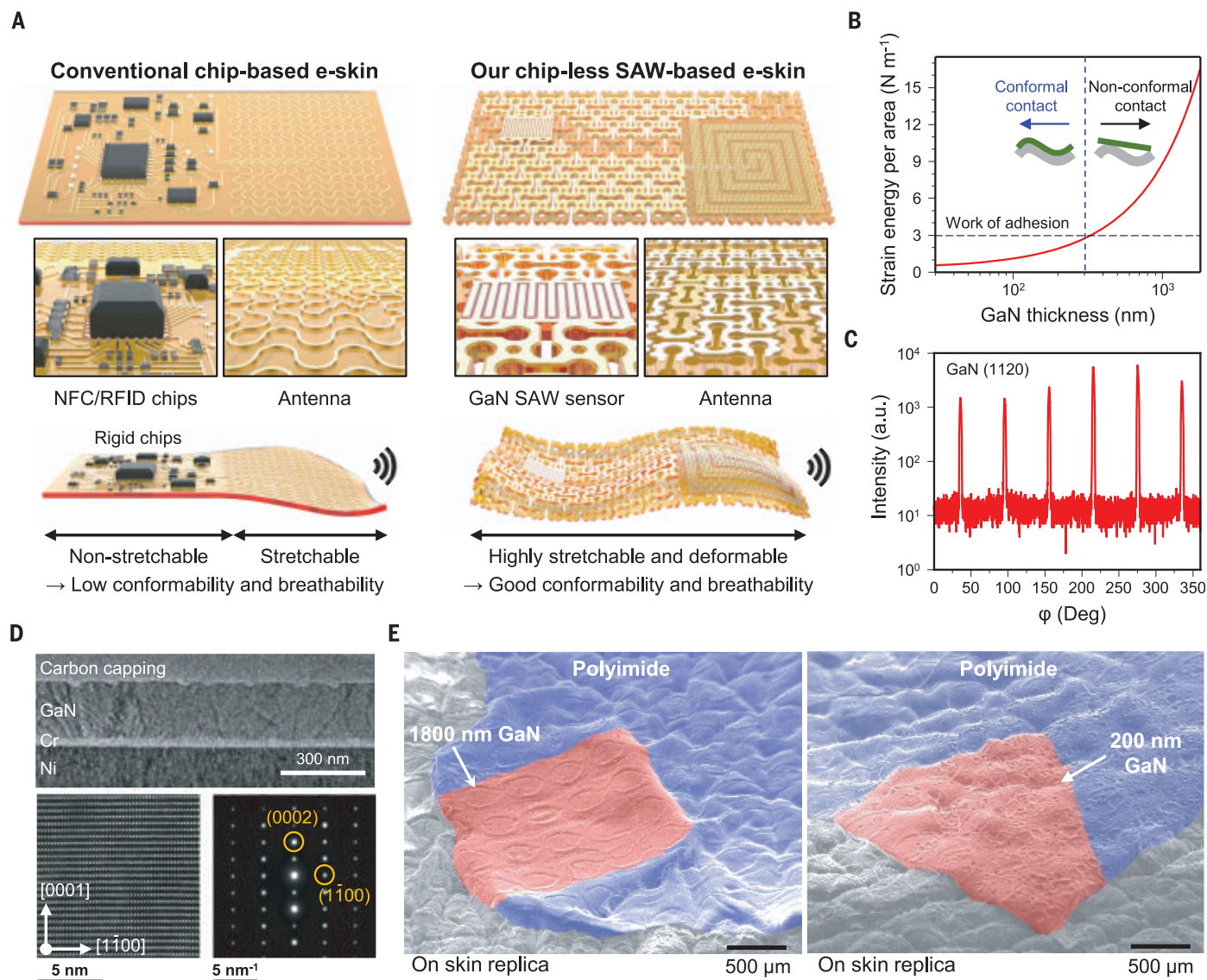


Fig. 1. Chip-less wireless e-skin based on single-crystalline freestanding nano-membranes of GaN and its mechanical properties. (A) Comparison between (left) conventional wireless e-skin based on integrated circuit chips and (right) our chip-less wireless e-skin based on surface acoustic wave (SAW) devices made of GaN freestanding membranes. (B) Estimation of minimum GaN thickness required for conformal lamination on human skin. Strain energies on curved surfaces per area depending on GaN thickness and the work of adhesion of a PDMS skin patch

were calculated and compared. (C) HRXRD phi scan of 200-nm-thick remote epitaxial GaN film. a.u., arbitrary units. (D) TEM image and associated selective-area diffraction images of the freestanding 200-nm-thick GaN nanomembrane. (E) SEM images of GaN e-skins with (left) 1800-nm-thick and (right) 200-nm-thick GaN attached to skin replica samples. The 1800-nm-thick GaN film (left) cannot fully conform to the microscale features of skin, whereas the 200-nm-thick film (right) can deform to follow the pits and curvatures.

(SEM) images]. We integrated our resulting ultrathin GaN membranes into our e-skin (figs. S2 and S4 to S8; see methods for more details).

To study the optoelectronic performance of our GaN nanomembrane device, we fabricated GaN-metal Schottky junction diodes using 200-nm-thick membranes of single-crystalline GaN, obtained by means of remote epitaxy and 2DLT, and polycrystalline GaN, obtained on poor-growth substrates, and compared their ultraviolet (UV) sensitivities. UV radiation is an important health indicator that existing chip-less wireless e-skins based on an LC resonator lack the semiconductor component to

detect. Our UV sensing results (Fig. 2A) indicate a UV responsivity of 10.06 A W^{-1} at 15.90 mW/cm^2 for a single-crystalline GaN diode, which is 37-fold higher than that of a polycrystalline GaN diode. This responsivity is also higher than those reported for e-skin sensors based on polycrystalline inorganic materials (14) or single-crystalline Si, which has poor optical absorption in the UV wavelength regimes (15), and comparable to that of the state-of-the-art single-crystalline GaN UV sensors on “rigid” wafers (16). A single-crystalline GaN diode also exhibits higher UV sensing speed, recovery time, and selectivity (for UV

light over white light) than those of a polycrystalline GaN diode, as illustrated in Fig. 2, B and C.

The excellent piezoelectricity and perfect single-crystallinity of our ultrathin GaN film enable wireless communication without NFC or RFID chips. We conceived our chip-less wireless e-skin by (i) discovering the formation of highly sensitive SAWs on freestanding ultrathin single-crystalline piezoelectric GaN membranes and (ii) reinventing the freestanding SAW device as a biosensing platform. Upon successful lamination on the human body, our e-skin can generate SAW

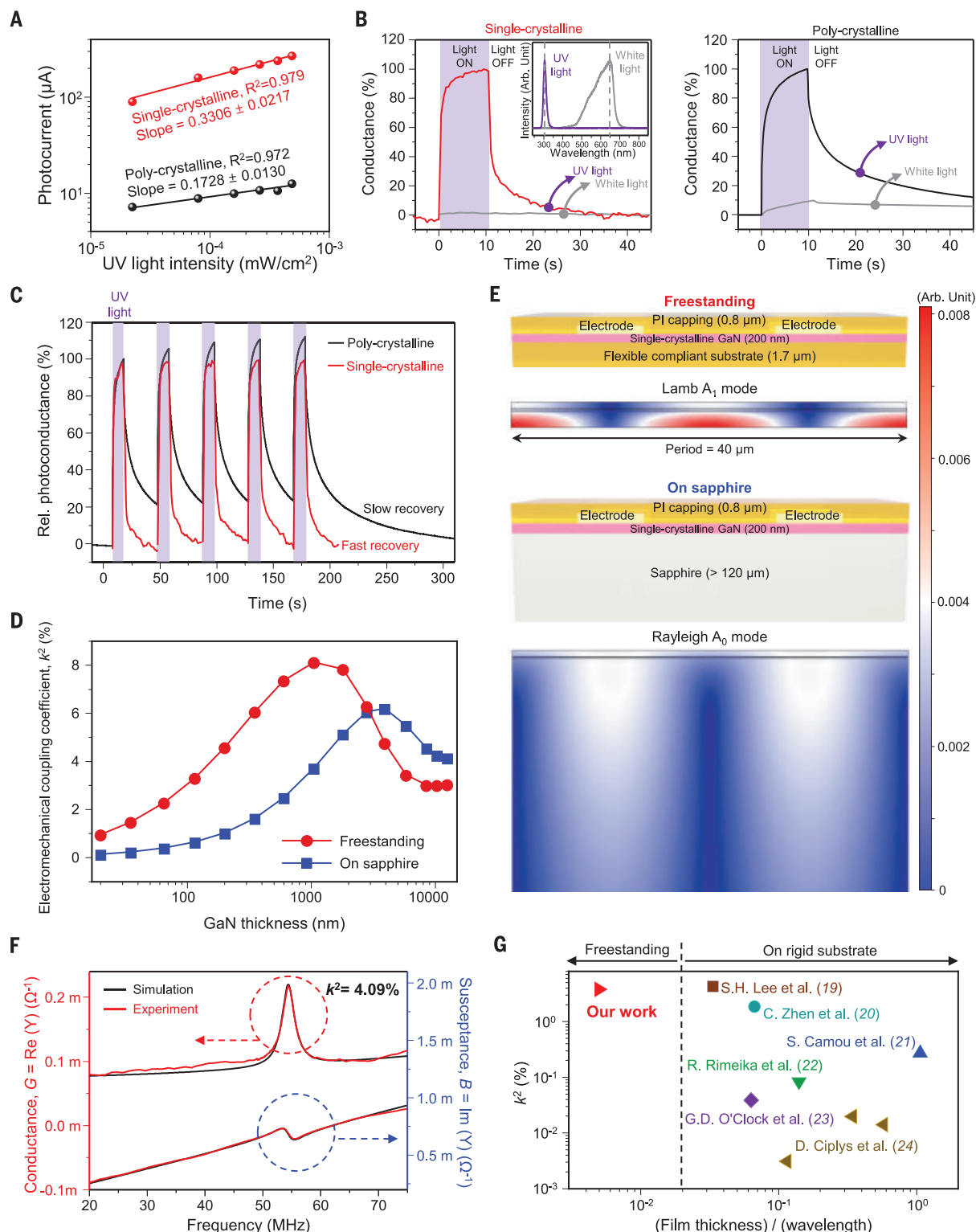


Fig. 2. High optoelectronic and surface acoustic performance of GaN-based single-crystalline e-skins. (A to C) GaN-metal Schottky diode UV sensors made of single-crystalline and polycrystalline GaN nanomembranes. (A) Responsivity of GaN UV sensors. The changes in photocurrent of GaN diodes in response to UV exposure with varying intensities. (B) Response and recovery speeds and selectivities for UV light over white light for (left) single-crystalline and (right) polycrystalline GaN UV sensors. The inset shows emission spectra of UV light and white light. (C) Consistency of UV response of GaN UV sensors. Slow switching speed of polycrystalline GaN sensors induces a gradual increase in remnant photoconductance.

(D and E) Simulation result of SAW generation in freestanding GaN membrane and GaN on sapphire. (D) Calculated electromechanical coupling coefficient (k^2) of GaN SAW devices by the function of GaN thickness. (E) The displacement of GaN SAW. The freestanding GaN has higher displacement than GaN on sapphire. (F) Conductance and susceptance of our single-crystalline GaN SAW devices were used to extract experimental k^2 . (G) Benchmark of extracted k^2 as a function of normalized thicknesses of GaN (19–24). Our freestanding single-crystalline GaN nanomembranes enable SAW generation at ultrathin GaN thickness, leading to k^2 as high as those of thick GaN layers on rigid substrates.

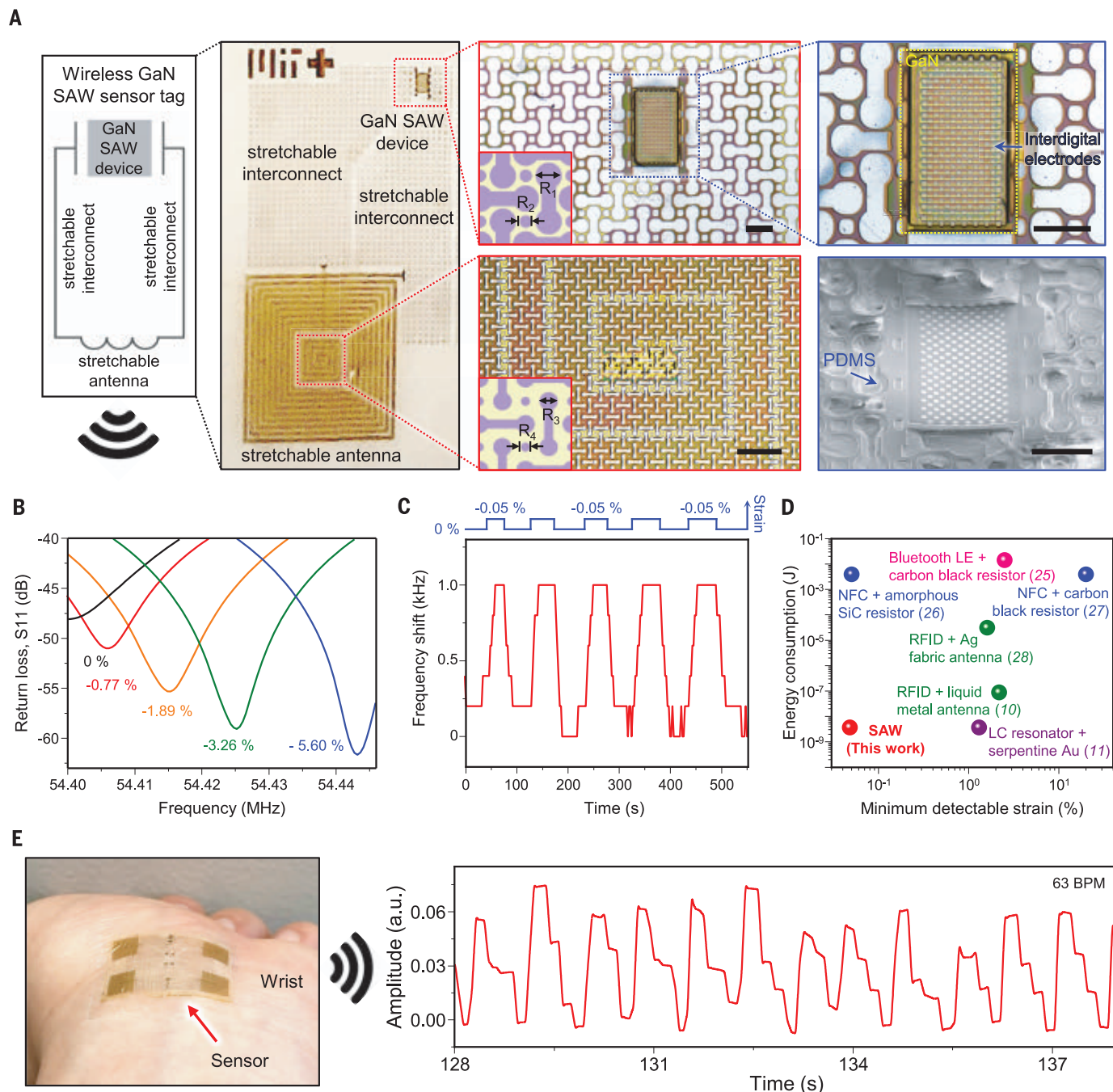


Fig. 3. Wireless GaN SAW strain sensors on e-skins free of communication chips or power source. (A) Schematic illustration and optical images of our wireless GaN SAW e-skin strain sensor. R1, R2, R3, and R4 in insets are 120, 50, 20, and 10 μm , respectively. Scale bars, 200 μm . (B) Resonant frequency shift as a function of strain for GaN SAW e-skin strain sensors.

(C) Measurement of the minimum detectable strain of our GaN SAW e-skin strain sensors. (D) Benchmark of minimum detectable strain and energy consumption for battery-less wireless e-skin strain sensors reported previously (10, 11, 25–28). (E) Wireless pulse measurements using our GaN SAW e-skin strain sensors.

that responds sensitively to physiological activities, the changes of which can be detected wirelessly through the antenna. Although previous studies note that SAW generated by an ultrathin piezoelectric film grown on a sapphire substrate is relatively negligible owing to the strong binding of the film to the substrate (17, 18), we have discovered that highly

crystalline GaN films that are decoupled from the substrate can generate SAWs with an ideal electromechanical coupling value.

Simulation of SAW generation in the GaN membrane (Fig. 2, D and E) showed that the electromechanical coupling coefficient k^2 is negligible for substrate-bound GaN films that are thinner than 300 nm (at a resonant fre-

quency of ~ 54 MHz), because substrate binding alters the acoustic mode and substantially reduces the displacement amplitude of acoustic vibration. However, decoupling of the GaN layer from the substrate substantially enhances electromechanical coupling by eliminating the binding effect. We experimentally confirmed that the k^2 value of our freestanding

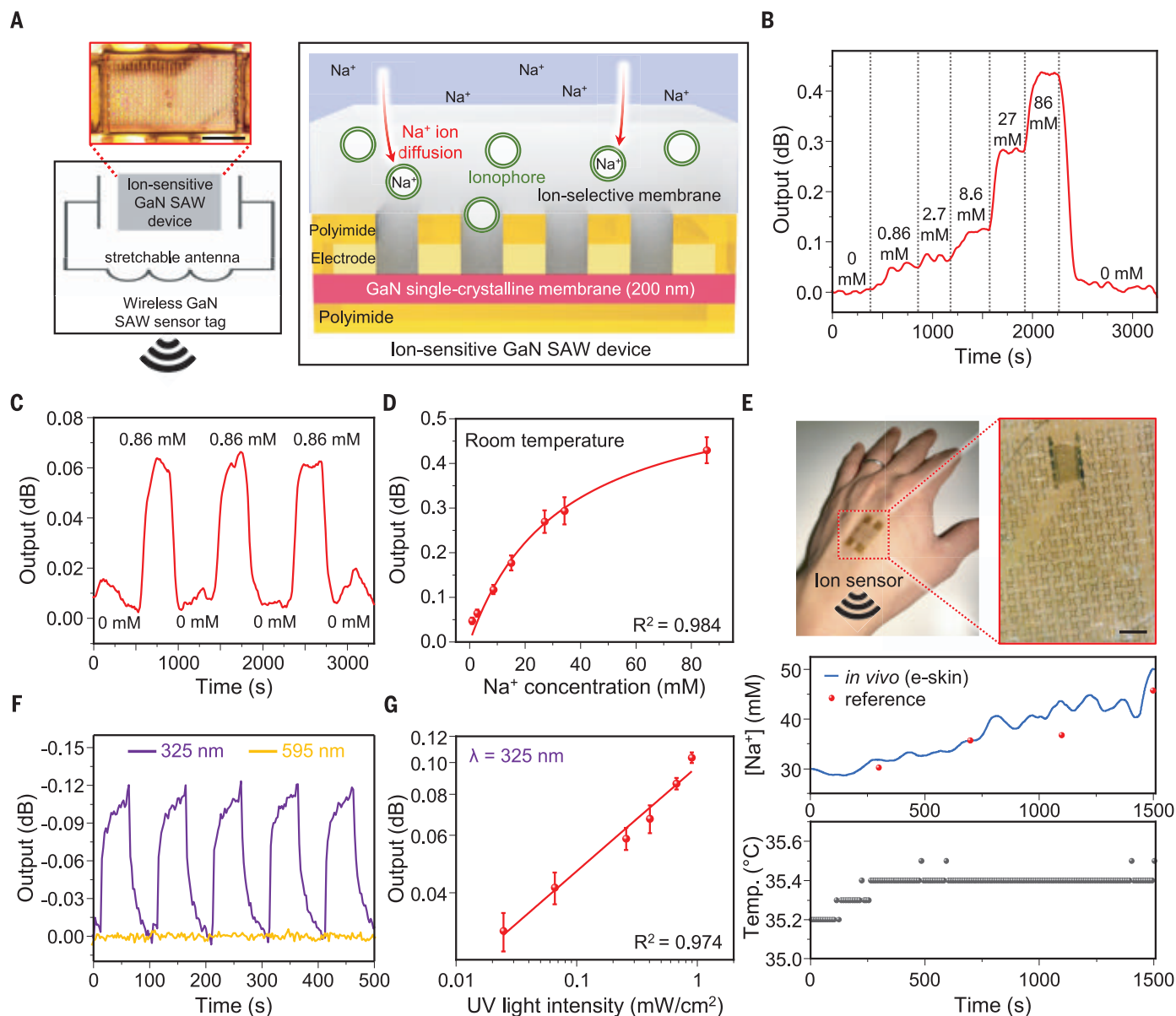


Fig. 4. Chip-free battery-less wireless GaN SAW ion sensors and UV sensors. (A) Schematic illustrations and optical microscope image of wireless ion sensors based on GaN SAW device coated with Na^+ ion-selective membranes. Scale bar, 200 μm . (B) Resonant frequency shift in the wireless signals obtained from a GaN SAW ion sensor in response to changes in Na^+ ion concentration. (C) Continuous wireless recordings collected from a SAW ion sensor during a series of alternating injections of 0.86 mM NaCl solution and distilled water over the e-skin, indicating consistent response and recovery characteristics. (D) Calibration of the responsivity of GaN SAW ion sensors to variation in Na^+ ion concentration. The error bars represent standard deviation in 5-min continuous measurements of the output signal for each concentration. (E) Photograph

and microscopy image of an e-skin attached on the back of a hand (top), in vivo recordings of the variation in Na^+ ion concentration in sweat using wireless GaN SAW-based e-skin (blue) and a reference conductometer (red; middle), and in vivo recording of the skin temperature obtained by a commercially available thermometer (bottom). Putting a glove on the hand and placing heating pads on body induces sweating. Scale bar, 500 μm . (F) Continuous wireless recordings collected by a SAW UV sensor in response to exposures of UV light (purple) and white light (orange), indicating the sensor's selectivity. (G) Calibration of the responsivity of GaN SAW UV sensors to exposures of different UV light intensities. Each data point and error bar indicate the average and standard deviation, respectively, from eight different measurements.

200-nm-thick GaN obtained by 2DLT is close to the value of 4.09% (Fig. 2F) that was reported for a 2.0- μm -thick GaN SAW sensor on a sapphire substrate (19). As shown in the benchmark plot in Fig. 2G (19–24), the k^2 value of our GaN film is on par with values previously achieved by epitaxial GaN SAW sensors with greater thicknesses bound on

sapphire wafers. A high k^2 value is essential for wireless detection, as it increases the signal-to-noise ratio in the resonant frequency shift of the SAW device on human skin.

Figure 3A shows the schematic illustration and microscopy images of our SAW-based chip-less wireless e-skin system. The GaN SAW device on a PDMS skin patch is designed

to be freestanding and suspended in air to maximize device sensitivity (see supplementary text for detailed device structures). SAW resonant peak frequency changes in response to mechanical strain and mass due to absorption or desorption of ions, as well UV exposure due to optical absorption by GaN (see supplementary text for detailed mechanisms). By scanning

the return loss (S_{11}) over a range of frequencies using the external wireless reader, the resonant frequency of GaN SAW (53.95 MHz) was recorded wirelessly (see figs. S9 and S10 for details).

We demonstrated wireless strain sensing by first calibrating the resonant peak shifts in the SAW device in response to strain induced by bending the patch (Fig. 3B and fig. S11). Compared with previously reported battery-less wireless e-skin systems (10, 11, 25–28), our single-crystalline GaN-based e-skin exhibits higher strain sensitivity, smaller minimum detectable strain (0.048%), and lower power consumption owing to chip-less operation (Fig. 3, C and D, and figs. S12 and S13). Although LC resonator-based e-skins can also achieve low-power sensing (Fig. 3D), they suffer from low sensitivity and limited sensing modality outside that of mechanical stimuli (11, 29, 30). Their low sensitivity also necessitates highly sophisticated and costly vector network analyzers with low trace noise for wireless measurement.

The high strain sensitivity of a SAW sensor on e-skin allows the continuous chip-less wireless measurement of arterial pulse waves on the wrist. Figure 3E and movie S1 illustrate the continuously wireless monitoring of pulse signals using our e-skin. Figure S14 shows the results of daytime (worn for ~17 hours/day) monitoring of heart rate and pulse waveforms (measured after exercise) over 7 days, which demonstrates the reusability and long-term wearability of our e-skin. Continuous wireless recording of strain through bending (fig. S15) and stretching (10.3% strain; fig. S16) cycles shows that our e-skin can undergo reversible bending and stretching without fracturing of the GaN owing to thin, deformable metal interconnects (30).

Our SAW sensor's communication range is ~14 mm in the z direction, ~7.5 mm in the x direction, or a rotation of ~30° (fig. S17). The relatively short communication range leads to limited monitoring of heart rate during active body movement (fig. S18). Replacing the near-field electrically small antenna with a far-field loop antenna may lead to longer-distance wireless communication thanks to the very low power consumption of our SAW sensor (see Fig. 3D for power comparison; methods and fig. S13 for estimation of power consumption in SAW sensors; and supplementary text for wireless distance and comparison with chip-based e-skins).

We also explored the wireless monitoring of ion concentrations in sweat, which can serve as indicators for conditions such as hyponatremia, kidney failure, and hypertension (31), using our SAW-based e-skin platform. GaN has an extremely low dissolution rate in aqueous solutions and can therefore yield a stable, biocompatible sweat sensor. We coated

the surface of a GaN SAW device with ion-selective membranes (ISMs) that can trap specific ions, which induces changes in the viscosity and mass of ISMs (see Fig. 4A, fig. S19, and table S2 for the design and composition of the SAW ion sensor). The resonant peak shifts in an ISM-coated SAW device can be used to wirelessly detect variation in ionic concentrations in surrounding fluids.

Figure 4, B to D, illustrates the results of in vitro wireless detection of Na^+ ions using an Na^+ ISM-coated GaN SAW device on e-skin. Continuous recordings in Fig. 4, B and C, indicate clear and consistent response and recovery of the output signal, collected by exposing the e-skin to aqueous NaCl solutions containing varying concentrations of Na^+ ions (see methods for detailed methodology). Calibration data in Fig. 4D, which represent the time-averaged response of the SAW sensor from 5-min continuous recordings, also indicate consistent sensor behavior. The detection limit of 0.86 mM represents a small value compared with the biologically relevant range of >10 mM in sweat, indicating the high sensitivity of the GaN SAW ion sensor. The sensor selectivity for Na^+ ions was confirmed by monitoring its response to flows of ionic solutions with different compositions (fig. S20).

Figure 4E shows images of a GaN SAW-based e-skin attached on the back of a hand for in vivo sweat analysis (see fig. S21 for measurement setup). Na^+ ion concentration in sweat was monitored simultaneously by a SAW sensor and a reference conductometer, while a commercial thermometer recorded skin temperature. The results show that the concentration of Na^+ ions in sweat gradually increases as perspiration continues (5). Integration of multiple types of ISMs on SAW devices may yield a wireless e-skin platform with improved versatility for sweat analysis.

Strong optoelectronic characteristics and piezoelectricity of GaN also enable wireless detection of UV light. SAW UV sensors (see fig. S22 for structures) respond to UV light (wavelength: ~325 nm) but not to white light (wavelength: ~595 nm), as shown in Fig. 4F. The results highlight the sensor's selectivity for UV owing to the matching bandgap of GaN, which eliminates the need for an optical filter and simplifies sensor design (fig. S23). Ion and UV (Fig. 4G) sensing capabilities of a GaN SAW-based e-skin illustrate the diverse sensing options that can be achieved using our chip-less wireless platform. Figure S24 also illustrates our sensors' capability to distinguish different types of input stimuli.

Here, we report a chip-free wireless e-skin platform based on SAW sensors made of free-standing ultrathin single-crystalline piezoelectric GaN films prepared by remote homoepitaxy and 2DLT to yield SAW devices with a high electromechanical coupling coefficient. SAW-

based e-skins offer a versatile biomedical sensing platform with high sensitivity, low power consumption, and long-term wearability.

REFERENCES AND NOTES

1. Y. Lee et al., *Sci. Adv.* **7**, eabg9180 (2021).
2. D.-H. Kim et al., *Science* **320**, 507–511 (2008).
3. L. Tian et al., *Nat. Biomed. Eng.* **3**, 194–205 (2019).
4. H. U. Chung et al., *Science* **363**, eaau0780 (2019).
5. W. Gao et al., *Nature* **529**, 509–514 (2016).
6. D. Son et al., *Nat. Nanotechnol.* **9**, 397–404 (2014).
7. K. Myrny, *Nat. Electron.* **1**, 30–39 (2018).
8. B. E. Jonsson, "An empirical approach to finding energy efficient ADC architectures," IMEKO TC4 International Workshop on ADC Modelling, Testing and Data Converter Analysis and Design 2011 (IWADC 2011) and IEEE 2011 ADC Forum, Orvieto, Italy, 30 June to 1 July 2011.
9. M. C. Vu et al., *ACS Appl. Mater. Interfaces* **12**, 26413–26423 (2020).
10. L. Teng et al., *Soft Robot.* **6**, 82–94 (2019).
11. X. Huang et al., *Adv. Funct. Mater.* **24**, 3846–3854 (2014).
12. Y. Kim et al., *Nature* **544**, 340–343 (2017).
13. H. Yeon et al., *Sci. Adv.* **7**, eabg8459 (2021).
14. Q. Hua et al., *Nat. Commun.* **9**, 244 (2018).
15. L. Shi, S. Ntintanov, *IEEE Sens. J.* **12**, 2453–2459 (2012).
16. R. Velazquez, A. Aldabahi, M. Rivera, P. Feng, *AIP Adv.* **6**, 085117 (2016).
17. C. R. Gorla et al., *J. Appl. Phys.* **85**, 2595–2602 (1999).
18. A. Shankar et al., "Impact of gamma irradiation on GaN/sapphire surface acoustic wave resonators," 2014 IEEE International Ultrasonics Symposium, Chicago, IL, USA, 3 to 6 September 2014.
19. S.-H. Lee et al., *IEEE Trans. Electron Dev.* **48**, 524–529 (2001).
20. Z. Chen et al., *Chin. Phys. Lett.* **18**, 1418–1419 (2001).
21. S. Camou, T. Pastureaud, H. Schenk, S. Ballandras, V. Laude, *Electron. Lett.* **37**, 1053–1055 (2001).
22. R. Rimeika et al., *Phys. Status Solidi B* **234**, 897–900 (2002).
23. G. O'Clock Jr., M. Duffy, *Appl. Phys. Lett.* **23**, 55–56 (1973).
24. D. Ciplý et al., *Electron. Lett.* **36**, 591–592 (2000).
25. A. D. Mickle et al., *Nature* **565**, 361–365 (2019).
26. Y. Gao et al., *Adv. Funct. Mater.* **29**, 1806786 (2019).
27. R. Lin et al., *Nat. Commun.* **11**, 444 (2020).
28. O. O. Rakibet, C. V. Rumens, J. C. Batchelor, S. J. Holder, *IEEE Antennas Wirel. Propag. Lett.* **13**, 814–817 (2014).
29. S. Niu et al., *Nat. Electron.* **2**, 361–368 (2019).
30. D.-H. Kim et al., *Science* **333**, 838–843 (2011).
31. J. Choi, R. Ghaffari, L. B. Baker, J. A. Rogers, *Sci. Adv.* **4**, eaar3921 (2018).

ACKNOWLEDGMENTS

We thank M. R. Abdelhamid and A. P. Chandrakasan for allowing us to use their vector network analyzer. **Funding:** This work was supported by AMOREPACIFIC. **Author contributions:** Y.K. and Je.K. conceptualized this work. Y.K., J.M.S., H.Y., J.L., S.Ki., T.P., Y.S.L., and K.L. did the formal analysis. Y.K., J.M.S., J.S., Y.L., H.Y., K.Q., H.S.K., H.E.L., C.C., D.L., J.-H.K., J.A.P., Y.P., L.K., J.P., M.-C.P., H.K., S.-H.B., W.K., J.H., and Je.K. developed the methodology. Y.K., J.M.S., Y.L., J.S., H.Y., K.Q., H.S.K., C.K., H.E.L., C.C., H.K., B.-I.P., S.Ka., Ji.K., K.W., K.K., and W.K. performed experiments. Y.K., J.M.S., H.Y., and S.Ki. visualized data. H.Y. and Je.K. acquired funding. Je.K. supervised this project. Y.K., J.M.S., H.Y., H.E.L., and Je.K. wrote the original draft. All authors reviewed and edited the manuscript. **Competing interests:** Y.K., J.M.S., and Je.K. are inventors on patent application number 63/355531 submitted by the Massachusetts Institute of Technology that covers devices (e.g., resonators) comprising a single-crystalline material and related systems and methods. **Data and materials availability:** All data are available in the main text or the supplementary materials. **License information:** Copyright © 2022 the authors, some rights reserved; exclusive licensee American Association for the Advancement of Science. No claim to original US government works. <https://www.science.org/about/science-licenses-journal-article-reuse>

SUPPLEMENTARY MATERIALS

science.org/doi/10.1126/science.abn7325

Materials and Methods
Supplementary Text
Figs. S1 to S24
Tables S1 and S2
References (32–42)
Movie S1

Submitted 16 December 2021; accepted 7 July 2022
10.1126/science.abn7325

METALLOENZYMES

Structures of the nitrogenase complex prepared under catalytic turnover conditions

Hannah L. Rutledge, Brian D. Cook, Hoang P. M. Nguyen, Mark A. Herzik Jr.*, F. Akif Tezcan*

The enzyme nitrogenase couples adenosine triphosphate (ATP) hydrolysis to the multielectron reduction of atmospheric dinitrogen into ammonia. Despite extensive research, the mechanistic details of ATP-dependent energy transduction and dinitrogen reduction by nitrogenase are not well understood, requiring new strategies to monitor its structural dynamics during catalytic action. Here, we report cryo-electron microscopy structures of the nitrogenase complex prepared under enzymatic turnover conditions. We observe that asymmetry governs all aspects of the nitrogenase mechanism, including ATP hydrolysis, protein-protein interactions, and catalysis. Conformational changes near the catalytic iron-molybdenum cofactor are correlated with the nucleotide-hydrolysis state of the enzyme.

Reduced forms of nitrogen are essential for the biosynthesis of amino acids and nucleic acids as well as the production of fertilizers and many commodity chemicals (1). As the only enzyme capable of nitrogen fixation, nitrogenase catalyzes the eight-electron reduction of atmospheric nitrogen (N_2) and protons (H^+) into ammonia (NH_3) and hydrogen (H_2) (2, 3) (Fig. 1A). Nitrogenase

is a two-component enzyme, which, in its most common form, consists of the iron protein FeP (a γ_2 homodimer) and the molybdenum-iron protein MoFeP (an $\alpha_2\beta_2$ heterotetramer) (Fig. 1B) (4, 5). Nitrogenase is distinct from most redox enzymes in its requirement for adenosine triphosphate (ATP) hydrolysis to enable the successive transfer of electrons and protons for substrate reduction (6, 7). The coupling

of ATP hydrolysis to electron transfer (ET) is mediated by FeP, which forms a specific, nucleotide-dependent complex with MoFeP and hydrolyzes two ATP molecules for the transfer of an electron to MoFeP (4–7). This part of nitrogenase catalysis is termed the FeP cycle (Fig. 1A) (2, 8). In the MoFeP cycle (Fig. 1A) (2, 8), the electrons from FeP are received by the P-cluster (an $[8Fe:7S]$ complex) of MoFeP and relayed to the iron-molybdenum cofactor FeMoco (a $[7Fe:9S:C:Mo]$ -homocitrate complex), where N_2 binding and reduction occur. Specific ATP-dependent interactions between FeP and MoFeP are necessary not only for interprotein ET but also for gated ET between the P-cluster and FeMoco through long-distance conformational perturbations, the nature of which are not understood (6, 7).

Although the dynamic coupling between ATP hydrolysis and ET ultimately drives N_2 fixation, it also creates experimental challenges for a mechanistic understanding of

Department of Chemistry and Biochemistry, University of California, San Diego, La Jolla, CA 92093, USA.

*Corresponding author. Email: tezcan@ucsd.edu (F.A.T.); mherzik@ucsd.edu (M.A.H.)

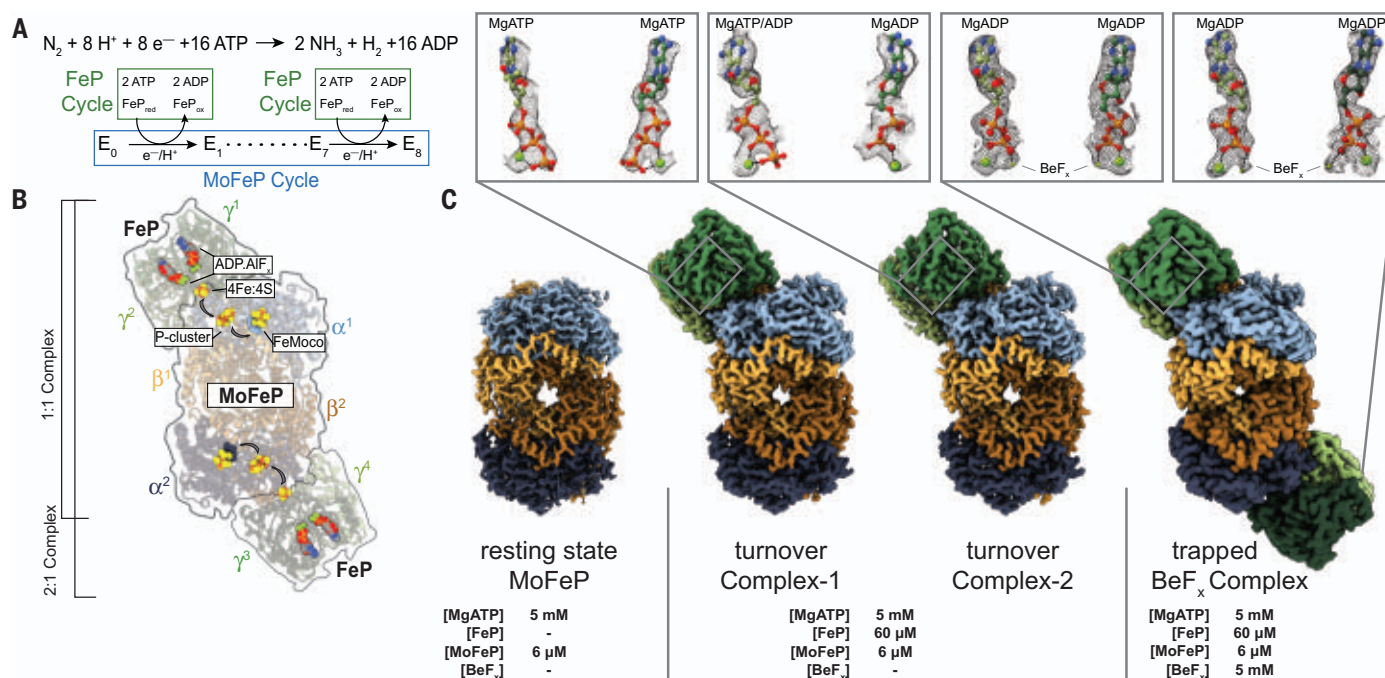


Fig. 1. Catalytic cycle for nitrogenase and its structural characterization under nonturnover and turnover conditions. (A) Chemical reaction catalyzed by nitrogenase. There are eight FeP cycles in each MoFeP cycle. (B) Crystal structure (PDB ID 1M34) (10) of the 2:1 FeP:MoFeP complex stabilized by MgADP.AIF_x, showing the relative positions of the individual FeP (γ^1 to γ^4) and MoFeP ($\alpha^1\beta^1\alpha^2\beta^2$) subunits, the nucleotides, and the metallocusters. The FeP subunits are shown in dark green (γ^1 or γ^3) and light green (γ^2 or γ^4), and the MoFeP subunits are highlighted in light blue (α^1), dark blue (α^2), light orange (β^1), and dark orange (β^2). Black arrows

indicate the path of electron flow. (C) Cryo-EM maps of $^{15}MoFeP$ (~1.8-Å resolution) obtained in the absence of FeP; $^{15}Complex-1$ (~2.3-Å resolution) and $^{15}Complex-2$ (~2.3-Å resolution) obtained under turnover conditions; and the BeF_x -trapped FeP-MoFeP complex (~2.4-Å resolution). Coloring scheme for the subunits is the same as in (B). Cryo-EM maps for nucleotides are shown as a gray mesh and contoured at the following levels: $^{15}MoFeP$, 0.008; $^{15}Complex-1$, 0.17; and $^{15}Complex-2$, 0.075. Magnified views of the nucleotides bound to the nitrogenase complexes and their corresponding cryo-EM densities are shown in boxes.

nitrogenase. First, substrates and inhibitors can only bind reduced forms of FeMoco, whose generation requires continuous turnover conditions that include ATP and reduced FeP (2, 3). Because MoFeP is also an inherent hydrogenase, such reduced forms of FeMoco promptly return to the resting state through H₂ evolution upon termination of ATP hydrolysis (8, 9), rendering substrate-bound states of FeMoco too fleeting for structural characterization. Second, the necessity of continuous ATP hydrolysis for catalysis leads to a heterogeneous distribution of nitrogenase substates that are difficult to interrogate experimentally. These substates differ not only in the FeP-MoFeP complexation state and the extent of ATP hydrolysis within the FeP cycle but also in the oxidation states of the metal cofactors and the reaction intermediates on FeMoco (E₀ to E₈) within the MoFeP cycle (Fig. 1, A and B).

Previous crystallographic studies have provided detailed views of the nucleotide-dependent conformations of the FeP-MoFeP complexes and outlined the path of ET in nitrogenase (Fig. 1B) (10, 11). Yet, these static views, which were obtained under nonturnover conditions and constrained by crystal lattice, showed no variation in the structure of MoFeP, providing little insight into the mechanism of ATP/FeP-mediated redox events within this protein. Recent crystallographic studies of MoFeP and its vanadium analog, VFe-protein, revealed possible modes of ligand interactions with FeMoco and showed that the cofactor is capable of undergoing compositional changes (12–14). However, these structural snapshots were obtained using crystals that formed hours to days after the last enzymatic turnover reaction, and their catalytic relevance remains an open question. In parallel, extensive freeze-quench spectroscopic studies of nitrogenase have characterized substrate- and intermediate-bound states of FeMoco (15, 16). Yet, these methods do not report on the atomic structure of the cofactor as a whole and provide little information regarding how the local cofactor-ligand interactions are linked to global ATP/FeP-dependent structural dynamics of MoFeP. Consequently, we lack a detailed understanding of why and how ATP hydrolysis is used to drive N₂ fixation and how catalysis at FeMoco proceeds. Clearly, new experimental approaches are needed to structurally interrogate nitrogenase during catalysis at or near atomic resolution to simultaneously characterize the ATP-dependent FeP-MoFeP interactions and the associated structural dynamics within each protein.

We sought to overcome some limitations of prior studies by using cryo-electron microscopy (cryo-EM) to directly visualize nitrogenase under enzymatic turnover conditions. We prepared cryo-EM samples of *Azotobacter*

vinelandii nitrogenase under high-electron flux turnover conditions (see supplementary methods), which contained a 10-fold molar excess of FeP over MoFeP and low ionic strength (≤ 25 mM NaCl) to favor the formation of electrostatically driven FeP-MoFeP complexes. We included sufficient MgATP and dithionite (5 mM each) to ensure that they are not depleted during turnover while minimizing background electron scattering. Turnover samples were prepared anaerobically under a N₂ atmosphere in an anaerobic glovebox and flash frozen in liquid N₂ within 15 s after initiation of turnover. For purposes of rapid manual freezing of cryo-EM grids, these turnover samples were removed from the glovebox, thawed, applied to grids, blotted, and frozen within <15 s. The ~ 30 -s total preparation period was sufficiently long to ensure that steady-state catalytic conditions were reached but short enough such that there was still remaining reductant and MgATP in solution (see supplementary methods). We collected a large cryo-EM dataset ($>15,000$ movies) that yielded >4.5 million usable particles (figs. S1 and S2 and table S1). Through exhaustive two-dimensional (2D) and 3D classification and refinement, we isolated free MoFeP ($\sim 60\%$) and FeP particles ($\sim 5\%$), as well as FeP-MoFeP nitrogenase assemblies ($\sim 35\%$), from this heterogeneous mixture. We determined the structures of two conformationally distinct 1:1 FeP:MoFeP complexes under turnover conditions, designated ^{56}Fe Complex-1 and ^{56}Fe Complex-2, at ~ 2.3 -Å resolution (Fig. 1C). Both complexes contain intact FeP and reduced, all-ferrous P-clusters (vide infra), indicating the lack of potential oxidation or damage by O₂ to the clusters. As a reference, we also obtained a ~ 1.8 -Å resolution cryo-EM structure of resting-state MoFeP, termed ^{56}Fe MoFeP, using the same turnover conditions but in the absence of FeP (Fig. 1C, fig. S3, and table S2).

Given the C₂ symmetry of MoFeP and the large separation (>65 Å) between the nearest clusters from the symmetry-related $\alpha\beta$ subunits, it has long been assumed that the two $\alpha\beta$ halves of MoFeP function independently from one another (2, 8). In support of this assumption, the crystal structures of various FeP-MoFeP complexes in different nucleotide-bound states largely possess a 2:1 FeP:MoFeP stoichiometry (Fig. 1B) (10, 11, 17). Unexpectedly, our turnover samples did not contain any particles that could be assigned to a 2:1 FeP:MoFeP complex (Fig. 1C and fig. S1). We considered the possibility that the exclusive observation of 1:1 complexes in our turnover samples could arise from an experimental artifact such as protein degradation or an increase in ionic strength during cryo-EM grid preparation. Therefore, we prepared a second set of turnover samples in the same manner as above that also included 5 mM beryllium fluo-

ride (BeF₃), which is known to arrest ATP hydrolysis in a transition-like state to yield quasi-irreversible, solution-stable 2:1 and 1:1 FeP-MoFeP complexes (18). Accordingly, our cryo-EM samples contained a large fraction of 2:1 FeP:MoFeP complexes alongside 1:1 species but no detectable free MoFeP particles (figs. S4 and S5 and table S3). We determined the structure of the MgADP.BeF₃-bound 2:1 FeP:MoFeP at ~ 2.4 -Å resolution and found it to be isostructural to the crystal structure of the related MgADP.AIF₃-bound 2:1 FeP:MoFeP complex [Protein Data Bank (PDB) ID 1M34; Fig. 1C and fig. S5]. These observations affirm that our cryo-EM samples contain intact proteins and operate under native turnover conditions, in turn indicating that the 1:1 FeP:MoFeP stoichiometry is the predominant nitrogenase assembly state during catalysis.

Prior work using pre-steady-state kinetics measurements revealed that the extents of interprotein ET and ATP hydrolysis were approximately half of what would be expected if there were two independent FeP binding sites on MoFeP (19). Originally, such half-reactivity was attributed to either partial inactivity of FeP molecules (19) or to the possible existence of an alternative interaction mode between FeP and MoFeP (20). Recent studies favored a model of negative cooperativity within a 2:1 FeP:MoFeP complex, whereby one of the bound FeP molecules suppresses ATP hydrolysis by the other bound FeP and the redox activity of the opposite $\alpha\beta$ half of MoFeP (21, 22). Our cryo-EM structures instead suggest that half-reactivity and negative cooperativity in nitrogenase arise from MoFeP binding to only one FeP molecule at a time during turnover.

^{56}Fe Complex-1 and ^{56}Fe Complex-2 were distinguished during cryo-EM data processing primarily on the basis of the structural variability of the FeP components. Thus, we first examined whether these differences are associated with the ATP-hydrolysis state of the two complexes. Earlier crystal structures identified at least three nucleotide state-dependent FeP-MoFeP docking geometries (DG1 to DG3) and led to the hypothesis that FeP moves in a unidirectional fashion across the MoFeP surface during turnover (Fig. 2A) (6, 11). The DG1 state predominates in the absence of nucleotides but is also populated in the presence of ATP (23) and corresponds to an electrostatically guided encounter complex wherein FeP largely interacts with the β subunit of MoFeP. DG2 is the activated nitrogenase complex in which ATP hydrolysis is coupled to interprotein ET, with FeP occupying the quasi-symmetric surface of MoFeP shared between α and β subunits (Figs. 1B and 2A) (10, 11). Finally, DG3 is formed by adenosine diphosphate (ADP)-bound FeP and primarily uses the α -subunit surface of MoFeP (11). The cryo-EM analysis of our

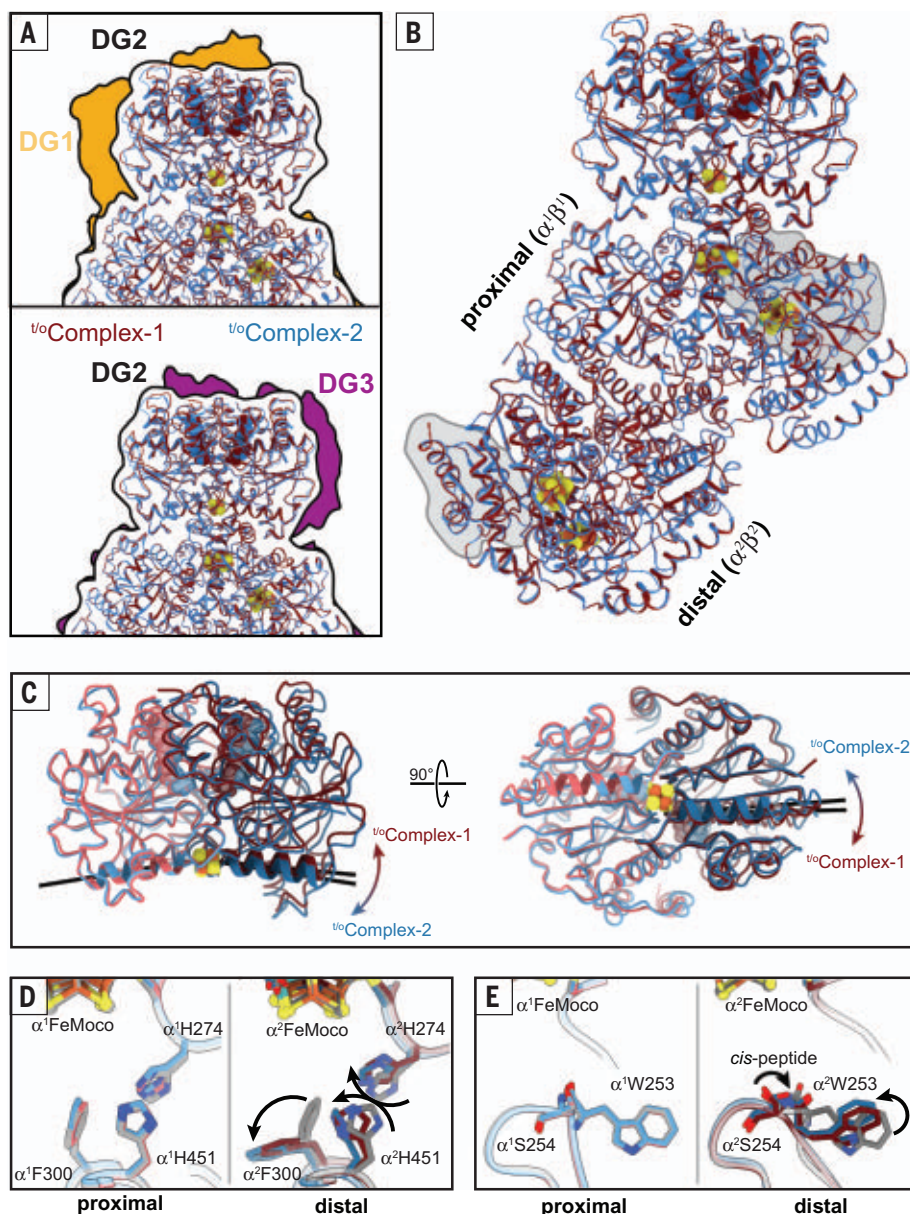


Fig. 2. Structural details of nitrogenase complexes characterized under turnover conditions. (A) The FeP:MoFeP docking geometry (DG) in t/o Complex-1 (maroon) and t/o Complex-2 (blue) observed in the DG2 configuration (black outline) compared with the DG1 (gold; PDB ID 2AFH) and DG3 (purple; PDB ID 2AFI) configurations characterized by x-ray crystallography (11). (B) Structural overlay of t/o Complex-1 and t/o Complex-2, indicating that the only large-scale conformational changes are observed in FeP. “Proximal” and “distal” refer to the $\alpha^1\beta^1$ and $\alpha^2\beta^2$ halves of MoFeP bound and not bound to FeP, respectively. The α II domains of MoFeP are outlined in gray. (C) Structural overlay of the FeP components in t/o Complex-1 and t/o Complex-2, highlighting the nucleotide-dependent conformational differences [hinging (left) and twisting (right)] motions of the γ^1 and γ^2 subunits relative to one another during ATP hydrolysis. The axes of the γ 100's helices (residues γ 98 to γ 112) that radiate from the [4Fe:4S] cluster are shown as black lines to illustrate these conformational differences. (D and E) Residues in the vicinity of FeMoco [(D) α His²⁷⁴, α Phe³⁰⁰, and α His⁴⁵¹; (E) α Trp²⁵³] that have undergone conformational changes in the distal subunit (α^2) of MoFeP during turnover. Movements between the resting-state (t^o MoFeP) (gray) and the turnover structures (maroon and blue) are indicated with arrows. F, Phe; H, His; S, Ser; W, Trp.

turnover samples revealed that t/o Complex-1 and t/o Complex-2 were exclusively in DG2 (Fig. 2A), implying that this configuration has a higher stability and/or longer residence time

relative to DG1 and DG3. Characteristic of a DG2 configuration, both complexes feature extensive interactions between FeP and MoFeP (buried surface areas >3600 Å²) and a short

[4Fe:4S]-to-P-cluster edge-to-edge distance of ~ 15 Å, primed for rapid interprotein ET (Fig. 2B). In t/o Complex-1, both FeP γ subunits (γ^1 and γ^2) are occupied by ATP molecules with clear densities for the γ -phosphate groups and associated Mg^{2+} ions (Fig. 1C). By contrast, the γ^1 subunit of t/o Complex-2 features an ATP molecule with weak density for the γ -phosphate, whereas the γ^2 subunit is ADP-bound and the γ -phosphate is completely absent from the nucleotide binding pocket, indicative of asymmetry in ATP hydrolysis (Fig. 1C). This observation is consistent with the crystal structure of a mixed-nucleotide FeP-MoFeP complex, in which AMPPCP (a nonhydrolyzable ATP analog) and ADP were selectively bound to the γ^1 and γ^2 subunits, respectively (24). The differences in the nucleotide occupancies of t/o Complex-1 and t/o Complex-2 are reflected in their distinct FeP conformations (Fig. 2C), which is further corroborated by a principal components analysis of available FeP structures (fig. S6). Collectively, we infer that (i) our cryo-EM structures report on active turnover states from the standpoint of ATP hydrolysis by FeP, (ii) the hydrolysis of two ATP molecules in each FeP cycle occurs in a stepwise fashion, and (iii) t/o Complex-1 and t/o Complex-2 correspond, respectively, to pre- and mid-ATP hydrolysis states of the nitrogenase complex that are populated along the catalytic reaction coordinate.

The asymmetry present both in ATP hydrolysis and FeP-MoFeP interactions has important implications for the timing of ET events during catalysis. Compared with a concerted process, stepwise nucleotide hydrolysis by FeP would be expected to increase the lifetime of the activated DG2 complex and provide additional conformational states for orchestrating the multistep redox reactions that occur at FeMoco and the P-cluster (6, 24). Similarly, an alternating docking mechanism between FeP and MoFeP (as imposed by negative cooperativity between the $\alpha\beta$ halves) would effectively slow down successive ET steps to a given $\alpha\beta$ subunit, providing sufficient time for anticipated protein and metallocluster rearrangements during N_2 reduction. This is consistent with the suggestion of Thorneley and Lowe that the slow kinetics of nitrogenase [turnover rate (k_{turnover}) ≈ 1 s⁻¹] governed by FeP-MoFeP interactions may be a mechanistic imperative to favor N_2 fixation over the competing but less demanding H^+ reduction (8).

Having analyzed t/o Complex-1 and t/o Complex-2 in the context of the FeP cycle, we next investigated whether they exhibited any conformational changes in their MoFeP components that may be correlated with the ATP hydrolysis state. In both t/o Complex-1 and t/o Complex-2, the P-clusters are in their fully reduced, all-ferrous (P^N) forms (fig. S7), and the protein

backbone arrangements of MoFeP's in both complexes are essentially indistinguishable from one another as well as from those in $^{rs}\text{MoFeP}$ and previously determined MoFeP crystal structures ($C\alpha$ root mean square deviation of 0.2 Å; Fig. 2B, fig. S8, and table S4). We observed no large-scale conformational changes that could account for mechanical coupling and negative cooperativity between symmetry-related FeP docking surfaces on MoFeP, implicating the involvement of a dynamic allosteric mechanism (e.g., FeP-induced changes in MoFeP conformational entropy) (fig. S9) (25). Yet, a detailed inspection of the structures revealed that the FeP-free (i.e., “distal”) $\alpha^2\beta^2$ half in both $^{t/o}\text{Complex-1}$ and $^{t/o}\text{Complex-2}$ possessed several features that distinguish it from the FeP-bound (i.e., “proximal”) $\alpha^1\beta^1$ half and $^{rs}\text{MoFeP}$.

First, there are several conserved residues ($\alpha^2\text{Trp}^{253}$, $\alpha^2\text{His}^{274}$, $\alpha^2\text{Phe}^{300}$, $\alpha^2\text{His}^{451}$) (26) in the vicinity of the distal FeMoco that adopt non-resting state conformations (Fig. 2, D and E). $\alpha^2\text{Trp}^{253}$ is particular in its *cis* peptide bond to $\alpha^2\text{Ser}^{254}$ and its position in a proposed substrate access channel from the protein surface to FeMoco (27, 28). The observed conformational flip in $\alpha^2\text{Trp}^{253}$ leads to the diversion of this putative channel to an alternate face of FeMoco (Fig. 2E and fig. S10). $\alpha^2\text{His}^{274}$, $\alpha^2\text{Phe}^{300}$, and $\alpha^2\text{His}^{451}$ side chains appear to have undergone a concerted motion compared with their resting state (Fig. 2D), whereby $\alpha^2\text{His}^{274}$ and $\alpha^2\text{Phe}^{300}$ assume a similar configuration as that seen in the low-pH crystal structure of MoFeP (fig. S11) (29). This $\alpha^2\text{His}^{274}$ configuration was proposed to form a water-bridged H bond to a protonated belt sulfur (S5A) of FeMoco (29). Along these lines, the observed rearrangement of the $\alpha^2\text{His}^{274}$ side chain in the turnover complexes could be envisioned to stabilize a protonated FeMoco intermediate and/or to increase the reduction potential of the cofactor, thus promoting its reduction by the P-cluster.

Second, the cryo-EM densities surrounding the $\alpha^2\text{His}^{442}$ and homocitrate ligands to the Mo center of the distal FeMoco are considerably less well defined compared with their counterparts in the proximal $\alpha\beta$ half and the residues in the vicinity (fig. S12) and cannot be modeled with the resting-state configurations of these ligands (Fig. 3). The reduction in map density is particularly pronounced for $^{t/o}\text{Complex-2}$ (i.e., mid-ATP hydrolysis) compared with that of $^{t/o}\text{Complex-1}$ (i.e., pre-ATP hydrolysis). These observations suggest that $\alpha^2\text{His}^{442}$ and homocitrate are mobile during turnover and that Mo undergoes changes in inner-sphere coordination in a way that is correlated with the nucleotide hydrolysis state of FeP bound to the opposing $\alpha\beta$ half of MoFeP. The substitution of Mo with V or Fe in alternative nitrogenases, the replacement of homocitrate with citrate, and alterations in H bonding to homocitrate have been shown to substantially diminish N_2 reduction activity and alter substrate specificity (2, 30–32). Indeed, the direct involvement of the Mo center in N_2 reduction has been proposed early on (2, 33), although recent experimental findings have shifted the focus to the central Fe centers of FeMoco as being the primary sites for substrate activation (15, 16). Our cryo-EM observations provide evidence that the Mo-homocitrate moiety may also participate in dynamic structural transformations that accompany catalysis at FeMoco.

Third, portions of a large domain in the distal $\alpha\beta$ subunit comprising residues α^25 to α^48 and α^378 to α^403 (particularly in $^{t/o}\text{Complex-2}$) possess increased mobility compared with the rest of the MoFeP (fig. S13). This so-called α^3 domain forms a lid above FeMoco and includes residues $\alpha^2\text{Glu}^{380}$ and $\alpha^2\text{Phe}^{381}$, which form close contacts with FeMoco (Figs. 2B and 3). In resting-state MoFeP, $\alpha^3\text{III}$ is well ordered, $\alpha^2\text{Glu}^{380}$ forms water-bridged H bonds to the Mo-ligated $\alpha^2\text{His}^{442}$ side chain and homocitrate, and $\alpha^2\text{Phe}^{381}$ is in van der Waals contact with the labile belt sulfide S2B of FeMoco (Fig. 3A). By contrast, in the distal $\alpha\beta$ halves of $^{t/o}\text{Complex-1}$ and $^{t/o}\text{Complex-2}$, the cryo-EM densities for $\alpha^3\text{III}$ and the side chains of $\alpha^2\text{Glu}^{380}$ and $\alpha^2\text{Phe}^{381}$ are either diffuse or entirely missing (Fig. 3B and fig. S13). This movement is likely coupled to the dynamics of the Mo ligands and FeMoco as a whole. $\alpha^3\text{III}$ has also been shown to undergo major structural rearrangements associated with the insertion of FeMoco into MoFeP (34). Furthermore, $\alpha^3\text{III}$ displays some of the highest temperature factors in MoFeP crystal structures and is positioned away from lattice contacts (table S5)

Third, portions of a large domain in the distal $\alpha\beta$ subunit comprising residues α^25 to α^48 and α^378 to α^403 (particularly in $^{t/o}\text{Complex-2}$) possess increased mobility compared with the rest of the MoFeP (fig. S13). This so-called α^3 domain forms a lid above FeMoco and includes residues $\alpha^2\text{Glu}^{380}$ and $\alpha^2\text{Phe}^{381}$, which form close contacts with FeMoco (Figs. 2B and 3). In resting-state MoFeP, $\alpha^3\text{III}$ is well ordered, $\alpha^2\text{Glu}^{380}$ forms water-bridged H bonds to the Mo-ligated $\alpha^2\text{His}^{442}$ side chain and homocitrate, and $\alpha^2\text{Phe}^{381}$ is in van der Waals contact with the labile belt sulfide S2B of FeMoco (Fig. 3A). By contrast, in the distal $\alpha\beta$ halves of $^{t/o}\text{Complex-1}$ and $^{t/o}\text{Complex-2}$, the cryo-EM densities for $\alpha^3\text{III}$ and the side chains of $\alpha^2\text{Glu}^{380}$ and $\alpha^2\text{Phe}^{381}$ are either diffuse or entirely missing (Fig. 3B and fig. S13). This movement is likely coupled to the dynamics of the Mo ligands and FeMoco as a whole. $\alpha^3\text{III}$ has also been shown to undergo major structural rearrangements associated with the insertion of FeMoco into MoFeP (34). Furthermore, $\alpha^3\text{III}$ displays some of the highest temperature factors in MoFeP crystal structures and is positioned away from lattice contacts (table S5)

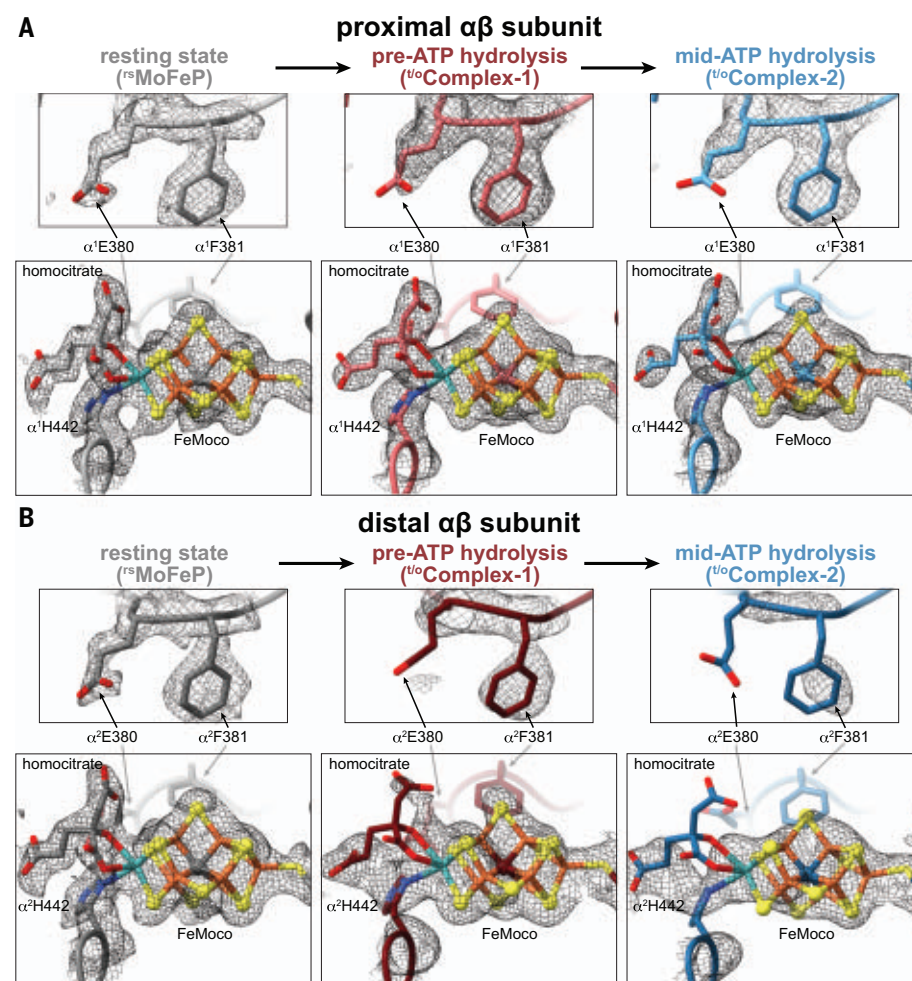


Fig. 3. Changes in the FeMoco environment observed during catalytic turnover. (A and B) Views of FeMoco and the nearby residues $\alpha^2\text{Glu}^{380}$ and $\alpha^2\text{Phe}^{381}$ in the proximal (A) and distal (B) $\alpha\beta$ halves of MoFeP in $^{rs}\text{MoFeP}$ (gray), $^{t/o}\text{Complex-1}$ (maroon), and $^{t/o}\text{Complex-2}$ (blue) structures. Cryo-EM maps for each individual structure are shown as a gray mesh and contoured at the following levels: $^{rs}\text{MoFeP}$, 0.008; $^{t/o}\text{Complex-1}$, 0.065; and $^{t/o}\text{Complex-2}$, 0.075. E, Glu.

(10, 11, 24, 29, 35), implying that it is inherently more flexible than other parts of MoFeP. Combined with this observation, ^{16}O Complex-1 and ^{16}O Complex-2 structures point to a possible role of αIII mobility in nitrogenase catalysis. Notably, αIII abuts the docking surface of MoFeP for MgADP-bound FeP in DG3 and may lie in the trajectory of FeP moving directionally across the MoFeP surface during ATP hydrolysis (11). Thus, a dynamic αIII domain could also provide a direct mechanical conduit between FeP and the proximal FeMoco, further linking the timing of nucleotide-dependent FeP-MoFeP interactions to redox transformations at FeMoco. The increased mobility of the αIII domain and the lack of a capping FeP could also allow more efficient substrate or molecular access to or exit from FeMoco.

Based on the available structures, it is not obvious (i) how FeP docking induces conformational changes in the distal $\alpha\beta$ subunit of MoFeP over a distance of ≥ 80 Å or (ii) to which states of the MoFeP cycle (i.e., E_0 to E_8) the observed nitrogenase complexes correspond. It is safe to assume, however, that all copies of FeMoco in these complexes represent the more stable or longer-lived of the many catalytic intermediates present in the turnover solution. The density maps for the proximal FeMoco's are essentially identical to those for the resting-state cofactor (Fig. 3). Thus, an assignment of E_0 for the proximal cofactors is plausible, although E_1 to E_4 are also reasonable because these states have been proposed as hydride-bound FeMoco intermediates (15, 16), which may be structurally indistinguishable from E_0 at the current resolution of these cryo-EM maps. At the same time, the obvious deviations between the densities of distal and proximal FeMoco's indicate that the distal cofactors in ^{16}O Complex-1 and ^{16}O Complex-2 might represent an E_x state or a mixture of E_x states that are different from the proximal cofactors and previous crystal structures solved in the resting state of FeMoco. It is thus possible that this structure represents a more advanced state in the MoFeP cycle (i.e., $\geq E_1$) than the proximal FeMoco's and involves the participation of the Mo center. We also note that the overall map density for the distal FeMoco in ^{16}O Complex-2 is less well defined than in those in ^{16}O MoFeP, ^{16}O Complex-1, or the proximal subunit in ^{16}O Complex-2, which may further indicate conformational changes in the cofactor during turnover such as the displacement of belt sulfurs or ligand binding (12–14). Given the asymmetry between the FeMoco's in the two $\alpha\beta$ halves, it is tempting to propose a “ping-pong”-type mechanism in which the cofactors proceed through each of the eight catalytic steps in an alternating fashion. This scenario would assign a dual role to FeP: (i) to deliver an electron to one $\alpha\beta$ subunit of MoFeP

and (ii) to suppress FeP binding to the opposite $\alpha\beta$ subunit while priming it for catalytic transformations through long-distance activation of electron, H^+ , and/or substrate access pathways to the distal FeMoco. Establishing whether such a mechanism is operative will require future studies, but our current work illustrates that it is possible to characterize nitrogenase under turnover conditions by cryo-EM at near-atomic resolution, representing a critical step toward understanding the mechanism of this enigmatic enzyme in full structural detail.

REFERENCES AND NOTES

- V. Smil, *Sci. Am.* **277**, 76–81 (1997).
- B. K. Burgess, D. J. Lowe, *Chem. Rev.* **96**, 2983–3012 (1996).
- R. Thorneley, D. Lowe, *J. Biol. Inorg. Chem.* **1**, 576–580 (1996).
- D. C. Rees *et al.*, *Philos. Trans. Royal Soc. London Ser. A* **363**, 971–984 (2005).
- O. Einsle, D. C. Rees, *Chem. Rev.* **120**, 4969–5004 (2020).
- H. L. Rutledge, F. A. Tezcan, *Chem. Rev.* **120**, 5158–5193 (2020).
- L. C. Seefeldt *et al.*, *Acc. Chem. Res.* **51**, 2179–2186 (2018).
- D. J. Lowe, R. N. Thorneley, *Biochem. J.* **224**, 877–886 (1984).
- R. N. Thorneley, D. J. Lowe, *Biochem. J.* **224**, 887–894 (1984).
- B. Schmid *et al.*, *Biochemistry* **41**, 15557–15565 (2002).
- F. A. Tezcan *et al.*, *Science* **309**, 1377–1380 (2005).
- T. Spatzal, K. A. Perez, O. Einsle, J. B. Howard, D. C. Rees, *Science* **345**, 1620–1623 (2014).
- D. Sippel *et al.*, *Science* **359**, 1484–1489 (2018).
- W. Kang, C. C. Lee, A. J. Jasniowski, M. W. Ribbe, Y. Hu, *Science* **368**, 1381–1385 (2020).
- B. M. Hoffman, D. Lukoyanov, Z.-Y. Yang, D. R. Dean, L. C. Seefeldt, *Chem. Rev.* **114**, 4041–4062 (2014).
- L. C. Seefeldt *et al.*, *Chem. Rev.* **120**, 5082–5106 (2020).
- H. Chiu *et al.*, *Biochemistry* **40**, 641–650 (2001).
- T. A. Clarke, F. K. Yousafzai, R. R. Eady, *Biochemistry* **38**, 9906–9913 (1999).
- G. A. Ashby, R. N. F. Thorneley, *Biochem. J.* **246**, 455–465 (1987).
- T. A. Clarke, S. Fairhurst, D. J. Lowe, N. Y. Watmough, R. R. Eady, *Biochem. J.* **39**, 201–206 (2011).
- K. Danyal *et al.*, *Proc. Natl. Acad. Sci. U.S.A.* **113**, E5783–E5791 (2016).
- Q. Huang *et al.*, *PLOS Comput. Biol.* **17**, e1008719 (2021).
- C. P. Owens, F. E. Katz, C. H. Carter, M. A. Luca, F. A. Tezcan, *J. Am. Chem. Soc.* **137**, 12704–12712 (2015).
- F. A. Tezcan, J. T. Kaiser, J. B. Howard, D. C. Rees, *J. Am. Chem. Soc.* **137**, 146–149 (2015).
- H. N. Motlagh, J. O. Wrabl, J. Li, V. J. Hilser, *Nature* **508**, 331–339 (2014).
- J. B. Howard, K. J. Kechris, D. C. Rees, A. N. Glazer, *PLOS ONE* **8**, e72751 (2013).
- R. Y. Igarashi, L. C. Seefeldt, *Crit. Rev. Biochem. Mol. Biol.* **38**, 351–384 (2003).
- C. N. Morrison, J. A. Hoy, L. Zhang, O. Einsle, D. C. Rees, *Biochemistry* **54**, 2052–2060 (2015).
- C. N. Morrison, T. Spatzal, D. C. Rees, *J. Am. Chem. Soc.* **139**, 10856–10862 (2017).
- R. R. Eady, *Chem. Rev.* **96**, 3013–3030 (1996).

- P. A. McLean, R. A. Dixon, *Nature* **292**, 655–656 (1981).
- M. C. Durrant, A. Francis, D. J. Lowe, W. E. Newton, K. Fisher, *Biochem. J.* **397**, 261–270 (2006).
- C. J. Pickett, *J. Biol. Inorg. Chem.* **1**, 601–606 (1996).
- B. Schmid *et al.*, *Science* **296**, 352–356 (2002).
- O. Einsle *et al.*, *Science* **297**, 1696–1700 (2002).

ACKNOWLEDGMENTS

We thank K. Corbett, S. Narehood, J. Figueroa, and R. Subramanian for critical discussions and members of the Tezcan and Herzik labs for their assistance. Molecular graphics and analyses were performed with UCSF ChimeraX, developed by the Resource for Biocomputing, Visualization, and Informatics at the University of California, San Francisco (UCSF), with support from National Institutes of Health (NIH) grant R01-GM129325 and the Office of Cyber Infrastructure and Computational Biology, National Institute of Allergy and Infectious Diseases. We also thank members of the University of California, San Diego (UCSD)'s Cryo-EM Facility, the Stanford-SLAC Cryo-EM Center (S^2C^2), and UCSD's Physics Computing Facility for help in data collection, data processing, and computational support. **Funding:** This work was supported by NIH grant R01-GM099813 (F.A.T.), NIH grant R35-GM138206 (M.A.H.), NIH grant T32-GM008326 (H.L.R. and H.P.M.N.), NASA grant 80NSSC18M0093 (F.A.T. and H.L.R.), ENIGMA: Evolution of Nanomachines in Geospheres and Microbial Ancestors, NASA Astrobiology Institute Cycle 8), and the Searle Scholars Program (M.A.H.). Cryo-EM experiments were conducted at UCSD's Cryo-EM Facility as well as the Stanford-SLAC Cryo-EM Center (S^2C^2) supported by the NIH Common Fund Transformative High-Resolution Cryoelectron Microscopy program (U24 GM129541). **Author contributions:** Conceptualization: H.L.R., M.A.H., F.A.T.; Methodology: H.L.R., B.D.C., M.A.H., F.A.T.; Investigation: H.L.R., B.D.C., H.P.M.N., M.A.H., F.A.T.; Visualization: H.L.R., B.D.C., M.A.H.; Funding acquisition: M.A.H., F.A.T.; Project administration: M.A.H., F.A.T.; Supervision: M.A.H., F.A.T.; Writing – original draft: H.L.R., M.A.H., F.A.T.; Writing – review and editing: H.L.R., B.D.C., M.A.H., F.A.T. **Competing interests:** The authors declare that they have no competing interests. **Data and materials availability:** Structural models have been deposited in the Protein Data Bank with accession codes 7UT6 (^{16}O MoFeP, C_1 symmetry), 7UT7 (^{16}O MoFeP, C_2 symmetry), 7UT8 (^{16}O Complex-1), 7UT9 (^{16}O Complex-2), and 7UTA (BeF_x-trapped complex). The corresponding cryo-EM maps are available at the Electron Microscopy Data Bank (www.ebi.ac.uk/emdb/) with accession codes EMD-26756 (^{16}O MoFeP, C_1 symmetry), EMD-26757 (^{16}O MoFeP, C_2 symmetry), EMD-26758 (^{16}O Complex-1 consensus MoFeP), EMD-26759 (^{16}O Complex-1 locally refined FeP), EMD-26760 (^{16}O Complex-1), EMD-26761 (^{16}O Complex-2 consensus MoFeP), EMD-26762 (^{16}O Complex-1 locally refined FeP), EMD-26763 (^{16}O Complex-2), and EMD-26764 (BeF_x-trapped complex). All other data are available in the main text or the supplementary materials. **License information:** Copyright © 2022 the authors, some rights reserved; exclusive licensee American Association for the Advancement of Science. No claim to original US government works. <https://www.science.org/about/science-licenses-journal-article-reuse>

SUPPLEMENTARY MATERIALS

science.org/doi/10.1126/science.abq7641
Materials and Methods
Figs. S1 to S13
Tables S1 to S5
References (36–51)
MDAR Reproducibility Checklist

Submitted 28 April 2022; accepted 14 July 2022
10.1126/science.abq7641

NANOMATERIALS

Nanocrystals with metastable high-pressure phases under ambient conditions

Tianyuan Xiao¹, Yasutaka Nagaoka^{1†}, Xirui Wang^{1‡}, Tian Jiang^{1‡}, Derek LaMontagne¹, Qiang Zhang¹, Can Cao^{1§}, Xizheng Diao¹, Jiahua Qiu¹, Yiruo Lu¹, Zhongwu Wang², Y. Charles Cao^{1*}

The ambient metastability of the rock-salt phase in well-defined model systems comprising nanospheres or nanorods of cadmium selenide, cadmium sulfide, or both was investigated as a function of composition, initial crystal phase, particle structure, shape, surface functionalization, and ordering level of their assemblies. Our experiments show that these nanocrystal systems exhibit ligand-tailorable reversibility in the rock salt-to-zinc blende solid-phase transformation. Interparticle sintering was used to engineer kinetic barriers in the phase transformation to produce ambient-pressure metastable rock-salt structures in a controllable manner. Interconnected nanocrystal networks were identified as an essential structure that hosted metastable high-energy phases at ambient conditions. These findings suggest general rules for transformation-barrier engineering that are useful in the rational design of next-generation materials.

Solids from a collection of atoms can adopt a variety of structural phases with their respective physical and chemical properties, providing the foundation for materials discovery (1–3). At ambient temperature and pressure, there is often one thermodynamically stable phase for a given atomic collection, and the rest can potentially become metastable as kinetically trapped phases with positive free energy above the equilibrium state (4). However, a general strategy for engineering kinetic barriers has

yet to be developed but is essential for the rational synthesis of new materials and for expanding the space of synthesizable metastable materials (5, 6).

Phase transformations in bulk solids exhibit complex kinetics involving different microscopic pathways that occur in parallel at different locations within one crystal domain, which are thus difficult to determine experimentally (7). However, transition pressures measured in experiments match well with the theoretical values determined from electronic

structure calculations. For example, the thermodynamic transition in silicon from a diamond to a β -tin structure was calculated to be 8.0 GPa, and this transformation was observed experimentally in the range of 8.8 to 12.5 GPa (8). However, based on elastic stability analysis, Mizushima, Yip, and Kaxiras (MYK) theoretically predicted that defect- and strain-free bulk silicon can remain metastable in the diamond structure up to 64 GPa, which implies a huge intrinsic activation barrier (~ 0.3 eV per atom) in the structural transformation (9).

This discrepancy indicates that the predicted intrinsic energy barrier in an ideal crystal is drastically decreased by mechanisms associated with defects in real bulk solids during high-pressure experiments and is reflected in high-pressure phases of most bulk solids relaxing back to the ambient phase upon release of pressure. Importantly, the MYK calculation predicts that most high-energy solid phases are theoretically metastable at ambient conditions, if their hosting crystals are defect- and strain-free (8, 9). This insight allows for

¹Department of Chemistry, University of Florida, Gainesville, FL 32611, USA. ²Cornell High Energy Synchrotron Source, Cornell University, Ithaca, NY 14853, USA.

*Corresponding author. Email: cao@chem.ufl.edu

†Present address: Department of Chemistry, Brown University, Providence, RI 02912, USA. ‡These authors contributed equally to this work. §Present address: Warren Alpert Medical School of Brown University, Providence, RI 02903, USA.

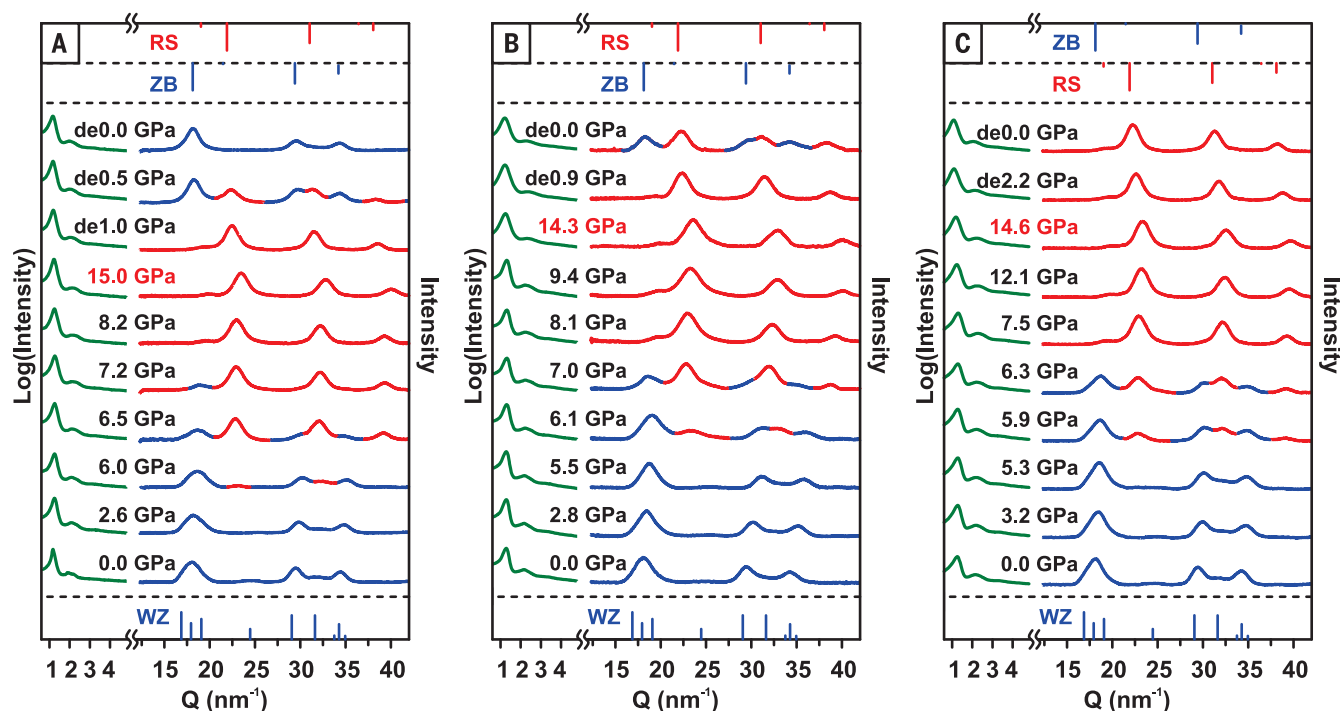


Fig. 1. Ligand-tailorable reversibility of the RS-ZB solid-phase transformation in superlattices of 4.8-nm WZ CdSe nanocrystals. (A to C) WAXS and SAXS patterns collected during compression and decompression (de) at different pressures. CdSe NCs were functionalized with octylamine of (A) 92% surface coverage and of (B) 62% surface coverage and (C) capped with

a mixture of octylamine and CTAB (with a molar ratio of 5:1) of 63% surface coverage in terms of hydrocarbon chains. SAXS patterns are shown in green. WAXS diffraction patterns from the WZ/ZB structure and from the RS structure are shown in blue and red, respectively. See supplementary materials for details on composition-ratio determinations. Q , scattering vector, calculated as $4\pi \sin(2\theta)/\lambda$.

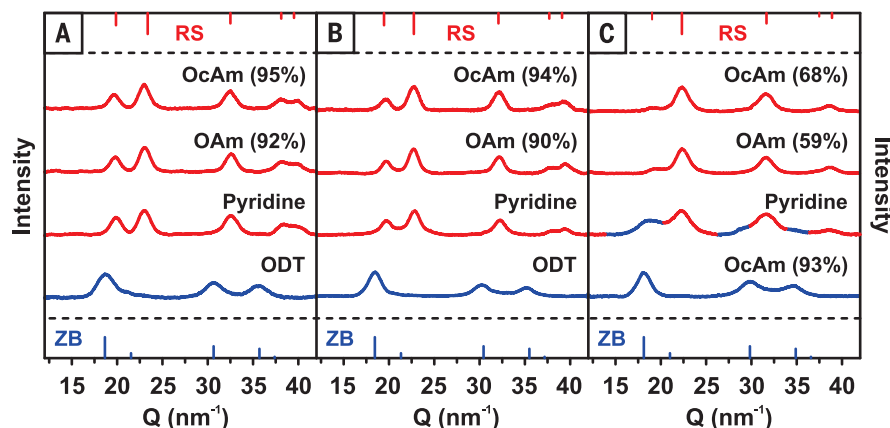


Fig. 2. Ligand-tailorable ambient metastability of the RS phase in 4.8-nm nanospheres. (A to C) WAXS patterns of NC assemblies decompressed from a pressure greater than 10.4 GPa: (A) ZB CdS NCs, (B) WZ CdSe/CdS core/shell NCs, and (C) WZ CdS/CdSe core/shell NCs. The type of ligand and surface coverage are given on the corresponding curves for octylamine (OcAm) or oleylamine (OAm). Pyridine ligand is of ~100% surface coverage, and ODT ligand is in excess amount corresponding to ~150% surface coverage. The corresponding WAXS and SAXS patterns obtained at different pressures can be found in figs. S12 to S14 and S16. See supplementary materials for details on ligand composition-ratio determinations.

the development of a general approach for making ambient metastable materials of given chemical compositions based on further understanding of kinetic pathways in solid-solid phase transformations (8).

High-quality colloidal CdSe semiconductor nanocrystals (NCs) (10) have been extensively used as models to study the phase transition from a four-coordinate hexagonal wurtzite (WZ) to a six-coordinate cubic rock-salt (RS) structure (6, 11–16). Bulk CdSe undergoes a WZ-to-RS phase transition at ~2.5 GPa, whereas defect-free WZ CdSe NCs can be metastable at pressures above 6.0 GPa (6, 11), which provides solid evidence for reliability of the MYK calculation (9). Because these NCs can act as single structural domains under high pressures, their phase-transition kinetics are simpler than those of bulk solids and are highly reproducible (12). Such advantages allowed for experimental measurements of fundamental properties—such as the energy, volume, and entropy of activation—of the WZ-to-RS transition in CdSe NCs that revealed direction-dependent nucleation through a sliding-plane mechanism (13, 14). However, detailed kinetic pathways for the reverse phase transformation from the six-coordinate RS to the four-coordinate cubic zinc-blende (ZB) structure remain unclear (14–17).

There exists evidence that under some conditions, high-pressure phases can be retained in NCs upon release of pressure. At ambient conditions, a sample of 11-nm CdSe NCs was composed of ~20% metastable RS structure (15), and a sample of 13-nm PbS nanocubes was composed of 37.2% metastable high-pressure phase (18). Additionally, the RS phase of CdSe/ZnS and CdS NCs could fully persist in a metastable state at ambient pressure (19–23).

These observations suggest the existence of unknown mechanisms for eliminating crystal defects from high-pressure structures (8, 9). To test this hypothesis, we performed a mechanistic study on the reversibility of the RS-ZB transformation in systems comprising spherical NCs or nanorods of CdSe, CdS, or both. We obtained insight into the mechanisms and microscopic processes that determine the kinetic barrier height between two crystal phases.

The ambient metastability of the RS phase in NCs of CdSe, CdS, or both was studied as a function of composition, initial crystal phase, particle structure, shape, surface functionalization, and ordering level of their assemblies. We synthesized six types of spherical NCs with 4.8-nm diameter and one type of CdSe/CdS nanorod with 23.8-nm length and 4.8-nm diameter that exhibited a narrow size distribution and high crystallinity, as confirmed with transmission electron microscopy (TEM), ultraviolet-visible absorption, and fluorescence spectroscopy (figs. S1 to S5). The NC surfaces were precisely controlled through ligand exchange with a designed surface density. We arbitrarily assigned a surface density of five ligands per nm² as 100% ligand coverage. Assemblies of these NCs were prepared either directly on the flat surface of a diamond anvil or at the air-liquid interface of diethylene glycol. To introduce deviatoric stress for promoting interparticle interactions, high-pressure experiments were performed in a diamond anvil cell without the use of a pressure medium (24–27). The solid-state phase structures as a function of pressure were determined with simultaneous measurements of both small-angle and wide-angle x-ray scattering (SAXS and WAXS) at the Cornell High Energy Synchrotron Source.

At ambient conditions, octylamine-capped WZ CdSe NCs (92% coverage; fig. S6A) formed superlattices in a face-centered-cubic (fcc) structure with an interparticle distance of 6.76 nm (Fig. 1A). Upon increasing pressure, the superlattice unit-cell size decreased gradually until 7.2 GPa, above which point the superstructure distorted, whereas the atomic WZ unit-cell volume decreased smoothly up to a threshold pressure (~6.0 GPa), at which point there was an abrupt decrease in unit-cell volume caused by the phase transformation to the RS structure (Fig. 1A). Upon decompression, the distorted fcc superlattice structure recovered in large part, whereas the atomic lattice system completely transformed to a four-coordinate ZB structure (Fig. 1A). Solid-phase transition of the atomic lattice exhibited a hysteresis of ~6.0 GPa, which was close to those measured under a pressure-media environment (6, 14). By contrast, in the sample of CdSe NCs capped with 93% butylamine coverage, a 4.8% RS phase was preserved back to ambient pressure (fig. S7A). These results suggested that ligand-shell thickness would play a major role in tailoring the reversibility of the RS-ZB phase transition in CdSe NC systems.

We performed more than 50 synchrotron-based high-pressure experiments to investigate the ambient metastability of RS CdSe structures as functions of amine ligand coverage and alkyl-chain length, the extent of long-range order in NC assemblies, applied pressure (up to 22 GPa), and decompression rate. At optimized conditions, only 50 to 60% of the RS structures were preserved in decompressed CdSe NC samples (Fig. 1B and fig. S7B). This result indicated that the surface binding of amine ligands may have been too strong and minimized effective interactions between neighboring NCs. However, when pyridine, a weakly binding ligand, was used, the NC assemblies exhibited nearly no long-range order, and no RS structure was retained in the NC system decompressed from 15.0 GPa, whereas after decompression from 16.2 GPa, 3.9% of RS structures were retained (fig. S8). These results suggest that the order of NC assemblies should play a role in the preservation of RS CdSe structures at ambient conditions.

To weaken the average ligand-binding strength while retaining the ability of the NCs to form ordered superstructures, we used a dual-ligand approach with a mixture of a primary amine (as the stronger binding ligand) and cetyltrimethylammonium bromide (CTAB) (as the weaker binding ligand; fig. S6B). The assembly of CdSe NCs functionalized with octylamine and CTAB (5:1 with a coverage of 63%; fig. S6A) formed an fcc superlattice with d_{111} -spacing of 5.03 nm (Fig. 1C). The RS-ZB transition became completely irreversible in these assemblies, and the RS CdSe structure was fully preserved at ambient conditions (Fig. 1C). The lattice constant of the fcc superstructure

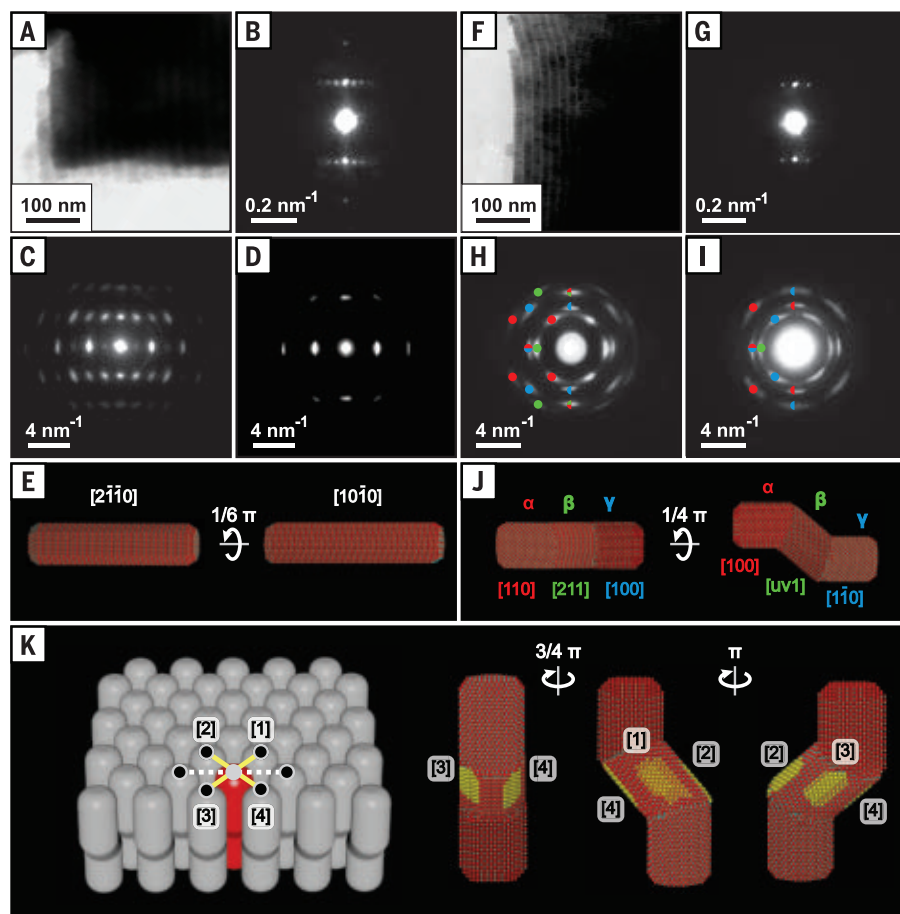


Fig. 3. Superlattice structures of CdSe/CdS WZ nanorods and RS nanorods. (A to D) Superlattices of WZ nanorods before compression: (A) TEM image, (B) small-angle electron diffraction (SAED) pattern at a 0°-tilt condition, and the wide-angle electron diffraction (WAED) pattern at a (C) 0°-tilt condition with $[2\bar{1}10]$ zone axis and at a (D) 30°-tilt condition with $[10\bar{1}0]$ zone axis. (E) 3D atomic nanorod model viewed along the zone axis of corresponding ED patterns shown in (C) and (D), respectively. (F to I) Superlattices of RS nanorods: (F) TEM image, (G) SAED pattern at a 0°-tilt condition, and the WAED pattern at a (H) 0°-tilt condition and at a (I) 45°-tilt condition, superimposed with simulated diffraction spots from the three corresponding RS domains (see figs. S18 and S19 for details). (J) 3D atomic model of a double-bend nanorod with three RS domains (α , β , γ) viewed at angles corresponding to those for ED patterns in (H) and (I), with labeled zone axes, where $u = (\sqrt{3} - 1)$ and $v = (\sqrt{3} - 2)$ at an off-axis direction (see fig. S20 for details). (K) Reconstructed 3D superlattice model showing each RS nanorod atomically overlapping with its four neighboring rods at corresponding rectangular areas on their β domains (fig. S22). The RS structures were extremely sensitive to electron beam irradiation and limited our ability to use conventional high-resolution TEM to study detailed features in RS nanostructures (fig. S26).

gradually decreased with a pressure increase up to 7.5 GPa. Above this pressure, the superstructure started to distort (indicated by a continuous expansion of its d_{111} -spacing) and then irreversibly transformed into a lamellar structure at pressures above ~ 12.0 GPa (fig. S9). Upon decompression to ambient pressure, the lamellar structure retained its integrity, and its d -spacing further increased to 5.81 nm (Fig. 1C and fig. S9).

Our TEM observations showed that the RS CdSe NCs existed only in the form of aggregates (fig. S10C). After sonication, they could be redispersed into 4.8-nm colloidal particles in

chloroform, but their crystal phase transformed into the ZB structure (fig. S10D). Altogether, these results suggest that strong interparticle associations (such as sintering) may have occurred within the lamellar structures that could be associated with the ambient metastability of the RS CdSe structure. Similar ligand-tailorable phenomena were observed in CdSe NCs capped with butylamine and CTAB ligands (fig. S7C).

The formation energy of ZB CdSe is 1.0 meV per atom lower than that of the WZ form, and such NCs were enclosed by crystal facets different from those of WZ (28). However, no substantial differences were observed between

4.8-nm ZB and WZ CdSe NCs in both the pressure-induced transformation to the RS structure and the ligand-tailorable reversibility of the RS-ZB phase transitions (fig. S11). Pure ambient metastable RS CdSe NCs can also be synthesized from ZB NCs (fig. S11B), showing that the initial crystal phase was not important for the ambient metastability of the resulting RS structures, and RS NCs that were transformed from the ZB and WZ phases could have degenerate three-dimensional (3D) atomic fine structures (29).

Bulk CdS, like CdSe, undergoes a reversible solid-phase transformation from a four- to six-coordinate structure at a pressure of ~ 2.5 GPa (30). However, CdS NCs exhibited substantial differences in the ligand-tailorable reversibility of their RS-ZB phase transition when compared with their CdSe counterparts (Fig. 2A). Dual-ligand functionalization was not necessary for making ambient metastable RS CdS NCs. Upon decompression from a pressure above 10.4 GPa, the RS phase was fully preserved in assemblies made from 4.8-nm ZB CdS NCs capped with amine ligand coverage as high as 95%, or even capped with 100% pyridine ligands, in which case NC assemblies exhibited no long-range order (Fig. 2A and fig. S12, A to C). By contrast, in assemblies of CdS NCs functionalized with excess octadecanethiol (ODT) (a stronger binding ligand than amines, for isolating CdS NCs as separate particles at high pressures), the RS-ZB phase transformation was completely reversible even when decompressed from 15.2 GPa (Fig. 2A and fig. S12D). These results demonstrated that the RS CdS phase was not intrinsically metastable at the nanometer scale, suggesting that the observed metastability in CdS NCs should also be related to strong interparticle associations, as in the case of RS CdSe NCs.

To further explore effects induced by chemical composition and particle structure, we synthesized 4.8-nm CdSe/CdS core/shell NCs in a WZ or ZB structure for corresponding 3.4-nm CdSe cores, and 4.8-nm WZ CdS/CdSe core/shell NCs from 3.4-nm CdS cores (figs. S3 and S4). In terms of the ligand-tailorable reversibility of the RS-ZB phase transition, both WZ and ZB CdSe/CdS NCs exhibited a nearly identical property to CdS NCs (Fig. 2B and figs. S13 to S15), whereas the behavior of CdS/CdSe NCs was in between that of CdS and CdSe NCs (Fig. 2C and fig. S16). Together, these results demonstrate that the composition of shell and core both play important roles in maintaining the RS phase at ambient conditions.

To study NC shape effects, we prepared atomically aligned nanorod superlattices at an air-liquid interface using 23.8-nm WZ CdSe/CdS nanorods functionalized with 95% octylamine coverage. These superlattices could be indexed as a simple hexagonal structure with lattice parameters of $a = 6.72$ nm and $c = 26.2$ nm, where the atomic WZ lattice of the CdSe/CdS

nanorods was coaxially aligned with the superlattice (fig. S17, A to C, and Fig. 3, A to E). After the pressure increase to 6.3 GPa, CdSe/CdS nanorods exhibited a WZ-RS phase transition at a pressure range slightly lower than that of the 4.8-nm CdSe/CdS core/shell nanospheres.

When decompressed from a pressure greater than ~10.0 GPa, the RS phase was fully preserved at ambient conditions (fig. S17A). During this process, the hexagonal superlattice structure was largely retained but was accompanied by a substantial d-spacing decrease in the *c*-axis direction, adopting a new set of lattice parameters of *a* = 6.97 nm and *c* = 17.5 nm (Fig. 3, F and G, and fig. S17A). As indicated by the dot-like electron diffraction (ED) patterns, the three-dimensionally ordered atomic alignments of CdSe/CdS nanorods persisted in the RS phase in the superlattices (Fig. 3, H and I). Altogether, our experimental data suggest that in this process, WZ CdSe/CdS nanorods transformed into double-bend RS nanorods with three domains, exhibiting a height of ~15.8 nm and an angle of 125.3° between neighboring domains (Fig. 3, F to J, and figs. S18 to S20). This shape change involved a shearing motion of the (0001) WZ crystal planes, which is consistent with the direction-dependent nucleation model of the

WZ-to-RS transition proposed by Alivisatos and co-workers (12, 14, 16).

The formation of three-domain nanorods is also consistent with TEM observations of the ZB nanorods recovered from RS aggregates (fig. S10, K and L). The recovered nanorods, having sizes similar to those of the nanorods before compression, exhibited traces of shape deformation and contained multiple crystalline domains and curved lattice fringes caused by strain (fig. S21). Based on all of the structural data, a reconstructed superlattice model showed that each double-bend nanorod atomically overlapped with four neighbors at the corresponding rectangular areas on the surfaces of their β domains, suggesting the existence of interparticle sintering, which would be responsible for the metastability of the RS phase (Fig. 3K and fig. S22). Indeed, in the assemblies of CdSe/CdS nanorods functionalized with excess strong-binding ODT ligands, the RS-ZB phase transition became fully reversible, and no detectable RS phase was observed when decompressed even from 12.5 GPa (figs. S10J and S17D).

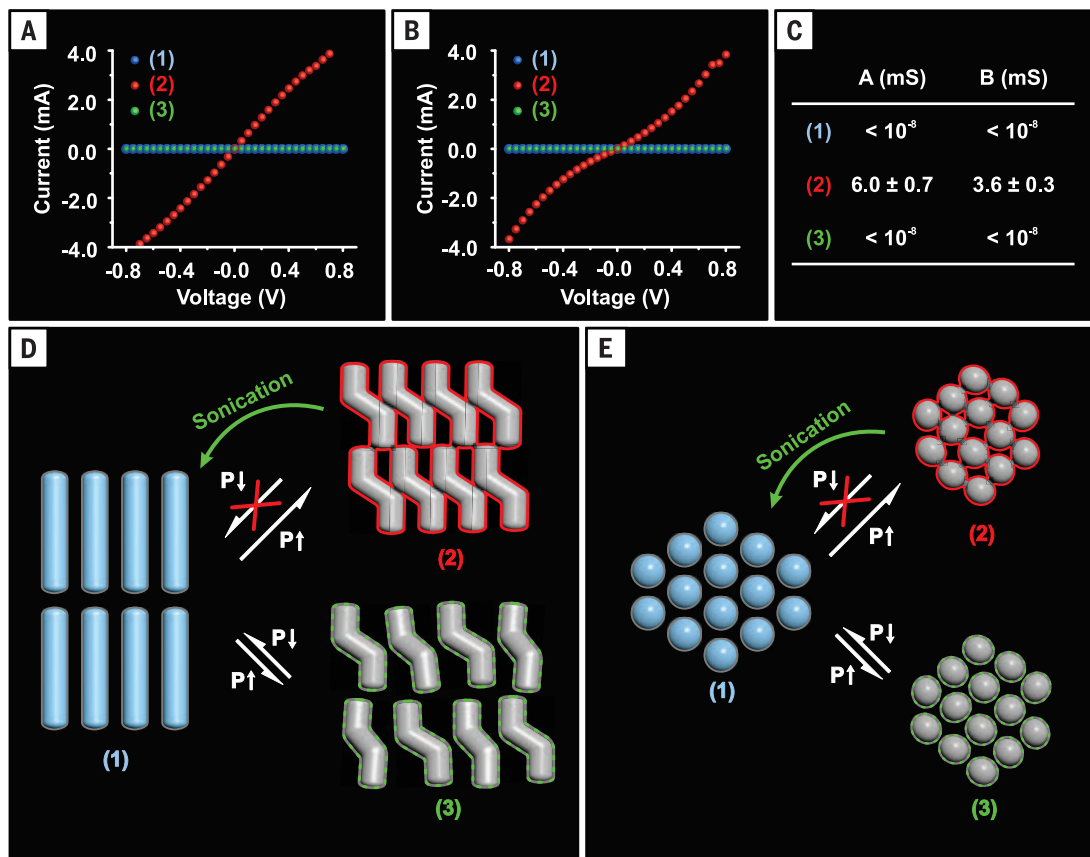
Additional information regarding interparticle sintering was obtained from electrical conductivity measurements (31). Films, composed of either WZ structures recovered before

the WZ-RS transition or ZB structures that transformed from the RS phase, were insulating below the detection limit (<10 pS), whereas the films of RS structures exhibited conductivities at least eight orders of magnitude higher, ranging from 3.0 to 8.0 mS (Fig. 4, A to C). These results, together with TEM observations, provide evidence that the ambient metastable RS phase existed in the form of three-dimensionally interconnected and partially fused NC networks created by interparticle sintering (Figs. 3 and 4 and fig. S10). These findings also suggest that the observed ligand-tailorable reversibility of their RS-ZB phase transition was caused by ligand effects during interparticle sintering, in which surface-ligand rearrangement was the initial step for the surface-atom diffusion and chemical-bond formation (32).

Based on these results, we propose that interparticle sintering was a main process that eliminated crystal defects and relaxed lattice distortions from high-pressure RS structures. The partial restoration of the intrinsic kinetic barrier in ideal crystals (as predicted by MYK) created ambient metastable nanostructures (Fig. 4, D and E). The RS NCs that formed from pressure-induced solid-phase transitions comprised a large quantity of high-energy crystal

Fig. 4. Electrical conductivity as indicator of interparticle sintering. (A and B) The current-voltage curve for films composed of assemblies of

(A) 23.8-nm WZ CdSe/CdS nanorods and (B) 4.8-nm WZ CdSe/CdS core/shell nanospheres in (1) the WZ phase before phase transition obtained by decompression from ~1.8 GPa, (2) the ambient stable RS phase obtained by decompression from ~10.4 GPa, or (3) the ZB phase that transformed from RS NCs with excess ODT after decompression from ~12.5 GPa. (C) Measured conductivity is shown in column A for nanorods and column B for nanospheres. (D and E) Schematic of proposed interparticle sintering mechanism for nanorods and nanospheres, respectively: (1) initial nanostructures at ambient pressure, (2) the RS phase in the form of interconnected NC networks at a high pressure (fig. S10, C, G, and K), and (3) the RS phase in the form of “free” NCs isolated with strong-binding ligands at high pressures. In recovered samples after decompression, either no or low degrees of interparticle sintering were observed with TEM (fig. S10, B, F, and J). P, pressure.



defects and lattice distortions (12) and served as nucleation sites for the rapid RS-to-ZB and RS-to-WZ transitions observed in the systems with no or low degrees of interparticle sintering (fig. S10, B, F, and J) (6, 11–14). In high-pressure-and/or deviatoric-stress-induced interparticle sintering, solid-state chemical reactions—driven by the minimization of Gibbs free energy—take place between surface atoms, forming effective sinks to absorb local high-energy defects and lattice distortions (33). These reactions produce grain and/or twin boundaries (GTBs) between neighboring particles (fig. S23, A and B) to form three-dimensionally interconnected nanocrystal networks in which crystal defects can be delocalized through stress-driven diffusion or propagation (34). This process allowed delocalized and collective GTB-defect interactions within an interconnected network where GTBs act as sources, sinks, or both to eliminate crystal defects through absorption and annihilation (note that GTBs also occurred within a single double-bend nanorod; fig. S23B) (35, 36).

Moreover, GTBs further acted as obstacles to block or jam dislocation motions and stabilize and harden interconnected NC networks (37, 38) and provided additional mechanisms to raise the activation barrier height for the RS-to-ZB transformation (fig. S23, C and D). These defect-elimination and strain-relaxation mechanisms depended on the hydrostatic and deviatoric stress applied on the system (24, 25). Our experimental findings showed that the activation barrier height in resulting RS structures was strongly dependent on the highest applied pressure, indicated by the observed partial reversibility of the RS-ZB transition in samples decompressed from lower pressures (figs. S13, S17, and S24). These results further demonstrate a critical pressure for a given NC system, above which point the resulting interconnected NC networks can fully retain the RS phase at ambient conditions (fig. S24).

This interparticle sintering (or partial fusion) mechanism is in good agreement with the entire set of experimental observations as well as the MYK prediction (8, 9). Without pressure media, the formation of three-dimensionally interconnected NC networks strongly interplays with an emergent phenomenon called force chain networks (39), which are created by interparticle interactions and by the topological patterns of pressure applied within the system (39, 40). Thus, the order of NC assemblies affects the degree of interparticle sintering as well as the mechanical integrity and strain uniformity of the resulting interconnected networks (Figs. 1C and 2C and fig. S8). In disordered systems, NC shape anisotropy promotes the formation of anisotropic force-chain-network architectures (40, 41), yielding strained-NC networks and thus imposing additional effects

on the ambient metastability of high-pressure phases. Indeed, when the ordering level of hexagonal-superlattice structures was decreased, CdSe/CdS nanorod assemblies retained 77.8% of the RS phase, whereas 100% was still preserved in totally disordered assemblies of CdSe/CdS nanospheres (figs. S14A and S25). In addition, the observed composition dependence in the ligand-tailorable reversibility of the RS-ZB phase transition likely originated from differences in the chemical and mechanical properties regarding interparticle sintering, as well as the formation, elimination, propagation, and annihilation of crystal defects and the relaxation of lattice distortions in the interconnected NC systems (29, 32–41).

To date, metastable RS CdSe, CdS, and CdSe/CdS samples in our lab have been fully preserved under ambient conditions for more than 6 years. This extended lifetime shows that an apparent activation-energy barrier of more than 1.3 eV per particle was created in the RS-to-ZB solid phase transformation (8, 20). The strategy for engineering transformation barriers established in this work is readily generalizable for making ambient metastable high-energy phases of other materials such as IV-VI and III-V semiconductors and transition-metal chalcogenides. In addition, our findings identify interconnected nanocrystal networks as a new form of matter that can effectively host metastable high-energy phases at ambient conditions. This approach allows for the rational design of synthetic methods for metastable materials through low-pressure routes (42), opening new opportunities for materials discovery and fabrication (2–5).

REFERENCES AND NOTES

- W. F. Smith, *Principles of Materials Science and Engineering* (McGraw-Hill, ed. 3, 1996).
- W. Sun et al., *Sci. Adv.* **2**, e1600225 (2016).
- H. Koinuma, I. Takeuchi, *Nat. Mater.* **3**, 429–438 (2004).
- A. Parija, G. R. Waetzig, J. L. Andrews, S. Banerjee, *J. Phys. Chem. C* **122**, 25709–25728 (2018).
- M. Aykol, S. S. Dwaraknath, W. Sun, K. A. Persson, *Sci. Adv.* **4**, eaq0148 (2018).
- C. C. Chen, A. B. Herhold, C. S. Johnson, A. P. Alivisatos, *Science* **276**, 398–401 (1997).
- J. M. Besson et al., *Phys. Rev. B* **44**, 4214–4234 (1991).
- L. E. Brus, J. A. W. Harkless, F. H. Stillinger, *J. Am. Chem. Soc.* **118**, 4834–4838 (1996).
- K. Mizushima, S. Yip, E. Kaxiras, *Phys. Rev. B* **50**, 14952–14959 (1994).
- C. B. Murray, D. J. Norris, M. G. Bawendi, *J. Am. Chem. Soc.* **115**, 8706–8715 (1993).
- S. H. Tolbert, A. P. Alivisatos, *Science* **265**, 373–376 (1994).
- J. N. Wickham, A. B. Herhold, A. P. Alivisatos, *Phys. Rev. Lett.* **84**, 923–926 (2000).
- K. Jacobs, A. P. Alivisatos, *Rev. Mineral. Geochem.* **44**, 59–72 (2001).
- K. Jacobs, D. Zaziski, E. C. Scher, A. B. Herhold, A. Paul Alivisatos, *Science* **293**, 1803–1806 (2001).
- K. Jacobs, J. Wickham, A. P. Alivisatos, *J. Phys. Chem. B* **106**, 3759–3762 (2002).
- D. Zaziski et al., *Nano Lett.* **4**, 943–946 (2004).
- M. Grünwald, E. Rabani, C. Dellago, *Phys. Rev. Lett.* **96**, 255701 (2006).
- T. Wang et al., *Adv. Mater.* **27**, 4544–4549 (2015).
- Z. Li et al., *Phys. Status Solidi B* **248**, 1149–1153 (2011).

- M. Grünwald, K. Lutker, A. P. Alivisatos, E. Rabani, P. L. Geissler, *Nano Lett.* **13**, 1367–1372 (2013).
- R. Martín-Rodríguez et al., *J. Appl. Phys.* **111**, 063516 (2012).
- H. Zhu et al., *J. Am. Chem. Soc.* **139**, 8408–8411 (2017).
- L. Meng et al., *J. Am. Chem. Soc.* **142**, 6505–6510 (2020).
- W. Li, H. Fan, J. Li, *Nano Lett.* **14**, 4951–4958 (2014).
- B. Li et al., *Sci. Adv.* **3**, e1602916 (2017).
- K. Bian, A. K. Singh, R. G. Hennig, Z. Wang, T. Hanrath, *Nano Lett.* **14**, 4763–4766 (2014).
- P. Podsiadlo et al., *Nano Lett.* **11**, 579–588 (2011).
- The Materials Project, Materials Project database; <https://materialsproject.org>.
- B. H. Kim et al., *Science* **368**, 60–67 (2020).
- H. Sowa, *Solid State Sci.* **7**, 73–78 (2005).
- D. Yu, C. Wang, P. Guyot-Sionnest, *Science* **300**, 1277–1280 (2003).
- L. Wang et al., *Science* **337**, 825–828 (2012).
- S. Tanaka, in *Materials Chemistry of Ceramics*, J. Hojo, Ed. (Springer, 2019).
- P. Heitjans, J. Karger, Eds., *Diffusion in Condensed Matter: Methods, Materials, Models* (Birkhäuser, ed. 2, 2005).
- X. M. Bai, A. F. Voter, R. G. Hoagland, M. Nastasi, B. P. Uberuaga, *Science* **327**, 1631–1634 (2010).
- J. Beyerlein, M. J. Demkowicz, A. Misra, B. P. Uberuaga, *Prog. Mater. Sci.* **74**, 125–210 (2015).
- K. Lu, *Nat. Rev. Mater.* **1**, 16019 (2016).
- X. Zhou, X. Y. Li, K. Lu, *Science* **360**, 526–530 (2018).
- S. Ostojic, E. Somfai, B. Nienhuis, *Nature* **439**, 828–830 (2006).
- K. P. Krishnaraj, P. R. Nott, *Phys. Rev. Lett.* **124**, 198002 (2020).
- E. Azéma, F. Radjai, *Phys. Rev. E* **85**, 031303 (2012).
- P. F. McMillan, *Nat. Mater.* **1**, 19–25 (2002).

ACKNOWLEDGMENTS

T.J. and X.W. contributed equally to this work. We thank the Research Service Centers (RSC) at the University of Florida for TEM usage. We thank B. Gao for the use of a thermogravimetric analyzer. We thank F. So in the Department of Materials Science and Engineering at the North Carolina State University for electric conductivity measurements. **Funding:** This work was supported by the National Science Foundation (DMR1710509, DMR1309798, DMR-1332208, and DMR-1829070) and special funds from the College of Liberal Arts and Science of the University of Florida. **Author contributions:** Y.C.C., T.X., and Y.N. conceived and designed experiments. T.X., T.J., X.W., C.C., and Y.N. performed the experiments and analyzed data. D.L., Y.L., J.Q., and Q.Z. participated in the early stages of the project, synthesized nanocrystals, and participated in data analysis. T.X., T.J., Y.N., J.Q., Q.Z., and X.D. designed, performed beamline synchrotron studies. T.X. and Y.N. performed TEM measurements and data simulations. Z.W. initiated this project, designed beamline synchrotron studies, and analyzed data. Y.C.C. supervised the entire project, analyzed data, and participated in simulations. Y.C.C., Z.W., and T.X. co-wrote the paper. All authors discussed the results and commented on the manuscript. **Competing interests:** The authors declare that they have no competing interests. **Data and materials availability:** All data needed to evaluate the conclusions in the paper are present in the main text or the supplementary materials. The samples can be provided by the authors upon reasonable request under a materials transfer agreement with the University of Florida. Requests for materials should be addressed to the corresponding author. **License information:** Copyright © 2022 the authors, some rights reserved; exclusive licensee American Association for the Advancement of Science. No claim to original US government works. <https://www.science.org/about/science-licenses-journal-article-reuse>

SUPPLEMENTARY MATERIALS

science.org/doi/10.1126/science.abq7684
Materials and Methods
Supplementary Text
Figs. S1 to S30
Table S1
References (43–50)

Submitted 29 April 2022; accepted 30 June 2022
10.1126/science.abq7684

IMMUNOLOGY

Cryo-EM structure of the human IgM B cell receptor

Qiang Su^{1,2,*†}, Mengying Chen^{3†}, Yan Shi^{1,2,4†}, Xiaofeng Zhang^{1,2}, Gaoxingyu Huang^{1,2},
Bangdong Huang^{1,2}, Dongwei Liu⁴, Zhangsuo Liu⁴, Yigong Shi^{1,2,3*}

The B cell receptor (BCR) initiates immune responses through antigen recognition. We report a 3.3-angstrom cryo-electron microscopy structure of human immunoglobulin M (IgM)-BCR in the resting state. IgM-BCR comprises two heavy chains, two light chains, and the Ig α /Ig β heterodimer. The ectodomains of the heavy chains closely stack against those of Ig α /Ig β , with one heavy chain locked between Ig α and Ig β in the juxtamembrane region. Extracellular interactions may determine isotype specificity of the BCR. The transmembrane helices of IgM-BCR form a four-helix bundle that appears to be conserved among all BCR isotypes. This structure contains 14 glycosylation sites on the IgM-BCR ectodomains and reveals three potential surface binding sites. Our work reveals the organizational principles of the BCR and may facilitate the design of antibody-based therapeutics.

B cells provide specific and long-lasting protection against a variety of pathogens (1, 2). B cell activation, initiated by antigen binding to the B cell receptor (BCR), results in B cell proliferation and differentiation into either plasma cells or memory cells (3). The BCR consists of a membrane-bound immunoglobulin (mIg) and two signal-transducing subunits, Ig α and Ig β (4, 5). The five mIg isotypes (A, D, E, G, and M) each comprise two heavy chains and two light chains (6). Mature naïve B cells express IgD and IgM, whereas memory B cells express IgA, IgG, or IgE (7). Antigen binding to the BCR triggers signal transduction by Ig α and Ig β (8), each of which consists of an Ig-like extracellular domain (ECD) and an intracellular immunoreceptor tyrosine-based activation motif (ITAM) (8).

Upon antigen binding, the BCRs are clustered on the plasma membrane, leading to phosphorylation of the ITAMs (3). ITAM phosphorylation triggers activation of downstream kinases exemplified by the spleen tyrosine kinase (SYK) and Bruton tyrosine kinase (BTK) (3). In addition, antigen-bound BCR complexes are internalized and processed, and antigenic peptides are presented to helper T cells (3). Activation of these kinases and participation of helper T cells drive the proliferation and differentiation of B cells (7, 9).

Several different models of BCR activation have been postulated, but the underlying mechanisms remain an open question (8, 10, 11).

The BCR pathway constitutes a key therapeutic target for B cell malignancies (12, 13). Small-molecule BTK inhibitors, such as ibrutinib and orelabrutinib, are used to treat several types of B cell lymphoma (14, 15). Polatuzumab vedotin, an Ig β -targeting monoclonal antibody conjugated to an antimetabolic agent, has been approved for the treatment of diffuse large B cell lymphoma (16). Abnormal BCR signaling also causes immune disorders, such as type 1 diabetes and systemic lupus erythematosus (17) and agammaglobulinemia (18).

Although the structures of sIg and the ECD of Ig β have been reported (19, 20), the architecture and organization of an intact BCR remain to be elucidated. Among all BCR isotypes, IgM-BCR is particularly important for B cell development and activation of naïve B cells as well as for oncogenic BCR signaling in most B cell malignancies (21). VRC01-IgM-BCR, with the variable domain replaced by that of the HIV neutralizing antibody VRC01, recognizes gp120 (22). Here, we report the cryo-electron microscopy (cryo-EM) structure of VRC01-IgM-BCR (referred to as IgM-BCR hereafter) in complex with a Fab fragment of polatuzumab.

An intact IgM-BCR consists of six chains: two heavy chains (μ), two light chains (κ), Ig α , and Ig β . To facilitate purification, we fused the recombinant κ chain and Ig α /Ig β to affinity tags (fig. S1A). To assist protein folding, we coexpressed IgM-BCR with pERp1, which promotes oxidative folding of IgM (23). In addition, H₂O₂ was used to preserve disulfide bonds in IgM-BCR. The purified IgM-BCR exhibited good solution behavior (fig. S1B). We also purified recombinant gp120 monomer and gp120 trimer (fig. S1C). As anticipated, IgM-BCR recognized both forms of gp120, with much greater avidities toward the trimer (fig. S1D). IgM-BCR formed a stable complex with the Fab of polatuzumab (fig. S1E).

The IgM-BCR complex was analyzed by cryo-EM (fig. S2A). We performed a seed-facilitated two-dimensional (2D) classification and heterorefinement using cryoSPARC (24), generating a reconstruction at 3.9 Å resolution (figs. S2B and S3). After 3D classification and refinement, the final reconstruction displayed an average resolution of 3.3 Å (fig. S4 and table S1). The EM maps displayed fine features for side-chain assignment (figs. S5 and S6), with local resolution reaching 2.8 Å (Fig. 1A). We modeled three Ig-like domains (C μ 2, C μ 3, and C μ 4) and a μ transmembrane region (TM μ) for each heavy chain (μ_A and μ_B), as well as the ECDs and TMs for Ig α /Ig β (Fig. 1B). The Fab domain (V μ -C μ 1/V κ -C κ) remained poorly resolved, likely reflecting its mobile position. In the low-pass-filtered EM map (Fig. 1C), two lobes of dumbbell-shaped density are connected to that of the Fc domain and may accommodate the Fab domains.

Another lobe of EM density is connected to that for Ig β and likely comes from polatuzumab-Fab. This conjecture was confirmed by the EM reconstruction of the polatuzumab-free IgM-BCR (fig. S7, A to D), which closely resembles that of the polatuzumab-bound IgM-BCR but lacks the suspected density (fig. S7, E and F). Thus, polatuzumab binding likely causes little structural alteration, consistent with the observation that polatuzumab recognizes the disordered N terminus of Ig β (25).

Each heavy chain spatially consists of five Ig modules (V μ , C μ 1, C μ 2, C μ 3, and C μ 4), a linker segment, L μ , and a transmembrane helix, TM μ (Fig. 1D). Each light chain comprises two Ig modules, V κ and C κ , which together with V μ and C μ 1 assemble into a Fab domain. Within the Fc domain, C μ 2, C μ 3, and C μ 4 from each heavy chain are twisted relative to each other (Fig. 1D). C μ 2_A and C μ 4_A interact with C μ 2_B/C μ 3_B and C μ 4_B, respectively. Furthermore, C μ 3_A is spatially separated from C μ 3_B, resulting in a large central hole in the Fc domain (Fig. 1, D and E).

C μ 2_A associates symmetrically with C μ 2_B, mainly through van der Waals interactions, with two Cys³³⁷ residues forming an inter-chain disulfide bond (Fig. 1E). C μ 2_A also recognizes the surface loops of C μ 3_B. In particular, Arg²⁵¹ and Arg²⁴³ of C μ 2_A donate three hydrogen bonds (H-bonds) to Asp³⁷⁶/Thr⁴³¹/Leu⁴³³ of C μ 3_B, whereas Leu³¹³ of C μ 2_A accepts an H-bond from Thr⁴²⁹ of C μ 3_B. Similar to the interface between C μ 2_A and C μ 2_B, the interface between C μ 4_A and C μ 4_B is symmetric and dominated by van der Waals contacts (Fig. 1F). The residues at the interface between the two C μ chains are invariant among mammals but show some variation in birds and fish (fig. S8A).

The Fc domain is connected to TM μ through L μ . TM μ_A associates with TM μ_B asymmetrically in the membrane. A number of hydrophobic residues from TM μ_A stack closely against the

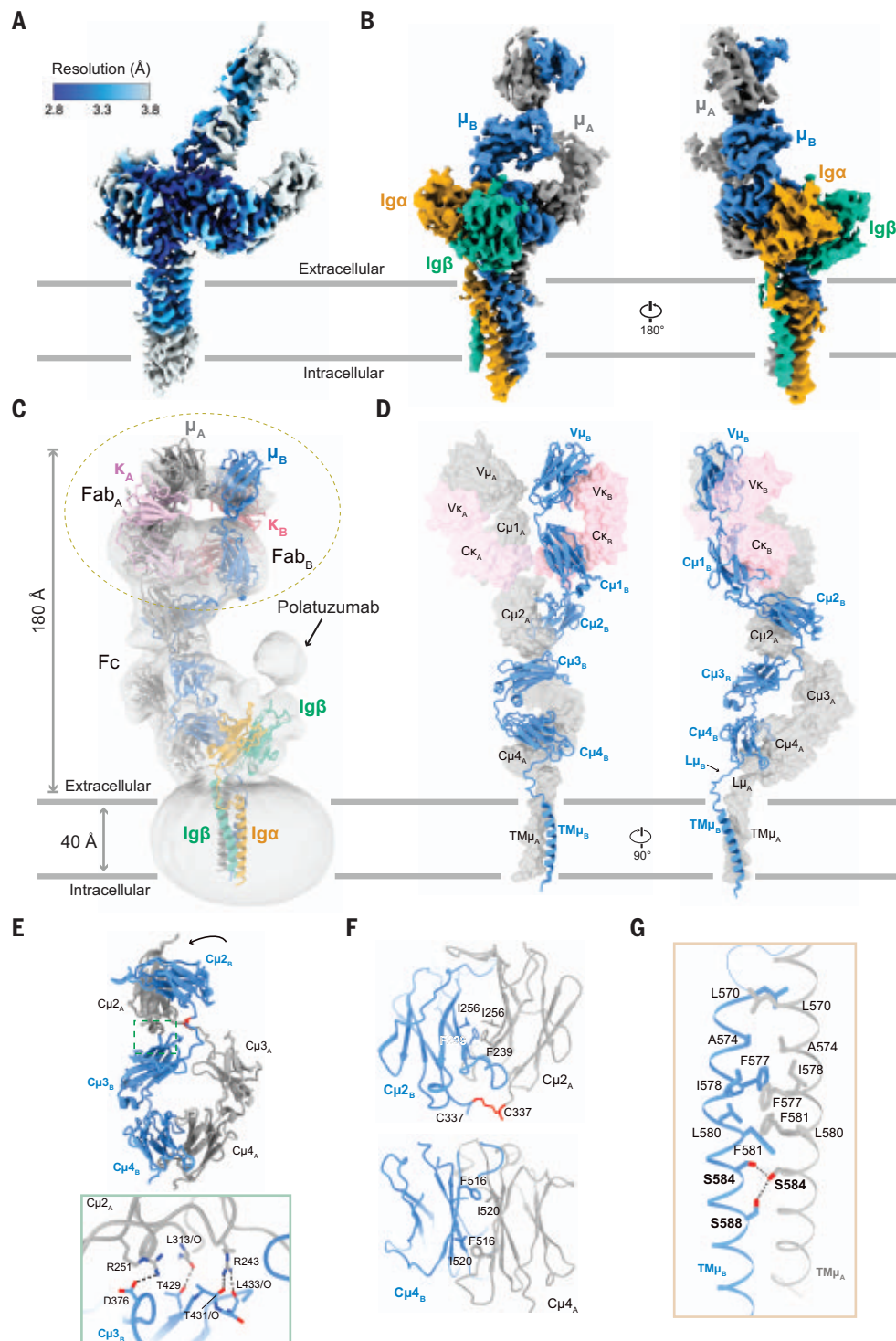
¹Research Center for Industries of the Future, Key Laboratory of Structural Biology of Zhejiang Province, School of Life Sciences, Westlake University, Institute of Biology, Westlake Institute for Advanced Study, Xihu District, Hangzhou 310024, Zhejiang Province, China. ²Westlake Laboratory of Life Sciences and Biomedicine, Xihu District, Hangzhou 310024, Zhejiang Province, China. ³Beijing Advanced Innovation Center for Structural Biology, Tsinghua-Peking Joint Center for Life Sciences, School of Life Sciences, School of Medicine, Tsinghua University, Beijing 100084, China. ⁴Department of Integrated Traditional and Western Nephrology, First Affiliated Hospital of Zhengzhou University, Henan Province Research Center for Kidney Disease, Zhengzhou 450052, P. R. China.

*Corresponding author. Email: syg@westlake.edu.cn (Y.S.); suqiang@westlake.edu.cn (Q.S.)

†These authors contributed equally to this work.

Fig. 1. Structure of the human IgM-BCR.

(A) Cryo-EM reconstruction of the human IgM-BCR at an average resolution of 3.3 Å. The local resolution is color-coded. The densities are contoured at 10 σ . **(B)** The structurally resolved IgM-BCR contains Ig α (gold), Ig β (teal), and two heavy chains, μ_A (gray) and μ_B (blue). Two views of the EM densities (contoured at 11 σ) are shown. The coloring scheme used in this panel is maintained throughout. **(C)** The low-pass filtered (to 15 Å) EM map of the human IgM-BCR shows the location of the Fab domains. Two Fab domains are docked into the EM density. The putative location of polatuzumab is indicated. The densities are contoured at 4 σ . **(D)** Modeled structure of the entire mIgM. Each heavy chain comprises five Ig-like domains ($V\mu$, $C\mu1$, $C\mu2$, $C\mu3$, and $C\mu4$), a linker $L\mu$, and a trans-membrane (TM) region. $C\mu2$, $C\mu4$, and TM domains in μ_A interact with the corresponding domains in μ_B . For clarity, the μ_B chain is shown in cartoon. All other chains are represented by transparent surface. Two orthogonal views are shown. **(E)** $C\mu2_A$ interacts with both $C\mu2_B$ and $C\mu3_B$. The lower panel is a magnified view showing the interface between $C\mu2_A$ and the surface loops of $C\mu3_B$. H-bonds are indicated by black dashed lines. **(F)** Magnified views of the $C\mu2_A/C\mu2_B$ (top) and $C\mu4_A/C\mu4_B$ (bottom) interfaces. **(G)** A magnified view of the interface between $TM\mu_A$ and $TM\mu_B$. All structural figures were prepared using UCSF ChimeraX (40) unless otherwise indicated.



corresponding residues from $TM\mu_B$ (Fig. 1G). Notably, there are two membrane-embedded, interchain H-bonds. The hydroxyl side chain of Ser⁵⁸⁴ from $TM\mu_A$ makes bifurcated H-bonds to the side chains of Ser⁵⁸⁴ and Ser⁵⁸⁸ from $TM\mu_B$. These H-bonds may help maintain the register between $TM\mu_A$ and $TM\mu_B$. The residues at this interface are invariant among the heavy chains of all organisms examined (fig. S8A).

Unlike mIgM, sIgM exists as a pentamer or hexamer (19, 26). Both mIgM and sIgM share the same sequences in the $C\mu$ region. Structural comparison between mIgM and sIgM (19) reveals a similar conformation for $C\mu3$ and $C\mu4$, with a root mean squared deviation (RMSD) of 1.1 Å over 225 aligned $C\alpha$ atoms (fig. S8B). Outside this region, mIgM and sIgM display substantial structural variations. Two

C-terminal β strands (known as tailpieces) of sIgM $C\mu4$ mediate sIgM oligomerization (19). By contrast, two C-terminal α helices, $TM\mu_A$ and $TM\mu_B$, of $C\mu4$ anchor mIgM on the cell membrane.

The Ig α /Ig β heterodimer is an obligate component of all BCRs (4, 6). The primary sequences of Ig α and Ig β are conserved from fish to humans (fig. S9, A and B). The Ig α /Ig β

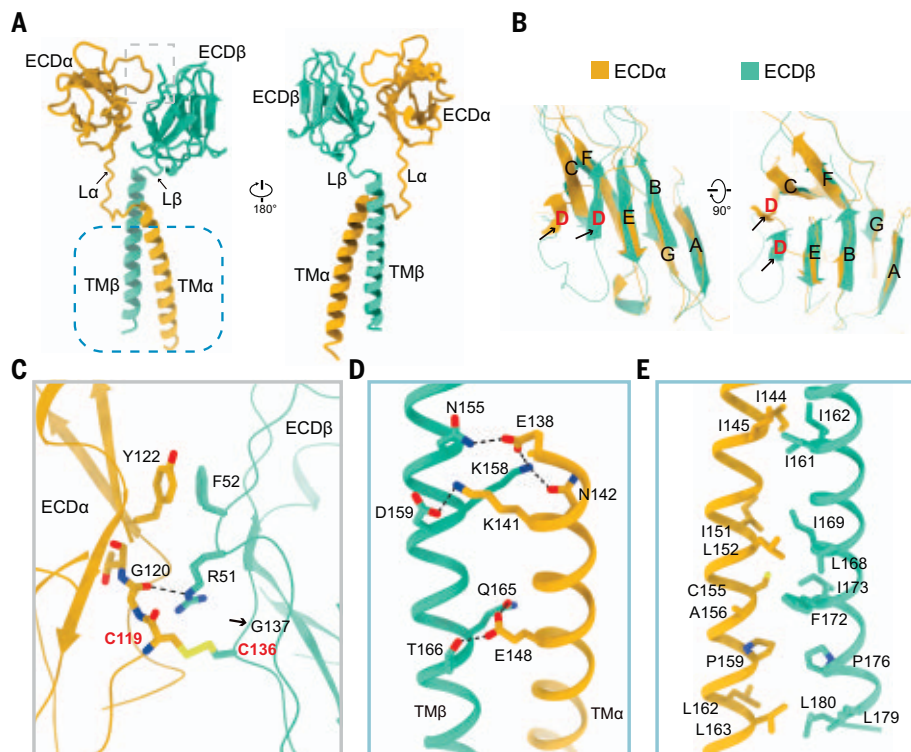


Fig. 2. Structure of the Igα/Igβ heterodimer. (A) Overall structure of the Igα/Igβ heterodimer. Igα or Igβ comprises an ECD, a linker, and a TM. Two views are provided. (B) ECDα and ECDβ are structurally similar. Strand D is positioned quite differently between ECDα and ECDβ, however. (C) A magnified view of the interface between ECDα and ECDβ. Cys¹¹⁹ of ECDα and Cys¹³⁶ of ECDβ form a disulfide bond. H-bonds are indicated by black dashed lines. The location of the disease mutation G137S in Igβ is indicated by a black arrow. (D) The interface between TMα and TMβ features several specific H-bonds. In the juxtamembrane region, three residues from each TM participate in a network of four H-bonds. In the middle of the TM, Glu¹⁴⁸ from TMα accepts two H-bonds from the side chains of Gln¹⁶⁵ and Thr¹⁶⁶. (E) The interface between TMα and TMβ involves extensive van der Waals contacts.

structure resembles a pair of scissors (Fig. 2A), each consisting of an ECD, a linker, and a TM. ECDα and ECDβ share 25% sequence identity (fig. S9C) and have a similar conformation with 0.87 Å RMSD over 83 aligned Cα atoms (Fig. 2B). The only notable difference is a positional shift of ~8 Å for strand D.

Igα interacts with Igβ through ECDα/ECDβ on the extracellular side and TMα/TMβ within the membrane. Cys¹¹⁹ of ECDα and Cys¹³⁶ of ECDβ form a disulfide bond (Fig. 2C), confirming a reported finding (20, 27). The disulfide bond is buttressed by π - π stacking between Tyr¹²² of Igα and Phe⁵² of Igβ and an H-bond between Gly¹²⁰ of Igα and Arg⁵¹ of Igβ. All these residues are highly conserved across species (fig. S9, A and B), suggesting conservation of the ECDα/ECDβ interface. The agammaglobulinemia-causing mutation G137S in Igβ impairs BCR assembly by reducing disulfide bond formation between Igα and Igβ (28). In our structure, Gly¹³⁷ is positioned next to the interchain disulfide bond (Fig. 2C) and the mutation G137S may perturb the local conformation.

The TMα/TMβ interface registers at least six specific H-bonds (Fig. 2D). At the juxtamembrane region, the Glu¹³⁸ side chain of TMα accepts two H-bonds from Asn¹⁵⁵ and Lys¹⁵⁸ of TMβ. Lys¹⁴¹ and Asn¹⁴² of TMα mediate two H-bonds to Asp¹⁵⁹ and Lys¹⁵⁸ of TMβ, respectively. In the transmembrane region, Asp¹⁴⁸ of TMα makes two H-bonds to Gln¹⁶⁵ and Thr¹⁶⁶ of TMβ (Fig. 2D). Moreover, the TMα/TMβ interface also features extensive van der Waals contacts (Fig. 2E). The residues involved in these interactions are highly conserved across species (fig. S9, A and B), again suggesting a conserved transmembrane interface. The elaborate H-bonds between TMα and TMβ argue against a marked interhelical shift in response to antigen recognition by BCR. However, this analysis does not rule out the possibility that antigen binding may lead to a new pattern of specific interactions in the TM region.

Consistent with previous characterization (5, 29), mIgM noncovalently associates with Igα/Igβ (Fig. 3A). Remarkably, the linker L_μB traverses through a hollow structure (referred

to as the O-ring) that is formed between Igα and Igβ. This O-ring is sealed on the extracellular side and the membrane side by ECDα/ECDβ and TMα/TMβ, respectively. This strongly suggests that cofolding between the heavy chain of mIgM and Igα/Igβ occurs during assembly of IgM-BCR. Consistent with the structural implication, mIgM exhibits no detectable binding to the Igα/Igβ heterodimer in vitro (fig. S10A). Only through their coexpression and cofolding in the endoplasmic reticulum can Igα/Igβ and mIgM assemble into an intact, functional IgM-BCR that is targeted to the plasma membrane (30).

In the transmembrane region, TM_μA and TM_μB are in parallel with TMβ and TMα, respectively (Fig. 3B). The interfaces between TM_μA/TM_μB and TMβ/TMα are dominated by van der Waals contacts. Nonetheless, there are three buried H-bonds within the membrane-spanning region: between Tyr⁵⁸⁷ of TM_μB and Thr¹⁶¹ of TMα, between Thr⁵⁷³ of TM_μB and Thr¹⁴⁶ of TMα, and between Glu⁵⁶⁸ of TM_μA and Gln¹⁵⁰ of TMβ. Tyr⁵⁸⁷ has been shown to be critical for complex formation between mIgM and Igα/Igβ (31). Among these residues, Thr⁵⁷³/Tyr⁵⁸⁷ of TM_μB and Thr¹⁴⁶/Thr¹⁶¹ of TMα are invariant across species, whereas Glu⁵⁶⁸ of TM_μA and Gln¹⁵⁰ of TMβ are invariant among mammals (figs. S8A and S9).

In the juxtamembrane region, L_μB is oriented mainly by three positively charged residues of ECDβ through the O-ring (Fig. 3C). Specifically, the guanidinium group of Arg⁵⁷ from ECDβ donates two H-bonds to Glu⁵⁶⁵ and Ala⁵⁶², and stacks against Phe⁵⁶⁷ through a cation- π interaction. Lys⁵⁶ and Arg⁵⁵ of ECDβ make H-bonds to Glu⁵⁵⁷ and Asp⁵⁵³, respectively. Thus, L_μ appears to play a key role in the association with Igα/Igβ, consistent with its requirement for BCR assembly (29).

On the extracellular side, ECDα/ECDβ stacks against C_μ3_B/C_μ4_B through an extended interface (Fig. 3D). On one side, Asn⁷³ and Thr⁷⁵ of ECDα mediate H-bonds to Gln⁴⁹³ and Gln⁴⁸⁷ of C_μ4_B, respectively. The aromatic side chain of Trp⁷⁶ of ECDα is sandwiched by Phe³⁵⁸ of C_μ3_B and Phe⁴⁸⁵ of C_μ4_B. On the other side, ECDβ only contacts C_μ4_B. Arg⁵⁵, Lys⁶², and Tyr⁶⁶ of ECDβ make three H-bonds to Thr⁵³³, Thr⁵³⁰, and Arg⁴⁹¹ of C_μ4_B, respectively (Fig. 3D). These residues are highly conserved across species (figs. S8A and S9), suggesting a conserved mode of interaction.

To corroborate these findings, we assessed the impact of mutations on IgM-BCR assembly. Consistent with our structural observations, mutations affecting the TM interfaces between the μ chain and Igα/Igβ (T573A/Y587A, F577W, or F581W in μ chain; L152W or A156W in Igα; I161W in Igβ) blocked IgM-BCR assembly (fig. S10B). Furthermore, mutations (D553A/E565A in L_μB; R55A/K56A/R57A in ECDβ) affecting the interface between L_μB and ECDβ also

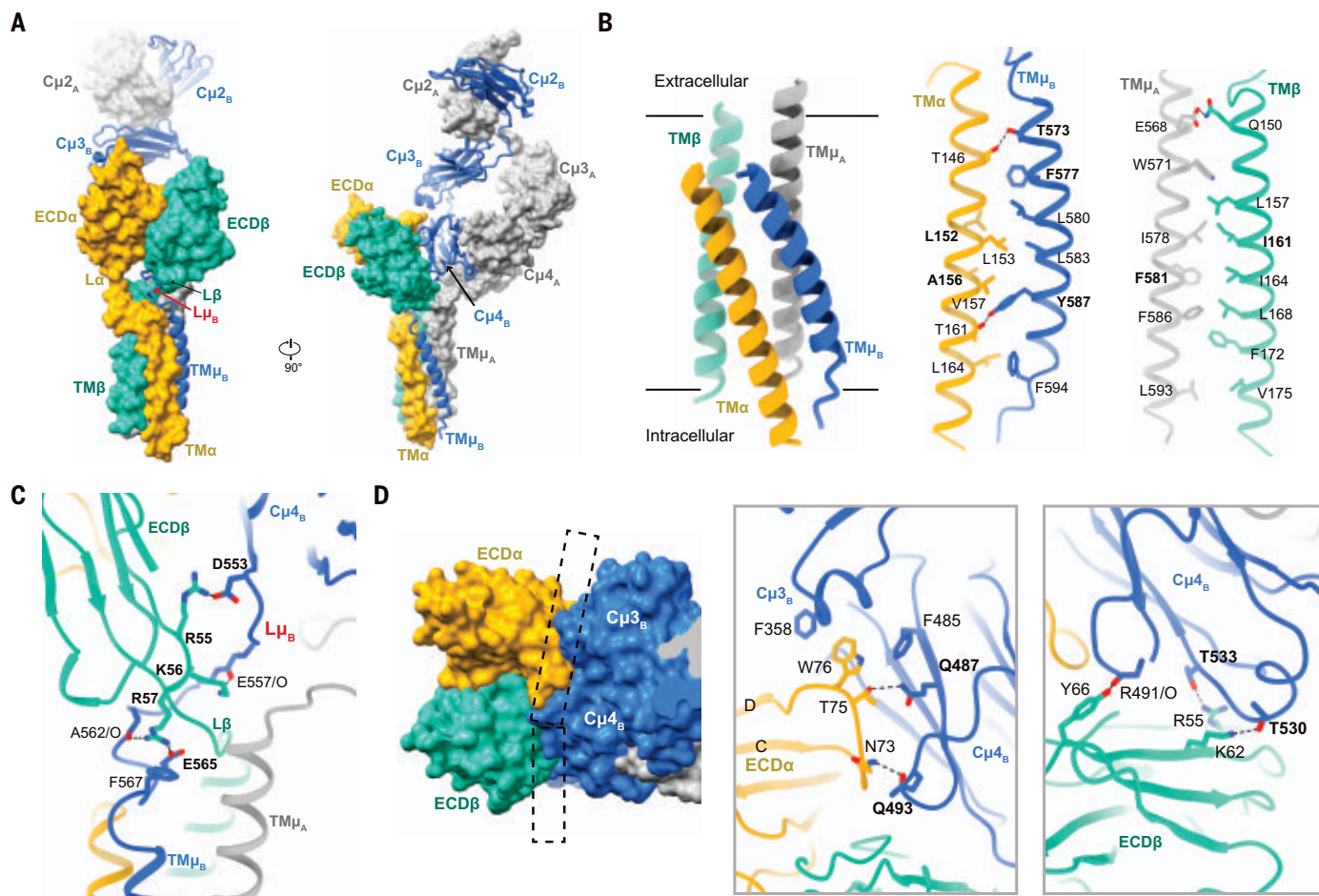


Fig. 3. Assembly of mIgM and Igα/Igβ into intact IgM-BCR. (A) The heavy chain μ_B traverses through a hollow structure (O-ring) formed by the Igα/Igβ heterodimer. Two perpendicular views are provided. The μ_B chain is displayed in cartoon. All other chains are represented by surface. (B) The TMs of mIgM and Igα/Igβ form a four-helix bundle. The pairwise interfaces for TM μ_B /TM α and TM μ_A /TM β are shown in the center and right panels,

respectively. (C) A magnified view of the accommodation of L μ_B in the O-ring. Residues from L μ_B primarily engage three positively charged residues (Arg⁵⁵, Lys⁵⁶, Arg⁵⁷) of ECD β in the juxtamembrane region. (D) ECD α /ECD β directly interacts with C μ_3 _B and C μ_4 _B. Left: Surface representation of this interface. Center and right: Magnified views between ECD α and C μ_4 _B/C μ_3 _B and between ECD β and C μ_4 _B.

crippled IgM-BCR formation. By contrast, mutations affecting the interface between C μ_4 _B and ECD α /β (Q487A/Q493A and T530A/T533A in μ chain) had little impact on IgM-BCR formation (fig. S10B). Thus, the TMs and L μ_B —but not the ectodomains particularly—play a key role in the assembly of IgM-BCR.

IgM-BCR is heavily glycosylated (27, 29). Our EM map allows identification of 14 glycans (fig. S6F). ECD α has six N-linked glycosylation sites (Asn⁵⁷, Asn⁶³, Asn⁷³, Asn⁸⁸, Asn⁹⁷, and Asn¹¹²), whereas ECD β has two such sites (Asn⁷³ and Asn¹⁰¹) (Fig. 4A). Three additional glycosylation sites are located on each heavy chain: Asn³³² on C μ_2 and Asn³⁹⁵/Asn⁴⁰² on C μ_3 (Fig. 4B). Analysis of glycan distribution reveals three surface patches that are free of glycosylation (Fig. 4C). Patch-1 is formed by the surface of ECD α and C μ_4 _B on one side of IgM-BCR. Patch-2, located on the opposite side of Patch-1, consists of the surface of ECD β and C μ_4 _B. Patch-3 covers the

surface between ECD α and ECD β and overlaps with Patch-1.

These patches represent potential epitopes for recognition by antibodies or miniproteins. Each patch contains one or more hydrophilic surface loops (Fig. 4D and table S2), which display high scores of antigenicity (32). However, recognition by bulky antibody may be hindered by steric hindrance, as these loops are relatively short and appear to be ordered. Consistent with this notion, the N-terminal flexible sequences of Ig β constitute the only recognition site for polatuzumab and other antibodies to Ig β (25). Nonetheless, smaller binders such as designed nanobodies and miniproteins may serve as other viable alternatives.

The residues at the interchain interfaces of IgM-BCR are conserved from zebrafish to humans (figs. S8A and S9), suggesting evolutionary conservation of the IgM-BCR assembly. In particular, key residues at the TM μ_A /TM μ_B

interface are almost invariant in the five mIgs. Thus, the register-maintaining H-bonds observed in mIgM are most likely preserved in the other four BCRs. Tyr⁵⁸⁷, invariant among all five BCRs, plays a key role in anchoring TM α (Fig. 3B). This strongly suggests a conserved interface in the TMs of all five BCRs. The structure of C μ_4 is almost identical among the five mIgs (fig. S11B) (19, 33–35). However, the residues at the interface between C μ_4 and ECD α /ECD β show major variations (fig. S11A). Thus, a conserved interface between mIg and Igα/Igβ appears to exist in the TM region, but not on the extracellular side, among the five BCRs (36). Accordingly, the TM shows greater sequence conservation than the ectodomains (fig. S11C).

The molecular basis for different signaling properties of the BCRs is partially suggested by structural and sequence analysis. The sequences in the linker and ectodomain are highly variable

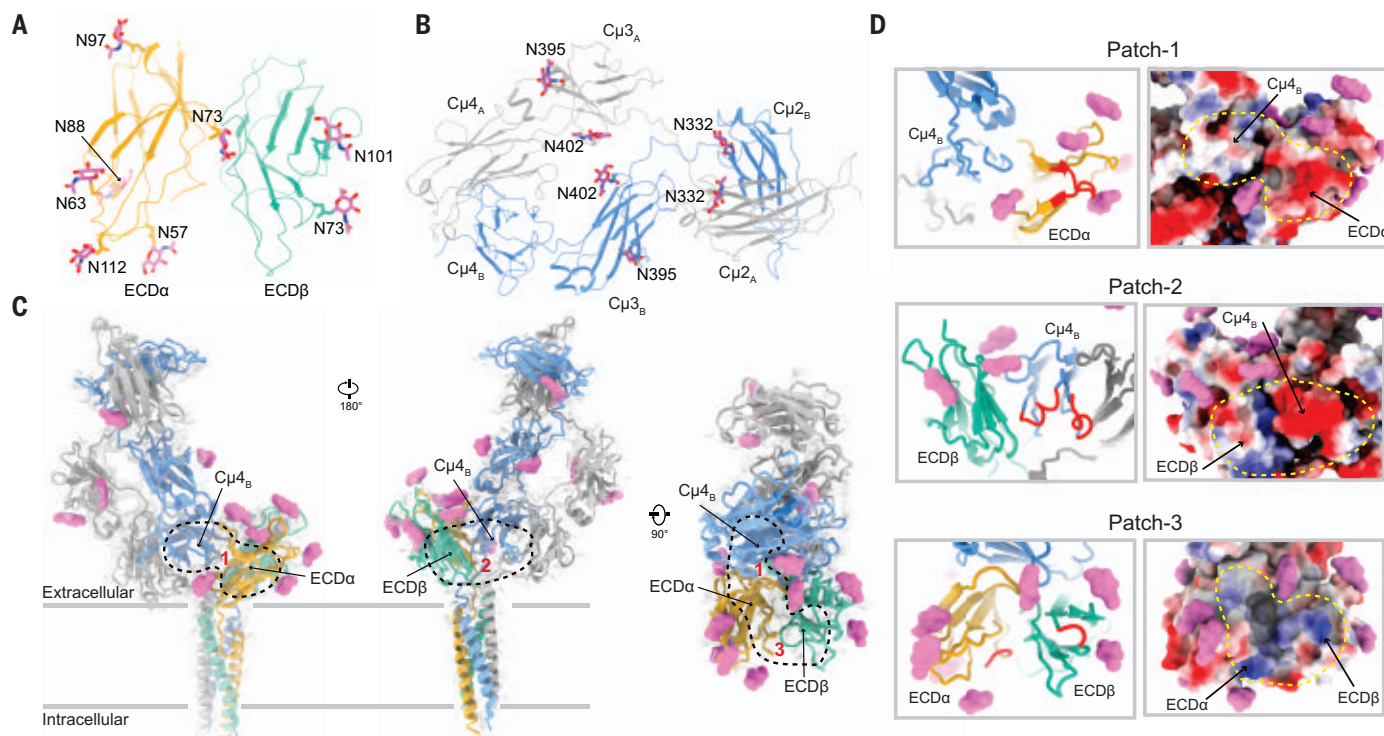


Fig. 4. N-linked glycosylation sites in the ectodomains of IgM-BCR.

(A) Eight glycosylation sites—six on ECDα and two on ECDβ—are structurally identified in the Igα/Igβ heterodimer. (B) Structural identification of six glycosylation sites in the Fc domain. Two sites are located on each Cμ3 and one site on each Cμ2. (C) Identification of three surface epitopes in IgM-BCR for recognition by antibody or miniprotein. Three views of the glycosylated

IgM-BCR are shown. The glycans are represented as magenta surfaces. The glycan-free surface epitopes are indicated by black dashed circles. (D) Magnified views of the three surface epitopes. Left: Hydrophilic surface loops are colored red. Right: These surface loops are enriched by charged amino acids. The glycan-free candidate epitopes are indicated by yellow dashed circles.

among different classes of mIg. Therefore, the Igα/Igβ binding mode of the ectodomain is likely to differ among the different BCR classes. This has been partially confirmed by the described structural variation between IgM-BCR and IgG-BCR (36). Such differences in ectodomain engagement may constitute a form of conformational signaling.

The inhibition of BCR signaling constitutes an effective strategy for disease treatment (12). Patch-1 and Patch-2 each contains a sizable surface area from both mIgM and Igα/Igβ (Fig. 4D), constituting a binding site specific for IgM-BCR, but not for sIgM or other BCRs. A specific binder conjugated to an antitumor drug could potentially be designed for the depletion of IgM⁺ B cells. Moreover, a specific binder could be fused to a Fc fragment for ligation of IgM-BCR with its inhibitory co-receptor, FcγRIIb, to suppress IgM-BCR signaling in chronic lymphocytic leukemia (37). Thus, our structure reveals concrete clues for future drug discovery efforts.

During BCR activation, co-receptors such as CD19, CD81, and CD20 are thought to associate with IgM-BCR in the TM region (27). The mutation Y587V/S588V in the TM of mIgM, which impairs its association with Igα/Igβ, suppresses downstream signaling events de-

spite normal antigen recognition (27, 31). Thus, small molecules that bind the conserved TM region may negatively affect assembly of IgM-BCR and block BCR signaling.

The stoichiometric ratio between mIg and Igα/Igβ was originally thought to be 1:2 (4, 38), but subsequent studies suggested the ratio to be 1:1 (5, 39) (fig. S12A). In our resting-state IgM-BCR structure, the ECDs of Igα/Igβ bind Cμ4B, while Cμ4A is close to the membrane. If Cμ4A also binds Igα/Igβ, the ECDs of Igα/Igβ will sterically clash with the cell membrane. Thus, the structural features of IgM-BCR are incompatible with the 1:2 molar ratio (fig. S12B).

Several models of BCR activation have been proposed, including the dissociation activation model, conformation-induced oligomerization model, and collision coupling model (8, 10, 11). Our current structure does not conflict with such models, and additional studies will be needed to definitively resolve this ongoing debate. For recombinant BCR in solution, the Fab domain is quite flexible relative to the Fc domain, and antigen binding is unlikely to transduce a conformational change from the Fab to the Fc domain in solution. However, endogenous IgM-BCR is restricted to the cell membrane, which is more conducive to binding-induced conformational changes. In addition,

co-receptors may contribute to force transmission. Elucidation of the activation mechanism may be greatly facilitated by structural determination of the activated BCR from native B cells by cryo-EM and direct visualization of the activated BCR in cells by cryo-electron tomography (cryo-ET).

REFERENCES AND NOTES

1. T. W. LeBien, T. F. Tedder, *Blood* **112**, 1570–1580 (2008).
2. F. A. Bonilla, H. C. Oettgen, *J. Allergy Clin. Immunol.* **125** (suppl. 2), S33–S40 (2010).
3. N. E. Harwood, F. D. Batista, *Annu. Rev. Immunol.* **28**, 185–210 (2010).
4. J. Hombach, T. Tsubata, L. Leclercq, H. Stappert, M. Reth, *Nature* **343**, 760–762 (1990).
5. W. W. Schamel, M. Reth, *Immunity* **13**, 5–14 (2000).
6. A. R. Venkitaraman, G. T. Williams, P. Dariavach, M. S. Neuberg, *Nature* **352**, 777–781 (1991).
7. K. Kwak, M. Akkaya, S. K. Pierce, *Nat. Immunol.* **20**, 963–969 (2019).
8. B. Treanor, *Immunology* **136**, 21–27 (2012).
9. R. J. Brezski, J. G. Monroe, *Adv. Exp. Med. Biol.* **640**, 12–21 (2008).
10. J. Yang, M. Reth, *Nature* **467**, 465–469 (2010).
11. S. K. Pierce, W. Liu, *Nat. Rev. Immunol.* **10**, 767–777 (2010).
12. J. A. Burger, A. Wiestner, *Nat. Rev. Cancer* **18**, 148–167 (2018).
13. D. G. Efremov, S. Turkali, L. Laurenti, *Cancers* **12**, 1396 (2020).
14. S. Dhillion, *Drugs* **81**, 503–507 (2021).
15. A. Charalambous, M. A. Schwarzlich, M. Witzens-Harig, *Recent Results Cancer Res.* **212**, 133–168 (2018).
16. E. D. Deeks, *Drugs* **79**, 1467–1475 (2019).
17. D. J. Rawlings, G. Metzler, M. Wray-Dutra, S. W. Jackson, *Nat. Rev. Immunol.* **17**, 421–436 (2017).
18. L. Yel et al., *N. Engl. J. Med.* **335**, 1486–1493 (1996).

19. Y. Li et al., *Science* **367**, 1014–1017 (2020).
20. S. Radaev et al., *Structure* **18**, 934–943 (2010).
21. M. R. Gold, M. G. Reth, *Annu. Rev. Immunol.* **37**, 97–123 (2019).
22. Z. Shen et al., *eLife* **8**, e42271 (2019).
23. E. van Anken et al., *Proc. Natl. Acad. Sci. U.S.A.* **106**, 17019–17024 (2009).
24. A. Punjani, J. L. Rubinstein, D. J. Fleet, M. A. Brubaker, *Nat. Methods* **14**, 290–296 (2017).
25. B. Zheng et al., *Mol. Cancer Ther.* **8**, 2937–2946 (2009).
26. R. Müller et al., *Proc. Natl. Acad. Sci. U.S.A.* **110**, 10183–10188 (2013).
27. K. S. Campbell, J. C. Cambier, *EMBO J.* **9**, 441–448 (1990).
28. A. K. Dobbs et al., *J. Immunol.* **179**, 2055–2059 (2007).
29. W. W. Schamel, M. Reth, *Mol. Immunol.* **37**, 253–259 (2000).
30. G. S. Brouns, E. de Vries, J. Borst, *Int. Immunol.* **7**, 359–368 (1995).
31. S. A. Grupp, K. Campbell, R. N. Mitchell, J. C. Cambier, A. K. Abbas, *J. Biol. Chem.* **268**, 25776–25779 (1993).
32. J. Ponomarenko et al., *BMC Bioinformatics* **9**, 514 (2008).
33. T. Wan et al., *Nat. Immunol.* **3**, 681–686 (2002).
34. N. Kumar, C. P. Arthur, C. Ciferri, M. L. Matsumoto, *Science* **367**, 1008–1014 (2020).
35. E. O. Saphire et al., *Science* **293**, 1155–1159 (2001).
36. X. Ma et al., *Science* **377**, 880–885 (2022).
37. R. Bosch et al., *Haematologica* **106**, 306–309 (2021).
38. M. Reth et al., *Immunol. Today* **12**, 196–201 (1991).
39. P. Tolar, H. W. Sohn, S. K. Pierce, *Nat. Immunol.* **6**, 1168–1176 (2005).
40. E. F. Pettersen et al., *Protein Sci.* **30**, 70–82 (2021).

ACKNOWLEDGMENTS

We thank L. Huang, X. Wang, and Z. Jiang of Westlake University Cryo-EM facility for technical assistance; the High-Performance Computing Center and Mass Spectrometry & Metabolomics Core Facility for support; and P. Zhang of the Protein Characterization and Crystallography Facility for advice. **Funding:** Supported by National Natural Science Foundation of China grants 31930059 and 81920108015 (Yi.S.), 81970633 (Z.L.), and U1904146 (D.L.), and by Key R&D Program of Zhejiang Province grant 2020C04001 and National Key R&D Program of China grant 2020YFA0509300 (Yi.S.). **Author contributions:** Q.S. conceived the project and designed the experiments. Ya.S. conducted cloning, protein purification, and biochemical analysis. M.C. performed cryo-EM analysis. All authors contributed to data analysis. Yi.S. and Q.S. wrote the manuscript. Yi.S. supervised the project. **Competing interests:** The authors declare no competing interests. **Data and materials availability:** The atomic coordinates

for IgM-BCR-polatuzumab have been deposited in the PDB with accession code 7XQ8. The EM maps of IgM-BCR and IgM-BCR-polatuzumab have been deposited in the EMDB with accession codes EMD-33438 and EMD-33390, respectively. All other data needed to support the conclusions in this manuscript can be found in the main text or supplementary materials. All materials are available from the corresponding authors upon request. **License information:** Copyright © 2022 the authors, some rights reserved; exclusive licensee American Association for the Advancement of Science. No claim to original US government works. www.science.org/about/science-licenses-journal-article-reuse

SUPPLEMENTARY MATERIALS

science.org/doi/10.1126/science.abc3923
Materials and Methods
Figs. S1 to S12
Tables S1 and S2
References (41–59)

Submitted 31 January 2022; accepted 11 July 2022
10.1126/science.abc3923

IMMUNOLOGY

Cryo-EM structures of two human B cell receptor isotypes

Xinyu Ma[†], Yuwei Zhu[†], De Dong[†], Yan Chen[†], Shubo Wang, Dehui Yang, Zhuo Ma, Anqi Zhang, Fan Zhang, Changyou Guo, Zhiwei Huang*

The B cell receptor (BCR) complex plays a critical role in B cell development and immune responses. The assembly mechanisms underlying the BCR complex remain unknown. We determined the cryo-electron microscopy (cryo-EM) structures of human IgG-BCR and IgM-BCR, which consist of membrane-bound immunoglobulin molecules (mIg) and Igα/β subunits at a 1:1 stoichiometry. Assembly of both BCR complexes involves their extracellular domains, membrane-proximal connection peptides, and transmembrane (TM) helices. The TM helices of mIgG and mIgM share a conserved set of hydrophobic and polar interactions with Igα/β TM helices. By contrast, the IgG-Cγ3 and IgM-Cμ4 domains interact with extracellular Ig-like domains of Igα/β through head-to-tail and side-by-side modes, respectively. This work reveals the structural basis for BCR assembly and provides insights into BCR triggering.

B cell immune responses involve recognition of antigens by B cell receptors (BCRs) (1–3). The BCR structure comprises a homodimeric antigen-binding membrane-bound form of immunoglobulin (mIg) and a membrane-bound signaling apparatus of Igα/β (CD79a/CD79b) heterodimer at a stoichiometry of 1:1 (4, 5). mIg consists of a tetramer with two identical membrane-bound heavy chains and two identical light chains (fig. S1A). The four subunits of disulfide-linked homodimeric heavy chains of mIg and disulfide-linked heterodimeric Igα/β in the BCR complex are type I transmembrane proteins. The BCR can be divided into five major classes according to their various heavy chains (6–8).

HIT Center for Life Sciences, School of Life Science and Technology, Harbin Institute of Technology, Harbin 150080, China.

*Corresponding author. Email: huangzhiwei@hit.edu.cn

[†]These authors contributed equally to this work.

The BCR complex plays a critical role in B cell development and function (9). Antigen engagement of the BCR induces phosphorylation of intracellular immunoreceptor tyrosine-based activation motifs (ITAMs) in the Igα/β subunits by the kinase Lyn. The phosphorylation event then triggers a cascade of signaling events, resulting in B cell activation, differentiation, and antibody production (10).

Several models of BCR triggering have been proposed (10, 11). The cross-linking model proposes that BCRs redistribute to form microclusters for signaling upon BCR engagement with multivalent antigens (12). Another, the conformation-induced oligomerization model (10, 13), contends that antigen engagement of BCRs induces a conformational change in the Fc domain of mIg, thereby triggering BCR oligomerization and signaling (14, 15).

Over the past few decades, many structures of antibodies and antigen recognition by antibodies have been reported (16–19). However,

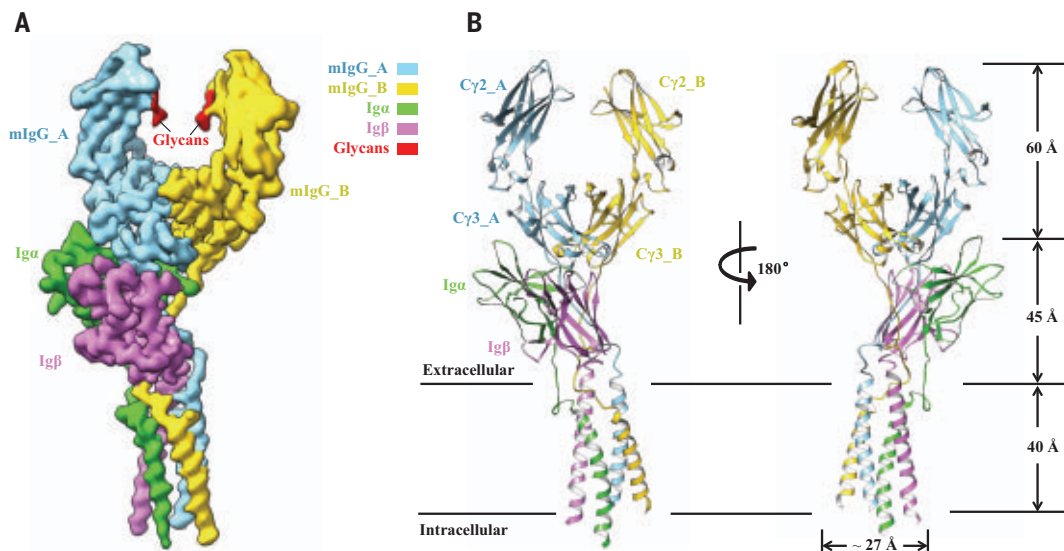
the organization and structure of the entire BCR complex has remained undetermined. The assembly mechanism for the BCR complex is important for our understanding of B cell activation but also for the development of effective immunotherapies targeting this complex.

We subjected a human IgG-BCR (VRC01) that targets the receptor binding site within HIV-1 gp120 (20) to cryo-electron microscopy (cryo-EM) analysis. Using a modified method for purification of the T cell receptor (TCR) (21), we reconstituted the IgG-BCR complex containing the heavy and light chains of mIgG and Igα/β subunits (fig. S1B). Three-dimensional reconstruction of the reconstituted IgG-BCR complex by single-particle analysis produced a cryo-EM map at a resolution of 3.0 Å (Fig. 1A and fig. S2). This reconstruction enabled us to build models for the Fc domains, the connecting peptides (CPs) and transmembrane (TM) helices of mIgG, and the two extracellular Ig-like domains, CPs, and TM helices of Igα/β (Fig. 1B, fig. S4A, and table S1).

The human IgG-BCR complex structure is composed of the heterodimeric Igα/β and mIgG with a 1:1 stoichiometry, consistent with previous studies (4). The conical structure of the BCR complex measures ~145 Å in height (Fig. 1B) with the Cγ2 and Cγ3 domains on top and the four parallel TMs forming a helical bundle-like structure below. The two Ig-like domains of Igα/β interacting with Cγ3 domains and CPs of mIgG constitute the central component of the BCR complex (Fig. 1B). The Fc, which links the two Fabs, is positioned distal and perpendicular to the plasma membrane (PM). The cytosolic tails of the BCR subunits and the two Fab domains are not visible, presumably because of structural flexibility (Fig. 1B). Six N-linked glycans at residues of asparagine

Fig. 1. 3D reconstruction and atomic model of the human IgG-BCR complex.

(A) Side view of the final cryo-EM map of the human IgG-BCR complex. Color codes for the subunits of the complex are indicated. (B) Different views of the overall structure of the IgG-BCR complex shown in cartoon. Color codes for the subunits of the IgG-BCR complex: light blue, IgG heavy chain_A; yellow, IgG heavy chain_B; green, Ig α ; magenta, Ig β .



are also well defined in the EM density (Fig. 1B and fig. S5).

The two heavy chains of mIgG form a homodimer mediated by the Fc (residues Gly²⁴¹ to Leu⁴⁴⁷), CP (Ser⁴⁴⁸ to Asp⁴⁶⁶), and TM (Gly⁴⁶⁷ to Phe⁴⁹²) domains (Fig. 2A). The two Fc domains adopt a classic Ig fold and interact with one another (Fig. 2A) to form a classic horseshoe-shaped structure that is nearly identical to the ligand-free Fc domain of VRC01 antibody (19) (fig. S6). Thus, the conformation of the Fc domain is conserved in both secretory antibody and membrane-bound forms. The homodimeric TM helices of the two heavy chains arrange with a helix-crossing angle of $\sim 15^\circ$ in the membrane. These two TM helices form extensive interactions mainly via hydrophobic contacts (Fig. 2A, right). Moreover, a Ser⁴⁸²-mediated hydrogen bond is formed between TM_A and TM_B (Fig. 2A). The interactions between the homodimeric heavy chains are further strengthened by a disulfide bond, Cys⁴⁵⁷-Cys⁴⁵⁷, at the center of the CPs (Fig. 2A).

The Ig α / β heterodimer—like the CD3 $\gamma\epsilon$ and CD3 $\delta\epsilon$ heterodimers of the TCR-CD3 complex—contains a pair of Ig-like domains located in Leu³³-Val¹²⁵ for Ig α and Ser⁴⁴-Met¹⁴³ for Ig β (Fig. 2B). The interface between the two extracellular domains of Ig α / β is mainly mediated by a disulfide bond between Ig α -Cys¹¹⁹ and Ig β -Cys¹³⁶ (Fig. 2B). Two hydrogen bonds between the main chains of Pro³⁹ and Gly¹²⁰ from Ig α and the side chain of Arg⁵¹ from Ig β at the center further stabilize the interface (Fig. 2B). Additionally, hydrophobic packing of Phe¹⁷² from Ig β against its neighboring residues from Ig α also contributes to Ig α / β heterodimerization. The Ig α _TM (residues Glu¹³⁸ to Trp¹⁶⁹) and Ig β _TM (residues Gln¹⁵⁰ to Asp¹⁸²) helices form a coiled-coil structure and make extensive hydrophobic contacts be-

tween them (Fig. 2B). The coiled-coil structure is further stabilized by polar interactions and van der Waals packing around the N-terminal sides of the two TM helices (Fig. 2B). A negative-charged residue Glu¹⁴⁸ of Ig α is partially exposed to the membrane. Moreover, a portion of the preceding CP (residues Pro¹³⁰ to Gly¹³⁷) of Ig α packs against the TM helix of Ig β in a nearly parallel manner, further stabilizing the Ig α / β interaction (Fig. 2B). A homozygous point mutation of G135S in Ig β in a patient with immunodeficiency and defect in B cell development is consistent with our observation that this mutation is located at the interface of Ig α / β heterodimer (22).

The extracellular assembly of the IgG-BCR complex involves interactions between the Ig-like domains of Ig α / β and the disulfide bond-linked γ _CPs (Fig. 3A). γ _CP_A binds along the interface between the Ig-like domains of Ig α / β , with its N-terminal portion tightly packing against the protruding CD loop (residues Val⁶⁹ to Pro⁷⁸) of Ig α on one side and Trp⁴⁷ of Ig β on the other (Fig. 3, B and C). Additionally, the two aromatic residues, Tyr⁷⁴ and Trp⁷⁶, of the CD loop make stacking contacts with Pro³⁵⁶ residues from the two C γ 3 domains. A main-chain hydrogen bond between Ig α -Trp⁷⁶ and C γ 3_B-Arg³⁵⁹ also contributes to the CD loop-mediated interactions. The CD loop of Ig α binds to the interface of homodimeric mIgG, thereby occluding another copy of Ig α / β to bind to the same site. Thus, it precludes a 2:1 stoichiometry between Ig α / β and mIgG. The central portion of γ _CP_A preceding residue Cys⁴⁵⁷ of γ _CP_A makes three main-chain hydrogen bonds with a β strand (residues Arg⁵¹ to Lys⁵⁶) of Ig β , forming a β sheet-like structure (Fig. 3D). The C-terminal side of γ _CP_A packs against the CP of Ig β . By comparison, the N-terminal side of γ _CP_B largely interacts with Ig α , whereas its central portion

is sandwiched between Ig α / β at the membrane-proximal side (Fig. 3D). Assembly of the CP region of the IgG-BCR complex is mainly organized by the C-terminal side of γ _CP_B.

The two C γ 3 domains are also involved in mediating assembly of the IgG-BCR complex. A short α helix (Lys⁴¹⁵-Gly⁴²⁴) between the β _E and β _F strands of C γ 3_A tightly packs against the N-terminal loop region of Ig β (Fig. 3C). Two aromatic residues of Ig β , Tyr⁶⁶ and Trp⁴⁷, stack against the N-terminal side of the short α helix. The loop region (Gln¹⁰⁹-Tyr¹¹⁵) linking the β _F and β _G strands of Ig α establishes contacts with the outer surface side of the β sheet. Furthermore, the Ig-like domains of Ig α / β also interact with the N-termini of TM segments. The two intra-chain disulfide bonds, Cys⁴⁵⁷-Cys⁴⁵⁷ and Ig α -Cys¹¹⁹-Ig β -Cys¹³⁶ (Fig. 3, A and D), further reinforce the ternary interaction between mIgG and Ig α / β . The interaction between mIgG and the Ig α / β heterodimer was greatly compromised by mutations of W76R, P77W, and R124A of Ig α , F52W and W47A of Ig β , or E454A, E455A, and E459A of the heavy chain of mIgG (fig. S7), which demonstrates the functional relevance of these molecular interactions.

The two Ig α / β _TM helices establish extensive hydrophobic interactions with the two γ _TM helices, resulting in formation of a four-helix bundle structure in the membrane (Fig. 3E). The two face-to-face γ _TM helices interact with the Ig α / β _TM helices at one side, leaving the other side exposed to the PM. The Ig α _TM helix interacts with both γ _TM helices of mIgG, forming a three-helix bundle structure. By comparison, the Ig β _TM helix only contacts the γ _TM_A helix, which allows the γ _TM_B helix to mainly interact with Ig α _TM helix in the membrane. The Ig α / β _TM segment packs against the γ _TM_B

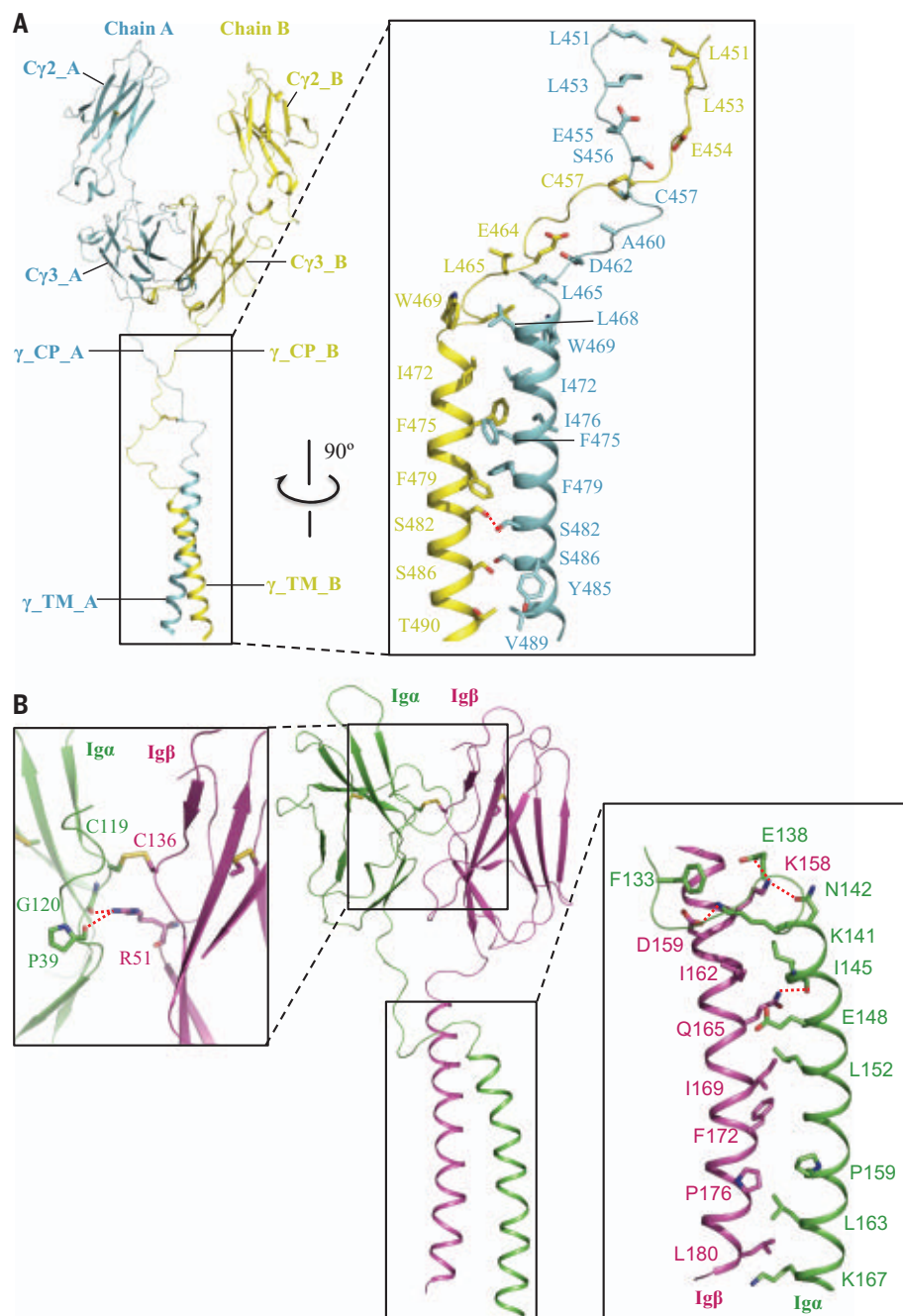


Fig. 2. Structures of the mIgG and Ig α / β subunits. (A) Left: Side view of the structure of the two component chains of the mIgG homodimer. Right: Detailed interactions within the mIgG homodimer. TM and CP indicate transmembrane and connecting peptide, respectively. Light blue, heavy chain_A; yellow, heavy chain_B. (B) Structure of the Ig α / β subunits. Shown in the middle is a side view of the structure. Detailed interactions between the two Ig-like domains and TM segments of Ig α / β are shown on the left and right, respectively. Polar interactions are indicated by dashed lines. Ig α and Ig β subunits are colored green and magenta, respectively.

helix via extensive hydrophobic interactions (Fig. 3F). The carbonyl oxygen atom of Val¹⁵⁷ from Ig α forms a hydrogen bond with Tyr⁴⁸⁵ of γ _TM_B (Fig. 3F). Ig α / β _TM helices contact the γ _TM_A helix through hydrophobic packing, forming the second three-helix bundle structure in the PM (Fig. 3G). In addition to

hydrophobic residues, polar interactions located at the N terminus of the helix bundles of Ig α / β _TM and γ _TM (Fig. 3, F and G) contribute to the assembly of the BCR subunits in the membrane. This is reminiscent of the charged residues participating in TM helix interactions between TCR and CD3 subunits (21). Those

residues from γ _TM_A or B chain involved in interactions with Ig α / β are conserved among the five classes of mIg-BCR heavy chains, which suggests a conserved TM structure of these BCR complexes. Mutations of conserved residues mIgM-Tyr⁶⁰⁰/Ser⁶⁰¹ [equivalent to Tyr⁴⁸⁵/Ser⁴⁸⁶ of mIgG (fig. S6)] completely disrupt the association of mIgM with Ig α / β as well as BCR clustering and intracellular calcium responses (14, 23), highlighting the critical role played by polar interactions in the IgG-BCR assembly. By contrast, mutations of mIgM-Ser⁵⁸⁸/Thr⁵⁸⁹ (equivalent to Thr⁴⁷³/Ile⁴⁷⁴ of mIgG), which are not involved in interaction with Ig α / β subunits in the complex, have no effect on BCR signaling (24).

IgG- and IgM-BCR have distinct sensitivities and thresholds to antigen engagement (25, 26), suggesting their structural differences. In addition to different cytosolic tails, the flexible hinge region connecting Fab and Fc of mIgG is replaced by a C μ 2 domain in mIgM (fig. S8). To investigate the assembly mechanism of IgM-BCR, we determined the cryo-EM structure of a human IgM-BCR complex at 3.6 Å (figs. S1 and S3 and table S1). The quality of the density was sufficient for sequence assignment of the extracellular Fc domains (C μ 2 to C μ 4 domains), CP region, and TM helices of mIgM and the two extracellular Ig-like domains, CP region, and TM segments of Ig α / β subunits (Fig. 4, A and B, and figs. S3 and S4B). Two densities adjacent to the Fc domain corresponding to two Fab domains of mIgM were visible at low thresholds (fig. S9), which suggests that they are relatively flexible. We identified 14 N-linked glycosylation sites on the extracellular domains of Ig α / β and mIgM (fig. S5B).

Like Ig α / β and mIgG in the IgG-BCR complex, Ig α / β and mIgM have a 1:1 stoichiometry in the IgG-BCR complex. The asymmetric structure of mIgM_Fc (C μ 2 to C μ 4 domains) is composed of two contacting homodimers of C μ 2-C μ 2 and C μ 4-C μ 4 at the membrane distal and proximal ends (Fig. 4, A and B), respectively. The overall heights of IgG-BCR and IgM-BCR are largely similar, although the IgM-BCR contains two C μ 2 domains (Fig. 4C and fig. S1A). As predicted, the C μ 2 domain assumes a typical Ig structure and forms a homodimer in the IgM-BCR (Fig. 4, B and C). The mIgM_Fc dimer has a structure similar to that of mIgM_Fc, but the positioning differs strikingly between the two complexes (Fig. 4C). As a result of its shortened CPs, the Fc of mIgM is much more proximal to the PM as compared to that of mIgG. Likely for this reason, the arrangement of the two CPs of mIgM is markedly different from that of the CPs of mIgG. Despite the differences, the TM helices of IgM are positioned similarly to those of IgG (Fig. 4D). The overall structure of the Ig α / β subunits in IgM-BCR resembles that of Ig α / β in the IgG-BCR complex, with an

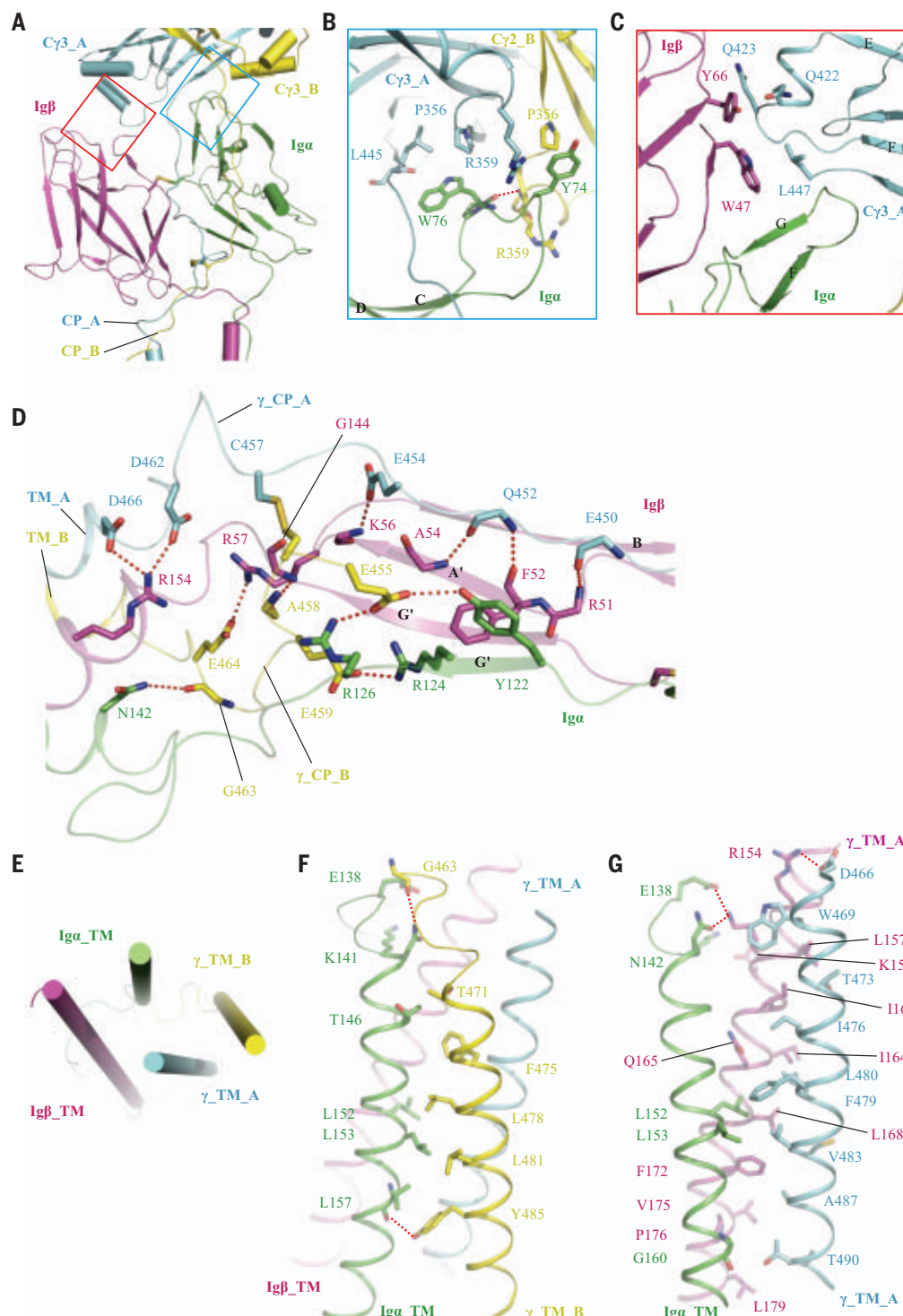


Fig. 3. Extracellular and transmembrane assembly of the IgG-BCR complex.

(A) Side view of the extracellular domains of the IgG-BCR complex. Red and blue boxes highlight the mIgG and Igα/β interfaces, respectively. Igα, Igβ, heavy chain_A, and heavy chain_B are colored green, magenta, light blue, and yellow, respectively.

(B and C) Detailed interactions of the interfaces highlighted in (A). (D) Detailed interactions of CP regions between mIgG and Igα/β modules. (E) Top view of the TM segment of the IgG-BCR complex. (F and G) The intramembrane interfaces between mIgG and Igα/β modules. Hydrogen bonds are shown as dashed lines.

RMSD of 1.92 Å over 268 Cα atoms (fig. S10A). In the IgM-BCR structure, the interactions between mIgM and Igα/β—as observed for the IgG-BCR—are mediated through extra-

cellular mIgM_Fc contact with Ig-like domains of Igα/β and mIgM_TM helices packing against Igα/β_TM helices in the PM (Fig. 4, B and C). The interactions between mIgM and

Igα/β within the PM are largely conserved in the IgG-BCR complex (Fig. 4D and figs. S10, B to D, and S11). The residues of mIgM and mIgG involved in interaction with Igα/β_TM

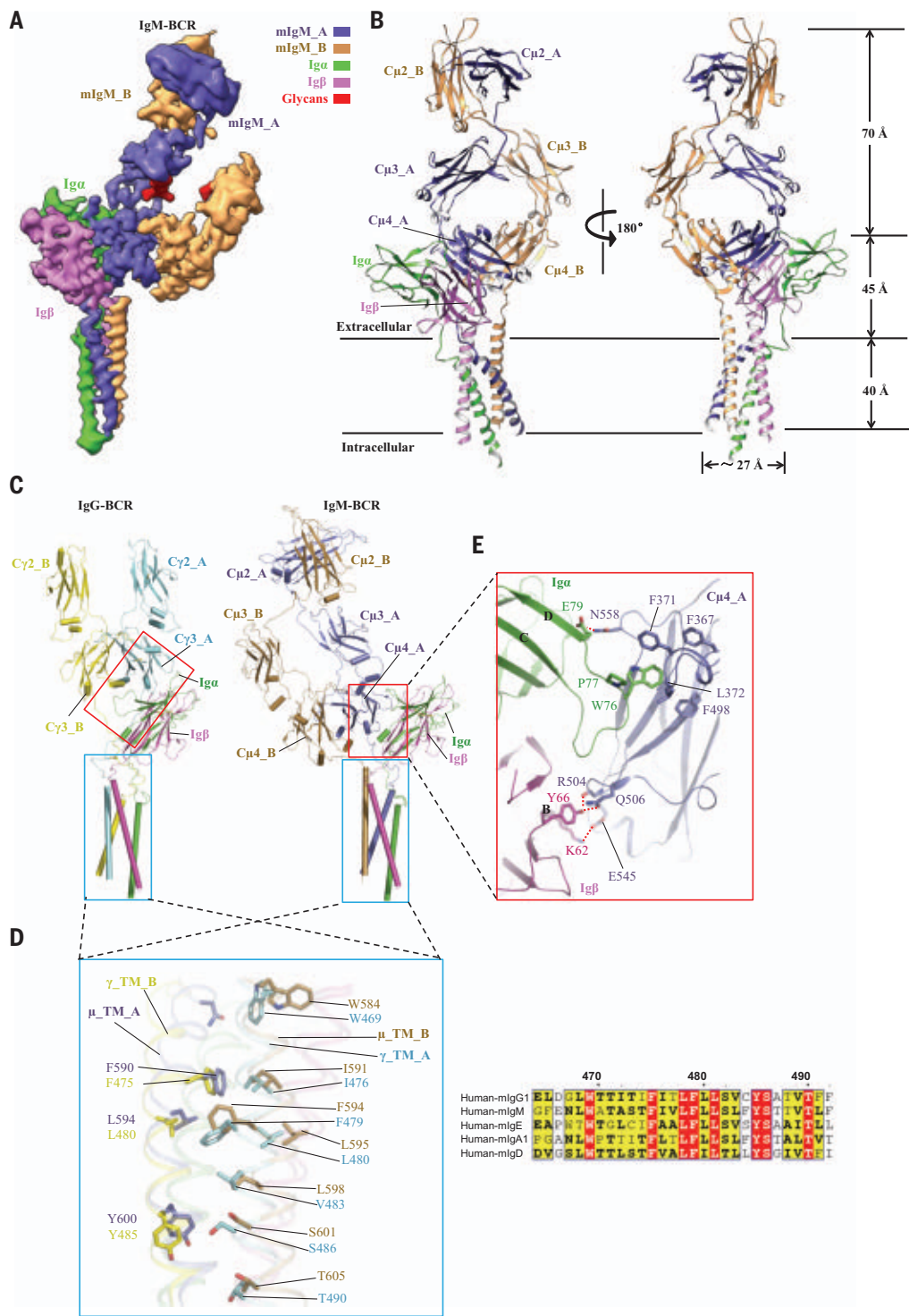


Fig. 4. Structural comparison of the human IgM-BCR and IgG-BCR. (A) Side view of the cryo-EM map of the human IgM-BCR complex. Igα, Igβ, mIgG_A, mIgG_B, mIgM_A, and mIgM_B are colored green, magenta, light blue, yellow, purple, and gold, respectively. (B) Different views of the overall structure of the IgM-BCR complex shown in cartoon. Color codes for subunits are the same as

those shown in (A). (C) Structural comparison of IgM-BCR with IgG-BCR. (D) Overlaid IgM-BCR_TM and IgG-BCR_TM. Conserved residues are shown as sticks. Left: Sequence alignment of heavy chains from five BCR isotypes. Right: Conserved and similar residues are highlighted in red and yellow, respectively. (E) Close-up view of the extracellular domain interfaces of IgM-BCR.

are conserved among all five mIg classes and are similarly positioned (Fig. 4D). Thus, all five isotypes of BCR may share a conserved conformation in the membrane.

Notable differences exist in the extracellular assembly of the IgG-BCR and IgM-BCR complexes. The mIgG homodimer plays a role in the extracellular assembly of IgG-BCR, whereas

only mIgM_A interacts with the Ig-like domains of Igα/β. Moreover, the Cμ4 domain of IgM-BCR rather than the CP as seen in the IgG-BCR complex makes simultaneous contacts

with the Ig-like domains of Ig α / β from IgM-BCR in a side-by-side mode (Fig. 4C), which is reminiscent of recognition of TCR by CD3 subunits (21). Despite these differences, the Ig-like domains of Ig α / β use the same surface side for interaction with mIgM_A. Notably, the protruding CD loop of Ig α packs against the concave surface of C μ 4_A (Fig. 4E) via hydrophobic contacts (Fig. 4E). At the periphery, Glu⁷⁹ of Ig α and Tyr⁶⁶ and Lys⁶² of Ig β establish three hydrogen bonds and a salt bridge with Asn⁵⁵⁸, Arg⁵⁰⁴, Gln⁵⁰⁶, and Glu⁵⁴⁵ of C μ 4_A (Fig. 4E), respectively, stabilizing the extracellular assembly of the BCR complex. Structural superimposition revealed that the CD loop of Ig α swings $\sim 90^\circ$ to contact IgG-C γ 3 and IgM-C μ 4 (fig. S10A), respectively.

IgG-BCR_C γ 3 and IgM-BCR_C μ 4 domains are required for antigen-induced BCR oligomerization (13). The C μ 4 and C α 3 domains of secretory IgM and IgA, respectively, are involved in pentamerization. However, the C μ 4 domain of IgM-BCR is likely inaccessible for oligomerization in the resting state (13). Structural superposition of IgM-BCR and the secretory IgM (sIgM) (PDB 6KXS) (or sIgA, PDB 7K0C) pentamer (16, 17) revealed that Ig α completely overlaps with the neighboring sIgM_C μ 4 domain (fig. S12). Moreover, the FG loop of Ig α overlaps with the FG loop of C μ 4 of sIgM_Fc2, which is involved in the direct contacts within each sIgM_Fc monomer. Future studies will be needed to establish whether the pentamerization surface of sIgM_C μ 4 is also required for BCR oligomerization.

BCR clustering induced by antigen engagement is shown to be an early and critical event (11). Although the C μ 4 domain of IgM-BCR is not accessible for oligomerization in the absence of antigen, antigen binding to the BCR may bring the C μ 4 domain into an oligomerization-receptive conformation (13). Moreover, it has been shown that the C μ 4 domain of mIgM or the C γ 3 domain of mIgG spontaneously forms clusters and activates B cells (14). These data and our cryo-EM structures lead us to propose that the extracellular domains of Ig α / β bind to C μ 4 or C γ 3 to sterically block mIg oligomerization in the resting state. Antigen engagement may impose mechanical forces on the Fab domains to trigger the structural changes in mIg_Fc, thereby releasing the clustering interface of C γ 3 or C μ 4 occupied by Ig α / β , leading to IgM-BCR clustering and downstream signaling. In contrast to the conserved assembly mechanism between Ig α / β and mIg isotypes (27), the different extracellular assemblies observed in the IgG-BCR (head-to-tail mode) and IgM-BCR (side-by-side mode) (Fig. 4C) complexes and the distinct flexibility of the Fab domains (fig. S9) may inform their distinct signaling features (28, 29). However, the underlying mechanism remains an open question.

REFERENCES AND NOTES

1. L. J. McHeyzer-Williams, M. G. McHeyzer-Williams, *Annu. Rev. Immunol.* **23**, 487–513 (2005).
2. M. Reth, J. Wienands, *Annu. Rev. Immunol.* **15**, 453–479 (1997).
3. M. Reth, *Annu. Rev. Immunol.* **10**, 97–121 (1992).
4. W. W. Schamel, M. Reth, *Immunity* **13**, 5–14 (2000).
5. K. S. Campbell, J. C. Cambier, *EMBO J.* **9**, 441–448 (1990).
6. A. R. Venkitaraman, G. T. Williams, P. Dariavach, M. S. Neuberger, *Nature* **352**, 777–781 (1991).
7. G. Alber, H. Flaswinkel, K.-M. Kim, P. Weiser, M. Reth, *Prog. Immunol.* **8**, 27–33 (1993).
8. J. Hombach, T. Tsubata, L. Leclercq, H. Stappert, M. Reth, *Nature* **343**, 760–762 (1990).
9. T. Kurosaki, H. Shinohara, Y. Baba, *Annu. Rev. Immunol.* **28**, 21–55 (2010).
10. S. K. Pierce, W. Liu, *Nat. Rev. Immunol.* **10**, 767–777 (2010).
11. N. E. Harwood, F. D. Batista, *Annu. Rev. Immunol.* **28**, 185–210 (2010).
12. P. Tolar, H. W. Sohn, S. K. Pierce, *Nat. Immunol.* **6**, 1168–1176 (2005).
13. P. Tolar, S. K. Pierce, *Curr. Top. Microbiol. Immunol.* **340**, 155–169 (2010).
14. P. Tolar, J. Hanna, P. D. Krueger, S. K. Pierce, *Immunity* **30**, 44–55 (2009).
15. C. Ketchum, H. Miller, W. Song, A. Upadhyaya, *Biophys. J.* **106**, 26–36 (2014).
16. N. Kumar, C. P. Arthur, C. Ciferri, M. L. Matsumoto, *Science* **367**, 1008–1014 (2020).
17. Y. Li et al., *Science* **367**, 1014–1017 (2020).
18. E. O. Saphire et al., *Science* **293**, 1155–1159 (2001).
19. S. Radaev et al., *Structure* **18**, 934–943 (2010).
20. T. Zhou et al., *Science* **329**, 811–817 (2010).
21. D. Dong et al., *Nature* **573**, 546–552 (2019).
22. A. K. Dobbs et al., *J. Immunol.* **179**, 2055–2059 (2007).
23. A. C. Shaw et al., *Cell* **63**, 381–392 (1990).
24. S. A. Grupp, K. Campbell, R. N. Mitchell, J. C. Cambier, A. K. Abbas, *J. Biol. Chem.* **268**, 25776–25779 (1993).
25. Z. Wan et al., *J. Cell Biol.* **217**, 2565–2582 (2018).
26. A. M. Davey, S. K. Pierce, *J. Immunol.* **188**, 3332–3341 (2012).
27. Q. Su et al., *Science* **377**, 875–880 (2022).
28. C. Wakabayashi, T. Adachi, J. Wienands, T. Tsubata, *Science* **298**, 2392–2395 (2002).
29. M. Noviski et al., *eLife* **7**, e35074 (2018).

ACKNOWLEDGMENTS

We thank J. J. Chai (University of Cologne) for critical reading of this manuscript, and the Core Facility at School of Life Science and Technology of Harbin Institute of Technology for their help with negative-staining EM and cryo-EM data collection. **Funding:** Supported by National Natural Science Foundation of China grants 31825008, 31422014, and U21A20276, and by the Tencent Foundation and Heilongjiang Touyan Team HITTY-20190034 (Z.H.). **Author contributions:** Z.H. conceived and supervised the whole project. X.M., D.D., S.W., and D.Y. prepared the protein samples for negative staining and cryo-EM. X.M., Y.Z., Y.C., Z.M., A.Z., and C.G. performed negative staining, prepared the cryo-EM grids, and collected the cryo-EM data. X.L. performed functional experiments. F.Z. performed bioinformatics analyses. Y.Z. and Z.H. performed cryo-EM data processing and model building. Z.H. wrote the manuscript with contributions from all authors. **Competing interests:** The authors declare no competing interests. **Data and materials availability:** The atomic coordinates of IgG-BCR and IgM-BCR have been deposited in the Worldwide Protein Data Bank (wwPDB) with accession codes 7WSO and 7XT6, respectively. The corresponding maps have been deposited in the Electron Microscopy Data Bank (EMDB) with accession codes EMD-32762 and EMD-33440. All other data needed to support the conclusions in this manuscript can be found in the main text or supplementary materials. **License information:** Copyright © 2022 the authors, some rights reserved; exclusive licensee American Association for the Advancement of Science. No claim to original US government works. www.science.org/about/science-licenses-journal-article-reuse

SUPPLEMENTARY MATERIALS

science.org/doi/10.1126/science.abc3828

Materials and Methods

Figs. S1 to S12

Table S1

References (30–40)

Submitted 30 January 2022; accepted 11 July 2022
10.1126/science.abc3828

QUANTUM PHYSICS

Tweezer-programmable 2D quantum walks in a Hubbard-regime lattice

Aaron W. Young¹, William J. Eckner¹, Nathan Schine¹, Andrew M. Childs^{2,3}, Adam M. Kaufman^{1*}

Quantum walks provide a framework for designing quantum algorithms that is both intuitive and universal. To leverage the computational power of these walks, it is important to be able to programmatically modify the graph a walker traverses while maintaining coherence. We do this by combining the fast, programmable control provided by optical tweezers with the scalable, homogeneous environment of an optical lattice. With these tools we study continuous-time quantum walks of single atoms on a square lattice and perform proof-of-principle demonstrations of spatial search with these walks. When scaled to more particles, the capabilities demonstrated can be extended to study a variety of problems in quantum information science, including performing more effective versions of spatial search using a larger graph with increased connectivity.

The ability of quantum systems to coherently explore their Hilbert space, exhibiting wavelike superposition and interference, is a key ingredient in quantum algorithms. Quantum walks are one intuitive framework for understanding the algorithmic speedups that these ingredients can provide. In this framework, states in Hilbert space are mapped to the locations of a walker on a graph (1); the walker can then

traverse this graph through a superposition of interfering paths. Even in the restrictive

¹JILA, University of Colorado and National Institute of Standards and Technology, and Department of Physics, University of Colorado, Boulder, CO 80309, USA.

²Department of Computer Science, University of Maryland, College Park, MD 20742, USA. ³Institute for Advanced Computer Studies and Joint Center for Quantum Information and Computer Science, University of Maryland, College Park, MD 20742, USA.

*Corresponding author. Email: adam.kaufman@colorado.edu.

case of real, equal-valued couplings and local, time-independent control, this simple framework is capable of universal quantum computation (2, 3) and has inspired the development of various quantum algorithms including those for spatial search (4), graph traversal (5), element distinctness (6), and formula evaluation (7). When scaled to many particles, systems that realize quantum walks further allow for rich studies of quantum information and many-body physics: controlled tunneling of many noninteracting particles maps to sampling problems of interest in complexity theory (8, 9) and the combination of interactions and itinerance underlies a broad class of condensed-matter Hubbard models (10, 11). In this work we introduce a platform for realizing programmable quantum walks and lattice models that combines favorable properties of optical tweezers and optical lattices. We use this platform to demonstrate spatial search by continuous-time quantum walks with neutral atoms.

Because of their broad applicability, quantum walks have been realized in a number of experimental platforms, including with photons (12–14), nuclear magnetic resonance (15), matter waves (16), trapped ions (17, 18), and superconducting qubits (19, 20). Optically trapped neutral atoms are particularly amenable to realizing quantum walks (21, 22) because they allow for high-fidelity creation

and detection of individual, physically identical walkers. One approach to studying quantum walks of neutral atoms is with quantum gas microscopes, which load degenerate gases containing thousands of particles into optical lattices containing thousands of sites (23, 24). Sophisticated techniques have been developed to “cookie-cut” desired initial states out of these complicated many-body states (22, 25, 26). A complementary approach is to rapidly assemble such states with optical tweezer arrays. In this case it is possible for individual atoms to be deterministically assembled into nearly arbitrary geometries (27, 28) and rapidly laser-cooled to their three-dimensional (3D) motional ground state (29–35). Pioneering studies have used tweezers to explore tunneling between up to eight sites (26, 36, 37); however, such systems are sensitive to disorder, making it difficult to realize coherent itinerance across many sites. We present an alternative solution that uses optical tweezers and high-fidelity laser cooling for fast, programmable implantation and control of single atoms in a Hubbard-regime optical lattice.

We use this approach to study quantum walks of individual atoms spanning hundreds of sites in a 2D lattice and to locally control those walks to realize a spatial search algorithm. In this case, elements of the search space are represented by sites in the lattice; the location of the atom, or walker, is ini-

tialized through tweezer implantation and the search oracle is created with dynamically programmable tweezers superimposed on the lattice (4). The techniques demonstrated here may advance studies of nonequilibrium and ground-state Hubbard physics, where fast cycle times, versatile state preparation, and site-resolved potentials can advance entanglement-measurement protocols and implement certain sampling problems (8, 9, 38–40). These tools could be further extended to other types of systems, like molecules (34, 41), that are less amenable to evaporative cooling but are powerful in terms of many-body physics and quantum information.

Our experiments begin by trapping and cooling individual strontium (^{88}Sr) atoms in optical tweezers (32). The atoms are then transferred into one 2D layer of a 3D optical lattice (Fig. 1A). This transfer need not be fully adiabatic with respect to on-site motional timescales because the tightly confining optical lattice allows for higher-fidelity optical cooling than can be performed in the tweezers, yielding a typical 3D motional ground state fraction of $100 \pm 7\%$ (42). This lattice is composed of a 1D crossed-beam lattice which is aligned along gravity and a 2D bowtie lattice. The depths of these two lattices are independently tunable and are reduced to $26.0E_R^{\text{Ax}}$ and $5.0E_R^{2\text{D}}$, respectively, to study tunneling after optically cooling the atoms, where E_R^{Ax}

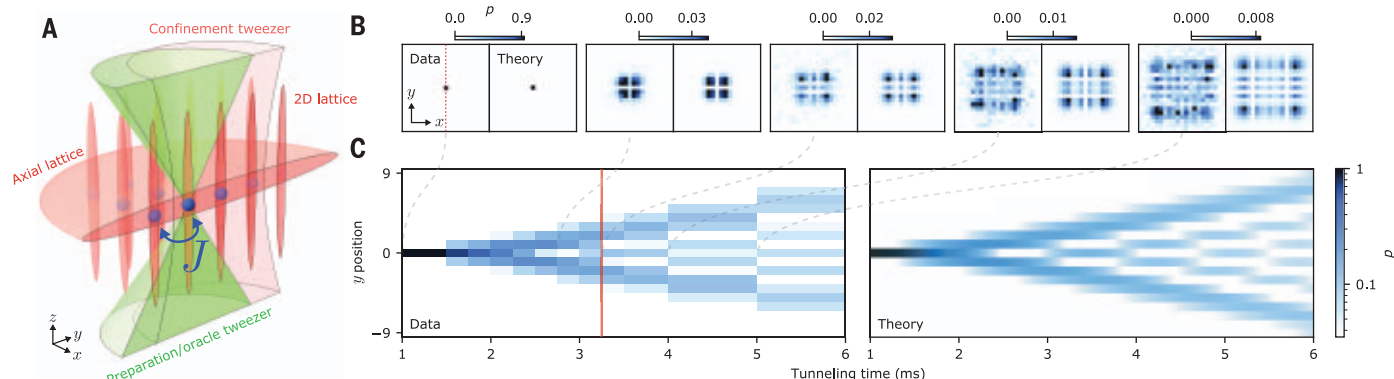


Fig. 1. Continuous-time 2D quantum walks with tweezer-implanted atoms in a lattice. (A) Individual ^{88}Sr atoms (solid blue sphere) are loaded and cooled in optical tweezers (preparation/oracle tweezer, green), and then implanted into single sites of a 3D optical lattice composed of a 1D crossed-beam lattice aligned along gravity (axial lattice, red half-disk), and a bowtie lattice (2D lattice, red). The 2D lattice contains more than 2000 sites that are compatible with high-fidelity imaging and ground state cooling (42) and is tunable to a regime where nearest-neighbor sites are coupled with a tunneling energy J , allowing the atoms to move through the lattice (translucent blue spheres). The preparation tweezers used to implant atoms can further be used to programmatically modify the depth of individual sites in this lattice and a large-waisted tweezer (confinement tweezer, pink) can be used to apply a tunable harmonic confining potential that spans many lattice sites. (B) Atoms implanted in this lattice undergo continuous-time quantum walks in 2D, such that the probability density p corresponding to their measured position (left panels)

exhibits ballistic expansion and wavelike interference; this is in good agreement with theory with fitted values of the tunneling energy (right panels) up to an evolution time of 5 ms, where the atoms have coherently explored a region spanning ~ 200 lattice sites. Each pixel in these plots represents a single lattice site. (C) Tracing out the x axis of this 2D quantum walk yields a 1D quantum walk along the y axis (left panel), which is in good agreement with theory (right panel). Sampling times in these plots correspond to the leading edge of each colored region. For data to the left of the red line, multiple atoms can be implanted in different regions of the lattice for faster data collection (42). Here, each point in time is averaged over 200 repetitions of the experiment. For data to the right of the red line a single atom is implanted in the center of the lattice to avoid overlapping atomic wavefunctions and averaging over inhomogeneous regions in the lattice. Here, each point up to and including 3.5 ms is averaged over 3000 repetitions. The points at 4 and 5 ms are averaged over 6000 and 14,000 repetitions, respectively.

and E_R^{2D} are the recoil energies of the two respective lattices (42). The detuning between sites in the axial lattice caused by gravity suppresses tunneling along this axis, whereas atoms tunnel freely in the 2D lattice with an average tunneling energy of $J_0/\hbar = 2\pi \times 163$ Hz, corresponding to a characteristic tunneling time of $\tau = \hbar/J_0 = 0.975$ ms (the tunneling energy differs slightly between the two axes of the lattice) (42).

The evolution of the system in this regime can be understood as a quantum walk on a graph where each site $|i\rangle$ in the lattice is represented by a node, and nodes corresponding to tunnel-coupled sites are connected by an edge. Such a graph can be represented by its adjacency matrix A , where $A_{ij} = 0$ unless nodes i and j are connected in which case $A_{ij} = 1$. Given this definition the Hamiltonian of the system is:

$$H_{\text{Lat}} = -J \sum_{i,j} A_{ij} |i\rangle \langle j| - \sum_i V_i |i\rangle \langle i| \quad (1)$$

where J is the tunneling energy; we have also included a local energy shift V_i that is present as a result of the finite extent of our lattice beams (42) and can be programmably modified through two sets of optical tweezers (Fig. 1A). If the tweezers are fully extinguished, given the lattice uniformity, $|V_i| \ll J$ and this term can be disregarded. In this case, an atom implanted in one site of the lattice undergoes a continuous-time quantum walk in 2D (Fig. 1B). The evolution of this atom's wavefunction is in good agreement with the theoretical prediction for a flat lattice with constant V_i and a distant boundary, exhibiting the formation of fringes in the probability density p of the atom's measured position thanks to interference between the multiple paths by which the atom can arrive at a given site after its evolution. This is in contrast to the behavior of classical random walks, which exhibit diffusive expansion of a Gaussian probability density distribution. We can trace out one of the atom's two spatial coordinates (Fig. 1C) which, given the form of H_{Lat} for a 2D square lattice, results in a 1D quantum walk along the remaining axis. The resulting data are in good agreement with theory, showing the expected ballistic or light-cone-like spreading of the atomic probability density (4). For the latest time shown here of $t = 5.0$ ms, the probability density continues to exhibit clear interference fringes (42), suggesting that the atom has maintained phase coherence while exploring a region spanning ~ 200 lattice sites. At later times the atom begins to sample the inhomogeneous potential resulting from the finite extent of the lattice beams and the infinite flat lattice approximation breaks down (42).

This coherent exploration of Hilbert space through continuous-time quantum walks can

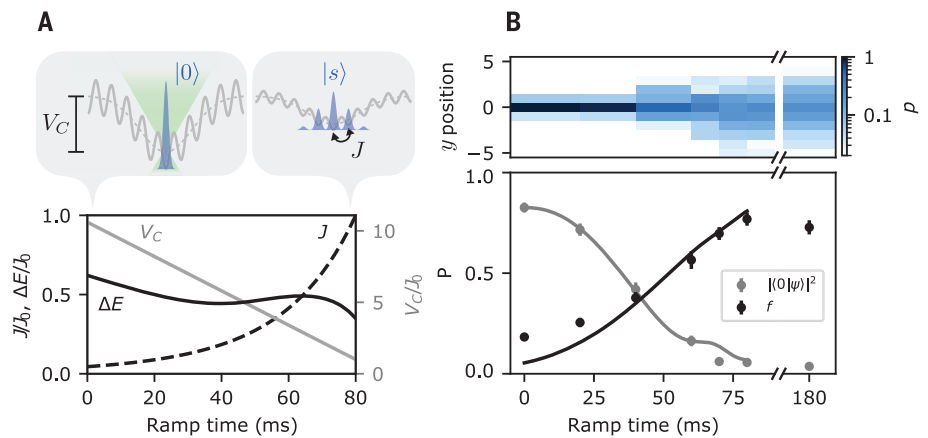


Fig. 2. Adiabatic resource state preparation. (A) An atom implanted in the site with the lowest energy in a deep lattice with no tunneling (left callout), which we label as being in state $|0\rangle$, can be adiabatically connected to the ground state $|s\rangle$ of a shallow lattice with tunneling (right callout) through an adiabatic ramp of the tunneling energy (J) and the depth (V_C) of the confinement tweezer. In the callouts the gray dashed line denotes the potential provided by the confinement tweezer and the solid gray line indicates the sum of the tweezer and lattice potentials. The preparation tweezer used to initially implant the atom in $|0\rangle$ is shown schematically in green. By ramping J and V_C together we can maintain a roughly fixed energy gap ΔE between the ground and first excited states of the system throughout the ramp. (B) As an atom evolves under this ramp its amplitude spreads over many sites in the 2D lattice. Here, the x coordinate has been traced out for illustration purposes, showing the spread in the atom's y position (top). During this ramp, the population on the initial site (gray points) decreases and the overlap f (see main text) between the classical probability distributions corresponding to the prepared state $|\psi\rangle$ and the expected lattice ground state $|s\rangle$ (black points) increases, eventually reaching 76.9(3.3)%. This is in reasonable agreement with theory (solid lines) given the independently measured parameters in our ramp, and an overall scale factor to account for filtering and loss due to imperfect preparation of the atoms in their 3D motional ground states (42). The prepared state is not observed to substantially evolve even after more than 100 tunneling times (right side of the broken axis), suggesting that it is indeed the lattice ground state. Each data point corresponds to 500 repetitions of the experiment except for the points at 70 and 180 ms which are averaged over 1500 repetitions.

be harnessed in a variety of quantum algorithms including those for spatial search (4). Spatial search is a specialization of the unstructured search problem with additional constraints on how the space can be explored. A continuous-time analog of Grover's search algorithm (43) performs search by quantum walk in the limiting case of a fully connected graph. The problem becomes more difficult when edges are removed from the graph, which may preclude the quadratic Grover speedup depending on the graph structure. Surprisingly, quadratic speedup can persist even for much less well connected graphs. In particular, for N -vertex square lattice graphs the search can be performed in time $O(\sqrt{N} \text{ polylog } N)$ in only four dimensions (4) whereas the full, optimal (43) quadratic speedup is recovered in five or more dimensions (4). Although the behavior of these single-particle walks can be captured by a classical wave equation involving N coupled oscillators (44), in the specific setting of searching a memory that is distributed in real space with a local probe (45), quantum walks of even a single particle can provide a notable quantum advantage (42).

In these algorithms the lack of structure in the search space suggests that a natural starting point is the uniform superposition

$$|S\rangle = \sum_{i=1}^N |i\rangle / \sqrt{N} \text{ over all standard basis}$$

states in the relevant Hilbert space. Assuming periodic boundary conditions, this resource state $|S\rangle$ is precisely the ground state of H_{Lat} with constant V_i . To approximate this resource state we prepare the ground state $|s\rangle$ of H_{Lat} (Fig. 2) in the presence of a potential V_i provided by an extra confinement tweezer (Fig. 1A). This tweezer has a nearly Gaussian profile with a fixed waist of $5.8a$, where a is the 2D lattice spacing, and tunable overall depth V_C . At fixed J , the lattice ground state $|s\rangle$ is similar to $|S\rangle$ except with an approximately Gaussian envelope with a width determined by the value of V_C .

To prepare the state $|s\rangle$ we implant an atom in the deepest site of the combined potential generated by the lattice and the confinement tweezer, which we label as being in state $|0\rangle$. This is the ground state of the system when the lattice is deep and $J \ll V_C$. The state $|0\rangle$ can be adiabatically connected to the ground state $|s\rangle$ in a shallow lattice through a ramp of the

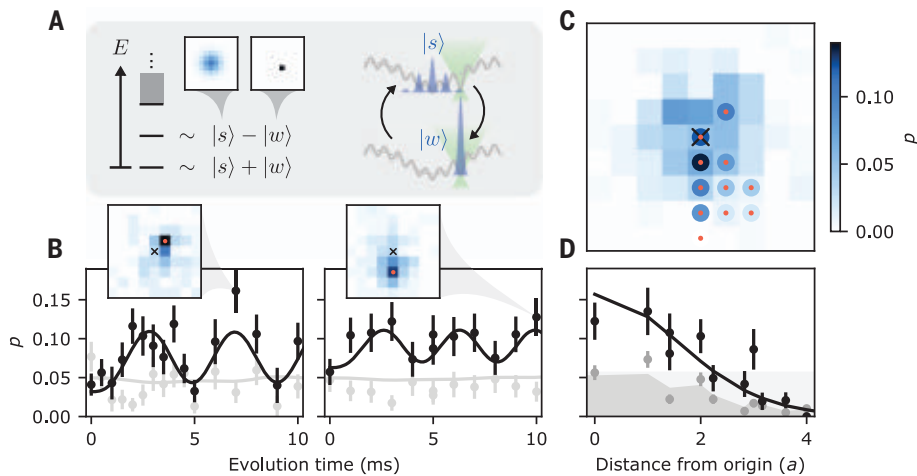


Fig. 3. Spatial search by continuous-time quantum walks. (A) When applying an oracle Hamiltonian $H_w = -V_w|w\rangle\langle w|$ through a tweezer (green) that selects for an arbitrary marked site $|w\rangle$ with appropriate strength, the spectrum of the system includes ground and first excited states that are approximately even and odd superpositions of $|w\rangle$ and the lattice ground state or resource state $|s\rangle$ (42). Consequently, evolving $|s\rangle$ under H_w results in coherent oscillations between $|s\rangle$ and $|w\rangle$. (B) Measurements of the resulting oscillations in the populations on the marked sites (black points) are in good agreement with theory, up to an overall offset, with independently characterized values of the state preparation fidelity, tunneling rate, and confinement potential (black lines) (42). For comparison we also plot the population in $|0\rangle$, at the center of the lattice (gray points and theory curves). (Insets) measured populations versus position at the peak of these oscillations where the location of the relevant oracle is marked by a red point and the lattice center by a cross. (C) The population on the marked site after a 2.46 ms quench is plotted for a selection of oracles (the lattice center is marked by a cross, and the position of each oracle by a red point, with the corresponding population shown in the surrounding circle. For comparison, the measured amplitudes in $|s\rangle$ are shown in the background). (D) Plotting the amplitudes from (C) as a function of oracle distance from the lattice center (black points, $a = 813/\sqrt{2}$ nm refers to lattice spacing) reveals quench behavior that is in good agreement with a theory prediction (black curve) with no free parameters (42). In a region spanning ~ 13 lattice sites the marked site can be found by looking for the highest amplitude site after the quench. At longer distances the amplitude on the marked site still increases from its value in $|s\rangle$ (theoretical and measured amplitudes in $|s\rangle$ shown in dark gray shading and points, respectively), but can be exceeded by the population at the origin in $|s\rangle$ (light gray shading), limiting the size of the search space. Color scale is shared across this figure and all data points are averaged over 500 to 600 repetitions of the experiment.

tunneling energy (Fig. 2A). In practice we perform a linear ramp of the lattice depth V_L as a function of time t resulting in a nonlinear ramp in the tunneling energy (42). We also ramp the depth V_C of the confinement tweezer to maintain an approximately constant value of the energy gap ΔE between the ground and first excited states during the ramp, which substantially relaxes the requirements on adiabaticity and improves the fidelity with which we can prepare $|s\rangle$. The observed evolution during this ramp is in reasonable agreement with theory (Fig. 2B), where the atoms start out primarily in $|0\rangle$ and smoothly delocalize over many sites over the course of an adiabatic ramp of V_C and J that is 80 ms in length. The prepared state $|\psi\rangle$ can be compared with $|s\rangle$ by computing the overlap between their populations, namely with the classical fidelity $f = \left(\sum_i \sqrt{p_{\psi,i} p_{s,i}}\right)^2$, where $p_{\psi,i}$ and $p_{s,i}$ denote the populations on site i in states $|\psi\rangle$ and

$|s\rangle$, respectively. This yields an upper bound on the fidelity with which we have prepared $|s\rangle$ of 76.9(3.3)% but does not certify any phase coherence between the amplitudes occupying different sites. However, the prepared state is not observed to substantially evolve over more than 100 tunneling times and the adiabatic ramp can be reversed to recover 57(5)% of the atoms in $|0\rangle$ (excluding loss caused by filtering of hot atoms) (42). This suggests that $|s\rangle$ has been prepared with a fidelity of 76(3)% in agreement with the bound set by the classical fidelity; we can thus proceed with the search procedure. Note that in this work and the associated supplementary materials all confidence intervals refer to one standard error of the mean.

The central idea in quantum-walk-based search algorithms is the presence of two competing terms in the Hamiltonian: a diffusion term H_{Lat} corresponding to tunneling, whose ground state is $|s\rangle$, and an oracle term $H_w =$

$-V_w|w\rangle\langle w|$, whose ground state marks a specific site $|w\rangle$. H_w can be applied to the system with variable drive strength V_w , but the choice of $|w\rangle$ is unknown to the experimenter and is the quantity being searched for. Given a sufficiently connected graph and appropriate choice of V_w , the states $|s\rangle$ and $|w\rangle$ are similar in energy and coupled under the full search Hamiltonian $H = H_{\text{Lat}} + H_w$. This results in ground and first excited states $|\pm\rangle$ that are approximately the even and odd superpositions of $|s\rangle$ and $|w\rangle$, and are separated by an energy gap $\Delta E = O(1/\sqrt{N})$, where N is the number of elements in the search space (Fig. 3A) (42). As a result quenching to this Hamiltonian from the resource state $|s\rangle$ yields coherent oscillations to $|w\rangle$ and back with a characteristic period of $O(\sqrt{N})$ that is independent of the specific choice of $|w\rangle$. Measuring the position of the walker after a half period of this oscillation identifies the marked site $|w\rangle$. This procedure can also be run backward to prepare $|s\rangle$ from an atom implanted in a predetermined site $|w'\rangle$, avoiding any additional overhead associated with adiabatic resource state preparation (42).

The choice of V_w must be carefully finetuned to minimize the energy gap between $|\pm\rangle$ given N and the connectivity of the graph (4). Here we choose $V_w = 12.55(65)J_0$, which is biased deeper than the optimal value to avoid certain sources of technical noise (42). Even with optimal V_w in a 2D square lattice with cyclic boundary conditions $|\pm\rangle$ deviate from the even and odd superpositions of $|s\rangle$ and $|w\rangle$ and the scaling of ΔE with N is modified, resulting in an asymptotic runtime of $\geq O(N/\text{polylog } N)$ (4). This scaling is further modified by the nonperiodic boundary conditions in our experiment (42). Nonetheless, upon quenching to H starting in the state $|s\rangle$, we observe coherent oscillations in the population on the marked site $|w\rangle$ for a selection of different oracles (Fig. 3B). At the peak of these oscillations the marked site is readily identified as the highest amplitude site in the lattice. Critically, the amplitudes of these oscillations are in good agreement with theory and limited in magnitude not by technical noise but rather by the expected performance of this search procedure in a 2D square lattice (42).

It should be noted that in the case of open boundary conditions or in the presence of the confinement tweezer the behavior of these oscillations is dependent on the specific position of $|w\rangle$ (42). This position-dependent behavior sets the effective size of the search space where at greater range reduced overlap between $|w\rangle$ and $|s\rangle$ yields oscillations with reduced amplitude. In our experiment, for an oracle with a distance of $\sqrt{2}a$ from the center of the confinement tweezer (the origin) the optimal evolution time after the quench is 2.46 ms. Performing this quench and evolution

for a variety of different oracles (Fig. 3C), we find that the amplitude on the marked site after the evolution decreases as a function of distance from the origin, in agreement with theory (Fig. 3D). Within $2a$ —corresponding to a region spanning ~ 13 lattice sites—we can blind ourselves to the position of the oracle tweezer and identify the marked site by looking for the most probable location of the walker after the quench. At longer range the amplitude at the origin after the quench and subsequent evolution can exceed that of the marked site. However, within $\sqrt{13}a$ —corresponding to a region spanning ~ 45 lattice sites—there is still a several-fold increase in the amplitude on the marked site relative to what was present in the resource state. This suggests that the effective size of the search space could be increased with constant overhead by measuring the amplitude of these oscillations over time. Although not demonstrated here this would help to reject any background signal that remains near the origin or effects relating to variable oscillation frequencies for different oracles.

In this work we have performed a proof-of-principle demonstration of spatial search through continuous-time quantum walks of a single particle on a 2D square lattice. This is accomplished by introducing a platform that combines the programmability of optical tweezer arrays with a Hubbard-regime optical lattice which provides a clean environment for tunneling in addition to several thousand sites which are compatible with high-fidelity cooling, imaging, and coherent control (42, 46). Beyond studies with itinerance, these capabilities can also be used to prepare large, well-controlled ensembles of atomic qubits for quantum information, simulation, and metrology (35, 46, 47, 48, 49, 50).

In the specific context of spatial search the runtime of the algorithm demonstrated in this work does not exhibit a quadratic speedup in comparison to classical search algorithms as a result of our use of a 2D square lattice (4). A runtime of $O(\sqrt{N}\log N)$ is achievable with a single particle in such a lattice if an additional spin degree of freedom is used to implement a Dirac Hamiltonian (51) or a discrete-time quantum walk (52). This degree of freedom can be either internal to the walker or external and realized with a modified optical lattice containing an array of doublets (53). The optical clock qubit in strontium is a strong candidate for implementing this spin internally because it is well controlled (46) and long lived compared with the tunneling time (35). Moreover, it is possible to engineer state-dependent optical potentials for this qubit (54) to realize a broad class of discrete-time quantum walks (21, 55).

Although there is a setting in which such single-particle quantum walks can provide a uniquely quantum advantage (45), this advantage

can be extended to a broader class of problems by realizing these dynamics in a system whose state space scales rapidly with physical resources. This can be achieved by extending this work to multiple particles, where the state space and thus graph size grows exponentially with particle number (42). Given the cooling performance and single-particle control demonstrated here such experiments could be performed with tens to hundreds of atoms, where the appropriate many-body oracle is applied through tunable Rydberg-mediated interactions (42, 46). Beyond spatial search the programmable control and assembly of large-scale itinerant systems enabled by this platform provides one route toward programmable boson sampling with many particles (8, 9) as well as the direct assembly and characterization of Hubbard models (56, 57).

REFERENCES AND NOTES

- D. Reitzner, D. Nagaj, V. Buzek, *Acta Physica Slovaca* **61**, 603–725 (2011).
- A. M. Childs, *Phys. Rev. Lett.* **102**, 180501 (2009).
- A. M. Childs, D. Gosset, Z. Webb, *Science* **339**, 791–794 (2013).
- A. M. Childs, J. Goldstone, *Phys. Rev. A* **70**, 022314 (2004).
- A. M. Childs et al., in *Proceedings of the Thirty-Fifth Annual ACM Symposium on Theory of Computing* (Association for Computing Machinery, 2003), p. 59.
- A. Ambainis, in *45th Annual IEEE Symposium on Foundations of Computer Science* (IEEE Computer Society, 2004), pp. 22–31.
- E. Farhi, J. Goldstone, S. Gutmann, *Theory Comput.* **4**, 169–190 (2008).
- S. Aaronson, A. Arkhipov, in *Proceedings of the Forty-Third Annual ACM Symposium on Theory of Computing* (Association for Computing Machinery, 2011), pp. 333–342.
- G. Muralidharan, A. Miyake, I. H. Deutsch, *New J. Phys.* **21**, 055003 (2019).
- P. A. Lee, N. Nagaosa, X.-G. Wen, *Rev. Mod. Phys.* **78**, 17–85 (2006).
- I. Bloch, J. Dalibard, W. Zwerger, *Rev. Mod. Phys.* **80**, 885–964 (2008).
- A. Peruzzo et al., *Science* **329**, 1500–1503 (2010).
- A. Schreiber et al., *Phys. Rev. Lett.* **104**, 050502 (2010).
- L. Sansoni et al., *Phys. Rev. Lett.* **108**, 010502 (2012).
- C. A. Ryan, M. Laforest, J. C. Boileau, R. Laflamme, *Phys. Rev. A* **72**, 062317 (2005).
- E. J. Meier, F. A. An, B. Gadway, *Phys. Rev. A* **93**, 051602 (2016).
- H. Schmitz et al., *Phys. Rev. Lett.* **103**, 090504 (2009).
- F. Zähringer et al., *Phys. Rev. Lett.* **104**, 100503 (2010).
- Z. Yan et al., *Science* **364**, 753–756 (2019).
- M. Gong et al., *Science* **372**, 948–952 (2021).
- M. Karski et al., *Science* **325**, 174–177 (2009).
- P. M. Preiss et al., *Science* **347**, 1229–1233 (2015).
- W. S. Bakr, J. I. Gillen, A. Peng, S. Fölling, M. Greiner, *Nature* **462**, 74–77 (2009).
- J. F. Sherson et al., *Nature* **467**, 68–72 (2010).
- C. Weitenberg et al., *Nature* **471**, 319–324 (2011).
- B. M. Spar, E. Guardado-Sanchez, S. Chi, Z. Z. Yan, W. S. Bakr, *Phys. Rev. Lett.* **128**, 223202 (2022).
- M. Endres et al., *Science* **354**, 1024–1027 (2016).
- D. Barredo, S. de Léséleuc, V. Lienhard, T. Lahaye, A. Browaeys, *Science* **354**, 1021–1023 (2016).
- A. M. Kaufman, B. J. Lester, C. A. Regal, *Phys. Rev. X* **2**, 041014 (2012).
- X. Li, T. A. Corcovilos, Y. Wang, *Phys. Rev. Lett.* **108**, 103001 (2012).
- J. D. Thompson, T. G. Tiecke, A. S. Zibrov, V. Vuletić, M. D. Lukin, *Phys. Rev. Lett.* **110**, 133001 (2013).
- M. A. Norcia, A. W. Young, A. M. Kaufman, *Phys. Rev. X* **8**, 041054 (2018).
- A. Cooper et al., *Phys. Rev. X* **8**, 041055 (2018).
- L. R. Liu et al., *Phys. Rev. X* **9**, 021039 (2019).
- A. W. Young et al., *Nature* **588**, 408–413 (2020).
- A. M. Kaufman et al., *Science* **345**, 306–309 (2014).
- S. Murrmann et al., *Phys. Rev. Lett.* **114**, 080402 (2015).
- A. J. Daley, H. Pichler, J. Schachenmayer, P. Zoller, *Phys. Rev. Lett.* **109**, 020505 (2012).
- A. M. Kaufman et al., *Science* **353**, 794–800 (2016).
- A. Elben, B. Vermersch, M. Dalmonte, J. I. Cirac, P. Zoller, *Phys. Rev. Lett.* **120**, 050406 (2018).
- L. Andergegg et al., *Science* **365**, 1156–1158 (2019).
- See supplementary materials.
- E. Farhi, S. Gutmann, *Phys. Rev. A* **57**, 2403–2406 (1998).
- L. K. Grover, A. M. Sengupta, *Mathematics of Quantum Computation* (CRC Press, 2002).
- S. Aaronson, A. Ambainis, in *44th Annual IEEE Symposium on Foundations of Computer Science* (IEEE Computer Society, 2003), pp. 200–209.
- N. Schine, A. W. Young, W. J. Eckner, M. J. Martin, A. M. Kaufman, *Nat. Phys.* **18**, s41567–022–01678-w (2022).
- H. Levine et al., *Phys. Rev. Lett.* **123**, 170503 (2019).
- T. M. Graham et al., *Phys. Rev. Lett.* **123**, 230501 (2019).
- S. Ebadi et al., *Nature* **595**, 227–232 (2021).
- P. Scholl et al., *Nature* **595**, 233–238 (2021).
- A. M. Childs, J. Goldstone, *Phys. Rev. A* **70**, 042312 (2004).
- A. Ambainis, J. Kempe, A. Rivosh, in *Proceedings of the Sixteenth Annual ACM-SIAM Symposium on Discrete Algorithms* (Society for Industrial and Applied Mathematics, 2005), pp. 1099–1108.
- A. M. Childs, Y. Ge, *Phys. Rev. A* **89**, 052337 (2014).
- A. Heinz et al., *Phys. Rev. Lett.* **124**, 203201 (2020).
- T. Kitagawa, M. S. Rudner, E. Berg, E. Demler, *Phys. Rev. A* **82**, 033429 (2010).
- S. Onari, R. Arita, K. Kuroki, H. Aoki, *Phys. Rev. B* **70**, 094523 (2004).
- T. Ohgoe, T. Suzuki, N. Kawashima, *Phys. Rev. B* **86**, 054520 (2012).
- A. W. Young, W. J. Eckner, N. Schine, A. M. Childs, A. M. Kaufman, Tweezer-programmable 2D quantum walks in a Hubbard-regime lattice, Version 1, Zenodo (2022); <https://zenodo.org/record/6519158#.YuGM03bMI2w>.

ACKNOWLEDGMENTS

We acknowledge fruitful discussions with E. Knill, S. Geller, and M. O. Brown. We further thank A. M. Rey, K. Kim, S. Geller, and P. M. Preiss for close readings of the manuscript. **Funding:** This work was supported by the AFOSR (FA95501910079), ARO (W911NF1910223), the National Science Foundation Physics Frontier Center at JILA (1734006), and NIST. A.M.C. received support from the National Science Foundation (grant CCF-1813814 and QLCI grant OMA-2120757) and the Department of Energy, Office of Science, Office of Advanced Scientific Computing Research, Accelerated Research in Quantum Computing program. W.J.E. and N.S. acknowledge support from the NDSEG fellowship program, and the NRC research associateship program, respectively. **Author contributions:** A.W.Y., W.J.E., N.S., and A.M.C. contributed to developing the experiments. All authors contributed to analysis of the results and preparing the manuscript. **Competing interests:** The authors declare no competing interests. **Data and materials availability:** Experimental data and code used in this work are available on Zenodo (57). **License information:** Copyright © 2022 the authors, some rights reserved; exclusive licensee American Association for the Advancement of Science. No claim to original US government works. <https://www.sciencemag.org/about/science-licenses-journal-article-reuse>

SUPPLEMENTARY MATERIALS

science.org/doi/10.1126/science.aba0608
Materials and Methods
Supplementary Text
Figs. S1 to S8
Table S1
References (59–77)

Submitted 31 January 2022; accepted 8 July 2022
10.1126/science.aba0608

CORONAVIRUS

Omicron spike function and neutralizing activity elicited by a comprehensive panel of vaccines

John E. Bowen^{1†}, Amin Addetia^{1†}, Ha V. Dang², Cameron Stewart¹, Jack T. Brown¹, William K. Sharkey¹, Kaitlin R. Sprouse¹, Alexandra C. Walls^{1,3}, Ignacio G. Mazzitelli⁴, Jennifer K. Logue⁵, Nicholas M. Franko⁵, Nadine Czudnochowski², Abigail E. Powell², Exequiel Dellota Jr.², Kumail Ahmed⁶, Asefa Shariq Ansari⁶, Elisabetta Camerini⁷, Andrea Gori^{8,9,10}, Alessandra Bandera^{8,9,10}, Christine M. Posavad¹¹, Jennifer M. Dan^{12,13}, Zeli Zhang¹², Daniela Weiskopf¹², Alessandro Sette^{12,13}, Shane Crotty^{12,13}, Najeeha Talat Iqbal⁶, Davide Corti⁷, Jorge Geffner⁴, Gyorgy Snell², Renata Grifantini¹⁴, Helen Y. Chu⁵, David Veelsler^{1,3*}

The severe acute respiratory syndrome coronavirus 2 (SARS-CoV-2) Omicron variant of concern comprises several sublineages, with BA.2 and BA.2.12.1 having replaced the previously dominant BA.1 and with BA.4 and BA.5 increasing in prevalence worldwide. We show that the large number of Omicron sublineage spike mutations leads to enhanced angiotensin-converting enzyme 2 (ACE2) binding, reduced fusogenicity, and severe dampening of plasma neutralizing activity elicited by infection or seven clinical vaccines relative to the ancestral virus. Administration of a homologous or heterologous booster based on the Wuhan-Hu-1 spike sequence markedly increased neutralizing antibody titers and breadth against BA.1, BA.2, BA.2.12.1, BA.4, and BA.5 across all vaccines evaluated. Our data suggest that although Omicron sublineages evade polyclonal neutralizing antibody responses elicited by primary vaccine series, vaccine boosters may provide sufficient protection against Omicron-induced severe disease.

The ongoing COVID-19 pandemic has led to the emergence of severe acute respiratory syndrome coronavirus 2 (SARS-CoV-2) variants with increased transmissibility, viral fitness, and immune evasion (*1–10*). The most recently named variant of concern, Omicron, is characterized by the greatest known genetic divergence from the ancestral virus (Wuhan-Hu-1) and consists of several sublineages, including BA.1, BA.2, BA.3, BA.4, and BA.5. BA.1 was first detected in late 2021 and rapidly replaced Delta to become the globally dominant SARS-CoV-2 strain (*3, 9, 11*), aided by its high transmissibility and escape from neutralizing antibodies (*6, 12–18*). In early March of 2022, BA.2 became the most prevalent SARS-CoV-2 variant globally (*19, 20*)

(Fig. 1A), and the proportion of BA.2.12.1 in sequenced viruses peaked at >30% worldwide and >60% in the United States by late May of 2022 (Fig. 1B). However, BA.4 and BA.5, which share the same spike (S) glycoprotein sequence, are expected to reach global dominance owing to their increasing prevalence and successful replacement of BA.2 in South Africa (*21*) (Fig. 1C).

The receptor-binding domain (RBD) of the SARS-CoV-2 S glycoprotein interacts with the receptor angiotensin-converting enzyme 2 (ACE2) (*22–26*), promoting S conformational changes that lead to membrane fusion and viral entry (*27–29*). S is the main target of neutralizing antibodies, which have been shown to be a correlate of protection against SARS-CoV-2 (*30–38*), with RBD-targeting antibodies accounting for most neutralizing activity against vaccine-matched virus (*36, 38*) and nearly all cross-variant neutralizing activity (*39*). SARS-CoV-2 vaccines are based on the S glycoprotein [sometimes the RBD only (*30, 40, 41*)] or (inactivated) virus, and they utilize a variety of delivery technologies. Lipid-encapsulated prefusion-stabilized S-encoding mRNA vaccines include Moderna mRNA-1273 and Pfizer-BioNTech BNT162b2. Viral-vectored vaccines encoding for the SARS-CoV-2 S sequence include Janssen Ad26.COV2.S (human adenovirus 26), AstraZeneca AZD1222 (chimpanzee adenovirus), and Gamaleya National Center of Epidemiology and Microbiology Sputnik V (human adenovirus 26 and 5 for prime and boost, respectively). Novavax NVX-CoV2373 is a prefusion-stabilized S protein subunit vaccine formulated with a saponin-based matrix M adjuvant, whereas Sinopharm

BBIBP-CorV comprises inactivated virions. The primary vaccine series consisted of two doses for all of these vaccines except for Ad26.COV2.S, which was administered as a single dose.

We first aimed to understand how the different S mutations in the Omicron variant sublineages affect host receptor engagement and membrane fusion. Whereas the Delta RBD recognized human ACE2 with a comparable affinity to that of the Wuhan-Hu-1 RBD [1.1-fold enhancement by biolayer interferometry (BLI) (*3*) and 1.5-fold enhancement by surface plasmon resonance (SPR)], the ACE2 binding affinity was greater for the BA.1 RBD (4.4-fold by BLI and 2.6-fold by SPR) (*4, 12, 15*) and for the BA.2 RBD (3.7-fold by BLI and 2.3-fold by SPR) (Fig. 1, D and E; figs. S1 and S2; and tables S1 and S2). The BA.2.12.1 RBD—which differs from the BA.2 RBD only by the L452Q (substitution of leucine for glutamine at position 452) mutation—had an ACE2 binding affinity similar to that of the Wuhan-Hu-1 RBD (1.1-fold and 1.7-fold enhancements determined by BLI and SPR, respectively). The ACE2 binding affinity of the BA.4/BA.5 (BA.4/5) RBD was the greatest among the RBDs evaluated in this work, with 6.1-fold and 4.2-fold increases relative to Wuhan-Hu-1, as determined by BLI and SPR, respectively (Fig. 1, D and E; figs. S1 and S2; and tables S1 and S2).

We next compared the kinetics and magnitude of cell-cell fusion mediated by the Wuhan-Hu-1/G614, Delta, BA.1, BA.2, BA.2.12.2, and BA.4/5 S glycoproteins using a split green fluorescent protein (GFP) system (*42*) with VeroE6/TMPRSS2 (VeroE6 cells stably expressing TMPRSS2) target cells (expressing GFP β strands 1 to 10) and BHK-21 effector cells (expressing GFP β strand 11) and transiently transfected with S. We observed slower and markedly reduced overall fusogenicity for all tested Omicron sublineage S glycoproteins compared with Wuhan-Hu-1/G614 S and even more so relative to Delta S (*15, 19*) (Fig. 1, F to H; fig. S3; and movies S1 to S6), despite the higher apparent BA.4/5 S cell surface expression compared with other S trimers (fig. S4).

We next assessed the plasma neutralizing activity elicited in humans by each of the seven vaccines or SARS-CoV-2 infection and evaluated the immune evasion associated with the constellation of S mutations present in the BA.1, BA.2, BA.2.12.1, and BA.4/5 Omicron sublineages (table S3). We measured entry of vesicular stomatitis virus (VSV) pseudotyped with the SARS-CoV-2 Wuhan-Hu-1 S harboring the D614G, BA.1, BA.2, BA.2.12.1, or BA.4/5 mutations into VeroE6/TMPRSS2 target cells (*43*) in the presence of vaccinee or convalescent plasma (table S4). Plasma was obtained from individuals previously infected with a Washington-1-like SARS-CoV-2 strain based on time of infection. These samples were

¹Department of Biochemistry, University of Washington, Seattle, WA 98195, USA. ²Vir Biotechnology, San Francisco, CA 94158, USA. ³Howard Hughes Medical Institute, University of Washington, Seattle, WA 98195, USA. ⁴Instituto de Investigaciones Biomédicas en Retrovirus y SIDA (INIBRS), Facultad de Medicina, Buenos Aires C1121ABG, Argentina. ⁵Division of Allergy and Infectious Diseases, University of Washington, Seattle, WA 98195, USA. ⁶Departments of Paediatrics and Child Health and Biological and Biomedical Sciences, Aga Khan University, Karachi 74800, Pakistan. ⁷Humabs Biomed SA, a subsidiary of Vir Biotechnology, 6500 Bellinzona, Switzerland. ⁸Infectious Diseases Unit, Fondazione IRCCS Ca' Granda Ospedale Maggiore Policlinico, Milan, Italy. ⁹Department of Pathophysiology and Transplantation, University of Milan, Milan, Italy. ¹⁰Centre for Multidisciplinary Research in Health Science (MACH), University of Milan, Milan, Italy. ¹¹Vaccine and Infectious Disease Division, Fred Hutchinson Cancer Research Center, Seattle, WA 98109, USA. ¹²Center for Infectious Disease and Vaccine Research, La Jolla Institute for Immunology, La Jolla, CA 92037, USA. ¹³Department of Medicine, Division of Infectious Diseases and Global Public Health, University of California, San Diego, La Jolla, CA 92037, USA. ¹⁴INGM, Istituto Nazionale Genetica Molecolare "Romeo ed Enrica Invernizzi," Milan, Italy.

*Corresponding author. Email: dveesler@uw.edu

†These authors contributed equally to this work.

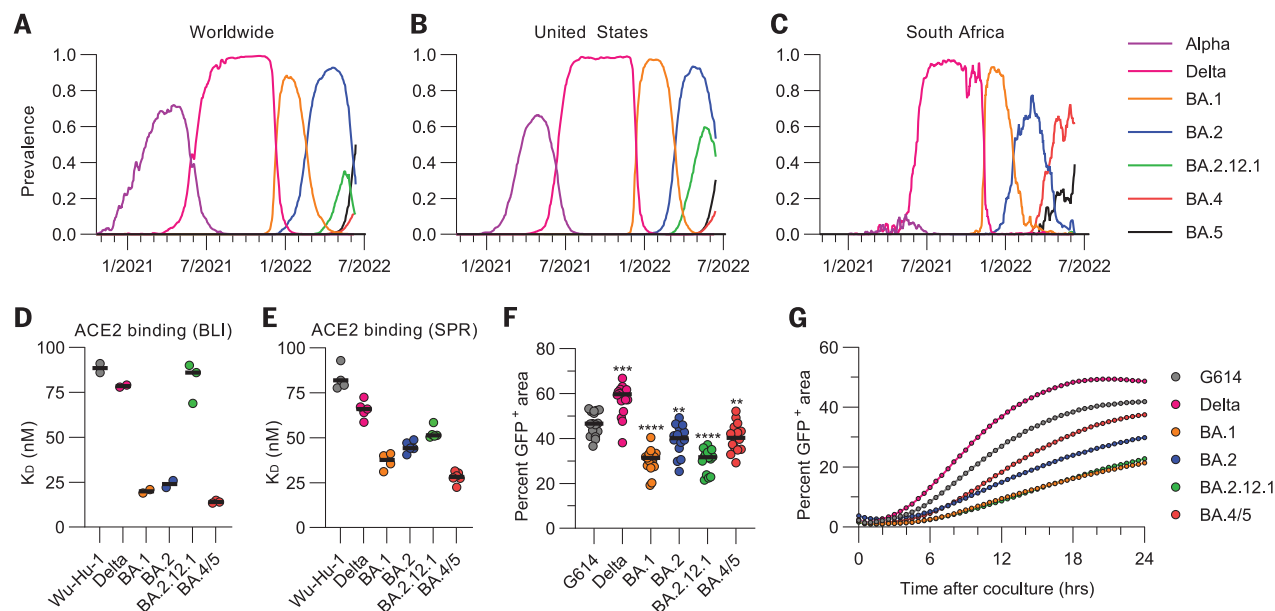


Fig. 1. Omicron sublineage RBDs bind ACE2 with enhanced affinity but exhibit impaired S-mediated fusogenicity relative to the ancestral virus.

(A to C) Prevalence of the different variants of concern measured globally (A), in the United States (B), or in South Africa (C). Alpha comprises B.1.1.7 and all Q sublineages; Delta comprises B.1.617.2 and all AY sublineages; and BA.1, BA.2, BA.4, and BA.5 comprise their respective sublineages (including BA.2.12.1 for BA.2). Prevalence calculations rely on shared GISAID (Global Initiative on Sharing Avian Influenza Data) sequences and may be biased by sampling. (D and E) Equilibrium dissociation constants (K_D) of binding of the monomeric ACE2 ectodomain to immobilized biotinylated Wuhan-Hu-1, Delta, BA.1, BA.2, BA.2.12.1, and BA.4/5 RBDs assessed by BLI (D) or SPR (E). Data presented are the results of at least two independent biological replicates

for BLI and for SPR (except for the BA.1 RBD SPR data, which come from four technical replicates). (F) Quantification of cell-cell fusion after 24 hours mediated by Wuhan-Hu-1/G614 S and other S variants expressed as the fraction of the total area with GFP fluorescence assessed using a split GFP system. Data are from 16 fields of view from a single experiment and are representative of results obtained from two independent biological replicates. Comparisons between fusion mediated by the Wuhan-Hu-1/G614 S and other S variants were completed using the Wilcoxon rank sum test. ** $P < 0.01$; *** $P < 0.001$; **** $P < 0.0001$. (G) Kinetics of cell-cell fusion mediated by Wuhan-Hu-1/G614 S and other S variants expressed as the fraction of the total area with GFP fluorescence assessed using a split GFP system.

obtained early in the pandemic, so individuals had not been vaccinated. We determined a plasma neutralizing geometric mean titer (GMT) of 39 against Wuhan-Hu-1/G614 S VSV pseudovirus, and only 5 of 24 individuals had detectable, albeit very weak, neutralizing activity against any of the four tested Omicron sublineages (Fig. 2 and fig. S5A). Plasma from subjects that received two doses of Moderna mRNA-1273 ~4 weeks apart had Wuhan-Hu-1/G614, BA.1, BA.2, BA.2.12.1, and BA.4/5 S VSV neutralizing GMTs of 633, 33, 44, 30, and 22, respectively, whereas plasma from subjects that received two doses of Pfizer BNT162b2 ~3 weeks apart had neutralizing GMTs of 340, 20, 29, 24, and 19, respectively (Fig. 2 and fig. S5, B and C). In total, 19 of 28, 21 of 28, 19 of 28, and 16 of 28 mRNA-vaccinated subjects retained neutralizing activity against BA.1, BA.2, BA.2.12.1, and BA.4/5 S VSV, respectively. The combined Moderna and Pfizer cohorts experienced ≥ 18 -fold, ≥ 13 -fold, ≥ 17 -fold, and ≥ 23 -fold GMT reductions against BA.1, BA.2, BA.2.12.1, and BA.4/5 S VSV, respectively. A similar trend was observed for plasma from individuals that received two doses of Novavax NVX-CoV2373 (44) in a double-blinded manner; however, these plasma samples were not obtained at

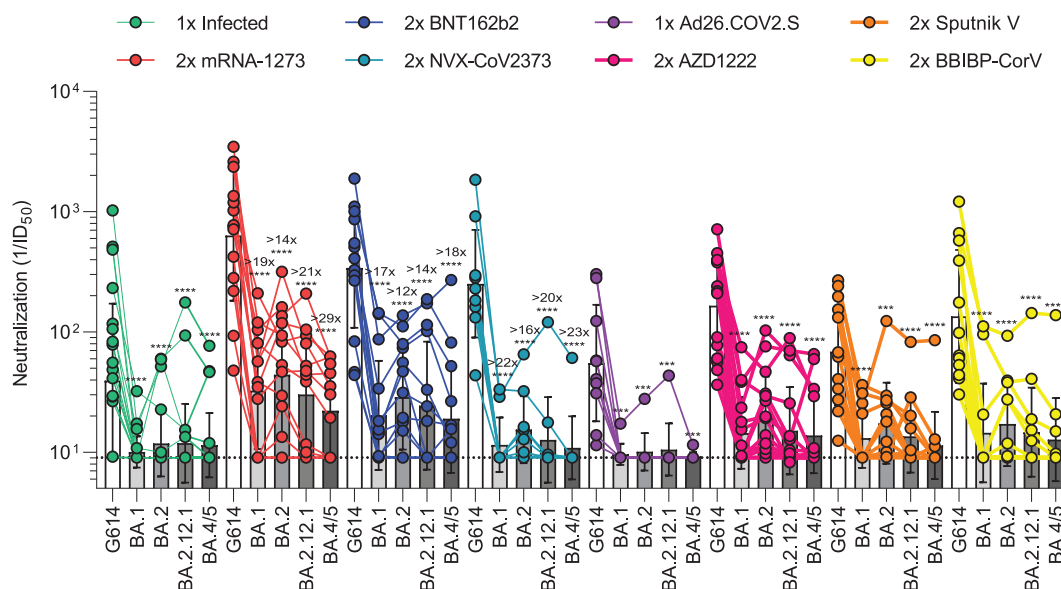
peak titers owing to the design of the clinical trial (figs. S6 and S7). From this group, we determined a neutralizing GMT of 252 against Wuhan-Hu-1/G614 S VSV with only 2 of 10 individuals having detectable neutralizing activity against BA.1 (GMT: 12, ≥ 22 -fold drop), 7 of 10 against BA.2 (GMT: 15, ≥ 16 -fold drop), 4 of 10 against BA.2.12.1 (GMT: 13, ≥ 20 -fold drop), and 1 of 10 against BA.4/5 (GMT: 11, ≥ 23 -fold drop) (Fig. 2 and fig. S5D). Plasma from individuals vaccinated with Janssen Ad26.COV2.S were obtained 9 to 142 days (mean, 79) after their single dose—a time frame expected to capture peak neutralizing titers (45). This resulted in a Wuhan-Hu-1/G614 S VSV GMT of 55, and only 1 of 12 subjects had detectable plasma neutralizing activity against any of the Omicron sublineages (Fig. 2 and fig. S5E). Two doses of AZD1222 4 weeks apart induced Wuhan-Hu-1/G614, BA.1, BA.2, BA.2.12.1, and BA.4/5 S VSV neutralizing GMTs of 165, 14, 19, 15, and 14, respectively, with 13 of 16 and 4 of 16 individuals having detectable neutralizing activity against any or all tested subvariants, respectively (Fig. 2 and fig. S5F). Sputnik V vaccinee plasma after two doses had Wuhan-Hu-1/G614, BA.1, BA.2, BA.2.12.1, and BA.4/5 S VSV GMTs of 69, 13, 17, 14, and 11, respectively (Fig. 2

and fig. S5G). Detectable neutralizing activity against any or all Omicron sublineages was observed for 7 of 13 and 2 of 13 individuals, respectively. Finally, plasma from subjects vaccinated with two doses of Sinopharm BBIBP-CorV had a neutralizing GMT against G614 S VSV of 135, with 3 of 12 samples retaining detectable neutralizing activity against BA.1 (GMT: 14), 7 of 12 against BA.2 (GMT: 17), 5 of 12 against BA.2.12.1 (GMT: 15), and 4 of 12 against BA.4/5 (GMT: 11) (Fig. 2 and fig. S5H). Overall, these data underscore the magnitude of evasion of polyclonal plasma neutralizing antibody responses for Omicron sublineages in humans after primary vaccine series or infection [resulting from the accumulation of S mutations (12)], with a subtle but consistently more marked effect for BA.1 and even more so for BA.4/5 compared with BA.2 and BA.2.12.1.

The emergence of the SARS-CoV-2 Delta and subsequently Omicron variants of concern led to an increasing number of reinfections and vaccine breakthrough cases (5, 46–48). Public health policies were therefore updated worldwide to recommend administration of an additional vaccine dose (booster) several months after the primary vaccine series, which

Fig. 2. SARS-CoV-2 Omicron sublineages evade human plasma neutralizing antibodies elicited by infection or primary vaccine series. Plasma

neutralizing antibody titers elicited by primary COVID-19 vaccination series determined using SARS-CoV-2 S VSV pseudotypes using VeroE6/TMPRSS2 as target cells. One-time (1×) infected samples ($n = 24$) were obtained 26 to 78 days (mean, 41) after symptom onset, two-dose (2×) mRNA-1273 samples ($n = 14$) were obtained 6 to 50 days (mean, 13) after second dose, 2× BNT162b2 samples ($n = 14$) were obtained 6 to 33 days (mean, 14) after second dose, 2× NVX-CoV2373 samples ($n = 10$) were obtained 17 to 168 days (mean, 82) after second dose, one-dose (1×) Ad26.COVS.2 samples ($n = 10$) were obtained 9 to 142 days (mean, 79) after first dose, 2× AZD1222 samples ($n = 16$) were obtained ~30 days after second dose, 2× Sputnik V samples ($n = 12$) were obtained 60 to 90 days after second dose, and BBIBP-CorV samples ($n = 12$) were obtained 9 to 104 days (mean, 69) after second dose. Individual points are representative geometric mean titers from



two independent experiments consisting of two replicates each. Bars represent geometric means, and error bars represent geometric standard deviations for each group. Statistical significance between groups of paired data was determined by Wilcoxon rank sum test. *** $P < 0.001$; **** $P < 0.0001$. Patient demographics are shown in table S4. Normalized curves and fits are shown in fig. S5. G614 indicates Wuhan-Hu-1/G614. ID₅₀, median inhibitory dose.

has been shown to increase the breadth and potency of neutralizing antibodies (5, 12, 17, 49). We thus assessed and compared the benefits provided by homologous or heterologous vaccine boosters on vaccinee plasma neutralizing activity against Wuhan-Hu-1/G614, BA.1, BA.2, BA.2.12.1, and BA.4/5 S VSV pseudotypes. Plasma samples of subjects that received three mRNA vaccine doses had neutralizing GMTs of 2371, 406, 448, 472, and 392 against Wuhan-Hu-1/G614, BA.1, BA.2, BA.2.12.1, and BA.4/5 S VSV, respectively (Fig. 3 and fig. S8A). The five- to sixfold potency losses against these variants are marked improvements over the >13- to >23-fold reductions observed after two vaccine doses, underscoring an increase in overall neutralizing antibody potency and breadth (5, 12). Individuals vaccinated with two doses of NVX-CoV2373 followed by a booster of mRNA-1273 (1 of 5 individuals) or NVX-CoV2373 (4 of 5 individuals) had neutralizing GMTs of 6978 for Wuhan-Hu-1/G614, 505 for BA.1 (14-fold reduction), 948 for BA.2 (sevenfold reduction), 935 for BA.2.12.1 (sevenfold reduction), and 330 for BA.4/5 (21-fold reduction) (Fig. 3 and fig. S8B). Plasma from individuals who received one dose of Ad26.COVS.2 followed by either a homologous Ad26.COVS.2 (12 of 14 individuals) or a heterologous BNT162b2 booster (2 of 14 individuals) ~4 months later had neutralizing GMTs of 363, 23, 50, 46, and 29 against Wuhan-Hu-1/G614, BA.1, BA.2, BA.2.12.1, and BA.4/5 S VSV, respectively, corresponding to damp-

ening ranging between ≥7- and ≥16-fold with 9 of 14 individuals maintaining neutralizing activity against all sublineages (Fig. 3 and fig. S8C). We also investigated individuals that received two doses of AZD1222 4 weeks apart followed by a BNT162b2 (17 of 18 individuals) or mRNA-1273 (1 of 18 individuals) booster ~6 months later. This cohort had respective neutralizing GMTs of 2167, 186, 269, 273, and 135 against Wuhan-Hu-1/G614, BA.1, BA.2, BA.2.12.1, and BA.4/5 S VSV, corresponding to 8- to 16-fold potency reductions (Fig. 3 and fig. S8D). Individuals vaccinated with two doses of Sputnik V and boosted with AZD1222 (11 of 12 individuals) or BNT162b2 (1 of 12 individuals) ~9 months later had neutralizing GMTs of 351, 68, 77, 72, and 35 for Wuhan-Hu-1/G614, BA.1, BA.2, BA.2.12.1, and BA.4/5, respectively, amounting to 5- to 10-fold reductions of potency (Fig. 3 and fig. S8E). BBIBP-CorV vaccinees boosted with either BNT162b2 (14 of 18 individuals) or mRNA-1273 (4 of 18 individuals) had GMTs of 2047 for G614, 439 for BA.1 (fivefold reduction), 375 for BA.2 (fivefold reduction), 430 for BA.2.12.1 (fivefold reduction), and 252 for BA.4/5 (eightfold reduction) (Fig. 3 and fig. S8F). The marked improvement in plasma neutralizing activity for subjects that received a booster dose over those that did not highlights the importance of vaccine boosters for eliciting potent neutralizing antibody responses against Omicron sublineages.

To assess the effect of target cell lines on apparent Omicron immune escape, we compared the aforementioned VeroE6/TMPRSS2 cells (43) with a stable ACE2-overexpressing HEK293T cell line (HEK293T/ACE2) (50) to determine plasma neutralizing activity for a cohort of mRNA-vaccinated individuals. After primary vaccine series, only three subjects had detectable neutralizing activity against any of the tested Omicron sublineage VSV pseudotypes when using HEK293T/ACE2 target cells. By contrast, all but one subject had detectable, albeit very weak, neutralizing activity against Omicron VSV pseudotypes using VeroE6/TMPRSS2 target cells, resulting in >17-fold, >14-fold, >20-fold, and >22-fold reductions against BA.1, BA.2, BA.2.12.1, and BA.4/5, respectively (figs. S9A and S10A). After a booster dose, we observed respective 7-fold, 7-fold, 11-fold, and 13-fold reductions of neutralizing activity against BA.1, BA.2, BA.2.12.1, and BA.4/5 VSV pseudotypes using HEK293T/ACE2 target cells, as compared with respective sevenfold, sixfold, fivefold, and eightfold reductions when using VeroE6/TMPRSS2 target cells (figs. S9B and S10B). This indicates that the target cell lines used in neutralization assays may affect the observed plasma neutralizing escape of SARS-CoV-2 variants, which may be further compounded on the basis of preferential entry routes (15, 23, 51).

We report that the BA.1, BA.2, BA.2.12.1, and BA.4/5 Omicron sublineages, which account

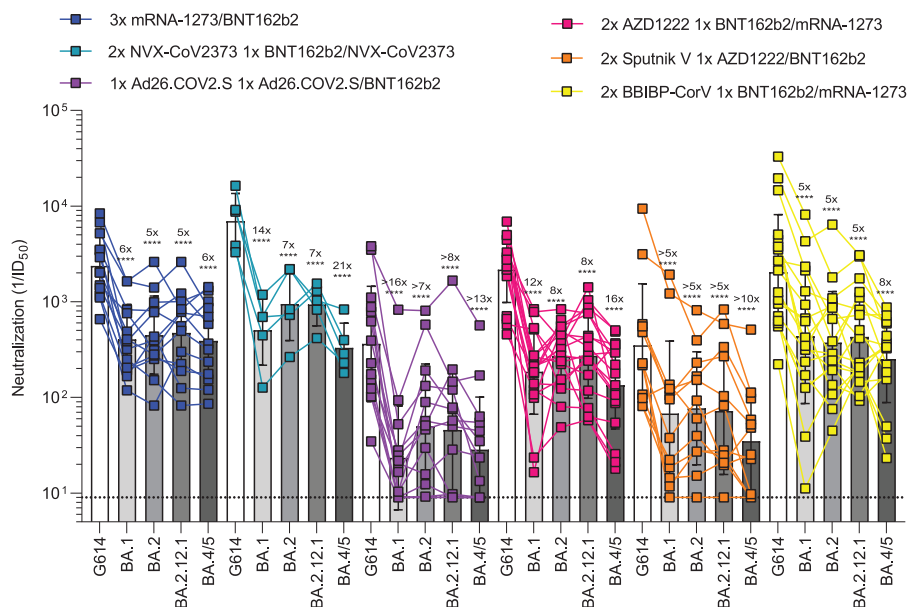


Fig. 3. Administration of a booster dose rescues neutralization potency against Omicron sublineages for all vaccines.

Plasma neutralizing antibody titers elicited by COVID-19 vaccine boosters determined using SARS-CoV-2 S VSV pseudotyped and VeroE6/TMPRSS2 as target cells. Three-dose (3×) mRNA-1273 or BNT162b2 samples ($n = 13$) were donated 13 to 97 days (mean, 30) after third dose; 2× NVX-CoV2373 plus 1× BNT162b2 or NVX-CoV2373 samples ($n = 5$) were donated 14 to 20 days (mean, 15) after third dose; 1× Ad26.COV2.S plus 1× Ad26.COV2.S or BNT162b2 samples ($n = 14$) were donated 12 to 16 days (mean, 14) after second dose; 2× AZD1222 plus 1× BNT162b2 or mRNA-1273 samples ($n = 18$) were donated 30 to 123 days (mean, 87) after third dose; 2× Sputnik V plus 1× AZD1222 or BNT162b2 samples ($n = 14$) were donated 45 to 60 days after third dose; and 2× BBIBP-CorV plus 1× BNT162b2 or mRNA-1273 samples ($n = 18$) were donated 29 to 89 days (mean, 50) after third dose. Individual points are representative geometric mean titers from two to four independent experiments consisting of two replicates each. Bars represent geometric means, and error bars represent geometric standard deviations for each group. Statistical significance between groups of paired data was determined by Wilcoxon rank sum test. $**P < 0.01$; $***P < 0.001$; $****P < 0.0001$. Patient demographics are shown in table S4. Normalized curves and fits are shown in fig. S8.

for >99% of all infections worldwide over the first half of 2022, have increased ACE2 binding affinity, have decreased fusogenicity, and markedly evade neutralizing antibody responses relative to the Wuhan-Hu-1 and Delta strains (3). Collectively, these data suggest that enhanced receptor engagement and immune evasion are key changes that may have promoted the rapid spread of these Omicron sublineages and could contribute to the current rise in prevalence of BA.4 and BA.5.

The development of life-saving vaccines is regarded as one of humanity's greatest medical and scientific achievements, which is exemplified by COVID-19 vaccines (52–54). Primary COVID-19 vaccine regimens or infection-elicited plasma neutralizing activity was severely dampened by Omicron sublineages BA.1, BA.2, BA.2.12.1, and BA.4/5. However, administration of a booster dose increased neutralizing antibody titers and breadth against all Omicron sublineages to appreciable levels regardless of the vaccine evaluated, concurring with findings for BA.1 (5, 12, 15, 17, 49, 55, 56). These results are consistent with previous

studies demonstrating that a third vaccine dose results in the recall and expansion of preexisting SARS-CoV-2 S-specific memory B cells, as well as de novo induction, leading to production of neutralizing antibodies with enhanced potency and breadth against variants (57, 58). Vaccinees receiving two doses of Ad26.COV2.S (4 months apart) had lesser Omicron immune escape than that in other two-dose vaccine recipients (3 to 4 weeks between doses) but greater than that observed in three-dose vaccinees. These findings suggest that the time interval between immunizations may affect the breadth and potency of vaccine-elicited plasma neutralizing activity and that a third dose may be beneficial for this cohort as well (59–62). Moreover, the induction by several currently available vaccines of robust cross-reactive cellular immunity against SARS-CoV-2 Omicron is likely playing a key role in the retained protection observed against severe disease (63, 64).

As SARS-CoV-2 progressively becomes endemic in the human population, vaccination strategies will need to be carefully considered

and optimized to provide long-lasting immunity. So far, elicitation of high titers of variant-neutralizing antibodies and protection against severe disease can be accomplished by dosing with the Wuhan-Hu-1 S antigen, as shown in animal models and studies of vaccine efficacy in humans (5, 48, 65, 66). In fact, an Omicron BA.1 (or other variant) S boost does not offer mice or nonhuman primates significantly more BA.1 protection than a Wuhan-Hu-1 S boost (67–71), and Omicron primary infections elicit neutralizing antibody and memory responses of narrow breadth (72–74). However, continued SARS-CoV-2 evolution will accentuate the antigenic divergence from the ancestral strain, and it is unknown whether vaccines based on Wuhan-Hu-1 S alone will provide satisfactory protection, either as boosters in vaccinated or infected individuals or as an initial vaccine in naïve individuals (mainly children). The recent evaluation of intranasal vaccine administration could also be important to not only prevent severe disease but also curtail viral infection and transmission through induction of mucosal immunity (75–78). For these reasons, it is important to monitor new variants, assess the effectiveness of currently available vaccines, and continue to test and implement new vaccination strategies that may provide stronger, longer-lasting, or broader protection against SARS-CoV-2 and the entire sarbecovirus subgenus (40, 79, 80).

REFERENCES AND NOTES

1. M. McCallum et al., *Science* **373**, 648–654 (2021).
2. E. B. Hodcroft et al., *Nature* **595**, 707–712 (2021).
3. M. McCallum et al., *Science* **374**, 1621–1626 (2021).
4. M. McCallum et al., *Science* **375**, 864–868 (2022).
5. A. C. Walls et al., *Cell* **185**, 872–880.e3 (2022).
6. S. Cele et al., *Nature* **602**, 654–656 (2022).
7. R. Viana et al., *Nature* **603**, 679–686 (2022).
8. H. Tegally et al., *Nature* **592**, 438–443 (2021).
9. P. Micochova et al., *Nature* **599**, 114–119 (2021).
10. D. A. Collier et al., *Nature* **593**, 136–141 (2021).
11. A. Saito et al., *Nature* **602**, 300–306 (2022).
12. E. Cameroni et al., *Nature* **602**, 664–670 (2022).
13. F. Schmidt et al., *N. Engl. J. Med.* **386**, 599–601 (2022).
14. A. Wilhelm et al., medRxiv 2021.12.07.21267432 [Preprint] (2021).
15. B. Meng et al., *Nature* **603**, 706–714 (2022).
16. H. Allen et al., medRxiv 2022.02.15.22271001 [Preprint] (2022).
17. W. Dejnirattisai et al., *Cell* **185**, 467–484.e15 (2022).
18. T. N. Starr et al., *Science* **377**, 420–424 (2022).
19. R. Suzuki et al., *Nature* **603**, 700–705 (2022).
20. D. Yamasoba et al., *Cell* **185**, 2103–2115.e19 (2022).
21. H. Tegally et al., medRxiv 2022.05.01.22274406 [Preprint] (2022).
22. A. C. Walls et al., *Cell* **181**, 281–292.e6 (2020).
23. M. Hoffmann et al., *Cell* **181**, 271–280.e8 (2020).
24. P. Zhou et al., *Nature* **579**, 270–273 (2020).
25. M. Letko, A. Marzi, V. Munster, *Nat. Microbiol.* **5**, 562–569 (2020).
26. D. Wrapp et al., *Science* **367**, 1260–1263 (2020).
27. A. C. Walls et al., *Proc. Natl. Acad. Sci. U.S.A.* **114**, 11157–11162 (2017).
28. Y. Cai et al., *Science* **369**, 1586–1592 (2020).
29. A. C. Walls et al., *Cell* **176**, 1026–1039.e15 (2019).
30. P. S. Arunachalam et al., *Nature* **594**, 253–258 (2021).
31. K. McMahan et al., *Nature* **590**, 630–634 (2021).
32. D. S. Khoury et al., *Nat. Med.* **27**, 1205–1211 (2021).
33. K. S. Corbett et al., *Science* **373**, eab0299 (2021).
34. P. B. Gilbert et al., *Science* **375**, 43–50 (2022).

35. D. Corti, L. A. Purcell, G. Snell, D. Veessler, *Cell* **184**, 3086–3108 (2021).
36. L. Piccoli *et al.*, *Cell* **183**, 1024–1042.e21 (2020).
37. L. Stamatatos *et al.*, *Science* **372**, 1413–1418 (2021).
38. A. J. Greaney *et al.*, *Sci. Transl. Med.* **13**, eabi9915 (2021).
39. J. E. Bowen *et al.*, bioRxiv 2021.12.19.473391 [Preprint] (2021).
40. A. C. Walls *et al.*, *Cell* **184**, 5432–5447.e16 (2021).
41. A. C. Walls *et al.*, *Cell* **183**, 1367–1382.e17 (2020).
42. M. Kodaka *et al.*, *Exp. Cell Res.* **336**, 171–181 (2015).
43. F. A. Lempp *et al.*, *Nature* **598**, 342–347 (2021).
44. Z. Zhang *et al.*, *Cell* **185**, 2434–2451.e17 (2022).
45. D. H. Barouch *et al.*, *N. Engl. J. Med.* **385**, 951–953 (2021).
46. T. A. Bates *et al.*, *JAMA* **327**, 179–181 (2022).
47. A.-r. Y. Collier *et al.*, *Sci. Transl. Med.* **14**, eabn6150 (2022).
48. Y.-J. Park *et al.*, bioRxiv 2022.05.08.491108 [Preprint] (2022).
49. W. F. Garcia-Beltran *et al.*, *Cell* **185**, 457–466.e4 (2022).
50. K. H. D. Crawford *et al.*, *Viruses* **12**, 513 (2020).
51. M. Hoffmann, H. Kleine-Weber, S. Pöhlmann, *Mol. Cell* **78**, 779–784.e5 (2020).
52. K. Wu *et al.*, *N. Engl. J. Med.* **384**, 1468–1470 (2021).
53. K. S. Corbett *et al.*, *Nature* **586**, 567–571 (2020).
54. E. E. Walsh *et al.*, *N. Engl. J. Med.* **383**, 2439–2450 (2020).
55. D. Planas *et al.*, *Nature* **602**, 671–675 (2022).
56. E. Pérez-Then *et al.*, *Nat. Med.* **28**, 481–485 (2022).
57. R. R. Goel *et al.*, *Cell* **185**, 1875–1887.e8 (2022).
58. F. Muecksch *et al.*, bioRxiv 2022.02.14.480394 [Preprint] (2022).
59. B. Grunau *et al.*, *JAMA* **327**, 279–281 (2022).
60. M. Voysey *et al.*, *Lancet* **397**, 881–891 (2021).
61. H. Parry *et al.*, *NPJ Vaccines* **7**, 14 (2022).
62. R. P. Payne *et al.*, *Cell* **184**, 5699–5714.e11 (2021).
63. J. Liu *et al.*, *Nature* **603**, 493–496 (2022).
64. A. Tarke *et al.*, *Cell* **185**, 847–859.e11 (2022).
65. N. Andrews *et al.*, *N. Engl. J. Med.* **386**, 1532–1546 (2022).
66. E. K. Accorsi *et al.*, *JAMA* **327**, 639–651 (2022).
67. B. Ying *et al.*, bioRxiv 2022.02.07.479419 [Preprint] (2022).
68. I.-J. Lee *et al.*, bioRxiv 2022.01.31.478406 [Preprint] (2022).
69. D. W. Hawman *et al.*, bioRxiv 2022.01.31.478520 [Preprint] (2022).
70. P. S. Arunachalam *et al.*, bioRxiv 2022.03.18.484950 [Preprint] (2022).
71. M. Gagne *et al.*, *Cell* **185**, 1556–1571.e18 (2022).
72. S. I. Richardson *et al.*, *Cell Host Microbe* **30**, 880–886.e4 (2022).
73. A. Rössler, L. Knabl, D. von Laer, J. Kimpel, *N. Engl. J. Med.* **386**, 1764–1766 (2022).

74. K. Stiasny *et al.*, *Research Square* [Preprint] (2022).
75. T. Mao *et al.*, bioRxiv 2022.01.24.477597 [Preprint] (2022).
76. J. E. Oh *et al.*, *Sci. Immunol.* **6**, eabi5129 (2021).
77. A. O. Hassan *et al.*, *Cell Rep. Med.* **2**, 100230 (2021).
78. S. N. Langel *et al.*, *Sci. Transl. Med.* 10.1126/scitranslmed.abn6868 (2022).
79. A. A. Cohen *et al.*, *Science* **371**, 735–741 (2021).
80. D. R. Martinez *et al.*, *Science* **373**, 991–998 (2021).

ACKNOWLEDGMENTS

We thank H. Tani (University of Toyama) for providing the reagents necessary for preparing VSV pseudotyped viruses. We thank J. R. Dillen and C. Ng for assistance with protein production.

Funding: This study was supported by the National Institute of Allergy and Infectious Diseases (NIAID) (DP1AI158186 and HHSN272201700059C to D.V.), the National Institutes of Health (NIH) Cellular and Molecular Biology training grant (T32GM007270 to A.A.), a Pew Biomedical Scholars Award (D.V.), an Investigators in the Pathogenesis of Infectious Disease Award from the Burroughs Wellcome Fund (D.V.), Fast grants (D.V.), the Bill & Melinda Gates Foundation (OPP1156262 to D.V.), the University of Washington Arnold and Mabel Beckman Center for Cryo-EM and the NIH grant S10OD032290 (to D.V.), and grant U01 AI151698 for the United World Antiviral Research Network (UWARN) as part of the Centers for Research in Emerging Infectious Diseases (CREID) Network. Additionally, work was supported by NIH NIAID grant CCHI AI142742 (S.C. and A.S.), NIAID contract no. 75N9301900065 (A.S. and D.W.), and U01 CA260541-01 (D.W.). D.V. is an investigator of the Howard Hughes Medical Institute. This project has been funded in part with federal funds from the NIAID, NIH, Department of Health and Human Services, under grant CCHI AI142742 (S.C. and A.S.). This work was additionally supported in part by LJI Institutional Funds. **Author contributions:** J.E.B., A.A., and D.V. conceived the project and designed experiments. J.E.B. and K.R.S. produced pseudotyped viruses. J.E.B. and A.A. performed neutralization assays. A.A. and H.V.D. carried out ACE2 binding assays. A.A. carried out cell-cell fusion assays. J.E.B., C.S., J.T.B., and W.K.S. carried out enzyme-linked immunosorbent assay (ELISA) binding assays. J.E.B., C.S., J.T.B., W.K.S., N.C., and A.E.P. expressed and purified glycoproteins. A.C.W., I.G.M., J.K.L., N.M.F., K.A., A.S., E.D., C.M.P., J.M.D., Z.Z., D.W., A.S., S.C., N.T.I., D.C., J.G., G.S., R.G., and H.Y.C. provided reagents. D.V. supervised the project and obtained funding. J.E.B., A.A., and D.V. analyzed the data and wrote the manuscript with input from all authors. **Competing interests:** D.C., H.V.D., N.C., A.E.P., E.D., and G.S. are employees of Vir Biotechnology Inc. and may hold shares in Vir Biotechnology Inc. A.C.W. and D.V. are named as

inventors on patent applications filed by the University of Washington for SARS-CoV-2 and sarbecovirus RBD nanoparticle vaccines. The Veessler laboratory has received a sponsored research agreement from Vir Biotechnology Inc. H.Y.C. reported consulting with Ellume, Pfizer, the Bill & Melinda Gates Foundation, Glaxo Smith Kline, and Merck. She has received research funding from Emergent Ventures, Gates Ventures, Sanofi Pasteur, and the Bill & Melinda Gates Foundation as well as support and reagents from Ellume and Cepheid outside of the submitted work. A.S. is a consultant for Gritstone Bio, Flow Pharma, ImmunoScape, Avalia, Moderna, Fortress, Repertoire, Gerson Lehrman Group, RiverVest, MedaCorp, and Guggenheim. S.C. has consulted for GSK, JP Morgan, Citi, Morgan Stanley, Avalia NZ, Nutcracker Therapeutics, University of California, California State Universities, United Airlines, Adagio, and Roche. The remaining authors declare that the research was conducted in the absence of any commercial or financial relationships that could be construed as a potential conflict of interest. **Data and materials availability:** All data associated with this manuscript are available in the main text or the supplementary materials. All further relevant source data that support the findings of this study are available from the corresponding author upon reasonable request. Materials are available through materials transfer agreements (UBMTAs or similar agreements) with the University of Washington. **License information:** This work is licensed under a Creative Commons Attribution 4.0 International (CC BY 4.0) license, which permits unrestricted use, distribution, and reproduction in any medium, provided the original work is properly cited. To view a copy of this license, visit <https://creativecommons.org/licenses/by/4.0/>. This license does not apply to figures/photos/artwork or other content included in the article that is credited to a third party; obtain authorization from the rights holder before using such material.

SUPPLEMENTARY MATERIALS

science.org/doi/10.1126/science.abq0203
Materials and Methods
Figs. S1 to S12
Tables S1 to S4
References (81–83)
Movies S1 to S6
MDAR Reproducibility Checklist

Submitted 16 March 2022; accepted 12 July 2022
Published online 19 July 2022
10.1126/science.abq0203

Sloan Kettering Institute

Celebrating over 75 years of breakthroughs

Join our faculty and help set the pace of biomedical science.

JOIN US

Successful candidates will hold an appointment in one of SKI's research programs. Candidates may apply to up to two programs. MSK is an equal opportunity and affirmative action employer committed to diversity and inclusion in all aspects of recruiting and employment.

Cancer Biology & Genetics

Chair: Scott Lowe, PhD

Cell Biology

Chair: Tobias Walther, PhD

Chemical Biology

Chair: Derek Tan, PhD

Computational & Systems Biology

Chair: Dana Pe'er, PhD

Developmental Biology

Chair: Anna-Katerina Hadjantonakis, PhD

Immunology

Chair: Alexander Rudensky, PhD

Molecular Biology

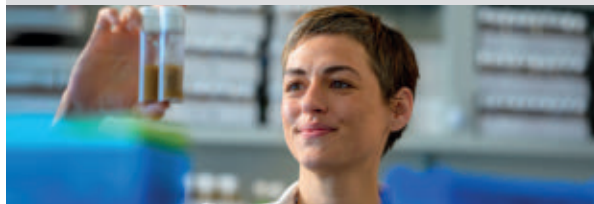
Chair: John Petrini, PhD

Molecular Pharmacology

Chair: David Scheinberg, MD, PhD

Structural Biology

Chair: Christopher Lima, PhD



Memorial Sloan Kettering
Cancer Center

AREAS OF BASIC AND TRANSLATIONAL RESEARCH

- Stem Cell Biology
- Developmental Oncology
- Regenerative Medicine
- Machine Learning
- 3D Single-Cell Modeling and Analysis
- Biophysics & Imaging
- Organelle Biology
- Chromatin & Gene Regulation
- Genome Integrity and Functional Genomics
- Chemistry & Chemical Biology
- Metastasis & Tumor Microenvironment
- Immunity, Host-Microbial Interactions and Microbiomes
- Tumor Immunobiology
- Experimental Therapeutics, Imaging and Bioengineering
- Protein Structure & Function
- Cancer Genetics

RESEARCH AND TRAINING

- 100 research laboratories housed in state-of-the-art buildings
- 26 Core facilities offering cutting-edge scientific services
- More than 900 pre- and postdoctoral trainees
- Appointments in the Gerstner Sloan Kettering Graduate School of Biomedical Sciences and the Weill Cornell Graduate School of Medical Sciences

Visit www.ski.edu to learn more.



MSK is an equal opportunity and affirmative action employer committed to diversity and inclusion in all aspects of recruiting and employment. All qualified individuals are encouraged to apply and will receive consideration without regard to race, color, gender, gender identity or expression, sexual orientation, national origin, age, religion, creed, disability, veteran status or any other factor which cannot lawfully be used as a basis for an employment decision.

Application deadline: **October 17, 2022** | Apply at: <https://facultysearch.ski.edu>

THE UNIVERSITY OF CHICAGO

Physician-Scientists – Rheumatology and Immunology

The University of Chicago's Department of Medicine, Section of Rheumatology, and the Committee on Immunology are searching for **full-time faculty members at any rank** to join an established, integrated and vibrant immunology community. We are interested in applicants from any area of immunology and especially welcome those whose research uses current molecular and computational approaches to understand important questions in autoimmunity, tolerance, peripheral immunity, lymphocyte biology, and inflammation. There are ample resources and opportunities for developing impactful research programs that seek to understand fundamental immunological mechanisms and how they contribute to human disease pathogenesis. In addition to research, successful applicants will be expected to engage in teaching and supervision of trainees and students, including undergraduates and graduates. Clinical appointees will have a mix of inpatient and outpatient clinical responsibilities primarily at our Hyde Park campus. Academic rank, tenure and compensation (including a generous package of fringe benefits) are dependent upon qualifications.

We anticipate that appointees will develop close interactions with other departments, divisions, centers and institutes at the University of Chicago, and the University of Chicago Medical Center Argonne National Laboratory, and/or the Marine Biological Laboratory. Appointees will have access to state-of-the-art core facilities and to outstanding colleagues and graduate students affiliated with numerous degree-granting programs within and outside the biological sciences including molecular engineering and the physical sciences. Competitive research space and start-up funding will be available. Faculty recruited through this effort will strengthen and diversify a collegial and internationally acclaimed research base that is making major contributions to the advancement of human health.

Prior to the start of employment, qualified applicants must: **1)** have a doctoral degree (MD, PhD, or MD/PhD) or equivalent. Clinical applicants must: **2)** hold or be eligible for medical licensure in the State of Illinois, and **3)** be Board Certified or Eligible in Rheumatology.

To be considered, those interested must apply through The University of Chicago's Academic Recruitment job board, which uses Interfolio to accept applications: <http://apply.interfolio.com/109756>. Applicants must upload: CV including bibliography, cover letter, and research statement.

Equal Employment Opportunity Statement

We seek a diverse pool of applicants who wish to join an academic community that places the highest value on rigorous inquiry and encourages diverse perspectives, experiences, groups of individuals, and ideas to inform and stimulate intellectual challenge, engagement, and exchange. The University's Statements on Diversity are at <https://provost.uchicago.edu/statements-diversity>.

The University of Chicago is an Affirmative Action/Equal Opportunity/Disabled/Veterans Employer and does not discriminate on the basis of race, color, religion, sex, sexual orientation, gender identity, national or ethnic origin, age, status as an individual with a disability, protected veteran status, genetic information, or other protected classes under the law. For additional information please see the University's Notice of Nondiscrimination.

Job seekers in need of a reasonable accommodation to complete the application process should call 773-834-3988 or email equalopportunity@uchicago.edu with their request.



POSTDOCTORAL RESEARCH ASSOCIATES

NRC Research Associateship Programs

The National Academies of Sciences, Engineering, and Medicine administers **postdoctoral** and **senior research** awards at participating federal laboratories and affiliated institutions at locations throughout the U.S and abroad.

We are seeking highly qualified candidates who hold, or anticipate earning, a doctorate in a variety of fields of science or engineering. Degrees from foreign universities should be equivalent in training and research experience to a doctoral degree from a U.S. institution. Citizenship eligibility varies among the sponsoring laboratories.

Application deadline dates (four annual review cycles):

- February 1
- May 1
- August 1
- November 1

Awardees have the opportunity to:

- Conduct independent research in an area compatible with the interests of the sponsoring laboratory
- Devote full-time effort to research and publication
- Access the excellent and often unique facilities of the federal research enterprise
- Collaborate with leading scientists and engineers at the sponsoring laboratories

Awardee benefits include:

- Stipends ranging from \$45,000 to \$94,500; may be higher based on experience
- Health insurance (including dental and vision), relocation benefits, and a professional travel allowance

For detailed program information, to search Research Opportunities, and to contact prospective Research Adviser(s) visit www.nas.edu/rap.



POSTDOCTORAL RESEARCH FELLOWS

Air Force Science & Technology Fellowship Program

The National Academies of Sciences, Engineering, and Medicine administers **postdoctoral** and **senior fellowship** awards at the U.S. Air Force Research Laboratory (AFRL), the U.S. Air Force Institute of Technology (AFIT), and the U.S. Air Force Academy (USAFA) under the Air Force Science & Technology Fellowship Program (AF STFP).

We are seeking highly qualified candidates who are U.S. citizens and hold, or anticipate earning, a doctorate in a variety of fields of science or engineering.

Application deadline dates (four annual review cycles):

- February 1
- May 1
- August 1
- November 1

Awardees have the opportunity to:

- Conduct independent research in an area compatible with the interests of the Air Force laboratories
- Devote full-time effort to research and publication
- Access the excellent and often unique Air Force research facilities
- Collaborate with leading scientists and engineers

Awardee benefits:

- Base stipend starting at \$76,542; may be higher based on experience
- Health insurance (including dental and vision), relocation benefits, and professional travel allowance

For detailed program information, to search for AFRL, AFIT, and USAFA Research Opportunities, and to contact prospective Research Adviser(s), visit www.nas.edu/afstfp.

THE UNIVERSITY OF CHICAGO

Description

The Biological Sciences Collegiate Division at the University of Chicago is accepting applications for an **Instructional Professor (IP)** (rank commensurate with experience) to be part of the Phoenix STEM Program team. Phoenix STEM is a new program whose goal is to promote the success of historically under-represented and first-generation students in STEM majors at the University of Chicago. The BSCD Phoenix STEM IP will be trained to teach collaborative learning workshops to help students succeed in Biology and Biochemistry courses in the Biology major. Anticipated topics are Cell Biology, Genetics, Developmental Biology, Physiology and Biochemistry. The BSCD Phoenix STEM IP will also work with the Phoenix STEM team to develop resources for Phoenix STEM students and serve as an academic advisor for these students. This position reports to the Phoenix STEM program director and the Master of the Biological Sciences Collegiate Division.

Qualifications

The successful candidate will have a Ph.D. in an area of Biology or Biochemistry and at least 2 years of teaching experience. Candidates with knowledge and experience in inclusion and diversity in STEM are particularly encouraged to apply.

Application Instructions

To apply for this position candidates must submit their application through the University of Chicago's Interfolio jobs board at <https://apply.interfolio.com/110503>, and upload a curriculum vitae, syllabus and teaching evaluations from one-two courses, a one page teaching statement, and the names and contact information for three references. This job will remain posted until filled.

This position will be part of the Service Employees International Union.

Equal Employment Opportunity Statement

We seek a diverse pool of applicants who wish to join an academic community that places the highest value on rigorous inquiry and encourages diverse perspectives, experiences, groups of individuals, and ideas to inform and stimulate intellectual challenge, engagement, and exchange. The University's Statements on Diversity are at <https://provost.uchicago.edu/statements-diversity>.

The University of Chicago is an Affirmative Action/Equal Opportunity/Disabled/Veterans Employer and does not discriminate on the basis of race, color, religion, sex, sexual orientation, gender identity, national or ethnic origin, age, status as an individual with a disability, protected veteran status, genetic information, or other protected classes under the law. For additional information please see the University's Notice of Nondiscrimination.

Job seekers in need of a reasonable accommodation to complete the application process should call 773-834-3988 or email equalopportunity@uchicago.edu with their request.



POSTDOCTORAL TRAINING IN NEUROBIOLOGY OF AGING, ALZHEIMER'S DISEASE AND RELATED NEURODEGENERATIVE DISORDERS

The collaborative and interactive Arizona postdoctoral fellowship program in Neurobiology of Aging, Alzheimer's Disease and Related Disorders that includes University of Arizona, Arizona State University, Barrow Neurological Institute, Translational Genomics Research Institute, Banner Alzheimer's Institute, Banner Sun Health Research Institute, and Mayo Clinic components of the statewide Arizona Alzheimer's Consortium is seeking highly qualified applicants for **positions supported by a National Institutes of Aging training grant**.

Training programs are intended to advance researcher development and studies in Alzheimer's disease, related disorders and non-pathological brain aging. Fellows can capitalize on programs in basic, cognitive, behavioral, clinical, neuropathological, brain imaging and omics research. Mentors have expertise in molecular biology, experimental, and neuropathological research, the study of transgenic and wild type mice, non-human primates, brain imaging, genomics, the computational and statistical analysis of complex data sets, experimental therapeutics, the early detection, diagnosis, treatment and prevention of Alzheimer's disease and related diseases, the development and application of new research methods, and other potential areas of interest. Trainees will benefit from a Professional Development Committee to foster career development, provide opportunities to work and learn across institutions all in an incredible place to live.

This is a U.S. Government funded training grant and is only available to U.S. citizens or Permanent Residents. All training program institutions value an inclusive academic community, which advances innovation and critical thinking. The program encourages applications from diverse candidates including people of color, women, LGBTQIA2S+, veterans, and individuals with disabilities.

Please send a CV, contact information for two references that have agreed to be contacted, and a letter describing your research interests to the program Admissions Director Dr. Elliott Mufson, Professor of Translational Neurosciences at the Barrow Neurological Institute c/o Katelyn.Kildoo@DignityHealth.org.



The University of Konstanz is one of eleven Universities of Excellence in Germany. Since 2007 it has been successful in the German Excellence Initiative and its follow-up programme, the Excellence Strategy.

The *Zukunftskolleg* is an Institute for Advanced Study for early career researchers in the natural sciences, humanities and social sciences. It is an central component of the university's strategy „creative.together“. The *Zukunftskolleg* promotes interdisciplinary discourse between distinguished researchers from Germany and abroad, and provides them with the resources to conduct their research independently and free from administrative constraints. The working language is English.

The *Zukunftskolleg* of the University of Konstanz offers:

One 5-year Research Fellowship at the Zukunftskolleg

(Salary Scale TV-L 14)

to develop and implement individual research projects and build up their own research group.

Fellowships will begin on June 1, 2023.

Reference number 2022/199

One 2-year Postdoctoral Fellowship at the Zukunftskolleg

(Salary Scale TV-L 13)

to develop and implement individual research projects. Conditionally on the submission of an external grant, the position can be extended for an additional year.

Fellowships will begin on May 1, 2023.

Reference number 2022/198



Applications, supporting materials and two letters of reference should be submitted in English by **31 October 2022 11:00 am (Konstanz time) using the Online Application Platform** <https://www.uni-konstanz.de/zukunftskolleg/online-application/>.

Details concerning the application, required documents, and information about the *Zukunftskolleg* are available on our website: <https://www.uni-konstanz.de/zukunftskolleg/>.

By Kaitlin Rasmussen

My life as a photon

Growing up, I asked a lot of questions. Many of them foretold my future in astronomy: Why is the Sun yellow? Why do the constellations look like that? Why does Jupiter have a spot? My parents answered what they could, and bought me books to answer the rest. But my most frequent question, starting when I was about 5 years old, was why am I a girl? And for that, my parents had no answer. In fact, in the 1990s, in the foothills of the Appalachians, no one did. It was my first encounter with a question that has no simple answer.

It faded in and out of my consciousness until middle school, when puberty brought feelings of dismay and disgust. Every day meant performing femininity while feeling increasingly isolated from it.

On the academic front, things weren't much better. In high school, I particularly hated freshman physics and its inflexible rules, which seemed to mirror the society I lived in. The same way we learned to expect a pendulum to swing, a block to slide down a slope, a ball to fall off a cliff, I felt I was expected to go to church, meet a man, marry young, and have kids. This seemingly inescapable trajectory left me depressed and numb to the world.

I went to college because I wanted out. I felt purposeless, hollow, void of meaning—but at the same time, standing at the crossroads to 1000 different futures. Like a particle atop a perfect sphere, I could have fallen in any direction. It was by pure chance that I wandered into a bookstore and saw Stephen Hawking's *The Grand Design* on the front table. I cannot tell you what inspired me to pick up a book on cosmology. But I did, and in a few short minutes I had discovered a doorway into a new kind of physics—the kind of physics that doesn't have all the answers, the kind of physics that disagrees with itself, the kind of physics that is messy and chaotic and, God forbid, *fun*. I changed my major to astrophysics the next week.

Over the following years, I learned about relativity, and how in the right circumstances time itself can slow. I learned about quantum mechanics, where anything can happen. Rules were no longer absolute. Things I had accepted as fact were really just approximations of unknowable truths.

In college, I would also hear the word “transgender” for the first time. I would meet queer folks in loving relationships. It was drastically different from my first brush with queerness—an encounter with a slur on a sign wielded by members of the Westboro Baptist Church, who came to my hometown to



“Being nonbinary means challenging the status quo every day.”

demonstrate when I was 13. At the end of college, I would realize that I myself am bisexual—attracted to my own gender as well as others, just as gravity draws every single thing in the universe to every other thing. It felt natural, like I had found a lower energy state of existence. Yet I still wasn't in my ground state.

That finally happened halfway through graduate school, when I found the label “nonbinary” through friends on Twitter. With its fluidity and disavowal of the traditional two-gender system, nonbinary felt right. It felt like home. It felt like I had spent my whole life trying to solve a chaotic system only to realize there wasn't one answer, but many. It was then I realized that I am a photon—possessing qualities inherent to either side of the binary, but ultimately belonging to neither.

It hasn't always been easy. I lived a bit of a double life for a while, authentic in my internet presence and closeted while I finished my Ph.D. But when I was ready, embracing my identity brought me into an incredible community.

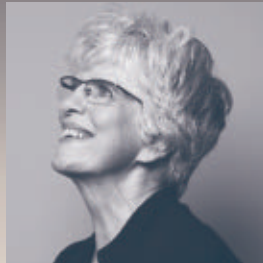
Now, I realize the power of my identity. Being nonbinary means challenging the status quo every day. It means everything can and must be questioned. It means exploring things others take to be fundamental in new ways from new angles. In my everyday life, my gender identity compels me to find unconventional solutions to difficult problems. I turn over unseen stones. I try unorthodox methods. I wrestle with big, fundamental questions. All of these things make me a better scientist.

Physics is always evolving, and gender is, too. When we understand that things are more complex than they appear, we learn. When scientists embrace the complexity of the universe, our science can only improve. ■

Kaitlin Rasmussen is a postdoc at the University of Washington, Seattle, and a member of the International Society of Nonbinary Scientists.

Your Legacy to Science

AN ESTATE GIFT TO THE
AMERICAN ASSOCIATION FOR THE ADVANCEMENT OF SCIENCE



Since 1848, our founding year, the American Association for the Advancement of Science (AAAS) has been deeply committed to advancing science, engineering and innovation around the world for the benefit of all people.

By making AAAS a beneficiary of your will, trust, retirement plan or life insurance policy, you become a member of our 1848 Society, joining Thomas Edison, Alexander Graham Bell and the many distinguished individuals whose vision led to the creation of AAAS and our world-renowned journal, *Science*, so many years ago.

Unlike many of its peers, *Science* is not for-profit. Your estate gift would provide long-term financial stability and durable annual income that will support operations and competitive innovation for years to come. **This support is vital.**

"As a teacher and instructor, I bear responsibility for the younger generations. If you have extra resources, concentrate them on organizations, like AAAS, that are doing work for all."

—Prof. Elisabeth Ervin-Blankenheim, 1848 Society member

If you intend to include AAAS in your estate plans, provide this information to your lawyer or financial adviser:

Legal Name: American Association for the Advancement of Science

Federal Tax ID Number: 53-0196568

Address: 1200 New York Avenue, NW, Washington, DC 20005

If you would like more information on making an estate gift to AAAS, cut out and return the form below or send an email to philanthropy@aaas.org. Additional details are also available online at www.aaas.org/1848Society.

cut here ✂

Yes, I would like more information about joining the AAAS 1848 Society.

PLEASE CONTACT ME AT:

Name: _____

Address: _____

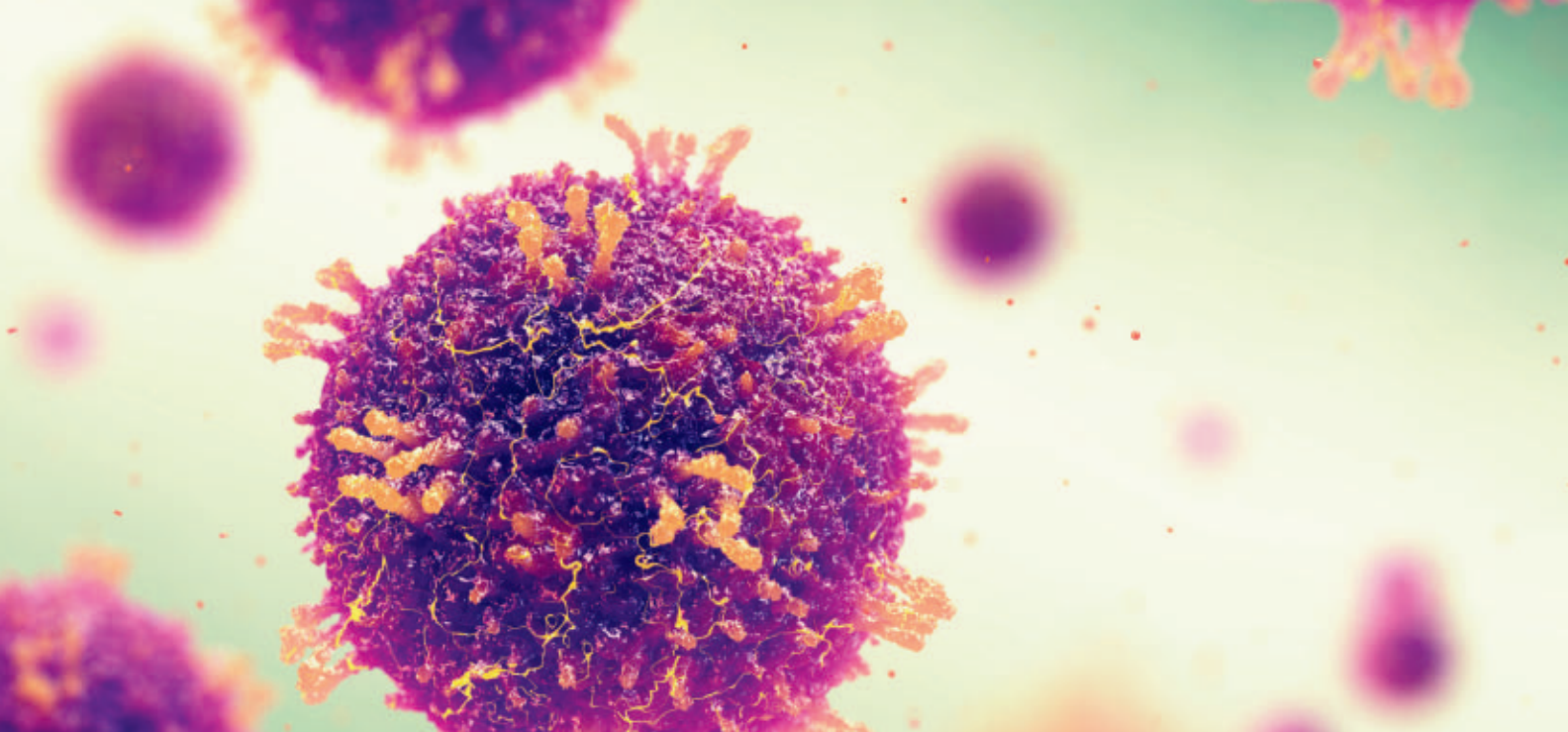
City: _____ State: _____ Zip code: _____ Country: _____

Email: _____ Phone: _____

RETURN THIS FORM TO:

AAAS Office of Philanthropy and Strategic Partnerships • 1200 New York Avenue, NW • Washington, DC 20005 USA





It's time to think differently.

Find out how NEB can support your infectious disease research and development.

Gaining a better understanding of infectious diseases, including their characterization, evolution and transmission, continues to be a priority, both from an R&D standpoint and as a public health issue. The COVID-19 pandemic has demonstrated the need for a wide range of tools to research infectious diseases, and has highlighted the importance of speed and the ability to pivot as new problems arise. This has emphasized the need for innovation and thinking differently about where to access those critical materials, including genomics reagents.

Many scientists know NEB as a trusted reagent supplier to the life science community, but what you may not know is that we also offer a portfolio of products that can be used in infectious disease research, development of diagnostics and therapies, and in epidemiological studies and disease surveillance. In fact, many of our products have supported the development of COVID-19 diagnostics and vaccines, and can also be utilized with other infectious diseases, such as influenza and malaria.



Benefit from almost 50 years of experience in molecular biology & enzymology



Partner with our OEM & Customized Solutions team to find the best solution for your needs



Take advantage of our expanded manufacturing capabilities



Access product formats, such as GMP-grade*, lyophilized, lyo-ready and glycerol-free



Be confident in your product performance with our expanded quality and regulatory systems



Ready to get started? Learn more at www.neb.com/InfectiousDiseases

*GMP-grade" is a branding term NEB uses to describe reagents manufactured at our Rowley, MA facility, where we utilize procedures and process controls to manufacture reagents in compliance with ISO 9001 and ISO 13485 quality management system standards. NEB does not manufacture or sell products known as Active Pharmaceutical Ingredients (APIs), nor do we manufacture products in compliance with all of the Current Good Manufacturing Practice regulations. One or more of these products are covered by patents, trademarks and/or copyrights owned or controlled by New England Biolabs, Inc. For more information, please email us at busdev@neb.com. The use of these products may require you to obtain additional third party intellectual property rights for certain applications. © Copyright 2022, New England Biolabs, Inc.; all rights reserved.



be INSPIRED
drive DISCOVERY
stay GENUINE